Cranfield Institute of Technology
School of Mechanical Engineering

Ph.D. Thesis

S. C. TAN

A Study of Particle Trajectories In A Gas Turbine Intake

Supervisor: Professor R. L. Elder

January 1988

This thesis is submitted for the degree of
Doctor of Philosophy

Abstract

An experimental and theoretical study of the particle trajectories in a gas turbine intake has been presented. A computer model was written to simulate a particle behaviour in flight in a theoretical flow which was assumed to inviscid, irrotational and incompressible. The model is also based on other assumptions which imposes several limitations on the accuracy of the predicted results. These limitations formed the objectives of the experimental investigation of the particle trajectories which was carried out in a 30.0 degree section of an axisymmetric helicopter inertial separator. The separator section was fully instrumented with wall pressure tappings to determine the near-wall flow condition. The flowfield at the central (vertical) plane of the separator was also measured with a two spot laser anemometer. The dust particles used in the tests were the spherical ballotini and irregular quartz particles with diameter ranging from 15.0 to 150.0 microns. These particles were seeded locally into the separator at three initial positions. The restitution ratios for the quartz particle were based on experimental data and the ballotini particle's ratios were based on a simple relation, which was derived by trial and error matching of predicted and experimental results. The particle trajectories, velocities and angles in the separator were measured at several stations using the laser anemometer. The measured results were compared with the predicted values from the model which has been modified to accept both the experimentally measured and inviscid flowfield. The particle shape factor was also included to account for the higher drag on the non-spherical particle. Further modification was also made to include the restitution ratios of the ballotini particle. Good agreement was found between measured and predicted particle trajectories, velocities and angles for both the spherical and non-spherical particle. The trajectories of the large particles

(>100.0um) are 'ballistic' in nature which are governed by the inertia forces.The trajectories of the smaller particles are influenced by the both aerodynamic and inertia forces.

Acknowledgement

I would like to express my sincere gratitude to Prof. R.L. Elder for his invaluable support and advice through the years. Credit is also due to Mr.R. Thorn and Mr.D.L.Mann for their undivided support. Special thanks to Mr.B.Scully who has always been in attendance to ensure the smooth running of the rig. Lastly, but not leastly, I gratefully acknowledgement the sponsorship of Rolls-Royce, without which this work would not have been possible.

CONTENTS

Page

Page

Appendices

A-1 Formulation of the Particle Equations Of Motion

A-2 Mathematical Model of the Particle Equations of Motion

A-3 Solution of the Particle Equations of Motion using the Kutta-Fehlberg Fifth Order Method

A-4 Polynomial Expansion of the Interpolation Functions for a Three dimensional Element

A-5 Formulation of the Jacobian Matrix of Transformation

A-6 Transformation of a Point defined in the Global Coordinate to the Local Coordinate.

A-7 Computation of the Unit Vector Normal to a Wall Surface.

FIGURES

Tables

Plates

Notations

A	Surface area
C_D	Drag coefficient
$c_k, \hat{c}_k$	Constant coefficients
D_p	Particle diameter
D	Drag force
D_R, D_Θ, D_Z	Component drag force in the Cylindrical coordinate system
E	Local truncation error
h	Step size
h_I, h_E, h_S	Heat transfer coefficient at the inlet, engine and scavenge section of a gas turbine separator
$\tilde{i}, \tilde{j}, \tilde{k}$	Unit vectors in the Cartesian coordinate system
$[J]$	Jacobian matrix of transformation
m_p	Particle mass
m_I, m_E, m_S	Massflow at the inlet, engine and scavenge section of a gas turbine separator
N_i	Shape function as applied in finite element interpolation function
$\tilde{N}, \tilde{T}$	Unit vector normal and tangent to a surface

P	Pressure
r_p, Θ_p, z_p	Particle's cylindrical coordinate
Re	Reynold Number
R,Θ,K	Unit vectors in the Cylindrical coordinate system
u,v,w	Component velocities in the Cartesian coordinate system
V_g, V_p	Gas and particle velocity vectors
$V_{rg}, V_{\Theta g}, V_{zg}$	Component gas velocities in the Cylindrical coordinate system
$V_{rp}, V_{\Theta p}, V_{zg}$	Component particle velocities in the Cylindrical coordinate system
V_{P1}, V_{P2}	Particle impact and rebound velocity vectors
V_{PN1}, V_{PN2}	Normal impact and rebound particle velocities
V_{PT1}, V_{PT2}	Tangential impact and rebound particle velocities
z	Shape factor
C_f	Correction factor

CHAPTER 1

INTRODUCTION

Modern gas turbine engines, especially helicopter engines, have to operate in hazardous environments such as the desert or an unprepared landing field where the atmosphere is heavily laden with dust particles. These dust particles, when ingested can seriously deteriorate engine performance by erosion. Helicopter engines, with a nominal rating of 1000 hours, have been known to reduce to 8 hours when flying unprotected in desert conditions. Most of the ingested dust particles are found to be between 0 to 1000 microns (um) in diameter. Small dust particles, less than 5 microns, do not erode but tend to deposit on engine components hence reducing their performances. Larger particles, between 5 and 200 microns (usually known as dust), are the major cause of erosion damage in gas turbine engines of today. The advent of new and advanced compressor blades are more prone to erosion damage due to increases in tip speed, reduced blade thickness and close running clearance. Particles greater than 200 microns, classified as foreign objects (FO), are large enough individually to cause damage to engine components.

The problem of erosion by dust particles in gas turbine engines has long been recognised by aircraft manufacturers. Steps have been taken to eradicate this problem by introducing intake filters such barrier filters and vortex tube panel filters. Filters have both their advantages and 'pitfalls' particularly relatively large pressure drops. Barrier filters, for example, require frequent cleaning and do have a tendency to dislodge dust particles due to engine vibration. Vortex tube panels, as shown in Figure 1, are efficient separator but they require large frontal area and installed volume. They are also highly dependent on their positioning on the airframe [Ref.1], for example, rotor

downwash effects can cause scavenge flow reversal. Vortex tube panel filters are still in service as an option for certain helicopter types. Inertial separators, on the other hand, offer the best compromise for engine protection due to their low weight, cost, convenient anti-icing capability while maintaining compactness. The modern inertial separator consists of a hub, shroud and a flow splitter as shown in Figure 2 and 3. The whole arrangement is similar to that of a bi-furcated duct where clean air enters the engine inlet and contaminated air enters the scavenge duct.

There are two main types of inertial separators, they being;

i) **swirl type configuration (Figure 2)**

This type of separator uses swirl vanes to introduce a centrifugal force field to the dust particles causing them to migrate to the outer wall or shroud, and into the scavenge duct. Application of this separator is found in the G.E. T700 helicopter engine. The main disadvantages of this system are the complication and necessity to de-swirl the flow before it enters the engine. The swirl vanes themselves can incur a pressure loss hence reducing compressor performance. The scavenge flow in this system is achieved by an auxiliary fan.

ii) **vaneless type configuration (Figure 3)**

This type of separator is relatively simpler than the swirl type separator without the need for the swirl vanes which induces performance penalties. It has a characteristic shape, contoured to deflect dust particles into the scavenge duct. The hub has a 'hump-shaped' wall and positioned in such a way as to deflect particles to the shroud wall and into the scavenge. Diagrammatic illustration of an ideal

operation of an inertial separator is shown in Figure 4. In this system, an ejector is used to achieve a scavenge flow of about 20 percent of the main engine flow, which is usually between 10 to 12 lb/s.

It is known that very small dust particles, less than 5 microns in diameter, tend to follow flow streamlines, whereas larger particles deviate from them due to their higher inertia. Such behaviour of the very small particles has found useful application in the field of laser anemometry techniques. They are used as seeding in high temperature flows where conventional liquid will vaporises. The 'ballistic' nature of the larger particles, greater than 50 microns, is the main reason behind the development of inertial separators. The trajectories of the dust particles between 5 and 50 microns are influenced by both the 'ballistic' and aerodynamic forces.

The performance of an inertial separator is determined by its separation efficiency tested under standard conditions which would simulate a dusty environment. Standard man-made dusts such as 'MIL-SPEC' sand (between 0 to 1000 microns) and AC coarse dust (between 0 to 200 microns), are used by most engine manufacturers in a dust test facility. Diagrammatic illustration of a standard dust test facility is shown in Figure 5. The separation efficiency is defined as,

$$S_{eff} = \frac{\text{mass of dust separated}}{\text{mass of dust at inlet}} \qquad \text{(as defined in U.S.A.)}$$

or,

$$S_{eff} = 1 - \frac{C_e}{C_i} = 1 - \frac{(1+S)W_e}{W_e + W_s} \qquad \text{(as defined in U.K.)}$$

where

C_e = dust concentration at the engine duct (compressor)
C_i = dust concentration at the inlet
W_e = weight of dust at the engine duct (compressor)
W_s = weight of dust at the scavenge duct
S = flow scavenge (bypass) ratio

Typical quoted separation efficiencies for AC coarse dust are between 80-85 percent, for example, the G.E.T700 helicopter engine was quoted at 85 percent [Ref.2].

Optimising the design of an inertial separator by experimentation only can be a costly exercise without first having obtained some predictive results. Hence, most engine manufacturers have developed three-dimensional particle trajectory programs [Ref.3, Ref.4, Ref.5, Ref.6] as a design tool to assess the performance of any new separator. Most prediction models compute particles trajectories by solving the particle equations of motion in a pre-defined flowfield. The computation is continued after a particle impact with a wall by applying a set of empirical relations which relate particle rebound characteristics with the initial condition. These empirical relations, also known as restitution ratios, are applicable only for a particular combination of target and dust particle material. Using the prediction model, a graph of predicted separation efficiencies versus particle sizes, as shown in Figure 86, can be obtained for a range of particle sizes. The overall separation efficiency for, say, AC coarse dust, is then calculated by integrating under the predicted separation curve between 1 and 200 microns.

Various prediction models are reported which appear to give reasonable agreement with experimental results. It is, however, necessary to validate these models as engine manufacturers become increasingly dependent on them as a design tool. Vittal [Ref.4] and Breitman [Ref.5] relied only on measured separation efficiencies to validate their pre-

diction models. As a result, an over-prediction of the separation efficiencies was found in the model which was then rectified by applying an experimentally obtained 'shape factor ' to the particle equations of motion. Application of this 'shape factor' was justified by the fact that non-spherical particles incur a higher drag than spherical particles which were initially assumed in the prediction models.

In this thesis, a model capable of predicting particle trajectories and separation efficiencies is developed together with an experimental programme designed to investigate particle trajectories. This prediction model calculates particle trajectory in a three dimensional gas turbine separator which includes the influence of the radial and tangential variation in the flowfield as well as the shape of the geometry. This study also examines factors which influence the particle trajectories. The experimental results are compared with the predicted values. A range of narrow bandwidth dust sizes, between 15 and 150 microns, were introduced into the flow at pre-determined locations. Subsequently measurements were made by traversing a laser '2-spots' anemometer at several stations giving an overall picture of their trajectories. The trajectory, velocity and angle at each station was then measured. Separation efficiency for each particle size is determined by taking the ratio of the amount of separated dust particles to the total amount of dust fed at the separator inlet. Comparisons were made between measured and predicted particle trajectories, absolute velocities and angles to reveal any discrepancies in the prediction model.

This thesis has been organised into the following chapters;

Chapter 2 presents the formulation and solution of the particle equations of motion. It also presents the three-dimensional interpolation for the flow

velocities. It also discusses the limitations and assumptions made in the prediction model.

Chapter 3 presents the initial conditions used in the prediction model to simulate particle trajectories in a gas turbine separator. It also reviews the assumptions made earlier and identifies the limitations as applied in this particular test separator.

Chapter 4 explains the experimental techniques employed in the measurement of the particle trajectories (absolute velocities and angles). Methods used in recording separation efficiencies are also presented. It also includes a detailed discussion of the experimental results.

Chapter 5 presents the experimental results and the comparisons made with predicted values calculated from the particle trajectory computer model. A comprehensive discussion of the results is also included.

Chapter 6 draws conclusions based upon the experimental results and comparisons made earlier and, recommends areas in the prediction model which could be improved to give a better prediction.

Chapter 2

Particle Trajectory Prediction Model

2.1 Introduction

The particle equations of motion were derived in cylindrical polar coordinates relative to the frame fixed in a gas turbine separator. In a gas-particle flow, the forces acting on a single, spherical particle are buoyancy, gravitational,kinematic and drag forces. For a particle with density of about 3 orders of magnitude (as was in the present studies), most of these forces are small compared to the drag force [Rudinger,Ref.31, Hinze,Ref.32]. Hence the drag force is considered as the only force of interaction between the particle and gas flow in the formulation of the particle equations of motion. These equations are then solved numerically using a Kutta-Felhberg method in a pre-defined flowfield. The inviscid, irrotational, incompressible flowfield was computed on a finite element mesh discretized in a gas turbine separator. The component flow velocities needed in the particle equations of motion were interpolated in this finite element mesh. An interpolation technique based on a finite element polynomial function was used to calculate the component flow velocities in each element or sub-domain. The particle trajectory computation after an impaction with a solid wall was continued by applying a set of empirical relations, known as the restitution ratios, which relate the particle rebound characteristics to their initial conditions. A description of the computational tasks and assumptions made in the prediction model is also presented.

2.2 Formulation of the Particle Equations of Motion

The behaviour of the flow around a spherical particle over different flow regimes has been well documented and studied by many researchers such as Massey [Ref.7], Lunnon [Ref.8], Winny [Ref.9], Stokes [Ref.10] and many others. The complexity of the problem associated with flow resistance makes it difficult to derive a simple equation which relates this resistance with the different flow regimes occurring around a sphere. However, by ignoring the inertia forces and for no body forces, the Navier-Stokes equations for a spherical particle in a steady, slow moving incompressible gas flow can be reduced to;

$$\text{GRAD } P = \mu_g \nabla^2(\tilde{V}_g) \qquad (2\text{-}1)$$

which yields the following expression for the drag force;

$$\tilde{D} = 3\Pi\mu_g D_p |\tilde{V}_{g\infty}| \qquad (2\text{-}2)$$

where

$$\tilde{V}_{g\infty} = (\tilde{V}_g - \tilde{V}_p)$$

Detail analysis of this formulation is found in Appendix A-1. The drag equation (2-2) is, however, valid for only small Reynold Number flows. For higher Reynold number flows, a correction factor is included in the drag equation. This factor, estimated from experimental results, has a different form depending on the flow regimes. Hence the drag equation (2-2) becomes;

$$\tilde{D} = 3\Pi\mu_g D_p(\tilde{V}_g - \tilde{V}_p)g(Re) \qquad (2\text{-}3)$$

where

$$g(Re) = C_D Re/24$$

and C_D is the drag coefficient for a spherical particle.

2.2.1 Drag Coefficient for Spherical Particle

The complete omission of the inertia terms resulted in the so called 'Creeping Motion' or Stokes equation [Happel & Brenner, Ref.11]. It also lead to a simplified linear partial differential equation which was used by Stokes [Ref.10] to solve for the motion of a sphere in a slow moving flow, i.e.

$$\tilde{D} = 3\Pi\mu_g D_p(\tilde{V}_g - \tilde{V}_p) \qquad (2\text{-}4)$$

Comparing equation (2-4) with (2-3) gives

$$C_D = 24/Re \qquad 0 < Re < 0.1 \qquad (2\text{-}5)$$

where

$$Re=(\rho_g D_p|(\tilde{V}_g - \tilde{V}_p)|)/\mu_g$$

Stokes equation is, however, valid for flow with Reynold number less than or equal to 0.1. Later Oseen [Ref.12, Boothroyd, Ref.13] took into account the inertia term and considered them only in that region of flow around the sphere where the velocity was approaching free stream value. The drag force equation on the sphere was found to be;

$$\tilde{D} = 3\Pi\mu_g D_p(\tilde{V}_g - \tilde{V}_p)[\ 1 + 3(Re)/16 + O(Re^2)\ ] \qquad (2\text{-}6)$$

Again, comparing this equation with (2-3) gives;

$$C_D = [\ 24(1 + 3(Re)/16)\ ]/Re \qquad 0.1 < Re < 1.0 \qquad (2\text{-}7)$$

This drag coefficient is valid for flow with Reynold number between 0.1 and 1.0. In higher Reynold number flow of up to 2000, Schlicthing [Ref.14] found from experimental that the drag coefficient was;

$$C_D = 21.9416\ Re^{-0.718} + 0.3240 \qquad 1.0 < Re < 2000 \qquad (2\text{-}8)$$

For Reynold number flow greater than 2000, for the practical interest of the present analysis, the drag coefficient is given as;

$$C_D = 0.4 \qquad Re > 2000 \qquad (2\text{-}9)$$

Theoretical investigation by Morsi and Alexander [Ref.15] found an expression for the drag coefficient which closely approximates the standard experimental drag-Reynold number relationship for spherical particle. This expression is valid for Stokes flow (Re <0.1) as well as Reynold number flow of up to 50000.The full drag coefficient from Morsi and Alexander, Chuen-Yen Chow, and Clift et al for a spherical particle in different flow regimes is found in Table I. Preliminary comparisons in the predicted results calculated using the drag data (from the above authors)show little difference hence the drag coefficient from Chuen-Yen Chow [Ref. 33]was chosen in the present study due to it's simpler form.

However, the above drag data is not applicable for non-spherical particles. Duffy [Ref.23] recognised this problem and sought to apply a shape factor to the particle equations of motion in order to give better agreement with test results. Duffy stated that this shape factor takes into account the drag on non-spherical particles and was empirically derived based on test results. The shape factor was defined as;

$$Z = \frac{\text{True Volume of non-spherical particle}}{\text{Equivalent Diameter of spherical particle}}$$

In the present study, this shape factor had been included in the prediction model when simulating trajectories of non-spherical particles. Further discussion of the shape factor can be found in Section 5.2.

2.2.2 Final Form of the Particle Equations of Motion

The drag equation given by (2-3) can be written to give;

$$\tilde{D} = \frac{\Pi D_p^2 \rho_g C_D (\tilde{v}_g - \tilde{v}_p)|(\tilde{v}_g - \tilde{v}_p)|}{8} \qquad (2\text{-}10)$$

since

$$Re = \frac{\rho_g D_p |(\tilde{v}_g - \tilde{v}_p)|}{\mu_g}$$

and,

$$g(Re) = C_D Re/24$$

Assuming that drag force is the only force acting on a single particle, the component drag force, as shown by the force diagram in Figure 6, can be resolved in a cylindrical polar coordinate system. Applying the 'Right Hand Rule' and resolving the forces in the axes direction gives;

$$m_p \ddot{r}_p - m_p r_p \dot{\Theta}_p^2 - D_R = 0$$

$$m_p r_p \ddot{\Theta}_p + 2 m_p \dot{r}_p \dot{\Theta}_p - D_\Theta = 0 \qquad (2\text{-}11)$$

$$m_p \ddot{z}_p - D_z = 0$$

where

$$\tilde{D} = D_R \tilde{R} + D_\Theta \tilde{\Theta} + D_Z \tilde{K}$$

Detail derivation of equation (2-11) is found in Appendix A-2. Resolving equation (2-10) into its components and substituting into equation (2-11) gives the final form of the particle equations of motion as follow;

$$\ddot{r}_p = G(V_{rg} - \frac{\partial r}{\partial t}p) + r_p \dot{\Theta}_p^2 \qquad (2\text{-}12)$$

$$r_p \ddot{\Theta}_p = G(V_{\Theta g} - r_p \frac{\partial r}{\partial t}p) - 2\dot{r}_p \dot{\Theta}_p \qquad (2\text{-}13)$$

$$\ddot{z}_p = G(V_{zg} - \frac{\partial z}{\partial t}p) \qquad (2\text{-}14)$$

where

$$m_p = \frac{4}{3}\Pi r_p^3 \rho_p$$

and,

$$G = \frac{3\rho_g C_D}{4\rho_p D_p} |(\tilde{v}_g - \tilde{v}_p)|$$

The centrifugal and coriolis acceleration terms are represented by the last terms on the right hand side of (2-12) and (2-13) respectively. The force of interaction between the two phases, G, per unit mass of particle, is dependent on the relative velocity between the particle and gas flow as well as particle size and shape. The drag coefficient, C_D, is dependent on the Reynold number which is

also based on the relative velocity between the particle and gas flow.

The particle equations of motion (2-12) to (2-14) can then be solved numerically to give the particle trajectory, velocity and trajectory angle. The particle trajectory after an impact with a solid wall depends on an important parameter called the restitution ratio, without which the particle rebound velocity and angle needed for continued computation cannot be obtained.

2.2.3 Particle Restitution Ratios

The continued computation of the particle trajectory after an impact with a solid wall is made possible using a set of empirical relations known as restitution ratios. These restitution relations provide the particle rebound characteristics as a function of its impact conditions. The reflection of a particle from a solid wall is, to some extent, a random process due to the irregular shape of the particle. Extensive experimental measurement were carried out by Tabakoff [Ref.16, Ref.17] and Grant [Ref.18] using high speed photography. High speed movies were also used to record the impact phenomenon as it allowed a large amount of data to be collected at the same time under the same flow condition.

Since rebound characteristics of particles are often irregular they are best described in a statistical sense requiring an extensive and lengthy analysis. More recently, laser velocimetry has become more common [Ref.20, Ref.21] due to its accuracy and ability to handle large amount of statistical data. Empirical relations were obtained by curve fitting experimental data as shown in Figure 8.1 to 8.8. The difficulties in forming accurate empirical relations is mainly due to the broad distribution in the measured reflected angles and velocities, as shown in Figure 8.1 to

8.4. Most prediction models [Ref.3, 4, 5], depend on these experimentally determined restitution ratios to compute particle trajectory after an impaction with a solid wall. Figure 8.1 to 8.4 shows that inaccuracies might easily have occurred in the curve-fitting routines due to the broad distribution in the rebound characteristics of the dust particles. Furthermore, this experimental data was recorded for a limited range of particle sizes, particle approach velocities and angles of attack. For example, the vast majority of the work by Tabakoff [Ref.16, 17] was carried out using mainly 200 microns dust particles whereas the range of interest lies between 10 to 250 microns. Breitman [Ref.5] found that test results revealed a discrepancy with analysis based on the restitution ratios from Tabakoff's data for large particles where bounce is the dominant mechanism. More recently, Armstrong [Ref.22] discovered that the restitution ratios obtained by impacting a solid target in a long tunnel [Tabakoff, Ref.16] reflect both the flowfield effect as well as the impingement phenomena which is hard to distinguish. As a result, the particles reflected from a stationary target were curved rather than straight, which would not show up clearly in double flash photographic technique. This technique was used in the early attempts to measure the restitution ratios which are still in use today. The difficulties in modelling the rebound characteristic accurately are reflected in the over- or underprediction of the separating efficiencies [Ref.3], by as much as 10 percent in some cases.

In the present thesis, the rebound characteristics used in the trajectory prediction model are based on Tabakoff's work. They are applicable to non-spherical particles, specifically quartz, impacting various target materials (2024 aluminium alloy, titanium alloy and stainless steel). These are reviewed in Table II. The restitution ratios for the spherical ballotini particle were obtained by trial and error matching the prediction with the measured results.

2.3 Methods of Solution

2.3.1 Solution of the Particle Equations of Motion using Kutta-Felhberg Fifth Order Method

The particle equations of motion were derived earlier in Section 2.2, they being;

$$\ddot{r}_p = G(V_{rg} - \frac{\partial r}{\partial t}p) + r_p\dot{\Theta}_p^2$$

$$r_p\ddot{\Theta}_p = G(V_{\Theta g} - r_p\frac{\partial r}{\partial t}p) - 2\dot{r}_p\dot{\Theta}_p \qquad (2\text{-}15)$$

$$\ddot{z}_p = G(V_{zg} - \frac{\partial z}{\partial t}p)$$

where

$$G = \frac{3\rho_g C_D}{4\rho_p D_p} |(\tilde{V}_g - \tilde{V}_p)|$$

$$|(\tilde{V}_g - \tilde{V}_p)| = [(V_{rg} - V_{rp})^2 + (V_{\Theta g} - V_{\Theta p})^2 + (V_{zg} - V_{zp})^2]^{0.5}$$

Ledermann [Ref.24] gives the Kutta-Felhberg Fifth order method in the form of ;

$$Y_1 = Y_0 + h\sum_{k=1}^{6} c_k f_k + O(h^6) \qquad (2\text{-}16)$$

and,

$$\hat{Y}_1 = Y_0 + h\sum_{k=1}^{8} \hat{c}_k f_k + O(h^7) \qquad (2\text{-}17)$$

where h is the step size used in the numerical method and coefficient c_k, $\hat{c}_k$ are the weighting coefficients which can

be found in Table III. The function f_k is given as;

$$f_k = f(x_0 + \alpha_k h, y_0 + h \sum_{\lambda=1}^{k} \beta_{k\lambda} f_\lambda) \qquad (2\text{-}18)$$

The coefficients α_k, $\beta_{k\lambda}$ are also found in Table III. The estimation of the leading truncation error term at every step in the Kutta-Felhberg technique involved calculating two approximations of the solution at the next point y_1. The difference between the two values gives the leading term in the local truncation error as;

$$E = h \sum_{k=1}^{6} [(c_k - \hat{c}_k) f_k + h(c_7 f_7 + c_8 f_8)]$$

and in simpler form;

$$E = [5h (f_1 + f_6 - f_7 - f_8)]/66 \qquad (2\text{-}19)$$

Equations (2-15) can be reduced to the first order differential form as follow;

$$\frac{\partial r_p}{\partial t} = V_{rp}, \quad \frac{\partial V_{rp}}{\partial t} = G(V_{rg} - V_{rp}) + \frac{V_{\Theta p}^2}{r_p}$$

$$r_p \frac{\partial_{\Theta p}}{\partial t} = V_{\Theta p}, \quad \frac{\partial V_{\Theta p}}{\partial t} = G(V_{\Theta g} - V_{\Theta p}) - \frac{2 V_{rp} V_{\Theta p}}{r_p} \qquad (2\text{-}20)$$

$$\frac{\partial z_p}{\partial t} = V_{zp}, \quad \frac{\partial V_{rp}}{\partial t} = G(V_{zg} - V_{zp})$$

Hence, six functions can be obtained, they being;

$$F_1 = V_{rp}, \quad F_4 = G(V_{rg} - V_{rp}) + \frac{V_{\Theta p}^2}{r_p}$$

$$F_2 = V_{\Theta p}', \quad F_5 = G(V_{\Theta g} - V_{\Theta p}) - \frac{2V_{rp}V_{\Theta p}}{r_p} \qquad (2\text{-}21)$$

$$F_3 = V_{zp}', \quad F_6 = G(V_{zg} - V_{zp})$$

Equation(2-21) has the general form;

$$F_j = F_j(r_p, V_{rp}, V_{\Theta p}, V_{zp}) \qquad j = 1,6 \qquad (2\text{-}22)$$

where F_j is time independent, hence in form of equation (2-16) to (2-18) gives;

$$Y_{n+1i} = Y_{ni} + h \sum_{k=1}^{6} c_k H_{jk} + O(h^6) \qquad (2\text{-}23)$$

$$\hat{Y}_{n+1i} = Y_{ni} + h \sum_{k=1}^{8} \hat{c}_k H_{jk} + O(h^7) \qquad (2\text{-}24)$$

and

$$H_{jk} = F_j(Y_i + h \sum_{\lambda=1}^{k} \beta_{k\lambda} H_{j\lambda}) \qquad k = 2,8 \qquad (2\text{-}25)$$

and the first term k=1

$$H_{j1} = F_j(Y_i) \qquad i = 1,4$$

where

$$Y_1 = r_p, \; Y_2 = V_{rp}, \; Y_3 = V_{\Theta p}, \; Y_4 = V_{zp}$$

Hence the local error gives;

$$E_j = [5h(H_{j1} + H_{j6} - H_{j7} - H_{j8})]/66 \qquad j=1,6 \qquad (2\text{-}26)$$

By defining an upper and lower limit to control the local truncation error, the iterative step size can be adjusted to give acceptable accuracy. The main advantage of this numerical method is the ability to optimise computational speed, by adjusting the computational error, when simulating a large amount of ingested dust particles. Detail analysis of the solution of the particle equations of motion using the Kutta-Felhberg method can be found in Appendix A-3.

2.3.2 Flowfield Computation in a 3-D Gas Turbine Separator

A typical gas turbine separator, as illustrated in Figure 3, has a highly contoured hub and shroud wall surfaces which need to be accurately modelled with some form of grid-fitting or mesh generating routines. It must be versatile enough to handle a complex region such as the flow splitter which is commonplace in inertial separators. In the swirl type inertial separator, the swirl and de-swirl vane blades would also need to be accurately represented. The main reason for this is that reflected particle trajectories depend on the accurate modelling of wall surfaces. Several techniques do exist which could cope with such strict requirements, for example, body-fitted coordinate or finite element methods. Meshes generated for such methods also have the advantage of being able to be used with many existing flowfield computation methods. Shieh [Ref.25] and Vittal [Ref.4] used an inviscid, irrotational flow model constructed with the stream function formulation for an arbitrary coordinate system. The governing equations for an axisymmetric flow were transformed to an arbitrary curvilinear coordinate and applied to a body-fitted coordinate system. Breitman [Ref.5] et. al.,however,computes

inviscid flowfield using a finite element through flow program.

In the present thesis, an inviscid, irrotational and incompressible flow computational technique was used to calculate the flowfield in a finite element mesh. A vaneless inertial gas turbine separator was discretized using a finite element mesh generator to give a mesh of elements or sub-domain (Figure 9). The mesh was used to calculate the flowfield using a heat transfer program by treating the nodal temperature as a potential function value. Since the heat transfer program was based on the same assumptions as an inviscid, irrotational, incompressible flow, by means of a heat/flow analogy, the flowfield can be computed in a finite element mesh (both the heat transfer program and mesh generator were developed in-house by Rolls-Royce). The analogy described by Mann [Ref.26] was as follows;

$$\text{Heat flow} \quad \Delta H = hA\Delta T$$

$$\text{Volume flow} \quad \Delta V = v_g A$$

By analogy,

$$\Delta H = \Delta V$$

Hence,

$$hA\Delta T = v_g A$$

Therefore,

$$h\Delta T = v_g \qquad (2\text{-}27)$$

The inflow and outflow velocities of the separator can be used as a first approximation in applying the equation (2-27) to the finite element mesh. Hence,

Inlet inflow velocity $V_{Inlet} = m_I/(\rho A_I)$

Engine outflow velocity $V_{Eng} = m_E/(\rho A_E)$

Scavenge outflow velocity $V_{Scav} = m_S/(\rho A_S)$

The boundary conditions required are as follows;

i) assume an initial temperature T_i at all the node points in the finite element mesh

ii) assume an initial temperature at those nodes which form the inflow and outflow boundary planes such that $(T_{plane}-T_i)$ is numerically large

iii) the heat transfer coefficients at the inflow and outflow boundary are derived (as a first approximation) as follow;

$$h_I = v_I/(\Delta T_{I-i})$$

$$= m_I/[\rho A_I(T_I - T_i)]$$

$$h_E = m_E/[\rho A_E(T_E - T_i)]$$

$$h_S = m_S/[\rho A_S(T_S - T_i)]$$

An iterative technique is employed to achieve the required inlet and outlet mass flow of the separator. Using the analogy, the nodal temperatures can be treated as nodal potential function values. A contour plot of the computed flowfield, based on the potential function, is shown in Figure 10.

2.3.3 Three Dimensional Interpolation for Flow Velocities using Finite Element Method

In Section 2.3.2, finite elements were used as the sub-domain in the computation of the flowfield which was based on the heat/flow analogy. The computed result was a set of potential function values at a set of node points. The component flow velocities, needed in the solution of the particle equations of motion, are computed from the finite element grid. Each element or sub-domain consists of a set of potential functions from which the flow velocity can be interpolated. The interpolation method is based in the classical variational method or Galerkin-weighted residual methods. The general interpolation function given by Chung [Ref.27, Connors, Ref.28, Livesley, Ref.29] over each element or sub-domain has the form,

$$U = a_0 + a_1x + a_2x^2 + a_3x^3 + ... \qquad (2\text{-}28)$$

where U is any variable value.

In general, the interpolation function are polynomials of various degrees but they may alternatively be given by the product of polynomials with trigonometric or exponential functions. Equation (2-28) represent a polynomial expansion approximated over a one dimensional element with a nodal value U. In a three dimensional element with 20 nodes (Figure 11), which was used in the present work, a higher order interpolation function with quadratic and some cubic variation in any variable nodal values is needed. They have the form;

$$U = a_1 + a_2S_1 + a_3S_2 + a_4S_3 + a_5S_1^2 + a_6S_2^2 + a_7S_3^2$$
$$+ a_8S_1S_2 + a_9S_1S_3 + a_{10}S_2S_3 + a_{11}S_1^2S_2 + a_{12}S_1^2S_3$$

$$+ a_{13}S_2{}^2S_1 + a_{14}S_2{}^2S_3 + a_{15}S_3{}^2S_1 + a_{16}S_3{}^2S_2$$
$$+ a_{17}S_1S_2S_3 + a_{18}S_1{}^2S_2S_3 + a_{19}S_2{}^2S_1S_3$$
$$+ a_{20}S_3{}^2S_1S_2 \qquad (2\text{-}29)$$

where U is any nodal function value in an element or sub-domain and S_1, S_2, S_3 are local coordinate.

The basic idea of the finite element technique lies in its ability to transform an element mesh or sub-domain created in the global coordinate axis system [Figure 9, 11] into a unit cubic element [Figure 12] in a local coordinate axis system with the origin at the centroid of the element. In a three dimensional cubic element [Figure 11, 12], the local coordinates can be defined as ξ, η, ζ which correspond to S_1, S_2, S_3 respectively in equation (2-29). The polynomial equation (2-29) can also be expressed as follow;

$$U = \sum_{i=1}^{20} N_i U_i \qquad (2\text{-}30)$$

where $N_i(\xi, \eta, \zeta)$ is the shape function. This shape function [Connor and Brenner, Ref.28] has a unit value at node i, and zero at all other nodes. It can be written in a different form depending on the location of the local origin and the arrangement of the node points. The shape functions for the 20 nodes element (Figure 11) used in the present work has the form;

at corner nodes (Figure 11)

where i=1, 3, 5, 7, 13, 15, 17, 19

$$N_i = [(1+\xi_i\xi)(1+\eta_i\eta)(1+\zeta_i\zeta)(\xi_i\xi+\eta_i\eta+\zeta_i\zeta-2)]/8 \qquad (2\text{-}31)$$

at midside nodes where i= 2, 6, 18, 14

$$N_i = [(1-\xi^2)(1+\eta_i\eta)(1+\zeta_i\zeta)]/4 \qquad (2\text{-}32)$$

at midside nodes where i= 9, 10, 11, 12

$$N_i = [(1-\zeta^2)(1+\eta_i\eta)(1+\xi_i\xi)]/4 \qquad (2\text{-}33)$$

at midside nodes where i= 4, 8, 16, 20

$$N_i = [(1-\eta^2)(1+\zeta_i\zeta)(1+\xi_i\xi)]/4 \qquad (2\text{-}34)$$

where ξ_i, η_i, ζ_i has a value of 1, 0 or -1 (TABLE IV) w.r.t. the local coordinate axes system. The complete expansion of the shape functions (2-31) to (2-34) is found in Appendix A-4.

The independent coefficients a_1 to a_{20} in equation (2-29) represent translation and rotation type terms that can be related to equation (2-30) as follow;

equation (2-29) can be rewritten in matrix form to gives;

$$\begin{bmatrix} u_1 \\ u_2 \\ \cdots \\ u_{20} \end{bmatrix} = \begin{bmatrix} 1, \xi_1, \eta_1, \zeta_1 \cdots\cdots\cdots\cdots \zeta_1^2 \xi_1 \eta_1 \\ 1, \xi_2, \eta_2, \zeta_2 \cdots\cdots\cdots\cdots \zeta_2^2 \xi_2 \eta_2 \\ \cdots\cdots\cdots\cdots\cdots\cdots\cdots\cdots\cdots\cdots \\ 1, \xi_{20}, \eta_{20}, \zeta_{20} \cdots\cdots \zeta_{20}^2 \xi_{20} \eta_{20} \end{bmatrix} \begin{bmatrix} a_1 \\ a_2 \\ \cdots \\ a_{20} \end{bmatrix} \qquad (2\text{-}35)$$

or,

$$[U]_i = [C][a]_i \qquad i=1,20 \qquad (2\text{-}36)$$

The matrix [U], [C] are known function values from the

nodes in an element and matrix [a] are independent coefficients which is obtained as follow;

$$[a]_i = [C]^{-1}[U]_i \qquad (2\text{-}37)$$

The required function variable Up at any position $P(\xi_p, \eta_p, \zeta_p)$ w.r.t. the local coordinate system can be interpolated by substituting equation (2-37) into equation (2-29) as follow;

$$U_p = [1, \xi_p, \eta_p, \zeta_p \ldots\ldots\ldots\ldots \zeta_p{}^2 \xi_p \eta_p] \begin{bmatrix} a_1 \\ a_2 \\ \ldots \\ a_{20} \end{bmatrix}$$

or,

$$U_p = [C_p][a]_i \qquad i = 1,20 \qquad (2\text{-}38)$$

substituting equation (2-37) into equation (2-38) gives,

$$U_p = [C_p][C]^{-1}[U]_i \qquad i = 1,20 \qquad (2\text{-}39)$$

Substituting the local coordinate of the position $P(\xi_p, \eta_p, \zeta_p)$ into equations (2-31) to (2-34) produced the same result, hence

$$U_p = \sum_{i=1}^{20} Ni(\xi_p, \eta_p, \zeta_p)Ui \qquad (2\text{-}40)$$

Equation (2-39) or (2-40) is the interpolated value for the variable U_p at the local coordinate ξ_p, η_p, ζ_p. Similar

expression can be written by replacing the function variable U with the potential nodal value or the global coordinate values x, y and z as follows;

$$\Phi = \sum_{i=1}^{20} N_i \Phi_i, \quad x = \sum_{i=1}^{20} N_i x_i, \quad y = \sum_{i=1}^{20} N_i y_i, \quad z = \sum_{i=1}^{20} N_i z_i \qquad (2\text{-}41)$$

In engineering applications, it is often that the derivatives of a variable function value with respect to the cartesian reference coordinate are of interest. In the present analysis, component flow velocities were obtained by taking the derivative of the potential function. Since the flow was assumed to be inviscid, irrotational and incompressible, the component flow velocities [Kuethe & Chow, Ref.30] can be expressed as follow;

$$\frac{\partial \Phi}{\partial x} = u, \quad \frac{\partial \Phi}{\partial y} = v, \quad \frac{\partial \Phi}{\partial z} = w \qquad (2\text{-}42)$$

The interpolation for component velocities could easily be obtained if only the potential values can be expressed as a function of the global cartesian coordinates. Since this is very difficult, they could only be obtained by applying the Jacobian matrix of transformation.

Since the potential values, Φ, can be expressed in the form given by equation (2-42), applying the Chain rule, their derivatives can be written as;

$$\frac{\partial \Phi}{\partial \xi} = \frac{\partial \Phi}{\partial x}\frac{\partial x}{\partial \xi} + \frac{\partial \Phi}{\partial y}\frac{\partial y}{\partial \xi} + \frac{\partial \Phi}{\partial z}\frac{\partial z}{\partial \xi}$$

$$\frac{\partial \Phi}{\partial \eta} = \frac{\partial \Phi}{\partial x}\frac{\partial x}{\partial \eta} + \frac{\partial \Phi}{\partial y}\frac{\partial y}{\partial \eta} + \frac{\partial \Phi}{dz}\frac{\partial z}{\partial \eta} \qquad (2\text{-}43)$$

$$\frac{\partial \Phi}{\partial \zeta} = \frac{\partial \Phi}{\partial x}\frac{\partial x}{\partial \zeta} + \frac{\partial \Phi}{\partial y}\frac{\partial y}{\partial \zeta} + \frac{\partial \Phi}{dz}\frac{\partial z}{\partial \zeta}$$

or in matrix form

$$\begin{bmatrix} \frac{\partial \Phi}{\partial \xi} \\ \frac{\partial \Phi}{\partial \eta} \\ \frac{\partial \Phi}{\partial \zeta} \end{bmatrix} = \begin{bmatrix} \frac{\partial x}{\partial \xi} & \frac{\partial y}{\partial \xi} & \frac{\partial z}{\partial \xi} \\ \frac{\partial x}{\partial \eta} & \frac{\partial y}{\partial \eta} & \frac{\partial z}{\partial \eta} \\ \frac{\partial x}{\partial \zeta} & \frac{\partial y}{\partial \zeta} & \frac{\partial z}{\partial \zeta} \end{bmatrix} \begin{bmatrix} \frac{\partial \Phi}{\partial x} \\ \frac{\partial \Phi}{\partial y} \\ \frac{\partial \Phi}{\partial z} \end{bmatrix} \qquad (2\text{-}44)$$

Hence the component flow velocities can be obtained by matrix inversion and applying equation (2-42) as follows;

$$\begin{bmatrix} \frac{\partial \Phi}{\partial x} \\ \frac{\partial \Phi}{\partial y} \\ \frac{\partial \Phi}{\partial z} \end{bmatrix} = [\ J\ ]^{-1} \begin{bmatrix} \frac{\partial \Phi}{\partial \xi} \\ \frac{\partial \Phi}{\partial \eta} \\ \frac{\partial \Phi}{\partial \zeta} \end{bmatrix} \qquad (2\text{-}45)$$

where matrix [J] is the Jacobian matrix of transformation

given by;

$$[\,J\,] = \begin{bmatrix} \frac{\partial x}{\partial \xi} & \frac{\partial y}{\partial \xi} & \frac{\partial z}{\partial \xi} \\ \frac{\partial x}{\partial \eta} & \frac{\partial y}{\partial \eta} & \frac{\partial z}{\partial \eta} \\ \frac{\partial x}{\partial \zeta} & \frac{\partial y}{\partial \zeta} & \frac{\partial z}{\partial \zeta} \end{bmatrix}$$

Detail mathematical derivation of the Jacobian matrix can be found in Appendix A-5.

The two matrices on the right hand side of equation (2-45) are obtained by substituting the local coordinate of the point where interpolation is required. The interpolation point is the computed particle trajectory from the particle equations of motion which was derived in the global coordinate axes system. This has to be transformed into the local coordinates in order to calculate the Jacobian and potential derivative matrices (equation (2-45)).The explicit expression for the local coordinate of a point ξ_p, η_p, z_p in term of the global coordinate x, y, z is not easily obtained, hence an iterative approach was used, as described below;

The polynomial equation (2-41) can be rewritten as follow in tensor notations;

$$F_j = \sum_{i=1}^{20} N_i X_{ij} - X_j = 0 \qquad j = 1,3 \qquad (2\text{-}46)$$

where

$$x_{i1} = x_i, \quad x_{i2} = y_i, \quad x_{i3} = z_i$$

and,

$$X_1 = x, \quad X_2 = y, \quad X_3 = z$$

Since equation (2-46) is non-linear in nature, the Newton-Raphson iterative method was employed to transform a point from global to the local coordinate. Detailed analysis of the method is found in Appendix A-6. Having obtained the local coordinate, the component flow velocities can then be calculated.

2.4 Analysis of the Particle Trajectory Prediction Program

The computation of the particle trajectory consist of the numerical integration of the particle equations of motion using the Kutta-Felhberg method. The component flow velocities are obtained by interpolation using the Finite Element technique. The main tasks involved in the computation of particle trajectory are;

a) the location of the element or sub-domain which contains the particle. A particle's position in cartesian or polar coordinate has to transformed into the local coordinate w.r.t. the local axes of the element which contained the particle. If the particle is on or within the selected element or sub-domain, then the absolute component value of it's local coordinate must be less or equal to unity. If it is greater than unity, the adjoining element or sub-domain in that axes direction (Figure 12)is then used to calculate for the new particle's local coordinate w.r.t. this new element's local axes system. Hence, the local coordinates of a particle can be treated as a vector quantity with the origin at the centroid of an element.

b) computation of the independent coefficients given by equation (2-37) of the interpolation function using the nodal values of the element or sub-domain. The nodal values in each element are potential function Φ, global coordinates x, y, z, and they varied with different element or sub-domain. The coefficients are needed in order to calculate the Jacobian matrix of transformation and the derivatives of the potential function in equation (2-45).

c) interpolating for the component flow velocities in an element. Having obtained the element which contains the particle, nodal potential function values is then used to interpolate for flow velocities using the method described in Section 2.3.3.

d) numerical integration of the particle equations of motion (2-12) to (2-14) using the Kutta-felhberg method described in Section 2.3.1. The interpolated component flow velocities are used to compute the particle trajectory in a stepwise manner. The main advantage of this numerical method is the ability to control the step size in order to optimise computational speed whilst only incurring acceptable inaccuracies.

e) the particle's position in the local coordinates computed from (a), above, is checked for possible interaction with the element which formed the part of the solid wall. The finite elements which were discretised in a gas turbine intake are divided into two types of element, they are either;

i) boundary element, which has one or more 'faces' (each element has 6 'faces') representing a solid wall eg. the shroud, hub and splitter surfaces,

or,

ii) ordinary element, which do not form part of a solid wall.

Sometimes, when the particle is close to a wall, near collision is possible, therefore the computation of the particle trajectory is carried to just outside the wall surface to ensure an impaction with the wall. This approach reduced the possibility of the particle just glancing past the wall surface with no wall interaction. If the absolute value of one or more of it's coordinates, in the direction of the 'face' which formed a solid wall, is about 1.0 (within computational error), an impact with the wall is assumed (a value greater than 1.0 means that the particle is outside the solid wall, Figure 12). Having assured a particle-wall interaction, the iteration is brought back one step and repeated again but with a reduced step size until the particle just impacts the wall. Hence, the unit vector normal at the point of impact is computed which enable the particle's rebound velocity and angle to be calculated (using the restitution ratios).

In summary, the particle trajectory positions computed from the particle equations of motion (d) are in cylindrical coordinates. The finite element which contains the particle has to be located before the flow velocities can be interpolated. This involved transforming the particle's position in cylindrical coordinates into a new set of local coordinates (a), with respect to the new axis system defined in the element or sub-domain which contains the particle. If there is no particle interaction with a solid surface, as described in (e), the nodal potential values from this new element are then used to compute the new component flow velocities (c). On an impaction, described as (e) above, the

rebound characteristic equations are then applied to calculate the rebound velocity and direction. The rebound equations (Table II) have the form;

$$V_{PT2}/V_{PT1} = C_1 + C_2\beta_1 + C_3\beta_1^2 + C_4\beta_1^3$$

$$V_{PN2}/V_{PN1} = K_1 + K_2\beta_1 + K_3\beta_1^2 + K_4\beta_1^3$$

$$V_{PN1} = -\tilde{V}_{P1}\cdot\tilde{N}$$

$$V_{PT1} = -\tilde{V}_{P1}\cdot\tilde{T}$$

similarly

$$V_{PN2} = -\tilde{V}_{P2}\cdot\tilde{N}$$

$$V_{PT2} = -\tilde{V}_{P2}\cdot\tilde{T}$$

where β_1 is the impact angle in radians. $\tilde{T}$, $\tilde{N}$ are the local unit vector normal and tangent to the wall surface at the point of impact respectively. The direction of the tangent vector is the same as the particle's tangential velocity component. The computation of the unit normal to the wall surface is described in Appendix A-7.

2.5 Limitation and Assumptions of the Prediction Model

The formulation of the particle equations of motion in Section 2.2 was based on several assumptions which are reviewed below;

a) the drag force being the only force of interaction between

the particle and gas flow. Other forces such as buoyancy, kinematics and gravitational forces are considered to be small compared to the drag force if the particle density is about 3 orders of magnitude greater than the gas density [Rudinger, Ref.31, Hinze, Ref.32]. The drag is a result of the relative velocity between the particle and gas flow. The gravitational force has to be taken into account for particle greater than 1000 microns.

b) the interaction of individual particle with the wakes of other particles is negligible if the average spacing between particle is about 50 or more diameters [Rudinger, Ref.31]. In effect, the particle concentration must be low. In standard dust ingestion test on a gas turbine intake, dust concentration is usually about 0.213 g/m^3 (6.0 mg/ft^3) to simulate normal operating condition. However, concentration of 0.706 g/m^3 (20.0 mg/ft^3) have been tested to simulate a severe condition for example, a dust cloud.

c) the effect of the particle on the flowfield must be negligible i.e. low dust concentration.

d) the solid particles are spheres of uniform diameter and physical properties. In a realistic application, the particles are irregularly shaped. However the assumption of sphericity of particles simplified the derivation of the particle equations of motion. Furthermore, the drag coefficient for different flow regimes is obtained from the standard drag curve for spherical particle. Vittal [Ref.4] and Breitman [Ref.5] applied a factor to the particle equations of motion, to take into account of the drag on an irregular shaped, non-spherical particle. This is discussed further in Chapter 5.

There are also other uncertainties such as the particle restitution ratios which can only be described in a statistical sense based on a large amount experimental data. Inaccuracies may have been incurred in assessing the particle rebound characteristics recorded using the photographic technique as was discovered by Armstong [Ref.22]. The effects of the particle size, particle approach velocity and boundary layer effects on the restitution ratios have not been thoroughly investigated. Most of earlier works were based on a particle size of 200 microns impacting the solid wall at three or four angle of attacks which does not provide the complete rebound characteristic for a broad range of particle impact angles. It was found that the restitution ratios are not invariant to the magnitude of the particle approach velocity.

The computation of the flowfield was based on an inviscid, irrotational and incompressible method. To a certain extent, the main core flow can be predicted quite accurately except in regions of separated flow, vortex or stagnation point, which commonly occur in separator. Their effects on the particles trajectories are largely felt by the small rather than large particles due to their higher inertia. Again, this is discussed further in Chapter 4.

In summary, the assumptions made in the prediction model imposes limitations on the accuracy in the computation of the particle trajectory. However, given these limitations, the majority of the particle trajectories can be predicted quite accurately (especially for larger particles) as shown in later chapters.

Chapter 3

Practical Application Of the Prediction Model In A Gas Turbine Separator

3.1 Introduction

The particle equations of motion (2-12) to (2-14) have been used to calculate particle trajectories in a three-dimensional inertial gas turbine separator. In Section 3.2, a vaneless axisymmetric separator has been discretized using finite element. The flowfield in the separator has been calculated using a heat transfer program (Section 2.3.2). This program provides the temperature values at the element node points which are treated as nodal potential function values (the flow is assumed be inviscid, irrotational and incompressible). The particle initial conditions have been discussed in detail in Section 3.3. These initial conditions are used in the computation of the particle trajectories. The computational errors in the prediction model, which represent the conditions for terminating the computation, are discussed in Section 3.3.1. In Section 3.3.2, sample calculations of the trajectories for two extreme particle sizes, and the effects on the particle behaviour are discussed. The particle shapes were assumed to be non-spherical and spherical, which represents the irregular quartz and ballotini glass beads respectively (they were the dust used in the experimental studies in Chapter 4). In the prediction model, the only difference between the two particle shapes was their restitution ratios. The predicted results and limitations of the prediction model as applied in the separator are also discussed in Section 3.4.

3.2 Analysis of the Flowfield In A Gas Turbine Separator

A vaneless, inertial gas turbine separator is used as a computational model in which to compute particle trajectories using the particle equations of motion. Ideally, the particle trajectory simulations would be calculated in a three-dimensional axisymmetric separator.However, in reality, this is impractical due to the enormous amount of computer storage and expensive computational time required. Since the flow in an axisymmetric separator does not vary at all in the circumferential direction, the flowfield can be treated as a two-dimensional flow. In the present analysis,a 45 degree section of a three-dimensional axisymmetric separator (provided by Rolls-Royce) is used as the flowfield computational model to calculate particle trajectories. In the experimental study of the particle trajectories (Chapter 4), a 30 (instead of the 45) degree section had been used. It was noted that the predicted velocities (and mass flow rates) were high but it was difficult to arrange for repeat predictions where the boundary conditions were better matched. The 20 nodes finite element arrangement (Figure 11, 12) has been used to discretize the separator to give a three-dimensional mesh from which the flowfield can be calculated (Section 2.3. 3). An illustration of the computational grid of the separator is shown in Figure 9.

It can be seen from Figure 4, that the hub and shroud wall surfaces are highly contoured, designed to deflect ingested dust particles into the scavenge duct. A finer mesh is required to accurately model these areas. However, since the heat transfer program can only be solved with a limited number of node points, some areas have to be modelled with a coarser mesh (for example the upstream section of the shroud wall surface, Figure 9). The effect of this coarse mesh on the particle trajectory calculations will be discussed in Section 3.4. Since the computational flow model is treated as a two-dimensional case, the side planes are treated as

solid walls. The three-dimensional separator has three distinct regions i.e. an inlet, scavenge and engine duct. This kind of separator is similar to the asymmetric inertial separator found in certain helicopter types, for example the A129 Mongoose attack helicopter.

By using the heat flow analogy (Section 2.3.2), potential function values are computed at the node points in the computational mesh. The flow velocities in the particle equations of motion can then be interpolated from the elemental nodes using the interpolation technique described in Section 2.3.3. A contour plot of the calculated nodal potential function is shown in Figure 10. From this figure, several areas of the separator with high or low flow velocities can be identified by the density of the contour lines. High velocity flows are found at the following areas;

i) at the shroud upstream of the 'hump' of the hub,
ii) at the peak of the 'hump' of the hub,
iii) at the underside of the splitter.

Conversely, areas of low velocity flow are;

i) at the shroud downstream of the 'hump' of the hub,
ii) at the stagnation region on the upperside of the splitter,
iii) at the base of the 'hump' of the hub.

Figure 13 shows the interpolated flow vectors at the node points calculated at a particular section of the separator model. The method of calculating these flow vectors has been described in Section 2.3.3 (i.e. simply by substituting known nodal potential functions and coordinate values into the matrices given in equation (2-45)).

Since the flowfield is assumed to be inviscid, irrotational and incompressible (Section 2.3.2), flow separation cannot be predicted at the region of adverse

velocity gradient. For example, in a flow visualisation test using wool tufts, flow separation was found at a region downstream of the peak of the 'hump' of the hub and yet the computed velocity is unable to simulate the process. The accuracy of this predicted flowfield will be compared in greater detail with measured values in Chapter 4.

The flow velocities required in the particle equations of motion can either be interpolated from the nodal potential functions or, from a mesh of interpolated nodal flow velocities. The advantage of using a mesh of interpolated nodal flow velocities is the improvement in the particle trajectory computation speed due to the reduced computational requirements. This is especially useful when simulating particle trajectories in severe conditions where large numbers of nodal points are involved.

In the present analysis, the nodal velocities, instead of the nodal potential function values, are used to calculate flow velocities.

3.3 Initial Conditions as Applied in the Gas Turbine Separator

The particle equations of motion can be solved in a pre-defined flowfield by applying initial conditions for different particle sizes and shapes. The particle trajectories in an experimental test can be simulated by applying similar initial conditions (for example, the restitution ratios and the initial particle conditions). In a standard dust test, man-made dusts are frequently used to assess the separation performance of a separator. These dust particles range from 0 to 1000 microns in diameter which are normally defined in terms of the maximum particle size and percentage of particles (by mass) below that particular size. AC coarse dust sizes usually range from 0 to 200 microns and, MIL-SPEC sand ranges from 0 to 1000 microns in

diameter. Occasionally narrow bandwidth dust between 10-20, 40-60, 100-150 and 700-1000 microns are also used to investigate different separator design.

In the present analysis, narrow bandwidth dust, similar to that used in the experimental work (Chapter 4), are used to compute particle trajectories in the separator. The particles are assumed to have uniform density and properties which includes both spherical and non-spherical particles. The range of dust sizes of interest in the present studies are between 15 and 150 microns in diameter. It is known from earlier works [Ref.16, 17, 18] that the trajectories of the large particles (>200 um) are influenced mainly by the particle's rebound characteristics where bounce is the predominant mechanism and the trajectories of the very small particles (<5 um) are affected mainly by the aerodynamic drag force. Hence, the present choice of particle sizes are chosen to reflect the influence of both the particle rebound characteristic and the aerodynamic drag force. The narrow bandwidth spherical dust used in the experimental investigation are also employed in the present simulation of the particle trajectories later in Chapter 5. The spherical dust sizes are;

i) 15 ± 3 microns
ii) 38-53 microns
iii) 53-65 microns
iv) 91-107 microns
v) 145-162 microns

The non-spherical dust sizes are;

i) 15 ± 3 microns
ii) 30.0 microns
iii) 60.0 microns
iv) 100.0 microns
v) 150.0 microns

Figure 14 shows a graph of the particles size distribution for both the spherical (Ballotini) and non-spherical (Quartz) particles. The upper and lower limits of the particle sizes are used to compute the particle trajectories so that the effect of the aerodynamic drag and rebound characteristics can be studied.

The particles initial radial location (in the cylindrical polar axes system) are defined at the inlet plane of the computational model, they being;

i) 105.50 mm
ii) 128.67 mm
iii) 151.80 mm

These particle initial locations represent the position at 20, 50 and 80 percent of the inlet annular height which was chosen for two main reasons, they are;

a) the predicted results from the three locations need to be verified with experimental measurements. Since it is impractical to investigate all the different particle locations experimentally, only three positions were chosen. These locations were chosen after some preliminary investigation of the flowfield (Chapter 4). Particle initial location (i), above, was chosen to investigate the effect of a vortex (discovered at the base of the 'hump' on the hub) on the particle trajectories (Chapter 4). The distance between the wall and the near-wall initial locations are spaced so that the particle will not interact with the walls of the inlet duct before the particle first impact with the hub.

b) the predicted particle trajectories, from the three locations, can be extrapolated to a wider distribution of initial particle locations without the need for further

computation. Since the particle trajectories in the present studies are affected only by the aerodynamic drag force and particle rebound characteristics, other factors such as the effect of the swirl vanes, which are not found in the present separator, can be ignored. However, if either the drag force or the bounce mechanism is predominant, particle trajectories for other initial locations are much more difficult to extrapolate without computation. The very small particles (<5 um) for example, can be entrained in a separation bubble or a vortex where the drag force is the predominant factor.

Since the flowfield is assumed to be two-dimensional in nature, the circumferential initial particle location can be at any position of model. The axial initial location, however, had to be 'just inside' the model so that initial flow velocities can be interpolated in the mesh.

The particle trajectories after an impact with a solid wall are calculated from the restitution ratios (particle rebound characteristic) which are applicable to a particular combination of particle and target material. The restitution ratios for the irregular, non-spherical particles representing the quartz particle were obtained from experimental work by Tabakoff [Ref.16, 17]. However, there are no such data for spherical particle (in this case, Ballotini glass beads), therefore a simple expression for the restitution ratios was employed, which had the form;

$$V_{PT2}/V_{PT1} = K_1$$

$$V_{PN2}/V_{PN1} = K_2$$

where V_{PT1} and V_{PN1} are the tangential and normal particle component velocities respectively and, vice versa for V_{PT2} and V_{PN2}. The constants K_1, K_2 can be determined by comparing measured with predicted particle trajectories

calculated using a guessed values for the constants until good agreement is found. Preliminary investigations give the two values as 0.8 and 0.78 respectively. Particle restitution ratios for non-spherical (quartz) can be found in TABLE II.

The drag coefficients, in the particle equations of motion, for spherical particles are based on the standard drag curve given in TABLE I. Since there are no available data for the irregular, non-spherical particles, the drag coefficients for spherical particles are used instead. The effect of applying these incorrect drag coefficients for non-spherical particles will be discussed in Chapter 5.

3.3.1 Conditions for the Termination of the Trajectory Computation

In the computation of the particle trajectory, several conditions had to be imposed in the solution in order to avoid severe computational errors. The main cause of computation errors are;

a) convergence to the incorrect roots during the solution of the non-linear equations (using Newton-Raphson method) due to the incorrect initial guessed values (Appendix A-6) or, there may not be any convergence at all due to severe element distortion.

b) the local truncation error in the Kutta - Felhberg method may be too large even though the time step used has been reduced to a very small value. This may be caused by condition (a) or, inaccurate interpolated flow velocity.

c) either condition (a) or (b) may lead to a failure to satisfy the particle-wall interaction condition.

In an event of the above failures, computation of the particle trajectory for that particular initial particle conditions is terminated and an error message is printed out. An inaccurate computed flow velocity near the wall can also lead to computation problems especially for the very small particles of less than 5 microns. An interpolated flow velocity across a solid wall (which is physically impossible in the present studies), due to either computational error or an inaccurate flowfield, may be small. However, this flow may cause the very small particles to 'cross' the solid wall thereby leading to 'multiple' impacts invoking the continuous computation of unit vector normal to the wall. This in itself would not cause a serious computational error but the computational time (for that particular particle) would increase. This effect can be eradicated by assuming the near-wall potential derivative (which gives the flow velocity) to be zero. Some of the above computational problems impose a limitation on the prediction model which will be discussed in Section 3.4.

3.3.2 Analysis of the Predicted Results

All the initial conditions mentioned in Section 3.3 are used to compute particle trajectories to be used as a comparison with experimental results. In order to study the particle trajectory prediction model, the following initial conditions were used;

i) Particle initial location : r_p = 0.12867 m; Θ_p = 87.0 deg ; z_p = 0.052 m,
ii) particle initial velocity V_p = 0.0 m/s,
iii) particle sizes : D_p = 15.0 um ; 150.0 um,
iv) particle material : Quartz (non-spherical) ; Ballotini (spherical),

v) particle density : 2650.0 kg/m3 (quartz); 2950.0 kg/m3 (ballotini),

vi) restitution ratios : Quartz-Al (non-spherical derived from Ref. 16 and 17); Ballotini (K_1 = 0.8, K_2 = 0.78)

In order to study the effects of the aerodynamic drag force and the particle rebound characteristics, two extreme particle sizes, 15 and 150 microns, were used. The drag coefficients for both spherical and non-spherical particles were obtained from the standard drag curve for spherical spheres derived by Chuen-Yen Chow [Ref.33] as shown in TABLE I. The results of the predicted particle trajectories, velocities and angles are plotted against the interpolated flow velocities and angles in Figure 15 (a) and (b) for the 15 and 150 microns spherical particle (ballotini) respectively and in Figure 16 for the non-spherical (quartz) particle.

Since the only differing factor in the predicted results between spherical and non-spherical particles is the restitution ratios, the effects on the particles trajectories can be grouped into two parts, they being;

i) <u>The Effect of Aerodynamic Drag on the Particles Trajectories.</u>

Figure 15 shows the predicted particles trajectories, absolute particles velocities and angles, interpolated absolute flow velocities and angles for 15 microns (Fig. 15(a)) and 150 microns (Fig.15(b)). These figures will be used to discuss the effect of the aerodynamic drag on the small particles (15 um) and large particles (150 um). At the initial position, both particle sizes had the same interpolated flow velocities and initial particle velocities. The drag force which is related to

the drag coefficient, is dependent on the relative velocity between the particle and flow, and the particle diameter. Hence, the small particles with a smaller Reynolds number, has a greater initial drag force acting on them. The result is a greater initial rate of increase in the particles velocities as shown in Figure 15. The small particles attained the flow velocity of about 80 m/s after travelling a distance of about 85 mm downstream of the inlet. Over the same distance, the large particles has only attained 28 m/s. The small particles achieved a maximum velocity of about 93 m/s while the large particles only manage about 42 m/s. The predicted particles trajectories of the small particles seem to be influenced mainly by the drag force whereas the large particles are mainly 'ballistic' in nature. The small particles can quickly 'adapt' to the changes in the flow velocities and angles while the large particles seem to be relatively unaffected. In general, the small particles's velocities and angles 'lag' behind the flowfield while the large particles maintained its trajectories by having a greater momentum due to it's inertia.

ii) <u>The Effect of the Particle Rebound Characteristics on the Particle Trajectories</u>

The predicted results for non-spherical particles in Figure 16 differ from the result for spherical particles Figure 15 only with respect to the particle rebound characteristics. While the restitution ratios for the spherical particles are based on a simple expression (Section 3.3), the non-spherical particles employed the restitution ratios obtained for quartz particles impacting aluminium wall surface. The predicted particle trajectories, velocities and angles, before the first impact position, for both spherical and non-spherical

particles, were similar. After the first impact, the small particles still displayed similar trajectories, velocities and angles except that the non-spherical particle has a smaller rebound angle. The larger particles, which are influenced mainly by the rebound characteristics, however, reflect at dissimilar impact positions, velocities and angles after the first impact position, for spherical and non-spherical particles. The non-spherical particles for both particle sizes suffered a greater loss in momentum during an impaction with a solid wall. In general, the trajectories of the larger particles are affected mainly by the particle rebound characteristics and, the smaller particles are mainly affected by the aerodynamic drag forces.

As the drag coefficients for non-spherical particles, and restitution ratios for spherical particles are in some doubt, the predicted trajectories (velocities and angles) have to be verified by experimental measurement. Other factors such as the viscosity of the flowfield can also affect the simulation of particle trajectories.

3.4 Limitations of the Prediction Model as Applied in the Gas Turbine Separator

Several limitations of the prediction model have already been mentioned in Section 3.3.2. In general, they can be grouped under the following effects;

a) the effect of viscosity on the particle trajectory.

It has been known that the present computational model is based on an inviscid, irrotational and incompressible flowfield calculated from a heat transfer program (Section 2.3.2). The predicted flowfield needs to be verified by experimental measurement (Chapter 4) because

of the effect of viscosity. Since the aerodynamic drag force is dependent on the relative velocity between the particle and flow, an inviscid flowfield might not predict the correct particle trajectories especially for the small particles. The effect on the larger particles is less likely to be affected, due to their greater inertia. Hence, their trajectories depend more on the restitution ratios than the aerodynamic drag force. Preliminary test carried on an experimental rig (based on the shape of the computational model) revealed the presence of a vortex at the base of the 'hump' in the upstream section, a separation 'bubble' just behind the peak of the 'hump' and, a transient flow separation at the shroud wall just after the peak of the 'hump' (as shown in PLATE 7 to 12). These observations found in the actual flowfield reveal the limitation of the present prediction model.

b) the effect of the drag coefficient on the particle trajectory.

Since there is no drag coefficient data for the non-spherical particles, the data from the standard drag curves were used throughout the analysis. Again, their effect on the predicted trajectories, velocities and angles can only be investigated experimentally. In general, their effect is largely felt by the smaller particles due to the greater aerodynamic drag force. An incorrectly predicted particle velocity, as a result of an incorrect aerodynamic drag force, can affect the calculation of the mass erosion parameter [Ref.16, 17, 18] which is a function of the particle impact and rebound velocities.

c) the effect of the restitution ratios on the particle trajectory.

In the present studies, the rebound characteristics for

the non-spherical particles has been obtained from experimental data (Section 2.2.3), but for spherical particles, a simple expression has to be used assuming that the particles have uniform density and other properties. This expression has to be verified by comparing measured particles trajectories with the prediction for various particle sizes. Since the rebound characteristics (restitution ratios) for quartz particle were obtained under limited conditions (Section 2.2.3), the predicted trajectories, velocities and angles will also need to be investigated experimentally.

d) the effect of the geometric modelling of the separator on the particle trajectory.

The flowfield computational model in the present separator consists of a mesh of finite elements and node points from which the potential function or temperature values can be calculated using the heat transfer program (Section 2.3.2, 3.2). Since this program can only handle a limited number of elements, some areas of the separator had to represented by a coarser mesh than desirable. This coarse mesh may consists of severely distorted elements for example, in Figure 15, the elements near the splitter lip have disproportionate sides. These distorted elements can affect the following calculations;

i) the rate of convergence in the Newton-Raphson method.

This method is used to transform a point in global coordinate into the local coordinate w.r.t. the axes in a particular element or sub-domain (Appendix A-6). Since the transformation involved solving a set of non-linear equations, the rate of convergence depend on the degree of element distortion. The iterative method usually converged to a solution after 3 iterations, however, it would takes twice as long to converge in a severely distorted element. Sometimes it will not converge at all

due to a poorly initial guessed values coupled with a severely distorted element. The overall effect is an increase in the number of iterations required for convergence, hence, an decrease in the overall computational speed.

ii) the accuracy in the computed unit vector normal to a wall at the point of impact on which the particle rebound velocity and angle are calculated (Section 2.4). The computation of the component tangential rebound velocity also depend on this vector normal (Appendix A-7). The accuracy in the calculation of the unit vector normal depends on the type of element used in modelling the areas prone to particle impacts for example, the 'hump' of the hub as shown in Figure 15 and 16. From these figures, the wall of the hub at the impact areas is represented by relatively coarse elements. Since the particle trajectories of the larger particles are influenced mainly by the rebound characteristics, an incorrect representation of this wall surface would lead to an inaccurate particle rebound velocity and angle. This in turn, could affect the computation of the overall separation efficiency of a separator, for particle sizes whose trajectories are predominantly 'ballistic' in nature. The effect of an incorrect unit normal on the particles trajectories which are influenced mainly by aerodynamic drag force is relatively small. The reason for this is that immediately after an impaction, the rebound particle is affected by the aerodynamic drag force. The accuracy in modelling the wall surfaces will be studied by comparing predicted trajectories with experimental measurement later in Chapter 4.

The computational model will be used throughout the present studies and their effect on the particle trajectories will be investigated in Chapter 4.

e) the effect of inter-element continuity on the particle trajectory.

The interpolation function (2-29) used in the interpolation for the flow velocity (Section 2.3.3) and the computation of the unit vector normal in a finite element, lacks inter-element continuity at the elemental node points. The result is a discontinuities in the interpolated flow velocity and vector normal at the node points shared by two or more adjacent elements. In general, this discontinuity in the interpolated flow velocity is usually small, however, coupled with a distorted element, the error can be significant. An example of this discontinuity in the predicted flow velocity can be seen in Figure 15 and 16, in the region where distorted elements exists (i.e. at the scavenge duct 300 mm from the inlet section). Although the effect of this discontinuity on the trajectory of the particles above 10 microns is small, this is not so for much smaller particles. Inter-elemental discontinuity in the computation of the unit vector normal can also occur at nodes shared by two or more adjacent elements. The result is the vector normal calculated using one element at a common node (shared with an adjacent element) will be different to that calculated from that adjacent element. The inter-elemental discontinuity is due to the interpolation function being of first order continuity [Connors, Ref.28], hence only inter-element continuity of the nodal function itself exist and no continuity exist in its' derivatives. In the present case, the nodal functions are the nodal global coordinate x, y, z and, the potential function value, Φ, and their derivatives are the vector normal to the wall and interpolated flow velocity respectively. The inter-elemental continuity can be obtained by using second order continuity interpolation function. However, this requires additional

nodal values such as V_x, V_y, V_z or V_{xy} in the interpolation of the flow velocity and, derivatives such as $\partial z/\partial x$, $\partial z/\partial y$ in the computation of the unit vector normal. As these additional terms cannot be calculated using the present flow model, inter-elemental discontinuity will exists.

The effects of (a) to (e) on the prediction of the particle trajectory are the present limitations which exist in the prediction model for the gas turbine separator. The effects (a) to (d) on the particles trajectories, velocities and angles will be studied experimentally in Chapter 4. Effect (d) would be reflected in the prediction of the particle rebound velocity (and angle), hence its effect was included into the experimental study of (c). Effect (e) is relatively small and can be ignored in the present studies.

In summary, the particle trajectory prediction model had been applied to a gas turbine separator which had an inviscid, incompressible and irrotational flowfield. The limitations of the model were studied experimentally (later in Chapter 4) for a range of particle sizes seeded at three initial height positions. Sample analysis of the predicted results for the 15.0 and 150.0 um particle had shown the effect of the aerodynamic drag and inertia forces (which are related to the above limitations) on their trajectories.

CHAPTER 4

Experimental Investigation of the Particle Trajectories in A Gas Turbine Separator

4.1 Introduction

Particle trajectory prediction models have been used to assess a separator's performance by predicting it's separation efficiency for a range for particle sizes. As a result, a curve can be obtained which relates the separation efficiency with the particle sizes. Therefore the overall separation efficiency for a particular dust type can be calculated. For example, the overall separation efficiency for the AC Coarse dust (0 to 200 um) can be obtained by integrating for the area under the curve (Figure 86), for the particle size between 0 and 200 um in diameter. Although these models can predict separation efficiency with some degree of success for the larger particles, most of them fail in their prediction for the smaller particles. The reason appears to be due to the limitations of the prediction model which has been discussed in detail in Section 3.4. These limitations can only be studied experimentally in a confined area, under pre-defined initial conditions. The usual method of assessing the separation efficiency of a separator was by feeding a known amount of dust, in the form of a cloud, at the separator inlet section (Figure 5) and, weighing the amount of dust separated in the scavenge section. The ratio of the separated dust to the total amount of dust fed at the inlet is the separation efficiency of the separator. Hence the measured separation efficiency for a particular dust size is compared with the result from the prediction model. This method of assessing a separator's performance lacks all the information involved in the behaviour of a particle in flight such as it's velocity or trajectory angle. Furthermore, the particle's

initial conditions such as the initial particle and flow velocity, which are vital to the successful prediction of the particle trajectories, cannot be obtained with the usual method of approach. During a particle's flight, it's velocity and angle cannot be recorded due to the inaccessibility of a conventional separator. In order to fully investigate the behaviour of a particle in flight and make detail comparison with the prediction model, the particle trajectory paths, velocities and angles have to be recorded. The only way of making such detailed observations is by studying and recording the particle's flight in a 'cut-away' section of an actual separator. The initial conditions can be controlled by feeding the dust particle at known positions where measurement of the particle and flow velocity can be made. Using the same initial conditions, the predicted particle trajectory, velocities and angles can then be compared with experimental measurements so that the limitations in the prediction model can be studied in greater detail. The comparisons for the different particle sizes can be made at several positions in the separator.

Limitations of Prediction Model (Review)

The limitations of the particle trajectory model have been discussed in detail earlier in Chapter 3. These limitations can summarized as follows;

a) the assumption of an inviscid, irrotational and incompressible flowfield
b) the use of the drag coefficient which is applicable for spherical particle only
c) the use of restitution ratios for non-spherical particles which were derived under limited conditions and, the assumption of a simple expression for spherical particles
d) the used of a coarse mesh to represent areas prone to

particle impacts

The effect of these limitations on the prediction model has to be fully investigated experimentally for a range of particle sizes and shapes. The particle trajectories of the small particles are affected mainly by the aerodynamic drag force, the application of the drag coefficient (derived for spherical particle only) for non-spherical particles give an incorrect results which include particle trajectories, velocities and angles. The prediction can also fail to give an accurate result if the modelling of the flowfield is incorrect. For example, the inviscid assumption used in the present studies cannot predict areas with separated flow or a vortex re-circulation. The flow velocities (from an inviscid flowfield) interpolated at these areas and hence the calculation of the Reynold number and drag coefficient was incorrect. The effect is felt largely by the small rather than the larger particle due to the greater influence of the flowfield on their trajectories. The larger particles, due to their inertia, depend on the accuracy of the rebound characteristics and the representation of the wall surfaces. These matters have been discussed in Section 2.2.3 where the restitution ratios (rebound characteristics) were obtained experimentally using mainly 200 um quartz particles, at only a few angle of attacks and approach velocities (no restitution ratios are found for ballotini particle). The inadequate experimental data used in the formulation of the restitution ratios could affect the particle rebound velocities, angles and trajectories. Furthermore, there are no experimental data on the effect of the boundary layer, flow separation or a vortex re-circulation on the particle trajectories. These flows phenomena are fairly common in the modern inertial separator which usually have highly contoured hub and shroud shapes, designed to deflect particles into the scavenge sections. Hence the flow has to negotiate the severe bend

and curvatures of the separator which could result in an area with adverse pressure gradient, and could lead to flow separation. The pressure loss, as a result of a separated flow, will incur a penalty in the engine performance. Since inertial separator do have these highly contoured hub and shroud surfaces, it was inevitable that these flow phenomena may occur. It is, therefore important to investigate these effects on the prediction of the particle trajectories.

4.2 Objectives

The objective of the present studies is to investigate the effects of the above limitations in the prediction model on the particle trajectories. The method of approach is to make comparison between measured and predicted results under the following conditions;

a) to investigate the difference between predicted and actual velocity of the flowfield on the particle trajectories, (velocities and angles) and to compare with predicted results. Since individual particle measurement was not possible with the equipment available, the particle mean trajectory positions, instead, were determined from the particle concentration curves, measured at several locations, in the separator. The particle concentration curves were obtained by traversing a Laser Anemometer across the particle's path and recording the intensity of the scattered light from the particles. Hence, local measurement of the particle velocities and angles can be made at these mean positions. The measured initial conditions can be used as an input for the prediction model so that local comparison of the velocities and angles at several stations in the separator can be made. The prediction will be carried out in the inviscid and

measured flowfield so that the comparisons with experimental data can be studied.

b) to investigate the effect of the drag coefficient on the particle trajectories, velocities and angles, and to compare with predicted result. The drag coefficient, used in the prediction model, for both the spherical and non-spherical particles is obtained from the standard drag curve derived for spherical particles. Hence, the measured particle velocities and angles using the spherical and non-spherical particles were compared with the prediction. The particle's absolute velocities and angles were measured with the Laser Anemometer at the mean trajectory positions (from (a)). The prediction was carried out in both inviscid and measured flowfield.

c) to investigate the effects of the restitution ratios on the particle trajectories (velocities and angles) and to compare with predicted results. The restitution ratios for the non-spherical particles were obtained from the experimental data by Tabakoff [Ref.16, 17], but for spherical particles, a simple expression (Section 3.3) was used. The accuracy of this expression and the restitution ratios (for non-spherical particles) was investigated by comparing the predicted trajectories and angles with measured results, using spherical and non-spherical particles, at the mean trajectory positions determined from (a).

The comparisons will be used to investigate the deficiency in the prediction model due to the limitations so that modification can be made to improve the model's accuracy in future predictions.

4.3 Particle Materials, Sizes, Shapes and Concentrations

The man-made dusts such as AC coarse and MIL-SPEC dusts used in standard dust tests are irregular and non-spherical in shape. AC coarse dust consists of particle ranging from 0 to 200 μm while MIL-SPEC sand ranges from 0 to 1000 μm. The dust used in the present studies, quartz and ballotini, are the narrow bandwidth dust which were graded to a particular size. The quartz and ballotini had similar properties to the AC coarse and MIL-SPEC dust. Analysis of particle sizes of the quartz (non-spherical) dust with a spectrum analyser gave their median diameter (i.e. 50 % below a particular size) as follows;

i) 30 microns
ii) 57 microns
iii) 102 microns
iv) 150 microns

The median diameter for the ballotini (spherical) particles had the following sizes;

i) 68 microns
ii) 105 microns
iii) 145 microns

Note that no independent analysis of the 30.0 um ballotini particles sizes were untaken and the only data available was that provided by the manufacturers.

The particle equations of motions were derived assuming that the particle is spherical and the drag coefficient is applicable for spherical particles only. Hence the spherical dust would be used as a test case for comparing with predicted results. In order to study the effect of the aerodynamic drag force on the particle trajectories, very small diameter dust particles, screened to 15 microns (± 3.0

um) for both ballotini and quartz were also used. The assumptions made in the derivation of the particle equations of motions (Section 2.5) had to be satisfied in the experimentation as well. They are;

a) the dust concentration has to be low enough so as not to affect flowfield. In standard dust tests, the dust concentration is usually about 0.213 g/m^3 (6.0 mg/ft^3). Sometimes, dust concentration of 0.706 g/m^3 (20.0 mg/ft^3) had been used to simulate severe conditions. In the present studies, the dust feedrate and concentration had been calibrated to be below 1.0 g/m^3. This dust concentration is based on solid particle seeding concentration used in the Laser Anemometry technique which will be discussed further in Section 4.4.2.

b) the particle density has to be about 3 orders of magnitude greater than the flow density so that only the drag force needs to be considered. The quartz and ballotini dust used in the present studies are 2650.0 and 2950.0 kg/m^3 respectively thereby satisfying this condition.

The laser anemometer, which has been used extensively throughout this investigation, depends on the scattered lights from the dust particles. Hence the dust particles has to be fairly reflective and uniformly sized. The ballotini and quartz dust has a refractive index of 1.60 and 1.46 respectively. The consistency of the dust sizes quoted by the supplier is that 90.0 percent of the particles to be within the quoted size. The dust used in the tests had been kept constantly dried in an oven set at 40.0 degrees Centigrade.

4.4 Experimental Set-Up

The experiment set-up is shown schematically in Figure 17 and PLATE 1. It consists of an inertial separator, laser anemometer and data acquisition systems, and a dust particle feeder assembly. The inertial separator is a 30 degree section of an actual axisymmetric gas turbine separator as shown in Figure 18 and 19. The separator consists of a highly contoured hub,shroud and splitter sections. They had been accurately machined (programming resolution is .001 mm) from Aluminium alloy using a numerically controlled machine (Hurco CNC).The three separate sections were then bolted on to a pair of end plates which has an annular inlet and two outlet holes which made up the air inlet,scavenge and engine flow outlets. Two 6.0 mm thick, toughened clear glass formed the side walls of the separator,allowing full optical access to the laser anemometer.The glass plates were sealed 'flush' against the three sections using an 'O-ring' seal which runs parallel to the wall edges. The glass plates, which had to be cleaned before each test, were removable by undoing 6 bolts for each plate. The removable glass plate also allowed easy access to the hub, shroud and splitter surfaces which need to be polished after each test using quartz particles. Since the quartz dust is very erosive in nature,due to their angular shapes, the wall surfaces (which were made of aluminium alloy) becomes roughened after each test. The ballotini dust particles, however, do not cause any damages to the wall surfaces due to their spherical shapes.

The inlet section of the front end-plate has a 'bellmouth' flare to guide the air into the separator. The annular scavenge and engine outlets were connected to two circular pipes via a pair of transition pipes. These pipes lead into a vacuum tank where the airflow is provided by a suction fan. The vacuum tank has a removable top section to allow access to the two pipe ends and a dust filter layer. In the dust ingestion test (later in Section 4.7), the dust

collected in two collector bags which are attached to the pipe ends can only be serviced regularly by removing the top section of the tank. The filter layer, which consists of two layers of fiberglass spun material, is sandwiched between two sets of wire mesh to prevent dust particles exhausting into the atmosphere. A pair of rubber ring seals are placed on the top and bottom of the wire mesh to prevent any dust getting through at the edges of the filter layer. The fiberglass material (Owens-Corning FM004) has a quoted separation efficiency of 85.0 percent for particle diameter greater than 0.5 microns. This filter layer had to be replaced regularly to avoid excessive pressure loss due to dust accumulations.

The suction fan can provide a maximum mass flow of about 1.70 lb/s, of which only 1.25 lb/s of air is required. However, there are other pressure losses that need to be considered, such as losses from the transition pipes and pressure loss across the filter layer. The required mass flows in the engine and scavenge pipes are 1.0416 and 0.2083 lb/s respectively in order to simulate a mass flow of 12.5 lb/s in actual engine flow with a 20.0 percent bypass (scavenge) ratio. The mass flows in the engine and scavenge pipes had to be adjusted daily to take into account of the everyday changes in the atmospheric conditions (Section 4.4.3). A pair of throttle valves in the pipes were used to maintain the required flow condition. A total pressure probe and three wall static pressure tappings were used to record the mass flow in each pipe. They were positioned at about 18 pipe diameters [B.S.1042, Ref.39] from the transition section in order to avoid the turbulent flows from the separator. The total and averaged static pressures were connected to a micromanometer via a scanivalve.

The hub, shroud and splitter walls had been fully instrumented with wall static pressure tappings which are connected to the micromanometer via a scanivalve. The tappings had been spaced so that areas with critical flows

such as the splitter region, has a higher density of static tappings.

4.4.1 Laser Anemometry (L2F) and Instrumentation

The non-intrusive measuring technique used for defining the absolute flow velocities and angles of a moving fluid is called Laser Anemometry (or L2F). This technique was used to measure the flowfield in the separator (Section 4.5), particle concentration, particle velocities and angles. The principle behind Laser Anemometry (Figure 20) is based on the detection of light pulses scattered by particles as they passed through the probe volume. The probe volume consists of two intense zones of light formed by two focused laser beams (Figure 21) at a known distance apart. The particle velocity, in the plane normal to the optical axis, is determined from the time of the particle's flight across the two spots. Hence, the measured particle transit time is translated into the velocity by the relation;

$$u=S/t$$

where S is the distance between the two spots and t is the particle transit time.

Since the basic principle of this technique is the detection of light scattering by the particles, different particle sizes can be used depending on the type of measurement required. In the measurement of a flowfield, sub-microns particle size of about 0.5 um in diameter are used due to their ability to follow the streamlines of the flow. However, in the present studies of the particle trajectories, the same principle was applied to measure the particle velocities and angles with sizes between 15.0 and 150.0 um in diameter (Section 4.6).

The scattered light from the two spots is detected by two photomultiplier tubes (PMT) representing the start and stop pulses. Random light such as flare from the background is conditioned by a process of amplification (light from particle) and discrimination (random light) [Mohsen, Ref.34] so that only light scattered by the particles are fed into a correlator (Figure 22). Each pulse train from each photomultiplier tube is fed into two channels in the correlator i.e. Channel A and B. The data stored in the correlator produces a probability histogram of time measurements. The highest probability that a particle travelling along the line of flow will be irradiated by both laser beam occur at the mean flow direction. The peak of the distribution curve (Figure 23) indicates the mean velocity whereas the maximum width of the curve near the baseline indicates the maximum velocity fluctuation. As the spots are rotated about the axis of the anemometer, the signal intensity changes as shown in Figure 24. The method of computing for the flow velocity is based on Ross's technique [Ref.35]. Since the detail of the velocity deduction technique is beyond the scope of the present studies, the method of analysis can be summarised as follows;

$$G(\tau,\alpha) = \frac{K\ s^2}{\tau^3} \exp\left[\frac{-(1/\tau-(U/s)\cos(\alpha-\alpha_0))^2}{(\sigma/U)^2\ (U/s)^2} \right]$$

where

U = mean velocity

α_0 = mean flow angle

σ/U = turbulence intensity

The area under the correlogram (Figure 23) at angle α is

given by;

$$P(\alpha) = K \exp\left[\frac{-U^2(\alpha-\alpha_0)^2}{\sigma^2} \right] \qquad (4\text{-}1)$$

Applying this equation for different angles α, yield the distribution curve in Figure 23. The correlogram at the angle closest to the mean flow angle α_0, is used to fit equation (4-1) yielding the mean velocity U, and turbulent intensity σ/U.

The laser instrumentation consists of two photo-multiplier tubes (PMT), a 35 mW Helium-Neon laser (Spectra Physics) and other optics. The whole assembly including the laser and photomultiplier tubes can rotate about it's optical axis, normal to the direction of the flow. The whole assembly is mounted on a milling bed with movement in the X, Y and Z axis, and, rotation is remotely controlled (PLATE 2). The transmitting lens has a focal length of 50 cm and spot separation is 450 um. The threshold level set in the amplifier and discriminator available with the PMT are suitable only for a high signal to noise ratio and not much background flare. Therefore an external LeCroy amplifier (X100) and discriminator (+ 200 X 16 uV maximum threshold) is added to each of the channels (from PMT) to overcome the situation of low signal to noise ratio. The threshold can be adjusted to give the best signal to noise ratio.

The signals are fed into a 50 nanoseconds correlator (K7023, Malvern) which is used on a cross correlator mode [Mayo, Ref.36]. During data collection, the quality and state of the histogram can be monitored on an oscilloscope (Gould) which is connected to the correlator store (PLATE 3). If the quality of the histogram is acceptable, the data is transferred to an online minicomputer (Amstrad PC1512) for analysis.

The accuracy of the results obtained by laser

anemometry depend on the equipment, seeding density and sizes and particle dynamics. A repeatability of ± 1 degree for the absolute flow angle has been claimed, and an uncertainty of less than ± 1 percent for the mean flow estimation has been reported [Mohsen, Ref.34] for the present equipment.

4.4.2 Dust Feeder Assembly

The dust feeder assembly consists of a dust feeder nozzle and dust hopper (PLATE 4). Two method of feeding dust into the nozzle (which will be discussed later) were used depending on the particle diameters. A pressurised, fluidised bed (Figure 25) was employed for the 15.0 um dust and, a laboratory burette was used for other dust sizes. All measurements were carried out inside the separator with the dust feeder nozzle exit plane at 50.0 mm downstream of the inlet. As a result, the nozzle had to satisfy the following requirements;

i) it had to deliver a steady flowrate and concentration of dust particles. This is necessary in order to obtained accurate measurement of the mean particle trajectories, velocities and angles using the laser anemometry technique. The particles must be produced at a rate sufficient for an acceptable signal rate in the measuring volume. In the measurement of the particles velocities and angles, the rate of delivery must be stable over a short time [Melling, Ref.37] for example, 1 minute.

ii) the dust concentration must satisfy the assumptions made in the formulation of the particle equations of motions (Section 2.5). The assumptions are that the

concentration must be low so that particle-particle interaction and their effect on the flowfield can be ignored.

iii) the nozzle must not cause too much disturbance to the flowfield. The nozzle end was placed at some distance downstream of the separator to coincide with the inlet plane of the flowfield computational model (Section 3.2). Since the computational model can only employ a limited number of finite elements, it cannot model the flow in the full length of the separator. As a result, the computation starts at 51.73 mm downstream of the actual separator inlet section and ends at 332.0 mm, just behind the leading edge of the splitter lip. Therefore the nozzle exit was placed at 50.0 mm downstream rather than at the inlet plane in order to reduce the inevitable 'spread' in the dust distribution exhausting from the nozzle end. The 'spread' is due to the orientation of the particles inside the nozzle and, the particle interaction with the wakes caused by the nozzle.

If the nozzle end was placed at the inlet position, a broad distribution in the dust particles would be obtained at the first measurement position of 51.73 mm. As a result, some particles would collide with the parallel walls (hub and shroud) of the inlet section before the originally intended hub surface target. The additional particle rebound trajectories would add to an already difficulty problem of determining the mean particle trajectory positions. Therefore, accurate measurements of the particles trajectories, velocities and angles is impossible due to the increase in the number of particles trajectories and rebound situations. The dust feeder nozzle had to be versatile enough so that measurements at the different particle initial positions can be carried out without causing

stoppages. Since there are 3 different nozzle radial heights (initial particle positions) and 12 traverse positions (discussed later in Section 4.6), it is important to keep the 'turnaround' time as low as possible. The nozzle diameter must also be large enough so as to avoid blockages due to the accumulation of the dust in the nozzle, especially for the 15.0 um dust which tends to agglomerate.

Since all the measurements of the particles trajectories, velocities and angles depend on the performance of the nozzle, the above requirements had to be satisfied. The dust feeder nozzle (PLATE 4) used in the present studies was based on the flow injector principle, with an L-shaped bend so that one end can be inserted into the flow (at 50.0 mm) and the other end acts as an inlet for dust feeding. The nozzle end (inside the flowfield) tube is 2.0 mm in diameter. It is welded to a 5.0 mm diameter tube which makes up the stem of the dust feeder nozzle. The whole assembly was clamped at several positions, which allowed only vertical movements, and placed on a fixed metal-based table. Pre-marked positions on the stem of the nozzle, which represent the different nozzle heights, enable quick changes of the nozzle height for different initial particle positions.

The two methods of feeding dust particles are the fluidised bed and 10 ml burette depending on the particles sizes. Since the quartz and ballotini dust between 30 and 150 um behaves like fluid, a laboratory 10 ml burette (PLATE 4) was found to be most suitable form of feeding dust into the nozzle under the gravitational effect only. TABLE V shows the results of the dust feedrate and concentration obtained for the burette. In general, a consistency of ± 7.0 percent and concentration of less than 0.6 g/m^3 was achieved in the calibration tests (Section 4.4.3). This method of feeding dust particles was, however, unsuitable for the 15

um dust due their agglomeration properties. Instead, a pressurised fluidised bed (PLATE 5), designed for solid particles seeding of 0.5 um, was used. The fluidised bed has quoted consistency of ±10.0 percent. Since the fluidised bed is pressurised, the particle velocities at the nozzle end were more difficult to control but generally they tend to be higher when fed under gravitational effect. However, earlier in Section 3.3.2, the trajectories of the 15.0 um particles were found to be influenced mainly by the flow-field, hence, they would quickly adapt to the flow even with a higher initial exit velocities. These consistency and concentration of the dust particles are necessary in the laser anemometry measurements. Since solid particle seedings used in the measurement of flow velocities are generated either by atomisation or fluidisation methods [A.Melling, Ref.37, Durst et al, Ref.38], they have to satisfy the above conditions (i) and (ii). The 'Puldoulit A' fluidised bed [A.Mellings, Ref.37] has an output in the concentration of less 1.0 g/m^3, while the Rotating Brush Generator [Ref.38]' can delivered between 20 mg/hr and 4.0 kg/hr of dust particles. The Cyclone Aerosol Generator [Ref.37] claimed an accuracy of 6.0 percent of the mean concentration. Since all these methods of solid particles seeding are applicable for particles less than 1.0 um and, they satisfied conditions (i) and (ii), the above consistency and concentration was used as a guideline in the present studies where the particles were between 15 and 150 um in diameter. Therefore, it can be argued that consistency and concentration obtained in the calibration of the nozzle (TABLE V) also automatically satisfied condition (i) and (ii).

In summary, the dust feeder nozzle could delivered solid particles with a consistency in the feedrate of less than ±10.0 percent and concentration of less than 0.6 g/m^3.

4.4.3 Calibration Tests

Calibration tests were carried out for the following;

a) mass flowrate in the scavenge and engine pipes

b) dust flowrate and concentration

a) The mass flowrate in a pipe was obtained by a single hole total probe and 3 static pressure tappings in the pipe wall. For calculation purpose, B.S.1042 [Ref.39] recommends that the pipe should be sub-divided into a set of annular concentric passageways and a number of diametral traverses made with station points. These station points divide the passageway into two rings of equal cross-sectional area as shown in Figure 26. The traverses were made at a position 18 pipe diameters downstream of the transition ducts where the flow is regular and uniform. Instead of traversing 10 stations in each pipe, a total of 21 equally spaced stations were measured from which the 10 readings were taken. The calculated mass flows and discharge coefficients are shown in TABLE VI. The discharge coefficient is defined as the ratio of the actual to the theoretical mass flow. Figure 27 shows the measured total pressure traverse across the engine and scavenge pipe for different throttle settings. The calculated discharge coefficient for the engine and scavenge pipe flow is 0.89 and 0.86 respectively. Having obtained the discharge coefficients, the total probes were placed at the centre of the pipes which remains unchanged throughout the tests. Subsequent mass flow calculation will take into account of the discharge coefficients and to adjust for the daily change in the atmospheric condition using the non-dimensionalised form as follows;

$$M_{actual} = \frac{M_{measured}\sqrt{(T/288.0)}}{(P/760.0)}$$

where T and P is the atmospheric temperature (deg. Kelvin), and pressure (mmHg) respectively. All the tests were carried at the design engine flow condition of 1.0416 lb/s (equivalent to 12.5 lb/s in actual engine) and a scavenge flow of 0.2083 lb/s giving a bypass ratio of 20.0 percent.

b) the dust flowrate is defined as the amount of dust particles per second. The method of determining this mass flowrate is as follows;

i) an amount of dried dust is weighed and recorded and, transferred into the 10.0 ml burette
ii) at design flow condition, the dust particles was fed into the dust feeder nozzle which was placed at the axial position of 50.0 mm downstream of the inlet
iii) the start and end time was recorded as the dust was seeded into the flow

Since the dust particles properties (eg. density, diameter) were known, the particle flowrate for a particular size can then be calculated. The above procedure is repeated for all the particle sizes at the 3 radial heights (i.e. 105.5, 128.67, 151.8 mm). TABLE V shows the measured dust flowrate for different particle sizes and shapes.

The dust concentration can be defined as the amount of dust per unit volume of air. Since the total mass flow was 1.25 lb/s, the volume, the dust concentration (g/m^3) can then be calculated by dividing the dust flowrate by the total mass flow of air per second.

4.5 Aerodynamic Performance Tests

The computational flowfield (Section 3.2) is based on an inviscid, irrotational and incompressible flow. The results from the potential function contour plot (Figure 10) and the flow vectors (Figure 13) shows the areas with adverse velocities gradient. Flow separations could have occurred at these areas in the actual flowfield in the separator. Therefore, aerodynamic measurements were taken in the separator so that comparisons could be made with the predicted flowfield. The performance of the separator was assessed with three methods, they were;

i) Flow Visualisation Using Wool Tufts.

The wall static pressure tappings in the hub, shroud and splitter were used as station for the wool tufts. Figure 28 illustrates the positions of the wall static tappings at the mid-section of the separator. Wool tufts about 6 mm long were fixed to pieces of wires and inserted into these static holes. The wire extend about 2 mm from the wall surfaces into the flow as shown in PLATE 7. When the design flow condition had been reached, the behaviour of the wool tufts were photographed using a 35 mm camera. PLATE 7 to 12 show the near-wall flow pattern photographed at the mid-section of the separator. The near-wall flow patterns can then be drawn from these photographic evidences as shown in Figure 29.

ii) Wall Pressure Distribution Using Wall Static Tappings.

When the flow visualisation recording had been completed, the wool tufts were removed to be used for

pressure measurements. The static tappings were connected to a micromanometer via a scanivalve for pressures measurements less than 3000.0 mm of water. A mercury filled U-tube manometer was also used to record the static pressure at the critical flow areas where limit of the micromanometer had been exceeded. Figure 30a shows the wall pressure distribution along the hub, shroud and splitter surfaces. The near wall velocities were calculated from the pressure distribution assuming isentropic conditions;

$$\frac{P_0}{P_{static}} = \left[1 + \frac{\Upsilon-1}{2} M^2 \right]^{(\Upsilon/\Upsilon-1)}$$

where M is the flow Mach number and Υ is the ratio of specific heats. Figure 30b show the near wall velocity distribution calculated from the pressure distribution using the above equation.

iii) Measurement of the Flowfield Using Laser Anemometry (L2F).

The laser anemometer (Section 4.4.1) was used to measure the flow's absolute velocities and angles at the mid-section of the separator. The separator has two clear glass plates acting as side walls, allowing full optical access to the Laser Anemometer (L2F) as shown in PLATE 6. The traverse stations were obtained by taking the element's node points from a mid-section of the computational finite element mesh (Section 3.2) as shown in Figure 31. The first set of traverse stations starts at 51.73 mm (to coincide with the inlet plane of the computational model) and the last was at 332.23 mm

(just behind the leading edge of the splitter lip) giving a total of 461 traverse stations. However, not all traverse stations could be used as measurement point due to obstruction caused by the annular shape of the separator as shown in Figure 31.

Liquid seeding (PROPYLENE GLYCOL) particles of 0.5 um were generated with an atomiser [A.Melling, Ref.37] and introduced into the flow through a half inch bore tube. The tube was placed at about 15.0 cm from the bellmouth of the separator so as not to cause disturbance in the airstream entering the separator. Occasionally, the tube had to be manoeuvred so that sufficient liquid seedings entered the measurement points. Movement of the measuring probe volume was achieved by the X, Y and Z movement of the milling bed on which the laser assembly was mounted (Section 4.4.1). At each measurement point (station), a minimum of 3 angle settings were needed to provide sufficient information for flow analysis. The data accumulation and analysis was carried out interactively where the correlogram obtained from each angle setting was transferred directly to the minicomputer. Obstruction due the annular shape of the separator may optically prevent measurement near the shroud and underside of the splitter surfaces (Figure 31), however, there are other areas where no measurement can be made due to the excessive optical noise which 'clouded' the scattered light. Areas such as flow separation, boundary layers or background flare reflected by solid wall surfaces could all result in poor signal to noise ratio condition. The effect was experienced by obtaining correlograms which were not sensitive to the orientation of the laser beams. The flow velocities at these areas were assumed to have a small value for computational reasons (which will be explained later in the section). Figure 32 show the measured flow vectors

at the mid-section of the separator obtained from the laser anemometry technique. The velocities at the shroud and underside of the splitter surfaces (where there were no measurements) were taken to be equal to the measured velocities at the nearest adjacent traverse station. The reason for doing so was that the computation of the very small particle's trajectories (which were influenced mainly by the flowfield)may fail as a result of the interpolated velocity of zero at certain areas.

In summary for this section, the results from the measured flowfield will be discussed in the following section. The predicted flowfield will also be compared with experimental data.

4.5.1 Analysis of the Aerodynamic Measurement Results

The different techniques of assessing the aerodynamics performance were carried out earlier in the above section where three different sets of results were recorded. The results from the flow visualisation techniques which present the near-wall flow behaviour are shown in PLATE 7 to 12. The photographic evidences produced some interesting near-wall flow behaviours, they were;

i) low velocities flows at the shroud wall (orientation of the wool tufts), just downstream of the peak of the 'hump' as shown in PLATE 7,
ii) a stable vortex re-circulation at the base of the 'hump' of the hub as shown in PLATE 8,
iii) a flow separation at the hub wall just downstream of the peak of the 'hump' as shown in PLATE 9,
iv) a flow separation at the shroud wall just downstream of the leading edge of the splitter as shown in PLATE 10

to 12,

v) flow reversal region at the leading edge of the splitter lip as shown in PLATE 10 to 12.

These photographs (PLATE 7 to 12) show the deficiency in the computational model (Section 3.2) to predict an accurate flowfield based on the inviscid, irrotational and incompressible assumptions. It did, however, show that the areas with low velocities coincided with the separated flows discovered in the separator. The areas of high velocities flows were difficult to identify from the photographic results alone. Hence, detailed measurements using wall static tappings had revealed the near-wall pressure distribution as shown in Figure 30a. Figure 30b shows the near-wall velocities calculated from the pressure distributions on the hub, shroud and splitter surfaces. The following results were found;

a) Along the Hub Surface

There was a gradual increase in the pressure ratio from the first tapping position (38.0 mm) to the vortex region (between 165.0 and 180.0 mm, from PLATE 8) at the base of the 'hump' of the hub surface. The calculated velocities show a gradual decrease from 78.0 m/s at the first tapping position (38.0 mm) to 48.0 m/s at the vortex region, over a distance of about 140.0 mm. This was followed by a sharp decrease in the pressure ratio from the vortex region to the peak of the 'hump' of the hub. Over this distance of just 63.0 mm, the flow had accelerated from 48.0 m/s at vortex region to 147.0 m/s at the peak of 'hump' (at 241.0 mm downstream of the inlet section). This sudden acceleration in the flow was caused firstly, by the severe 'bending' of the flow due to the hub shape, secondly, by the decreasing flow volume passage and, thirdly, by the blockage effect of the vortex region

(Figure 29). At the peak of the 'hump', the flow volume passage increases, leading to an expansion in the flow. This sudden expansion coupled with a high mass flow turning into the engine core flow resulted in an adverse pressure gradient forming behind the 'hump' of the hub. As a result, a separation 'bubble' (PLATE 7,9) was formed on the hub surface, just downstream of the peak of the 'hump' (between 254.0 and 284.0 mm) where the flow velocity had reduced to 96.0 m/s. This separation 'bubble' as shown in Figure 29, reduces the flow passage into the engine core flow where 80 percent (1.0416 lb/s) of the total mass flow passes through. The effect of this blockage would be to cause high velocities in between this constriction followed by expansion in the flow due to an increase of the flow passage after the separation 'bubble'. The flow velocity was reduced to 87.0 m/s (at 284.0 mm) and, at the last tapping station (533.0 mm), the velocity was 108.0 m/s.

b) Along the Shroud Surface

The flow velocity measured at the first static tapping position (38.0 mm) along the shroud surface was the same as the hub surface, i.e. 78.0 m/s, which suggests a uniform flow at the inlet. However, at the first 'bend' (114.0 mm), on the shroud surface, there was a sharp decrease in the measured pressure ratio where the flow velocity was calculated to be 129.0 m/s. Although this was followed by sharp increase in the pressure ratio, just after the 'bend', there was no flow separation which must be due to the blockage caused by the vortex region. The flow velocity calculated at just behind this 'bend' was 96.0 m/s. The gradually increasing pressure ratios caused a further gradual decrease in the flow velocity to 48.0 m/s near the scavenge's exit plane at 533.0 mm. The low velocity flow in the scavenge was due to the low mass flow

of 0.2083 lb/s, in a relatively large flow passage, when compared to the mass flow of 1.0416 lb/s in the engine core flow. A separation in the flow was also found on the shroud surface (Figure 29) behind the leading edge of the splitter lip, which was moving between tapping 11 (at 316.0 mm) and tapping 13 (at 368.0 mm), as shown in PLATE 10 to 12.

c) On the Splitter Lip

Perhaps the areas with the greatest change in the pressure ratios (hence, velocities) can be found near the leading edge of the splitter lip. The measured pressure ratio (Figure 30a) had dropped sharply from the upperside, at tapping 7, to the underside of the splitter, at tapping 5 (Figure 29). Photographic evidence taken near this region (PLATE 10 to 12) shows a reversal in the flow from the upperside to the underside of the splitter. The calculated flow velocities (Figure 30b) at tappings 7 and 5 were 54.0 m/s and 198.0 m/s respectively, showing a sharp increase in the flow velocity on the underside of the splitter. This high velocity flow areas was due to the high mass flow of 1.0416 lb/s (as compared to 0.2083 lb/s in the scavenge section) into a relatively small flow passage between the splitter lip and the hub wall. Although the flow passage is geometrically small, it was the separation 'bubble' at the hub surface (Figure 29) which caused further restriction in the flow but, without which flow separation would have occurred on the underside of the splitter. As the flow passed through this constriction into a larger area, it began to diffuse and the calculated velocity was 108.0 m/s, which matches the hub wall velocity, suggesting a uniform velocity at the engine exit plane.

On the upperside of the splitter lip, a stagnation region had formed between tapping 7 and tapping 8 (Figure

30) as shown in PLATE 10 to 12. The flow velocities on the upperside of the splitter were generally low due to the low mass flow and a relatively large flow passage. The flow velocities in this area had remained fairly constant at 48.0 m/s which matches the calculated shroud wall velocity near the exit plane, again suggesting a uniform flow.

The experimental results from wall static tappings and photographs, show good agreement in the near-wall flow patterns at the hub, shroud and splitter surfaces. However, the detailed measurement of the flowfield with the laser anemometer had produced a better overall flow pattern at the mid-section of the separator as shown in Figure 32. In this figure, three distinct areas where no measurement could be made (as explained in Section 4.5) could be identified and corroborated with photographic results;

i) the vortex region (PLATE 8) at the base of the 'hump' of the hub,
ii) the flow separation 'bubble' (PLATE 9) behind the peak of the 'hump',
iii) stagnation region (PLATE 10 to 12) near the leading edge, on the upperside of the splitter lip.

The flow vectors (Figure 32) show a directional and uniform flow between the parallel walls of the inlet section. The average measured inlet velocity was 77.0 m/s (at 51.73 mm). While the flow on the shroudside had gained momentum towards the first 'bend' position (110.0 m/s), the flow on the hubside had slowed down towards the vortex region (50.0 m/s). As the flow negotiated the first 'bend' between the shroud and hub walls, the flow passage began to decrease toward the peak of the 'hump', causing an overall increase in the flow velocities. The flow on the hubside shows a greater rate of increase in the velocity magnitudes

from the vortex region (50.0 m/s) to the peak of the hub (142.0 m/s). On the shroudside, the flow shows a decrease in the velocity magnitude from the first 'bend' position (110.0 m/s) to the position of the peak (68.7 m/s). At the peak of the 'hump', the flow vectors on the hubside indicates a high velocity flow area with a changing flow directions toward the engine section. The flow on the shroudside, however, had not gained momentum and the flow directions continued towards the scavenge section. As the hubside flow negotiates the peak of the 'hump', it continued to maintain a high velocity with a severe change in the flow direction. Figure 32 shows clearly the blockages and restriction caused by the separation 'bubble' on the hub surfaces. The flow vectors at this constriction show high measured velocities. The reduction in the flow passage into the engine section also resulted in the high velocities on the underside of the splitter lip but without which flow separation would have occurred. Photographic result (PLATE 11) did not show any flow separation on the underside of the splitter. Down-stream of the separation 'bubble' the flow passage in-creases. While the flow on the splitterside maintained a high velocities, the flow on the hubside shows a decrease in the measured velocity magnitudes. The mass flow on the engine section was 1.0416 lb/s (80 % of the total inlet mass flow) and the mass flow on the scavenge was 0.2083 lb/s. The velocity vectors between the shroud and the splitter indicates a low velocity flow areas which was due to the low mass flow and a relatively large flow passage. A stag-nation region and flow reversal had formed on the upper-side of the splitter lip.

The experimental results obtained from the 3 different techniques had shown good agreement and critical areas had been identified in the separator flowfield. A further comparison was made between the measured flowfield (L2F and wall static tappings) and the predicted flowfield (inviscid)

at the mid-section of the separator. The comparisons were made at the traverse stations in the computational mesh described earlier in Section 3.2. The predicted flow vectors, shown in Figure 13, were superimposed with the measured flow vectors (Figure 32) to give the result in Figure 33. The near-wall velocities calculated from the wall static pressures were also compared with the predicted velocities at the hub, shroud and splitter as shown in Figure 34.

Figures 34 show that the overall predicted flow velocities were higher than the measured velocities. In fact, the average predicted inlet velocity at 51.73 mm was 95.0 m/s whereas the average measured velocity (L2F) was only 77.0m/s which gave an error of 23.3 percent.This error was due to the incorrect boundary conditions used as described in Section 3.2. This difference in the velocity magnitudes was also found in Figure 34 where the comparison was made at the wall surfaces. Hence, a re-comparison with the measured flowfield was made with a 'scaled' predicted flowfield. The scale factor was based on the ratio of the average measured inlet velocity to the average predicted inlet velocity. The re-comparison can be found in the following figures;

a) Figure 35 shows the re-comparison in the flow vectors,
b) Figure 36 shows the velocities contours in the predicted and measured flowfield,
c) Figure 37 shows the re-comparison in the near-wall velocities on the hub, shroud and splitter surface,
d) Figure 38 shows the re-comparison in the wall pressure distribution

Figure 35 to 38 show good agreement exists between the 'scaled' predicted and measured flowfield except at the areas with critical flows. The re-comparison of the flow vectors in Figure 35 show almost identical results in terms

of the velocity magnitudes and directions. Main areas of difference were;

i) vortex region on the hub
ii) separation 'bubble' on the hub
iii) stagnation region on the splitter lip

The measured flow velocities at the restricted flow passage between the hub and splitter was expectably higher than predicted values. The velocity contour plots shown in Figure 36 also exhibit good agreement in terms of the high and low velocities areas. A detail comparison was made between the measured wall velocities and pressure (from the laser techniques and wall static tappings) and the predicted results were shown in Figure 37 and 38.

In Figure 37, along the hub surface, the predicted near-wall velocities show good agreement with the measured results from the inlet section until about the position (126.0 mm) just upstream of the vortex region. The prediction deviates from measured result at the vortex region. However, downstream of this region (at 191.0 mm), the predicted velocities show good agreement with the measured velocities until the position (253.0 mm) where the separation 'bubble' region (254.0 to 284.0 mm) begins. Beyond this region, the predicted flow velocities were lower than the measured values.

Along the shroud surface, the predicted velocities were slightly lower than the measured velocities from the inlet to the position at about 165.0 mm, downstream of the first 'bend' on the shroud wall. The prediction begins to deviate from the measured velocities beyond this position of 165.0 mm position.

Perhaps, the greatest discrepancies in the comparison of the velocities and pressure ratio were in the splitter region.The measured near-wall velocities on the underside of the splitter are much higher than the predicted velocities

which was due to the blockage caused by the separation 'bubble'. On the upperside of the splitter, the predicted velocities were, again, much lower than the measured values. The failure of the prediction could be due to the separation 'bubble' and the insufficient number of finite elements (Figure 15) used at this critical flow area.

In Figure 37 and 38, the measured results from the wall static tappings were also compared with those obtained with the laser anemometer (L2F). In general, good agreement in the measured results exists between laser anemometry and wall static pressure tappings. Since laser anemometry provides no data at areas with disturbed flows such as the vortex or separation regions, they were taken from the measured results of the nearest adjacent traverse stations. As a result, the comparison at these regions along the hub surface shows a slight difference in the measured velocities as shown in Figure 37. Along the shroud and the underside of the splitter wall, again, since the near-wall velocities cannot .be obtained with the laser technique (due to wall curvature obstructions), the value from the nearest traverse station was taken. Hence, slight discrepancy was found mostly at the areas with high radius of curvatures. The area with the greatest discrepancy was at the underside of the splitter where the measured velocities from the laser technique were lower than that calculated from the wall static tappings.

In summary to this section, the following flow phenomena were found;

i) vortex region between 165.0 and 180.0 mm at the hub surface,
ii) separation 'bubble' between 254.0 and 284.0 mm at the hub surface,
iii) moving flow separation between 316.0 and 368.0 mm on the shroud surface,

iv) high velocities flow region at the peak of the 'hump' on the hub surface,
v) high reverse flow region at the leading edge of the splitter lip,
vi) high velocities flow at the first 'bend' on the shroud surface.

These flow phenomena would affect the measurement of the particle trajectories, velocities and angles in the next section. Hence, the traverse planes for these measurements would be placed so that their effects on the particle's behaviours could be investigated.

4.6 Particle Trajectories Measurement

4.6.1 Initial Measurement Conditions

The objectives of the present investigation have been discussed in Section 4.2. In order to achieve these objectives, dust particles were seeded into the flowfield of the separator at pre-defined locations. Subsequently, their trajectories, velocities and angles were measured with the laser anemometer. Later in Section 4.6.2, the method of measuring the particle trajectories at several traverse planes will be described. The method of measuring the particle velocities and angles at the mean particle trajectory using the same laser technique will be described in Section 4.6.3.

All the measurements were carried out on the mid-section of the separator at design flow condition (i.e. 1.0416 and 0.2083 lb/s in the engine and scavenge section respectively). The dust feeder nozzle end was placed at 50.0 mm downstream of the separator inlet and the heights were at 105.5 mm (20.0 %), 128.67 mm (50.0 %) and 151.8 mm (80.0 %)

as shown in Figure 39. The first measurement plane was at 51.73 mm downstream on the inlet section which coincided with the inlet plane of the computational model (Section 4.4.2) and, the last plane was at 308.73 mm, just upstream of the leading edge of the splitter lip. Figure 39 and 40 shows all the traverse planes used, their axial positions were;

1) z_1 = 51.73 mm
2) z_2 = 81.73 mm
3) z_3 = 124.23 mm
4) z_4 = 151.23 mm
5) z_5 = 170.23 mm
6) z_6 = 190.98 mm
7) z_7 = 208.98 mm
8) z_8 = 224.98 mm
9) z_9 = 243.98 mm
10) z_{10} = 268.23 mm
11) z_{11} = 285.73 mm
12) z_{12} = 308.73 mm

These positions were chosen as a result of the analysis of the aerodynamic measurements found on the separator earlier in Section 4.5.1. Traverse plane 3 and 9 corresponded to the areas with high velocity flow at the shroud and hub surfaces respectively. Traverse plane 12 corresponds to the areas with low velocity flow at the shroud wall and high velocity flow reversal at the leading edge of the splitter lip. Traverse plane 5 lies in the region of vortex re-circulation at the base of the 'hump' of the hub. Traverse plane 10 and 11 lies in the separation 'bubble' at the hub surface. The particle trajectory measurements at these planes were used to investigate the effect of the restitution ratios, drag coefficient and viscosity on the particles behaviour. All the traverse planes were used to determine the particle trajectories, velocities and angles.

The dust particle materials (Section 4.3) used were quartz (non-spherical) and ballotini (spherical) with densities of 2650.0 and 2950.0 kg/m^3 respectively. The particle sizes (Section 4.3) for both quartz and ballotini were between 15.0 and 150.0 um in diameter. Some of the initial conditions had been discussed earlier in Section 3.3. In the present analysis, all the quartz and ballotini particles sizes were seeded at the mid-height location of 128.67 mm. The 15.0, 30.0 and 100.0 um dust (quartz and ballotini) were seeded at the upper height of 151.8 mm and lower height of 105.5 mm. The dust feeder nozzle had been calibrated to output a dust concentration of less than 1.0 g/m^3 and a consistency in the feedrate of less than $\pm$ 10.0 percent. The two methods of delivering the dust particles were;

1) a 10 ml laboratory burette was used for particle size between 30.0 and 150.0 um which were fed under gravitational effect,
2) a pressurised fluidised bed was used for particles of 15.0 um where the initial particle velocities were difficult to control.

These were the initial measurement conditions used in the following test.

4.6.2 Particles Concentration Measurements

In this section, the main task is the determination of the mean particle trajectory positions for the quartz and ballotini dust particle between 15.0 and 150.0 um, at the three nozzle heights. The mean particle trajectory positions at the 12 traverse planes would give an overall picture of the particle's flight paths at the mid-section of the separator. The mean position is determined from the particle

concentration curve measured with the laser anemometer. Since the basic principle of the laser anemometry (Section 4.4.1) is the detection of scattered lights from the particles, the strength of the reflected signal (proportional to the number of particles passing through the 2 beams) would provide the information on the dust concentration at the measuring volume. Hence, at each traverse plane, there were a number of traverse points (or stations) equally spaced at 3.175 mm apart. This spacing (equivalent to 1 revolution on the vertical spindle of the milling bed) was found to be sufficiently accurate bearing in mind of the inevitable 'spread' in the particle distribution normal to it's trajectory paths and the large number of traverse points involved. Furthermore, in the measurement of the particle rebound trajectories, a reduced spacing would not necessary give better resolution due to an even broader particle distribution.

Figure 39 shows the traverse points for each particle size at three nozzle heights. At each measurement point, the reading from Channel A (corresponding to the number of particles passing through the measuring volume) of the correlator was recorded after a period of sampling time. The number of readings and length of sampling time required depended on the quality of the readings from the correlator. For example, 3 to 5 readings, each lasting 3 to 5 seconds at each point were usually sufficient when an acceptable consistency in the readings had been obtained. Since the dust nozzle (Section 4.4.2) can output a fairly consistent amount of dust particles, the traverse points which lie in the trajectory paths (before the first impact areas) usually have a consistent number of particles passes through them. However, in certain areas (where multiple particles impaction with the wall exist), a consistency in the readings can be difficult to obtain. Therefore, a greater number of readings,each lasting a longer period of time,were needed. Hence, at these areas, usually 3 to 12 readings,

each lasting 5 to 8 seconds at each point were needed. In the test, the last three traverse planes, plane 10, 11 and 12, were found to be the most difficult measurement areas due to the large number of particles impacting the shroud wall at different angles of attack and reflected off with different rebound angles.

Before the particle concentration measurements were taken the noise from the background flare (light reflected from the glass plates or surrounding optical sources) was determined at all the points, in each plane, without any dust particles. The same measurement were made with dust particles and the signal(scattered light from the particles) was recorded. Hence, the particle concentration, at a particular point,was calculated by subtracting the background noise from the reflected signal (Channel A) by the particles.

The first impact area occurred at the hub surface and all subsequent impacts occurred at the shroud surface, where measurements close the wall could not be obtained due to the obstruction of the annular separator. The procedure for the particle concentration measurements were as follows;

1) Align the laser anemometer and set the datum point to be on the surface of the hub at the first traverse plane position (51.73 mm), at the mid-section of the separator,
2) record the corrected engine and scavenge mass flow at design flow condition,
3) set the nozzle at the appropriate height and axial position (50.0 mm),
4) before releasing dust into the nozzle, the noise from the background flare was recorded for all the traverse points at the first plane,
5) start sampling at the first point as the dust was released into the flow. The readings were recorded from Channel A and repeated at least 3 times depending on the quality of the signal. This was repeated until the last point (nearest to the wall edge) on the first plane was

reached,

6) the measuring volume was moved to the next traverse plane and step (4) to (5) were repeated until the last traverse plane.
7) The whole procedure was repeated at the next nozzle height position.

The particle concentration at each traverse point was obtained by subtracting the averaged background noise from the averaged particle's reflected signal. The combined particle concentrations at all the points gave the distribution curve at each traverse plane. Hence, the combined particle concentration distributed curves from all the traverse planes would give an overall picture of the particle trajectories. The above procedure was repeated for both quartz and ballotini dust for the different particle sizes. The results are shown in Figure 41 to 54 which will be discussed later in Section 4.8.

4.6.3 Particle Velocities and Angles Measurement

The dust particle concentration measurement (from Section 4.6.2) gave an overall picture of the particle trajectories for different initial conditions. The mean particle trajectory positions could then be obtained from these distribution curves. Hence, the absolute particle velocities and angles could be measured at these mean positions using the laser anemometry. The same principle of the laser anemometry as applied in the measurement of the flow velocities and angles in Section 4.5 was used to measure the velocities and angles of the particles. The only difference in this case was that the particles were comparatively larger i.e. greater than 15.0 um, instead of the 0.5 um used for measuring flow velocities.

The main task in this section was the measurement of the particle velocities and angles at the mean particle trajectory positions. The mean particle trajectory position at each traverse plane was taken to be the point with the highest calculated particle concentration from each distribution curve. Therefore, there are 12 mean particle trajectory positions for each particle size seeded at each initial nozzle height. At each mean position, the particle's absolute velocities and angles were measured using the laser anemometer. Two measurements were made at each position to ensure repeatability in both the velocities and angles. The repeatability for ballotini (spherical) particles were between 0.4 and 3.4 percent. For the quartz (non-spherical) particles, the repeatability were between 0.4 and 5.8 percent. However, such repeatability cannot be obtained for certain dust sizes or mean position for these reasons;

i) excessive noise due to background flare [Mohsen, Ref.34] from the wall surfaces. Some mean positions might be too close to the curvature of the wall edge especially at the shroud wall,
ii) the poor quality of the correlogram caused by scattered light from the particles at different angles of approach to the measuring volume. The randomness of the particle rebound angles at the shroud wall, especially for the larger particles, makes analysis difficult.

The effect of (i) and (ii), above, was a poor signal to noise ratio which could be conditioned and amplified to obtain a better signal for analysis. The procedure for the measurement of the particle's absolute velocities and angles were as follows;

1) Align the laser so that the measuring volume is at the mid-section of the separator,
2) set the flow at design condition,

3) set the nozzle to the appropriate height and axial position,
4) released the dried dust into the flow,
5) move the measuring volume to the mean trajectory position
6) adjust the sampling time and orientate the 2 beams until a good quality correlogram (observed from the oscilloscope) is obtained,
7) transfer the correlogram from the correlator to the on-line minicomputer and repeat with different angle setting,
8) when 3 or 4 readings had been obtained, analysis was carried out to calculate the particle velocity and angle,
9) particle velocity and angle measurements were repeated twice to ensure repeatability,
10) step (5) to (9) were repeated at all the mean positions for each particle size.

Figure 41 to 54 show the measured particle's absolute velocities and angles for the quartz and ballotini dust with sizes between 15.0 and 150.0 um.

4.7 Dust Ingestion Tests

The usual method of assessing a separator's performance is by measuring it's separation efficiency under certain test conditions which are applicable for a particular particle size distribution. The standard dust used is the AC Coarse (0 to 200 um) and MIL-SPEC (0 to 1000 um) sand. The usual method of determining the separation efficiency is by feeding a known amount of dust, in the form of a dust cloud, at the separator's inlet. The amount of dust entering the engine and scavenge section were collected by some form of filter layer. Hence, the separation efficiency of the separator is defined as the ratio of the amount of dust separated to the total amount of dust seeded into the flow.

In the present studies, the separation efficiency of the separator was measured for a particular dust size, at design flow condition. The dust particles were seeded at the three nozzle height positions which had been defined in the earlier section. A known equal amount of dust was seeded into the inlet section at each nozzle height. The dust particles were then collected with a pair of collector bags placed on the pipes ends in the vacuum tank. The top section of the vacuum tank is removable to allow access to these bags (Figure 17). The canvas bags were dried for an hour in an oven (set at 40.0 degree Centigrade) before and after each test so that moisture could be evaporated. And, at the end of each test, the engine and scavenge pipes were thoroughly cleaned with a pressurised air along their lengths to ensure no dust had accumulated in the pipes. The procedure for measuring the separation efficiency for a particular dust size was as follows;

1) dry and weigh three equal amount of dust,
2) dry and weigh the two canvas collector bags. Each bag was placed over the pipe end in the vacuum tank,
3) set the flow at the design condition,
4) set the nozzle to the appropriate height and axial position,
5) release the dust into the flow and, record dust flowrate and concentration,
6) step 4 and 5 was repeated for an equal amount dust particles at the next nozzle height,
7) the test was stopped when all the dust was seeded into the flow at the three nozzle heights,
8) the engine and scavenge pipes were cleaned with high pressure jet of air before the two collector bags were removed and left to dry for an hour,
9) the canvas bag and the dust were weighed and recorded

The separation efficiency for the different particle sizes

was calculated (from the Chapter 1) based on both the U.S.A. and U.K. definition. The results are shown in TABLE VII. A discussion of the results will be included later in Chapter 5.

4.8 Analysis of the Experimental Results

The experimental results from the aerodynamic measurements on the separator had revealed some interesting flow phenomenons which could not be predicted using the inviscid model. These flow phenomena (Figure 29) had been discussed in detail earlier in Section 4.5.1, they were;

i) vortex at the base of the 'hump' on the hub between 165.0 and 180.0 mm,
ii) separation 'bubble' behind the peak of the 'hump' between 254.0 and 284.0 mm,
iii) a moving flow separation on the shroud wall, between 316.0 and 368.0 mm,
iv) a stagnation region and flow reversal on the upperside of leading edge of the splitter lip.

The areas with high velocity flows (Figure 40) were;

i) at the first 'bend' on the shroud surface where the measured flow velocity was 129.0 m/s,
ii) at the peak of the 'hump' on the hub where the measured flow velocity was 147.0 m/s,
iii) near the leading edge, on the underside the splitter where the measured flow velocity was 198.0 m/s.

Although the inviscid flowfield model (Section 3.2) predicted a higher than measured overall velocities, it did, however, give reasonable agreement with experimental results (Section 4.5.1). The areas with high velocity flows had been

predicted and, the areas with low velocity correspond to the above flow phenomena.

The results for the particle concentration, particle velocities and angles measurements were discussed in the context of the measured flowfield. Later in Chapter 5, the particle trajectories results will be compared with the measured results. Figure 39 and 40 show the arrangement of the traverse planes for the measurement of the particle concentration distribution. The first and last traverse planes were at 51.73 and 308.73 mm respectively. The mean particle trajectory position was then determined from each distribution curve for the measurement of the particle's velocity and angle. Three different dust feeder nozzle heights of 105.5 (20.0%), 128.67 (50.0%) and 151.8 (80.0%) were used for these measurement. Particles with sizes of 15.0, 30.0 and 100.0 um were seeded at the extreme nozzle heights i.e. at 105.5 and 151.8 mm. However, all the particle sizes were used at the mid-height position of 128.67 mm. The nozzle end was placed at 50.0 mm downstream of the inlet of the separator. The results from the particle trajectories measurements (Section 4.6) have been arranged to present the results for ballotini, particles before the quartz particles. For each particle material, the results have been arranged as follows;

i) at nozzle height of 151.8 mm, the particle concentration plots have been arranged according to the particle sizes;

   a) 15.0 um
   b) 30.0 um
   c) 100.0 um

These are followed by the measured particle's absolute velocities angles at the mean trajectory positions.

ii) at nozzle mid-height of 128.67 mm, particle concentration plots, followed by particle's absolute velocities and angles plots, have been arranged according the following particle sizes;

a) 15.0 um
b) 30.0 um
c) 50.0 um
d) 100.0 um
e) 150.0 um

iii) at nozzle height of 105.5 mm, the arrangement is the same to that as (i) above.

4.8.1 Experimental Discussion for Ballotini (Spherical) Particles

The measured particle trajectories, velocities and angles for the ballotini particles are shown in Figure 41 to 47. The results have been arranged according to the nozzle heights as follows;

i) Figure 41 to 42 were the results for particles seeded at the nozzle height of 151.8 mm (80.0%),
ii) Figure 43 to 45 were the results for particles seeded at the nozzle height of 128.67 mm (50.0%),
iii) Figure 46 to 47 were the results for particles seeded at the nozzle height of 105.5 mm (20.0%)

The measured particle concentration plots in Figure 41 show three sets of distribution curves for the 15.0, 30.0 and 100.0 um particles respectively. In this figure, several points were noted;

i) all the particle sizes had the primary (or first impaction) with the hub surface
ii) the bulk of all particles of each size was collected in the scavenge,
iii) the 100.0 um particles had the widest distribution curves along the trajectory paths. On impaction, they also had broad reflected distribution,
iv) the 15.0 um particles seem to have a significant amount of dust entering the engine section.

The results for the 100.0 um particle show some dust entering the engine flow probably due to the particles reflected from the shroud wall. However, the majority of the dust particles had migrated into the scavenge flow section. The measured particle concentration at traverse plane 8, for the 15.0 um particle (Figure 41a) shows a broad distribution in the reflected particle trajectories from the hub surface. As a result, a significant amount of dust was entrained into the region with high velocity flows (Figure 40) at the peak of the 'hump' of the hub. In the analysis of the 15.0 um particle's trajectories, in Section 3.3.2, it was found that their trajectories were mainly influenced by the flowfield. Consequently, the reflected dust on the hubside (at traverse plane 8) was given an extra momentum by the high velocity flows whereas the dust on the shroudside was affected by a relatively low velocity flows. As a result, the particle concentration curves at traverse plane 9 and 10 show a twin 'peak' profiles. Beyond traverse plane 12 (308.73 mm), some dust particles might have interacted with the moving separated flow on the shroud wall (between 316.0 and 368.0 mm) or reflected into the flow reversal region on the splitter lip and, consequently, drawn into the engine core flow. This possibility was supported by earlier explanation which shows that their trajectories were influenced mainly by the aerodynamic drag force of the flow. Hence, the trajectories of the smaller particle tends to follow the

flowfield. However, as the particle size increases, the influence of the aerodynamic drag force decreases as the inertia force becomes dominant. This shift in role from the drag to inertia force effect could be observed by the increase in the particle rebound angles at traverse plane 6 to 8 as the particle size increases from 15.0 um (Figure 41a) to 100.0 um (Figure 41c). As the particle size increased from 15.0 to 30.0 um, the rebound angle, typified by the broad distributed curve shifted from plane 8 to 7 as shown in Figure 41a and 41b. For the 100.0 um particles, the rebound angles, typified by the broad distribution curve, shifted from plane 7 for the 30.0 um to plane 6 for the 100.0 um particle. At plane 6, the reflected particle trajectories of the 100.0 um were superimposed with the main particle trajectories to give a characteristic 'peak' and 'flat' distribution curve. The broad distributed curve at plane 8 for the 15.0 um particle has becomes a well defined curve for the 100.0 um particle at the same plane.

The 30.0 um particle (Figure 41b) shows that subsequent impacts occurred at the shroud surfaces from traverse plane 6 onwards which was well upstream of the peak of the hub. The measured distribution curves between plane 8 and 12 exhibit sharp peaks which are biased towards the shroud wall.

As for the 100.0 um (Figure 41c), the main second impact region occurred at the shroud wall between plane 5 and 6 which, again, was well upstream of the peak of the hub. The particle concentration curves have well defined peaks from plane 7 to 12 which show that the main reflected particle trajectories were away from the shroud wall in contrast to the 30.0 um particle. Since their trajectories are 'ballistic' in nature, some particles on impact with the shroud wall may be deflected towards the hubside of the separator. This was observed by the small number of particles recorded between planes 10 and 12 towards the hubside.

The mean particle positions (determined from the peaks

in each particle concentration curve), particle's absolute velocities and angles are shown in Figure 42. The results for all the particles sizes were plotted on the same axes for comparison purposes, In this figure, the following points were noted;

i) the 15.0 um particle has the highest overall velocities and angles except at the last traverse position. They also have the highest initial velocities,
ii) the mean trajectory positions for all particle sizes are similar before the first impacts with the hub wall

The high initial velocity for the 15.0 um dust is due to the high energy imparted by the pressurised, fluidised bed and not as a result of the flow velocity in the vicinity. The initial particle velocities for the 15.0, 30.0 and 100.0 um particles is 76.0, 20.0, 15.0 m/s respectively. The 30.0 and 100.0 um particles were fed under gravitational effect, hence the lower initial velocities.

The effect of the aerodynamic drag on the 15.0 um particles can be seen by the curved trajectory of the mean positions and steady rate of change in the particles angles. The measured particle velocities show a high measured particle velocity at position 8, at the peak of the 'hump' of the hub which was followed by a decrease at positions 9 to 12, where the flow velocities is comparatively lower. The negative measured particle angle at the last traverse position (12) shows a downward trend (from the horizontal) in the particle trajectory direction. At mean position 7, the high measured particle velocity and angle could be a result of the main trajectories or the reflected trajectories. These will be compared with predicted trajectories later in Chapter 5. At mean position 6, just before the initial impact with the hub, the high measured trajectory angle meant the angle of attack with the hub was low.

The measured particle velocities for the 30.0 um dust initially show a steady increase (position 1 to 6) before impaction with the hub surface. The particle impacted the hub between traverse plane 6 and 7. At mean position 7, the high velocity and angle were from the main particle trajectories as shown in Figure 41b. The measured rebound particle angles (between position 8 and 10) show a (positive) upward direction in the particle trajectories and a decrease in the velocities which means, either the measured particle angles are the result of the particle reflected from the hub surface, or the particle reflected from the secondary impacts with the shroud wall. And at mean position 11 and 12, the particle trajectory angles were in the (negative) downward direction which suggests that their positions might be in the path of the reflected particle trajectories. At mean position 6, the particle had impacted the wall with an angle of attack higher than the 15.0 um particle since the trajectory angle was lower. The mean trajectory positions, velocities and angles will be compared with predicted results and will discussed later in Chapter 5.

As in the 30.0 um particle, the 100.0 um particle shows a steady increase and decrease in it's velocities before and after impacting the hub. However, contrary to the 30.0 um dust, the position of impacts are much more clearly defined as shown in Figure 41c. The first main impact region is on the hub surface between plane 6 and 7, and the second main impact region is on the shroud surface between plane 5 and 6.Hence, the measured particle velocities and angles between mean position 8 and 12 (Figure 42 and 41c) are a result of the secondary impacts with the shroud surface. The measured particle angles after an impaction with the shroud surface (between 8 and 12) were in the upward (positive) direction. At mean position 6, the particle had the lowest trajectory angle, hence a high angle of attack with the hub. Again, the measured trajectories, velocities and angles will be

compared with predicted results in Chapter 5.

The measured particle concentration curves for the ballotini particles between 15.0 and 150.0 um, seeded at the mid-height nozzle position of 128.67 mm are shown in Figure 43 and 44. In these figures, the following points were noted;

i) all the particle sizes have the initial impact region on the hub wall,
ii) the bulk of all particles of each size was collected in the scavenge,
iii) large particles have a broader distributed particle concentration along their trajectory path

The measured particle concentration curves for the 15.0 um dust (Figure 43a) show a low rebound angles, typified by the bias in the distributed curve at traverse plane 6, toward the hub surface. The subsequent impacts region on the shroud surface occurred between traverse plane 7 and 12. The bias in the distributed curves between plane 10 and 12 towards the shroud wall, show that the reflected particle trajectories (from the shroud surface) were close to the wall where there are no measurements (due to obstruction of the wall edge). A small amount of dust (less than that seeded at the upper nozzle height position) can be seen entering the engine flow from the flow reversal region.

As the particle sizes increases to 30.0 um (Figure 43b), the rebound angle also increases as observed in the particle concentration curve at plane 7. The broad distribution curve at plane 7 for the 15.0 um particle (Figure 43a) had become the curve with a bias towards the shroudside for the 30.0 um particle.

These changes can also be seen in Figure 43c when the particle size increases further to 50.0 um. In this figure, a heavy concentration of particles had reflected off the hub

surface towards the shroud surface typified by the 'flat' portion of the distributed curve at plane 5. At plane 6, a small 'peak' had formed on the shroudside of the distribution curve. This 'peak', at plane 6, became well defined as the particle sizes increase further to 100.0 and 150.0 um as shown in Figure 44d and 44e respectively. The increase in the rebound angle as particle size increase can be observed in the distribution curve at plane 5. The 'flat' portion of the distributed curve, toward the shroudside, for the 50.0 um (Figure 43c) and 100.0 um (Figure 43d) had developed into a 'peak' for the 150.0 um particles. In fact, the particle concentration at plane 5 had three distinct shapes, firstly, there was a sharp 'peak' depicting the main particle trajectories before impact with the hub, secondly, there was a middle 'flat' portion depicting the reflected particle trajectories after an impact with the hub wall (toward the shroudside), and finally, a 'peak' on the shroudside of the curve depicting reflected particles from the shroud wall. The high rebound angles of the 150.0 um particles can also be observed in the distributed curve at plane 4 towards the shroudside. A shift in the reflected particle trajectories, away from the shroud wall, can be observed in the particle concentration curves between plane 7 and 12 from 15.0 to 150.0 um in diameters. The 30.0 um particle' second impact region on the shroud occurred between plane 5 and 6 while the particles between 50.0 and 150.0 um have second impact region between plane 4 and 5. These second impact region were well upstream of the peak of the hub.

The mean particle trajectory positions, particle velocities and angles, for all the particle sizes are shown in Figure 45. In this figure, the mean particle trajectory positions for all the particle sizes have similar positions (mean position 1 to 6) before an impaction with the hub surface. The mean positions 7 to 12 show the shift in the

reflected particle trajectories away from the shroud wall as the particle sizes increases from 15.0 to 150.0 um.

The measured particles velocities for all particle sizes except the 15.0 um, exhibit similar trend. The 15.0 um particles has a different form of velocity and angle curves because, firstly, their trajectories are governed mainly by the aerodynamic drag force and, secondly, the secondary impact regions (between plane 7 and 12) are different to that of the larger particle (between plane 4 to 6). The measured trajectory angles at the last two position, were in the downward (negative) direction which was most probably due to the reflected particles from the shroud wall.

For the particles between 30.0 and 150.0 um, there was a steady increase in their velocities before the first impacts with the hub surface and after further impaction with the shroud surface. The measured particles angles for particle between 30.0 and 150.0 um have comparatively 'shallow' reflected trajectory angles as compared to those measured for the 15.0 um particles. At mean position 5, all the particles had a low angle of approach to the hub wall, hence a high angle of attack with the hub wall.

The initial particle velocities for the 15.0, 30.0, 50.0, 100.0, and 150.0 um are 75.0, 19.0, 14.0, 11.0 and 10.0 m/s respectively. A comparison with the predicted particle trajectories, velocities and angles will be discussed later in Chapter 5.

Perhaps the most interesting results can be found in the particles trajectories for the particle seeded at the lower nozzle height position of 105.5 mm as shown in Figure 46, where traverse plane 5 lies in the vortex re-circulation region. The three different particles sizes 15.0 ,30.0 and 100.0 um seeded at this nozzle height, gave three different forms of distributed curves.

The centrifuging effect of the vortex forced the trajectories of the 15.0 um particles (Figure 46a) towards

the hub wall typified by the bias toward the hubside in the measured concentration curves at traverse plane 6 to 8. At traverse plane 8, near the peak of the 'hump' of the hub, the particles were given extra momentum by the high velocity flow. Hence, the well defined distributed curves at traverse plane 9 to 11. The main impact region occurred at the hub and the second impact region on the shroud wall occurred at between plane 10 and 12. At plane 12, a significant number of particles had entered into the engine flow via the reverse flow region.

The centrifuging effect on the 30.0 um particles (Figure 46b), however, had a different form to the 15.0 um particles. Contrary to the 15.0 um particles, the trajectories of the 30.0 um particles were dispersed by the vortex as shown by the broad distributed curves at plane 5 to 7. The curves show a bias toward the hubside at traverse plane 5 and a bias toward the shroudside from traverse plane 6 to 9. Hence, a high proportion of the dust had collisions with the shroud wall, between plane 6 to 9, with high angles of attack (with subsequent impact at between plane 9 and 12). Therefore, some dust particles could have been reflected into the engine core flow, as shown by the distribution curves at plane 10, on the hubside. At plane 12, a significant number of particle had also entered the engine flow which could be due to reflected particle and/or the reverse flow effect.

In the case of the 100.0 um particles, the concentration curves (Figure 46c) are different to those obtained for the 15.0 or 30.0 um dust. The high rebound angles from the hub wall,typified by distributed curves at plane 4 and 5 show the little effect of the vortex re-circulation had on the rebound trajectories. The second impact on the shroud wall occurred at between plane 3 and 4 and subsequent impact region seem to occur at between plane 7 and 12. The particle concentration curve at plane 6 show a strong bias toward the shroud surface (as opposed to that for the 15.0 or 30.0 um)

which was due to the rebound particles from the shroud wall. A significant number of dust particles had also migrated into the engine core flow probably due to the reflected particles from the shroud wall.

The measured particle velocities and angles at the mean particle trajectory positions are shown in Figure 47. Since the particles were seeded into an areas of decreasing flow velocity (Section 4.5.1), the 15.0 um particles, being mainly influenced by the aerodynamic drag force, show a decrease in the measured velocities from 84.0 m/s (position 1) to 66.0 m/s (position 5) just before an impaction with the hub surface.

The 30.0 and 100.0 um particle, however, due to the inertia, show increasing particle velocities from 20.0 m/s and 12.0 m/s (position 1) to 47.0 m/s and 30.0 m/s (position 5) respectively. The mean particle trajectory positions for all the particles sizes exhibited similar trajectories behaviour before the initial impact with the hub surface. The low trajectory angle at mean position 5 meant a high angle of attack with the hub wall for all particle sizes. The subsequent trajectory positions after impaction were different for the three particle sizes. The 15.0 um particle reflected mean trajectory positions show a bias toward the hub side while the 30.0 um particle were bias toward the shroud side. The 100.0 um particle had a different second impact region, hence, a different reflected trajectory positions.

The particle trajectory angles for the 15.0 and 30.0 um particle (or rebound angles) after the impaction with the hub surface, at traverse position 6, was measured to be 60.0 degrees. The particle velocities at that position were 50.0 m/s for both 15.0 and 30.0 um dust. The velocity of the 15.0 um particles continued to increase to a maximum at mean position 9, at the high flow velocity areas, while it's trajectory angle is decreasing. After position 9, the

particle velocity begun to decrease rapidly with a decreasing particle angle. The behaviour of the 15.0 um particle after the impaction with the hub surface (from position 6 onward), was due to the particle's tendency to follow the flowfield. Hence, between mean position 9 and 12, the particle seemed to follow the 'turning' flowfield but 'lag' behind the flow streamlines due it's relatively small inertia.

The 30.0 um particles, after the initial impact with the hub, also show an increasing velocity at high trajectory angles until the mean position 9 (close to the shroud wall), where a sharp drop in velocity and angle was recorded probably due to an impaction with the shroud wall. The continued drop in the trajectory angles and fairly constant velocities from mean position 9 to 12 suggested that the particles measured at these positions had undergone an earlier impaction with the shroud wall probably before plane 9.

The 100.0 um particles, after the impaction with the shroud wall, between plane 3 and 4 (Figure 46c), continued in their trajectories with increasing velocities and decreasing trajectory angles until the last mean position where there was a drop in both velocity and angle. The downward (negative) direction of the particle trajectory suggested that an earlier impaction had taken place.The particles trajectories, velocities and angles will be compared with the prediction later in Chapter 5.

In summary, the following were found in the trajectories of the ballotini particles;

i) the influence of the aerodynamic drag force on the particle trajectories increases as the particle sizes decreases. The smallest particles (15.0 um) have the highest overall velocities and angles, and their trajectories are much more affected by the flowfield,

ii) the influence of the inertia force on the particle trajectories increases as the particle size increases. The position of the particle's secondary and subsequent impact locations depends on the particle size and on the influence of the drag force,

iii) the vortex re-circulation affects (seen at the base of the hub,PLATE 8) mainly the trajectories of the 15.0 and 30.0 um particles while having very little effect on the 100.0 um particles.

iv) the vortex re-circulation at the base of the hub seem to be the main cause for the high proportion of dust entering the engine flow engine.

4.8.2 Experimental Discussion for Quartz (Non-Spherical) Particles

The measured particle trajectories, velocities and angles are shown in Figure 48 to 54. The results for the particles at the three nozzle heights were arranged as follows;

i) Figure 48 to 49 were the results for particles seeded at the nozzle height of 151.8 mm (80.0%),

ii) Figure 50 to 52 were the results for particles seeded at the nozzle height of 128.67 mm (50.0%),

iii) Figure 53 to 54 were the results for particles seeded at the nozzle height of 105.5 mm (20.0%)

The properties of the quartz particles differ from the ballotini particles in their chemical compositions, shapes and density.The quartz particles are non-spherical in shape and have a density of 2650.0 kg/m^3. The ballotini particle have a greater density of 2950.0 kg/m^3. Hence, the effect of the drag force would be expected to be greater for quartz

particles due to the lower density (inertia) and irregular shape. The restitution ratios (Section 2.2.3) for the quartz are also different to the ballotini.

The measured particle concentration for the 15.0, 30.0 and 100.0 um particles seeded at the upper position is shown in Figure 48. Several points were noted;

i) all the particles have most of their dust in the scavenge flow section and a small amount of dust entering the engine core flow,
ii) the larger particles have a wider 'spread' in the particle concentration curves along their trajectory path.

The particle concentration curves for the 15.0 um particle in Figure 48a shows that most of the dust did not have an initial collision with the hub surface, contrary to the (15 um) ballotini particle. Since there was no particle interaction with the hub surface, the distribution curves at all the traverse planes, except the last plane, have well defined curves. The particles have impaction with the shroud surface between plane 11 and 12. At traverse plane 8 and 9, no sign of an impact with the hub was evident (usually shown by the broad distribution at the planes), hence,all the dust was under the influence of the flow. At the last traverse plane,the effect of the moving flow separation on the shroud wall (between 316.0 and 368.0 mm) could have resulted in some dust entering the engine core flow via the reverse flow region.

As the particle size was increases to 30.0 um,the inertia forces began to take effect on the particle trajectories. The measured particle concentration, shown in Figure 48b, show a collision with the hub surface between plane 6 and 7. As a result, at plane 8, the reflected particles came under the effect of two different flow velocities, the high flow velocity on the hubside and the relatively low velocity flow

on the shroudside. The measured particle concentration curves at plane 9 and 10 have twin peaks, one due to the effect of the high velocity flow on the hubside, and the other due to the inertia of the reflected particles. The 30.0 um particles have a second impact region starting from between traverse planes 8 and 9. And subsequent impact on the shroud wall occurred at between plane 10 and 12. Some of the particles entering the engine flow section could be due to the reflection from the shroud wall, and some could be due to flowfield effect at the reverse flow region, on the upperside of the splitter lip.

As the particle size was increased further to 100.0 um in Figure 48c, the inertia forces began to take effect. The broad distribution in the concentration curves at plane 7 and 8 show the wide rebound angles of the larger particles. These particles have the second impact region starting from between traverse plane 7 and 8. And subsequent impact on the shroud wall occurred between planes 9 and 12. Again, some of the dust particles reflected from the shroud wall had entered the engine core flow. The small number of particles entering the engine flow section at plane 12, seem to be as a result of particles reflected from the shroud rather than due to flowfield effect.

The measured particle absolute velocities and angles at the mean particle position are shown in Figure 49. In this figure, the mean trajectory of the 15.0 um particles seem to follow the flowfield,exhibiting curved trajectory paths with no particle interaction with the wall surfaces until about the last two planes. At the last two mean positions (11 and 12), the particles have downward (negative) trajectories angles and low measured velocities suggesting that these positions might be particle rebound positions or part of the main curved trajectories.

The 30.0 um particles, had an impaction with the hub surface between traverse planes 6 and 7.These particle had a high approach angle at mean position 6, just before the

impaction, hence, a low angle of attack with the hub surface. As a result, a small loss in rebound velocity was measured at mean position 8. The high velocity and angle measured at mean position 7 could be due to the reflected trajectories (from the hub) or part of the main trajectories which had not collided with the hub. The particle trajectories continued with an increasing velocity until the last two mean positions, 11 and 12, where the measured particle trajectories were in a downward (negative) direction. The decrease in measured particle velocities at these position show, again, that these might be the particle rebound positions. The similarity in the measured velocity profiles between the 15.0 and 30.0 um particles suggested that the aerodynamic drag force might have a significant effect on the trajectories of the 30.0 um particle.

The 100.0 um particle impacted the hub surface with a high angle of attack (position 6 just before impact). This was followed by a sharp increase in the measured trajectory angle and a decrease in the rebound velocity at mean position 7. The particle continued to mean position 8 with an increase in the velocity and high trajectory angle. The low trajectory angles and the drop in the velocities from mean position 9 onwards suggested that these might be the rebound positions. In general,the 30.0 and 100.0 um particle collided with the shroud surface with a high angle of attack. The initial particle velocity for the 15.0, 30.0 and 100.0 um are 36.0, 25.0 and 10.0 m/s respectively. The measured results will be compared with the prediction later in Chapter 5.

The measured particle concentration curves for the quartz particles between 15.0 and 150.0 um, seeded at the mid-height position of 128.67 mm, are shown in Figure 50 and 51. In these figures,trends in the particle trajectories for particles between 30.0 and 150.0 um can be established, they are;

i) all the particles have the initial impact region with the hub between traverse plane 5 and 6,
ii) most of the dust entered the scavenge flow section.

The 15.0 um particles shown in Figure 50a, have the initial impact region at traverse plane 6. The measured rebound distribution curves show a bias towards the hubside at planes 7 and 8. At plane 8, the rebound particles are in the region with high flow velocities, hence the well defined curves at plane 9 to 11. The second impact region on the shroud wall is at traverse plane 12 near the region of moving flow separation. The particle interaction with these flows may have resulted in some dust entering the engine core flow via the reverse flow region.

The particle rebound distribution curves for the particles between 30.0 and 150.0 um could be observed in the broad distribution at planes 7 and 8. The 30.0 um particle had a second impact region from traverse plane 8 onwards while for particles greater than 50.0 um, it was between planes 7 and 8.However,all the particle sizes had subsequent impact on the shroud wall until and beyond the last plane.

Figure 52 shows the measured particle velocities and angles at the mean trajectory positions for particle between 15.0 and 150.0 um. All the particle sizes have similar measured velocity and trajectory angle profiles. The trajectory angles for all the particle sizes, except the 15.0 um particle, had a low approach angle to the hub wall, measured at mean position 5, hence a high angle of attack with the wall.

The 15.0 um particles had an even lower angle of attack, measured at mean position 6, as they collided with the hub surface. As a result, the measured particle velocity at mean position 7 had shown only a relatively small loss in the momentum after the impaction. The particle had also gained

the highest velocity at mean position 9, in the areas with high flow velocity. The subsequent mean positions show decreasing particle velocities and trajectory angles. The negative trajectory angles at position 11 and 12 were probably due to the curved particle trajectories rather than the particle reflected from the second impact region which was at traverse plane 12.

The 30.0 and 60.0 um particle had also gained a maximum velocity at mean position 9. At all the subsequent positions, there followed a decrease in the velocities with (negative angles) downward trajectory directions,which could be due to the reflected particles because of their greater inertia.

The 100.0 and 150.0 um particles, however, had an impaction with the shroud wall at between positions 8 and 9. The decrease in the measured particle velocities coupled with the low trajectory angles between position 9 and 12 might be due to the rebound particles.The initial velocities for the 15.0, 30.0, 50.0, 100.0 and 150.0 um particles were 35.0, 25.0, 14.0, 10.0 and 9.0 m/s respectively.

The measured particle concentration for the quartz particles seeded at the nozzle height of 105.5 mm is shown in Figure 53. In this figure, the measured particle distribution curves for the 30.0 um particle were very similar in form to the 15.0 um particle.

The 15.0 um particle concentration curves (Figure 53a) are similar to those obtained for the ballotini particles (Figure 46a) seeded at the same nozzle height. The particle trajectories after an impaction with the hub wall remained close the hub surface until traverse plane 8 where the particle come under the effect of the high velocity flow (near the 'peak' of the hub). The particle's initial impact region was in the vortex circulation region. The second impact region was at the shroud surface, from plane 10 to 12. Although most of the dust seems to enter the scavenge

flow, a high proportion had also entered the engine flow via the flow reversal region.

The centrifuging effect of the vortex on the 30.0 um particles (Figure 53b) also resulted in distribution curves similar to the 15.0 um particles, except with a broader distribution. However, the distribution curves for the reflected trajectories were not as widely distributed as for the 30.0 um ballotini particles (Figure 46b). Even the distribution curve at traverse plane 5 (inside the vortex) was not as widely distributed as with the 30.0 um ballotini particles. The bias towards the hub wall,in the distribution curves at planes 6 and 7 (reflected trajectories), could be due to the effect of the flowfield and/or the effect of the restitution ratios. The comparison with the predicted trajectories, later in Chapter 5, could provide an explanation. The particle initial impact region was at the hub surface and the second impact region was from traverse plane 9 onwards. Some dust particles had entered the engine flow due to the reflection off the shroud wall, others, via the flow reversal region.

The centrifuging effect of the vortex on the 100.0 um particle (Figure 53c) resulted in the broad distribution curves (planes 5 to 7) similar to that obtained for the 30.0 um ballotini particles (Figure 46b). But, their (100.0 um) trajectories are influenced mainly by the inertia force, therefore, the bias towards the hub wall in the distribution curves at plane 5 and 6 (reflected trajectories) can only be due to the restitution ratios rather the flowfield effect. The particles have the same initial impact region on the hub and the second impact region on the shroud is from plane 6 onwards.

The measured particle velocities and angles at the mean trajectory positions are shown in Figure 54. The 30.0 and 100.0 um particle sizes show a steady increase in the velocities just before the first initial impact region at the hub.

After the impaction with the hub,the 15.0 and 30.0um particle show similar velocity profiles. Both these particle sizes continued in their trajectories with increasing velocities until mean position 9. Both particle sizes show a drop in the measured velocities and angles from mean positions 10 to 12. These changes could be a result of an impaction with the shroud wall, or, the effect of the flowfield in a region of high velocity turning flow. The 100.0 um particles also show an increase in velocity after the impaction until mean position 9. After that mean position, the particles collide with the shroud surface with a high angle of attack where the measured results at mean positions 10 to 12 shown a decrease in velocity and, the trajectory angles were in the downward (negative) direction. However, a comparison will be made with the predicted results later in Chapter 5.

In summary, the influence of the aerodynamic drag and inertia force on the particle trajectories is similar to that observed for the ballotini particle. In general, these forces have a greater effect on the quartz particle due to the greater drag on angular shapes and smaller density. The trajectories of the 30.0 um quartz particles were found to be more affected by the flowfield than the 30.0 um ballotini. However, the main difference between the quartz and ballotini particle lies in the secondary impact region due to the different restitution ratios especially for sizes greater than 50.0 um where the inertia force takes effect on their trajectories. In general, the ballotini particle had higher rebound angles after an impaction with a wall surface. Hence, the ballotini particle usually had the second impact region well upstream of the 'hump' of the hub and, subsequent impactions well downstream of the 'hump'. The quartz particles usually had the second impact region occurring on the shroud wall near the peak of the 'hump' of the hub. They also usually had a higher angles of attack during an impaction with the shroud surface (second impact

region). The ballotini particle, seeded at the lower (bottom) nozzle height of 105.5 mm, also had the second impact region occurring on the shroud wall, near the peak of the 'hump'.

In summary to Section 4.8, for the results obtained for quartz and ballotini particle, the vortex re-circulation region appears to be the main cause for the ballotini particle entering the engine flow. As for the quartz particle, both the vortex re-circulation and the rebound characteristics are responsible for the dust entering the engine core flow. Since the 100.0 and 150.0 um (ballotini and quartz) particles are influenced mainly by the inertia force, the vortex re-circulation would have little effect on their trajectories. Therefore, the restitution ratios would be the main effect on the trajectories of the ballotini and quartz particles.The measured separation efficiency (by mass as shown in TABLE VII) for ballotini particle between 100.0 and 150.0 um shows an improvement over the quartz particle of less than 1.0 percent. As for the 50.0 um ballotini particle, an improvement of 1.7 percent over the 60.0 um quartz particle was found. The experimental results will be compared with the prediction using both the measured (Section 4.5) and inviscid (Section 3.2) flowfield later in Chapter 5.

CHAPTER 5

Discussion

The experimental results have been discussed in detail earlier in Chapter 4 and the general findings can be summarised as follow;

i) the influence of the aerodynamic drag forces increases as the particle sizes decreases,

ii) the influence of the inertia forces increases as the particle sizes increases,

iii) the influence of the inertia and aerodynamic drag forces were greater on the quartz particle (as opposed to the ballotini particle) due to their smaller mass and irregular shape,

iv) ballotini particles had the higher rebound angle on impact with a solid wall due to their higher coefficient of restitution,

v) both the quartz and ballotini particles between 30.0 - 150.0 um had the initial impaction on the hub surface but they had different second and subsequent impact regions. The ballotini particle had impact regions on the shroud wall occurring well upstream and downstream of the 'peak' of the hub except for those seeded at the lowest height position which gave similar results to the quartz particles.The quartz particles had second impact region occurring near the 'peak' of the hub.

The mean trajectory positions for each particle size seeded at each nozzle height have been determined from the particle concentration obtained at the 12 traverse planes (Section 4.8). Hence, the particle's velocities and angles were measured at the mean trajectory positions using the laser anemometer. In this chapter, the mean positions, velocities (and angles) are compared with the predicted

values from the particle trajectory prediction model (which had been discussed earlier in Chapter 2 and 3). The three main limitations of the prediction model are;

i) the difference in the predicted trajectories, velocities and angles using the measured and inviscid flowfield. The simulation of the particle trajectories was carried out in both the inviscid and measured flowfield. The measured flowfield at the mid-section of the separator was used as the representative flowfield in the entire domain. The difference between the actual and predicted (inviscid) flowfield has been discussed in detail earlier in Chapter 4, and the main critical areas found (in the actual flow) were the vortex re-circulation (at the base of the hub), flow separation on the hub and shroud, and high velocity flow areas. The predicted particle trajectories, velocities and angles were compared with the measured values.

ii) the effect of the drag coefficient on the prediction of the particle trajectories, velocities and angles. The analysis of the experimental results had shown that the non-spherical particle achieved higher overall velocities (due to the higher drag) compared to the spherical particles. In the prediction model, the drag coefficients are applicable for spherical particle only, therefore, a correction factor (and indirectly a shape factor) was included into the computation to account for the higher drag on non-spherical particles. Further discussion of this correction factor can be found in the discussion of the results for the quartz particles.

iii) the effect of the restitution ratios on the prediction of the particle trajectories, velocities and angles.

The restitution ratios for the quartz particle were obtained from the earlier works by Tabakoff [Ref.16]. Since there is no experimental data on the restitution ratios for the ballotini particles, a simple expression was derived by trial and error matching the experimental results with the prediction model. The predicted results were compared with measured particle trajectories (velocities and angles) for both the quartz and ballotini particles.

The initial conditions used in the prediction model were;

i) the measured initial particle velocity and angle,
ii) the initial particle position which is the nozzle position.

Other initial conditions (Section 3.3) were the particle's diameter, density and material. The predicted results were compared with the particle concentration curves, mean particle trajectory positions, velocities and angles. The figures have been arranged in the following order;

a) Figures 55 to 69 are the results for the spherica ballotini particles,
b) Figures 70 to 85 are the results for the non-spherical quartz particles,

5.1 Simulation of the Particle Trajectories for the Spherical Ballotini Particle

The ballotini particle formed the basis of the prediction model due to the assumptions (Section 2.5) made

in the formulation of the particle's equations of motion (a major assumption being that the solid particles are spheres of uniform diameter and furthermore the drag coefficients (used by the prediction model) are applicable only for spherical particle). The only unknown factor is the ballotini's restitution ratios which could only be derived by experimentation. Therefore simple expressions relating the particle rebound velocity to the impact velocity were employed in the model. They have the following form;

$$V_{PT2}/V_{PT1} = K_1$$

$$V_{PN2}/V_{PN1} = K_2$$

V_{PT2} = tangential component of the particle rebound velocity
V_{PT1} = tangential component of the particle impact velocity
V_{PN2} = normal component of the particle rebound velocity
V_{PN1} = normal component of the particle impact velocity

The constants K_1 and K_2, which were found by trial and error matching with experimental results, were 0.8 and 0.78 respectively, The results for the ballotini particle had been arranged as follows;

i) Figures 55 to 58 are the results for particles seeded at the upper nozzle height position,
ii) Figures 59 to 65 are the results for particles seeded at the middle nozzle height position,
iii) Figures 66 to 69 are the results for particles seeded at the lower nozzle height position.

The comparison between the predicted trajectories and measured particle concentration curves for the 15.0 um particle is shown in Figure 55a. The particle sizes used in the prediction were 12.0, 15.0 and 18.0 um in diameter. In this figure, the predicted trajectories using the measured

flowfield differ slightly from those predicted using the inviscid flowfield. Since their trajectories were influenced mainly by the aerodynamic drag force of the flowfield, small difference between the two flowfields could be felt by these particles. The main differences between the two flowfields could be found near critical areas such as the vortex re-circulation region and areas with separated flow. The effect of this difference was greater on the trajectories of the 12.0 um particle due to their relatively smaller mass. However, all the predicted trajectories shown an initial impaction with the hub surface and subsequent impacts which occurred at the shroud surface. The measured particle concentrations show good agreement with the trajectories of the 12.0 um particle predicted using measured flowfield and, the 12.0 and 15.0 um particle predicted using the inviscid flowfield. The broad particle concentration at plane 8 also shows good agreement with the reflected trajectories of the 12.0 to 18.0 um (inviscid flowfield) particle. The predicted trajectories show that the initial impact region occurred at the hub surface;the subsequent impact region occurred on the shroud surface in the obstructed areas. The end predicted positions were at the shroud surface near the region of moving separate flow.

As the particle sizes increase to between 38.0 and 53.0 um, Figure 55b, the difference in the predicted trajectories using the measured and inviscid flowfield were less, due to their greater inertia. The predicted particle trajectories show good agreement with the measured particle concentrations. The broad reflected particle concentration measured at plane 7 could be due to a wide range of particle rebound angles. The predictions also show that the reflected trajectories from the shroud surface, plane 10 onwards, were in the obstructed areas (Figure 19).These coincide with the bias (towards the shroudside) in the particle distributions measured at plane 10 to 12. The two main predicted impact regions on the shroud surface were at the upstream and

downstream positions of the 'peak' of the hub. Compared to the 12.0-18.0 um particles, the flow seems to have little effect on the particles reflected from the hub. The end predicted positions were also at the shroud surface near the region of moving separated flow.

In Figure 55c, the predicted trajectories for particles between 91.0 and 107.0 um show similar behaviour to 38.0-53.0 um particles except that the reflected trajectories have higher rebound angles. In general, the predicted trajectories show good agreement with the measured particle concentrations. The trajectories (predicted) of particles reflected from the shroud surface show a downward shift, away from the shroud surface (compared to the 38.0-53.0 um particles)which coincide with the peaks of the distributions measured at planes 7 to 11.The main impact region was at the hub surface but the second impact region on the shroud surface was further away from the 'peak' of the hub compared to that of the 38.0-53.0 um particles. However the two impact regions on the shroud surface were well upstream and then downstream of the 'peak' of the hub.

The detailed comparisons between measured and predicted particle trajectories (velocities and angles) are shown in Figures 56 to 58.

In Figure 56, the mean trajectory positions show good agreement with the predicted results using 12.0 um rather than 15.0 or 18.0 um particles. The predicted results using the two different flows (inviscid and measured) gave different particle trajectories (velocities and angles) but those predicted using the measured flow show better agreement with experimental measurements. The deviation in the particle velocities begins at the third mean position where the measured flow velocity near the shroudside was higher than that predicted flow (Figures 35 and 37). At the last position, the predicted velocities (based on the measured flow) were higher than the experimental measurement. This discrepancy was due to the effect of assuming the

near-wall flow velocities (no measurement in the obstructed areas) to be equal to those of the nearest adjacent points, which were higher than the actual values.

In Figure 57, the predicted trajectories, for particles between 38.0 and 53.0 um, using the two different flows show good agreement with the measured mean particle trajectory positions. The particle velocities, however, show slightly different results, but those predicted using the measured flow show the better agreement with the experimental data. The deviations in the predicted particle velocities (due to the higher measured flows than predicted as shown in Figure 37) also begin at the third mean position. The good agreement between the predicted and measured particle trajectory angles and velocities show that mean positions 8 to 11 were, in fact, particles reflected from the shroud surface.

Similar results to those observed in the above analysis were also observed for the larger particle between 91.0 and 107.0 um in diameter as shown in Figure 58. In general, the predicted results using the measured flow gave the better agreement with the experimental results. The predicted particle trajectories show slight deviation at mean position 8 and 9 which were due to the wide range of particle rebound angles involved. The good agreement between predicted and measured results show that mean position 8 to 12 lie within the path of the reflected trajectories from the shroud wall. The deviation in the predicted particle velocities (due to the higher measured flows than predicted as shown in Figure 37) also begin at the third mean position.

Figures 59 and 60 presents the comparative results for particles between 15.0 and 150.0 um in diameter seeded at the mid-height nozzle position.

In Figure 59a, the predicted trajectories for the 12.0, 15.0 and 18.0 um particles show good agreement with the measured particle concentrations. The effect of the two

flowfields can be seen from the different predicted impact positions on the shroud surface. The predictions also show the particles have the main impact with the hub wall and, subsequent impaction occurred on the shroud surface, in the obstructed areas. These coincide with the bias toward the shroudside, in the particle concentration curves measured at planes 10 to 12. The reflected particle from the hub surface also show good agreement with the measured concentration at planes 6 and 7.

The predicted trajectories for particles between 38.0 and 53.0 um, shown in Figure 59b, show good agreement with measured concentration curves. Again, the predicted results using the measured flow were different to those predicted from the inviscid flow. The prediction shows main impaction occurred on the hub wall; second and subsequent impact regions occurred on the shroud surface. The bias in the concentration curves, toward the shroudside, measured between planes 7 and 12 coincide with the predicted trajectories. The bias in the concentration curve, toward the hub, measured at plane 6 was most likely due to the main trajectories rather than reflected particles from the hub. The reflected particle trajectories from the hub surface were detected at both planes 5 and 6 which show the broad range of particle rebound angle.

In Figure 59c, the predicted trajectories for particles between 53.0 and 65.0 um in diameter show good agreement with the particle concentration curves. The impact regions were similar to those predicted for the 38.0-53.0 um particle but the two impact regions (on the shroud surface) were further away from the 'peak' of the hub. The reflected particle trajectories from the hub surface coincide with the measured results at plane 5. The small 'peak' in the measured concentration curve, toward the shroudside, was due to reflected particles from the shroud surface. The reflected trajectories also coincide with the peaks of the particle concentration curves which were measured between

planes 7 and 9. The curves at plane 11 and 12 were due to subsequent particle impaction with the shroud surfaces.

In Figure 60, the predicted results for the particles between 91.0 and 162.0 um show good agreement with the measured particle concentrations.

In Figure 60a, the reflected trajectories from the hub wall, for particle between 91.0-107.0 um, coincide with the 'flat' part of the measured concentration curve at plane 5. The subsequent particle reflected from the shroud wall also show good agreement with the 'peak' of the concentration curves measured at planes 6 to 9. Slight deviations from the predicted results were found at planes 10 to 12 which could be due to the broad rebound angles. The two impact regions (on the shroud surface) were at the upstream and downstream position of the 'peak' of the hub. Deviation also existed in the prediction between the results based on the measured and inviscid flowfield.

In Figure 60b, predicted trajectories for particles between 145.0 and 162.0 um also showed good agreement with measured concentration curves. The reflected trajectories from the shroud surface show a similar trend to the 91.0-107 um particle except there is a further downward shift, toward the hubside. The trajectories show good agreement with the concentration curves measured between planes 6 to 10 but the slight deviation at planes 11 and 12 could be due to the broad particle rebound angles. Deviation also exists in the predictions between the results based on the measured and inviscid flow. The predicted trajectories based on the inviscid flow show particle impacts with the 'peak' of the hub but the predicted results based on the measured flow show otherwise.

The detailed comparison between the predicted particle trajectories, velocities and angles for particles between 12.0 and 162.0 um are shown in Figure 61 to 65.

In Figure 61, the mean particle trajectory positions obtained for the particles between 12.0 and 18.0um show good

agreement with the predicted results. The comparison of the particle velocities shows that the predicted velocities for the 12.0-15.0 um, based on the measured flowfield, show the better agreement with the experimental results when compared to the 18.0 um particle. However, deviation in the particle velocities was found at mean positions 2 and 3, which could be due to the effect of the particle interaction with the wakes caused by the feeder nozzle.At mean positions 11 and 12, the measured velocities were lower than the prediction (based on the measured flow) which was due to the high near-wall flow velocities. Deviation in the predicted particle trajectories using the inviscid flow begins at the third mean position where the predicted impact positions differed from those predicted using the measured flow. The predicted velocities also show that the deviation begins at the third mean position which was in the area where deviation in the inviscid flow from the actual flow was found, due the vortex re-circulation.

In Figure 62, the predicted trajectories for particles, between 38.0 and 53.0 um, show good agreement with the mean trajectory positions. The comparisons of the particle velocities show that the predicted results based on the measured flowfield gave the better agreement with the experimental measurements. The measured particle velocities at mean positions 1 to 9 were within the predicted limit. As in the previous analysis, deviation in the predicted velocities using the inviscid flow begins at the third mean position although deviation in the trajectories was less obvious. The comparison in the particle trajectory angles show that the measured values at positions 7 to 12 were slightly lower than the predicted results. This could be due again to the wide range of reflected angles, which cannot be simulated with the simple restitution ratios used in the present analysis.

In Figure 63, the predicted trajectories for particles between 53.0 and 65.0 um show good agreement with

the measured mean trajectory positions. The measured particle velocities were within the predicted limit except at position 11 and 12. The predicted particle velocities and angles at these two positions were lower than the measured values because they lay in the path of the particles (predicted) reflected from the shroud although this may not be so. The measured particle trajectory angles, between positions 7 and 12, were slightly lower than the predicted values which suggested a lower rebound angle at the hub and a higher rebound angle at the second impact position on the shroud. The predicted results based on the measured flowfield gave the better comparison with the experimental measurements.

Similar results observed for the small particle between 38.0 (Figure 62) and 65.0 um (Figure 63), were also found for the large particle between 91.0 and 162.0 um in diameter as shown in Figure 64 and 65. In general, the predicted particle trajectories and velocities show reasonably good agreement with the measured values. The predicted velocities for the particle between 145.0 and 162.0 um, Figure 65, however, were slightly lower than the measured values. The comparison in the particle trajectory angles also shows that the measured values at positions 8 to 12 were slightly lower than predicted results, again, for the same reasons as the 38.0-53.0 um particle.

Figure 66 to 69 shows the comparison between the predicted and measured results for particle seeded at the lowest height position.

In Figure 66, the predicted particle trajectories using the measured and inviscid flowfield show an even greater difference compared to the particle seeded at the other positions. The presence of the vortex re-circulation region on the hub surface introduces two main uncertainties into the prediction model;

i) there is no experimental data on the particle rebound characteristics (both quartz and ballotini) involving vortex re-circulation flows. In the present analysis, the rebound characteristics for the ballotini particle was based on the simple relation which had, so far, given good agreement with the measured results. Therefore, the same relation was applied to the present case.

ii) the flow velocities at the node points near the vortex re-circulation region were assumed to have a small non-zero value because laser measurements were not possible due to the high level of turbulence intensity encountered in the flow. The effect on the prediction of the particle trajectories may be minimal due to the short duration which the particle spends in the region.

In Figure 66a, the predicted trajectories (based on the measured flow) for particles between 12.0 and 18.0 um in diameter show good agreement with the measured particle concentration curves. Since their trajectories are influenced mainly by the nature of the flow, the reflected trajectories from the hub would come under the immediate effect of the flow away from the vortex region. The predicted results based on the measured and inviscid flowfield gave different reflected trajectories from the hub surface but those predicted with the measured flow gave the better comparison. Given the above uncertainties in the vortex region, the measured particle concentrations between planes 1 and 9 show reasonably good agreement with the prediction but at plane 10, only general agreement was found. At planes 11 and 12, the predicted trajectories were in the obstructed areas which was detected by the bias in the curves toward the shroudside. The end position of the predicted trajectories were near the region of the moving separated flow.

As the particle size increases to 38.0-53.0 um, Figure 66b, the predicted trajectories based on the measured flow were also different to those predicted using the inviscid flow. The results based on the measured flowfield show the better agreement with the experimental data. Simulation of the wide reflected trajectories which were measured at planes 6 and 7, would not necessary be correct without further experimental information on the particle behaviour in the vortex region. However, the predicted results show reasonably good agreement with the measured concentration curves. The bias in the concentration curves toward the shroudside measured between planes 7 to 12 coincide with the predicted trajectories. The predicted impact region (based on the measured flow) on the shroud surface occurred at the 'peak' of the hub.

In Figure 66c, the predicted trajectories of the large particles between 91.0 and 107.0 um, reflected from the hub, were different for the two flowfields. The measured flow had a higher velocities than the inviscid flow, therefore it has a greater effect on the trajectories reflected from the hub. As a result, the predicted trajectories (based on the two flowfield) have different impact positions on the shroud surface, which ultimately affect their final trajectories. Although the measured concentration curve at plane 4 shows good agreement with the reflected trajectories from the hub, the comparison from planes 6 to 12 show otherwise. It seems that the rebound angle from the shroud should be higher and the uncertainties at the vortex may be the cause of the inaccuracies in the prediction.

The comparisons between the measured and predicted particle trajectories, velocities and angles are shown in Figures 67 to 69.

In Figure 67, the predicted trajectories for 12.0 to 18.0 um particle show good agreement with all the mean trajectory positions except with the tenth position. The comparison between the measured and predicted velocities

show good agreement except at the last mean position which was due to the higher than measured near-wall velocities. The predicted velocities using the inviscid flow were lower than those predicted with the measured flow (which gave better agreement with the experimental data) and deviation begins at the third mean position. The predicted particle trajectory angles also show good agreement with the measured trajectory angles.

The predicted trajectories (based on the measured flowfield), for the particles between 38.0 and 53.0 um, show reasonably good agreement with the mean particle positions, as shown in Figure 68. The comparison of the particle velocities gave good agreement at all the mean positions except at positions 6 to 8 where the measured velocities were higher than predicted. However, the comparison in the particle trajectories angles, at all the mean positions gave reasonably good agreement with the measured values although the broad reflected trajectories from the hub were measured but had not been simulated.

In Figure 69, the predicted trajectories for particles between 91.0 and 107.0 um shows some discrepancies mean positions 6 to 9. The predicted particle velocities (based on the measured flow) showed good agreement with the measured values at positions 1 to 5, before impaction with the hub but at positions 6 to 12, the measured velocities were higher than the prediction. However, the predicted particle angles show reasonably good agreement with the measured trajectory angles at all the positions.

In summary to this section, for the spherical ballotini particle, good agreement exists between the predicted and measured results for particle seeded at the upper and mid-height position. At the lower height position, the prediction shows reasonable agreement with the measured results after an impaction with the hub surface. However, good agreement exists between the measured and predicted

results at all the mean particle trajectory positions, at the three height positions,before the initial impaction with the hub. The present inviscid flow could reasonably predict the trajectories for particle seeded at the upper and mid-height position but predicted particle velocities would be lower than the measured values. At the lower height position, the prediction based on the measured flow gave the better comparison although some discrepancies were found for larger particles. In general, the predicted results using the measured flow gave the better agreement with the experimental data although the inviscid flowfield can be useful for predicting particle trajectories in an undisturbed flow (where separation and vortices do not exist). The simple expression, which was used for the restitution ratios for the spherical particles, has shown good agreement with measured values.

In general, the prediction model, which is based on the spherical partícle had shown good agreement with the experimental data obtained for the spherical ballotini particle.

5.2 Simulation of the Particle Trajectories for the Non-Spherical Quartz Particle

The particle prediction model has shown good agreement with the measured particle trajectories (velocities and angles) for spherical particles. The accuracy of the prediction is due to the several assumptions made in the model, one of which is the sphericity of the particle. Applying the same particle equations of motion to non - spherical particles (which have a higher drag) introduces inaccuracies into the prediction. The drag coefficient used in the prediction model was derived for a spherical particle applicable over a range of Reynold numbers.

Unfortunately, no such correlation exists for the irregular quartz particle, therefore, a factor had to be included into the drag coefficient to account for the higher drag force. Zenz and Othmer [Ref.40] introduce a shape factor which relates the diameter of a sphere, with the same projected area as the particle, to the volume of the particle. There are many definitions for the shape factor but an acceptable one has yet to be developed because the factor appears to vary under different flow conditions. Heywood [Ref.41] expressed the shape factor as the ratio of the volume of the particle to the diameter of the sphere which has the same projected area as the particle in the most stable orientation. In mathematical form;

$$Z = VOL_p/D_p^3$$

where VOL_p and D_p are the volume and the diameter of the particle respectively. Heywood gave the shape factor for the spheres as $\Pi/6$ and sand as 0.26. Johnstone, Pigford and Chapin [Ref.42] modified Heywood's approach by deriving a drag coefficient based on the mean projected area (average of the projected area in all possible orientations) of the particle. They plotted the drag coefficient for the Reynold numbers of between 10 and 300, for four types of irregular particle with the shape factor ranging from 0.28 to 0.4, and found that all the measured values of drag coefficient, C_D, lay within 15.0 percent of the curve for a sphere. They concluded that the drag coefficient could be used to predicted the motion of irregular particles.

In the present analysis, the shape factor was obtained by trial and error matching the predicted results with the experimental data. Instead of applying the shape factor directly into the drag coefficient, a correction factor was used because the particle equations of motion had initially been derived assuming that the particle was spherical. The correction factor can be related to the shape factor in the

force interaction term as follows;

$$G = \frac{3\ C_D\ \rho_g\ [(\tilde{V}_g - \tilde{V}_p)]}{4\ C_f\ \rho_p\ D_p}$$

Hence, re-writing to include the shape factor term gives;

$$G = \frac{\Pi\ C_D\ \rho_g}{8\ Z\ \rho_p\ D_p}\ [(\tilde{V}_g - \tilde{V}_p)]$$

where

$$Z = \Pi\ C_f/6$$

The shape factor for a spherical particle is $\Pi/6$ which gives a correction factor of 1.0. Hence the force interaction term remains unchanged for the spherical particle. The correction factor for quartz particle was found to be 0.4 which gives the shape factor as 0.21. This shape factor was found by matching the predicted trajectories (velocities and angles) with measured results,at mid-height location (128.67mm), for particle sizes between 15.0 and 150.0 um. Several values of the shape factor were repeated (with a resolution of .02) until the best fit was obtained. Zenz and Othmer [Ref.40] gave the shape factor for sand as between 0.26 and 0.28, however,the actual flow condition and sand's properties were undefined. Breitman [Ref.5] found the shape factor for AC Coarse sand to be 0.2618, by trial and error matching with experimental data. The proposed shape factor (0.21) for these studies therefore differs and lies modestly outside of the range (0.26 and 0.28) recommended by Zenz and Othmer.

Figures 71 to 85 shows the comparison between measured and predicted particle trajectories, velocities and angles

for the non-spherical particles. The prediction was carried out using the measured flowfield only due to the earlier predicted results for the ballotini particle which gave better comparison with experimental data. Also the measured particle velocity, angle and position at the second mean position had been used as the initial input condition for the prediction model. The reason for doing so was that the wake from the nozzle feeder affects the quartz particle more than the ballotini particle due to the smaller density(2650. kg/m^3 as compared 2950.0 kg/m^3) and non-spherical shape. The result was a discrepancy between the measured and predicted particle velocity at the second mean position as shown in Figure 70. The effect was most significant on the 15.0 and 30.0 um particles and less so on the larger particle due to their greater mass. This discrepancy was also found in in the prediction for the 15.0 um ballotini particle seeded at the mid-height position as shown in Figure 61.

The predicted results have been arranged in the following order;

Figures 71 to 74 are results for particles seeded at the upper height position,
Figures 75 to 81 are results for particles seeded at the mid-height position,
Figures 82 to 85 are results for particles seeded at the lower height position,

In Figure 71a, the predicted trajectories for 15.0 um quartz particles show good agreement with the measured particle concentration curves. The predicted results show no particle interaction with the wall surface except at the final position. This position was near the region of moving separated flow on the shroud surface.

As the particle is increased to 30.0 um, Figure 71b,the predicted trajectories show an initial impaction with the

hub (at plane 7) and second impaction at the shroud surface (between plane 10 and 11), just downstream of the 'peak' of the hub. The reflected trajectories (from the hub surface) correspond to the measured particle concentration at plane 8. The trajectories seem to coincide with the bias in the curve toward the shroudside, measured at planes 9 and 10 although the other peaks were most probably due to the trajectories of the smaller particles or the result of other rebound angles. The reflected trajectories from the shroud surface were in the obstructed areas which were also detected (bias in the curves toward the shroudside) at plane 11 and 12.

The predicted trajectories for the 100.0 um particles, Figure 71c, show reasonably good agreement with the measured particle concentration curves. The predicted results show an initial impact with the hub near plane 6; the second and final impact regions on the shroud occurred in the obstructed area near planes 8 and 11 respectively.The reflected trajectories from the hub were measured at planes 7 and 8 where broad rebound angles were detected apart from the main trajectories. However, the reflected trajectories from the shroud surface coincided with the bias (toward the shroudside) in the measured particle concentrations between planes 9 and 12.

Figure 72 shows the comparison between the measured and predicted particle trajectories (velocities and angles) for the 15.0 um particles seeded at the upper position. In this figure, good agreement exists between the measured and predicted results. The mean trajectory positions coincide with the predicted trajectories; measured particle velocities and angles also show good agreement with predicted results.

The predicted trajectories for the 30.0 um particles, Figure 73,show good agreement with mean trajectory positions 2 to 9.The discrepancy at position 10 is due to the parti-

cles being reflected from the hub at other rebound angles other than the predicted trajectories. Positions 11 and 12 were at the limit of measurement (due to obstruction of the wall), however, the relatively low measured and predicted particle velocities and angles indicate that they were indeed particle rebound positions (as were predicted). Reasonably good agreement between the predicted and measured particle velocities and angles were found between position 2 and 9 except at position 10 where discrepancy in the trajectory was also found.

In Figure 74, for the 100.0 um particles,good agreement between the predicted trajectories and mean positions were found between positions 2 and 8. The predicted trajectories between positions 9 and 12 were in the obstructed areas hence the discrepancies. However, the general agreement in the velocities and angles show the behaviour of the trajectories measured at these positions. The main reflected trajectories from the hub surface, at positions 7 and 8, show reasonably good agreement in the velocities and angles comparison.

The comparison between the measured and predicted results for the quartz particles seeded at the mid-height position are shown in Figures 75 and 76.

In Figure 75a,the predicted trajectories for the 15.0um particles show reasonably good agreement with the measured particle concentration curves. The prediction shows an impact with the hub near plane 6 and second impact near plane 12. Before the initial impact with the hub, the peak of the curves at planes 2 to 6 were slightly higher than the predicted trajectories; at planes 9 to 12, the opposite was found. The final predicted position was near the region of moving separated flow on the shroud surface.

The comparison between the measured concentration curves and predicted trajectories for the 30.0 um, Figure 75b, show good agreement. The reflected trajectories from

the hub were measured at planes 7 and 8. At planes 9 to 12, the bias towards the shroudside, in the concentration curves coincide with the trajectories near the shroud wall, in the obstructed areas. The main impact occurred at the hub wall; the second and subsequent impactions occurred at the shroud surface near the 'peak' of the hub. The final predicted trajectories were at the shroud wall, near the region of separated flow.

The predicted trajectories for the 60 um particles, as shown in Figure 75c, were generally similar to those predicted for the 30.0 um particles. The main difference was that the reflected trajectories, from the hub, for the 60.0 um particles had a higher rebound angle due to the higher inertia. The second impact region occurred near plane 9, as opposed to that of the 30.0 um particle which occurred near plane 10. The reflected trajectories from the hub were measured at planes 7 and 8.Between planes 9 and 12, the bias in the curves towards the shroudside coincide with the predicted trajectories at the shroud wall,in the obstructed areas.

In Figure 76, for the 100.0 and 150.0 um particle, the comparison between predicted and measured results exhibit trends which were similar to the trajectories of the 30.0 and 60.0 um particles. The main difference lies in the second impact region which was further away from the 'peak' of the hub due to their greater inertia and the small effect which the flowfield has on their trajectories. The reflected trajectories of the 100.0 and 150.0 um particles coincide with the broad distributed curves measured at planes 7 and 8, also, the bias in the curves, towards the shroudside, coincides with the trajectories in the obstructed areas.

The detailed comparison between the measured and predicted particle trajectories, velocities and angles are shown in Figures 77 to 81.

In Figure 77, the predicted trajectories for the 15.0 um particles were slightly lower than the mean positions

before the impaction with the hub; at positions 9 to 12, the predictions were higher. Good agreement exists between measured and predicted velocities (and angles) at all the mean positions except in position 10 to 12. At these three positions, the predicted velocities were slightly lower than the measured values, and predicted trajectory angles were slightly higher than measured.

The predicted trajectories for the 30.0 um particles, Figure 78, show reasonably good agreement with all the mean positions except at positions 10 to 12 (which were at the limit of measurements). The predicted particle velocities were slightly higher than the measured values at positions 2 to 6, before impaction with the hub. Although the reflected (predicted) trajectories were slightly lower than the measured values at the mean position 7 and 8, the comparison in the velocities and angles, however, showed good agreement. The comparison in the particle trajectory angles show good agreement with measured values although reflected trajectories from the shroud surface were in the obstructed areas. The low measured (and predicted) particle velocities and angles at position 10 to 12 show that they were indeed particle rebound positions.

In Figure 79, the predicted results for the 60.0 um particles show good agreement with the measured values at all the mean positions. The predicted trajectories at position 9 to 12 were in the obstructed areas, hence the difference with the mean positions. At mean positions 10 to 12, the low predicted and measured velocities and angles shows that they were particle rebound positions.

In Figure 80, good agreement exists between the measured and predicted particle velocities (and angles) for the 100.0 um particles even though discrepancies in the predicted and measured trajectories were found from positions 7 to 12. The fact that similar predicted and measured velocities (and angles) were found in positions 7 and 8, shows the wide range of particle rebound angles apart from

the main reflected trajectories.The particles reflected from the shroud surface (at the upstream position of the 'peak' of the hub) were represented by mean position 9 to 12 where measured and predicted particle velocities (and angles) show good agreement.

The above analysis for the 100.0 um particles was also found for the 150.0 um particle in Figure 81. The predicted and measured trajectories show reasonably good agreement at all the mean positions except those in the obstructed areas. The comparison in the velocities and angles also show reasonably good agreement. Positions 9 to 12 lie in the path of the particle reflected from the shroud surface (in the obstructed area) due to the reasonably good agreement between measured and predicted velocities (and angles).

The measured and predicted results for quartz particles seeded at the lowest height position are shown in Figures 82 to 85.

In Figure 82a, the predicted trajectories for the 15.0 um particles show good agreement with all the measured particle concentrations except in the last three traverse planes. The assumption of a low velocity area to represent the vortex region did not seems to have affected their trajectories. The prediction shows an initial impaction with the hub and the second impaction with the shroud. The end position of the predicted trajectories were at the shroud wall near the region of a moving separated flow.

The comparison between the measured and predicted trajectories for the 30.0 um particles, Figure 82b, also exhibits good agreement except at the last three positions. However, the bias in the concentration curves towards the shroudside were in general agreement with the predicted trajectories in the obstructed areas. The prediction shows that the second impact region occurred at the shroud surface near the 'peak' of the hub.

Similar impaction with the shroud surface predicted for

30.0 um particles was also found for the 100.0 um particles as shown in Figure 82c. The broad distributed curves measured at planes 6 and 7 show the wide range of particle rebound angles although only the main trajectories reflected from the hub were simulated. The reflected (predicted) trajectories from the shroud surface, which were in the obstructed areas, coincide with the bias in the curves measured from planes 8 to 12.

The comparison between the measured and predicted trajectories, velocities and angles are shown in Figures 83 to 85.

In Figure 83, the predicted trajectories for the 15.0 um particles show good agreement with mean positions 2 to 9. At positions 10 to 12, the prediction was higher than the measured mean positions, and their (predicted) velocities were lower than the measured values. At positions 2 to 5, before impacting the hub, the predicted velocities were slightly higher than the measured values although the comparison in the trajectory angles show good agreement. The prediction shows that between positions 5 and 6, several impactions had occurred with the hub surface. The comparison in the trajectory angles also show good agreement between measured and predicted values.

The results for the 30.0 um particles, Figure 84, show reasonably good agreement between measured and predicted values. The reflected trajectories from the hub surface re-impact the surface outside of the vortex region. The actual behaviour of the particles is difficult to predicted accurately without further experimental studies on the particle interaction with a vortex flow. The discrepancy at mean positions 10 to 12 was due to the obstruction of the wall curvature. However, the discrepancies in the particle velocities and angles at position 10 and 11, suggest that they were a result of other particles apart from the main trajectories reflected from the shroud surface. In general,

the measured and predicted velocities and angles show good agreement.

In Figure 85, the measured and predicted results for the 100.0 um particles show reasonably good agreement. The predicted trajectories were slightly lower than the mean positions 2 to 5 but the particle velocities and angles were in good agreement with measured values. The reflected trajectories from the hub, between positions 6 and 9, have high rebound angles (compared to the 30.0 um particle) due to their greater inertia. The reflected trajectories from the shroud surface were in the obstructed areas, hence the difference in the mean positions 9 to 12. However, the predicted velocities and angles show reasonably good agreement with measured values.

In summary to this section, good agreement between predicted and measured results was found for the irregular quartz particles. The predicted trajectories (velocities and angles) using the correction factor of 0.4 (shape factor of 0.21) had shown agreement with measured results especially in their particle velocities. Unlike the results for the ballotini particle seeded at the lower height position, the predicted results for quartz particle seem to show reasonably good agreement with the measured values even though the particle interaction with the vortex has not been simulated. Although the 100.0 um particle reflected from the hub surface were broadly distributed, the mean positions show reasonably good agreement with the reflected (predicted) trajectories. In order to accurately simulate these reflected trajectories, a more extensive experimental study of their rebound characteristics need to be carried out.The present restitution ratios (Section 2.2.3) have been derived from experimental studies which were based primarily on 200.0 um particles impacting a solid surface at only 3 or 4 angles of attack. However, in general, the predicted results (trajectories, velocities and angles) reflected

from the hub or shroud surfaces show reasonably good agreement with measured values at the mean positions although a much wider range of reflected trajectories were measured.

In general, the factors found to influence the prediction of particle trajectories, velocities and angles can be summarised from the results for the ballotini (spherical) and quartz (non-spherical) particles as follows;

i) <u>The difference in the predicted trajectories, velocities and angles using the measured and inviscid flowfield</u>

The deficiencies in the inviscid flowfield have been discussed in detail earlier in Chapter 4. In general, the presence of the vortex re-circulation region, separation 'bubble' and flow separation resulted in higher core flow velocities. Hence, the results predicted using the measured flow gave the better comparison with the experimental data. The effect was not only felt by the small 15.0 um particles but also the larger 150.0 um particles. The predicted particle velocities based on the measured flow were, in general, higher than those predicted using the inviscid flow. However the predicted trajectories, using the measured and inviscid flowfield, for the particle seeded at the upper and mid-height position show no major difference although some discrepancies were found for those seeded at the lower height position. But this could be due to the effect of the particle interaction with the vortex re-circulation which is impossible to simulate without further experimental information. However, the assumption of a non-zero value (in the measured flowfield) at that region shows only slight differences between measured and predicted trajectories for the quartz particle which could be a

result of their low rebound angle. The effect on the trajectories (predicted using the measured flow) of the ballotini particles, which have a much higher rebound angle, seems to occur well outside of the vortex region where the measured flow was higher than predicted. The results seem to suggest that due to the short duration which the particle spend in the vortex, the effect (of the vortex) on their trajectories is minimal. However, their predicted velocities (based on the measured flow) shows a 'dip'(Figures 83 to 85) near the vortex region which is due to the deceleration of the particle in the low velocity areas. The assumption of the near-wall velocities, at the shroud surface, to be equal to the measured values taken from the adjacent points had resulted in a higher velocities compared with those measured especially for the small particles. The particle interaction with the moving flow separation at the shroud surface could also give incorrect predicted results.

ii) <u>Effect of the drag coefficient on the prediction of the particle trajectories, velocities and angles.</u>

The drag coefficient which was used in the prediction model is applicable for the spherical particle, hence, the comparison for spherical ballotini particle formed an ideal test case. The predicted results (based on the measured flow and drag coefficient) for the ballotini particle show good agreement with the measured values especially in the comparison of the particle velocities. The computation of the particle velocities also depend on the theoretical modelling of the flow since the drag coefficient depends on the relative velocity between the particle and gas. The predicted velocities using the inviscid flow were, in general,

lower than those predicted using the measured flowfield.

In the case of the non-spherical quartz particles, the predicted particle velocities (based on the measured flow), based on the un-modified drag coefficient gave a lower than measured values. This is due to higher aerodynamic drag force on the irregular particles which had to be taken into account by including a correction factor into the drag coefficient computation. The correction factor of 0.4 (shape factor of 0.21) was found by trial and error matching of prediction with measured particle trajectories (velocities and angles). The comparison between the measured and predicted results (based on the measured flow) using the modified drag coefficient show good agreement for all the particle sizes.

iii) <u>Effect of the restitution ratios on the prediction of the particle trajectories, velocities and angles.</u>

The computation of reflected particle trajectories depends on the particle restitution ratios which relate the rebound velocities to the impact velocities. It also depends on the particle material, density and target material, and the accuracy in modelling the wall surface. The restitution ratios for the ballotini particle was based on a simple relationship which was found by trial and error matching with measured values. Although this has not been validated with experimentation, the predicted trajectories, velocities and angles show good agreement with measured results. However, the effect of the restitution ratios is mainly on the larger particles because their trajectories are influenced mainly by inertia forces hence their motions are ballistic in nature.

The restitution ratios for the quartz particle was obtained from the earlier experimental investigation by Tabakoff[Ref.16].The reflected (predicted) trajectories for the quartz particle have a lower rebound angle compared to the ballotini particle. As a result, the quartz particle has different impact positions, especially the second impaction with the shroud surface. The ballotini particle (greater than 60.0 um) had the second impact position occurring well upstream of the 'peak' of the hub while quartz particle's second impact positions were near the 'peak'. In general, the reflected trajectories, velocities and angles, predicted using the restitution ratios, show good agreement with the measured values. The simulation of the other trajectories, besides the main reflected trajectories, to represent the broad distributed curves measured at the planes which lie in the path of the reflected trajectories cannot be done without further experimental data on the restitution ratios for both the quartz and ballotini particle.

5.3 Comparison between Measured and Predicted Particle Separation Efficiency

The ballotini and quartz particles were seeded at the three height positions for each dust size between 30.0 and 150.0 um. The separation efficiency for each particle size (ballotini and quartz) was calculated and plotted in Figure 86. In this figure, the separation efficiency obtained on the actual axisymmetric separator was also included. The predicted separation efficiency for both ballotini and quartz particle was 100.0 percent, based on the predicted trajectories shown in Figure 55 to 85. However, the measured results were lower than predicted, and the deviation

increases as the particle's size decreases. The measured separation efficiency (by dust concentration defined in U.K.) for the 100.0 and 150.0 um quartz particle was 98.5 and 98.9 percent respectively; for the ballotini particle, they were 98.6 and 99.7 percent respectively. The difference between the quartz particles and ballotini particle was less than 1.0 percent while the difference from the prediction (for both particle type) was less than 2.0 percent. As the quartz particle's size decreases to 60.0 and 30.0 um, the measured separation efficiency was reduced to 96.6 (98.3 percent for 50.0 um ballotini) and 89.2 percent respectively which differed from the predicted efficiency by about 5.0 and 10.0 percent respectively. The dust lost (mostly through the filter bags) was assumed to be collected in the scavenge duct,hence,the measured separation efficiency may be slightly higher than indicted (for example, the separation efficiency (U.K.) for the 30.0 um quartz particles would rise by 0.43 percent for a 3.97 percent dust lost in this manner).

The projected difference between the measured and predicted separation efficiency for the 15.0 um particle (Figure 86)was about 25.0 percent. The deterioration in the separation efficiency for the small particles was due to the inaccurate modelling of the actual flowfield and the failure to simulate the broad range of reflected trajectories. These are related to the aerodynamic and inertia effects on the trajectories of particles less than 100.0 um. On the one hand, the trajectories of the 15.0 um particles are predominantly influenced by the aerodynamic drag of the flow while on the other hand, the 100.0 um particles are influenced mainly by the inertia forces. Furthermore, the end positions of the predicted trajectories for the 15.0 and 30.0 um were in the regions of moving separated flow, flow reversal and stagnation points which could affect their final positions. Limited evidence from the eroded pattern on the two glass plates (PLATE 13) shows a significant number of particles being 'drawn' from the upperside of the splitter lip to the

engine section due the high reverse flow (at the leading edge of the splitter). This evidence is somewhat circumspect, however, because the sidewall flows may differ signficantly from the central flow.

Although the trajectories of the 100 and 150 um particle are governed mainly by the inertia forces, the broad rebound angles could have caused some particles to be reflected into the engine section. However, the small difference of less than 2.0 percent shows that this did not affect the trajectories of the majority of the particles. But a combination of both broad rebound angles and aerodynamic effects could result in a significant proportion of dust entering the engine section. Clearly, the inviscid flow model cannot be used to accurately predict the trajectories of particles of less than 100.0 um apart from their main trajectories. The simulation of the reflected trajectories has to include the broad distribution of particle rebound angles, which depends on the accuracy of the restitution ratios.

Also in this figure, the measured separation efficiency in the actual axisymmetric separator was lower than that obtained in the test model although the trend was similar. The difference in the measured results is due mainly to the difference in the initial particle and flow conditions. The result obtained for the actual separator were carried out in a dust cloud where the initial conditions at the separator's inlet are generally unknown. On the contrary, all the initial particle (and flowfield) conditions in the present test model were known and yet similar trends were observed. Therefore, the measured results (based on the three initial positions)in the present model show that some dust particles in the actual separator behaved in similar manner.

Chapter 6

Review and Conclusions

Review

An experimental and theoretical study of particle trajectories in a gas turbine intake has been presented. Dust particles from 15.0 to 150.0um in diameter were locally seeded into a 30 degree section of an axisymmetric inertial separator at pre-defined initial positions. The dust particles used were the spherical ballotini glass beads and the irregular quartz particles (which are similar to AC Coarse and MIL-SPEC dust used in standard dust tests). The particle distribution (across a traverse plane) at several axial positions was determined with a laser anemometer. The particle velocity (speed and direction) was measured at the mean trajectory positions (from the particle distribution curves) using the same anemometer. The measured results were compared with a prediction of the particle trajectories (velocities and angles) using an analytical model, which was also developed as part of this project.

The particle trajectory prediction model is based on the solution of a set of particle equations of motion in a pre-defined flowfield. The pre-defined flowfield may be defined experimentally or predicted, in which case the flow was assumed to be inviscid, irrotational and incompressible. With such assumptions, the component flow velocities could be calculated from a set of potential function values.

The formulation of the particle equations of motion in Section 2.2 is based on the assumption of the drag force being the only force of interaction. Other assumptions included are that the dust concentration has to be sufficiently low so that there is no particle-particle interaction and the effect of the particle on the flowfield is negligible. Particles are also assumed to be spheres of

uniform density and approximately three orders of magnitude greater than the gas density (Section 2.5). During the experimental measurement of the particle trajectories (Chapter 4), these assumptions have been accommodated. The dust concentration used was kept to about 1.0 g/m^3 (which satisfies the requirement for a low dust concentration),also both the spherical ballotini and irregular quartz particles have densities of 2950.0 and 2650.0 kg/m^3 respectively (which satisfies the particle density requirement). The non-spherical quartz particle was included because in realistic conditions atmospheric dust particles are irregular in shape. The practical application of the prediction model in the investigation of particle trajectories,however,poses several limitations(Section 3.4) which formed the objectives of the present study, these limitations are:

a) the theoretical flowfield in the separator was assumed to be inviscid, irrotational and incompressible. In the present separator, flow separations and vortices (and their effects on the particle trajectories) exist in the actual flow but these have not been predicted,

b) the drag coefficient used in the prediction model was that derived for spherical particles. However,a different form of the drag coefficient may be required for the prediction of the trajectories for non-spherical quartz particles,

c) the restitution ratios (used to compute the particle re-bound velocity and angle) were those for non-spherical quartz particles (derived under limited conditions). Since no suitable data was found for the spherical ballotini particles, a simple expression (derived by trial and error matching of predicted and experimental results) was used to define a suitable restitution ratio.

In order to investigate the above limitations the particle trajectory prediction model has been modified to include a shape factor (Section 5.2) to account for the different drag force on non-spherical particles (limitation (b)), and, the restitution ratios (Section 3.3) for the spherical ballotini particle (limitation (c)). A further modification was also included to accept the experimental measured flowfield (limitation (a)). This measured flowfield was taken on the central (vertical) plane of the separator using the laser anemometer. Some areas of the separator were obstructed from measurement due to the curvature of the separator, for example, at the shroud surface and the under-side of the splitter lip. To overcome this problem the flow velocities and angles at these areas were assumed to be equal to the measured values from the nearest adjacent points. In other areas, such as the vortex re-circulation region and the areas with separated flows, the flow velocities were assumed to have a small non-zero value. It is appreciated, however, that these velocities require better definition.

Conclusions

The analysis of the predicted and measured results have been discussed in Chapter 5 and the conclusions can be summarised as follows;

a) the predicted results using the measured flowfield show good agreement with experimental data. The predicted particle velocities and angles using the inviscid flow were generally lower than the measured values, however, their trajectories show only slight difference from those predicted using the actual flow. The reason for the difference is due to the presence of a vortex re-circulation region at the base of the 'hump' of the hub,

a separation 'bubble' at the hub surface downstream of the peak of the 'hump', and flow separation at the shroud surface just downstream of the leading edge of the splitter. The blockage caused by this 'disturbed' flow resulted in a higher flow velocity although the main core flow directions remained relatively unchanged (except in certain areas).

b) the drag coefficients used in the prediction model gave good agreement with experimental data for the spherical ballotini particle. As for the irregular quartz particle, a correction factor of 0.4 (shape factor of 0.21) was included into the drag coefficient to account for the higher drag force. The predicted results using the modified drag coefficients gave good agreement with experimental data.

c) the restitution ratios for the quartz and ballotini particles has been found to be sufficiently accurate for predicting only the main particle trajectories reflected from a solid wall. However, the broadly distributed curves (Figures 55 to 85) which represent other reflected trajectories had not been simulated. The restitution ratios for the ballotini particle were obtained by trial and error matching with measured results. The restitution ratios for the quartz particle were obtained from the experimental studies by Tabakoff [Ref.16] although these were found to be inadequate (requiring further experimental study).

d) the trajectories of the 15.0 um particle are dominated by the aerodynamic drag force while the 100.0 and 150.0 um particle are influenced mainly by the inertia forces. As for the particles between 15.0 and 100.0 um, both the aerodynamic and inertia forces have an effect on their particle trajectories although it is hard to distinguish

which has the greater effect. In general, smaller particles achieved a higher velocities but their trajectories show a 'lag' behind the flow due to their small but significant inertia. The trajectories of the larger particle are 'ballistic' in nature where bounce is the main mechanism.

e) the predicted separation efficiency (using the actual and inviscid flow) for all the particle sizes ranging from 15.0 to 150.0 um was 100.0 percent. The measured separation efficiency for the 100.0 and 150.0 um (quartz and ballotini) particle was greater than 98.0 percent (the difference between measured and predicted separation efficiency for these sizes was less than 2.0 percent). Since the trajectories of these larger particles (greater 100.0 um) are predominantly 'ballistic' in nature, the inviscid flow was found to be sufficiently adequate (based on the small difference of less than 2.0 percent between measured and predicted separation efficiency). However, the trajectories of the smaller particles (less than 100.0 um) are influenced by both the aerodynamic and inertia forces but the particle behaviours in the vicinity of the flow separations and vortices cannot be simulated in the present inviscid flowfield. The measured separation efficiency for the 60.0 and 30.0 um quartz particle was 96.6 and 89.2 percent respectively although predicted efficiency was 100.0 percent. The measured separation efficiency for the 50.0 um ballotini particle was 98.3 percent. The difference (between the predicted and measured separation efficiency) appears to be due to the inaccurate modelling of the flowfield and the failure to simulate other (statistically) reflected trajectories.

In conclusion, it is considered that a model capable of modelling particle trajectories in a gas turbine intake has

been developed and through a series of tests using both ballotini and quartz particles (and a laser anemometer) the model has largely proved this capability and some areas of difficulty have been isolated. The areas which need further improvement are the better representation of the flowfield (which includes viscous effect) and a better formulation of the restitution ratios for the quartz particles. However, in general, the measured particle trajectories (velocities and angles) have shown good agreement with predicted results. Also, (although not presented in this thesis) the eroded surfaces observed after the quartz particle tests showed reasonably good agreement with predicted impact regions.However, erosion on the surface by ballotini particles was hard to distinguish due to their non-erosive properties.These studies also show that regions of separation exist within the separator and that the aerodynamics need improvement, and the studies have also highlighted the important role of the splitter.

Recommendation for further work.

Although the inviscid flowfield can be used to assess the separation performance of a gas turbine intake for particle greater than 100.0 um, it fails in the prediction for the smaller particle. One of the main causes appears to be the failure to model the actual flowfield (as described in (e) above). The inviscid model cannot truly represent the flow where flow separation and vortex re-circulation has taken place. The critical areas such as flow separation, stagnation regions and flow reversal on the splitter can affect the behaviour of a particle (especially a small particle). In the present separator, a significant amount of dust in the scavenge duct was found to have been 'drawn' from the upperside of the splitter lip into the engine section (by combining the effect of the flow reversal on the

splitter lip and flow separation on the shroud surface). To improve the situation it is proposed that a viscous, compressible code will be needed so that a better prediction of the particle trajectories can be obtained. Although the effect of these critical flows on the particle behaviour can be simulated, experimental validation may still be needed. Experimental studies would also need to investigate the particle interaction with not only these critical flows but the boundary layer effects as well. In the present studies, and in most other related studies, research such as those by Tabakoff [Ref.16], Breitman [Ref.5] and Lord [Ref.48], on the particle interaction with the boundary layer have been ignored due to the assumption of the short duration of time which the particle spend in them. This assumption may not always be true because of the high velocity gradient in the boundary layer which may affect the behaviour of the very small particles although the effect on the large particles is less so, due to their greater inertia. Experimental studies would be needed to investigate this effect on the particles less than 100.0 um in diameter.

The other deficiency in the prediction model is the inaccurate restitution ratios derived for the quartz particles. The uncertainty arising from the statistical factors in the restitution ratios for the quartz were found to be inadequate due to the insufficient data collected on the particle rebound characteristics. Most of the studies [Tabakoff, Ref.16] had been limited to 200.0 um particles impacting a solid surface at only 3 or 4 angles of attack. Further experimental studies are needed to derive more accurate restitution ratios (and deviations) for quartz particles less than 100.0um in diameter, impacting a solid wall at a wider range of angles of attack. The uncertainty in the restitution ratios can be used to predict other trajectories apart from the main reflected trajectories. The experimental technique developed in this study could significantly aid progress in this area.

Also, the prediction model does not take into account possible fragmentation (which was considered to be outside the scope of the current work) of a particle after an impact with a wall. Information on the particle fragmentation is sparse but Goodwin [Ref.49] (Mann, Ref.50) suggest that both the particle diameter and impact velocity have a significant effect on the degree of fragmentation. However, Goodwin's study was based on only three different particle diameters and three different impact velocities.Furthermore, the impact angle was kept to 90.0 degrees for only one target material. Further experimentation is needed to provide the necessary information on the effects of the particle impact speed and angle, particle diameter and target material on the particle fragmentation.

References

Ref.1 Rodgers,S.J., 'Evaluation of the Dust Cloud Generated by Helicopter Rotor Blade Downwash', 7th Annual Conference on Environmental Effects, Paper 67-ENV-1, 1967

Ref.2 Ray, M.G., Browne, J.L., 'T700 Engine Integral Inlet Separator', 6th European Rotorcraft and Powered Lift Aircraft Forum, Bristol, Sept. 1980

Ref.3 Ballard,J.R., Mann,D.L., Tan,S.C., ' Development of a 3-D Trajectory Prediction Technique for Helicopter Inlets ' MF2 Brochure 2A3/4L Final Report, Rolls-Royce Report LTN01018, May 1985

Ref.4 VITTAL,B.V.R.,TIPTON,D.L., BENNETT,W.A.,' Development of An Advanced Vaneless Inlet Particle Separator for Helicopter Engines', Allison Gas Turbine Division, Indianapolis

Ref.5 Breitman,D.S.,Dueck,E.G.,Habashi,W.G.,' Analysis of a Split Flow Inertial Particle Separator by Finite Element', Journal of Aircraft, Volume 22, No.2, Feb. 1985

Ref.6 Hamed,A., ' Particle Dynamics of an Inlet Flow Field with Swirling Vanes ',AIAA 81-0001, AIAA 19th Aerospace Sciences Meeting, Jan. 1981

Ref.7 Massey, B.S., 'Mechanics of Fluids ', 2nd. edn.,ch.10 Van Nost, Rein. Co., London 1976

Ref.8 Lunnon, R.G., ' Fluid resistance to Moving Sphere ', Proc. Roy. Soc., London A118,1928, pp.680-694

Ref.9 Winniy, H.F., ' Vortex System behind a Sphere Moving through Viscous Fluid ', Aero. Res. Comm., R&M, no.1531, 1932

Ref.10 Stokes,G.G., ' On the Effect of the Internal Friction of Fluid on the Motion of Pendulums ', Trans. Camb. Phil. Soc., no.9, 1851,pp.8-106

Ref.11 Happel & Brenner, ' Low Reynolds Hydrodynamics with special application to Particular Media ',Prentice Hall Inc., 1965, pp.40

Ref.12 Oseen,C.W., 'Uber die Stokessche Formel and Uber die Verwandte Aufgabe in der Hydrodynamik', Arkik fur Mathematik, Astronomi och Fysik 6, no.29, 1910

Ref.13 Boothroyd,R.G.,' Flowing Gas-Solid Suspensions',Chapman and Hall, London, 1971, pp.10

Ref.14 Schlichting,H., 'Boundary Layer Theory ', McGraw-Hill Inc. 1968, pp.104

Ref.15 Morsi, S.A., Alexander,A.J., ' An Investigation of Particle Trajectories in Two Phase Flow Systems', Journal of Fluid Mechanics, 1972, Vol.55, Part 2, pp.193-208

Ref.16 Tabakoff,W.,Hamed,A.,' Aerodynamic Effects on Erosion in Turbomachinery', JSME & ASME paper no.70, 1977 Joint Gas Turbine Congress, Tokyo, Japan, 1977, pp.574-581

Ref.17 Tabakoff,W., Wakeman,T., ' Test Facilities for Material Erosion at High Temperatures', ASTM pub., STP 664, 1978, pp.123-134

Ref.18 Grant,G.,Ball,R.,Tabakoff,W.,' An Experimental Study of Erosion Rebound Characteristics of High Speed Particle Impacting a Stationary Specimen', Univ. of Cincinatti,Technical Report no.33-36, May 1970, AO-760578

Ref.19 Tan,S.C., ' Availability of Particle Restitution Coefficients data for IPS Design ', Interim Research Note, Cranfield Inst. Of Technology, July 1987

Ref.20 Tabakoff,W.,Malak,M.F., ' Laser Measurement of Fly Ash Rebound Parameters for use in Trajectory Calculation ',ASME paper 85-GT-161, Gas Turbine Conference and Exhibit, Houston, Texas, March 1985

Ref.21 Tabakoff,W.,Malak,M.F.,Hamed,A., ' Laser Measurement Of Solid Particle Rebound Parameter Impacting ON 2024 Aluminium Alloy ', AIAA-85-1570, AIAA 18th Fluid Dynamics and Plasmadynamics and Laser Conference, July 1985, Cincinatti, Ohio

Ref.22 Armstrong,J.D., Collings,N., Shayler,P.J., ' Trajec- of Particle Rebounding off Target Plane', AIAA Journal, Feb. 1982

Ref.23 Duffy,R.J. et.al.,' Integral Engine Inlet Particle Separator Design Guide ',Vol II, USAAMRDL-TR-75-31B, Aug. 1975

Ref.24 Ledermann,W.,' Handbook of Applicable Mathematics', Vol III, John Wiley & Son

Ref.25 Shieh,C.F., Delaney,R.A., Tipton,D.L., ' Analysis of the Flow Field in an Engine Inlet Particle Separator', Allison Gas Turbine Operations, General

Motors Corp.,Indianapolis

Ref.26 Mann, D.,' Computer Prediction of Particle Trajectories for use in Particle Separator Design ',Leavesden Technical Note, Report no. LTN01181, Sept. 1986

Ref.27 Chung,T.J.,'Finite Element Analysis in Fluid Dynamics' McGraw-Hill Inc., 1978

Ref.28 Connors,J.J.,Brebbia,C.A.,' Finite Element Technique for Fluid Flow', Newnes-Butterworth,1976

Ref.29 Livesly,R.K.,' Finite Element. An Introduction for Engineer', Cambridge Univ. Press,1983

Ref.30 Kuethe,A.M.,Chow,C.Y.,' Foundation of Aerodynamics. Basics of Aerodynamics Design', 3rd Edn., John Wiley & Sons

Ref.31 Rudinger,G.,' Flow of Solid Particles in Gas', AGARD-AG-222, Oct.1976

Ref.32 Hinze, J.O.,' Turbulence', 2nd ed., McGraw-Hill Book Co., 1975

Ref.33 Chuen-Yen Chow, 'An Introduction to Computational Fluid Mechanics'

Ref.34 Mohsen, A.S.Mirzabozorg, 'Measurement And Computation of the Flow in an Axial Blade Row', Phd Thesis, Cranfield Institute Of Technology

Ref.35 Ross, M.M, 'Transit Laser Anemometry Data Reduction for Flow in Industrial Turbomachinery', Optica Acta Vol.27, No.4, P511-528, 1980

Ref.36 Mayo,W.T.Jr., Smart, A.E., 'Tutorial Digital Correlator Data Processing', Photo Correlation Techniques in Fluid Mechanics, Proceeding from the 4th International Conference, Stanford University, Stanford, California, 1980

Ref.37 Melling, A., 'Seeding for Laser Anemometry', Optical Measurement Techniques for Internal Flows, Short Course Notes, 1985, Cranfield Institute of Technology

Ref.38 Durst,F., Melling,A., Whitelaw,J.H., 'Principles and Practical of Laser Doppler Anemometry, Academic Press, 1976

Ref.39 B.S.1042:1943. 'Flow Measurement', Issued by British Standards Institute, 2, Park St., London W1

Ref.40 Zenz, A.F., Othmer, D.F., ' Fluidisation and Fluid-Particle Systems', Reinhold Chemical Series, Reinhold Publishing Co., 1960

Ref.41 Heywood, A., Proc. Inst. Mech. Engrs., (London), 140, 257 (1938), Chem. & Ind., (London), 56 149 (1937)

Ref.42 Johnstone, H.F., Pigford, R.L. and Chapin, J.H.,Transaction Am. Inst. Chem. Engrs., 37, 95 (1941)

Ref.43 Durand, W.F., 'Aerodynamic Theory', Vol.III, Berlin, Julius Springer, 1935, P.69

Ref.44 Hussein, M.F., Tabakoff,W., 'Calculation of Particle Trajectories in a Stationary 2-D Cascade', June 1972, Univ. of Cincinnati, Ohio

Ref.45 Spiegel, M.R.,'Advanced Mathematics For Engineers and Scientists', Schaum Series, McGraw-Hill Book Co.,1980

Ref.46 Goodman, A.W.,'Analytical Geometry And the Calculus', 4th. Ed., Collier MacMillan Int. Edits.

Ref.47 Kreyszig, E., 'Advanced Engineering Mathematics',4th. Ed., John Wiley and Sons.

Ref.48 Lord, M.J., Singh,U.K., 'Theoretical Study of Potential Turbine Erosion Hazard by Means of Particle Trajectory Calculations', Proc. 5th Int. Conf. on Erosion by Solid and Liquid Impact, 1979, Paper no.54

Ref.49 Goodwin,J.E., Sage,W. and Tilly, G.P., 'Study of Erosion by Solid Particles', Proc. of the I.Mech. E., Volume 184, Part 1, 1969-70.

Ref.50 Mann, D., Leavesden Technical Note, Report no. LTN01157 May, 1986

APPENDIX

A-1 Formulation of the Particle Equations Of Motion

The Navier-Stokes equation for the motion of a spherical particle in a steady, slow moving, incompressible flow is given as (ignoring inertia and body forces);

$$\text{GRAD } P = \mu_g \nabla^2(\tilde{V}_g) \qquad (1\text{-}1)$$

or,

$$\frac{\partial P}{\partial x} = \mu_g \nabla^2(U_g)$$

$$\frac{\partial P}{\partial y} = \mu_g \nabla^2(V_g)$$

$$\frac{\partial P}{\partial z} = \mu_g \nabla^2(W_g)$$

since $\tilde{V}_g = U_g\tilde{i} + V_g\tilde{j} + W_g\tilde{k}$ and $\tilde{i}$, $\tilde{j}$, $\tilde{k}$ are unit vectors in the cartesian coordinates.

The continuity equation can be written as;

$$\text{DIV } (\tilde{V}_g) = 0 \qquad (1\text{-}2)$$

Taking the divergence of both sides of equation (1-1) and (1-2) gives;

$$\text{DIV GRAD } P = \nabla.\nabla P = \nabla^2(P) = 0 \qquad (1\text{-}3)$$

The simplest form of the solution for equation (1-3) given by Durand [Ref.43] as;

$$P = \frac{-Ax}{r^3} \qquad (1\text{-}4)$$

where

$$r = (x^2 + y^2 + z^2)^{0.5}$$

Substituting (1-4) into (1-1) gives;

$$\nabla^2 U = \frac{A}{\mu_g}\left[\frac{3x^2}{r^5} - \frac{1}{r^3} \right]$$

$$\nabla^2 V = \frac{A}{\mu_g}\left[\frac{3xy}{r^5} \right]$$

$$\nabla^2 W = \frac{A}{\mu_g}\left[\frac{3xz}{r^5} \right]$$

The constant A given by Durand [Ref.43] was;

$$0.75\ \mu_g\ D_p\ |\tilde{V}_{g\infty}| \qquad (1\text{-}5)$$

where

$$\tilde{V}_{g\infty} = V_g - V_p$$

Substituting (1-5) into (1-4) gives;

$$P = -\frac{3\ \mu_g\ D_p\ |\tilde{V}_{g\infty}| x}{4\ r^3} \qquad (1\text{-}6)$$

and since $r = D_p/2$, equation (1-6) becomes;

$$P = - \frac{6 \mu_g D_p |\tilde{V}_{g\infty}| x}{D_p^2}$$

The pressure is greatest and least at point P_1 and P_2 (Figure 87) respectively, where $x = \pm D_p/2$.

At these points, the pressures are, [Hussein, Ref.44],

$$P = \pm \frac{3 \mu_g |\tilde{V}_{g\infty}|}{D_p}$$

There are no frictional forces at these points since $\partial u/\partial x$, $\partial u/\partial y$, $\partial u/\partial z$ are equal zero. However, frictional forces exists at other points on the sphere and they are greatest at the 'equator', i.e. x=0 (Figure 87). The shear force at the 'equator' being;

$$\tau = \frac{3 \mu_g |\tilde{V}_{g\infty}|}{D_p}$$

Durand [Ref.43] found that these shear forces are exactly equal to the surplus or deficit in pressure at point P_1 and P_2 respectively. The shear forces can be determined at every point on the surface of the sphere. Hussein [Ref.44] stated that the resultant of the pressure difference and friction forces has the same magnitude at all points and equal,

$$\frac{3 \mu_g |\tilde{V}_{g\infty}|}{Dp} \qquad (1-7)$$

Hence, the total drag force acting on the sphere can be determined by multiplying the resultant force per unit area (1-7) by the area of the surface of the sphere. This gives

$$\tilde{D} = \frac{3\ \mu_g\ |\tilde{v}_{g\infty}|\ 4\pi r^2}{D_p} \qquad (1\text{-}8)$$

Equation (1-8) is the well known 'Stokes Formula'.

A-2 Mathematical Model of the Particle Equations of Motion

A particle's position vector (Figure 7) in cylindrical coordinate can be written as;

$$\tilde{r}_p = r_p\tilde{R} + z_p\tilde{K} \qquad (2\text{-}1)$$

The Coriolis equation is given by;

$$\dot{\tilde{r}}_p = \frac{\partial \tilde{r}_p}{\partial t} + \omega \times \tilde{r}_p$$

Substituting equation (2-1) into the Coriolis equation gives;

$$\dot{\tilde{r}}_p = \frac{\partial}{\partial t}[r_p\tilde{R} + z_p\tilde{K}] + \dot{\Theta}_p\tilde{K} \times [r_p\tilde{R} + z_p\tilde{K}]$$

where $\omega = \dot{\Theta}_p \tilde{K}$. The above equation gives;

$$\dot{\tilde{r}}_p = \frac{\partial r_p}{\partial t}\tilde{R} + \frac{\partial z_p}{\partial t}\tilde{K} + r_p\dot{\Theta}_p\tilde{\Theta} \qquad (2\text{-}2)$$

Substituting equation (2-2) into the Coriolis equation again gives;

$$\ddot{\tilde{r}}_p = \frac{\partial}{\partial t}\left[\frac{\partial r_p}{\partial t}\tilde{R} + \frac{\partial z_p}{\partial t}\tilde{K} + r_p\dot{\Theta}_p\tilde{\Theta} \right]$$

$$+ \dot{\Theta}_p\tilde{K} \times \left[\frac{\partial r_p}{\partial t}\tilde{R} + \frac{\partial z_p}{\partial t}\tilde{K} + r_p\dot{\Theta}_p\tilde{\Theta} \right]$$

$$= [\ \ddot{r}_p - r_p\dot{\Theta}_p^2]\tilde{R} + [\ r_p\ddot{\Theta}_p + 2\dot{r}_p\dot{\Theta}_p\ ]\tilde{\Theta} + \ddot{z}_p\tilde{K} \qquad (2\text{-}3)$$

The component acceleration terms are shown in Figure 6 which also include the component drag forces. Hence, the resultant forces acting on a particle can be written in their direction as;

$\tilde{R}$ direction; $\quad m_p[\ \ddot{r}_p - r_p\dot{\Theta}_p^2] - D_R = 0$

$\tilde{\Theta}$ direction; $\quad m_p[\ r_p\ddot{\Theta}_p + 2\dot{r}_p\dot{\Theta}_p\ ] - D_\Theta = 0$

$\tilde{K}$ direction; $\quad m_p\ddot{z}_p - D_Z = 0$

where D_R, D_Θ and D_Z are the component drag forces.

A-3 Solution of the Particle Equations of Motion using the Kutta-Fehlberg Fifth Order Method

The six equations describing the particle equations of motion (2-21) are given as follows;

$$F_1 = V_{rp}, \quad F_4 = G(V_{rg} - V_{rp}) + \frac{V_{\Theta p}^2}{r_p}$$

$$F_2 = V_{\Theta p}, \quad F_5 = G(V_{\Theta g} - V_{\Theta p}) - \frac{2V_{rp}V_{\Theta p}}{r_p} \qquad (3\text{-}1)$$

$$F_3 = V_{zp}, \quad F_6 = G(V_{zg} - V_{zp})$$

Equation (2-23) can be expanded as follows;

$$r_{pn+1i} = r_{pni} + \Delta t \sum_{k=1}^{6} c_k H_{1k}$$

$$\Theta_{pn+1i} = \Theta_{pni} + \Delta t \sum_{k=1}^{6} c_k H_{2k}$$

$$z_{pn+1i} = z_{pni} + \Delta t \sum_{k=1}^{6} c_k H_{3k}$$

$$V_{rpn+1i} = V_{rpni} + \Delta t \sum_{k=1}^{6} c_k H_{4k}$$

$$V_{\Theta pn+1i} = V_{\Theta pni} + \Delta t \sum_{k=1}^{6} c_k H_{5k}$$

$$V_{zpn+1i} = V_{zpni} + \Delta t \sum_{k=1}^{6} c_k H_{6k}$$

and,

$$H_{1k} = F_1 \left(V_{rp} + \Delta t \sum_{\lambda=1}^{k} \beta_{k\lambda} H_{4\lambda}\right)$$

$$H_{2k} = F_2 \left(r_p + \Delta t \sum_{\lambda=1}^{k} \beta_{k\lambda} H_{1\lambda},\ V_{\Theta p} + \Delta t \sum_{\lambda=1}^{k} \beta_{k\lambda} H_{5\lambda}\right)$$

$$H_{3k} = F_3 \left(V_{zp} + \Delta t \sum_{\lambda=1}^{k} \beta_{k\lambda} H_{6\lambda}\right)$$

$$H_{4k} = F_4 \left(r_p + \Delta t \sum_{\lambda=1}^{k} \beta_{k\lambda} H_{1\lambda},\ V_{rp} + \Delta t \sum_{\lambda=1}^{k} \beta_{k\lambda} H_{4\lambda},\right.$$
$$\left. V_{\Theta p} + \Delta t \sum_{\lambda=1}^{k} \beta_{k\lambda} H_{5\lambda},\ V_{zp} + \Delta t \sum_{\lambda=1}^{k} \beta_{k\lambda} H_{6\lambda}\right)$$

$$H_{5k} = F_5 \left(r_p + \Delta t \sum_{\lambda=1}^{k} \beta_{k\lambda} H_{1\lambda},\ V_{rp} + \Delta t \sum_{\lambda=1}^{k} \beta_{k\lambda} H_{4\lambda},\right.$$
$$\left. V_{\Theta p} + \Delta t \sum_{\lambda=1}^{k} \beta_{k\lambda} H_{5\lambda},\ V_{zp} + \Delta t \sum_{\lambda=1}^{k} \beta_{k\lambda} H_{6\lambda}\right)$$

$$H_{6k} = F_6 \left(r_p + \Delta t \sum_{\lambda=1}^{k} \beta_{k\lambda} H_{1\lambda},\ V_{rp} + \Delta t \sum_{\lambda=1}^{k} \beta_{k\lambda} H_{4\lambda},\right.$$

$$V_{\Theta p} + \Delta t \sum_{\lambda=1}^{k} \beta_{k\lambda} H_{5\lambda},\ V_{zp} + \Delta t \sum_{\lambda=1}^{k} \beta_{k\lambda} H_{6\lambda})$$

where k = 2,8 and c_k, $\beta_{k\lambda}$ are coefficients of the Kutta-Fehlberg method given in TABLE III.

For the first term where k = 1,

$$H_{11} = F_1 (V_{rp})$$

$$H_{21} = F_2 (r_p, V_{\Theta p})$$

$$H_{31} = F_3 (V_{zp})$$

$$H_{41} = F_4 (r_p, V_{rp}, V_{\Theta p}, V_{zp})$$

$$H_{51} = F_5 (r_p, V_{rp}, V_{\Theta p}, V_{zp})$$

$$H_{61} = F_6 (r_p, V_{rp}, V_{\Theta p}, V_{zp})$$

The local truncation error yields;

$$E_1 = \frac{5}{66} \Delta t \ (H_{11} + H_{16} - H_{17} - H_{18})$$

$$E_2 = \frac{5}{66} \Delta t \ (H_{21} + H_{26} - H_{27} - H_{28})$$

$$E_3 = \frac{5}{66} \Delta t \ (H_{31} + H_{36} - H_{37} - H_{38})$$

$$E_4 = \frac{5}{66} \Delta t \left(H_{41} + H_{46} - H_{47} - H_{48} \right)$$

$$E_5 = \frac{5}{66} \Delta t \left(H_{51} + H_{56} - H_{57} - H_{58} \right)$$

$$E_6 = \frac{5}{66} \Delta t \left(H_{61} + H_{66} - H_{67} - H_{68} \right)$$

A-4 Polynomial Expansion of the Interpolation Functions for a Three dimensional Element

The shape function for a 20 node, three dimensional element is given in equation (2-32) to (2-34). The shape function for the corner nodes (Figure 11) where ξ_i, η_i, $\zeta_i = \pm 1$,

at i = 1, 3, 5, 7, 13, 15, 17, 19

$$N_1 = [(1+\xi)(1-\eta)(1-\zeta)(\xi-\eta-\zeta-2)]/8$$

$$N_3 = [(1-\xi)(1-\eta)(1-\zeta)(-\xi-\eta-\zeta-2)]/8$$

$$N_5 = [(1-\xi)(1+\eta)(1-\zeta)(-\xi+\eta-\zeta-2)]/8$$

$$N_7 = [(1+\xi)(1+\eta)(1-\zeta)(\xi+\eta-\zeta-2)]/8$$

$$N_{13} = [(1+\xi)(1-\eta)(1+\zeta)(\xi-\eta+\zeta-2)]/8$$

$$N_{15} = [(1-\xi)(1-\eta)(1+\zeta)(-\xi-\eta+\zeta-2)]/8$$

$$N_{17} = [(1-\xi)(1+\eta)(1+\zeta)(-\xi+\eta+\zeta-2)]/8$$

$$N_{19} = [(1+\xi)(1+\eta)(1+\zeta)(\xi+\eta+\zeta-2)]/8$$

and at other node points where ξ_i, ζ_i, $\eta_i = 0$ or ± 1,

at midside nodes where i= 2, 6, 18, 14

$$N_2 = [(1-\xi^2)(1-\eta)(1-\zeta)]/4$$

$$N_6 = [(1-\xi^2)(1+\eta)(1-\zeta)]/4$$

$$N_{18} = [(1-\xi^2)(1+\eta)(1+\zeta)]/4$$

$$N_{14} = [(1-\xi^2)(1-\eta)(1+\zeta)]/4$$

at midside nodes where i= 9, 10, 11, 12

$$N_9 = [(1-\zeta^2)(1+\eta)(1-\xi)]/4$$

$$N_{10} = [(1-\zeta^2)(1-\eta)(1-\xi)]/4$$

$$N_{11} = [(1-\zeta^2)(1-\eta)(1+\xi)]/4$$

$$N_{12} = [(1-\zeta^2)(1+\eta)(1+\xi)]/4$$

at midside nodes where i= 4, 8, 16, 20

$$N_4 = [(1-\eta^2)(1-\zeta)(1-\xi)]/4$$

$$N_8 = [(1-\eta^2)(1+\zeta)(1-\xi)]/4$$

$$N_{16} = [(1-\eta^2)(1-\zeta)(1+\xi)]/4$$

$$N_{20} = [(1-\eta^2)(1+\zeta)(1+\xi)]/4$$

A-5 Formulation of the Jacobian Matrix of Transformation

The Jacobian matrix is as follows;

$$[\ J\ ] = \begin{bmatrix} \frac{\partial x}{\partial \xi} & \frac{\partial y}{\partial \xi} & \frac{\partial z}{\partial \xi} \\ \frac{\partial x}{\partial \eta} & \frac{\partial y}{\partial \eta} & \frac{\partial z}{\partial \eta} \\ \frac{\partial x}{\partial \zeta} & \frac{\partial y}{\partial \zeta} & \frac{\partial z}{\partial \zeta} \end{bmatrix} \qquad (5\text{-}1)$$

The interpolation functions which are defined for isoparametric elements are given by equation (2-41) as;

$$\Phi = \sum_{i=1}^{20} N_i \Phi_i, \quad x = \sum_{i=1}^{20} N_i x_i, \quad y = \sum_{i=1}^{20} N_i y_i, \quad z = \sum_{i=1}^{20} N_i z_i$$

The full expansion of the interpolation can be found in equation (2-29) as follow;

$$\begin{aligned} U_j = {} & a_{j1} + a_{j2}\xi + a_{j3}\eta + a_{j4}\zeta + a_{j5}\xi^2 + a_{j6}\eta^2 + a_{j7}\zeta^2 \\ & + a_{j8}\xi\eta + a_{j9}\xi\zeta + a_{j10}\eta\zeta + a_{j11}\xi^2\eta + a_{j12}\xi^2\zeta \\ & + a_{j13}\eta^2\xi + a_{j14}\eta^2\zeta + a_{j15}\zeta^2\xi + a_{j16}\zeta^2\eta \\ & + a_{j17}\xi\eta\zeta + a_{j18}\xi^2\eta\zeta + a_{j19}\eta^2\xi\zeta \\ & + a_{j20}\zeta^2\xi\eta \end{aligned} \tag{5-2}$$

where the local coordinate S_1, S_2 and S_3 corresponds to ξ, η, ζ respectively and a_j are the independent coefficient. U_j corresponds to the function value Φ, x, y and z.

The terms on the right hand side of the Jacobian matrix (5-1) are derived by taking the derivatives of the interpolation function (5-2) w.r.t the local axes ξ, η and ζ as follows;

$$\begin{aligned} \frac{\partial U_j}{\partial \xi} = {} & a_{j2} + a_{j5}(2\xi) + a_{j8}(\eta) + a_{j9}(\zeta) + a_{j11}(2\xi\eta) \\ & + a_{j12}(2\xi\zeta) + a_{j13}(\eta^2) + a_{j15}(\zeta^2) + a_{j17}(\eta\zeta) \\ & + a_{j18}(2\xi\eta\zeta) + a_{j19}(\eta^2\zeta) + a_{j20}(\zeta^2\eta) \end{aligned}$$

$$\frac{\partial U_j}{\partial \eta} = a_{j3} + a_{j6}(2\eta) + a_{j8}(\xi) + a_{j10}(\zeta) + a_{j11}(\xi^2)$$

$$+ a_{j13}(2\xi\eta) + a_{j14}(2\eta\zeta) + a_{j16}(\zeta^2) + a_{j17}(\xi\zeta)$$
$$+ a_{j18}(\xi^2\zeta) + a_{j19}(2\xi\eta\zeta) + a_{j20}(\zeta^2\xi)$$

$$\frac{\partial U_j}{\partial \zeta} = a_{j4} + a_{j7}(2\zeta) + a_{j9}(\xi) + a_{j10}(\eta) + a_{j12}(\xi^2)$$
$$+ a_{j14}(\eta^2) + a_{j15}(2\zeta\xi) + a_{j16}(2\zeta\eta) + a_{j17}(\xi\eta)$$
$$+ a_{j18}(\xi^2\eta) + a_{j19}(\eta^2\xi) + a_{j20}(2\xi\eta\zeta)$$

The independent coefficients, a_j, are computed by substituting the local coordinate value (TABLE IV) and nodal function value from each node point in an element (Fig.12) into equation (5-2). Hence, 20 simultaneous equations (which is different for each finite element) is obtained for each element which can then be solved to give the coefficients values.

A-6 Transformation of a Point defined in the Global Coordinate to the Local Coordinate

A point can be defined in the global cartesian coordinates as x_p, y_p and z_p which can also be defined by another axes system (defined in a isoparametric element with its origin at the centroid). The non-linear equation (2-46) is given as;

$$F_1 = \sum_{i=1}^{20} N_i x_i - x \qquad F_2 = \sum_{i=1}^{20} N_i y_i - y \qquad F_3 = \sum_{i=1}^{20} N_i z_i - z \quad (6\text{-}1)$$

where $N_i = N(\xi,\eta,\zeta)$.

Hence,

$$F_j = \sum_{i=1}^{20} N_i X_{ij} - X_j = 0 \qquad j = 1,3 \qquad (6\text{-}2)$$

Differentiating the above equation (6-1) w.r.t. ξ, η and ζ, for example, for function F_1 gives,

$$\frac{\partial F_1}{\partial \xi} = \sum_{i=1}^{20} x_i \frac{\partial N_i}{\partial \xi}, \quad \frac{\partial F_1}{\partial \eta} = \sum_{i=1}^{20} x_i \frac{\partial N_i}{\partial \eta}, \quad \frac{\partial F_1}{\partial \zeta} = \sum_{i=1}^{20} x_i \frac{\partial N_i}{\partial \zeta}$$

since $\partial x/\partial \xi$, $\partial x/\partial \eta$ and $\partial x/\partial \zeta$ are zero.

Hence, 9 different equations can be obtained by differentiating equation (6-2);

$$\frac{\partial F_j}{\partial \xi} = \sum_{i=1}^{20} x_{ij} \frac{\partial N_i}{\partial \xi}, \quad \frac{\partial F_j}{\partial \eta} = \sum_{i=1}^{20} x_{ij} \frac{\partial N_i}{\partial \eta}, \quad \frac{\partial F_j}{\partial \zeta} = \sum_{i=1}^{20} x_{ij} \frac{\partial N_i}{\partial \zeta} \qquad (6\text{-}3)$$

where j=1,3 (=x,y,z) and i=1,20.

Expanding equation (6-2) in the Taylor's series gives;

$$dF_j = \frac{\partial F_j}{\partial \xi} \Delta\xi + \frac{\partial F_j}{\partial \eta} \Delta\eta + \frac{\partial F_j}{\partial \zeta} \Delta\zeta + O(\Delta\xi^2) + O(\Delta\eta^2) + O(\Delta\zeta^2) + \ldots \qquad (6\text{-}4)$$

and

$$dF_j = F_j - (F_j)o$$

$$= - (F_j)o$$

since $F_j = 0$ (from (6-2)).

Ignoring second order terms, equation (6-4) can be written in matrix form as follows;

$$\begin{bmatrix} (-F_1)o \\ (-F_2)o \\ (-F_3)o \end{bmatrix} = \begin{bmatrix} \frac{\partial x}{\partial \xi} & \frac{\partial x}{\partial \eta} & \frac{\partial x}{\partial \zeta} \\ \frac{\partial y}{\partial \xi} & \frac{\partial y}{\partial \eta} & \frac{\partial y}{\partial \zeta} \\ \frac{\partial z}{\partial \xi} & \frac{\partial z}{\partial \eta} & \frac{\partial z}{\partial \zeta} \end{bmatrix} \begin{bmatrix} \Delta\xi \\ \Delta\eta \\ \Delta\zeta \end{bmatrix}$$

$$= [J]^T \begin{bmatrix} \Delta\xi \\ \Delta\eta \\ \Delta\zeta \end{bmatrix}$$

where $[J]^T$ is the transpose of the Jacobian matrix of transformation (which had been derived in Appendix A-5). The terms in this matrix are calculated by substituting the global cartesian coordinate of a point (x,y,z). The terms in the L.H.S are calculated by substituting an initial guessed value of the point's local coordinates (for example, $\xi o = \eta o = \zeta o = 0.0$) and it's global coordinates into equation (6-1). The increment $\Delta\xi$, $\Delta\eta$ and $\Delta\zeta$ can then be obtained by Cramer's rule [Spiegel, Ref.45] as follows;

$$\Delta\xi = \begin{vmatrix} (-F_1)o & \frac{\partial x}{\partial \eta} & \frac{\partial x}{\partial \zeta} \\ (-F_2)o & \frac{\partial y}{\partial \eta} & \frac{\partial y}{\partial \zeta} \\ (-F_3)o & \frac{\partial z}{\partial \eta} & \frac{\partial z}{\partial \zeta} \end{vmatrix} / \left|[J]^T\right|$$

$$\Delta\eta = \begin{vmatrix} \frac{\partial x}{\partial \xi} & (-F_1)o & \frac{\partial x}{\partial \zeta} \\ \frac{\partial y}{\partial \xi} & (-F_2)o & \frac{\partial y}{\partial \zeta} \\ \frac{\partial z}{\partial \xi} & (-F_3)o & \frac{\partial z}{\partial \zeta} \end{vmatrix} / \left|[J]^T\right|$$

$$\Delta\zeta = \begin{vmatrix} \frac{\partial x}{\partial \xi} & \frac{\partial x}{\partial \eta} & (-F_1)o \\ \frac{dy}{\partial \xi} & \frac{dy}{\partial \eta} & (-F_2)o \\ \frac{\partial z}{\partial \xi} & \frac{\partial z}{\partial \eta} & (-F_3)o \end{vmatrix} / \left|[J]^T\right|$$

Thus, new value of the local coordinate ca be obtained;

$$\xi_{new} = \xi_{old} + \Delta\xi$$

$$\eta_{new} = \eta_{old} + \Delta\eta$$

$$\zeta_{new} = \zeta_{old} + \Delta\zeta$$

Having obtained the new values of ξ, η and ζ, they are then repeatedly substituted back into (6-2) and (6-3) until F_1, F_2 and F_3 approaches zero. However, the condition $F_j = 0$, is difficult to attain due to the truncation error of the Taylor's series, which has the second order of magnitude. Hence, a small tolerance was used to end the iterative process.

A-7 Computation of the Unit Vector Normal to a Wall Surface

The basic concept regarding the calculation of the unit vector normal to a surface has been discussed by Goodman [Ref.46], Kreyszig [Ref.47] and Spiegel [Ref.45]. In general, let a surface be defined by the function Z=f(X,Y) as shown in Figure 88. If the surface has a tangent plane ABC at point $P_0(X_0,Y_0,Z_0)$, then the plane must contain the lines P_0M and P_0N which are parallel to plane ZX and ZY respectively (Figure 88). If the surface is defined by the function Z=f(X,Y), then Z_x=df/dx is the rate of change of Z as X changes along the lines P_0M. Hence, a unit change in X produces a change in Z_x, in the Z direction along line P_0M, but remains unchanged in the Y direction. The vector

parallel to line P_0M is;

$$\tilde{V} = \tilde{i} + 0\tilde{j} + f_x(X_0,Y_0)\tilde{k}$$

since $Z_x=f_x(Xo,Yo)$ and, $\tilde{i},\tilde{j},\tilde{k}$ are unit vectors in the X,Y,Z direction respectively. Similarly the vector parallel to line P_0N is;

$$\tilde{W} = 0\tilde{i} + \tilde{j} + f_y(X_0,Y_0)\tilde{k}$$

The cross product of vectors $\tilde{V}$ and $\tilde{W}$ gives the unit vector normal at the point (X_0,Y_0) in the outward direction, hence;

$$\tilde{V} X \tilde{W} = - f_x\tilde{i} - f_y\tilde{j} + \tilde{k} \qquad (7\text{-}1)$$

In general, if a surface can be defined by the equation,

$$S = f(x,y,z) = \text{constant}$$

Then GRAD S gives the vector normal to the surface [Spiegel, Ref.45], hence,

$$\text{GRAD } S = \frac{\partial S}{\partial x}\tilde{i} + \frac{\partial S}{\partial y}\tilde{j} + \frac{\partial S}{\partial z}\tilde{k}$$

However, explicit expression for the function $S = f(X,Y,Z)$ is not always available but X,Y and Z can be expressed by

the local coordinate ξ, η and ζ, therefore,

$$\frac{\partial S}{\partial \xi} = \frac{\partial S}{\partial x}\frac{\partial x}{\partial \xi} + \frac{\partial S}{\partial y}\frac{\partial y}{\partial \xi} + \frac{\partial S}{\partial z}\frac{\partial z}{\partial \xi}$$

$$\frac{\partial S}{\partial \eta} = \frac{\partial S}{\partial x}\frac{\partial x}{\partial \eta} + \frac{\partial S}{\partial y}\frac{\partial y}{\partial \eta} + \frac{\partial S}{\partial z}\frac{\partial z}{\partial \eta}$$

$$\frac{\partial S}{\partial \zeta} = \frac{\partial S}{\partial x}\frac{\partial x}{\partial \zeta} + \frac{\partial S}{\partial y}\frac{\partial y}{\partial \zeta} + \frac{\partial S}{\partial z}\frac{\partial z}{\partial \zeta}$$

or in matrix form,

$$\begin{bmatrix} \frac{\partial S}{\partial \xi} \\ \frac{\partial S}{\partial \eta} \\ \frac{\partial S}{\partial \zeta} \end{bmatrix} = [J] \begin{bmatrix} \frac{\partial S}{\partial x} \\ \frac{\partial S}{\partial y} \\ \frac{\partial S}{\partial z} \end{bmatrix} \qquad (7\text{-}2)$$

where [J] is the Jacobian matrix of transformation (Appendix A-5). Taking the inverse of the matrix (7-2) gives the form similar to equation (7-1) as;

$$\begin{bmatrix} \frac{\partial S}{\partial x} \\ \frac{\partial S}{\partial y} \\ \frac{\partial S}{\partial z} \end{bmatrix} = [J]^{-1} \begin{bmatrix} \frac{\partial S}{\partial \xi} \\ \frac{\partial S}{\partial \eta} \\ \frac{\partial S}{\partial \zeta} \end{bmatrix} \qquad (7\text{-}3)$$

Function S=f(x,y,z)=constant can also be expressed as

$$S = f(x,y) + \text{constant} = z$$

Hence, replacing function S by function z in matrix (7-3) gives;

$$\begin{bmatrix} \frac{\partial z}{\partial x} \\ \frac{\partial z}{\partial y} \\ 1 \end{bmatrix} = [J]^{-1} \begin{bmatrix} \frac{\partial z}{\partial \xi} \\ \frac{\partial z}{\partial \eta} \\ \frac{\partial z}{\partial \zeta} \end{bmatrix} \qquad (7\text{-}4)$$

The L.H.S. of matrix (7-4) is also a unit vector normal to a surface defined by a function z. However, in this case, the terms on the R.H.S. of the equation can be calculated since x,y and z can be expressed as a function of ξ, η and ζ. The method of calculating these terms (R.H.S.) are shown in Appendix A-5.

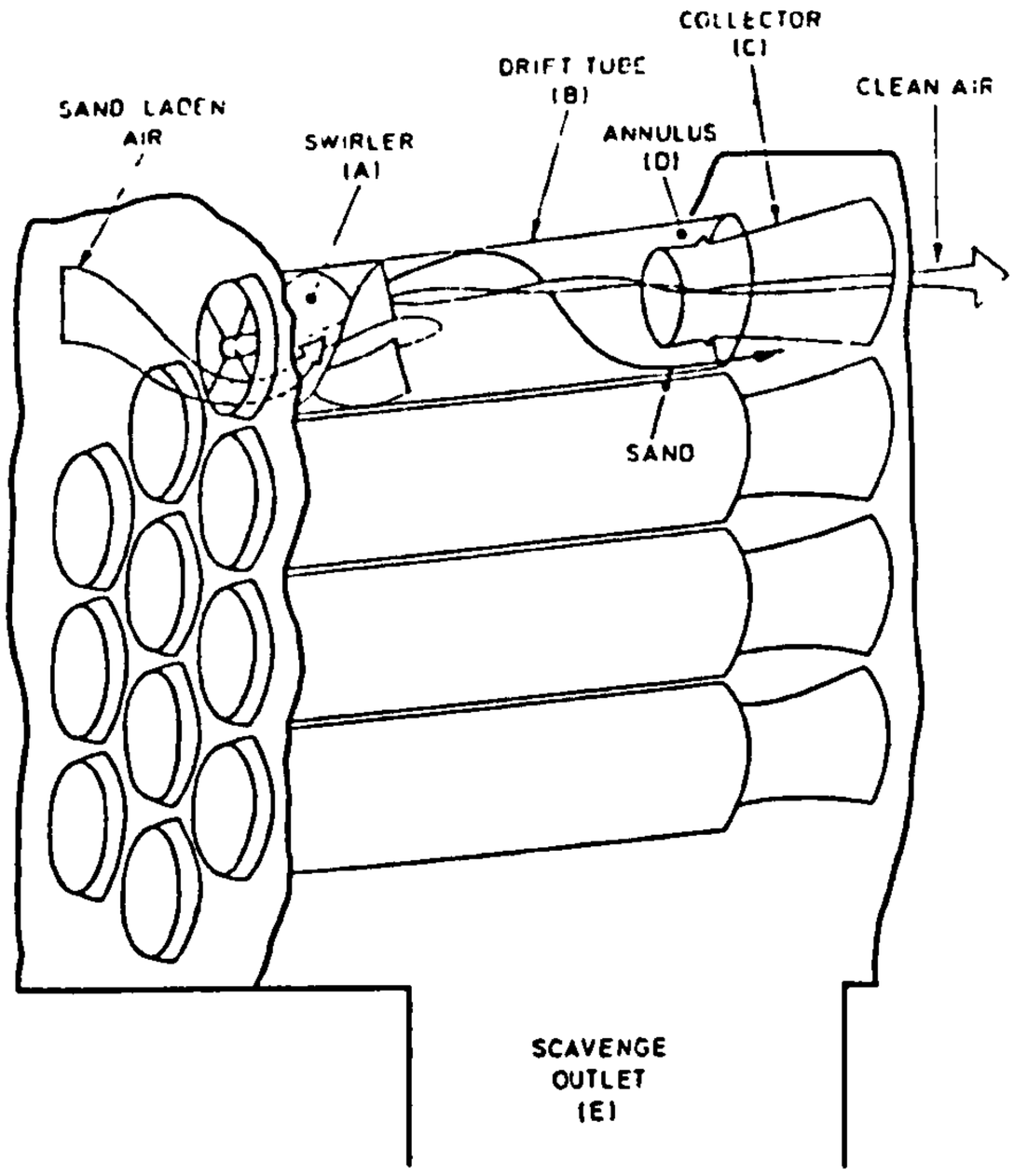

Vortex Tube Filter Pack: The basic principle of operation

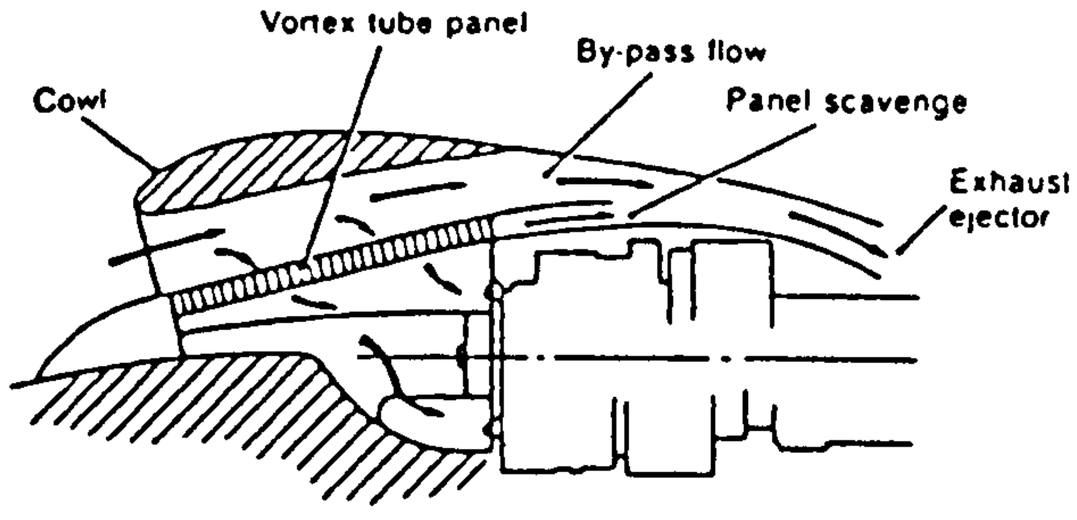

Configuration of a Cowled Vortex Tube Separator.

FIG.1 VORTEX TUBE PANEL FILTER

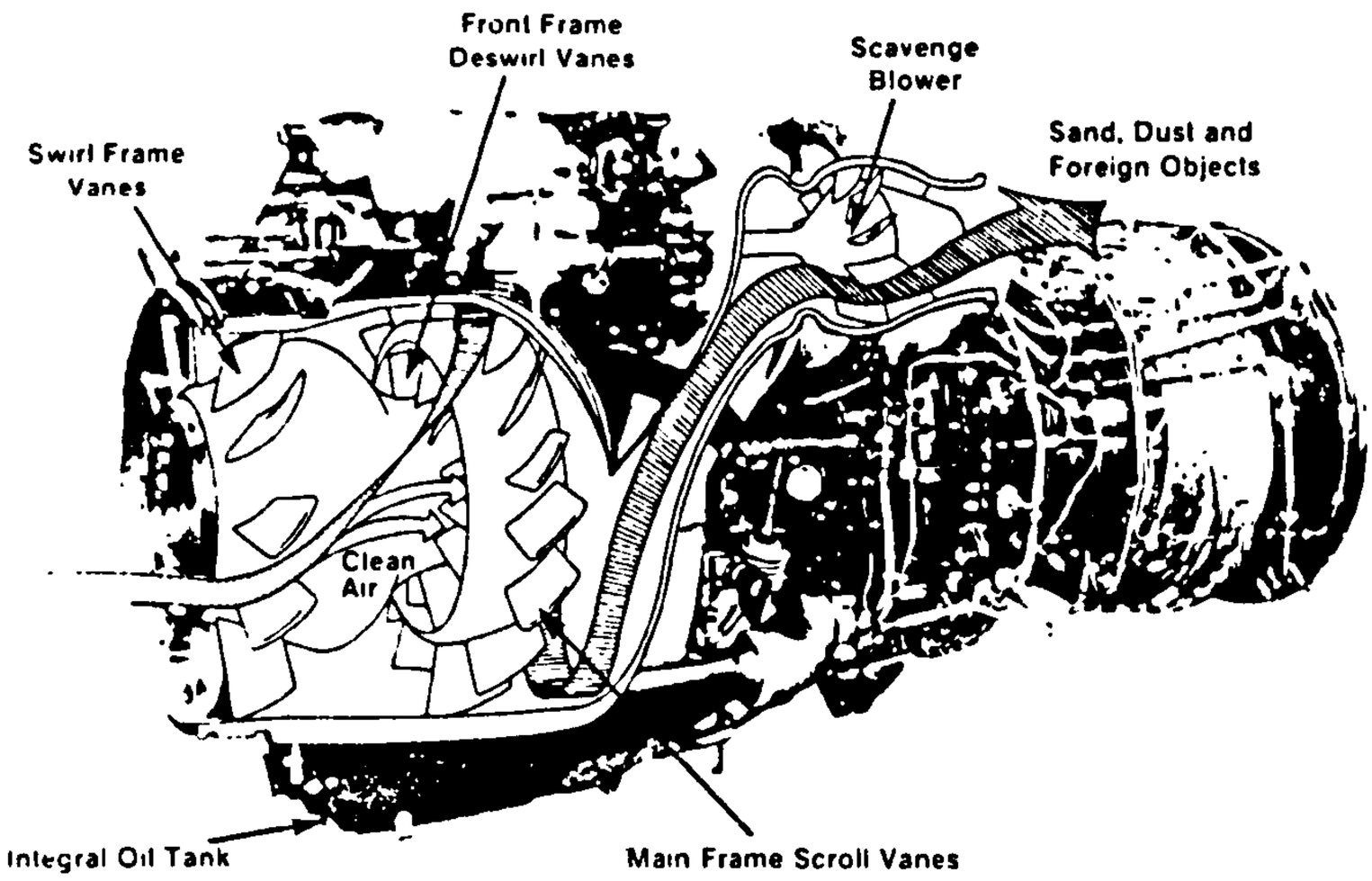

FIG.2 G.E. T700 HELICOPTER ENGINE
(SWIRL TYPE CONFIGURATION)

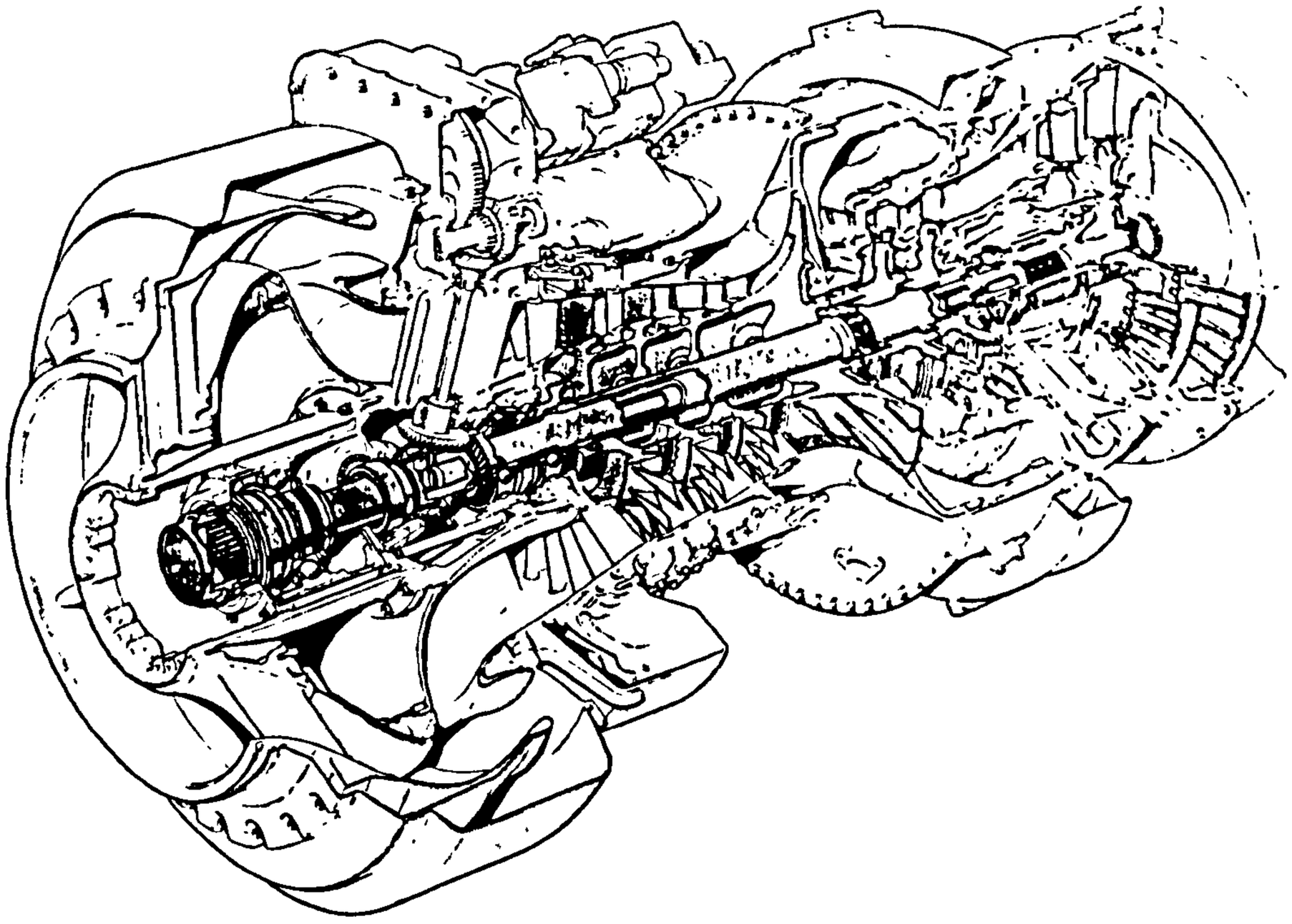

FIG.3 RTM322 HELICOPTER ENGINE
(VANELESS TYPE CONFIGURATION)

FIG.4 IDEAL OPERATION OF AN INERTIAL SEPARATOR

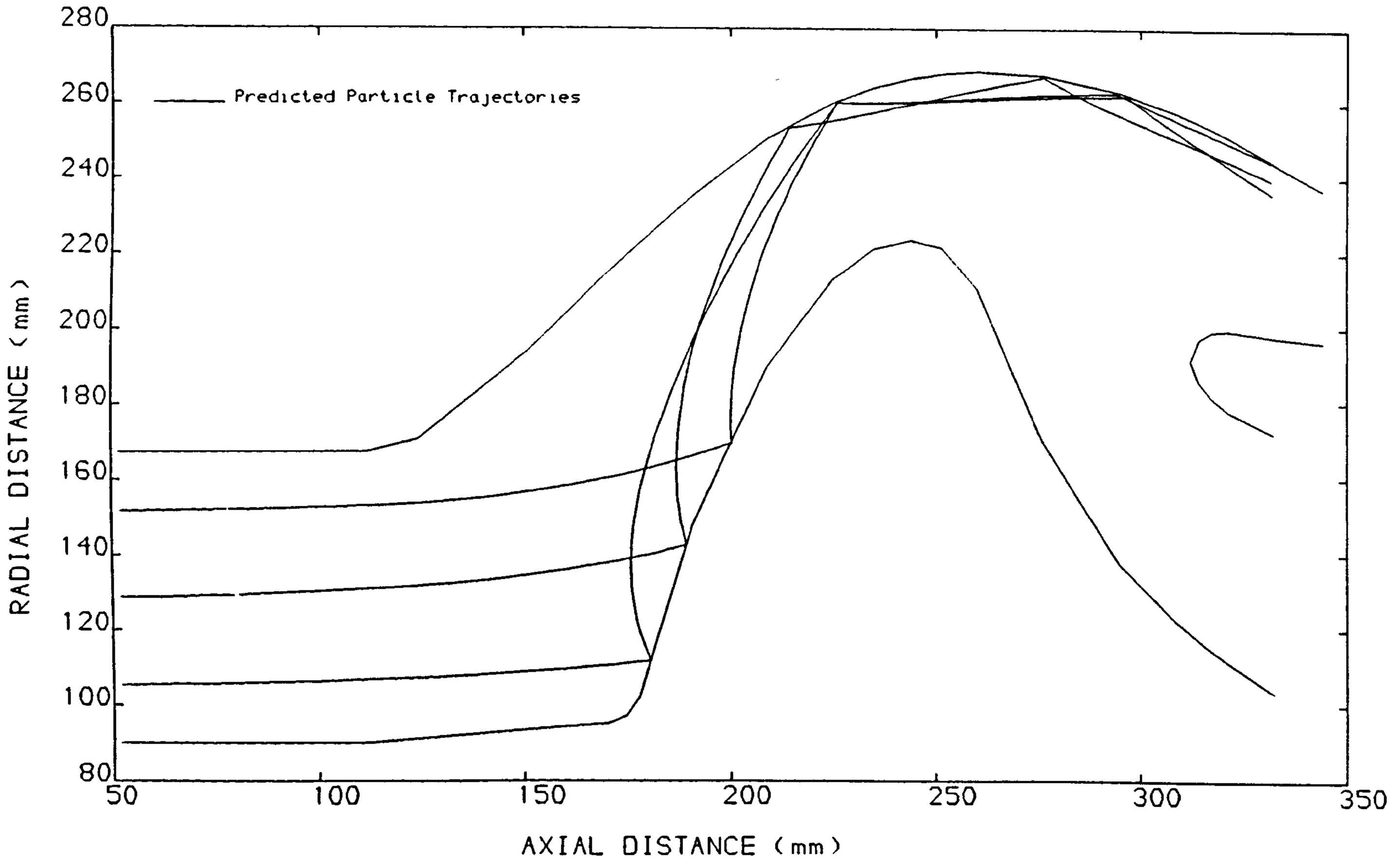

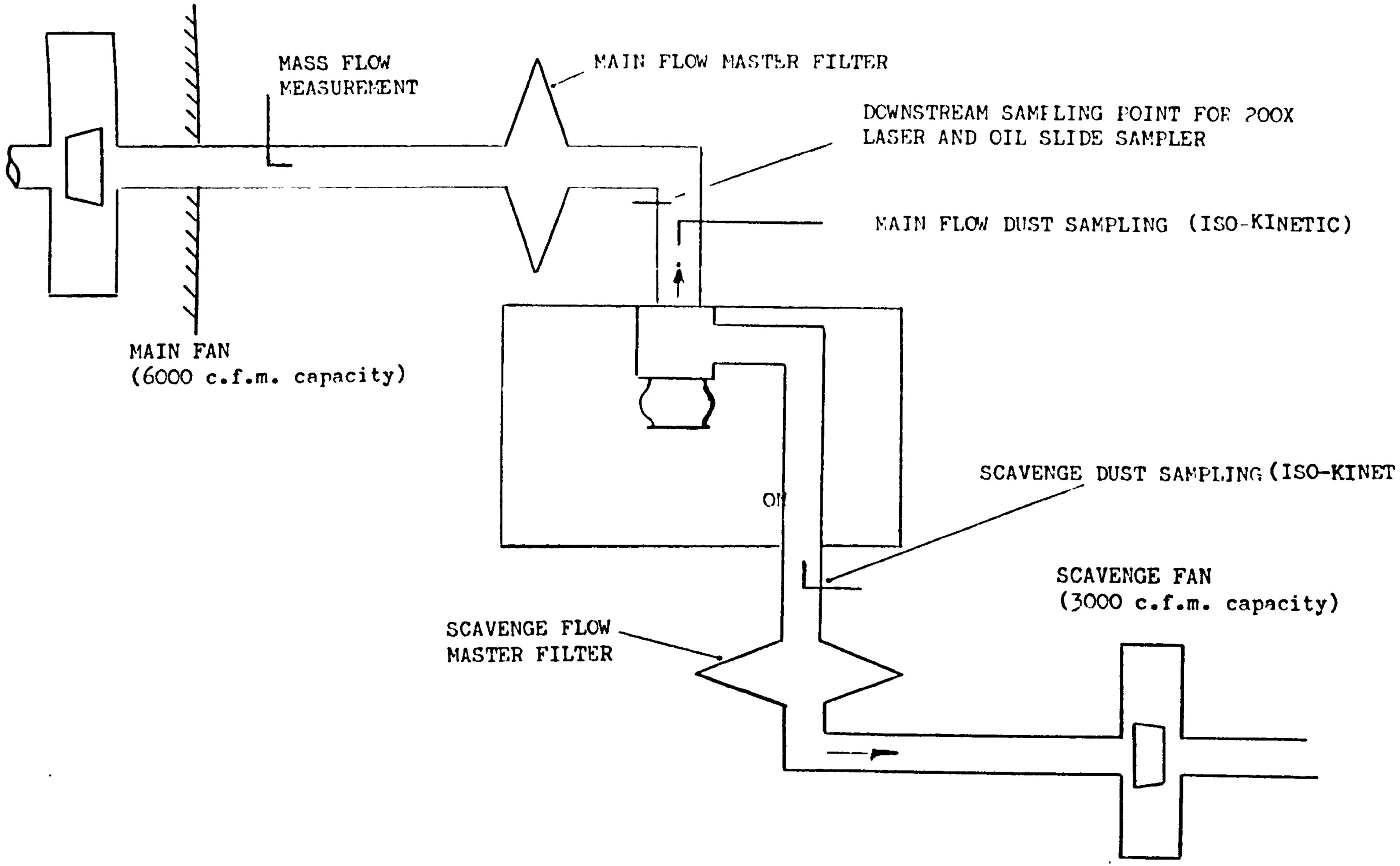

FIG.5 STANDARD DUST TEST FACILITY

FIG.6 FORCES ACTING ON A SINGLE SPHERICAL PARTICLE

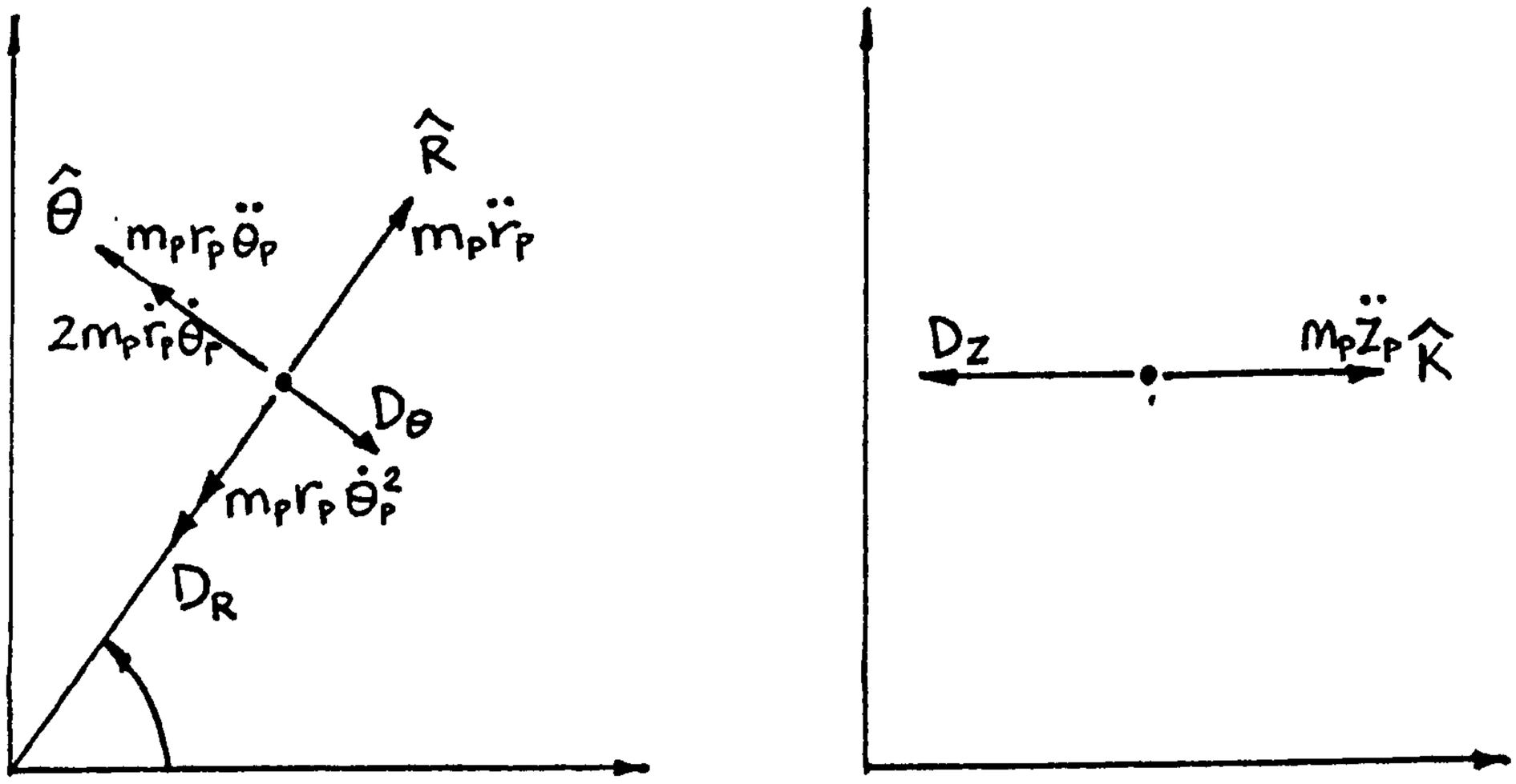

FIG.7 POSITION VECTOR OF A SINGLE PARTICLE W.R.T. THE CYLINDRICAL AXES SYSTEM

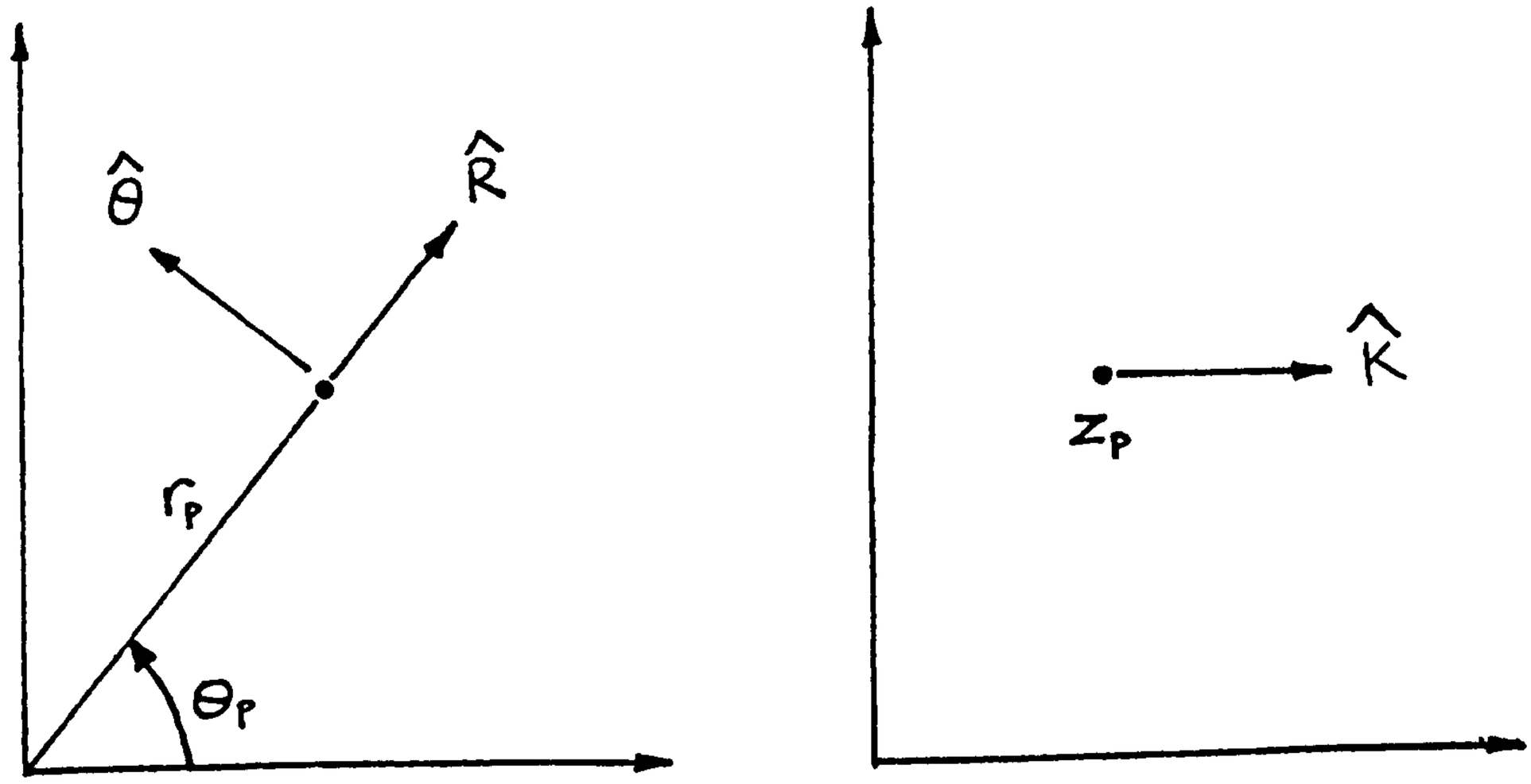

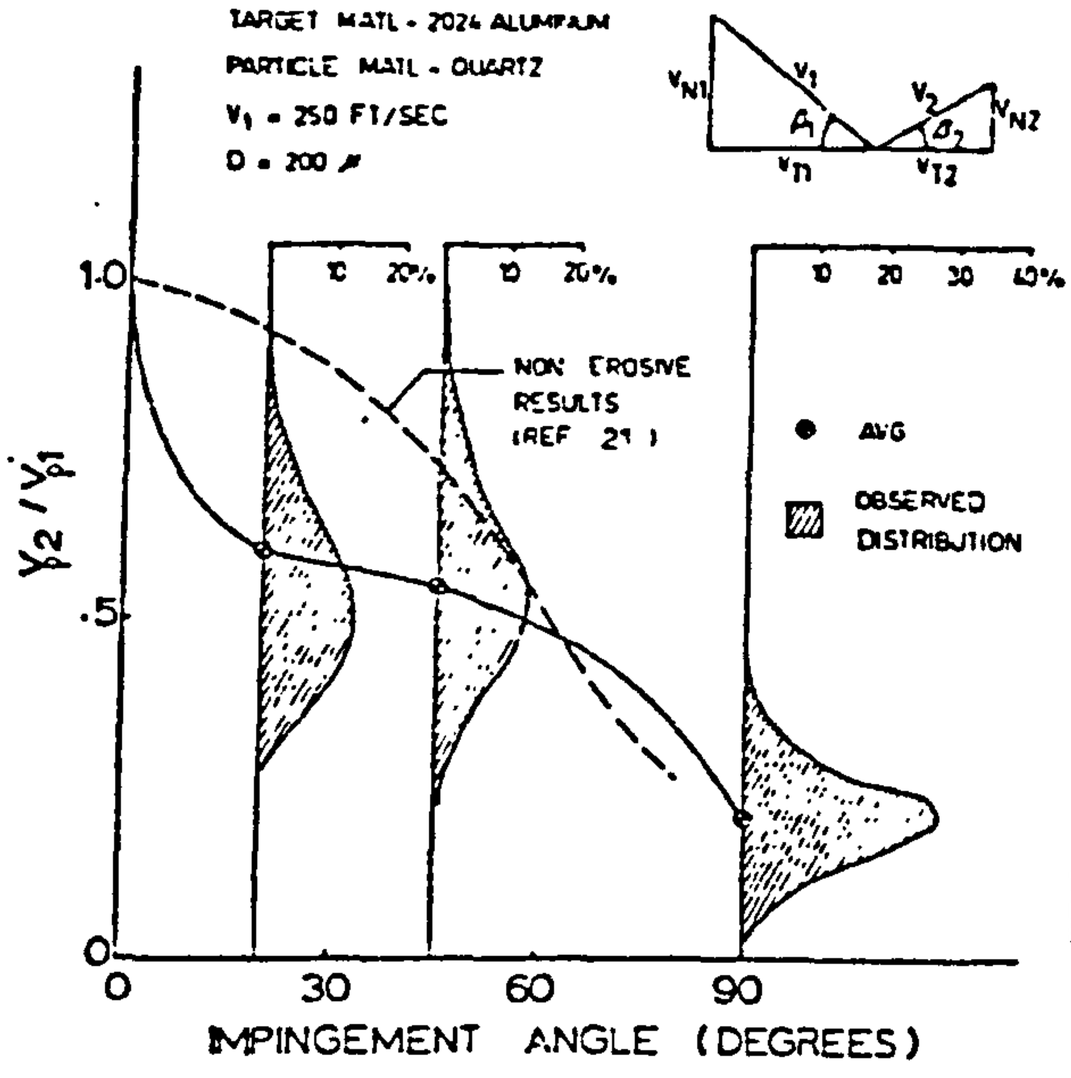

FIG.8.1 INFLUENCE OF IMPACT ANGLE ON THE EROSIVE PARTICLE VELOCITY RESTITUTION RATIO.

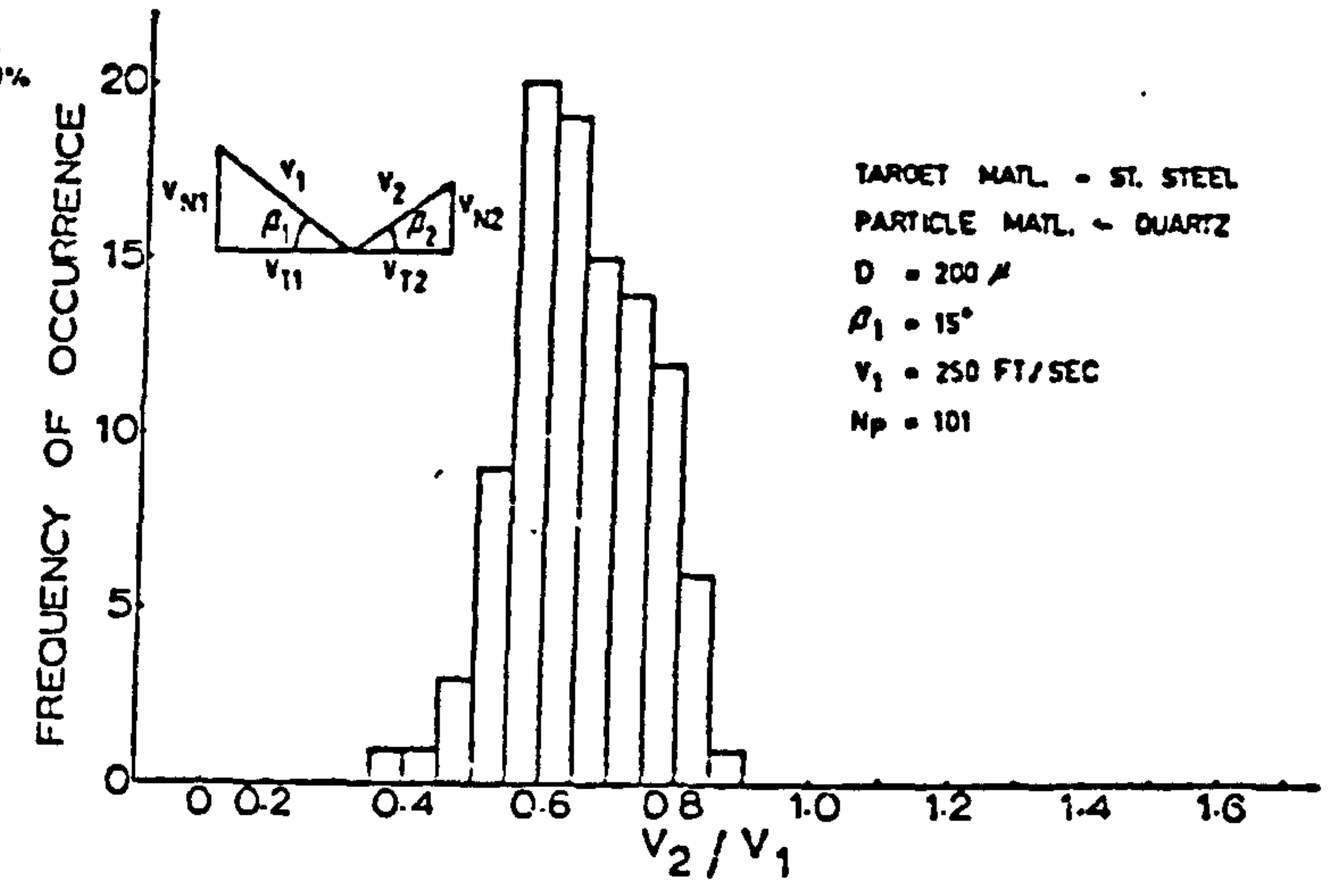

FIG.8.2 EROSIVE PARTICLE VELOCITY RESTITUTION RATIO DISTRIBUTION

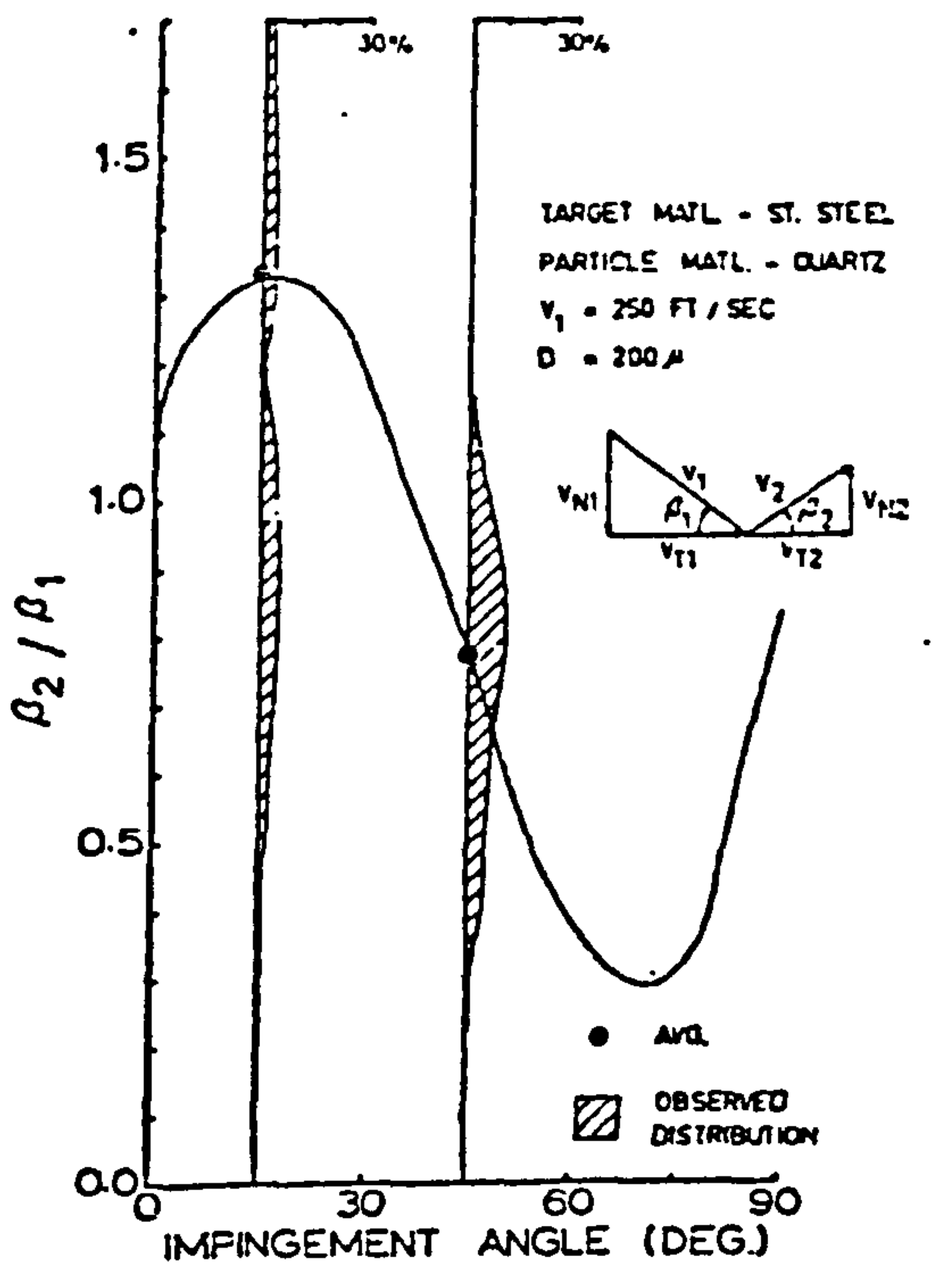

FIG.8.3 INFLUENCE OF IMPACT ANGLE ON THE EROSIVE PARTICLE DIRECTIONAL COEFFICIENT

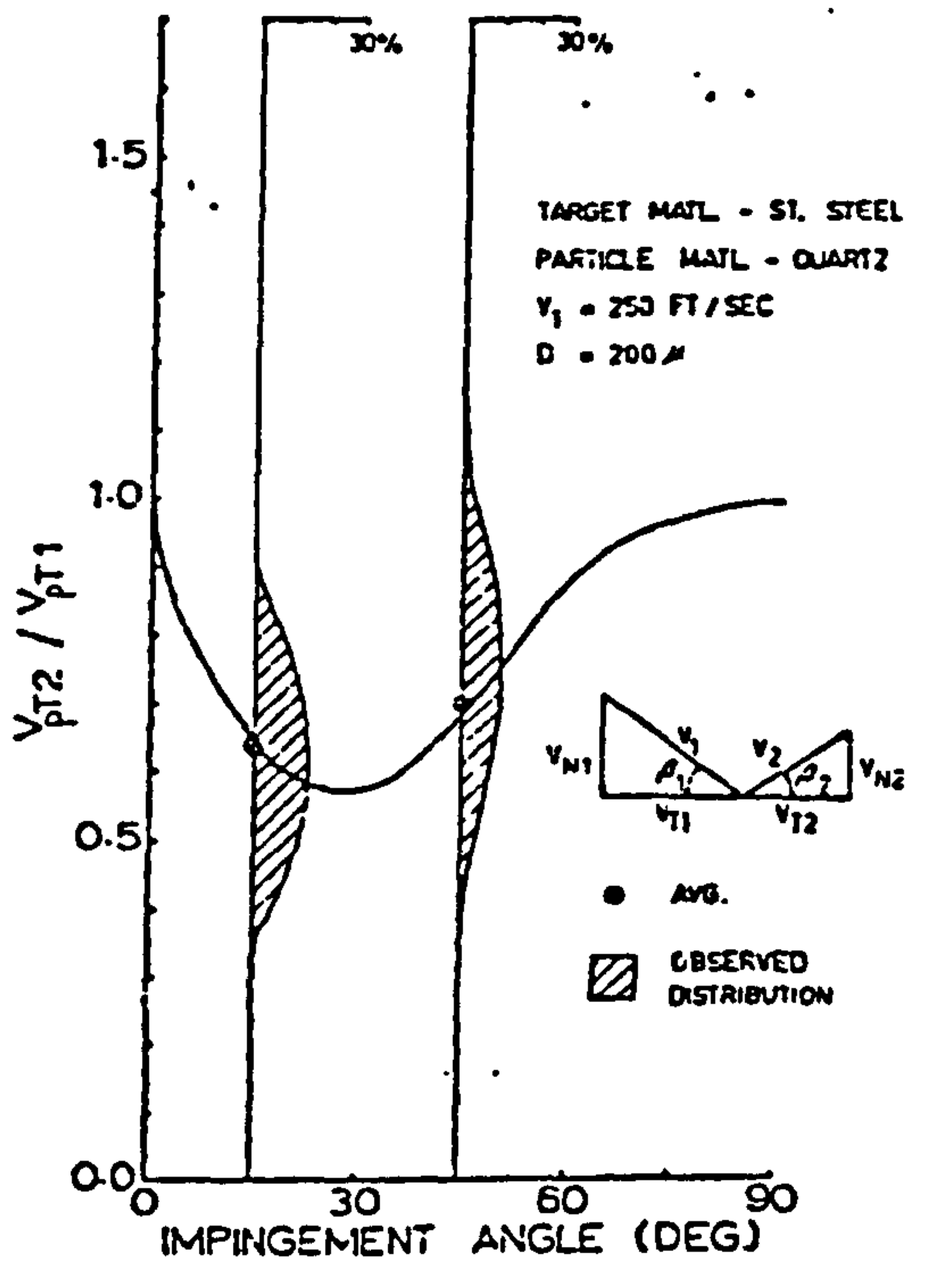

FIG.8.4 INFLUENCE OF IMPACT ANGLE ON THE EROSIVE PARTICLE TANGENTIAL VELOCITY RESTITUTION RATIO

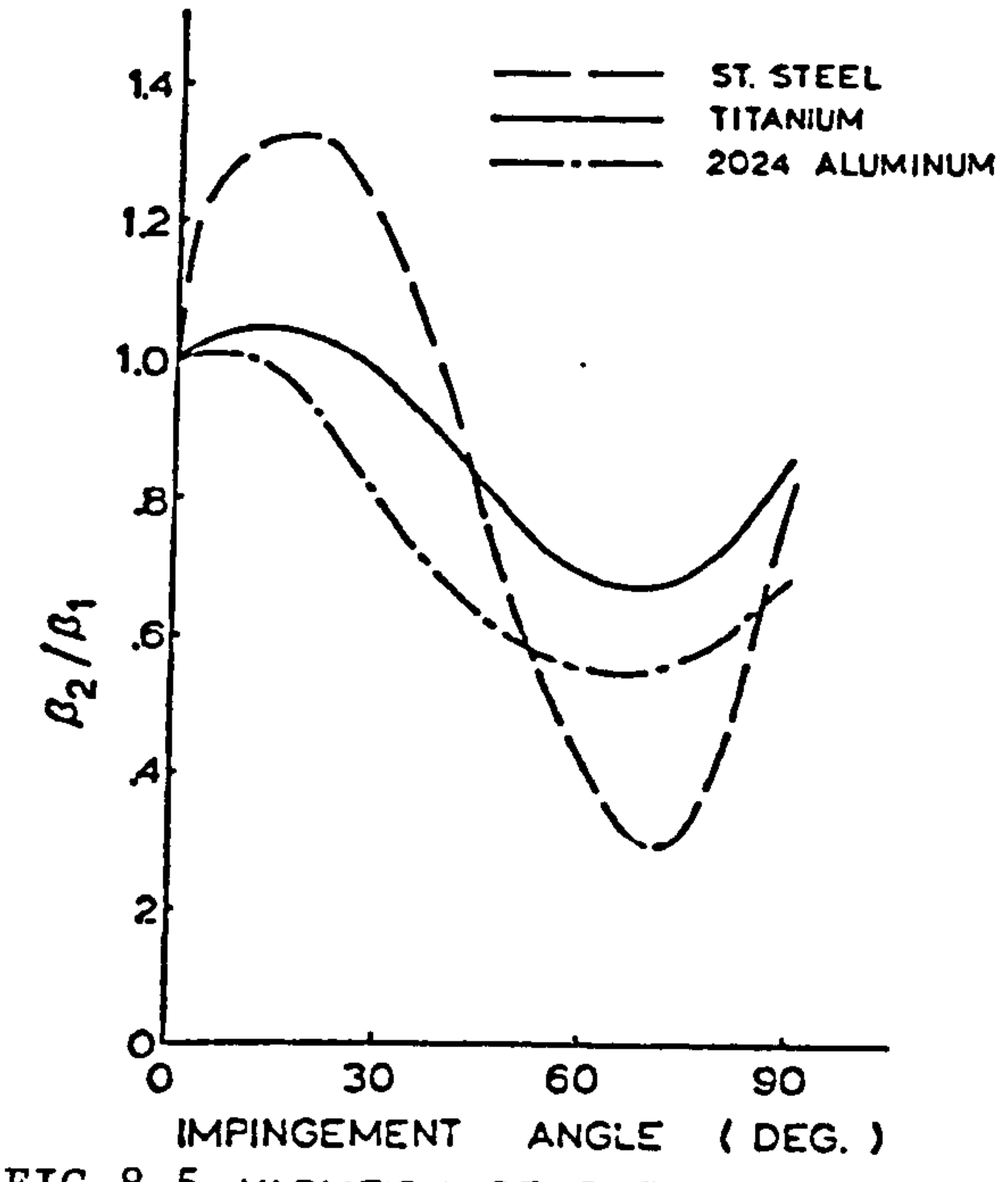

FIG.8.5 VARIATION OF THE DIRECTIONAL COEFFICIENT WITH TARGET MATERIAL

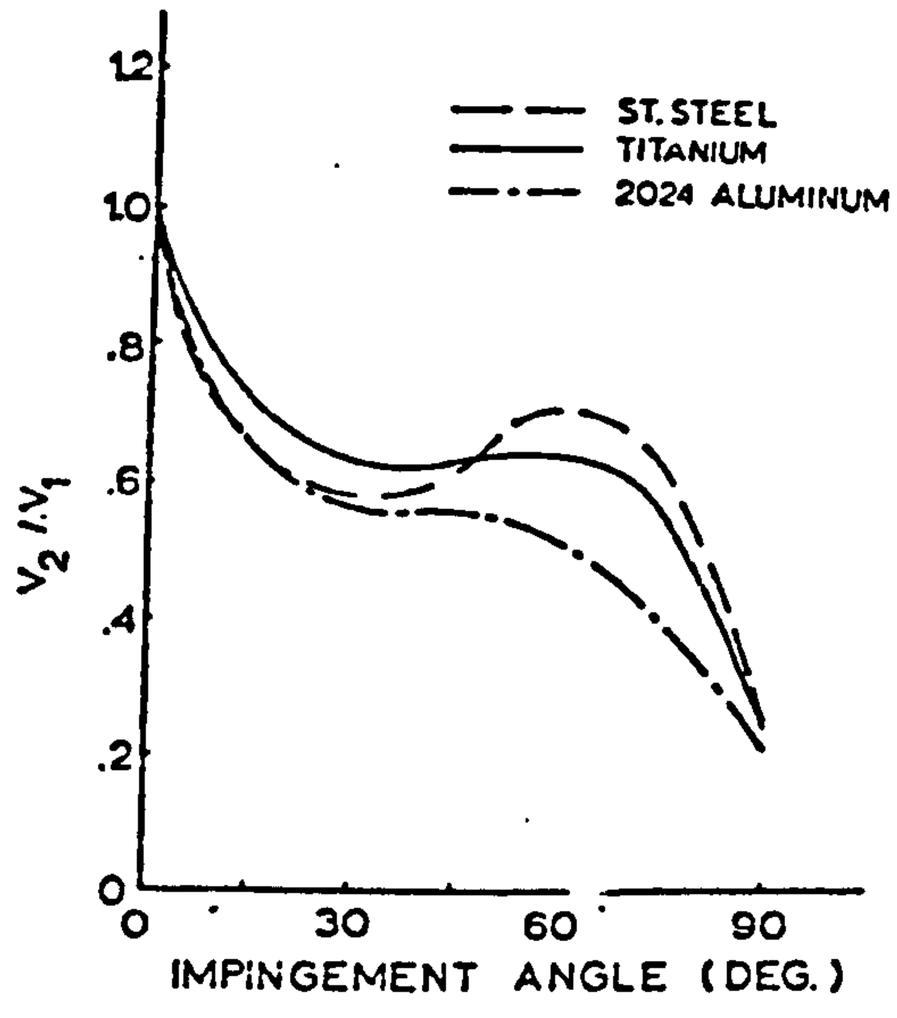

FIG.8.6 VARIATION OF THE RESTITUTION RATIO WITH TARGET MATERIAL

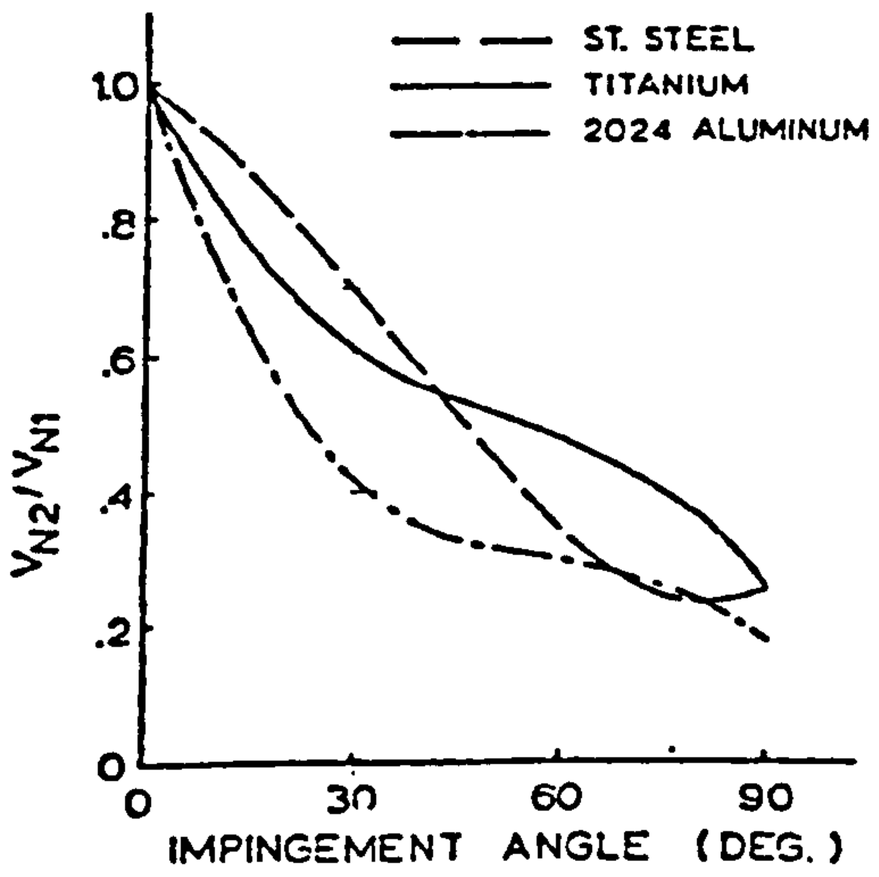

FIG.8.7 VARIATION OF THE NORMAL RESTITUTION RATIO WITH TARGET MATERIAL

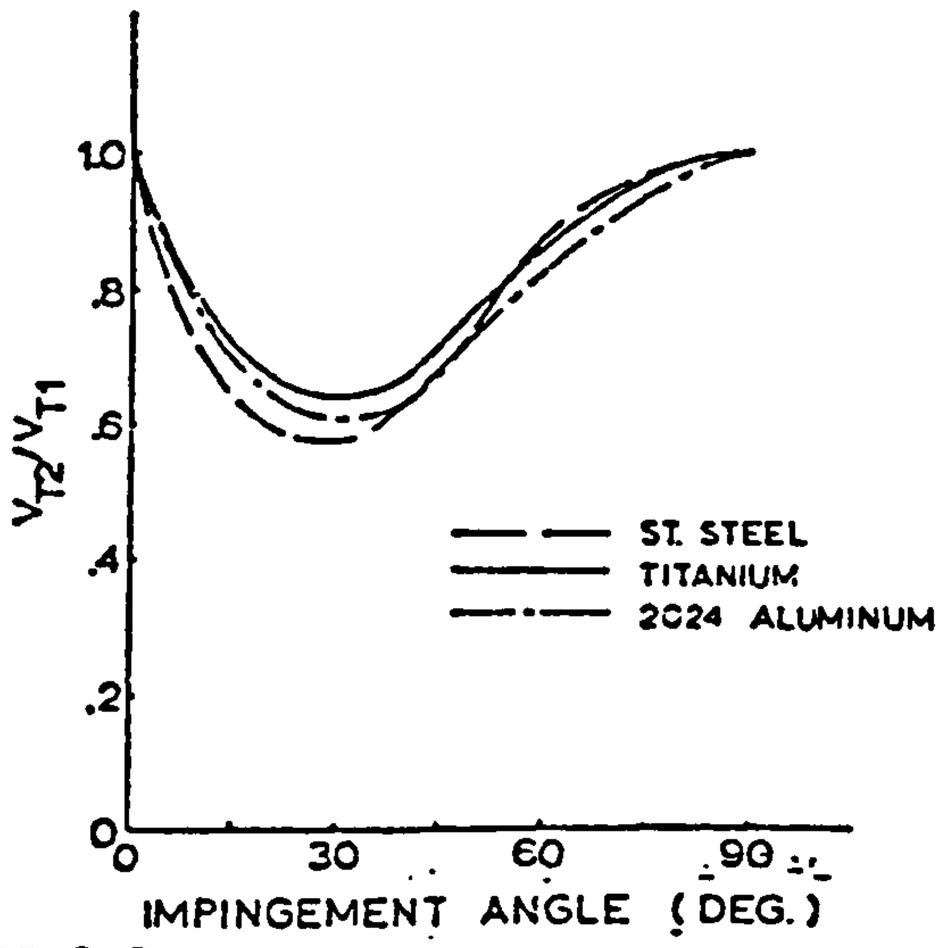

FIG.8.8 VARIATION OF THE TANGENTIAL RESTITUTION RATIO WITH TARGET MATERIAL

FIG.9 FINITE ELEMENT MESH OF A GAS TURBINE SEPARATOR

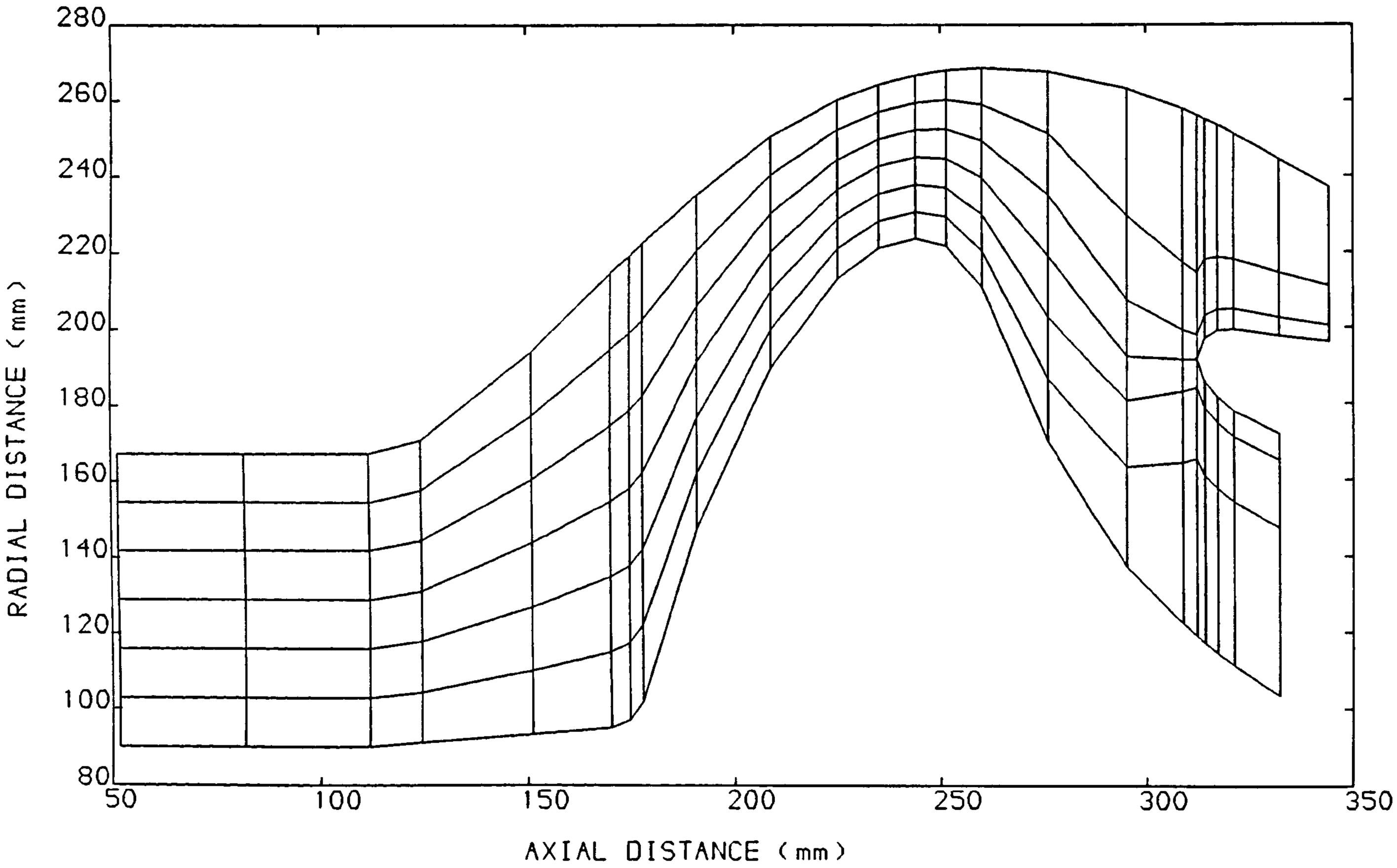

FIG.IO POTENTIAL FUNCTION CONTOUR PLOT

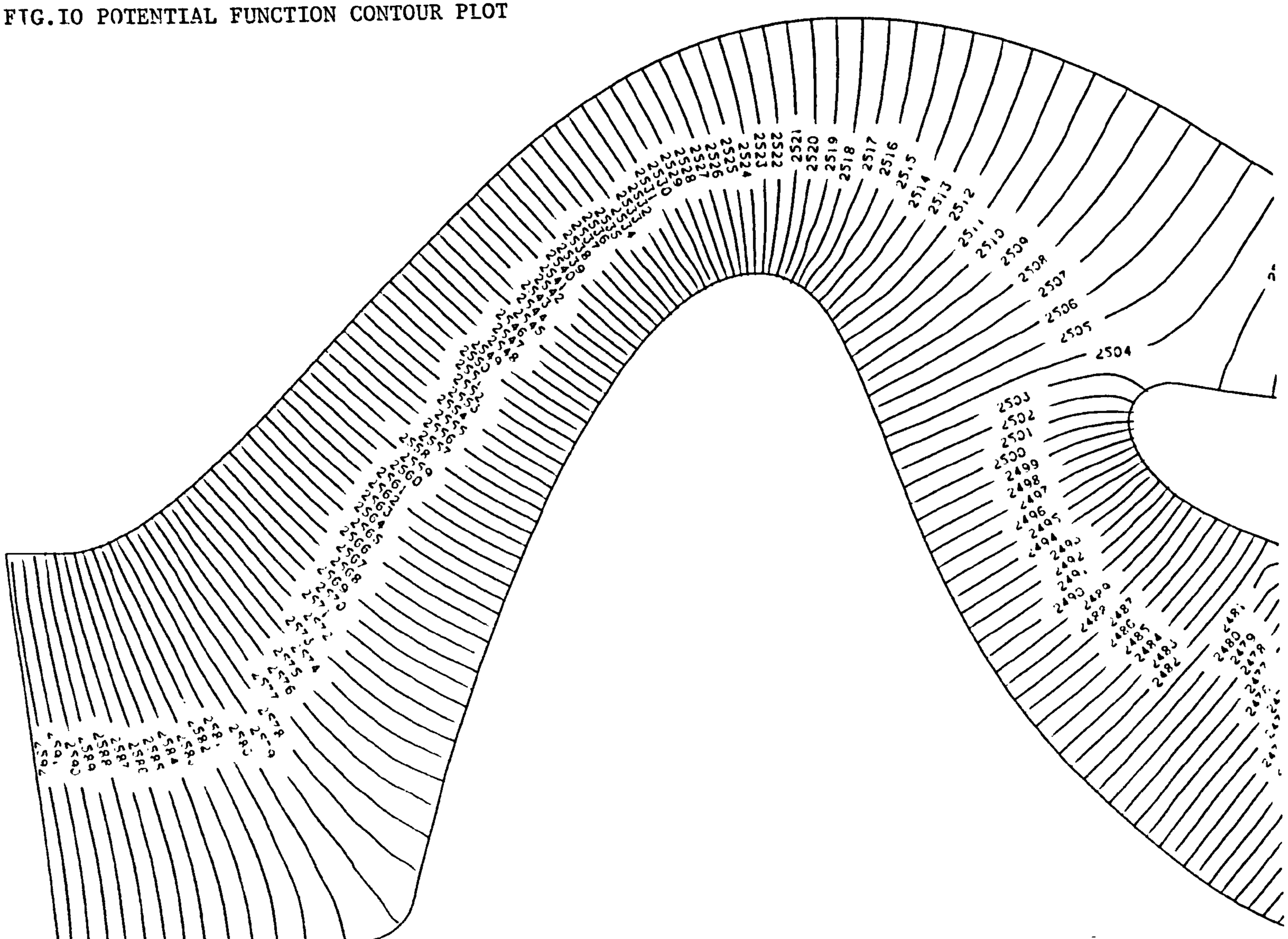

FIG.11 A 20 NODES CUBIC ELEMENT

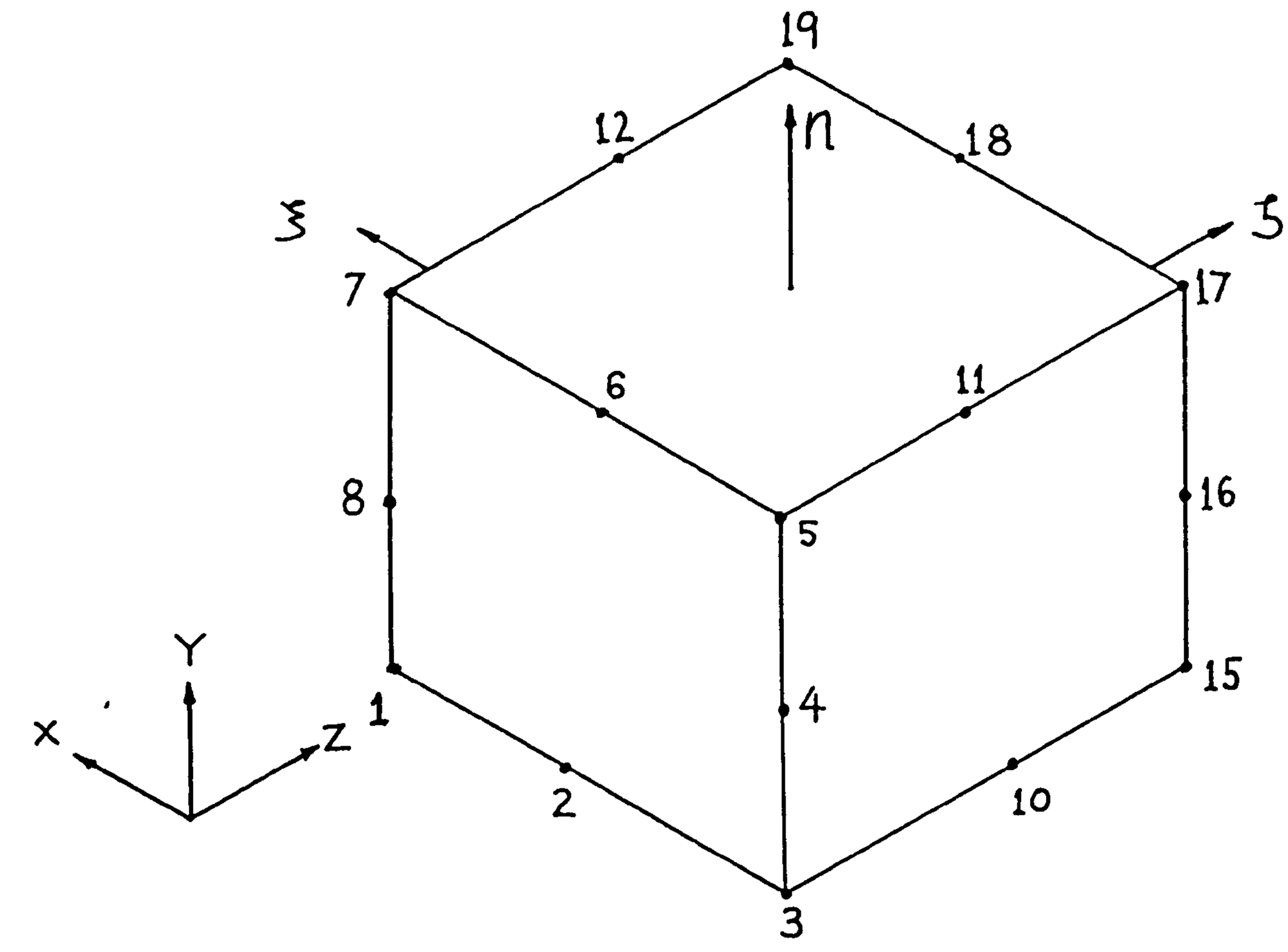

FIG.12 A 20 NODES ISOPARAMETRIC ELEMENT

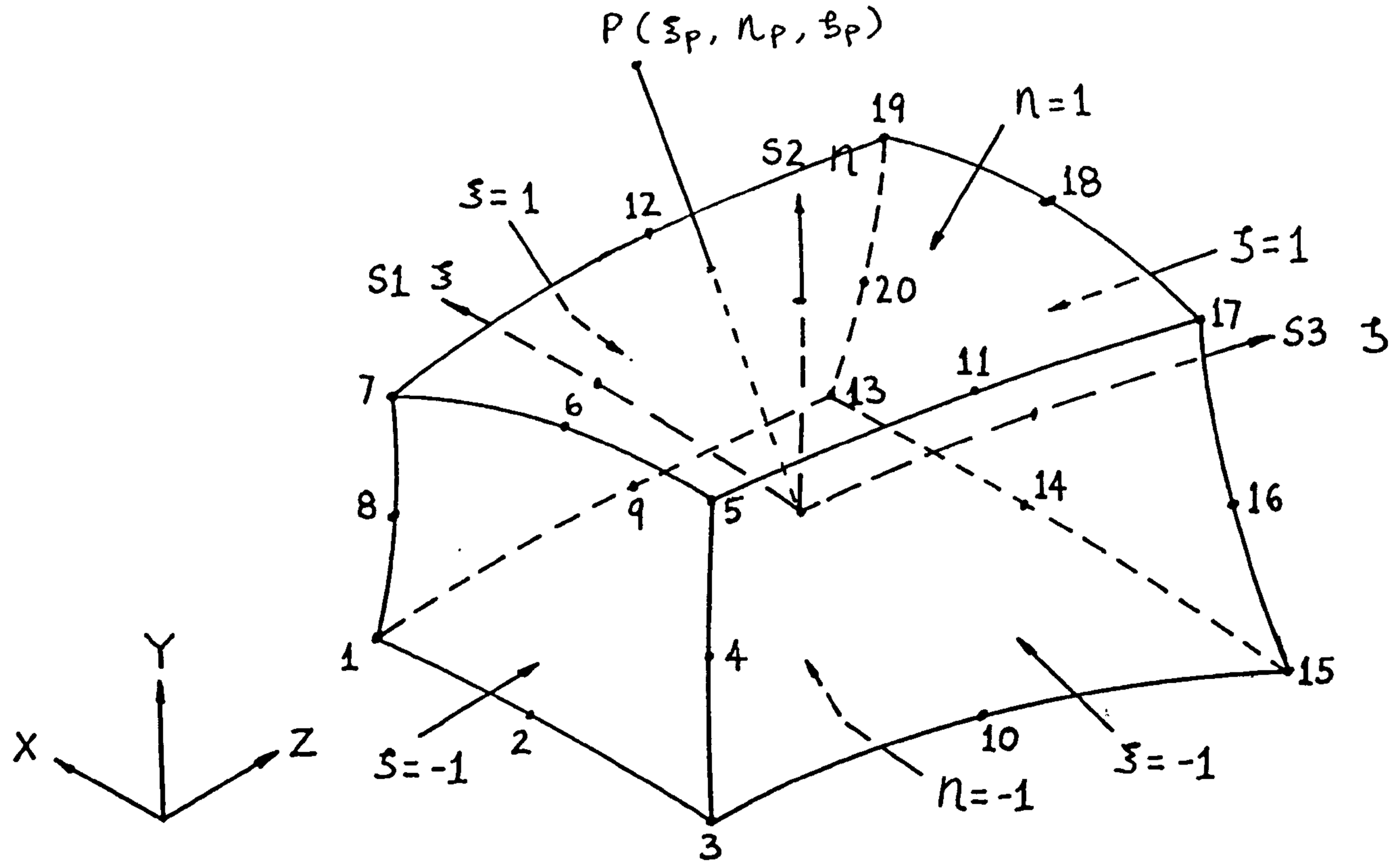

FIG.13 PREDICTED FLOW VECTORS IN A GAS TURBINE SEPARATOR

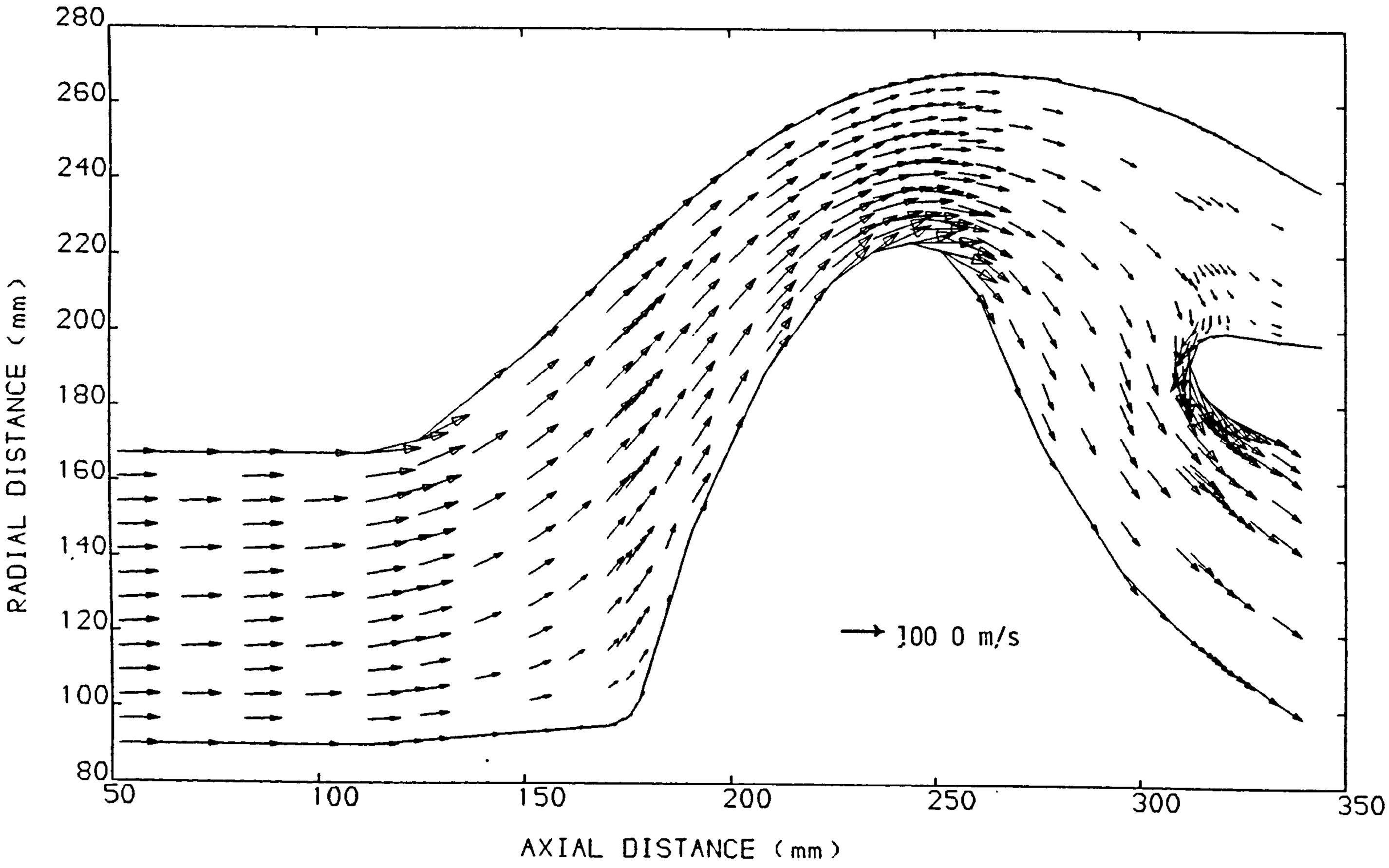

FIG I4 PARTICLE SIZES VS % BELOW SIZE

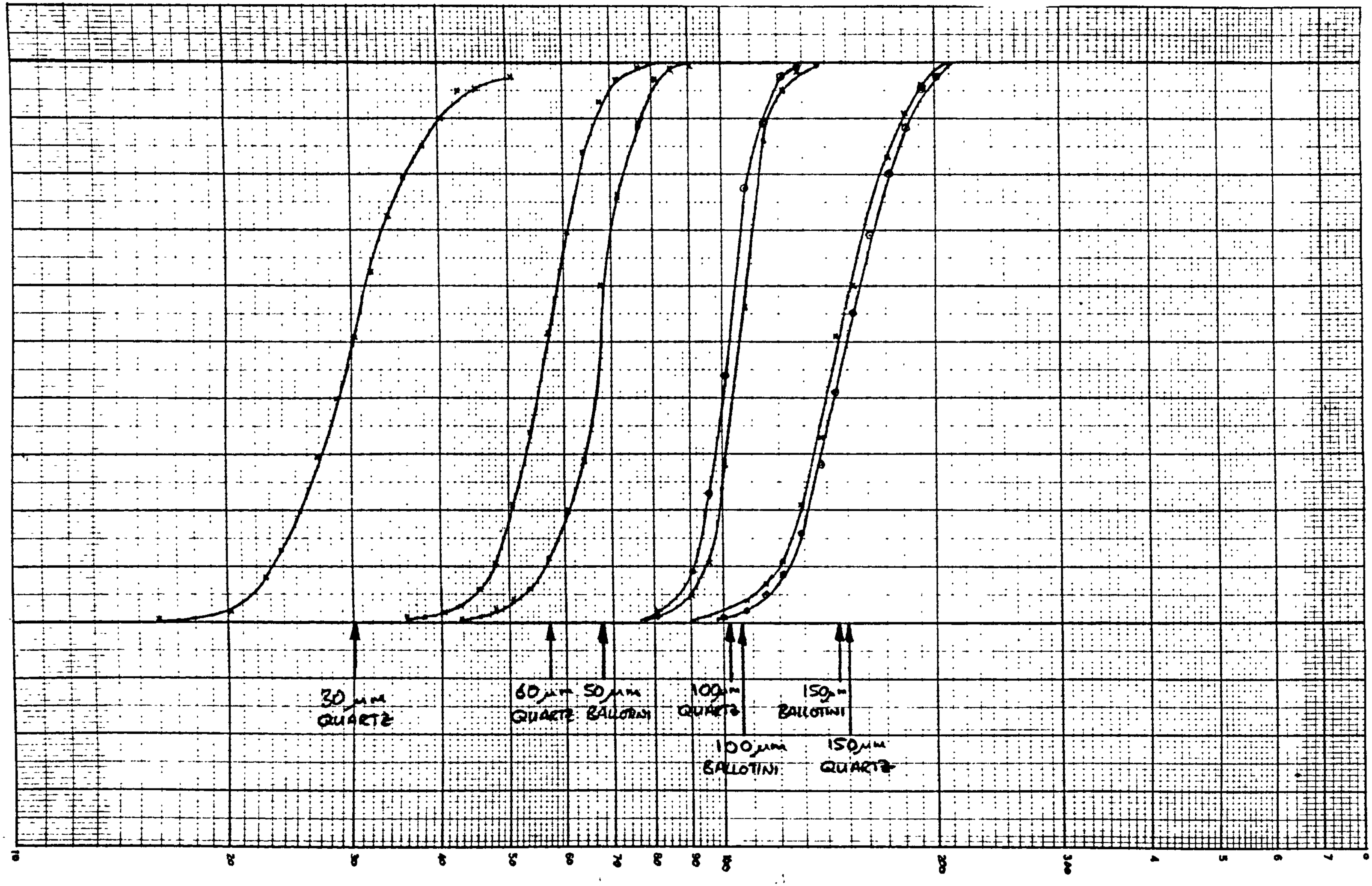

FIG.15a PREDICTED TRAJECTORIES FOR 15.0 um BALLOTINI PARTICLE

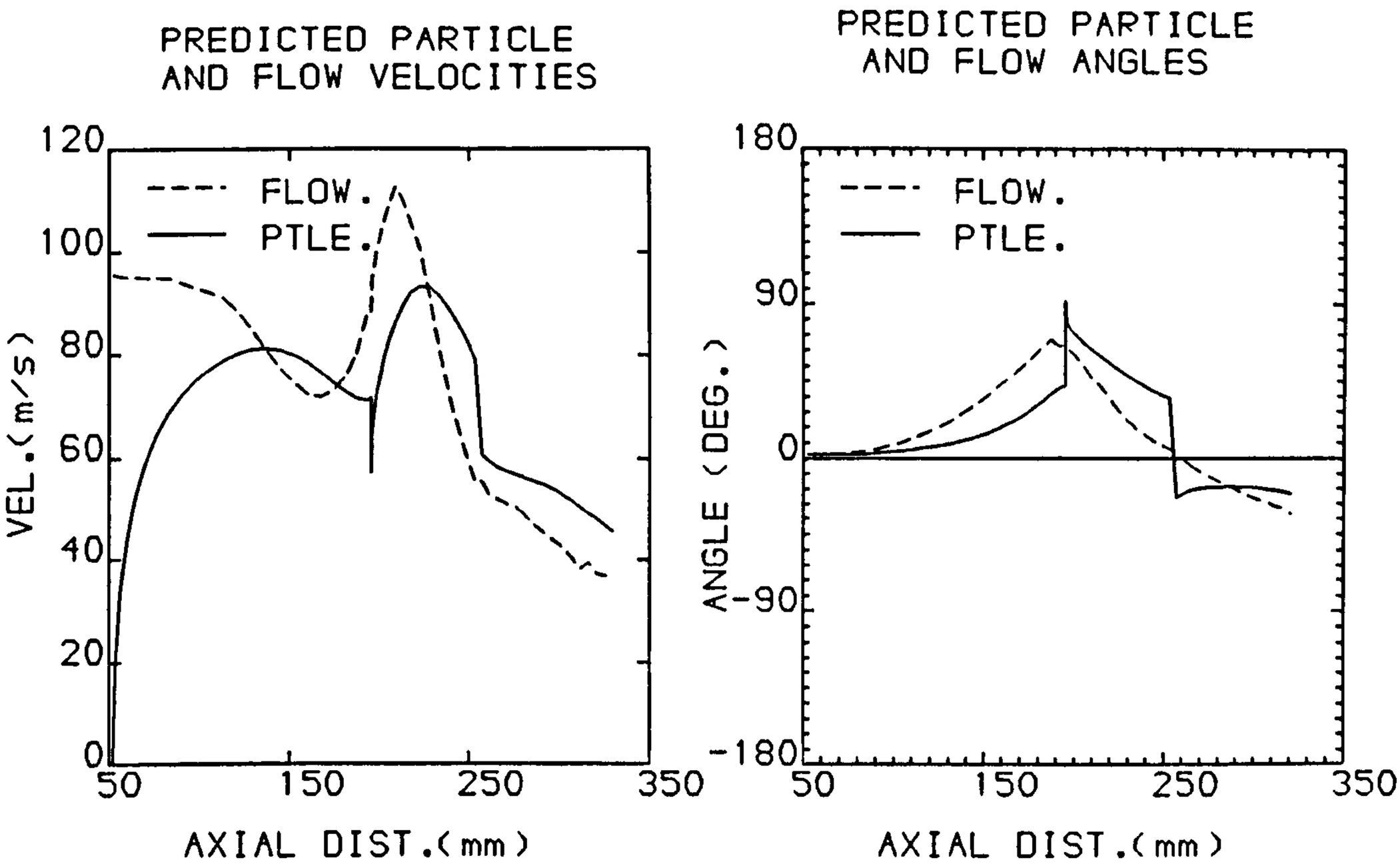

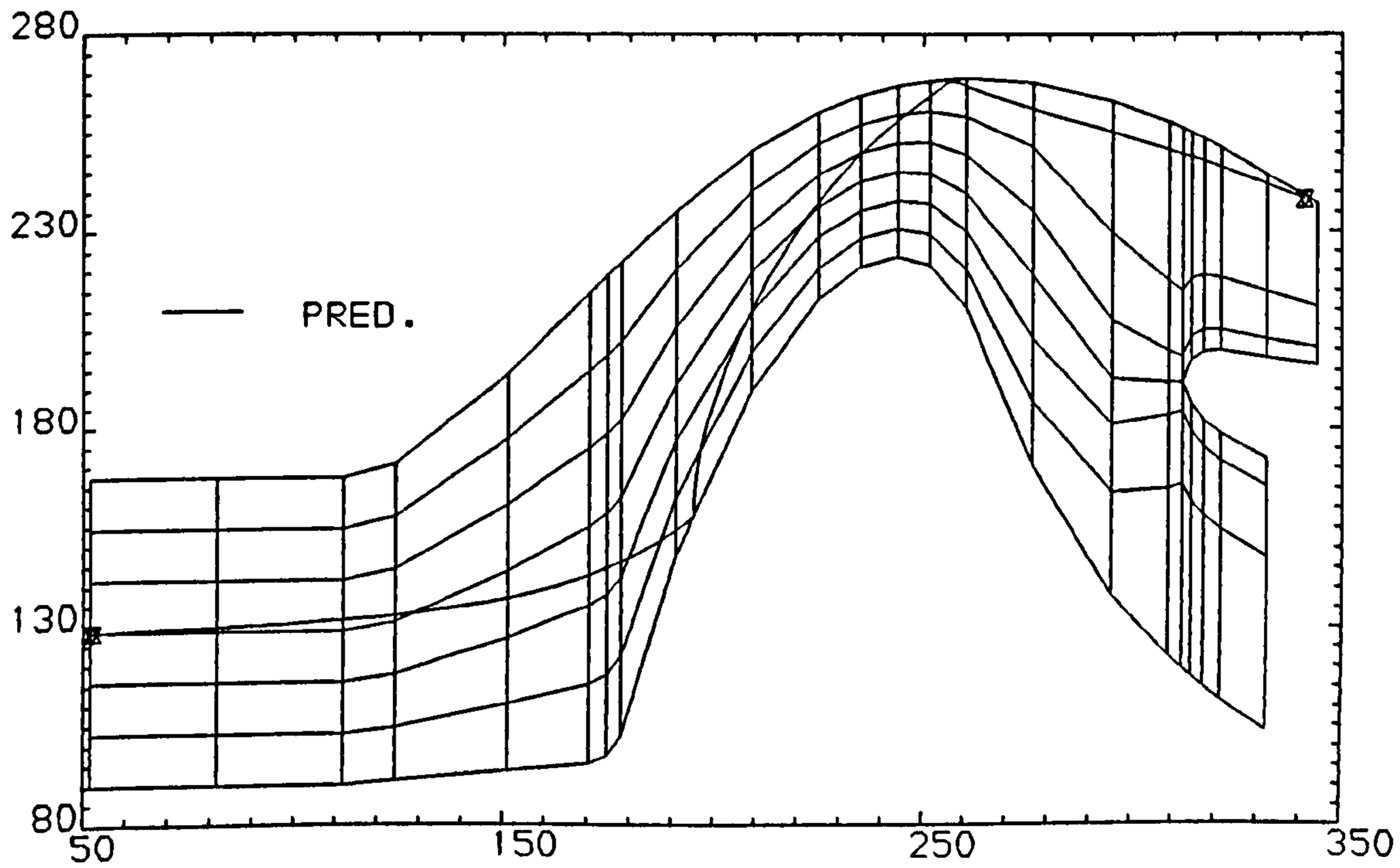

WALL MATL. = AL.
PTLE. MATL. = BALLOTINI
PTLE. DENSITY = 2950.0 kg/m3
PTLE. DIAMETER = 15.0 um
PTLE. INITIAL VEL.= 0.0 m/s

FIG.15b PREDICTED TRAJECTORIES FOR 150.0 um BALLOTINI PARTICLE

PREDICTED PARTICLE AND FLOW VELOCITIES

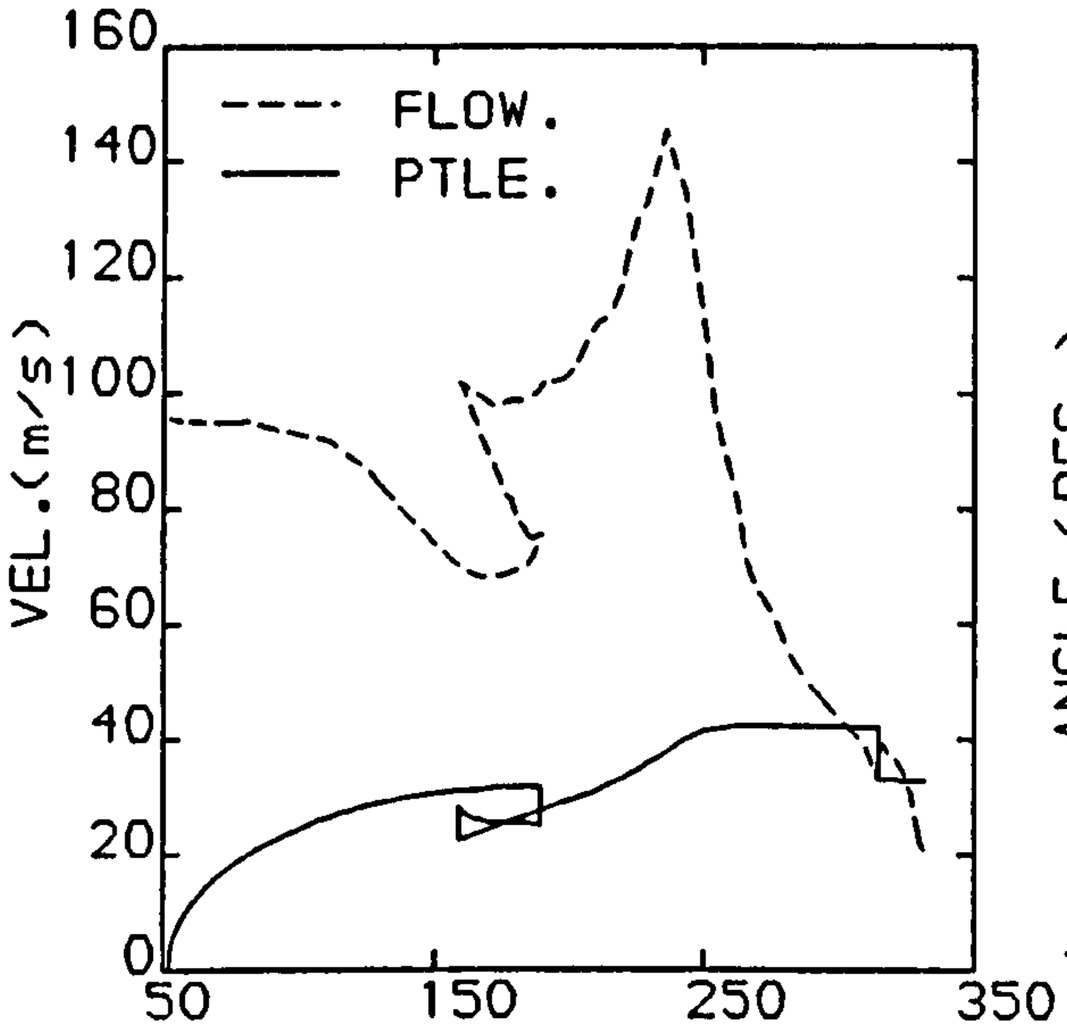

PREDICTED PARTICLE AND FLOW ANGLES

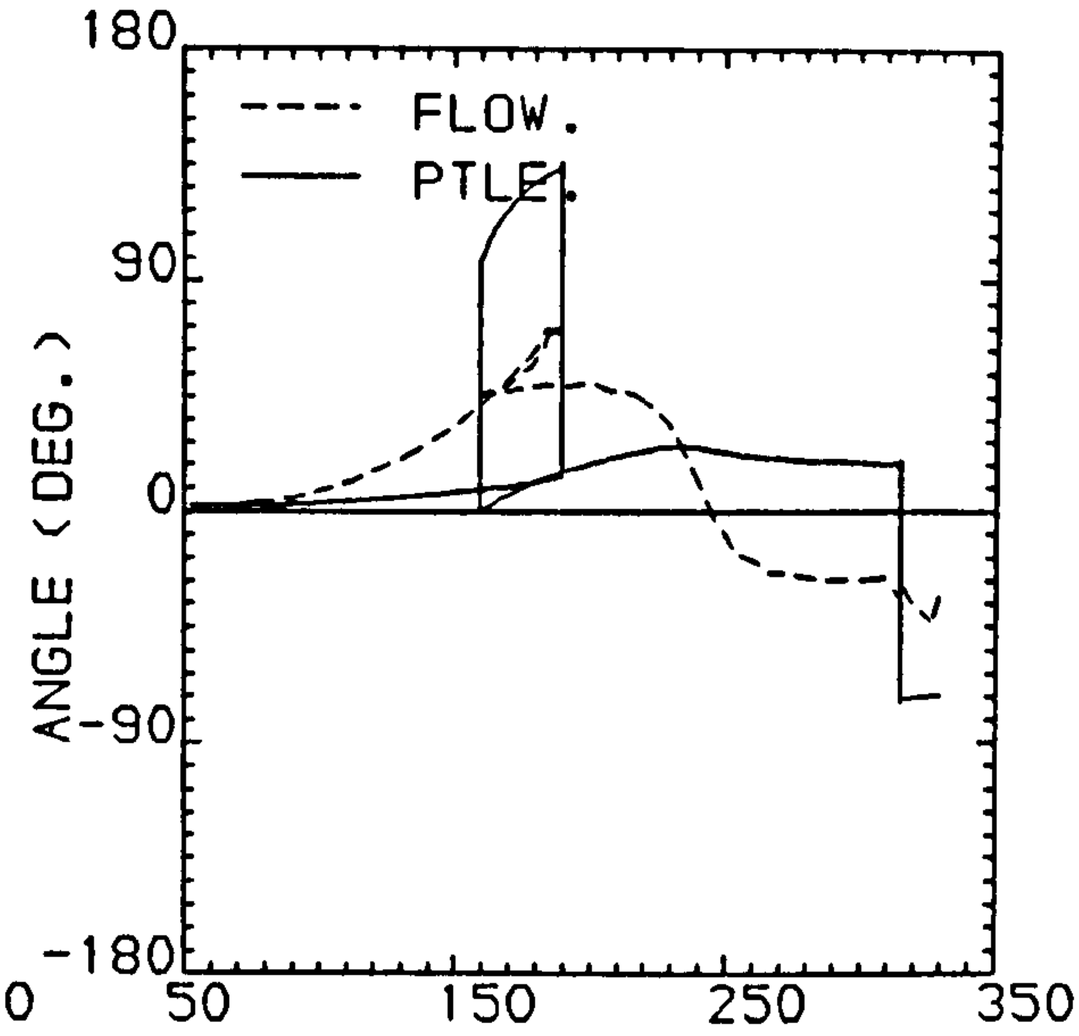

PREDICTED PARTICLE TRAJECTORIES

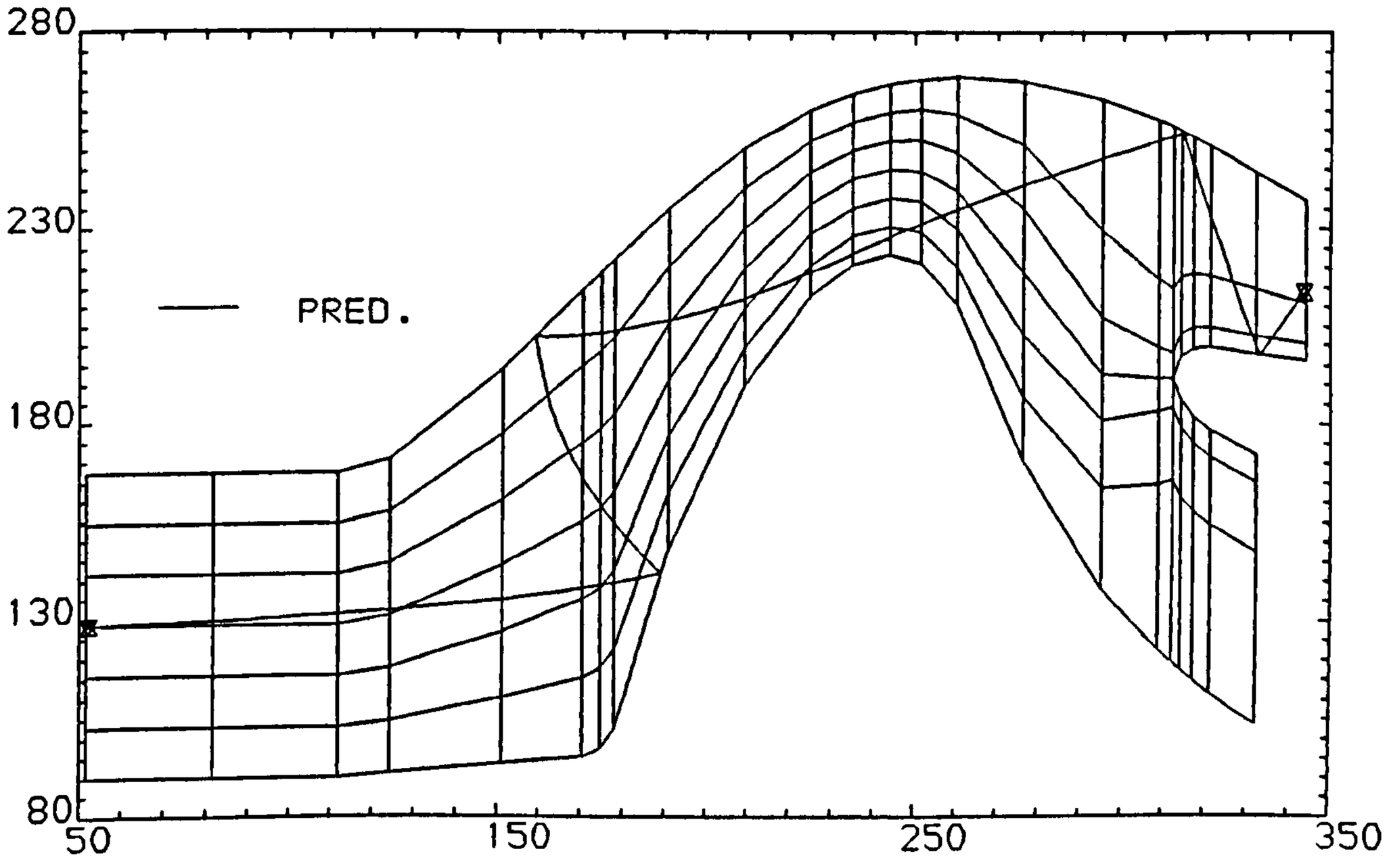

WALL MATL.	= AL.	PTLE. DIAMETER	= 150.0 um
PTLE. MATL.	= BALLOTINI	PTLE. INITIAL VEL.	= 0.0 m/s
PTLE. DENSITY	= 2950.0 kg/m3		

FIG.16a PREDICTED TRAJECTORIES FOR 15.0 um QUARTZ PARTICLE

PREDICTED PARTICLE AND FLOW VELOCITIES

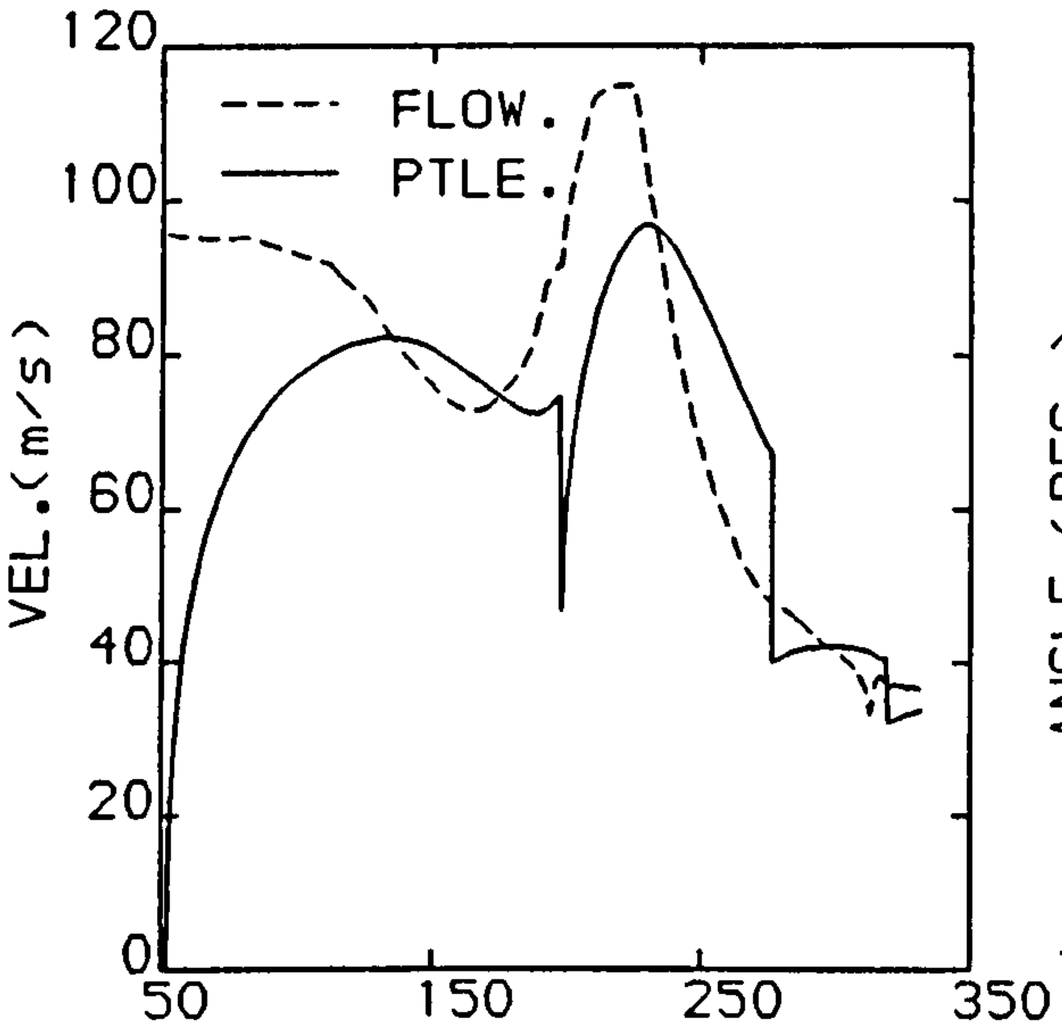

PREDICTED PARTICLE AND FLOW ANGLES

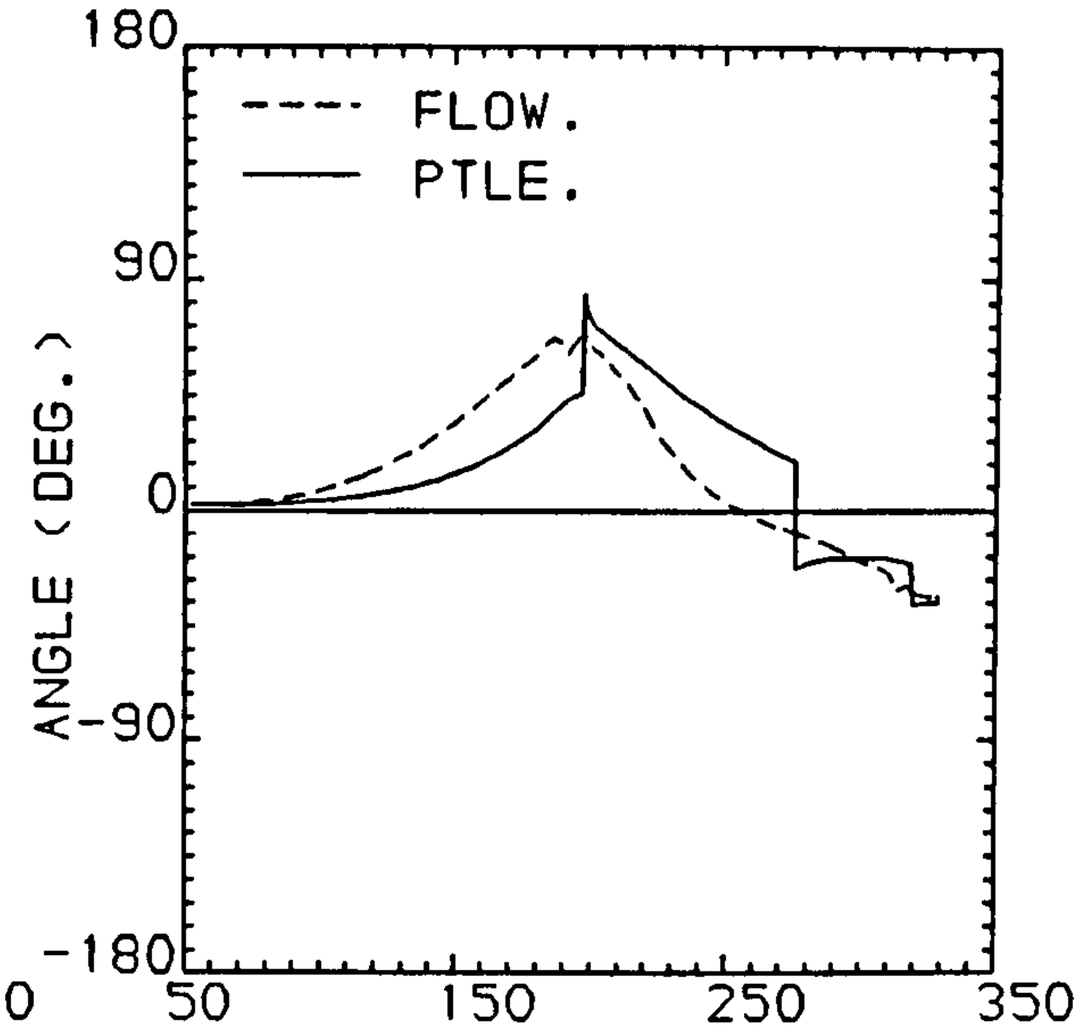

PREDICTED PARTICLE TRAJECTORIES

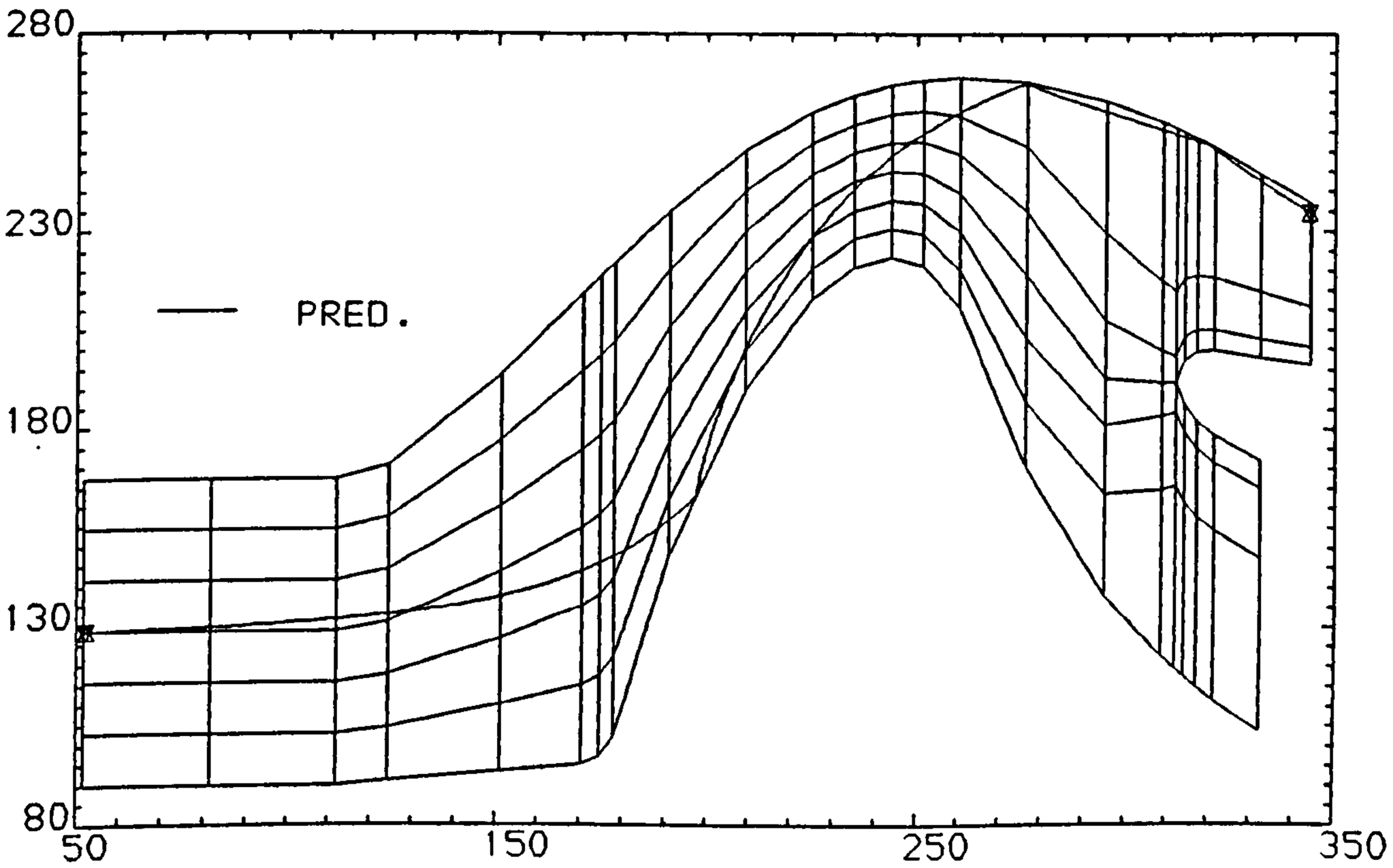

WALL MATL. = AL.
PTLE. MATL. = QUARTZ
PTLE. DENSITY = 2650.0 kg/m3
PTLE. DIAMETER = 15.0 um
PTLE. INITIAL VEL.= 0.0 m/s

FIG.16b PREDICTED TRAJECTORIES FOR 150.0 um QUARTZ PARTICLE

PREDICTED PARTICLE AND FLOW VELOCITIES

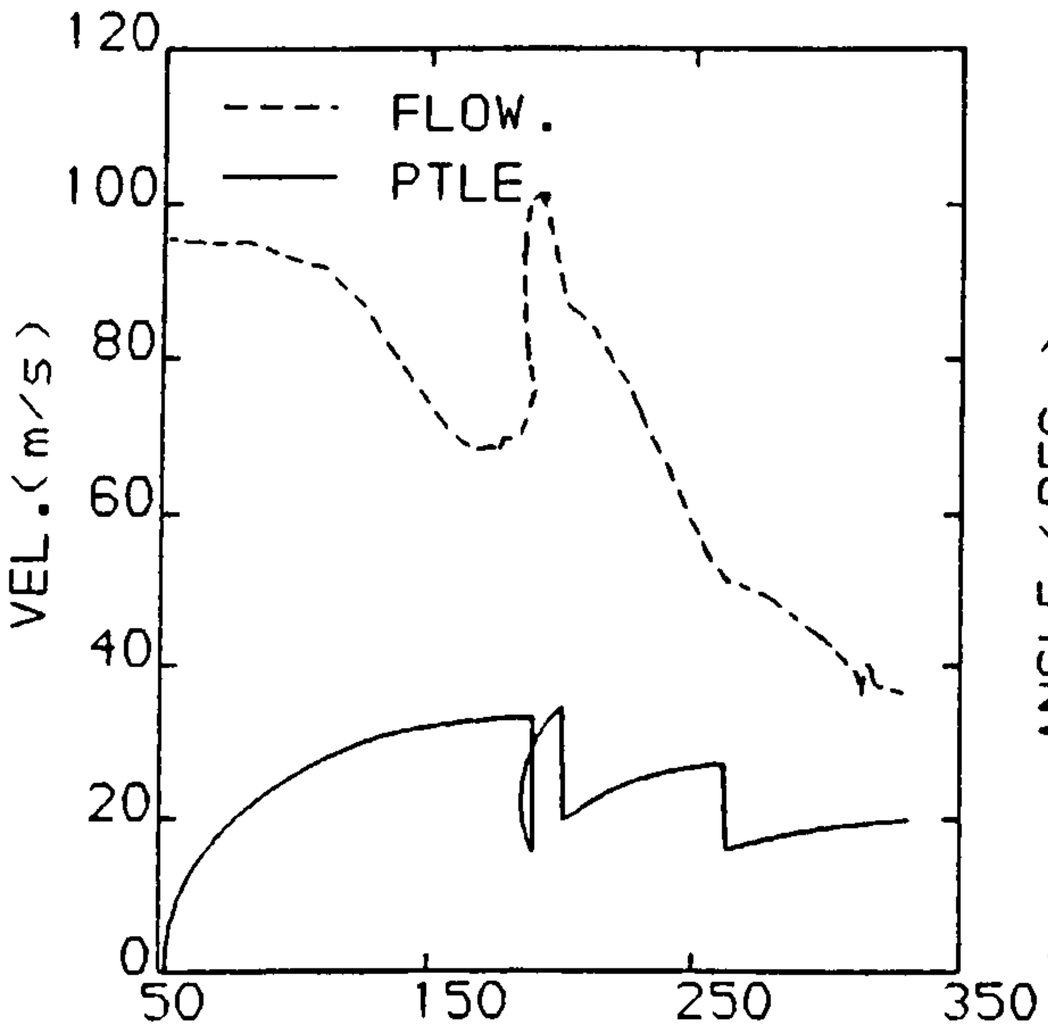

PREDICTED PAPTICLE AND FLOW ANGLES

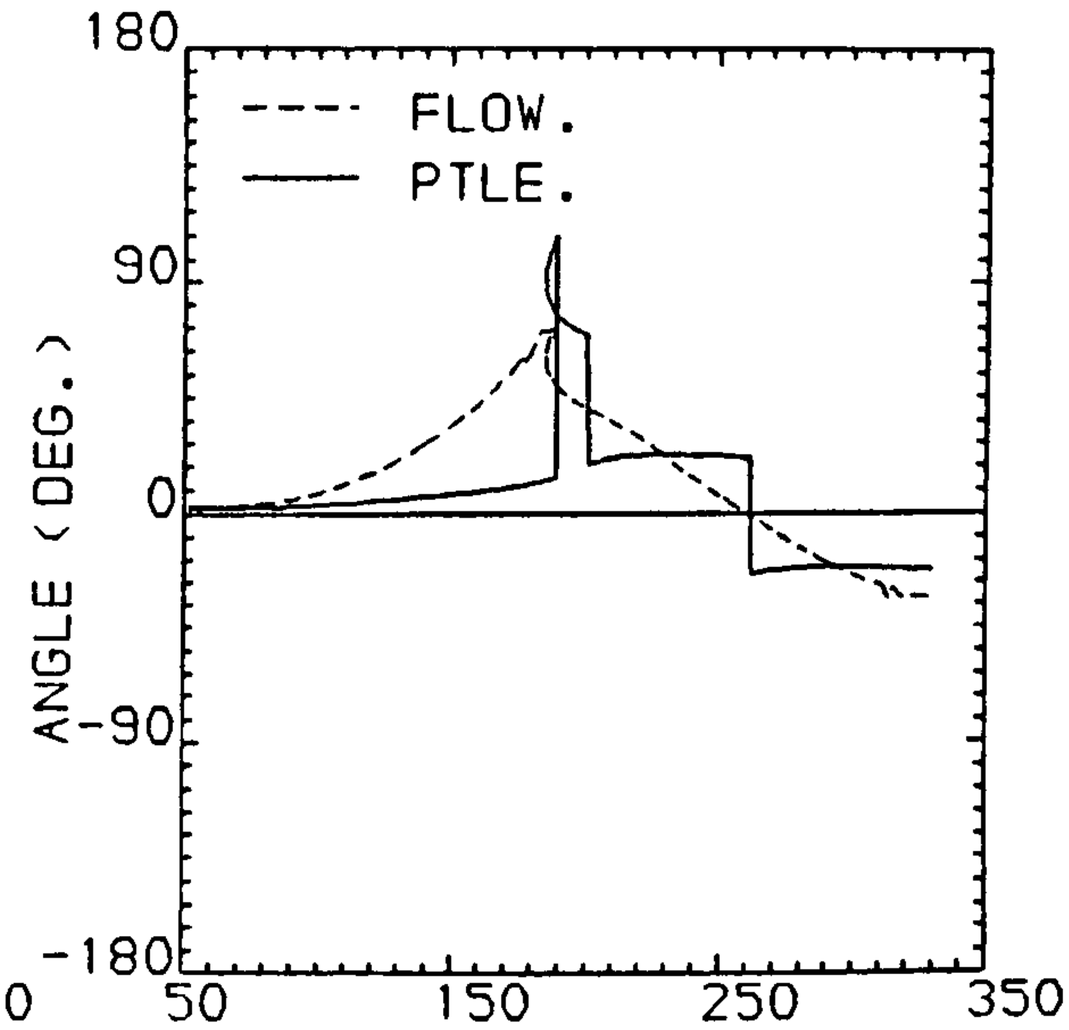

PREDICTED PARTICLE TRAJECTORIES

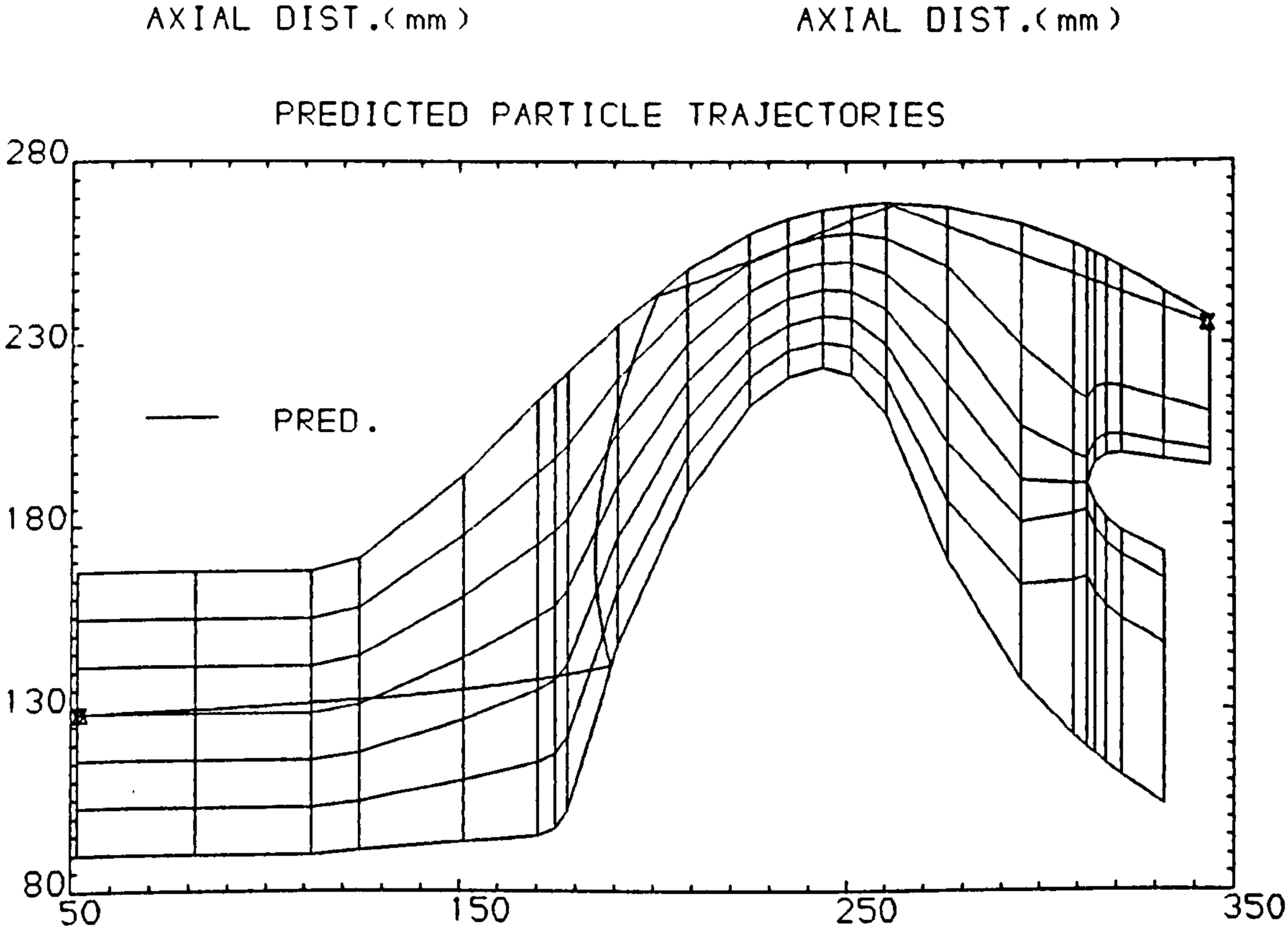

WALL MATL.	= AL.	PTLE. DIAMETER	= 150.0 um
PTLE. MATL.	= QUARTZ	PTLE. INITIAL VEL.	= 0.0 m/s
PTLE. DENSITY	= 2650.0 kg/m3		

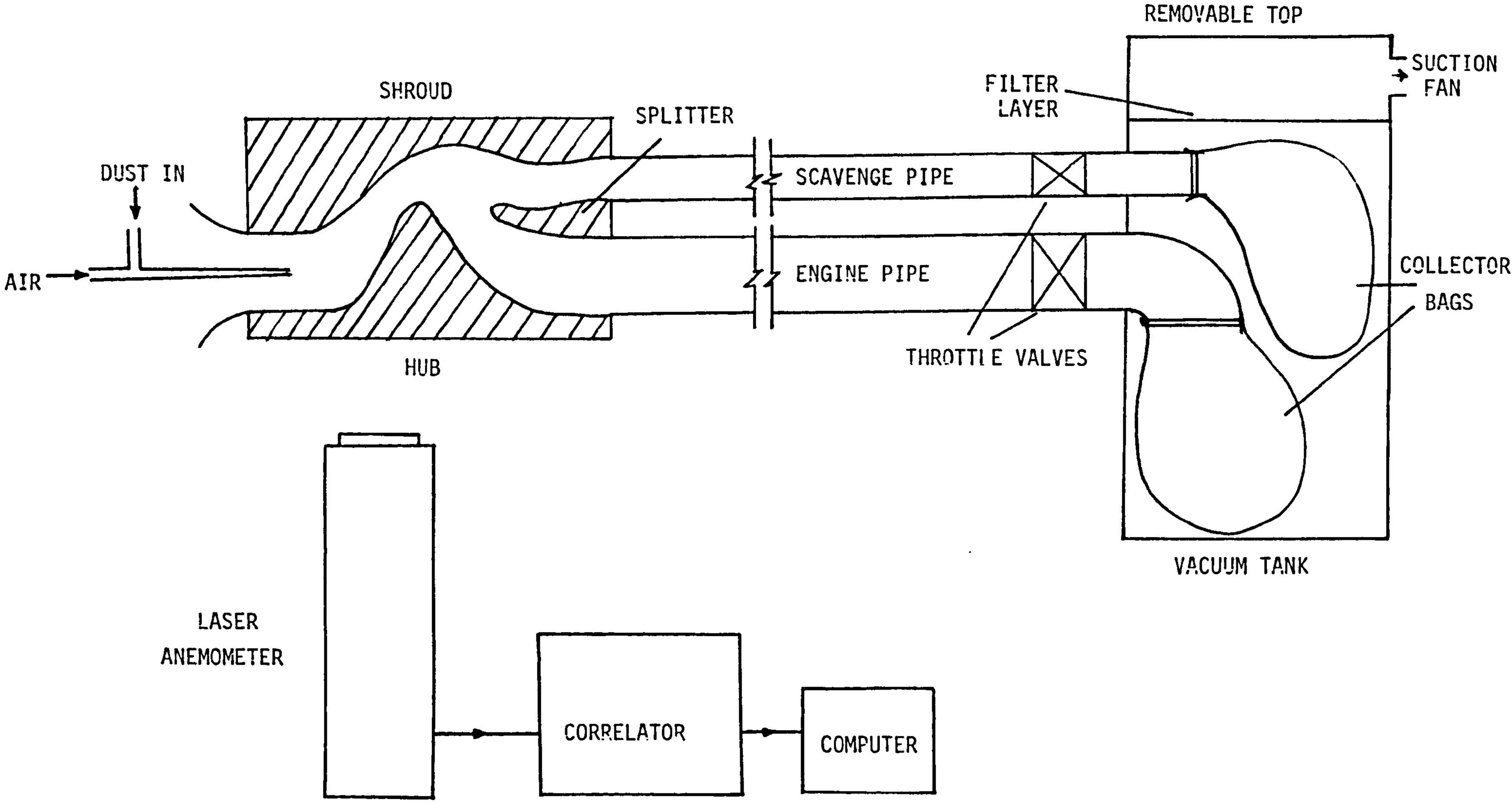

FIG.17 SCHEMATIC LAYOUT OF THE EXPERIMENTAL SET-UP

FIG.18 AN ISOMETRIC VIEW OF THE GAS TURBINE SEPARATOR

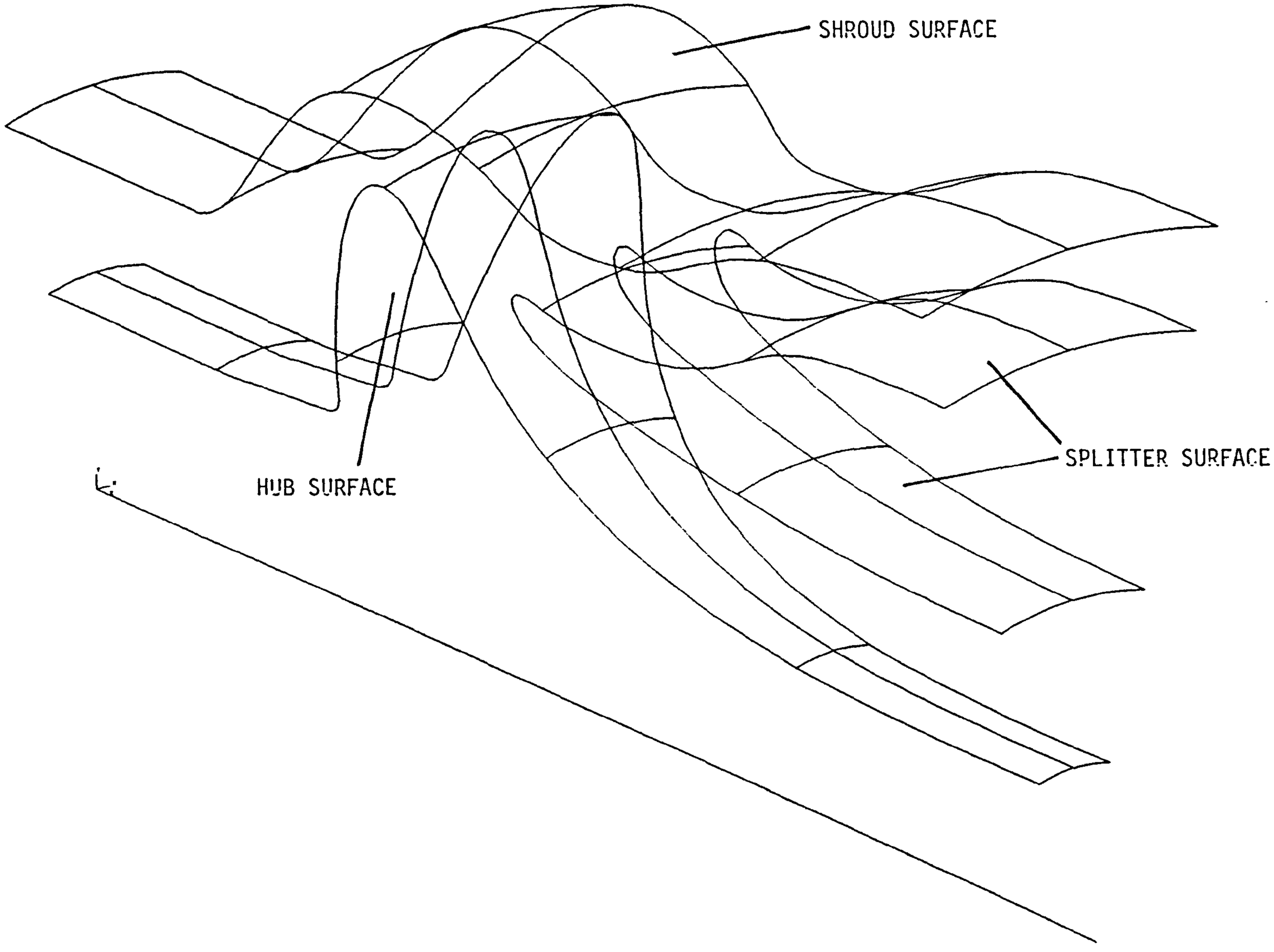

FIG.19 A 30 DEGREE SECTION OF AN AXISYMMETRIC GAS TURBINE SEPARATOR

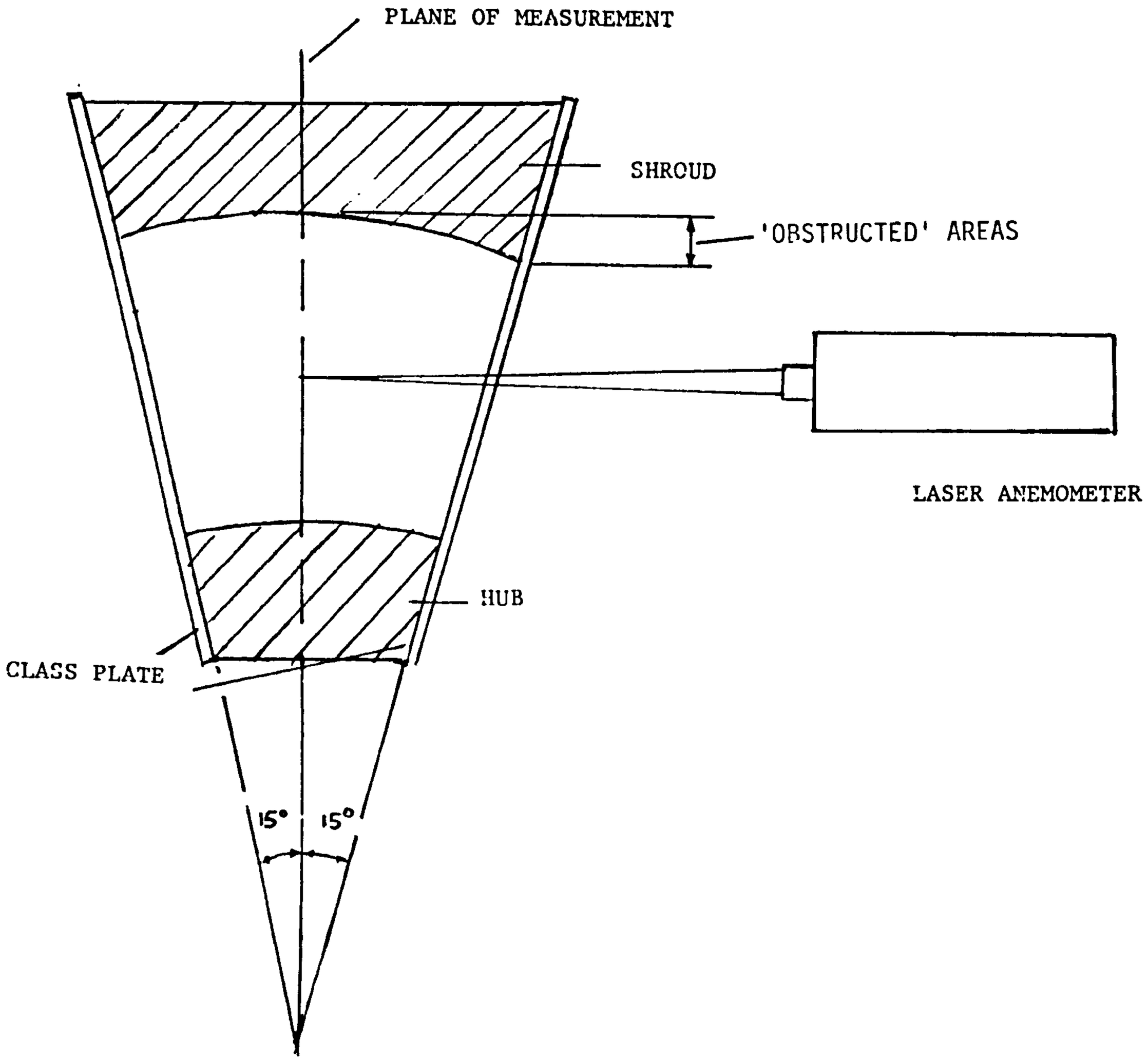

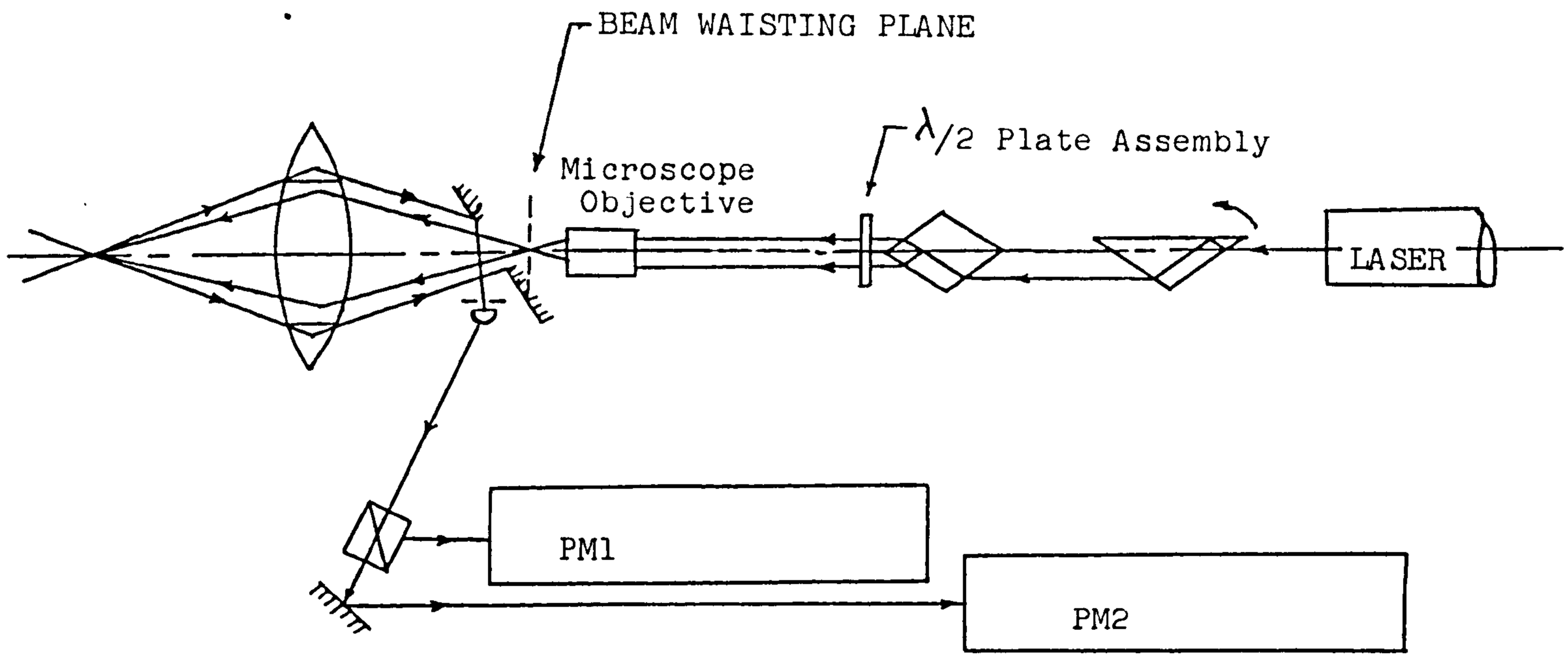

Fig. 20 The basic laser time of flight system.

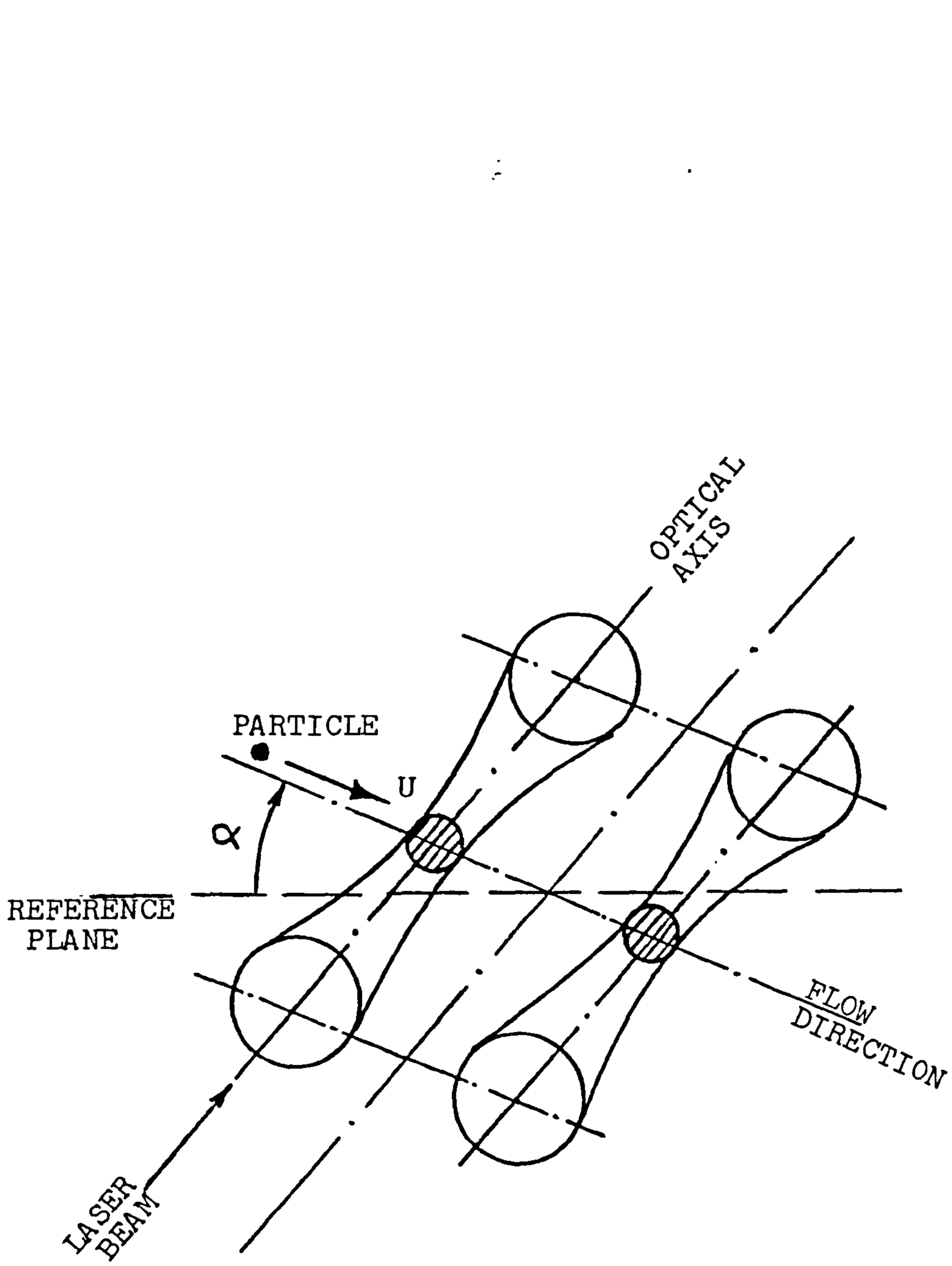

Fig. 2I Measuring volume of the two spot laser anemometer.

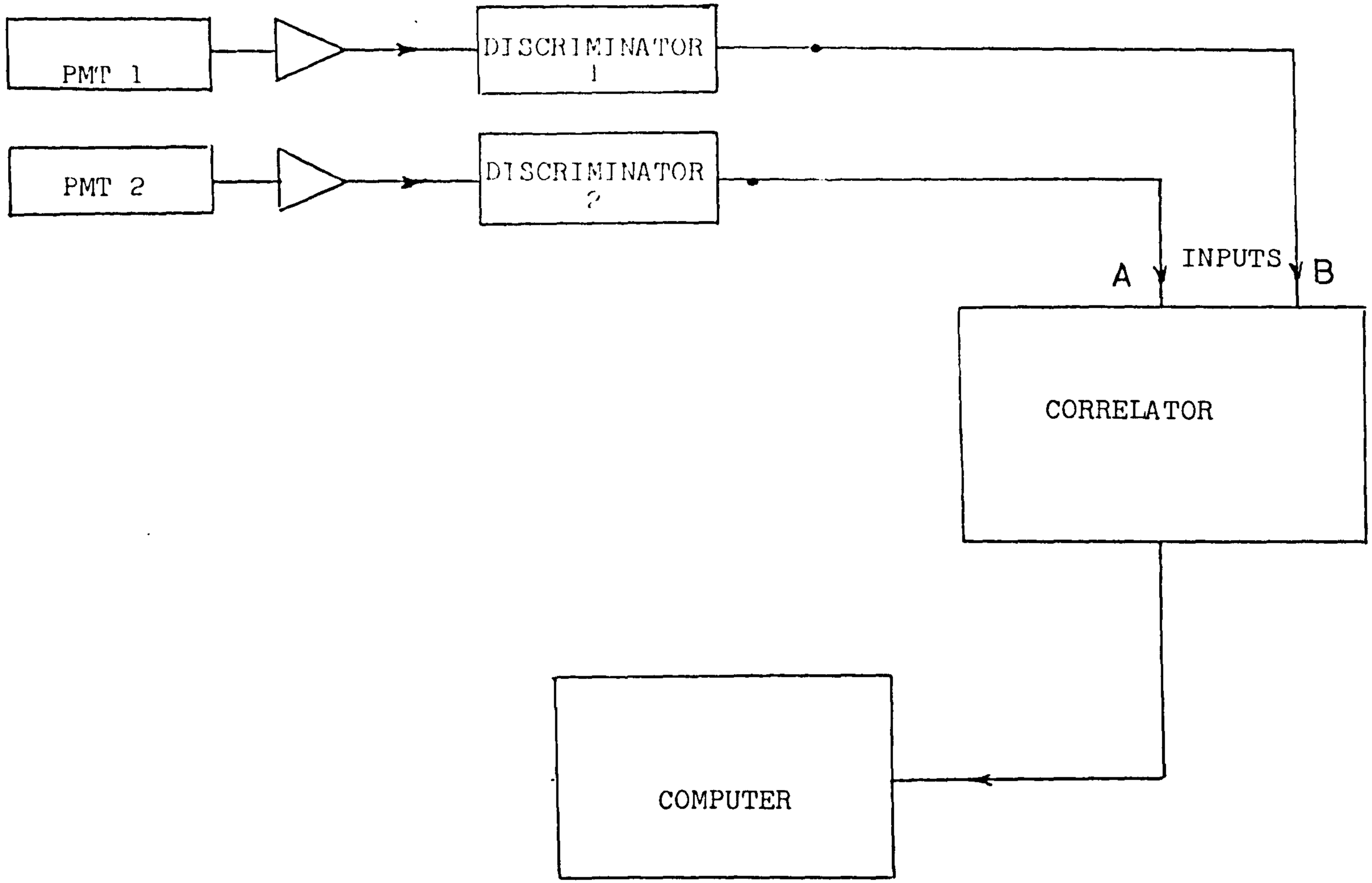

Fig. 22 Analysis of two spot data.

FIG.23 PROBABILITY CURVE VS FLOW ANGLE

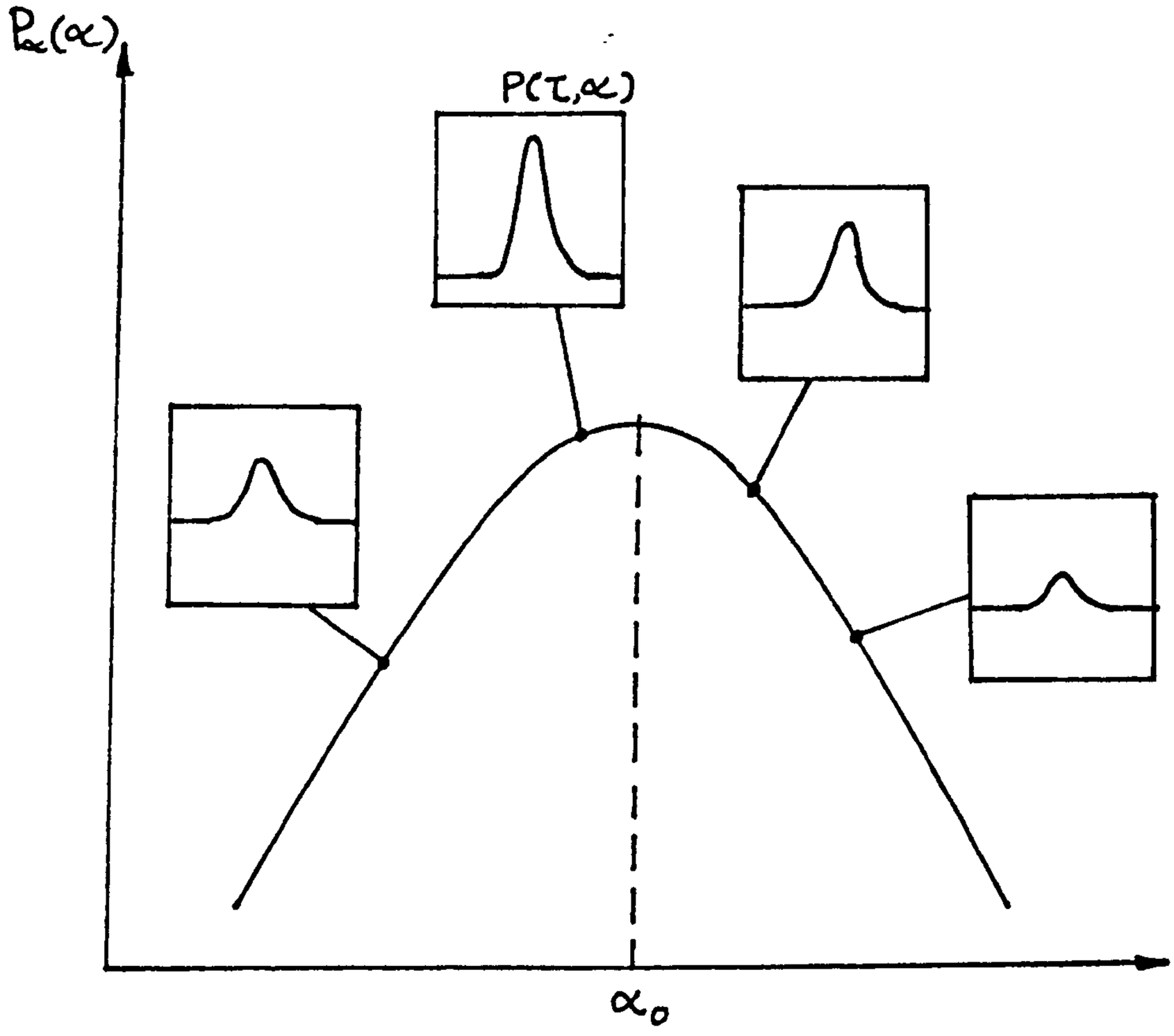

FIG.24 VARIATION OF THE PROBABILITY CURVE WITH FLOW ANGLE

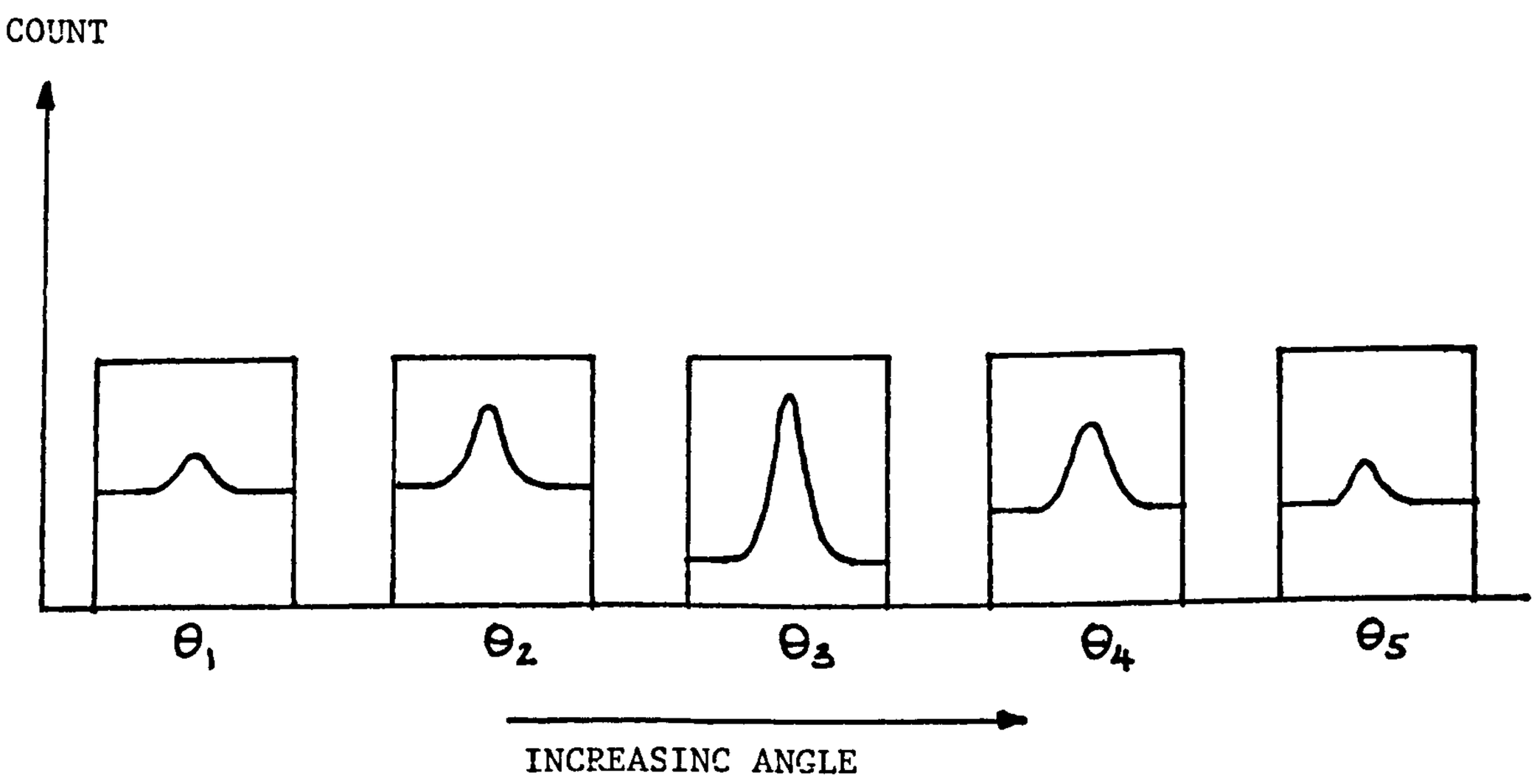

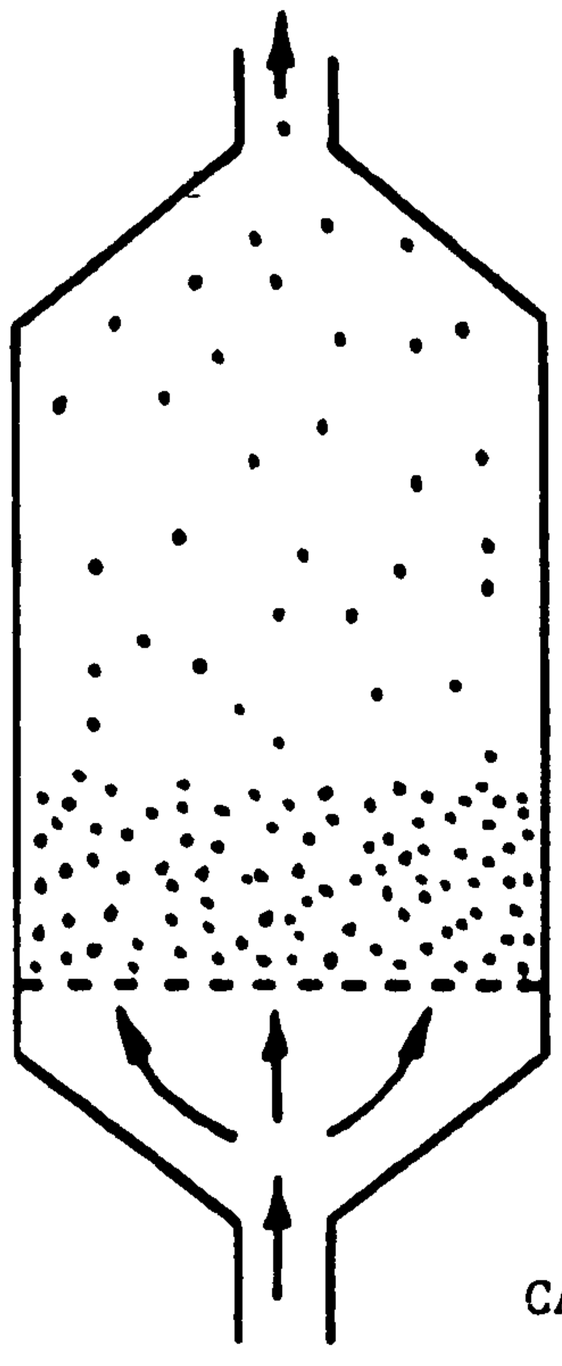

FIG.25 A PRESSURISED FLUIDISED BED

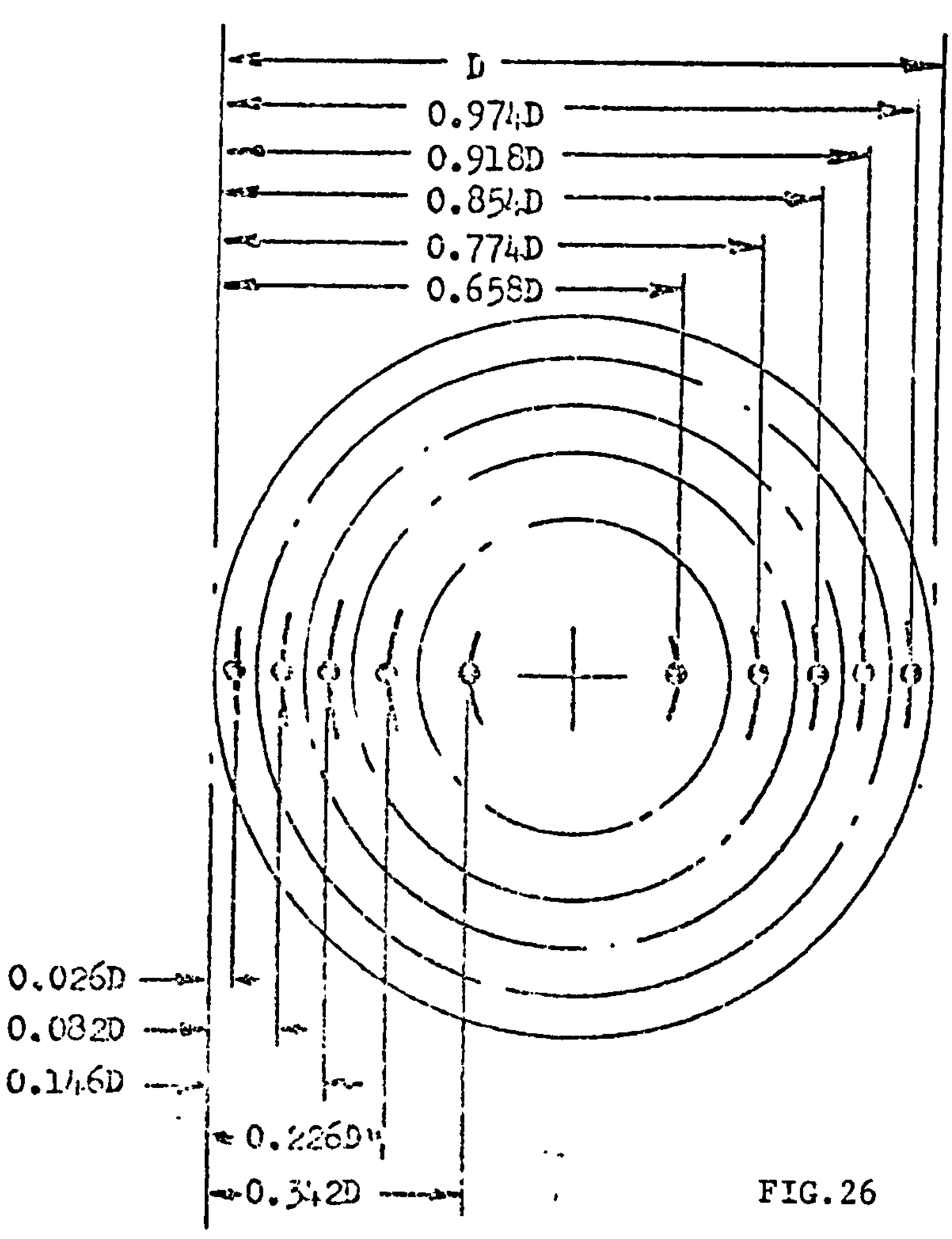

FIG.26 TRAVERSE STATIONS

FIG.27 PRESSURE TRAVERSE READINGS ACROSS THE ENGINE AND SCAVENGE PIPE

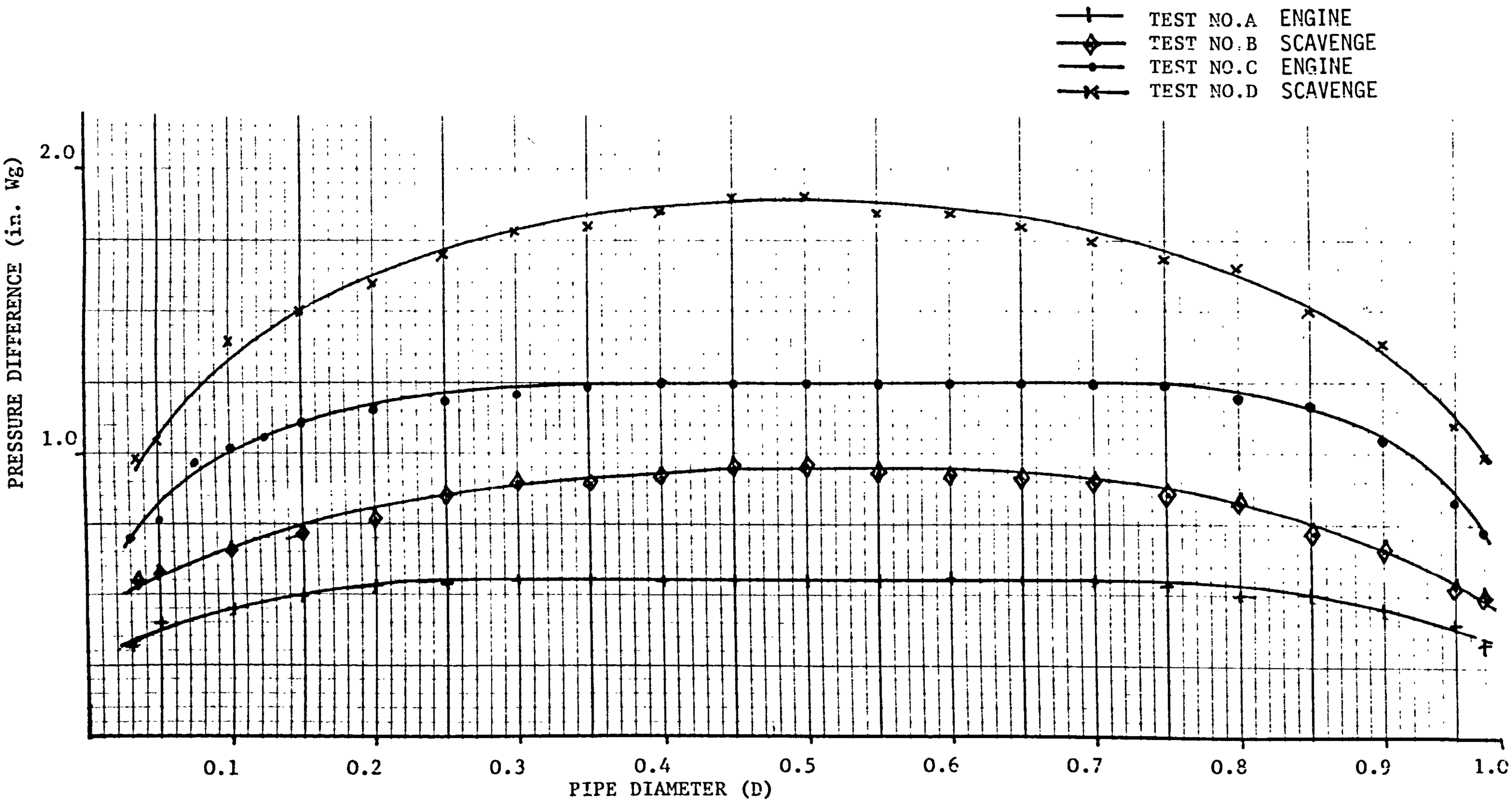

FIG.28 LOCATION OF THE WALL STATIC PRESSURE TAPPINGS IN THE SEPARATOR

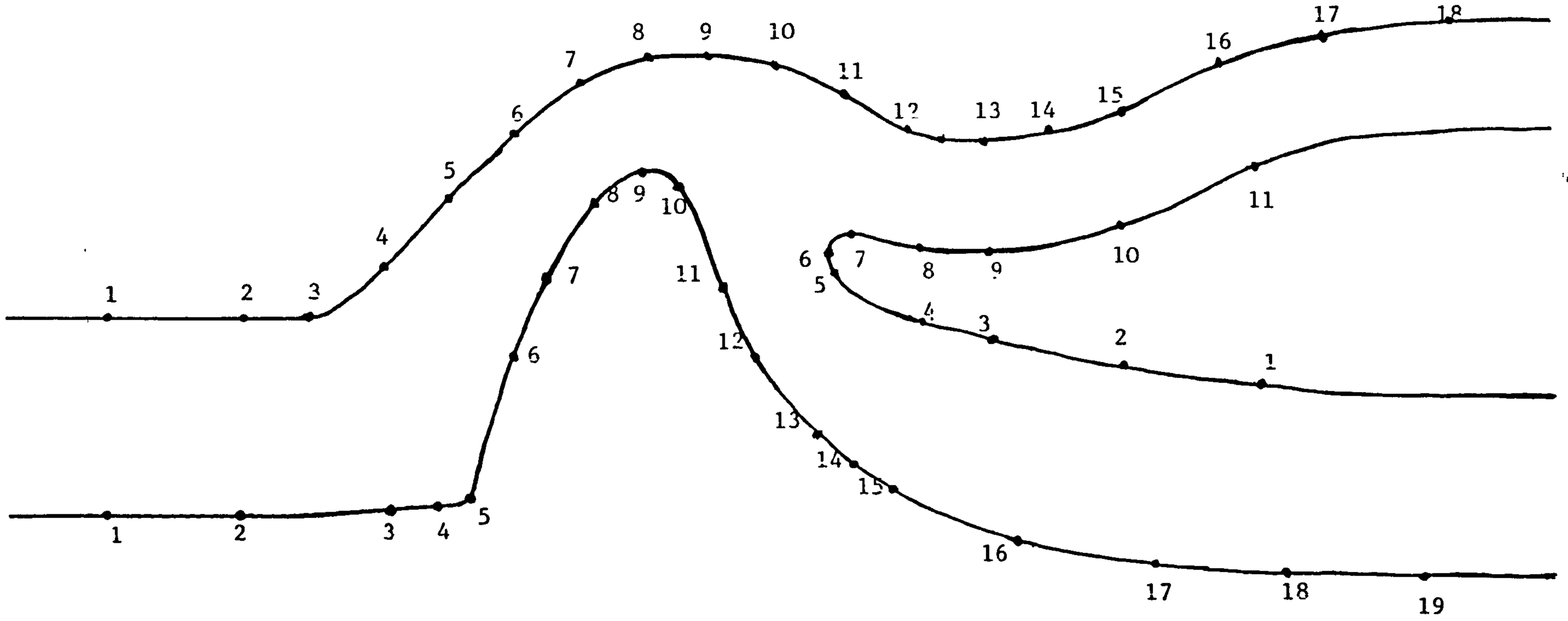

FIG.29 CRITICAL FLOW AREAS IN THE SEPARATOR

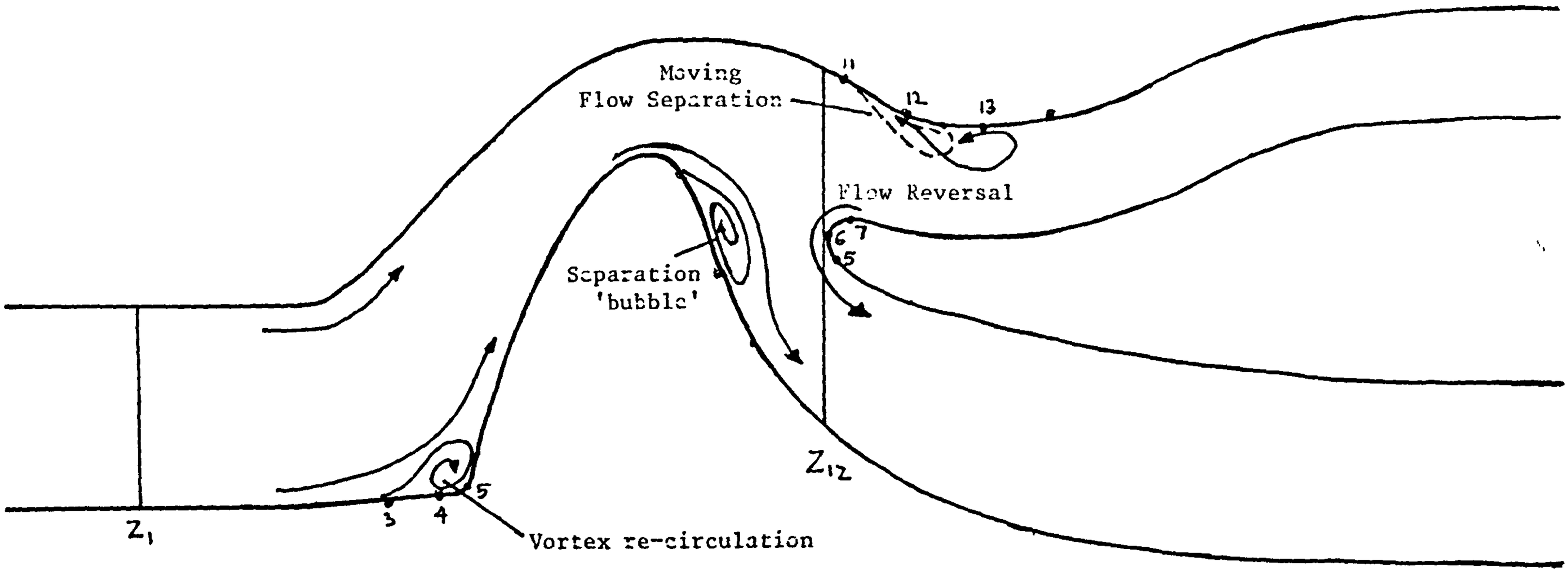

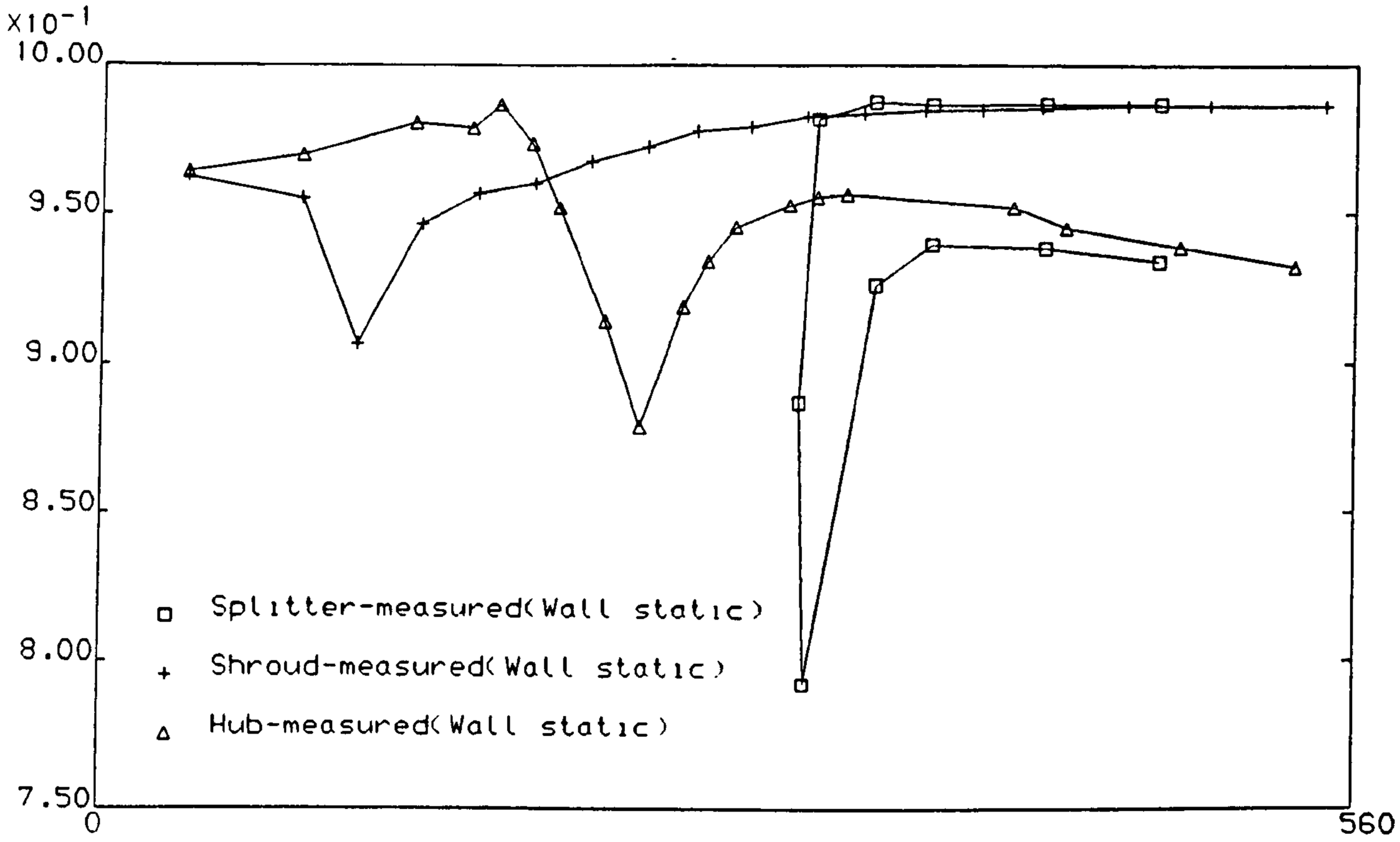

FIG30a MEASURED WALL PRESSURE DISTRIBUTION

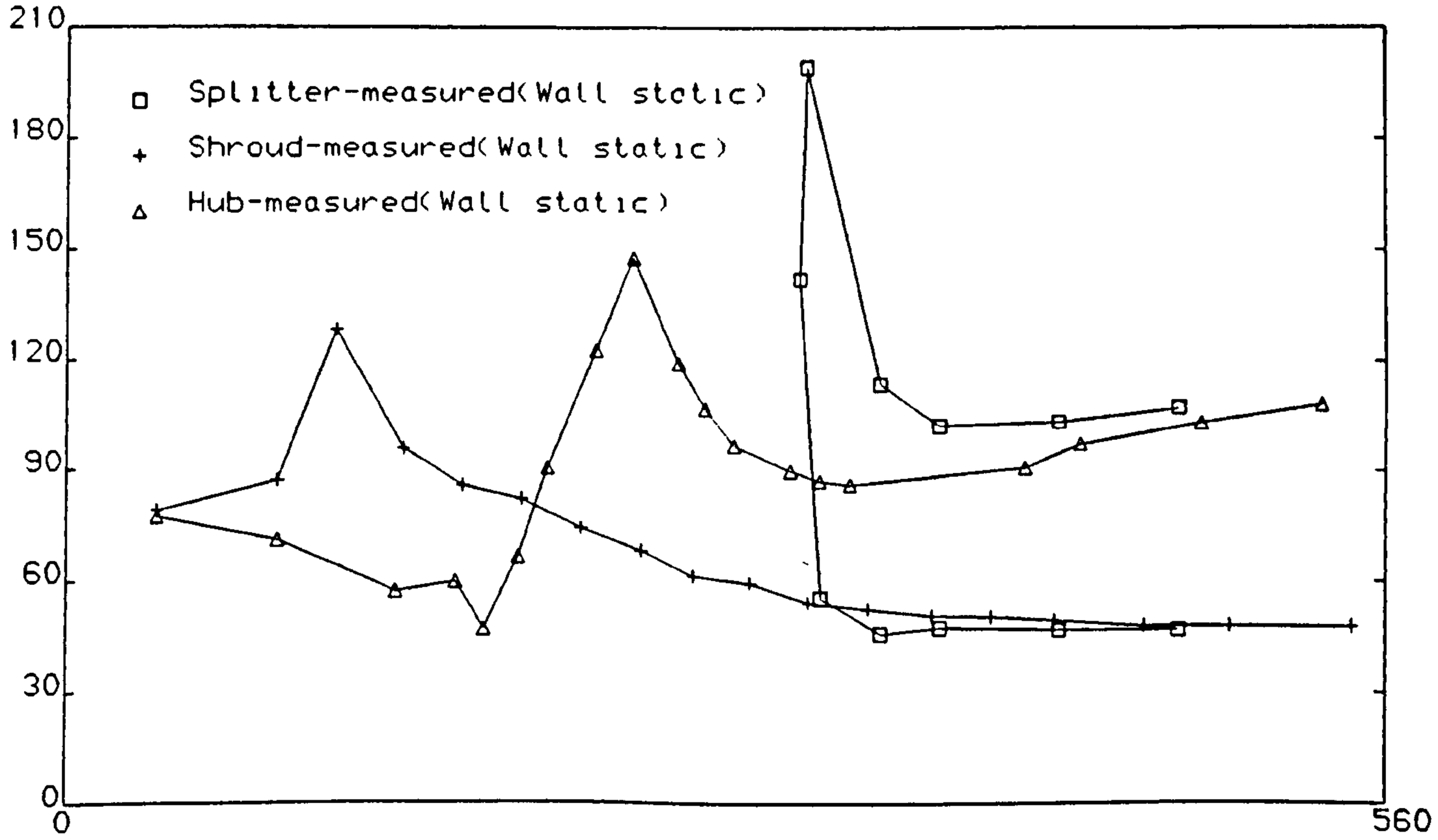

FIG30b MEASURED WALL VELOCITY DISTRIBUTION

FIG.31 TRAVERSE STATIONS FOR THE MEASUREMENT OF THE FLOWFIELD AT MID-SECTION OF THE G.T. SEPARATOR

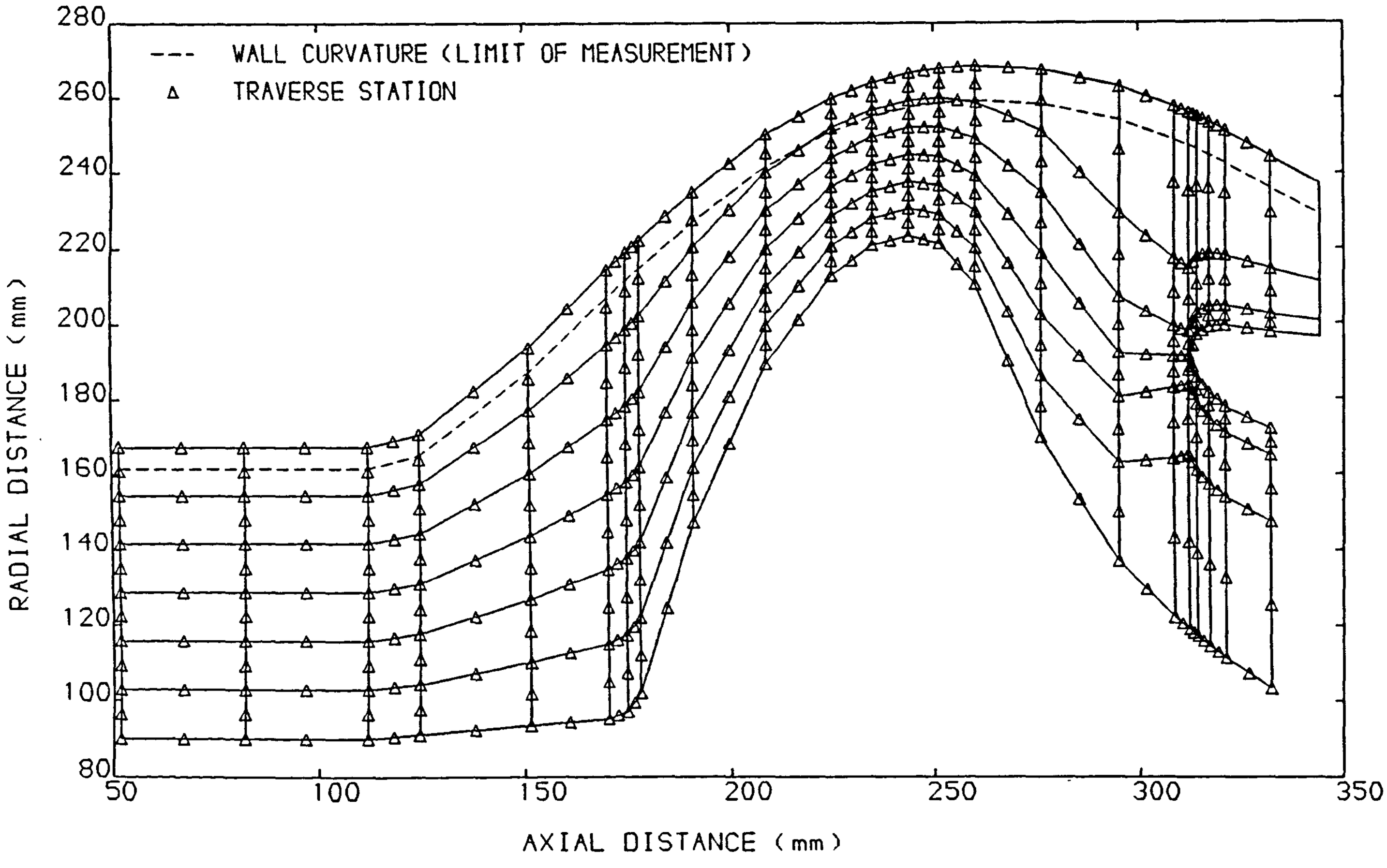

FIG.32 MEASURED FLOW VECTORS AT MID-SECTION OF A GAS TURBINE SEPARATOR

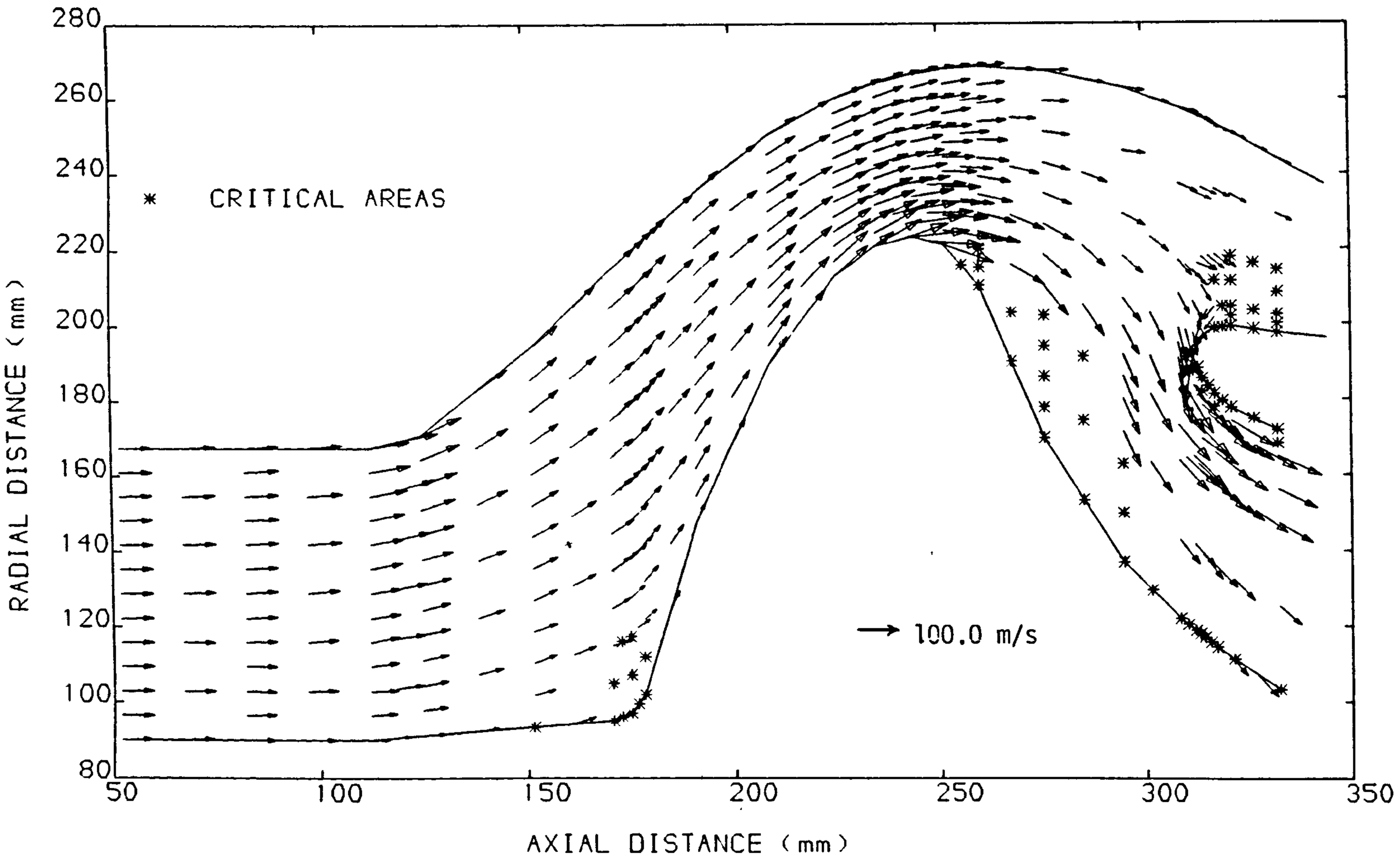

FIG.33 COMPARISION BETWEEN MEASURED AND PREDICTED FLOW VECTORS

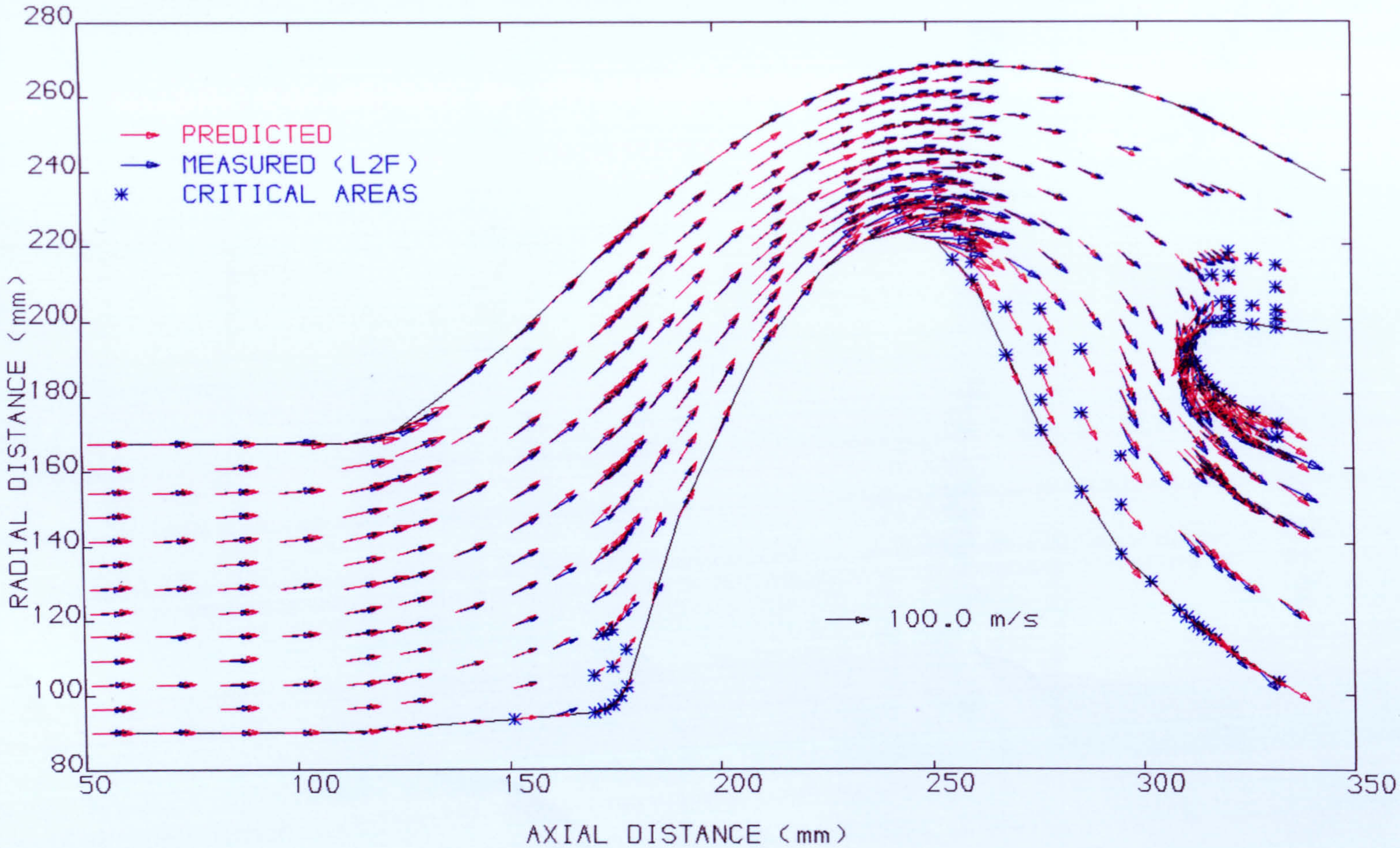

FIG.34 COMPARISION BETWEEN MEASURED AND PREDICTED FLOW VELOCITIES

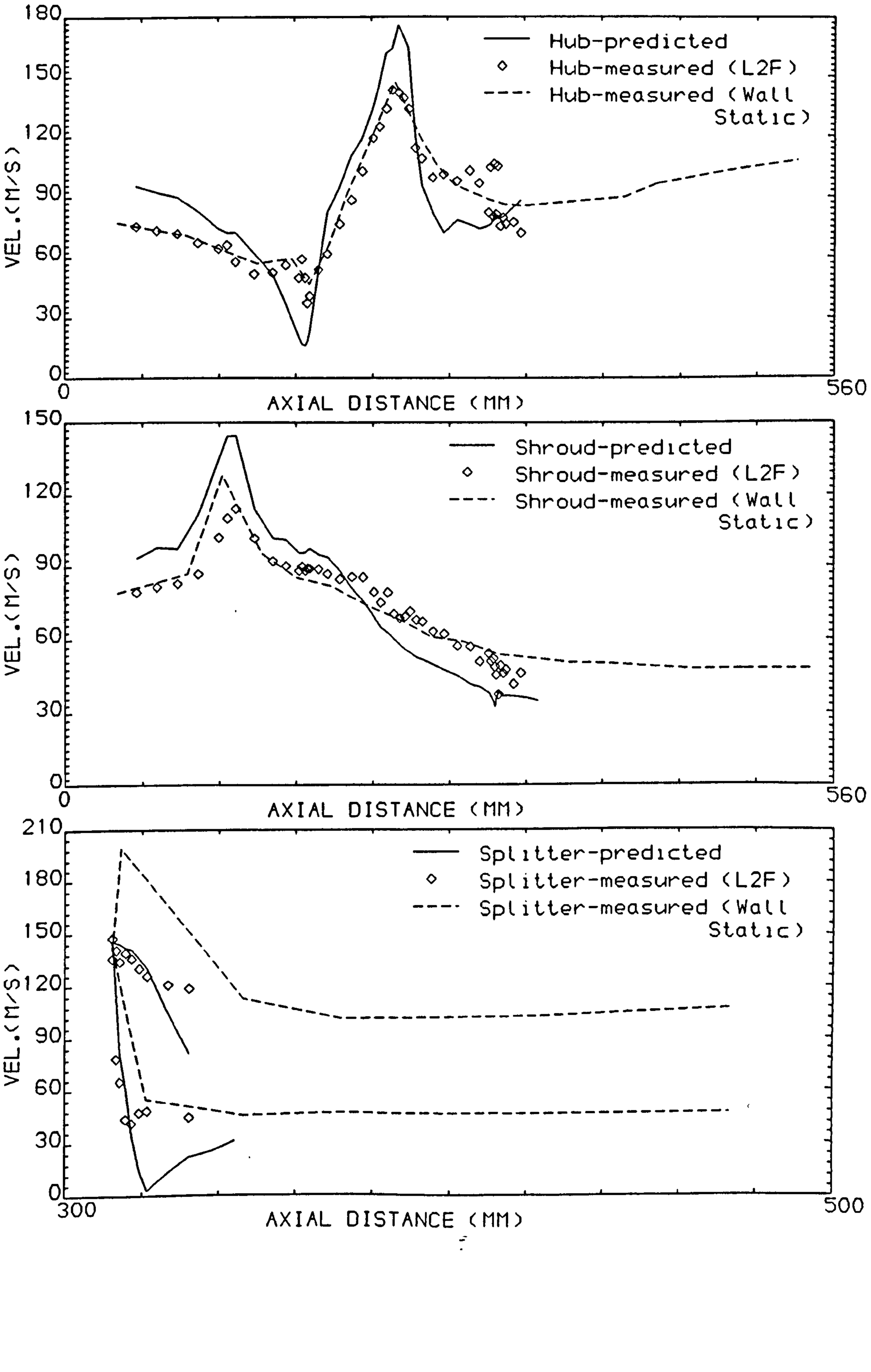

FIG.35 COMPARISION BETWEEN MEASURED AND PREDICTED (SCALED)
FLOW VECTORS

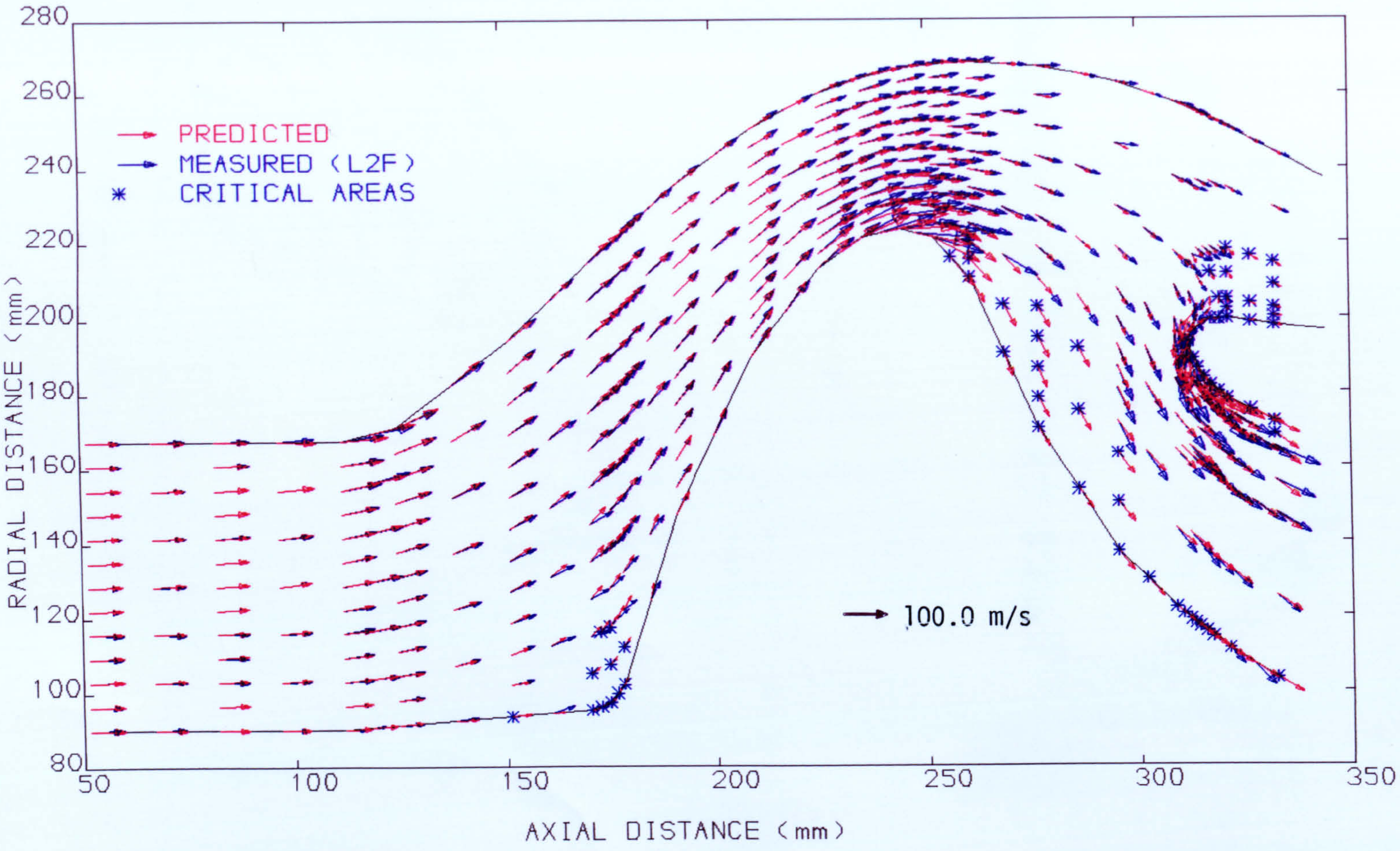

FIG.36 MEASURED AND PREDICTED FLOW VELOCITIES CONTOURS

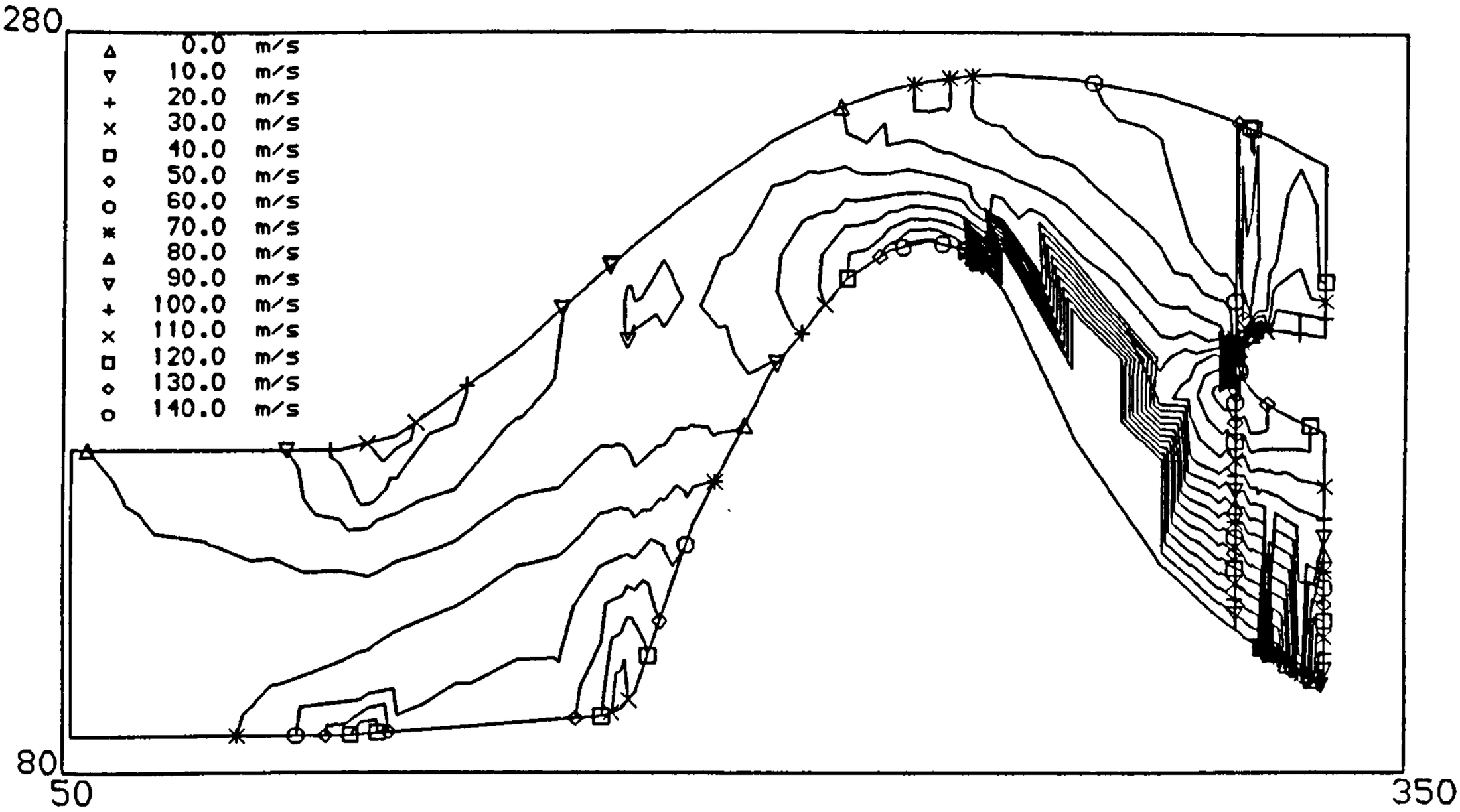

Measured Flowfield

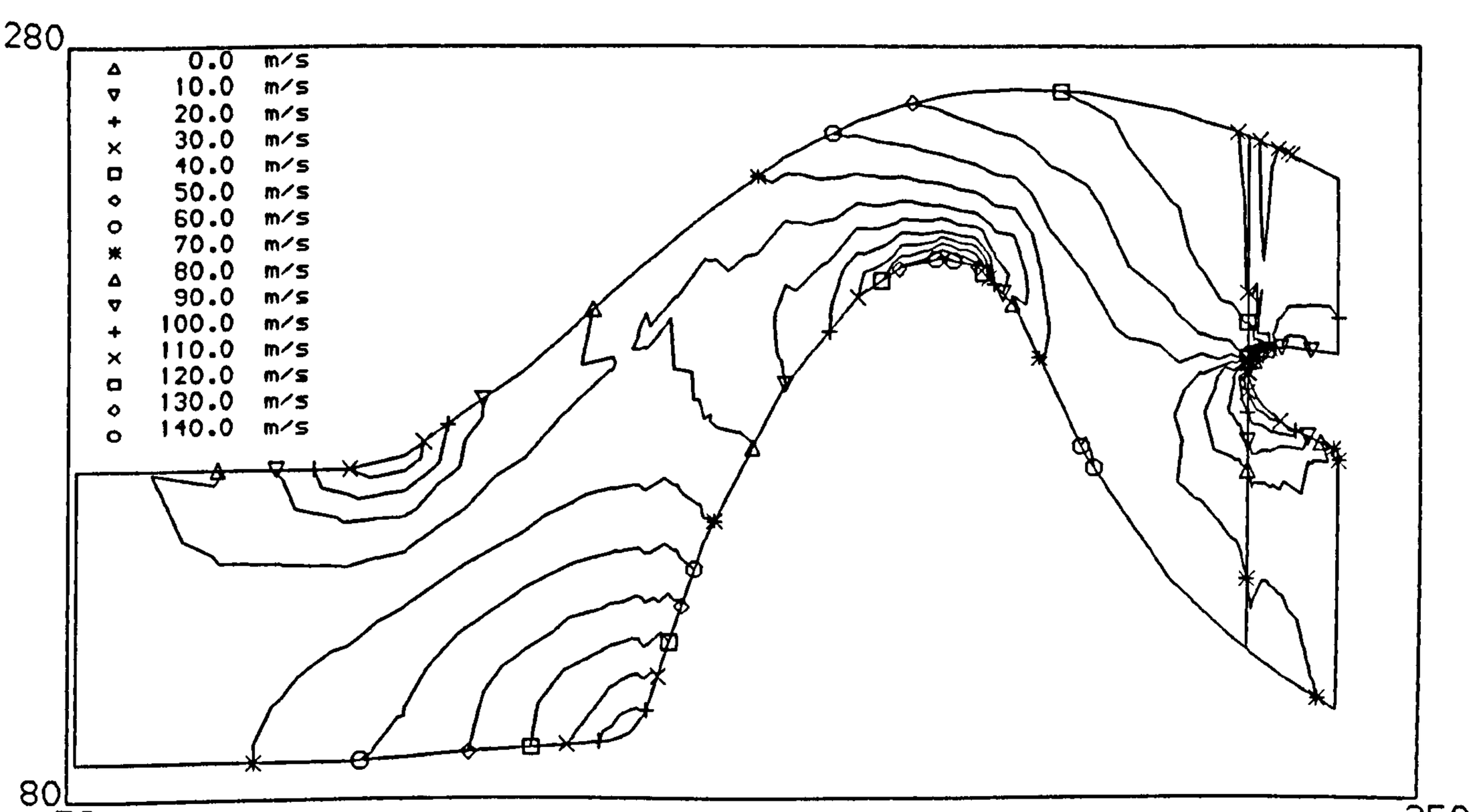

Predicted FlowField (Scaled)

FIG.37 COMPARISION BETWEEN MEASURED AND PREDICTED (SCALED) FLOW VELOCITIES

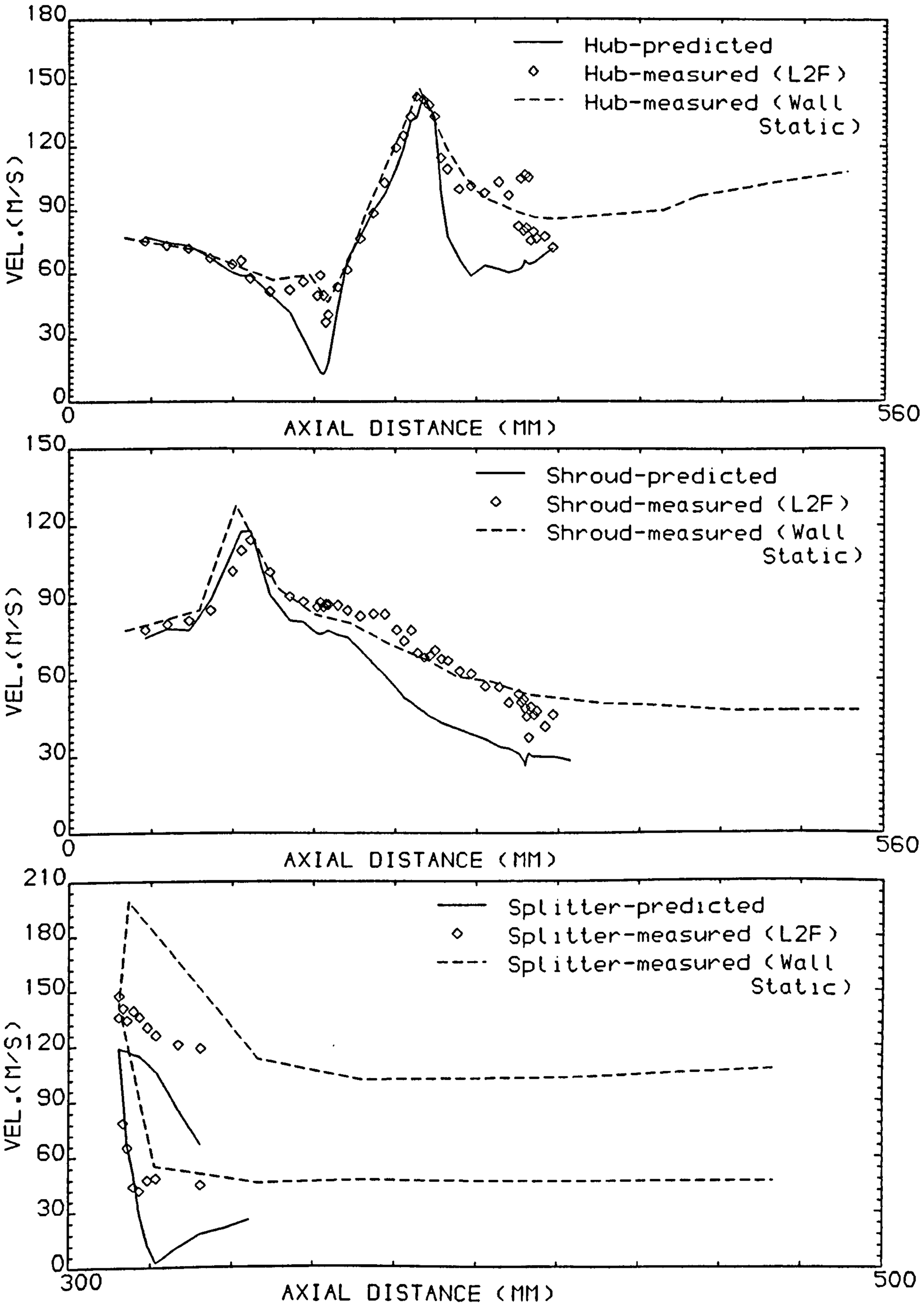

FIG.38 COMPARISION OF MEASURED AND PREDICTED (SCALED) WALL PRESSURE DISTRIBUTION

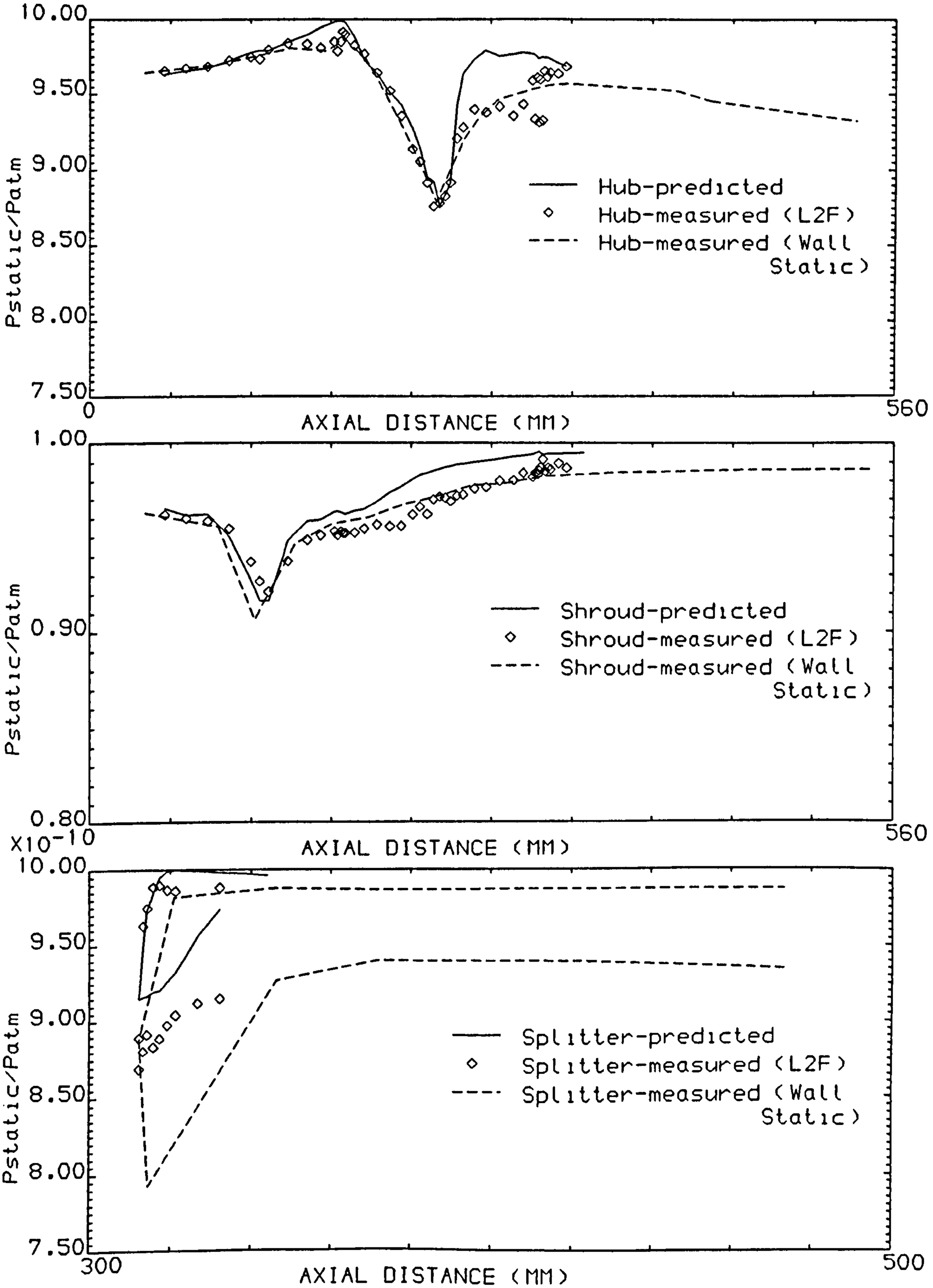

FIG.39 TRAVERSE STATIONS FOR THE MEASUREMENT OF PARTICLE TRAJECTORIES

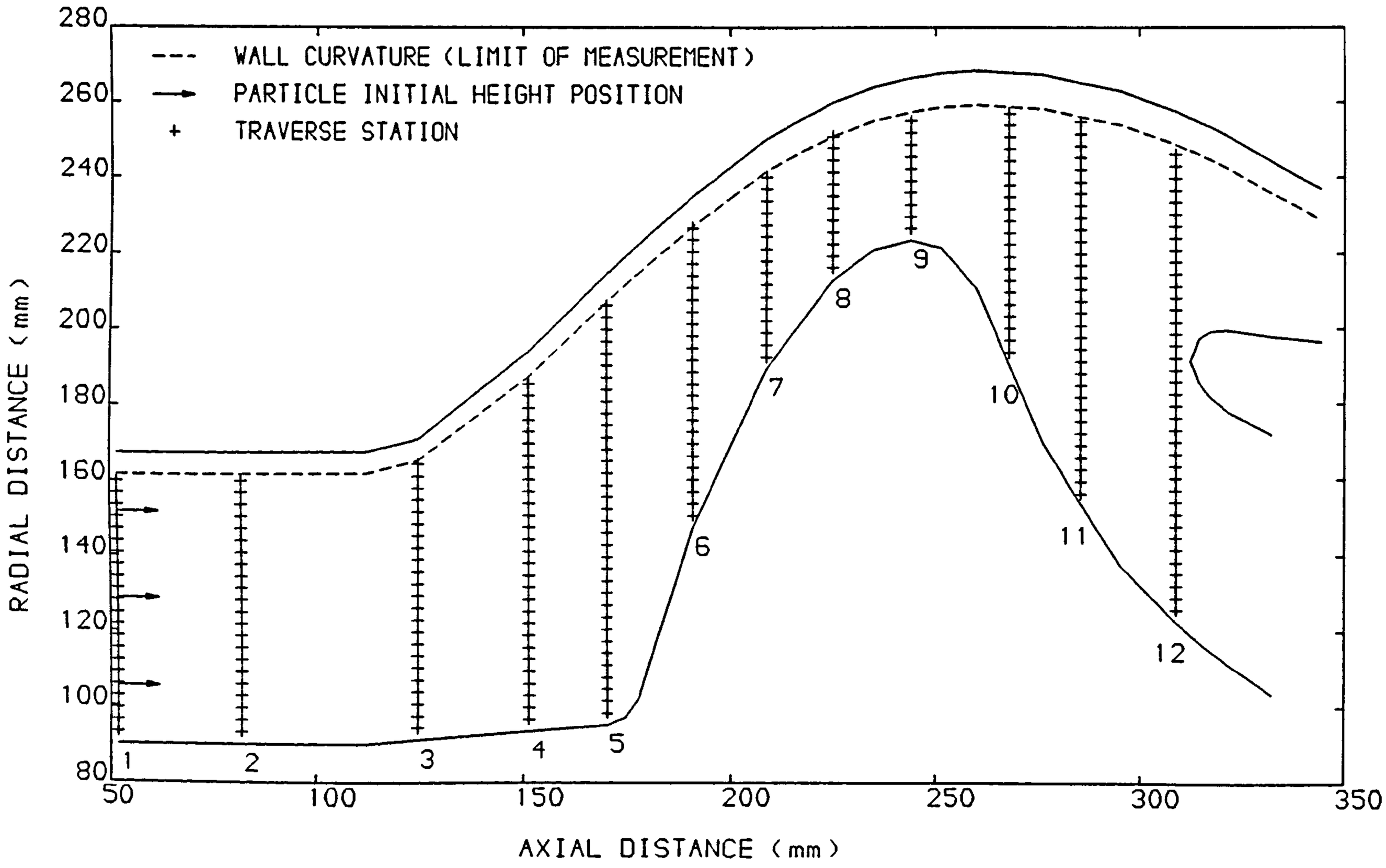

FIG.40 ARRANGEMENT OF THE TRAVERSE PLANES IN THE CRITICAL FLOW AREAS

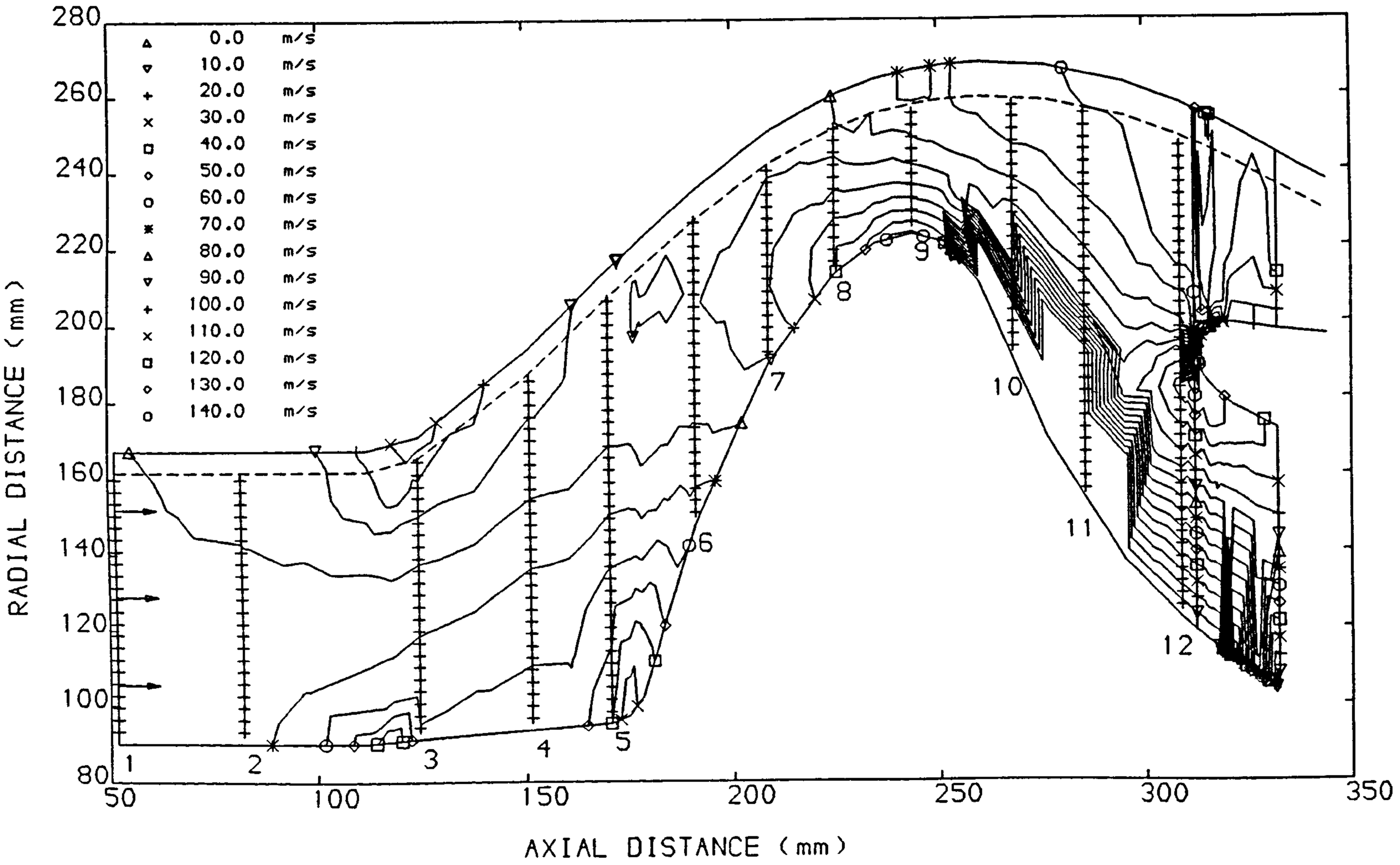

FIG.41 MEASURED PARTICLE CONCENTRATION DISTRIBUTION

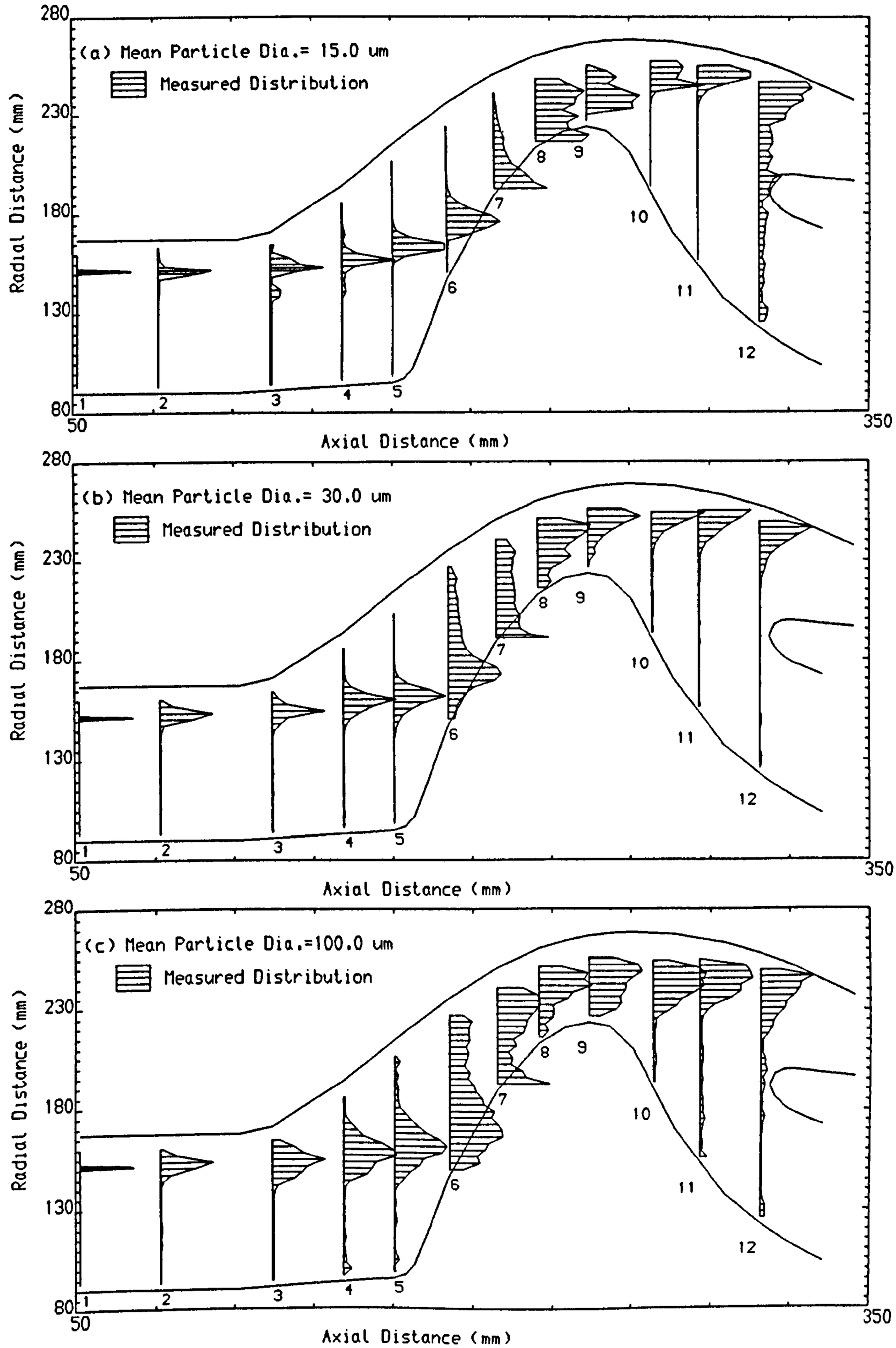

Wall matl. = AL.
Particle matl. = Ballotini

Particle initial location = 151.80 mm
Particle density = 2950.0 Kg/m3

FIG.42 MEASURED PARTICLE VELOCITIES AND ANGLES AT THE MEAN TRAJECTORY POSITIONS

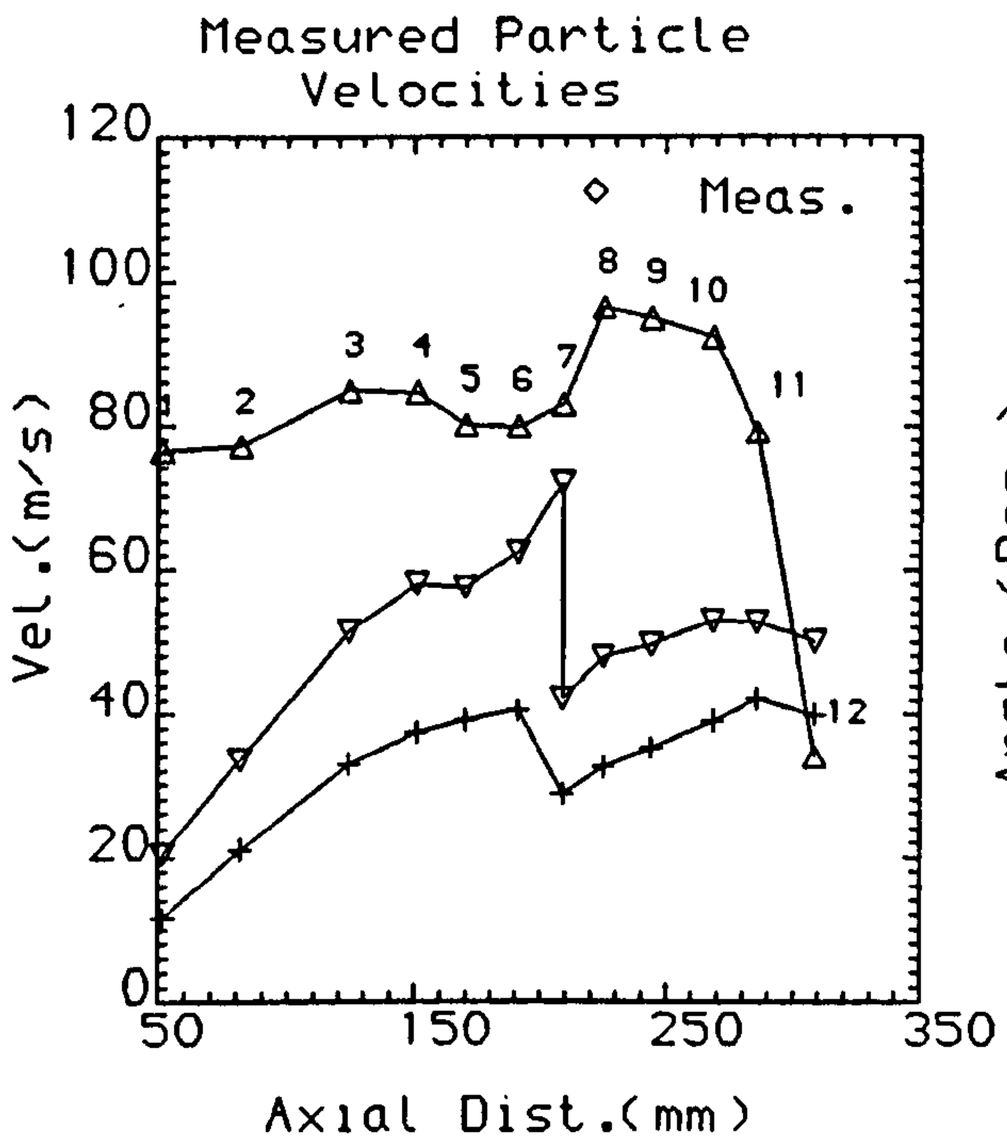

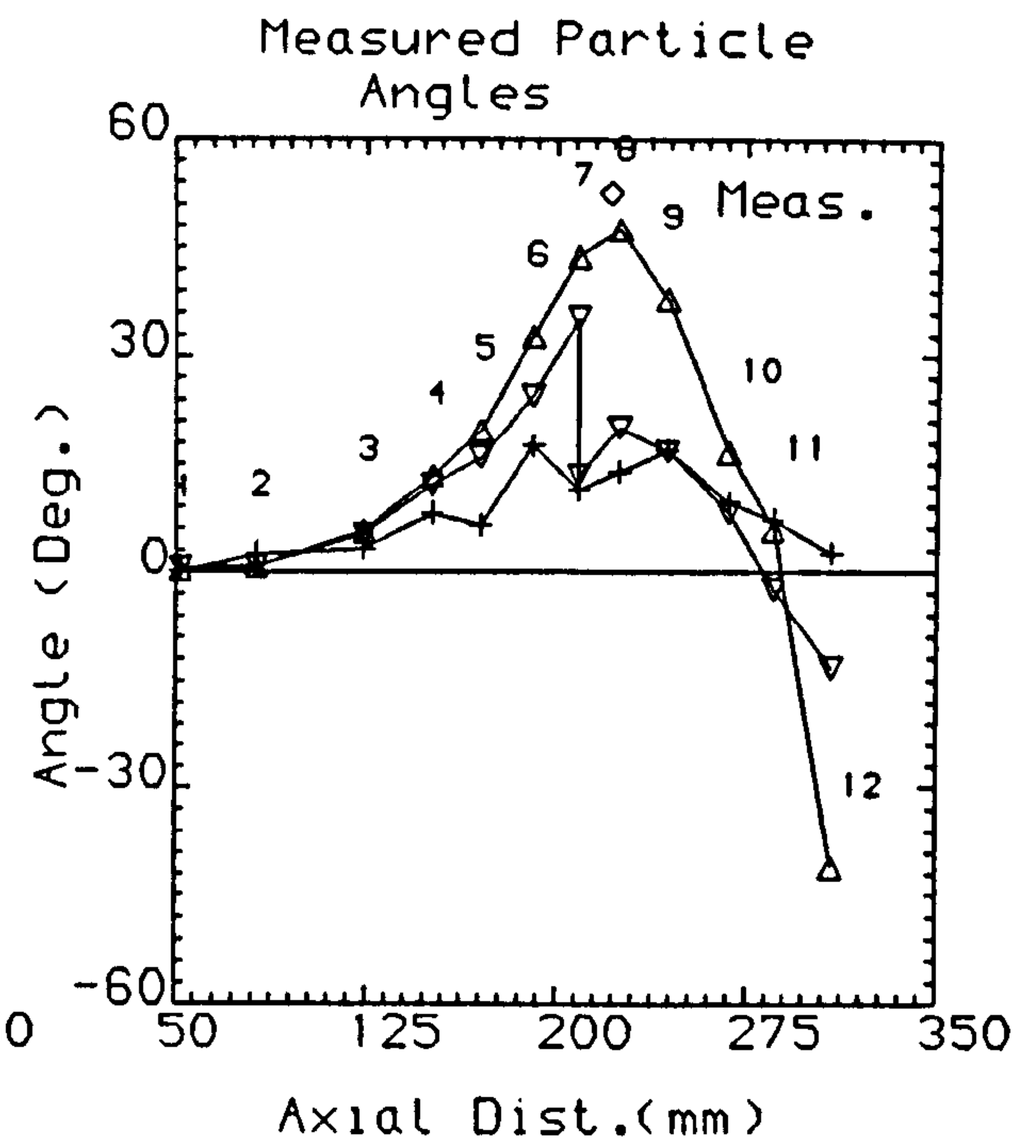

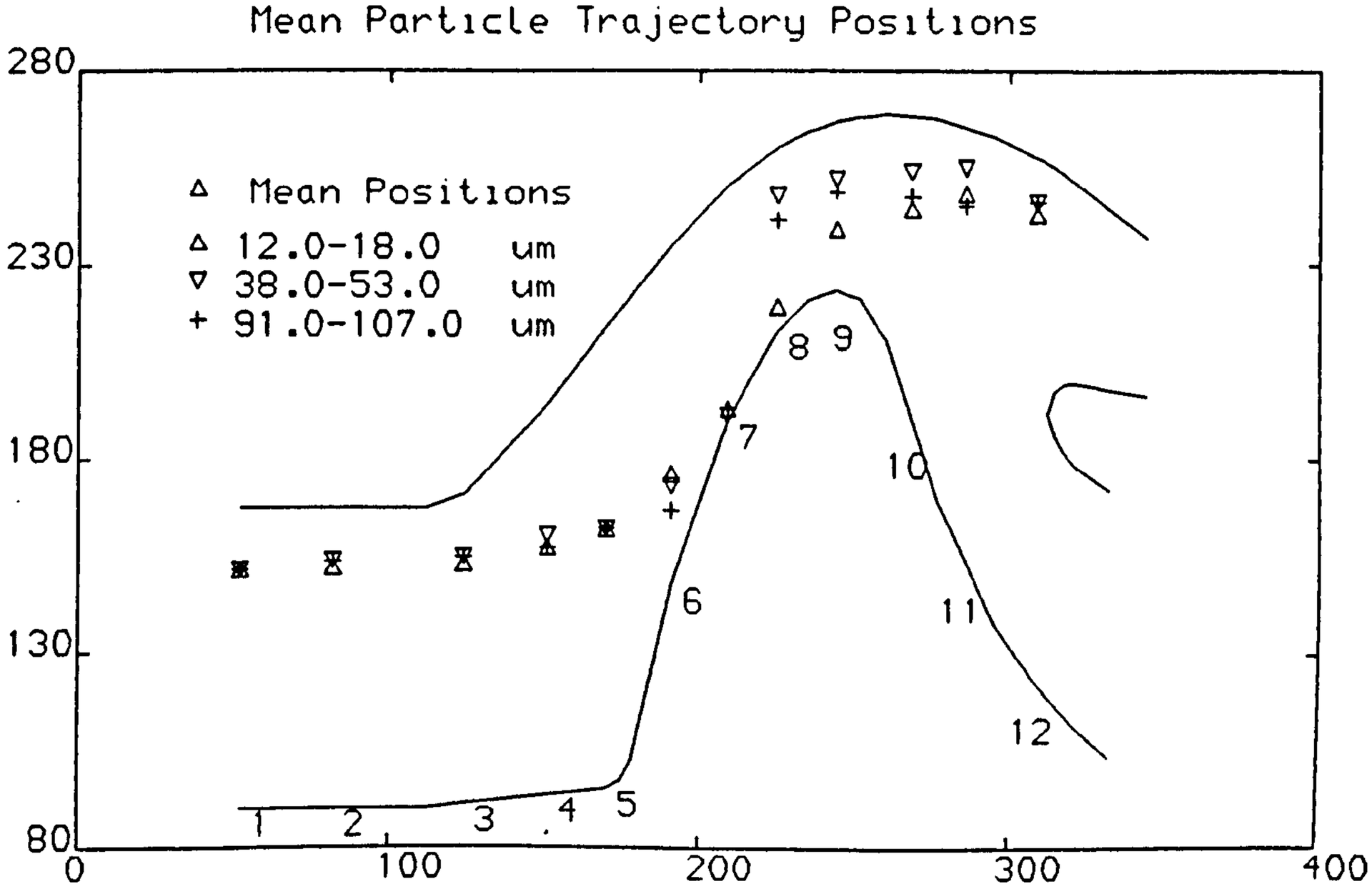

Wall Matl. = AL.

Ptle. Matl. = Ballotini

Ptle.Density= 2950.0 kg/m3

FIG.43 MEASURED PARTICLE CONCENTRATION DISTRIBUTION

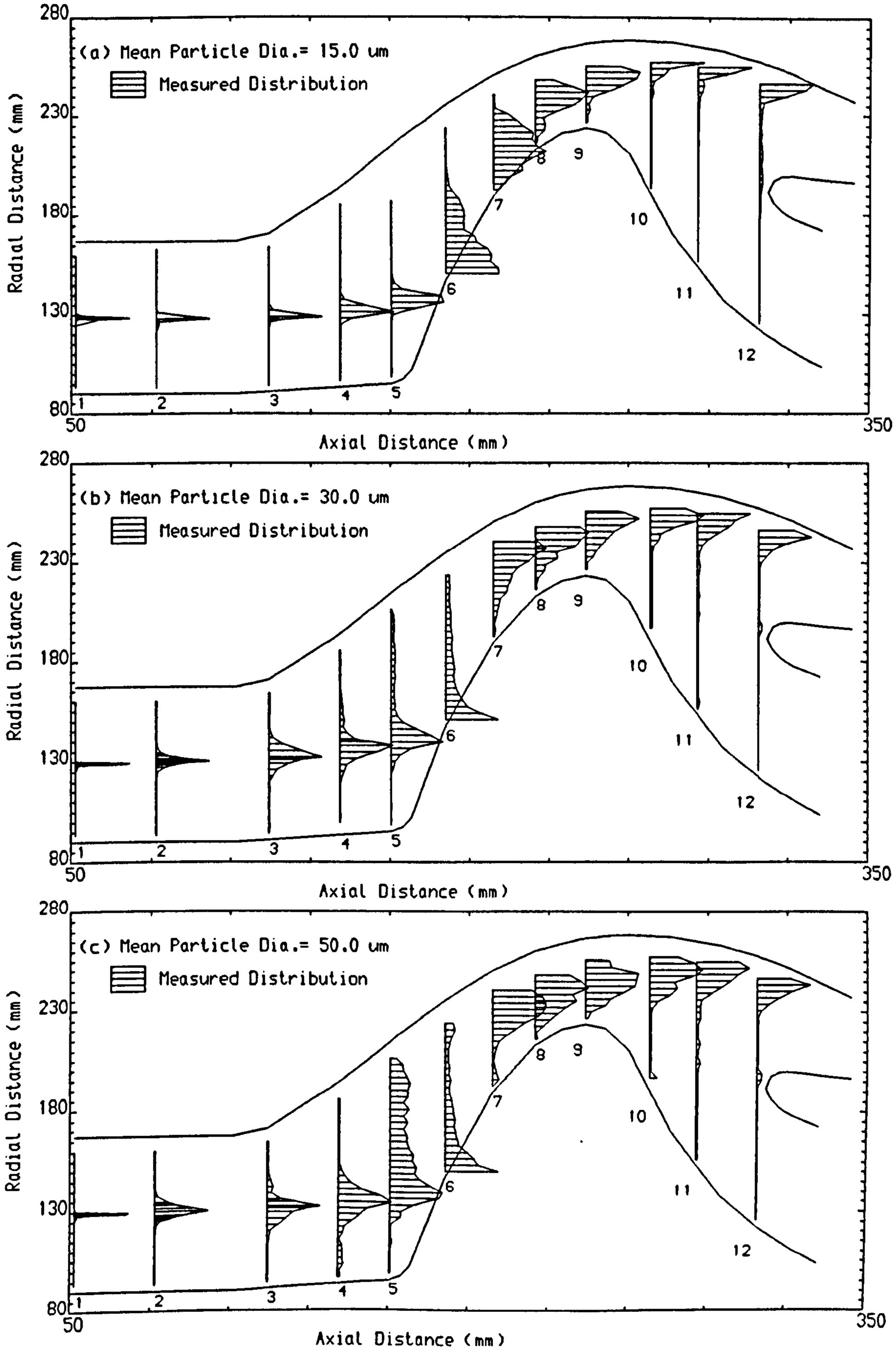

Wall matl. = AL.
Particle matl. = Ballotini
Particle initial location = 128.67 mm
Particle density = 2950.0 Kg/m3

FIG.44 MEASURED PARTICLE CONCENTRATION DISTRIBUTION

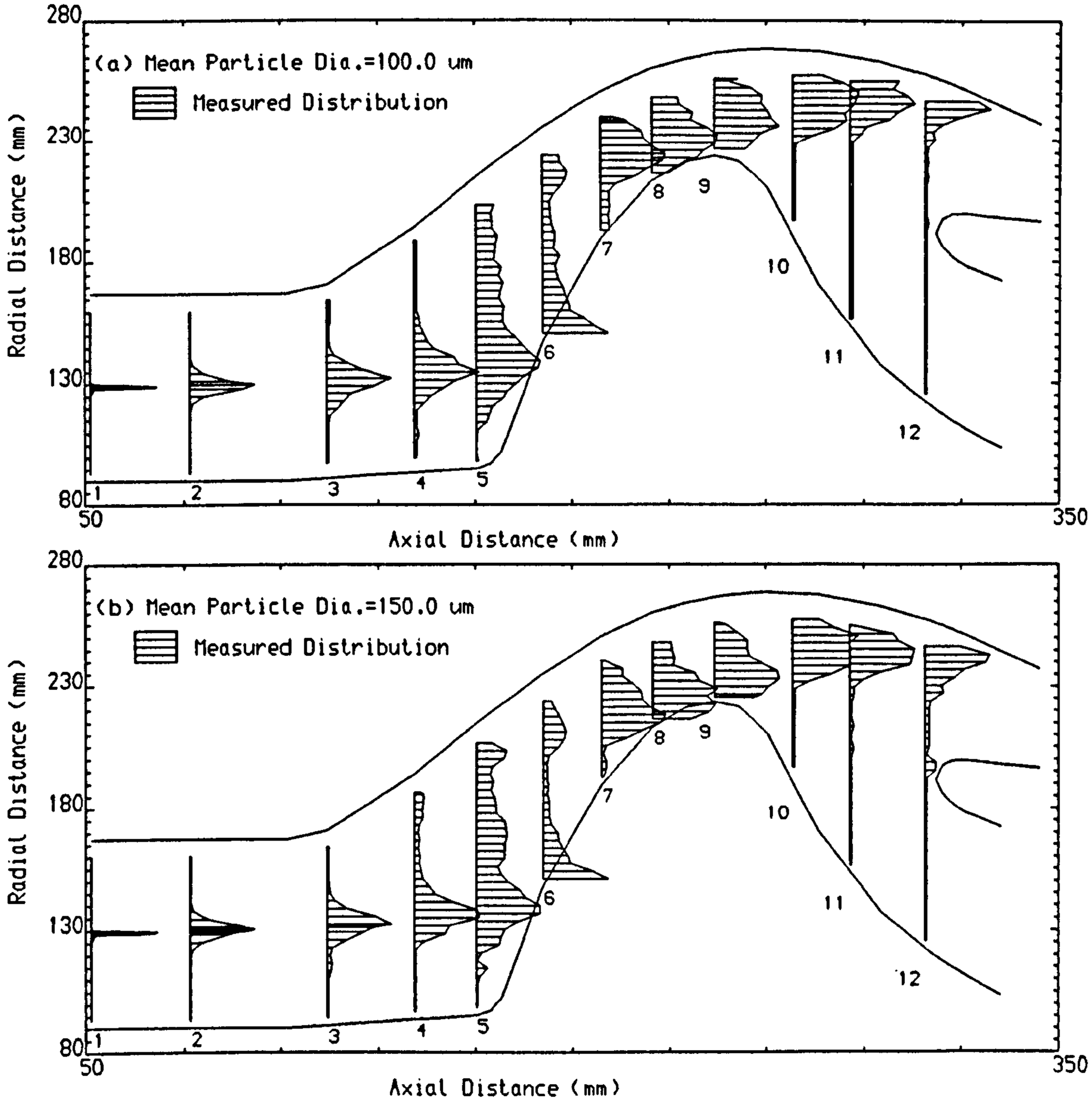

Wall matl. = AL.	Particle initial location = 128.67 mm
Particle matl. = Ballotini	Particle density = 2950.0 Kg/m3

FIG.45 MEASURED PARTICLE VELOCITIES AND ANGLES AT THE MEAN TRAJECTORY POSITIONS

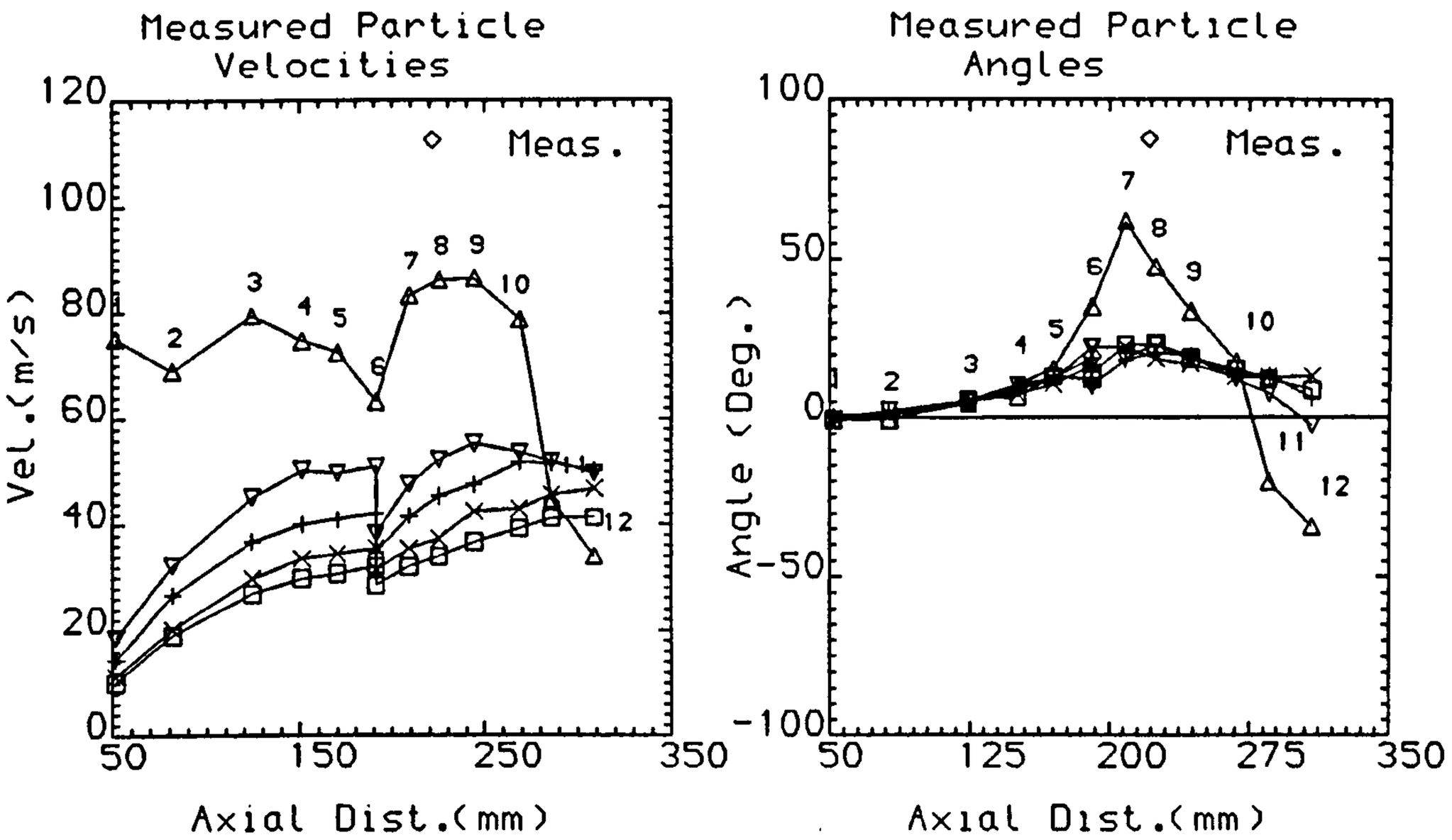

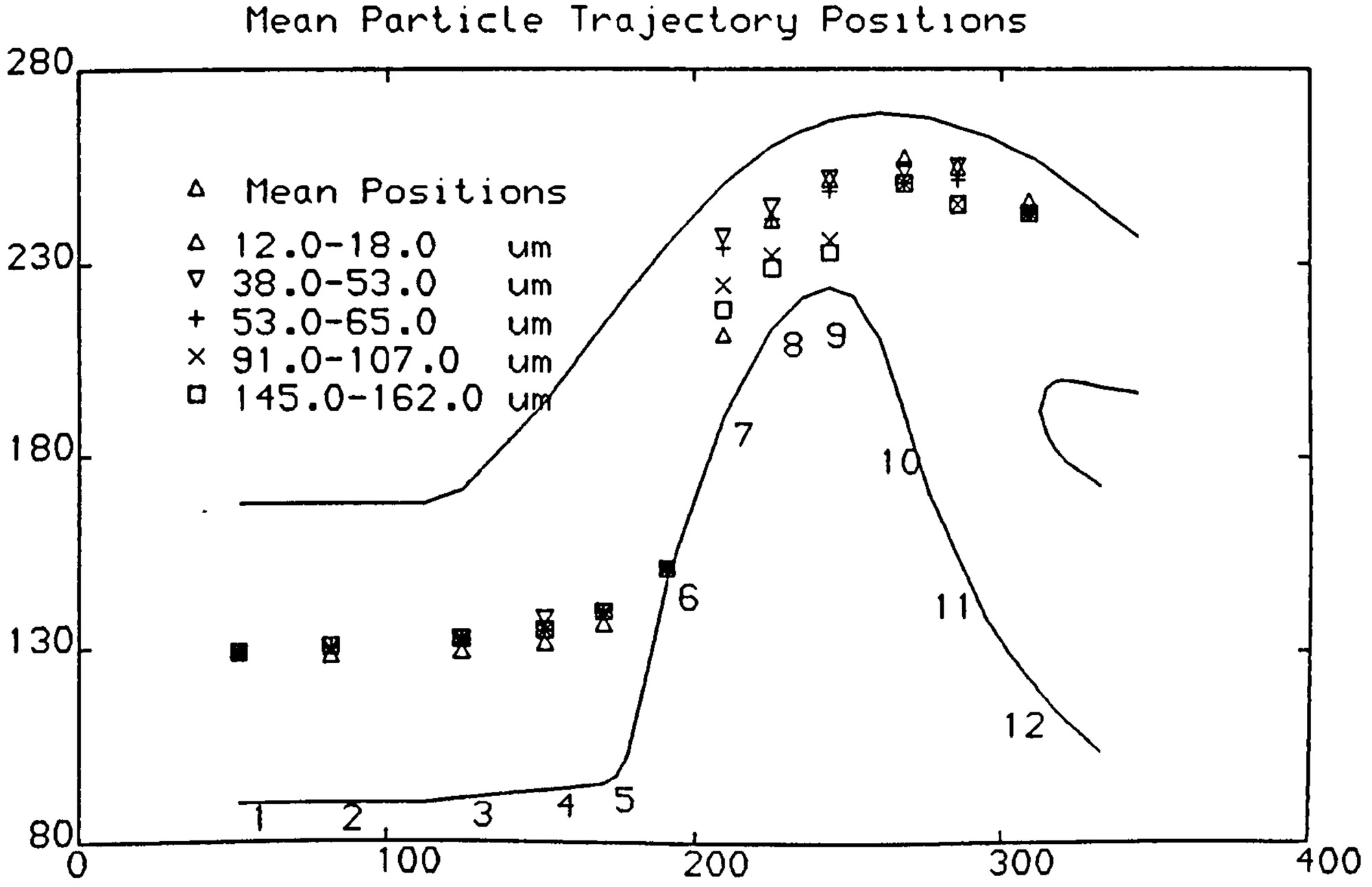

Wall Matl. = AL.
Ptle. Matl. = Ballotini
Ptle.Density= 2950.0 kg/m3

FIG.46 MEASURED PARTICLE CONCENTRATION DISTRIBUTION

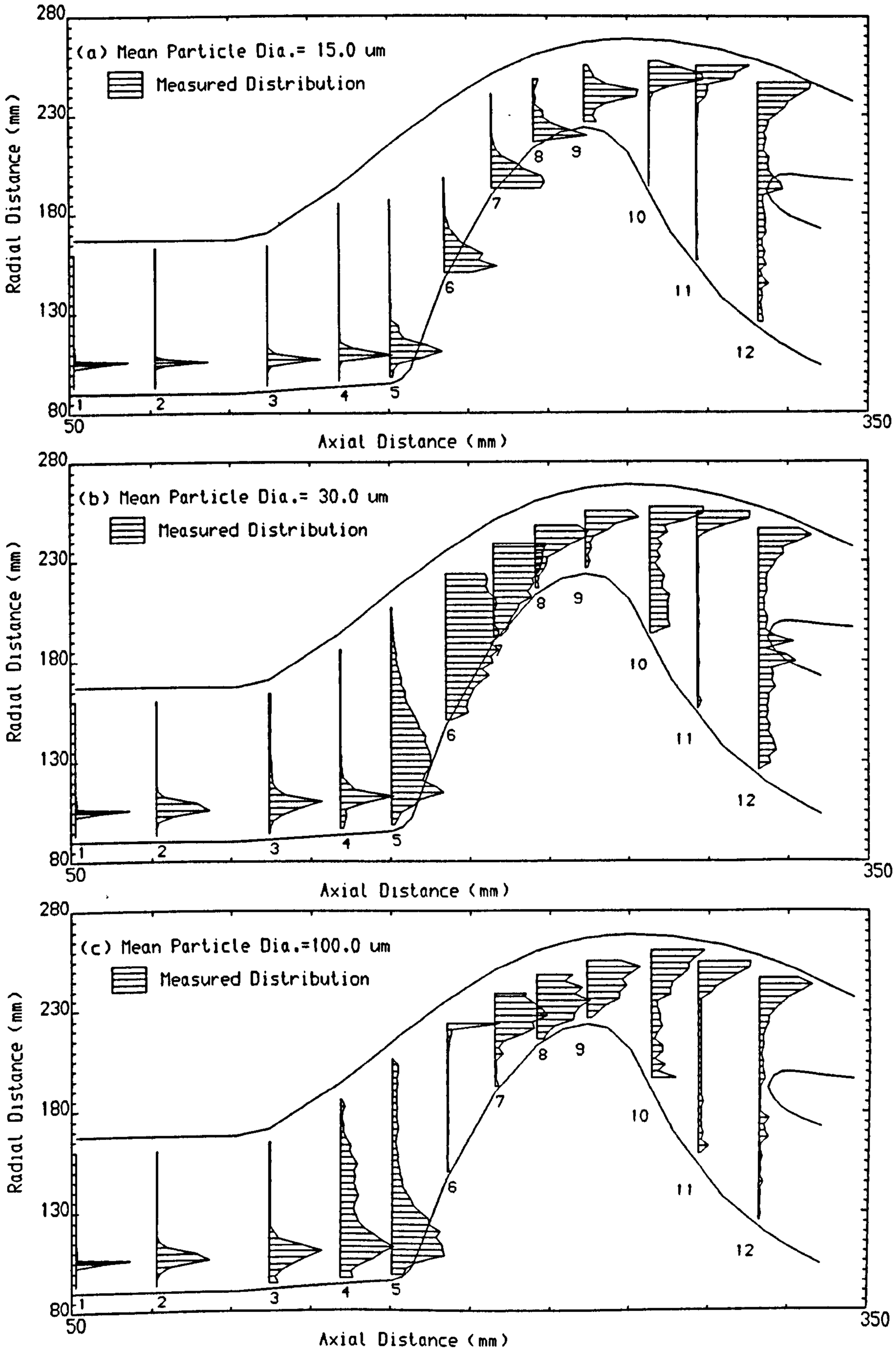

Wall matl. = AL.
Particle matl. = Ballotini
Particle initial location = 105.50 mm
Particle density = 2950.0 Kg/m3

FIG.47 MEASURED PARTICLE VELOCITIES AND ANGLES AT THE MEAN TRAJECTORY POSITIONS

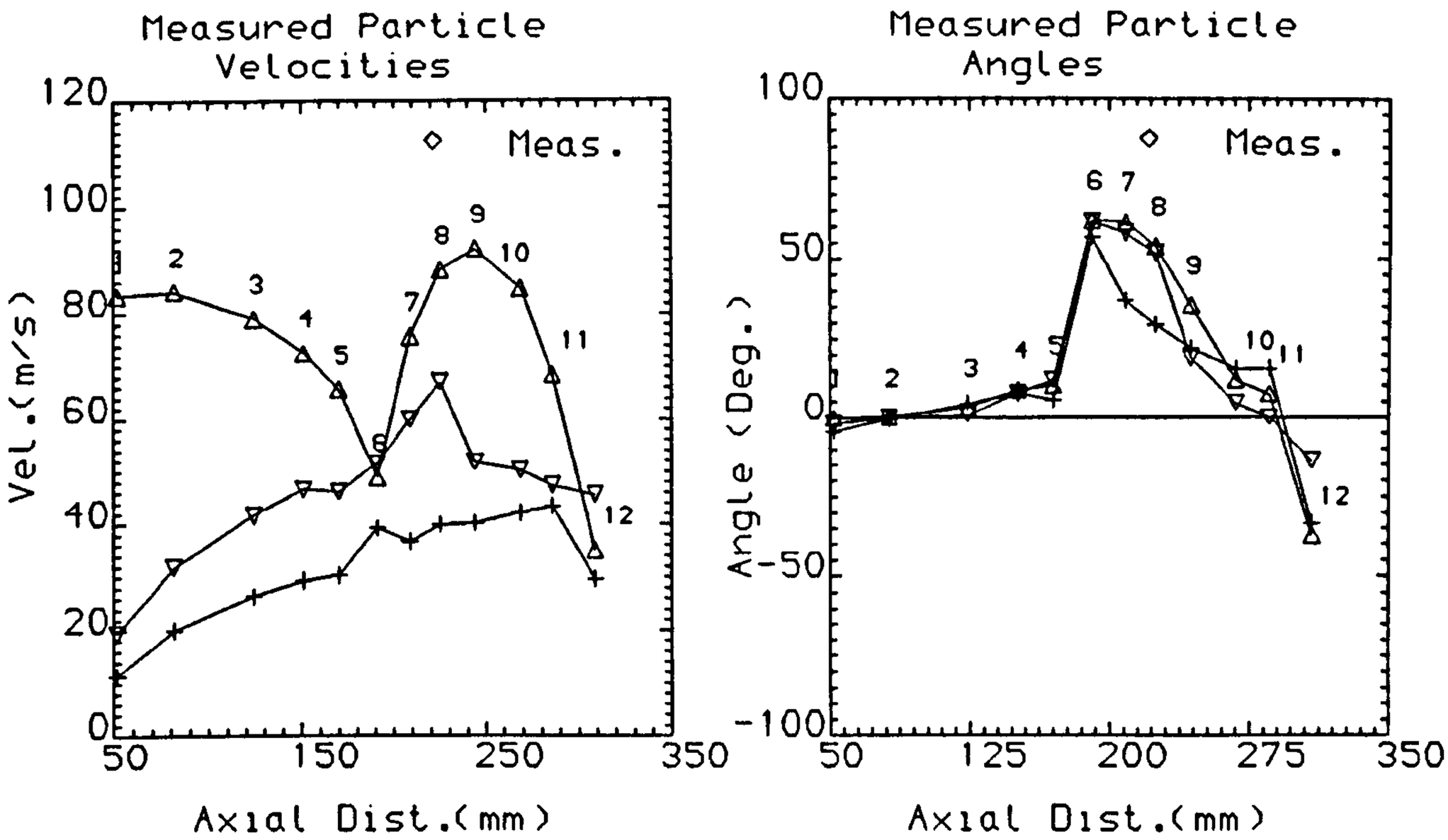

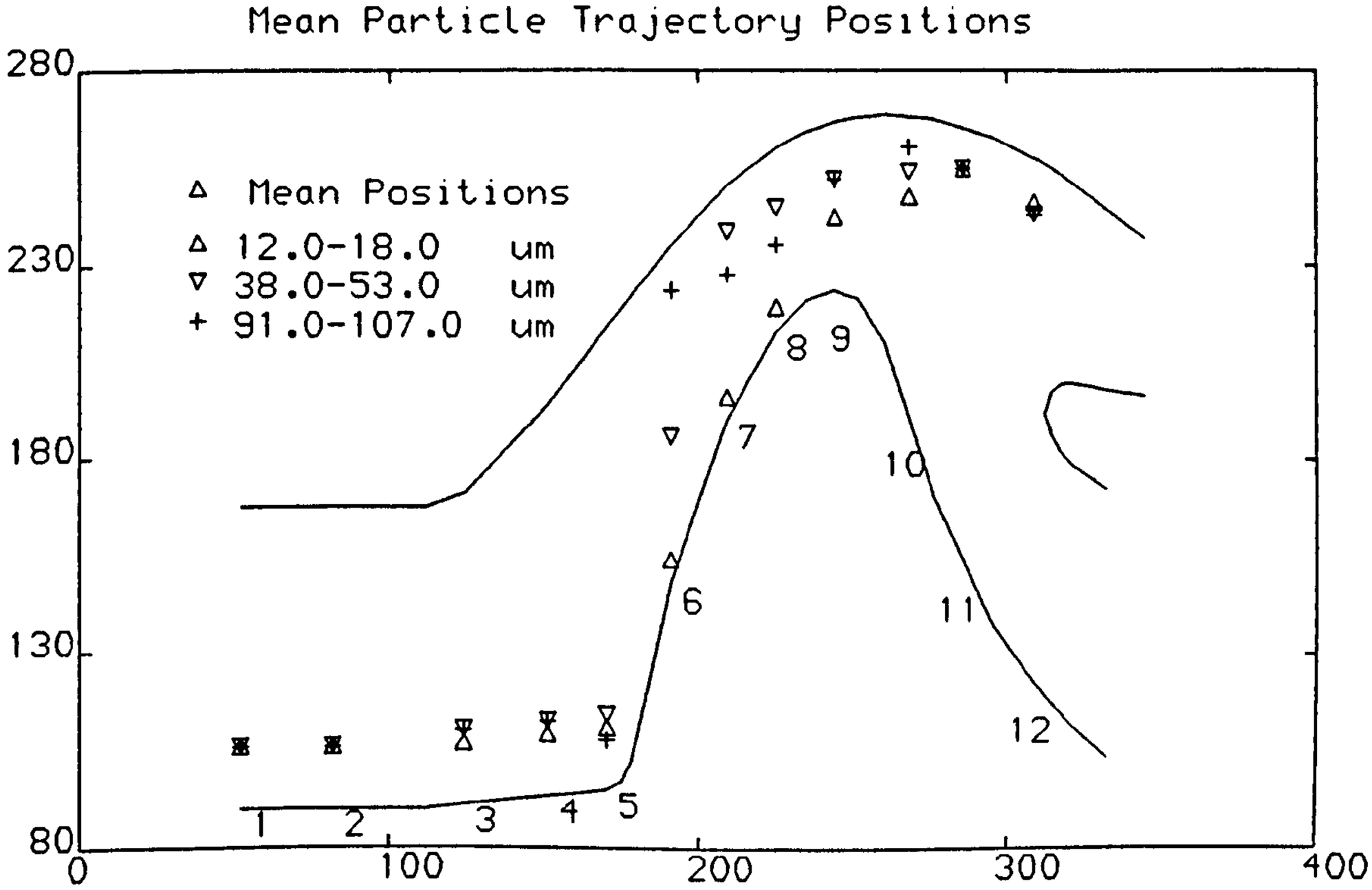

Wall Matl. = AL.
Ptle. Matl. = Ballotini
Ptle.Density= 2950.0 kg/m3

FIG.48 MEASURED PARTICLE CONCENTRATION DISTRIBUTION

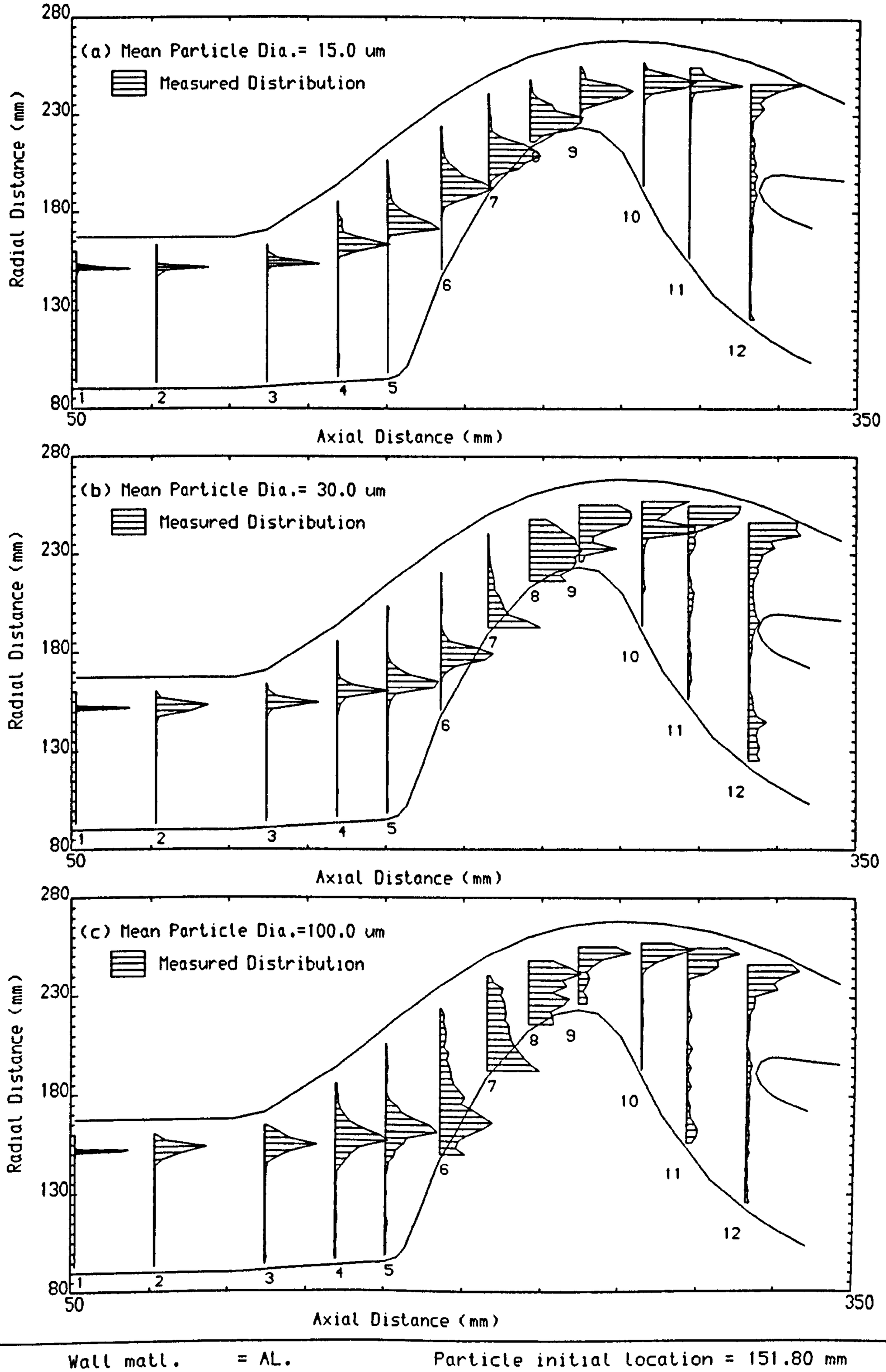

Wall matl. = AL.
Particle matl. = Quartz
Particle initial location = 151.80 mm
Particle density = 2650.0 Kg/m3

FIG.49 MEASURED PARTICLE VELOCITIES AND ANGLES AT THE MEAN TRAJECTORY POSITIONS

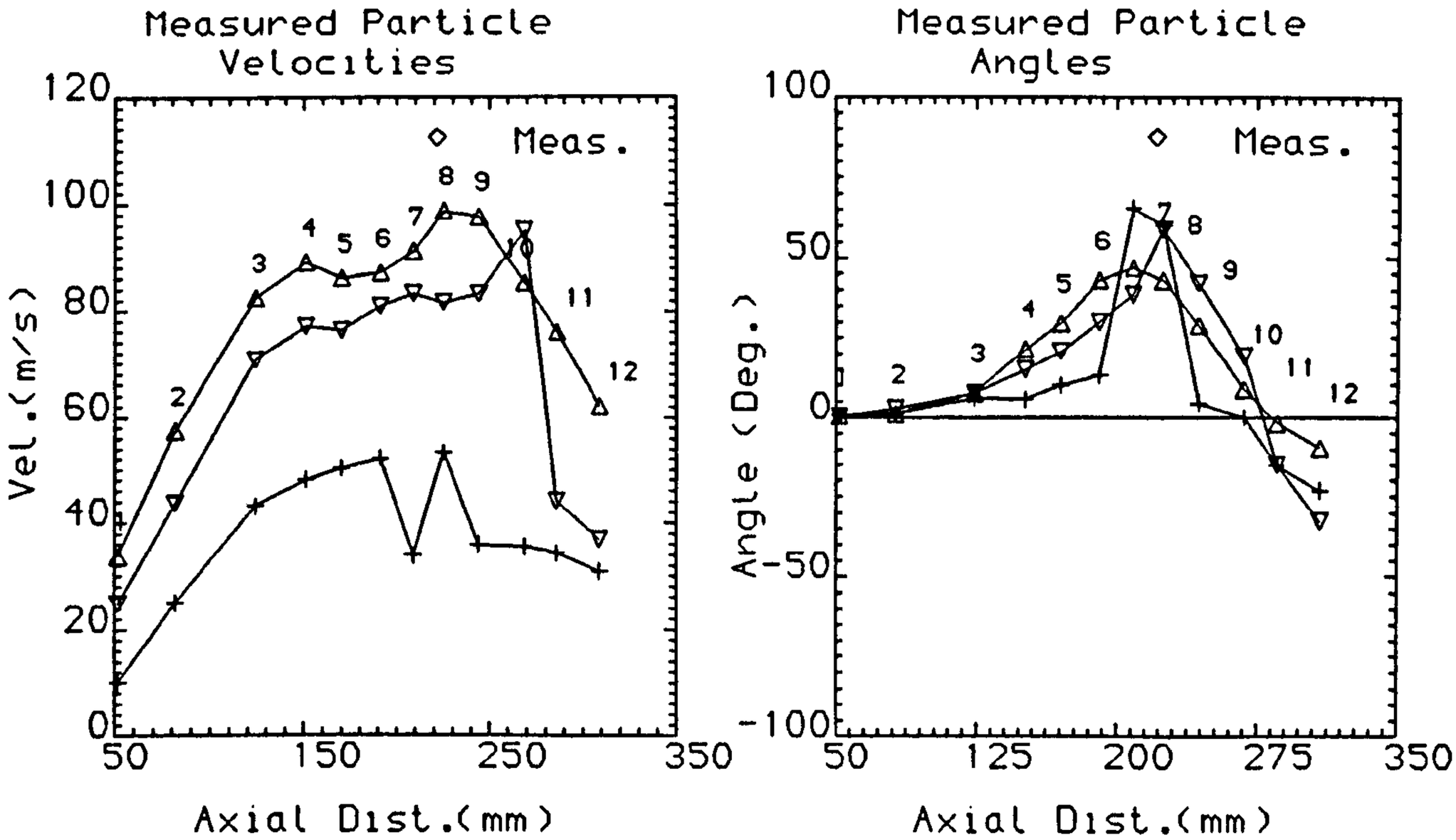

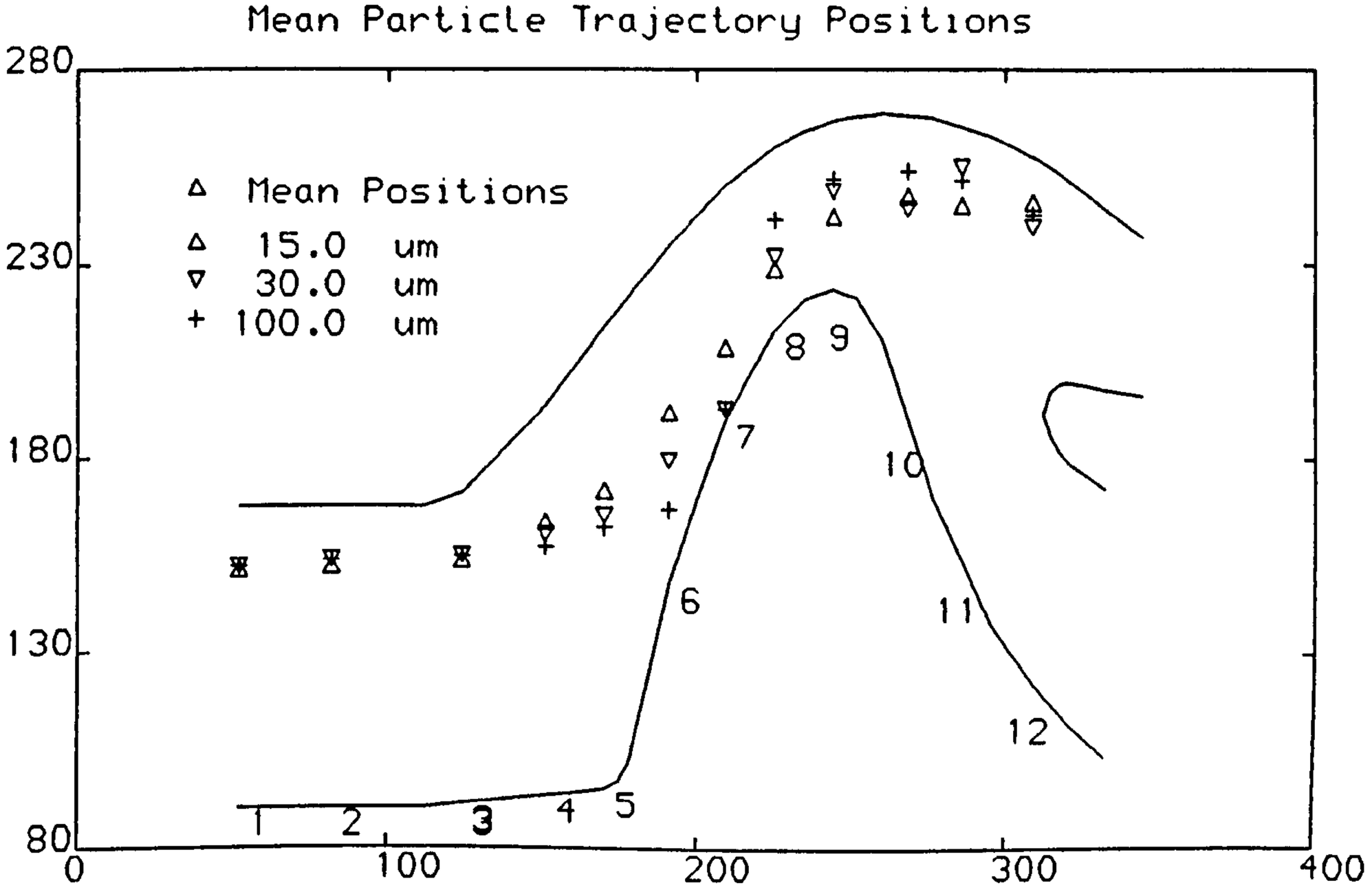

Wall Matl. = AL.
Ptle. Matl. = Quartz
Ptle.Density= 2650.0 kg/m3

FIG.50 MEASURED PARTICLE CONCENTRATION DISTRIBUTION

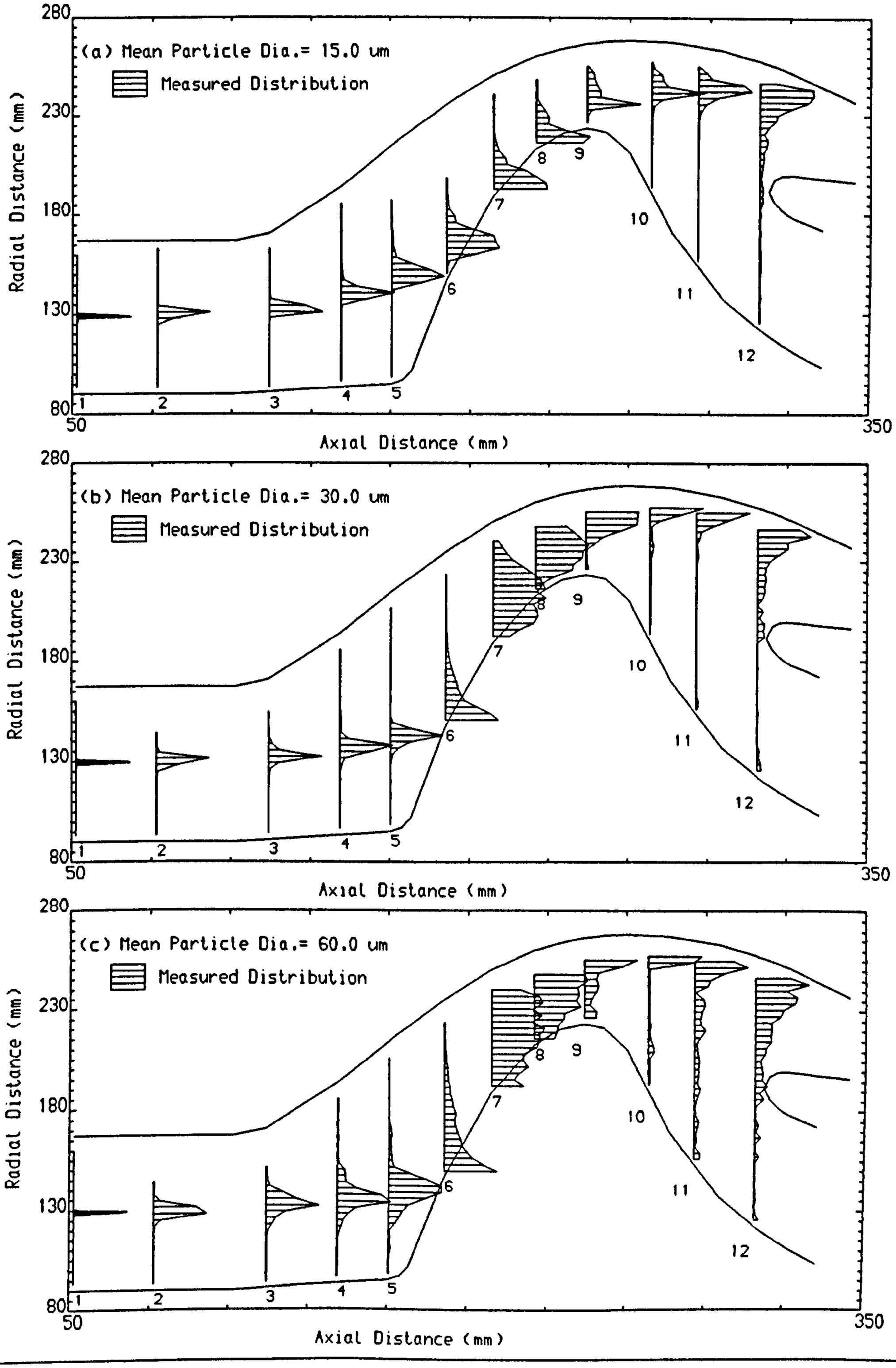

Wall matl. = AL.
Particle matl. = Quartz
Particle initial location = 128.67 mm
Particle density = 2650.0 Kg/m3

FIG.51 MEASURED PARTICLE CONCENTRATION DISTRIBUTION

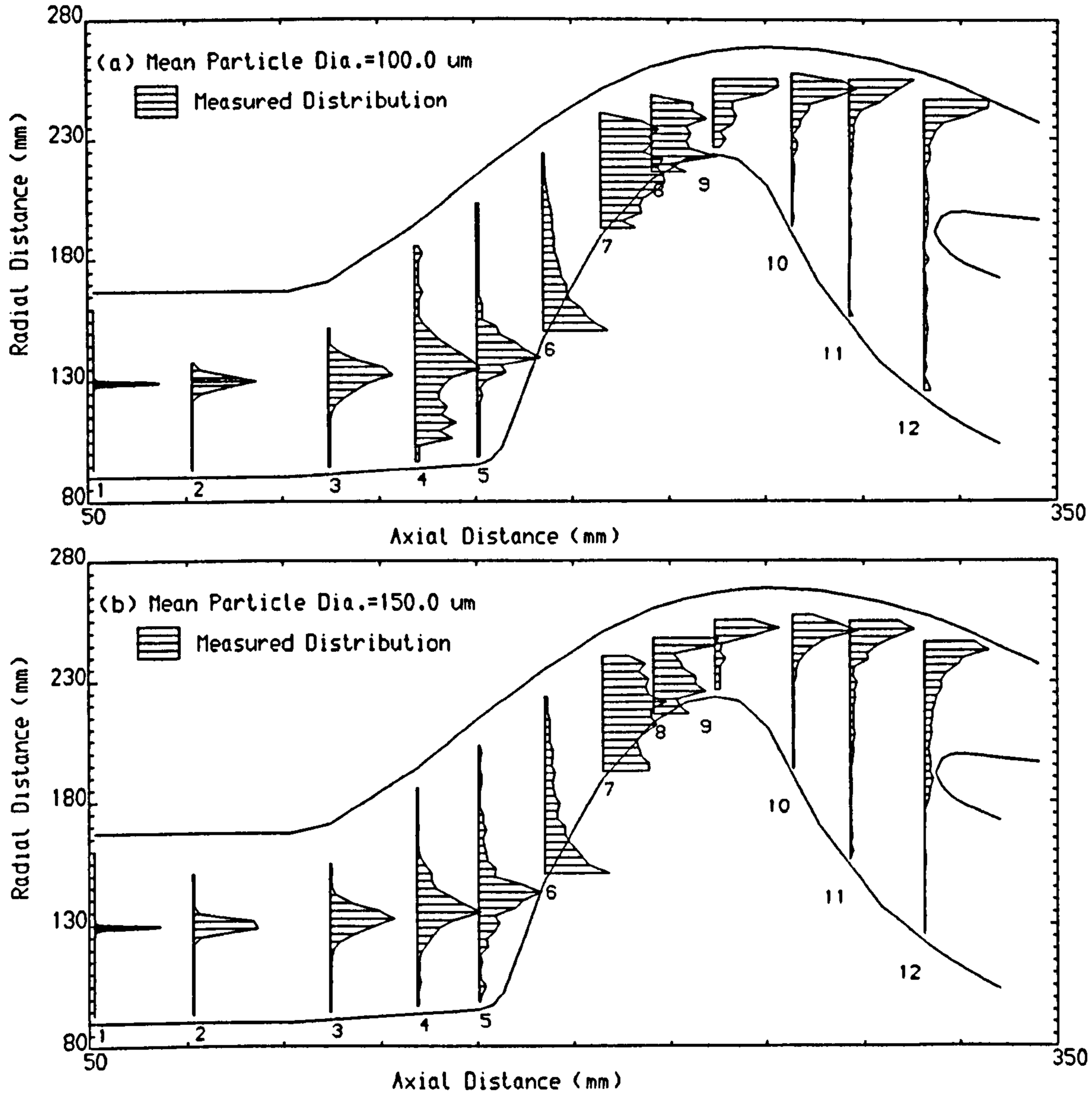

Wall matl. = AL.	Particle initial location = 128.67 mm
Particle matl. = Quartz	Particle density = 2650.0 Kg/m3

FIG.52 MEASURED PARTICLE VELOCITIES AND ANGLES AT THE MEAN TRAJECTORY POSITIONS

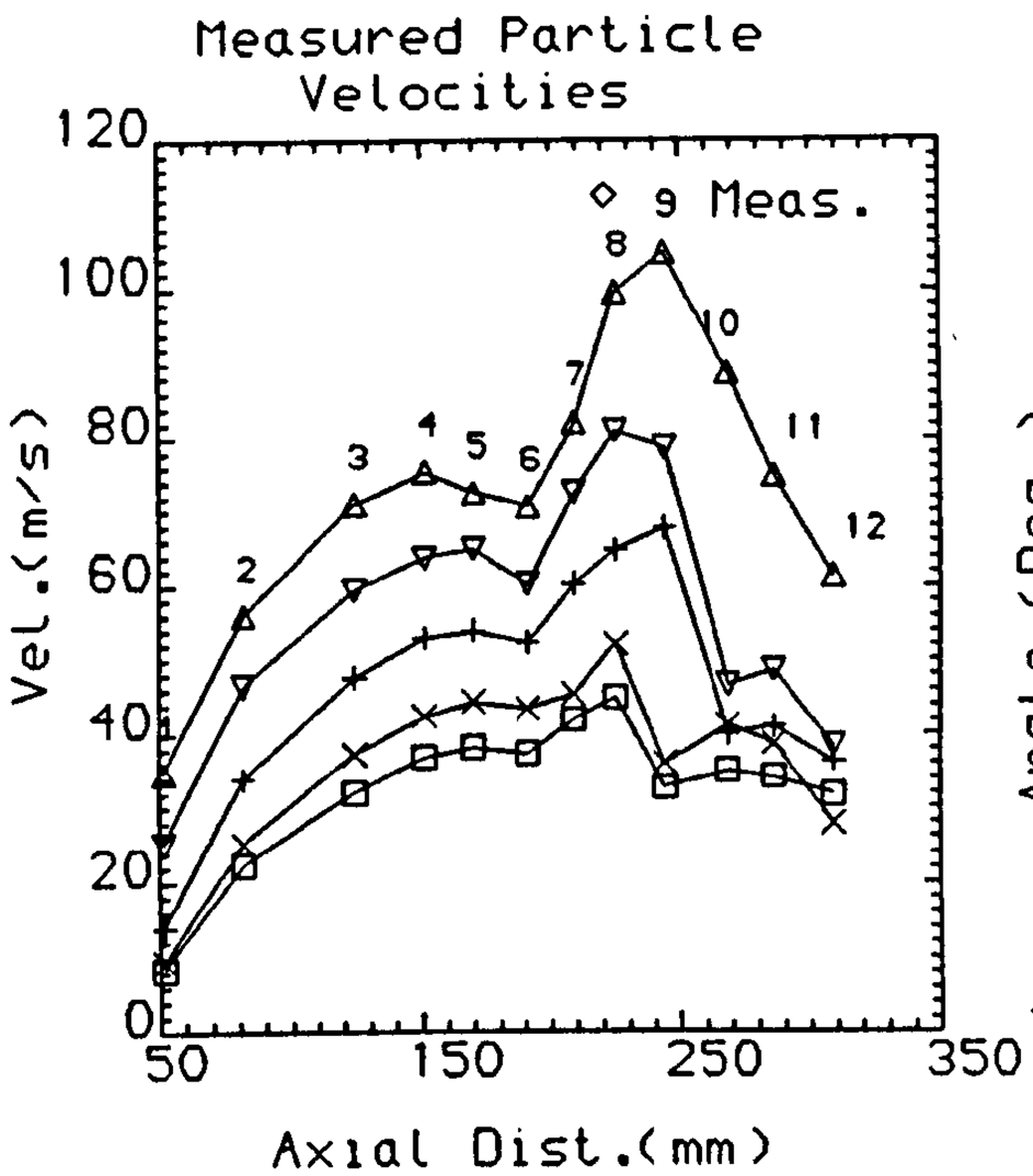

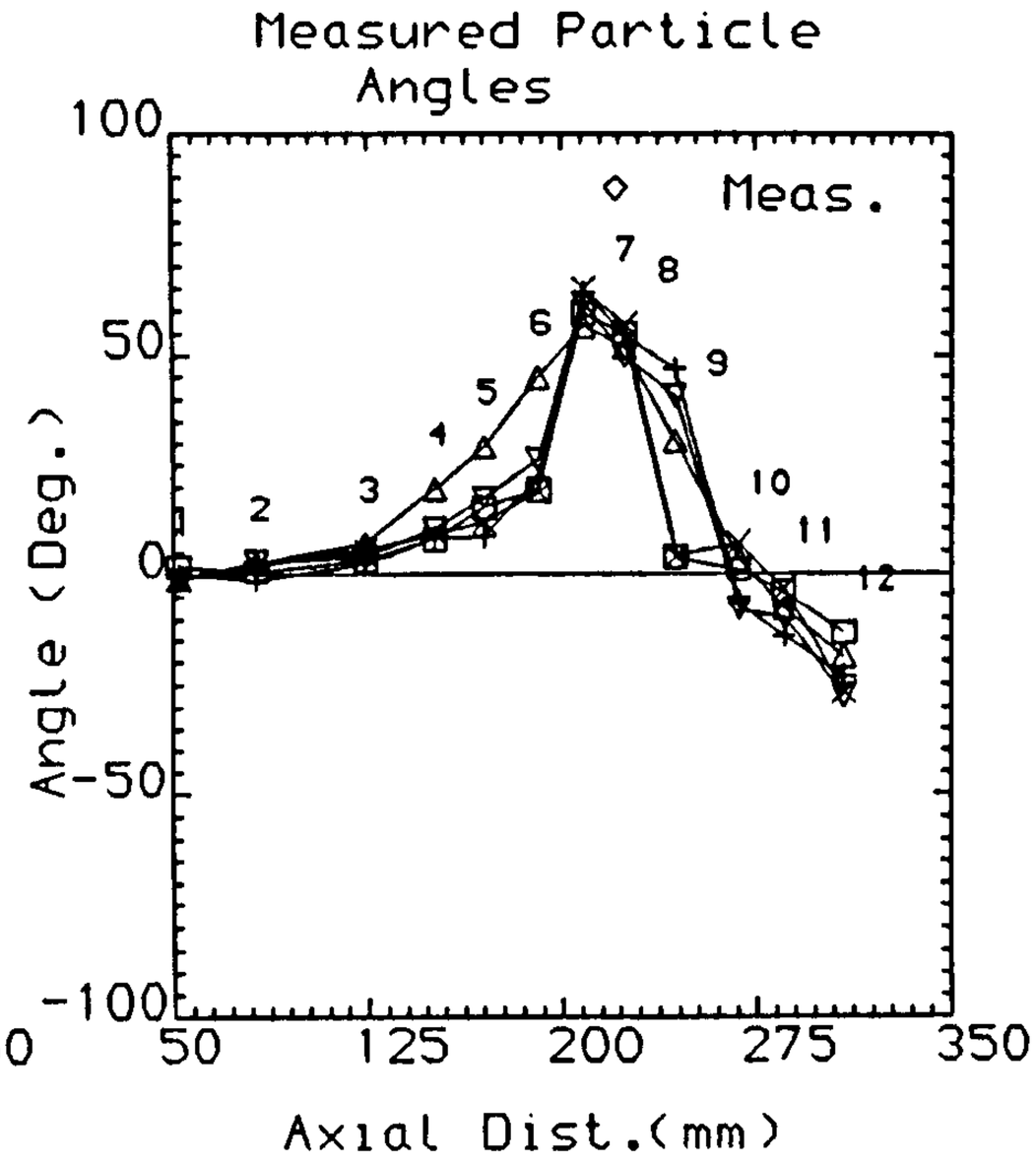

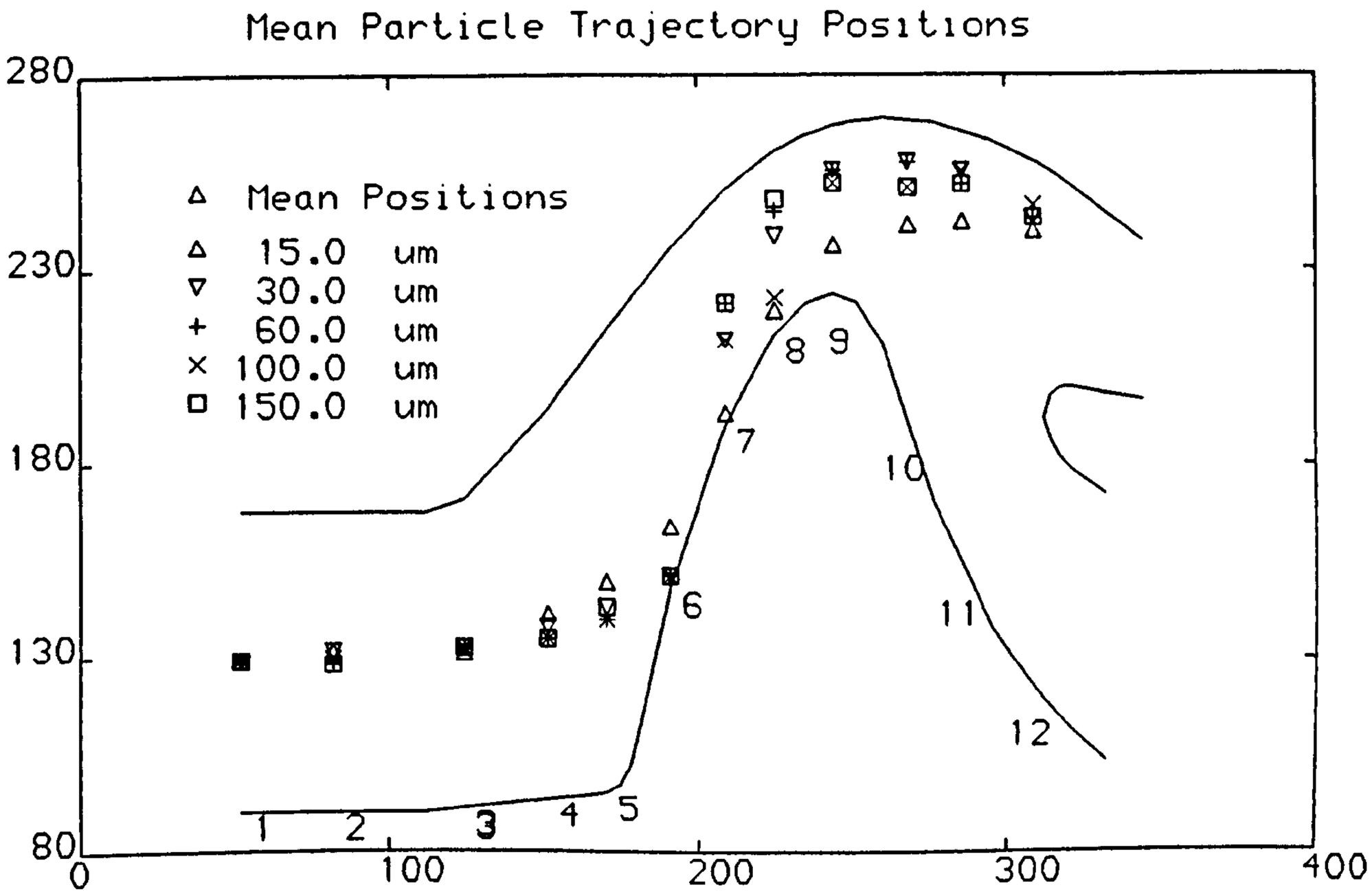

Wall Matl. = AL.
Ptle. Matl. = Quartz
Ptle.Density= 2650.0 kg/m3

FIG.53 MEASURED PARTICLE CONCENTRATION DISTRIBUTION

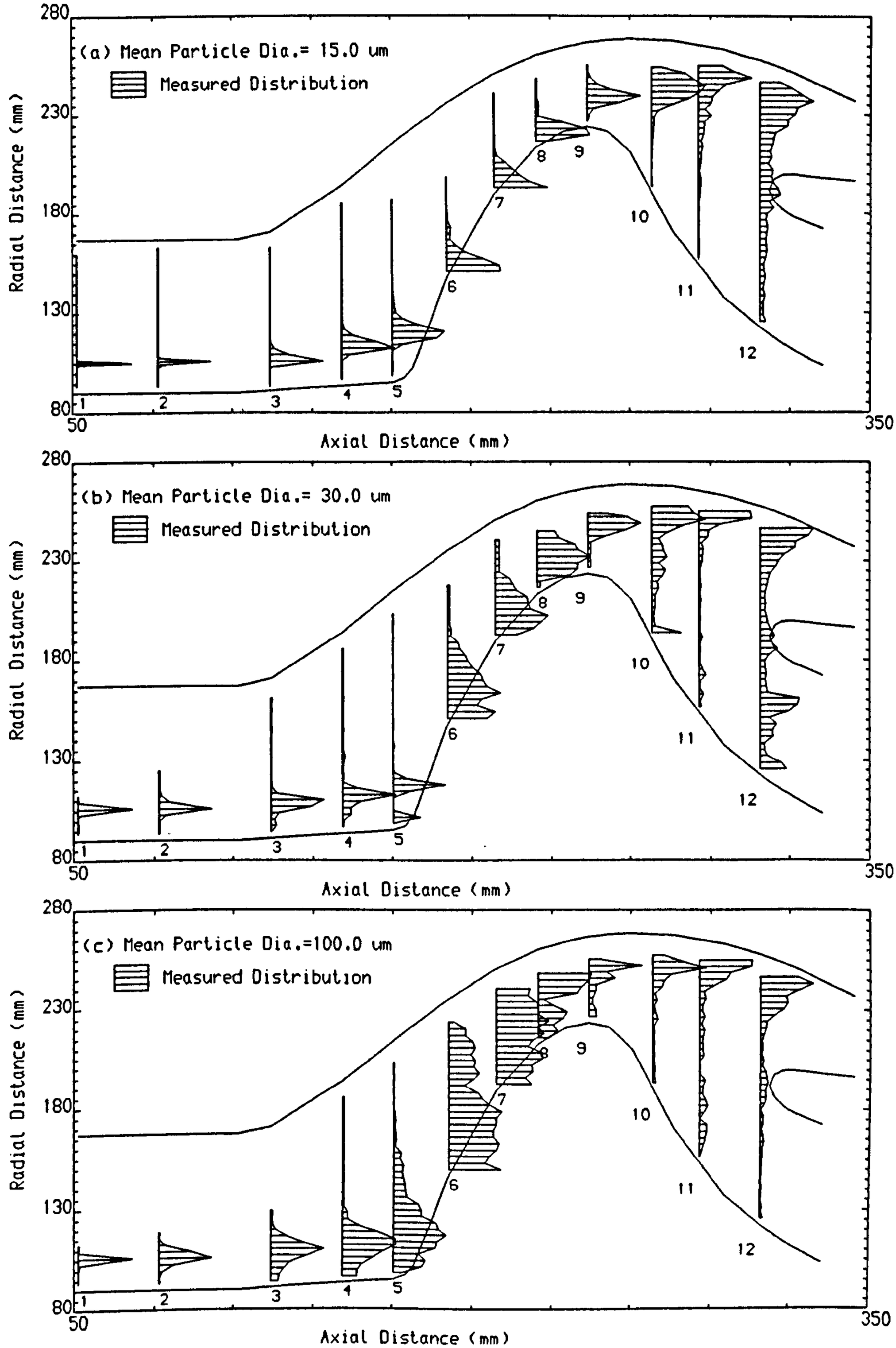

Wall matl. = AL.
Particle matl. = Quartz
Particle initial location = 105.50 mm
Particle density = 2650.0 Kg/m3

FIG.54 MEASURED PARTICLE VELOCITIES AND ANGLES
AT THE MEAN TRAJECTORY POSITIONS

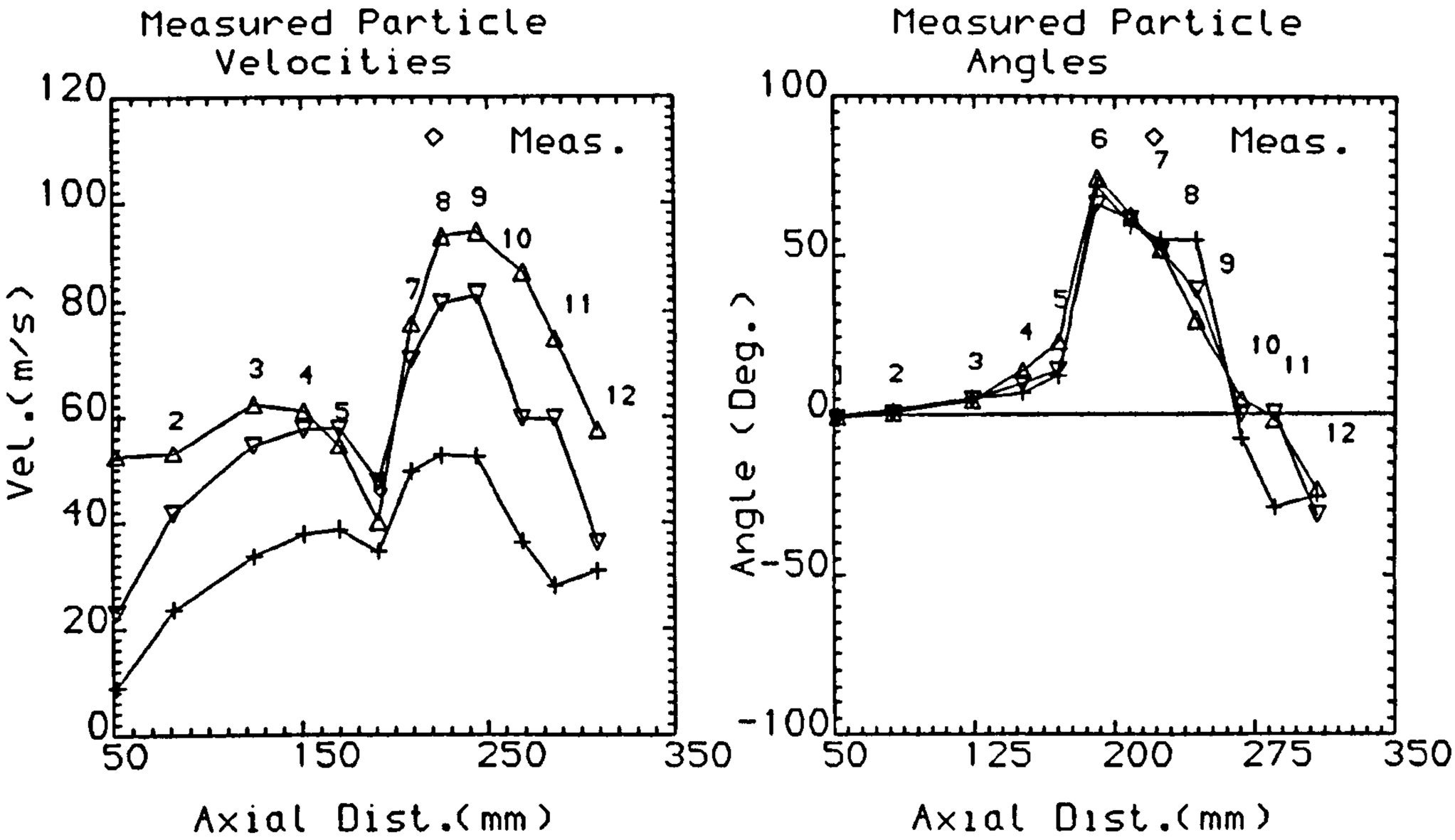

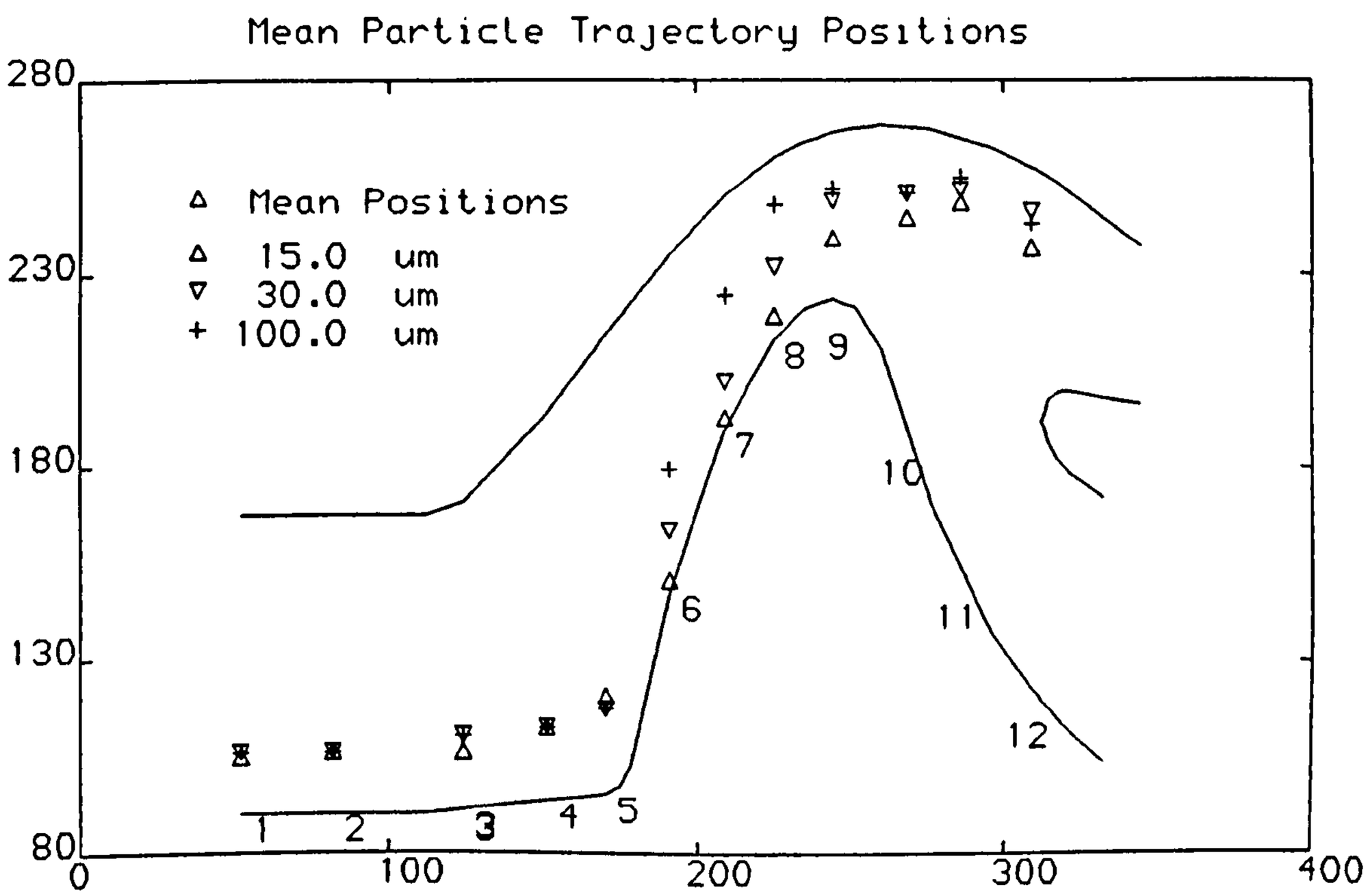

Wall Matl. = AL.
Ptle. Matl. = Quartz
Ptle.Density= 2650.0 kg/m3

FIG.55 PREDICTED AND MEASURED PARTICLE CONCENTRATION DISTRIBUTION

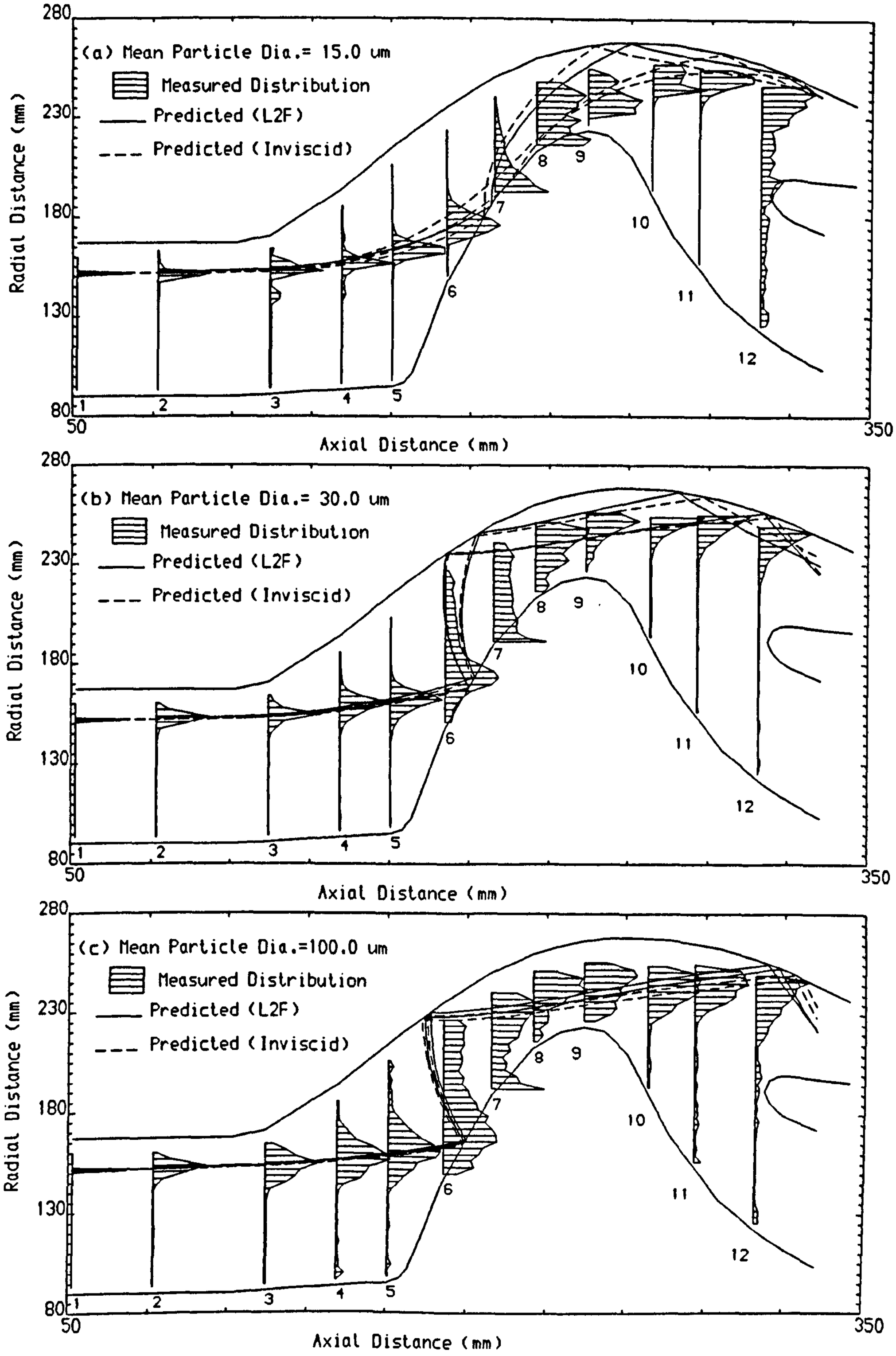

Wall matl. = AL.
Particle matl. = Ballotini
Particle initial location = 151.80 mm
Particle density = 2950.0 Kg/m3

FIG.56 MEASURED AND PREDICTED PARTICLE VELOCITIES AND ANGLES AT THE MEAN TRAJECTORY POSITIONS

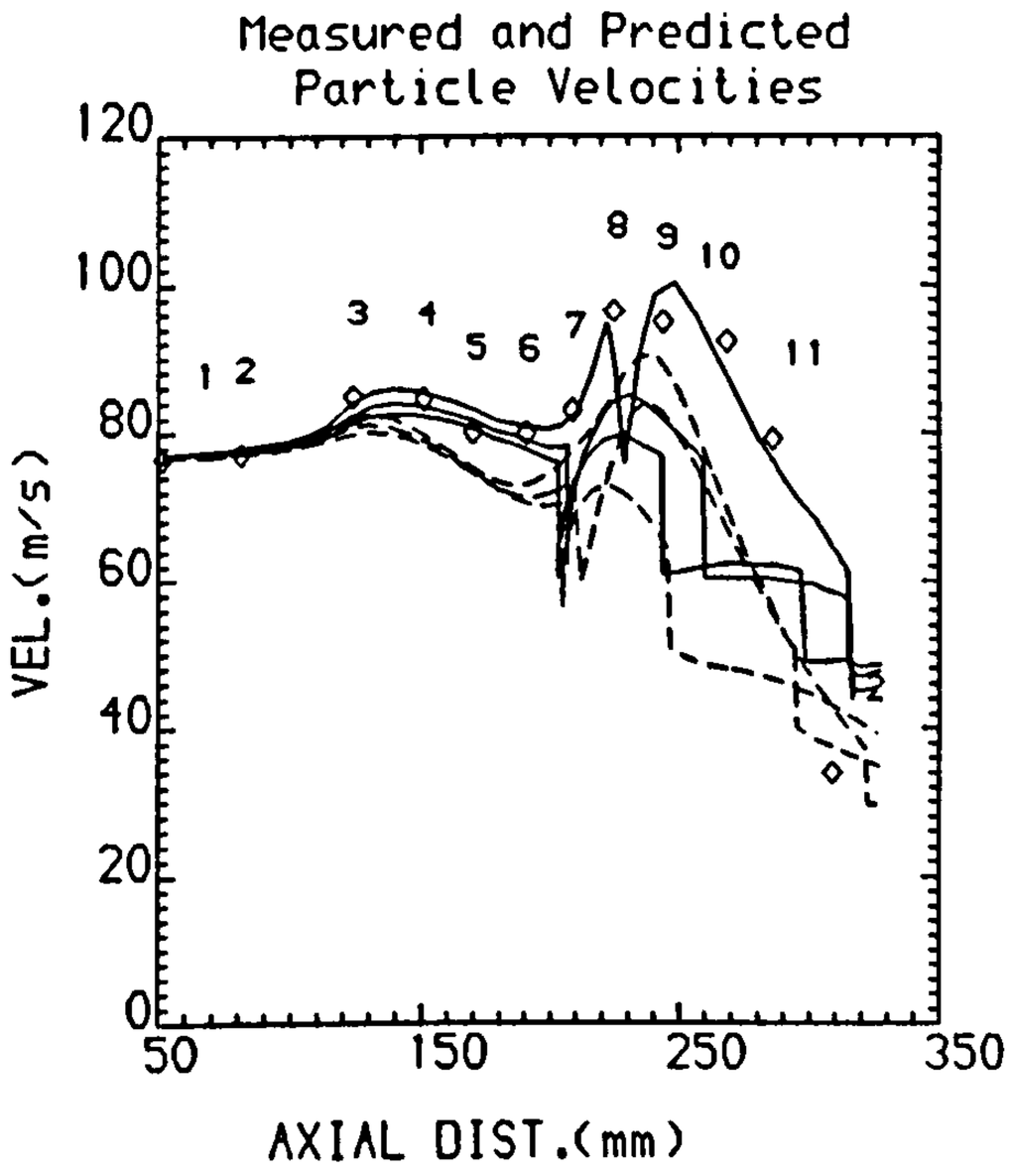

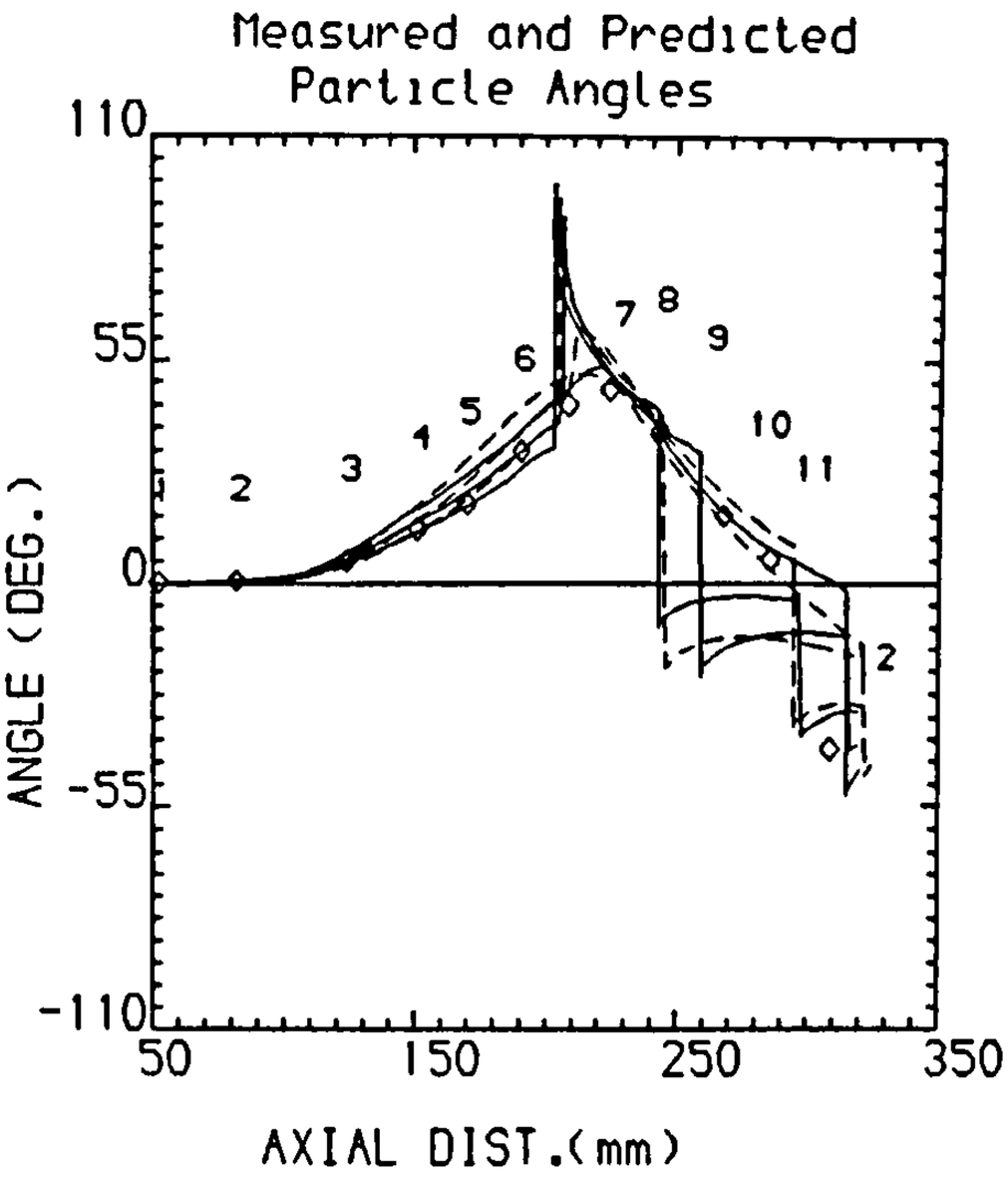

MEASURED AND PREDICTED PARTICLE TRAJECTORIES

WALL MATL. = AL.
PTLE. MATL. = BALLOTINI
PTLE. DEN. = 2950.0 kg/m3
PTLE. DIAMETER = 12.0-18.0 um
PTLE. INITIAL VEL.= 76.4 m/s

FIG.57 MEASURED AND PREDICTED PARTICLE VELOCITIES AND ANGLES AT THE MEAN TRAJECTORY POSITIONS

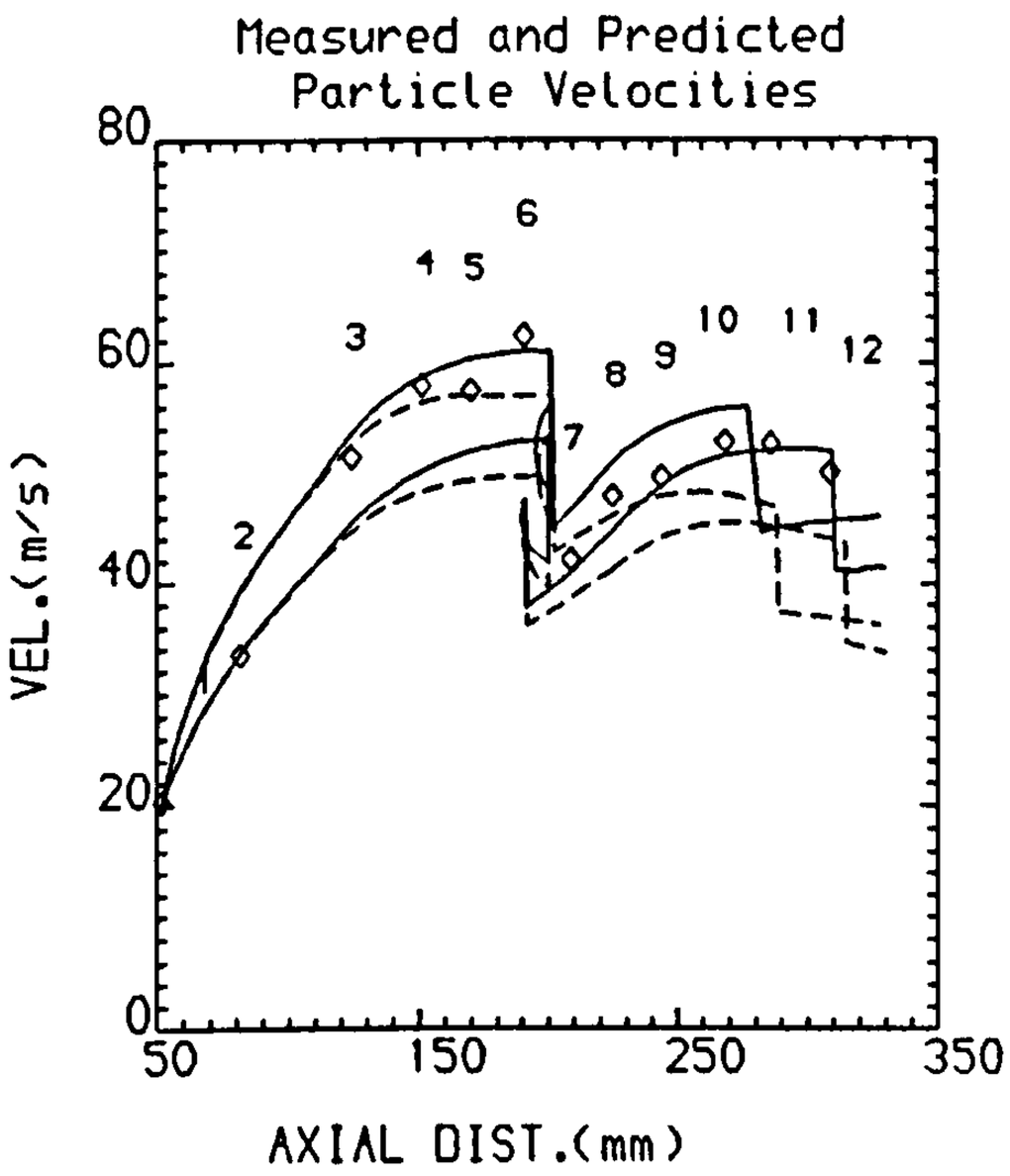

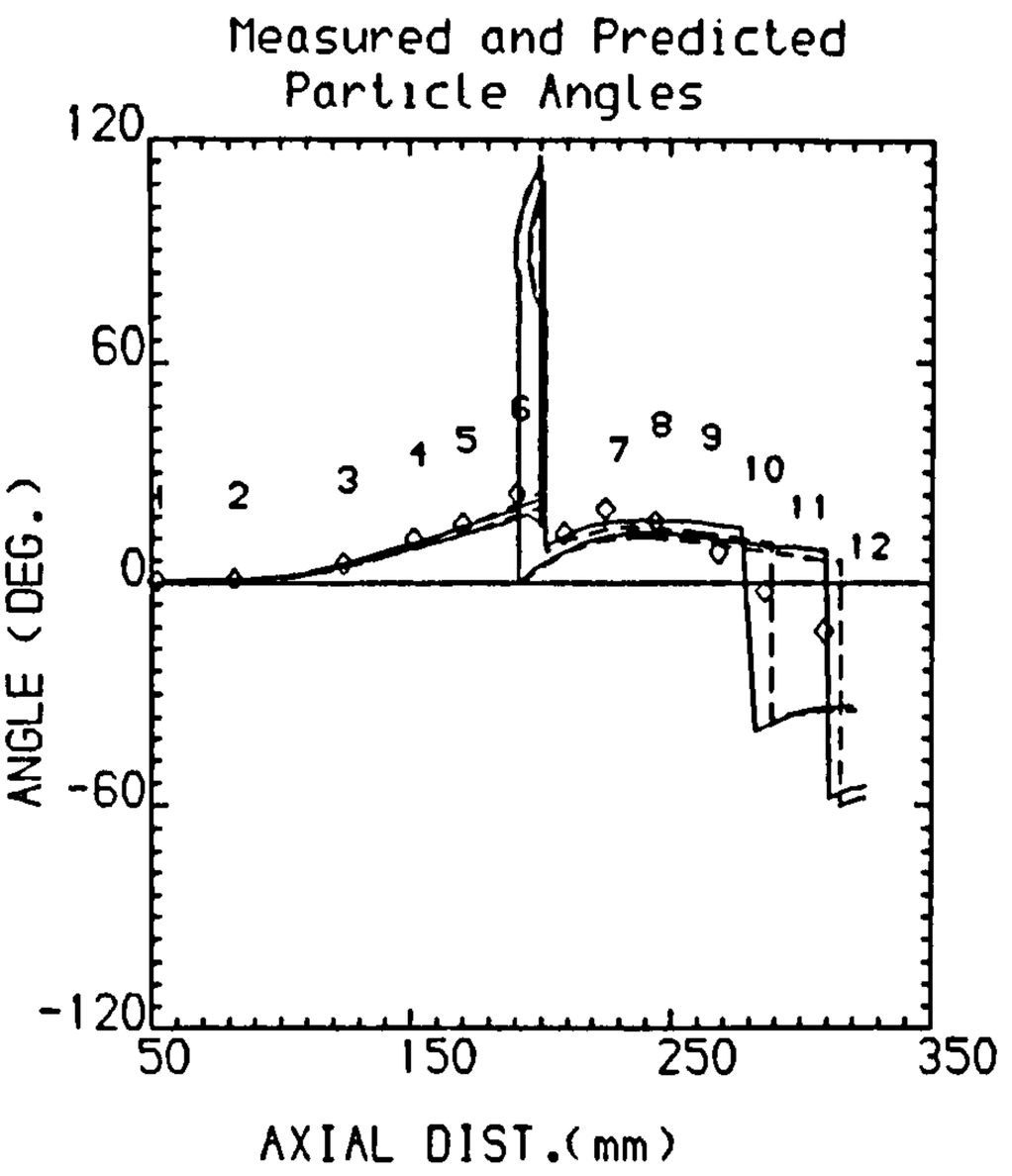

MEASURED AND PREDICTED PARTICLE TRAJECTORIES

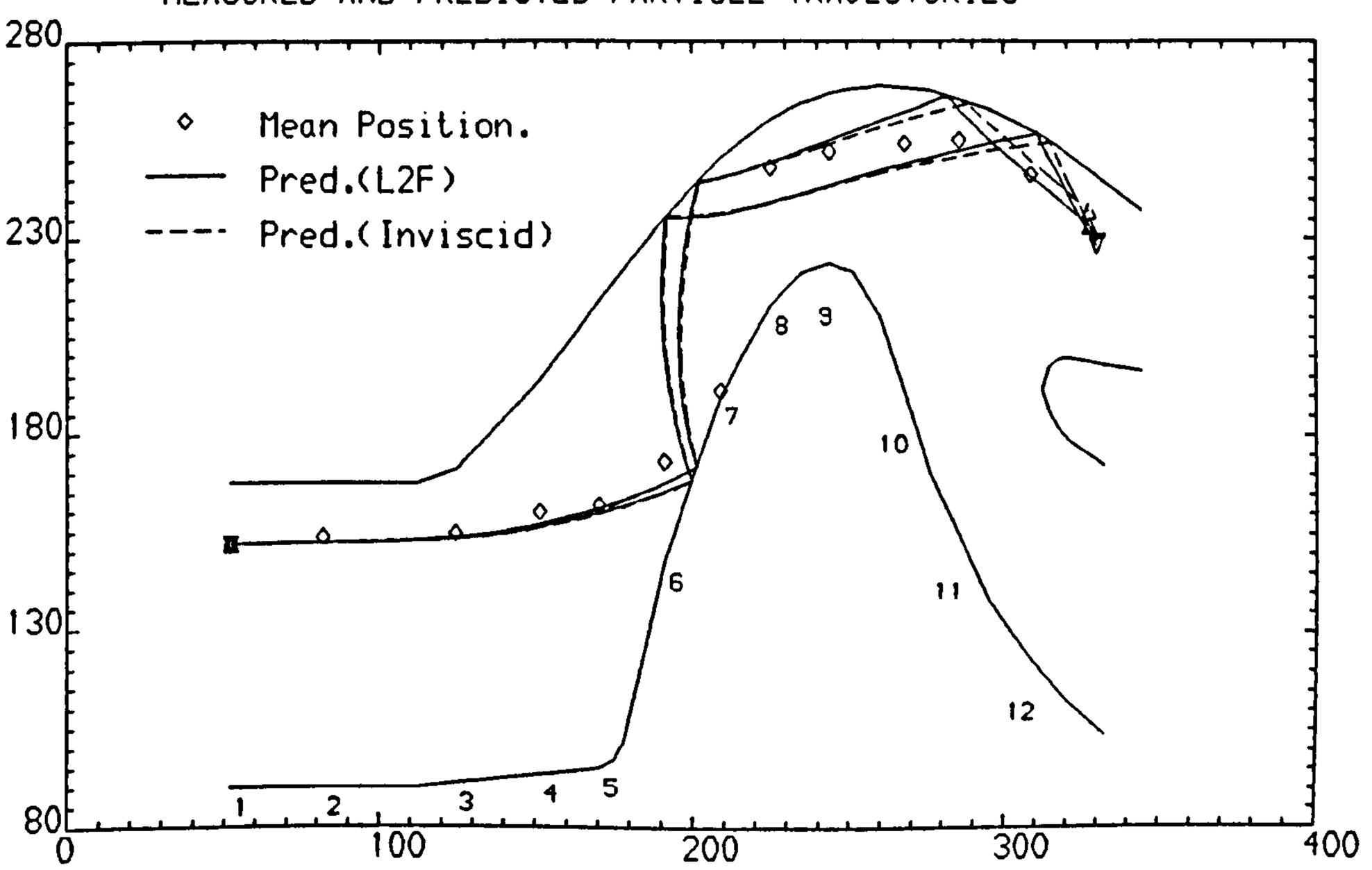

WALL MATL. = AL.	PTLE. DIAMETER = 38.0-53.0 um
PTLE. MATL. = BALLOTINI	PTLE. INITIAL VEL.= 20.4 m/s
PTLE. DEN. = 2950.0 kg/m3	

FIG.58 MEASURED AND PREDICTED PARTICLE VELOCITIES AND ANGLES AT THE MEAN TRAJECTORY POSITIONS

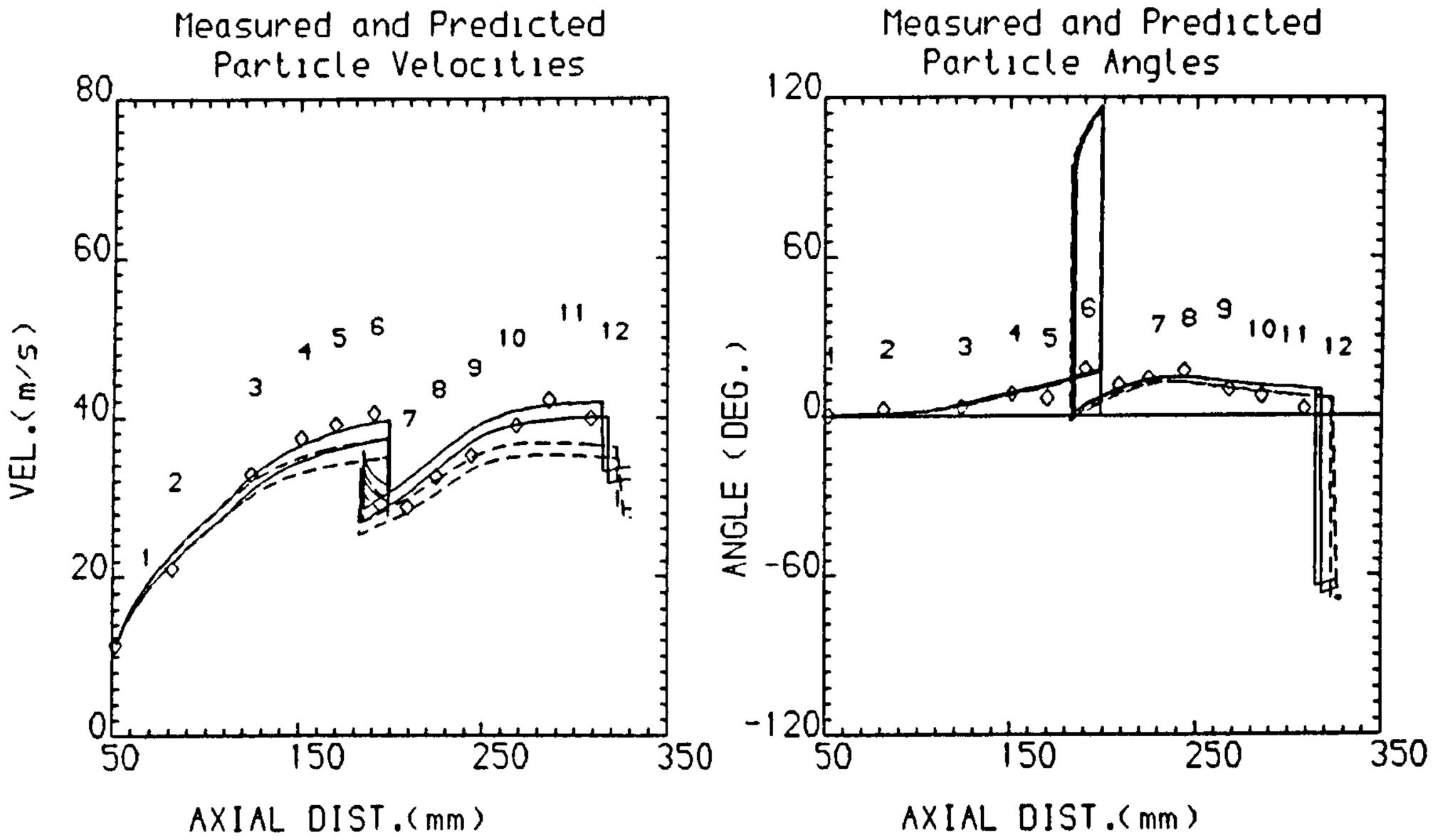

MEASURED AND PREDICTED PARTICLE TRAJECTORIES

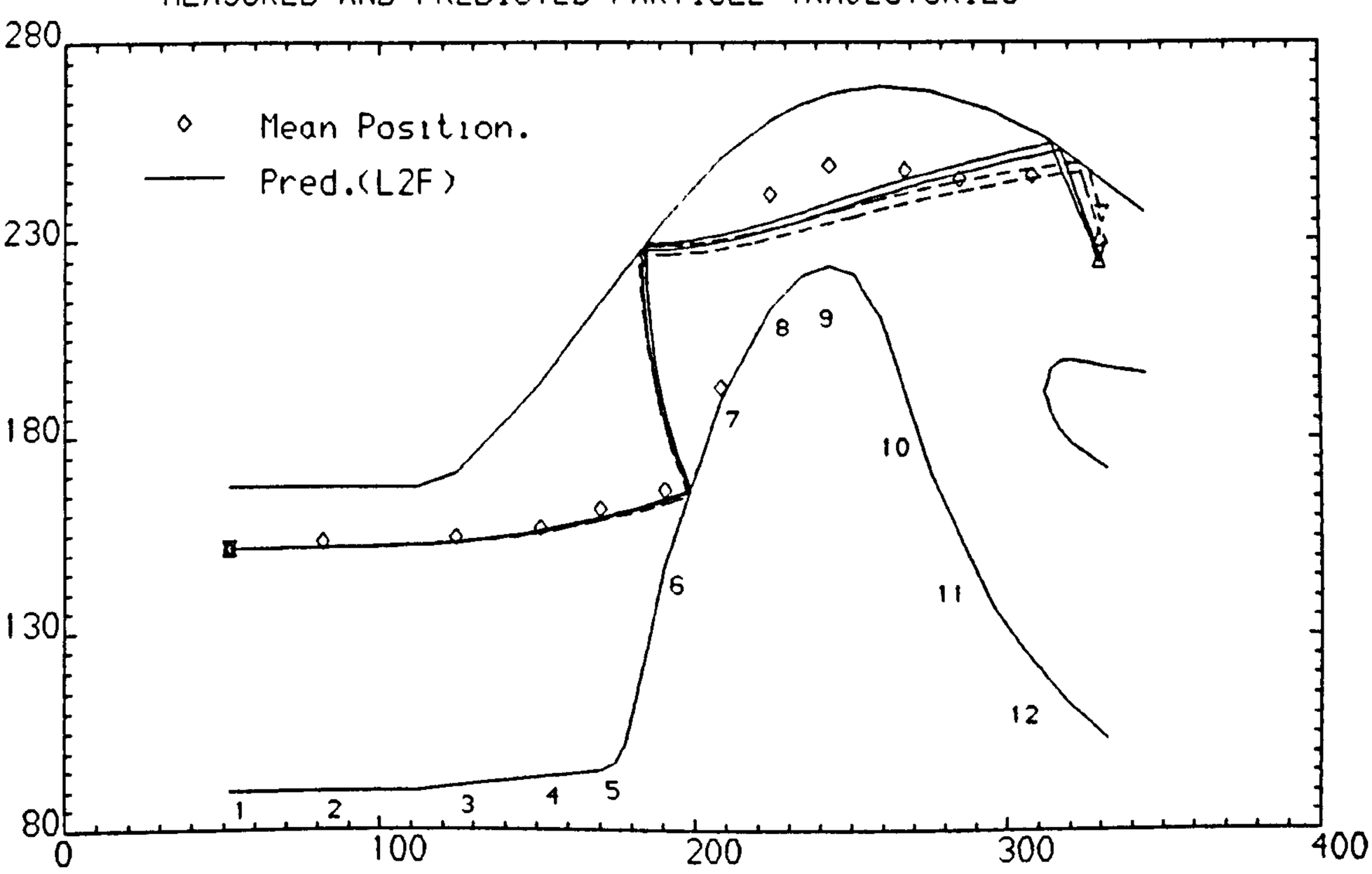

WALL MATL. = AL.
PTLE. MATL. = BALLOTINI
PTLE. DEN. = 2950.0 kg/m3
PTLE. DIAMETER = 91.0-107.0 um
PTLE. INITIAL VEL.= 11.5 m/s

FIG.59 PREDICTED AND MEASURED PARTICLE CONCENTRATION DISTRIBUTION

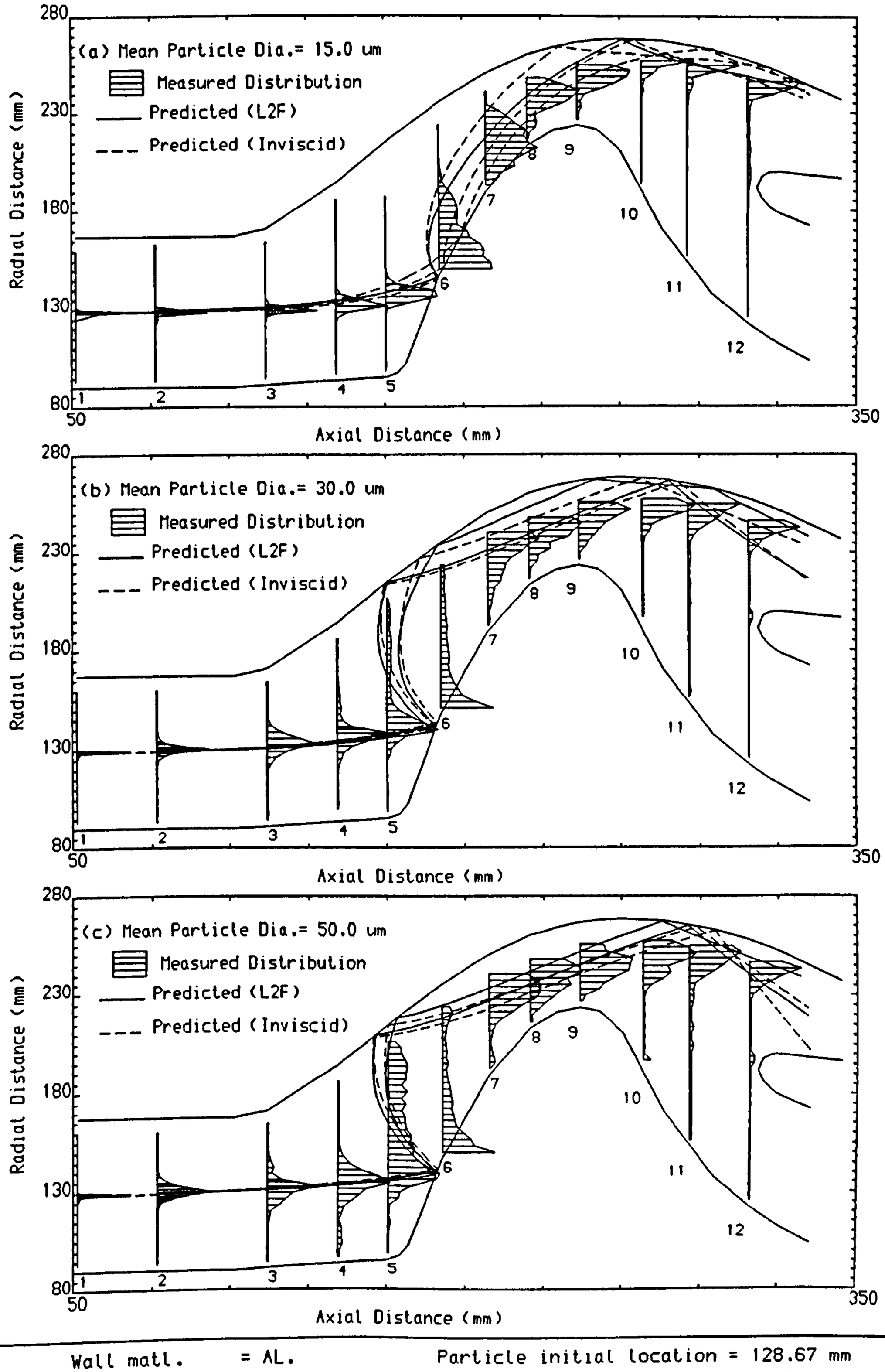

Wall matl. = AL.
Particle matl. = Ballotini
Particle initial location = 128.67 mm
Particle density = 2950.0 Kg/m3

FIG.60 PREDICTED AND MEASURED PARTICLE CONCENTRATION DISTRIBUTION

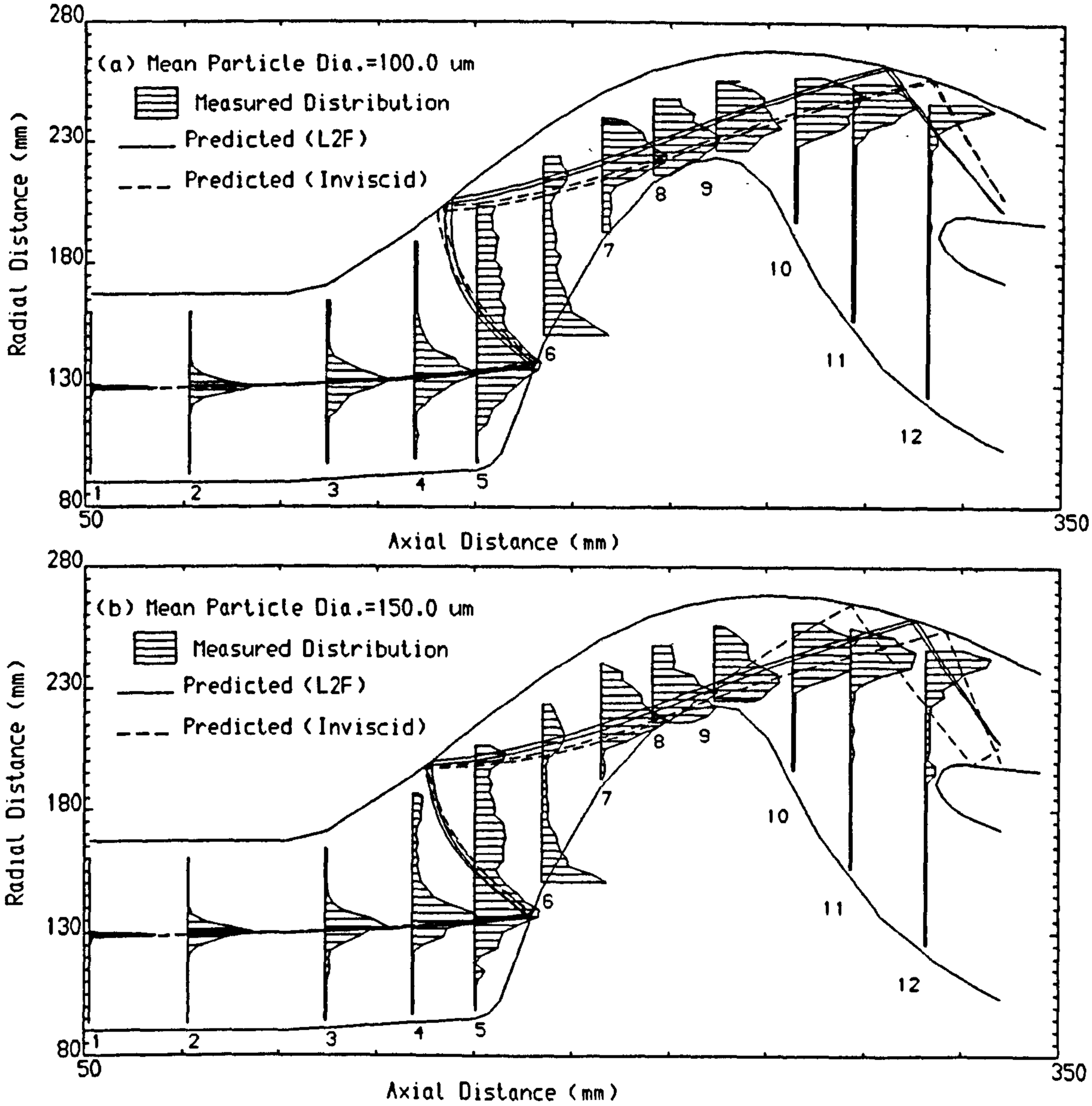

Wall matl. = AL.	Particle initial location = 128.67 mm
Particle matl. = Ballotini	Particle density = 2950.0 Kg/m3

FIG.61 MEASURED AND PREDICTED PARTICLE VELOCITIES AND ANGLES AT THE MEAN TRAJECTORY POSITIONS

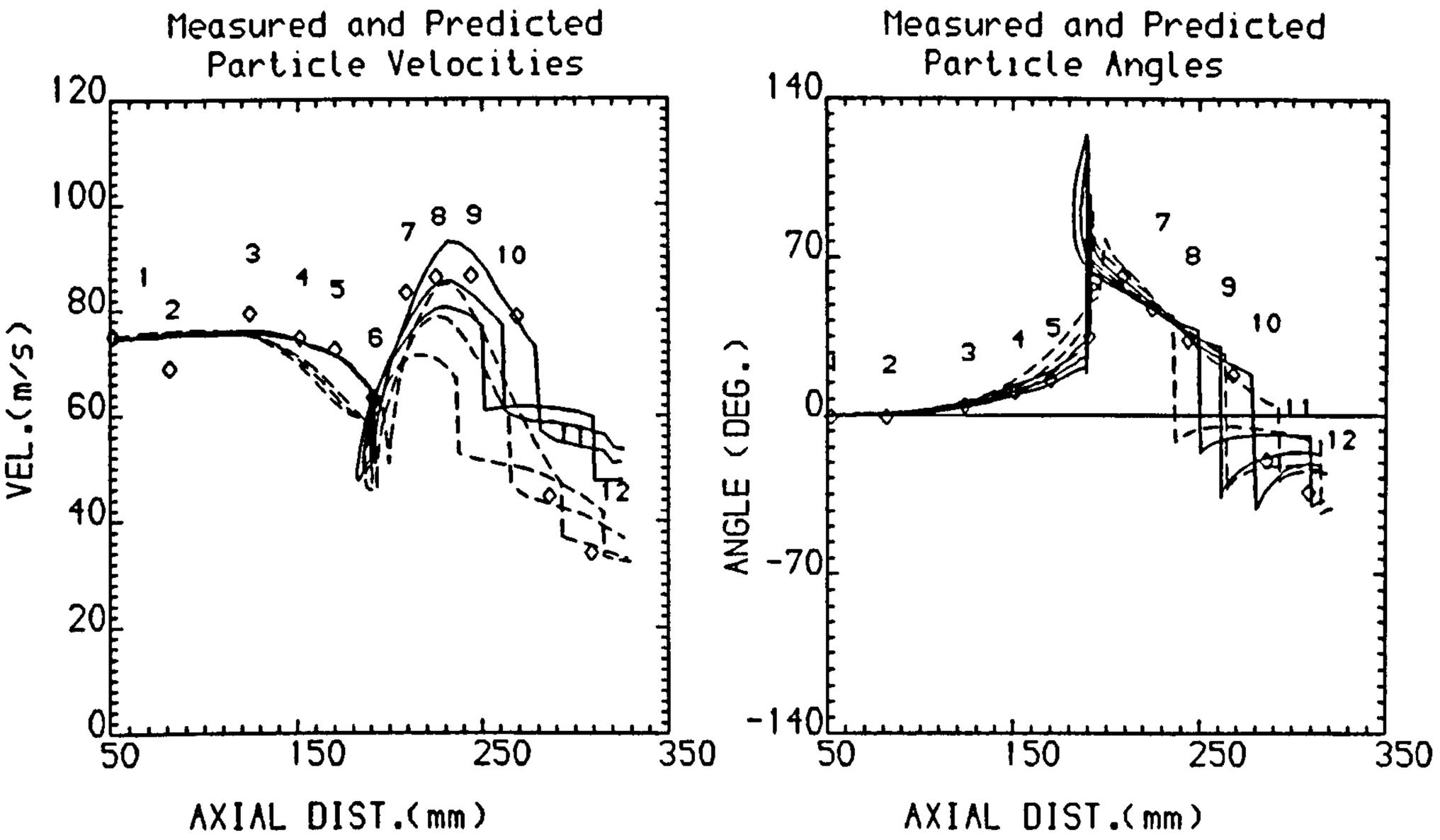

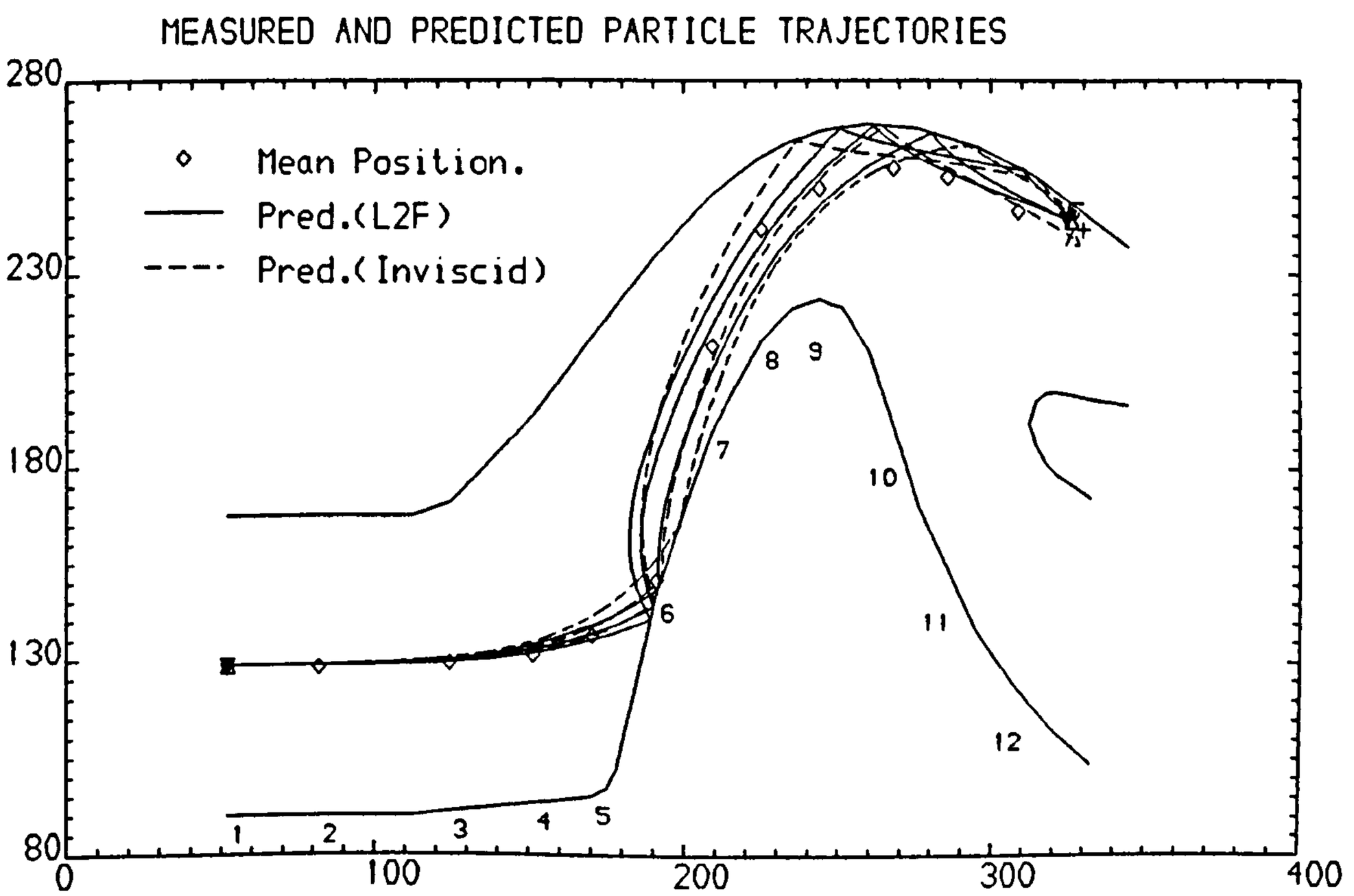

WALL MATL. = AL.	PTLE. DIAMETER = 12.0-18.0 um
PTLE. MATL. = BALLOTINI	PTLE. INITIAL VEL.= 75.1 m/s
PTLE. DEN. = 2950.0 kg/m3	

FIG.62 MEASURED AND PREDICTED PARTICLE VELOCITIES AND ANGLES AT THE MEAN TRAJECTORY POSITIONS

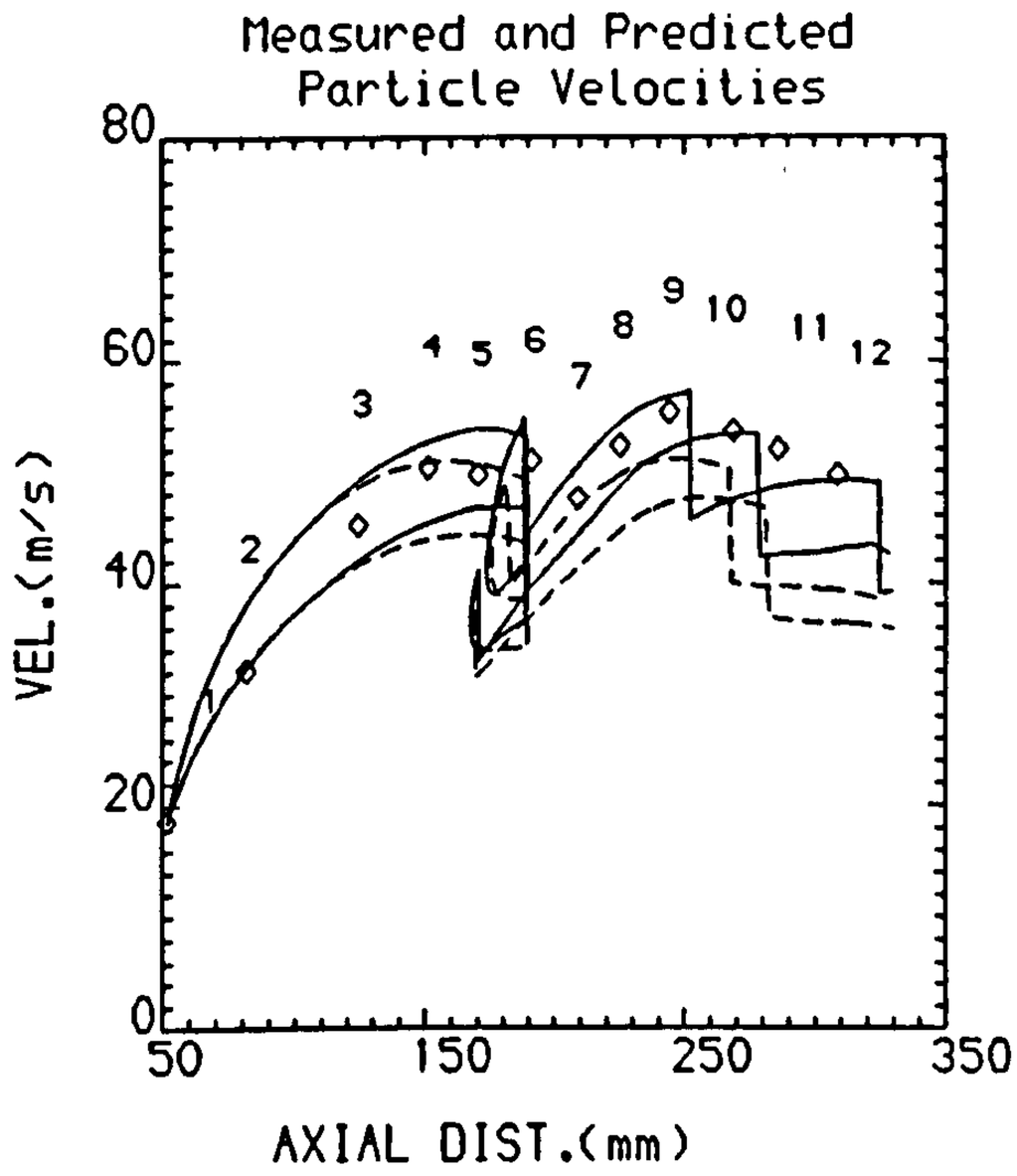

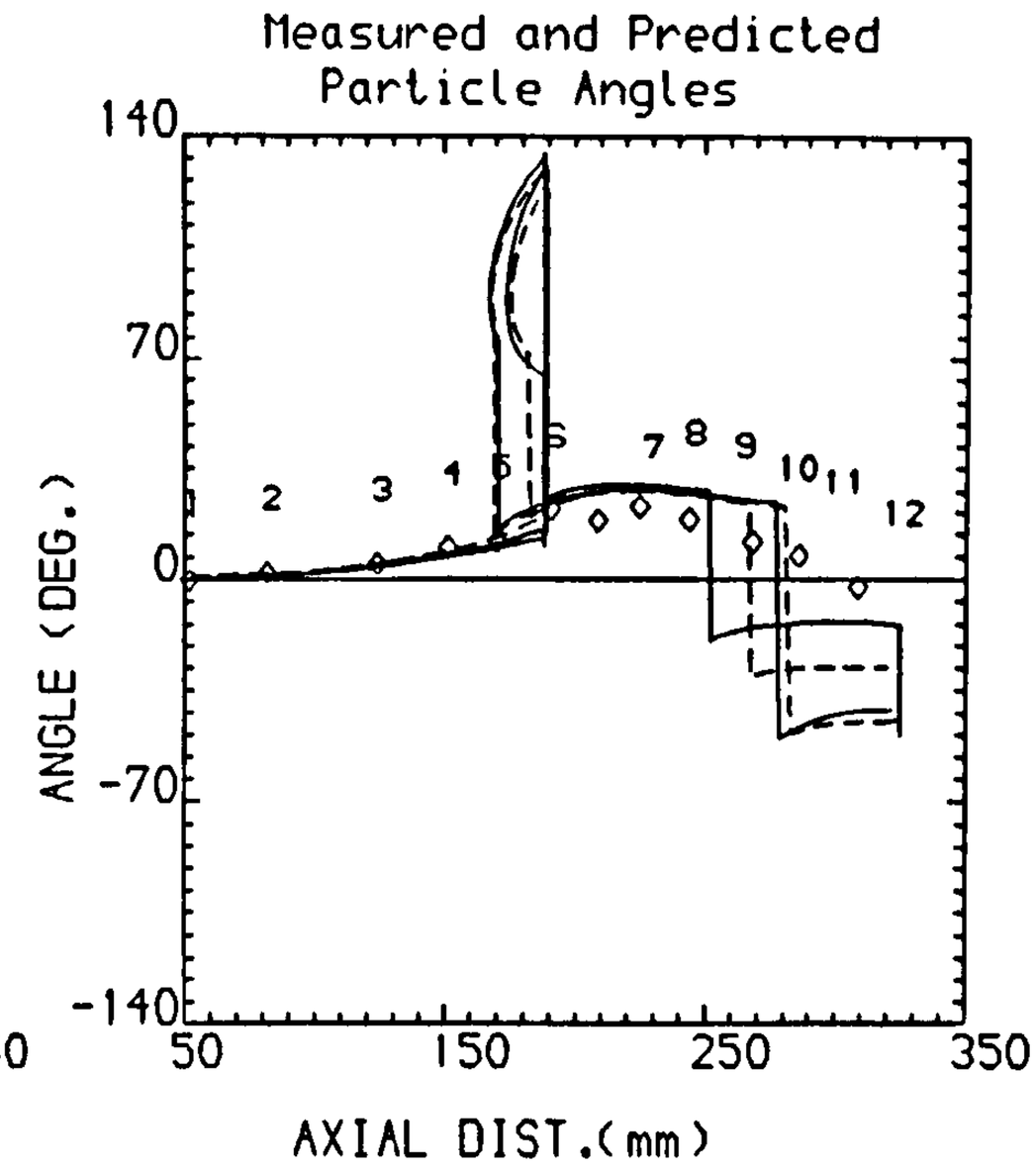

MEASURED AND PREDICTED PARTICLE TRAJECTORIES

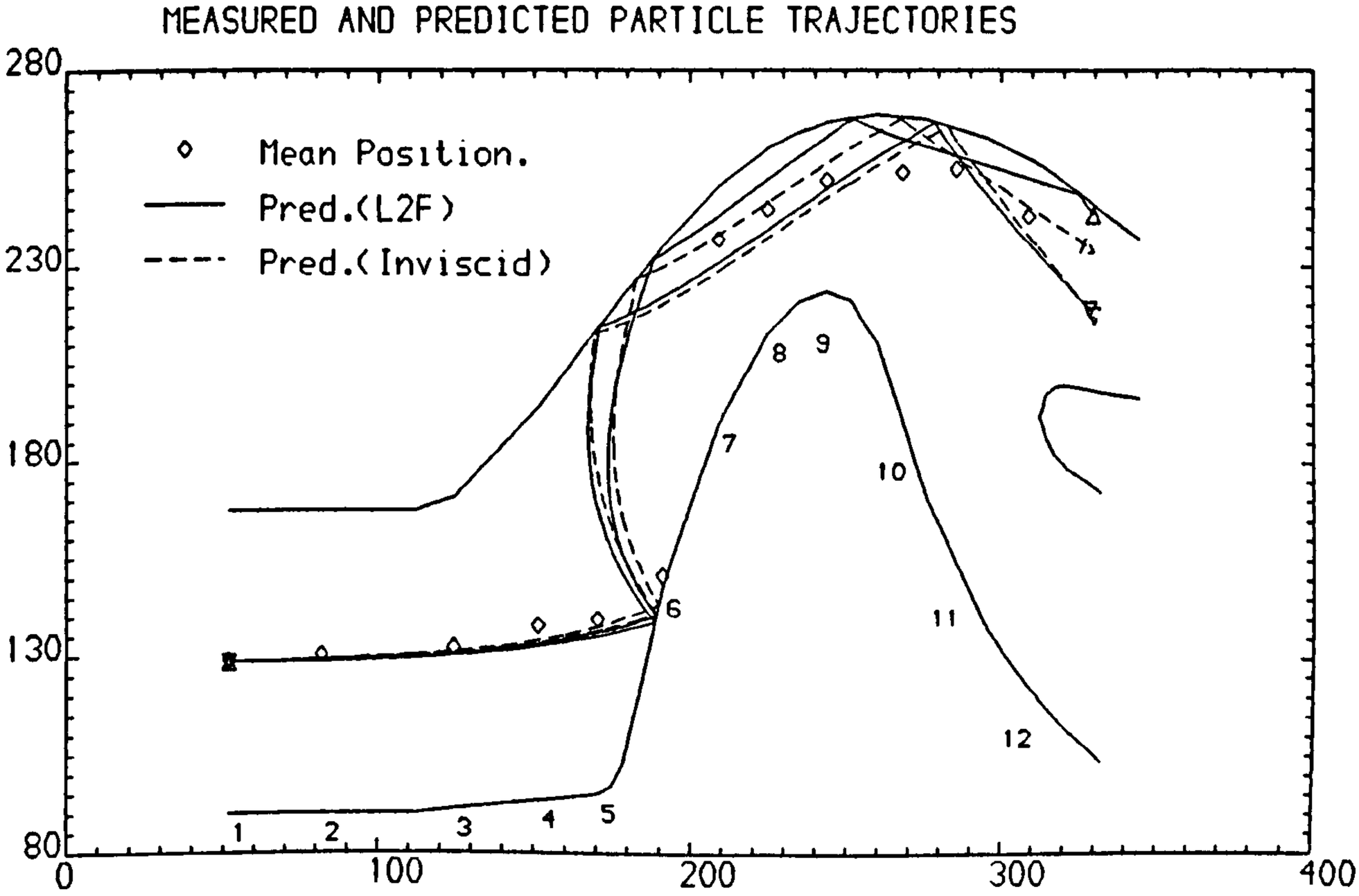

WALL MATL. = AL.
PTLE. MATL. = BALLOTINI
PTLE. DEN. = 2950.0 kg/m3
PTLE. DIAMETER = 38.0-53.0 um
PTLE. INITIAL VEL.= 18.6 m/s

FIG.63 MEASURED AND PREDICTED PARTICLE VELOCITIES AND ANGLES AT THE MEAN TRAJECTORY POSITIONS

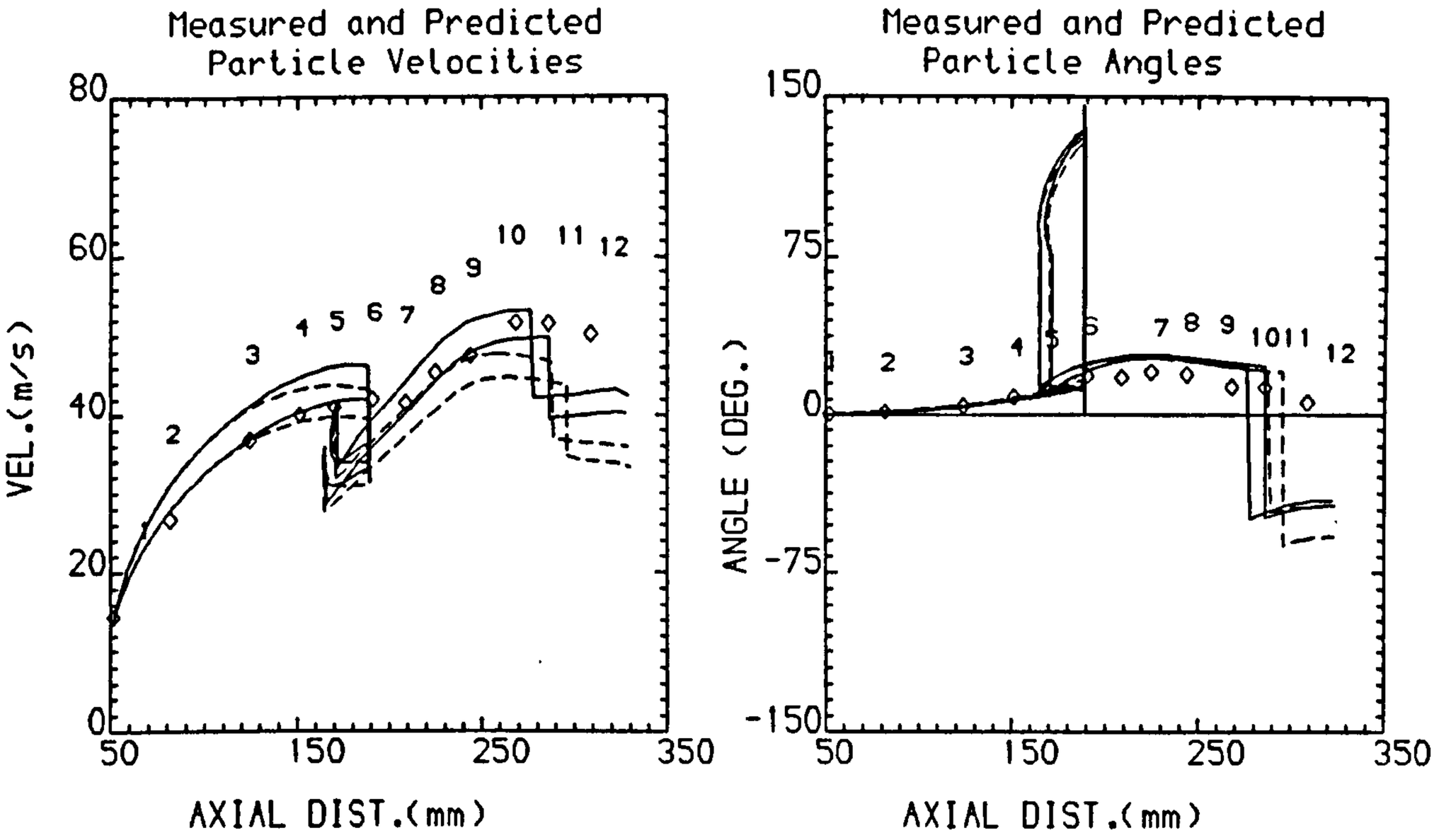

MEASURED AND PREDICTED PARTICLE TRAJECTORIES

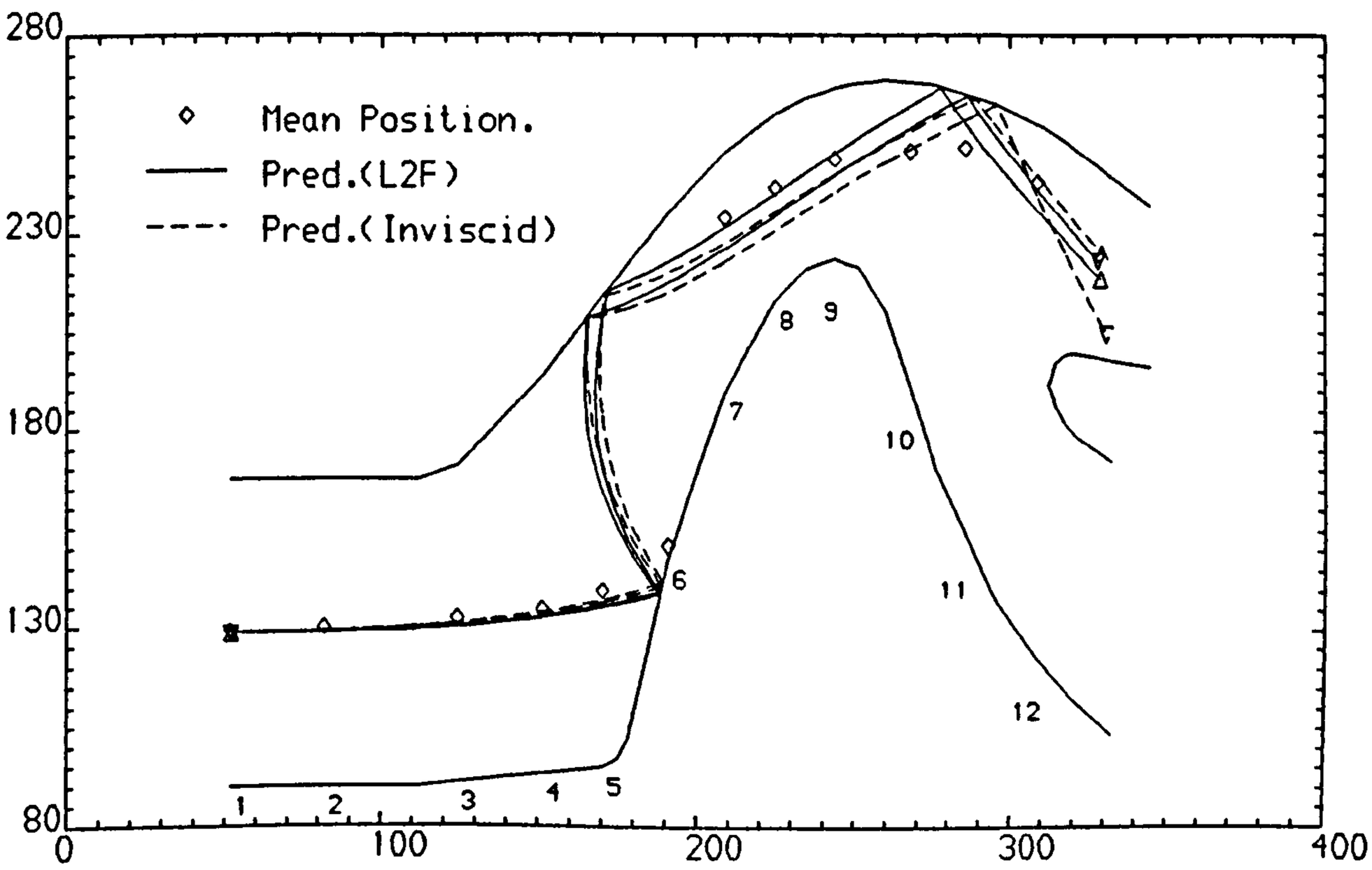

WALL MATL. = AL.	PTLE. DIAMETER = 53.0-65.0 um
PTLE. MATL. = BALLOTINI	PTLE. INITIAL VEL.= 14.4 m/s
PTLE. DEN. = 2950.0 kg/m3	

FIG.64 MEASURED AND PREDICTED PARTICLE VELOCITIES AND ANGLES AT THE MEAN TRAJECTORY POSITIONS

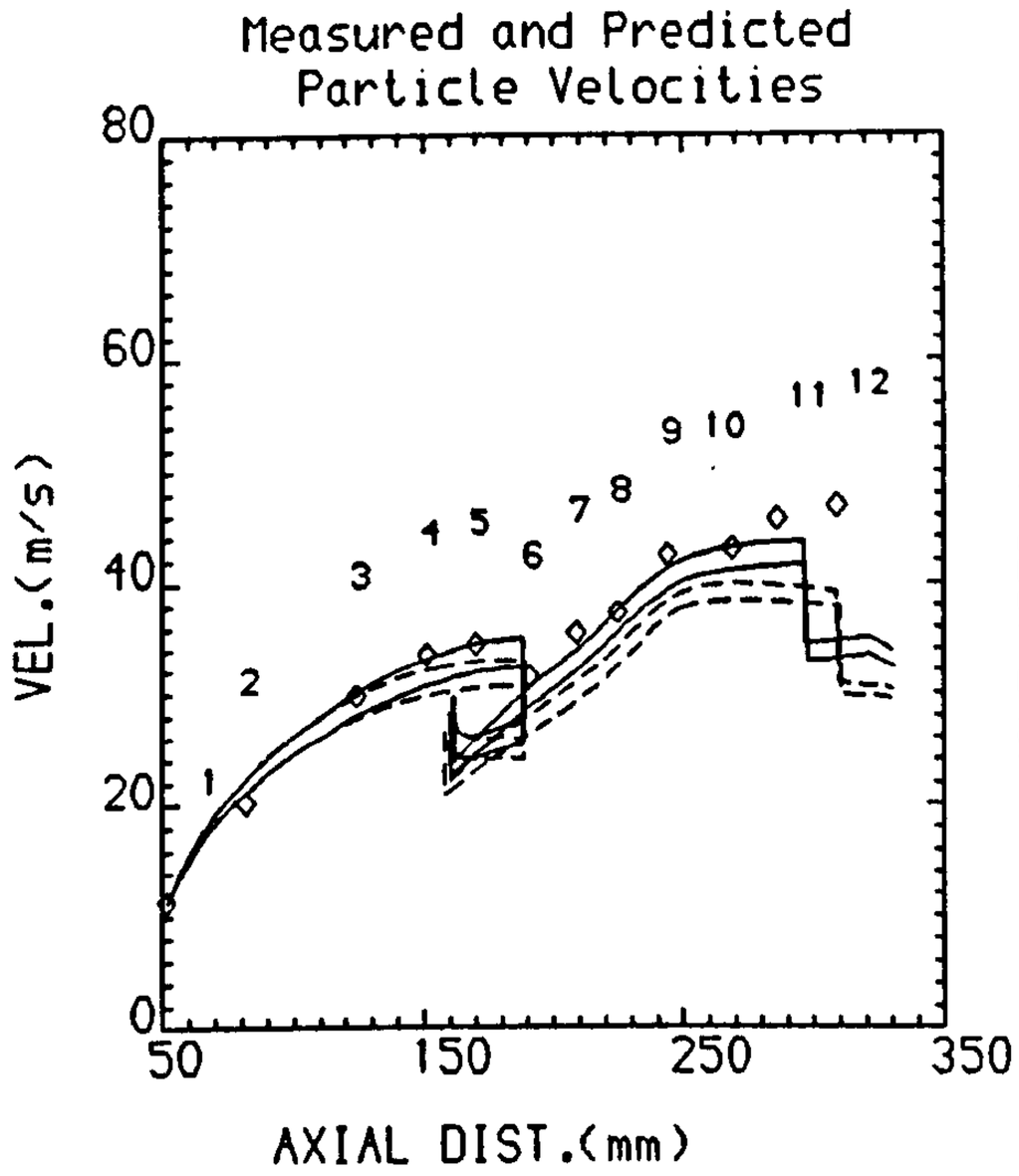

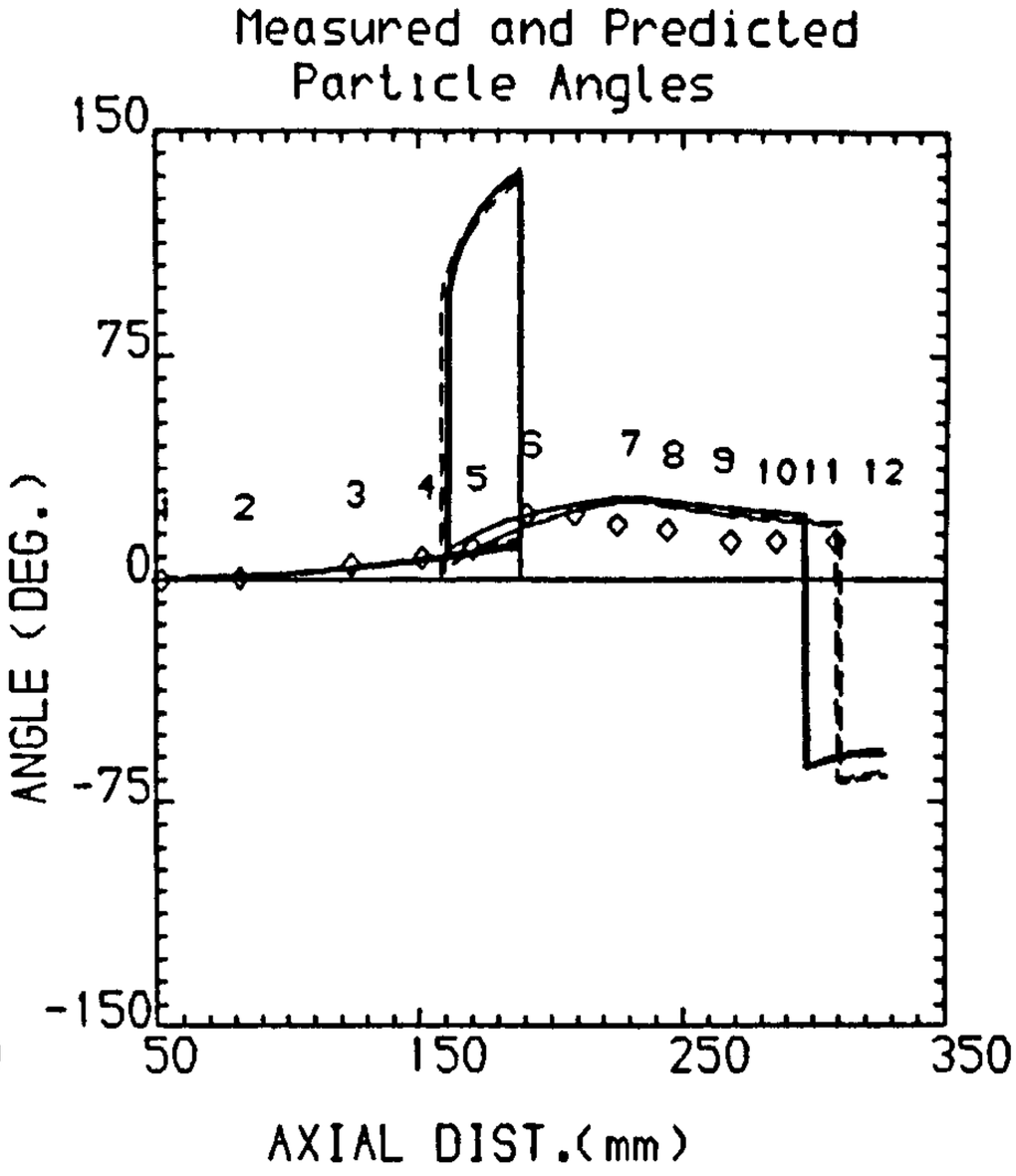

MEASURED AND PREDICTED PARTICLE TRAJECTORIES

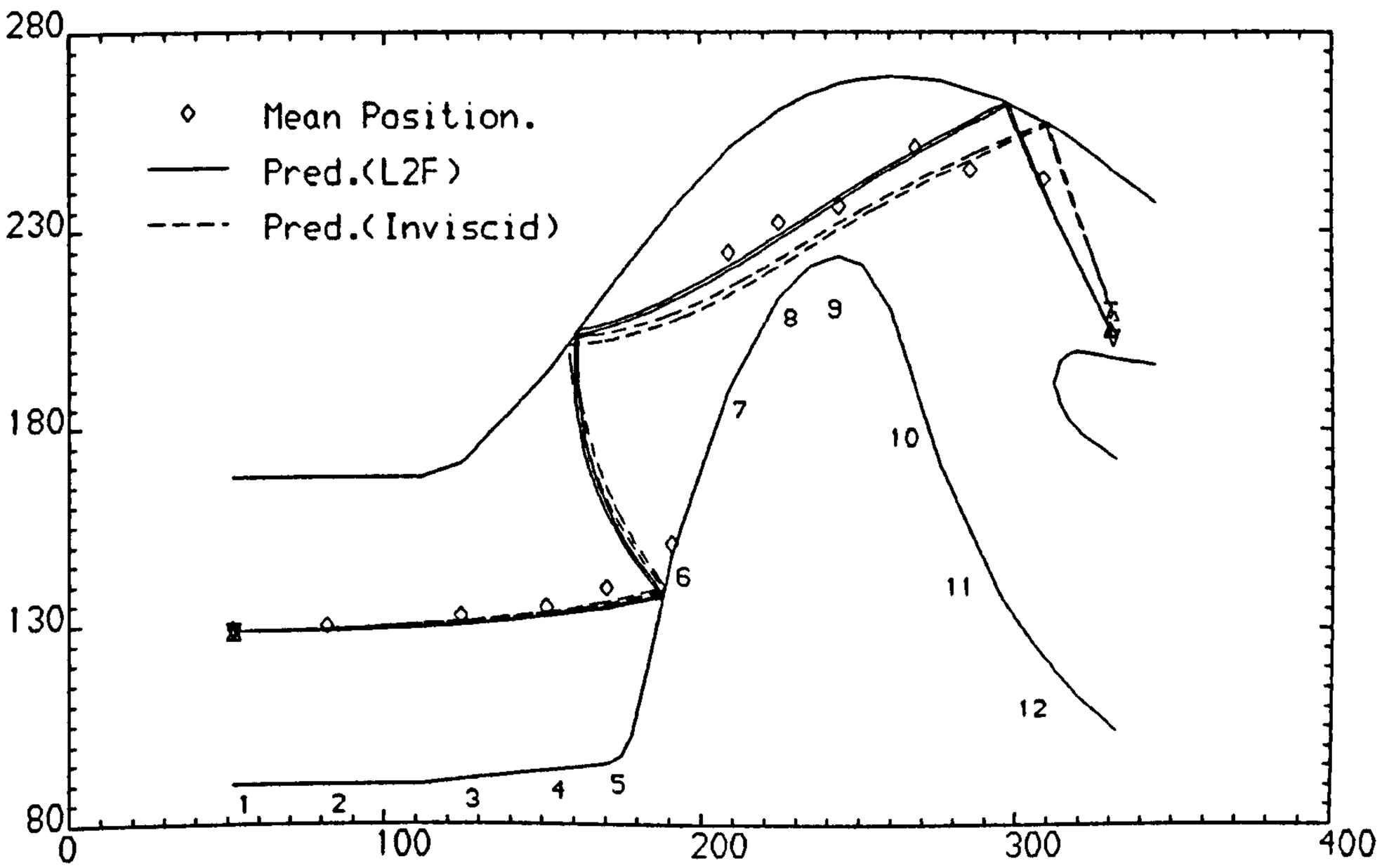

WALL MATL. = AL.

PTLE. MATL. = BALLOTINI

PTLE. DEN. = 2950.0 kg/m3

PTLE. DIAMETER = 91.0-107.0 um

PTLE. INITIAL VEL.= 11.3 m/s

FIG.65 MEASURED AND PREDICTED PARTICLE VELOCITIES AND ANGLES AT THE MEAN TRAJECTORY POSITIONS

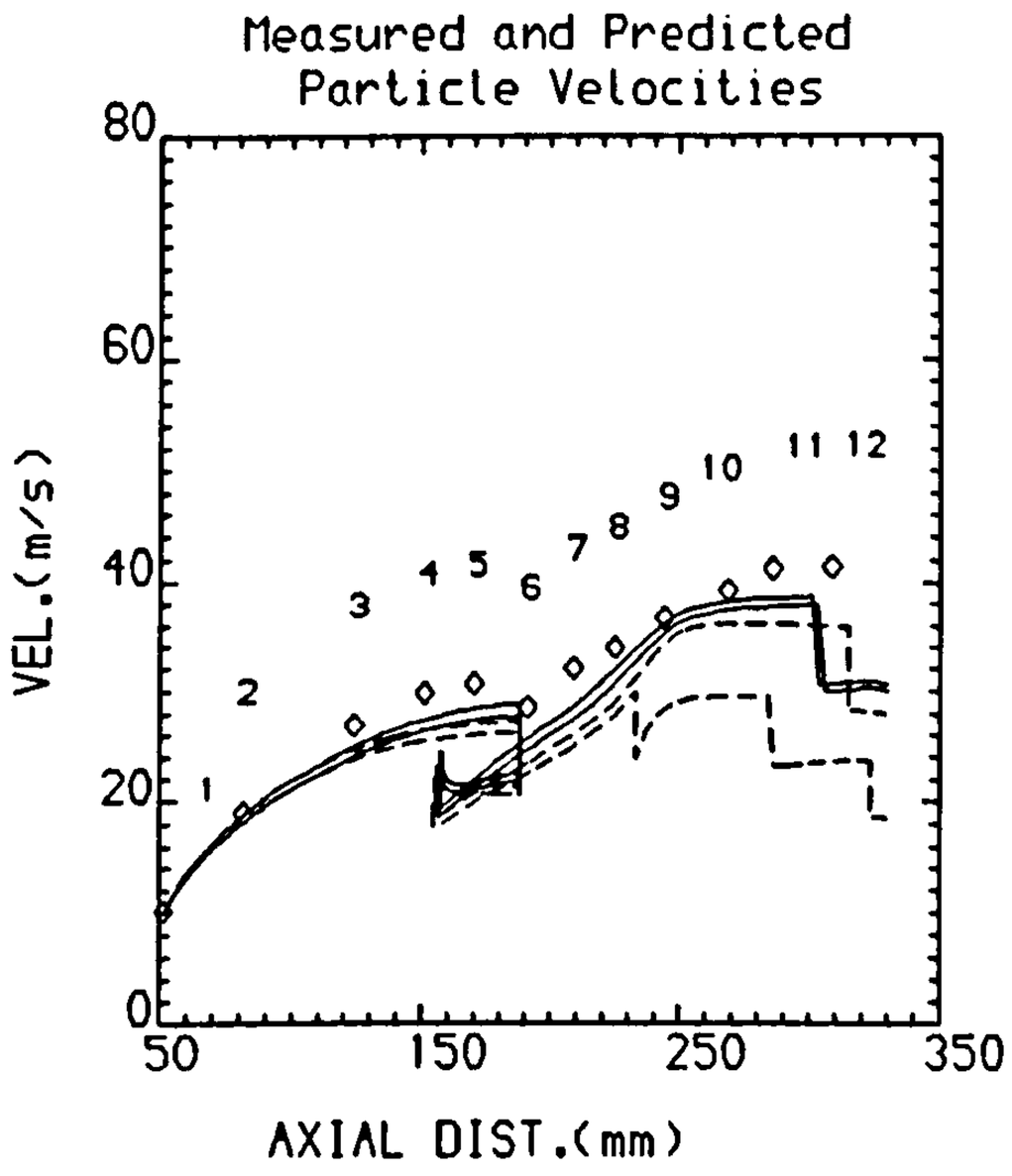

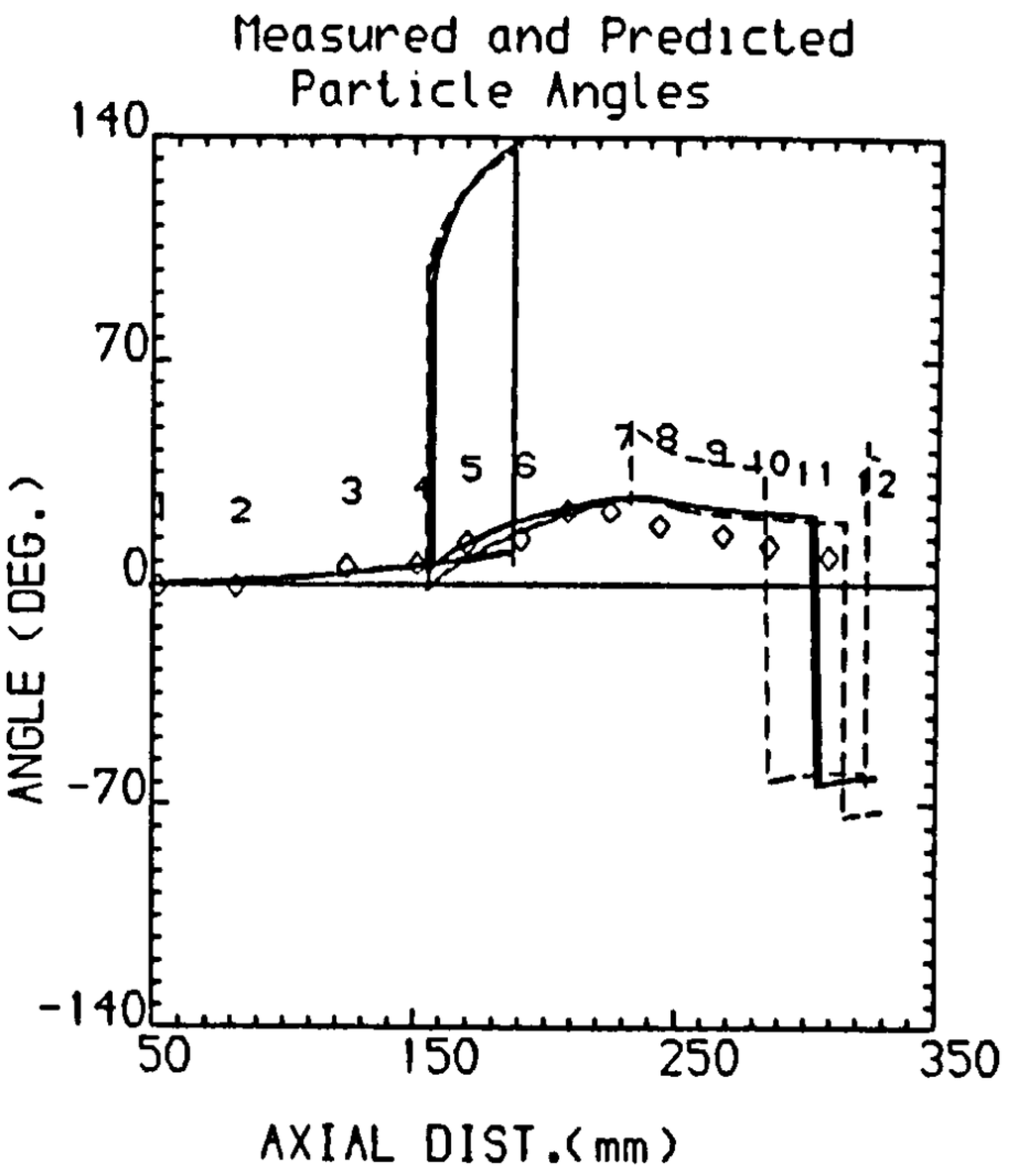

MEASURED AND PREDICTED PARTICLE TRAJECTORIES

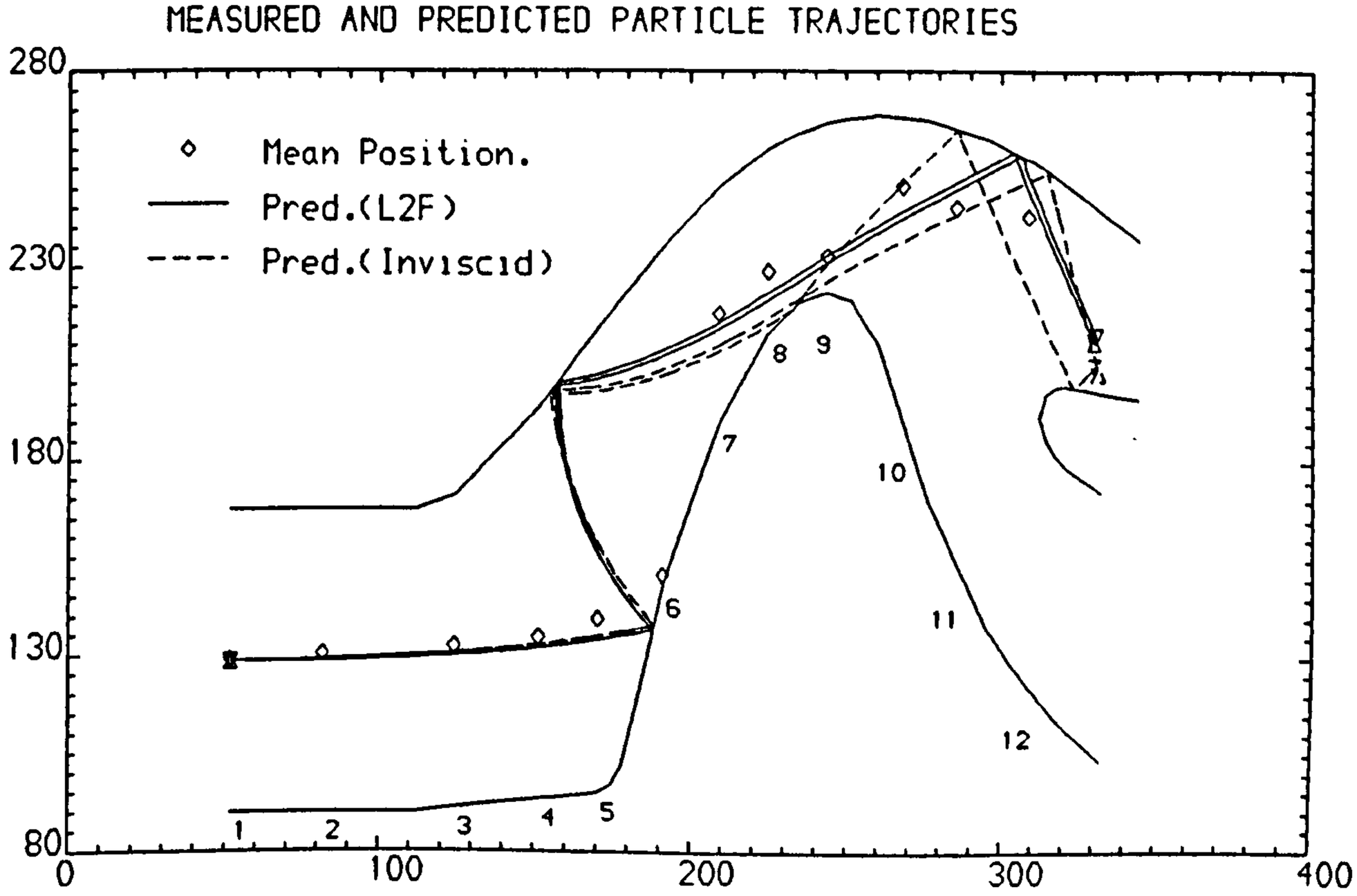

WALL MATL. = AL.

PTLE. MATL. = BALLOTINI

PTLE. DEN. = 2950.0 kg/m3

PTLE. DIAMETER = 145.0-162.0 um

PTLE. INITIAL VEL.= 10.2 m/s

FIG.66 PREDICTED AND MEASURED PARTICLE CONCENTRATION DISTRIBUTION

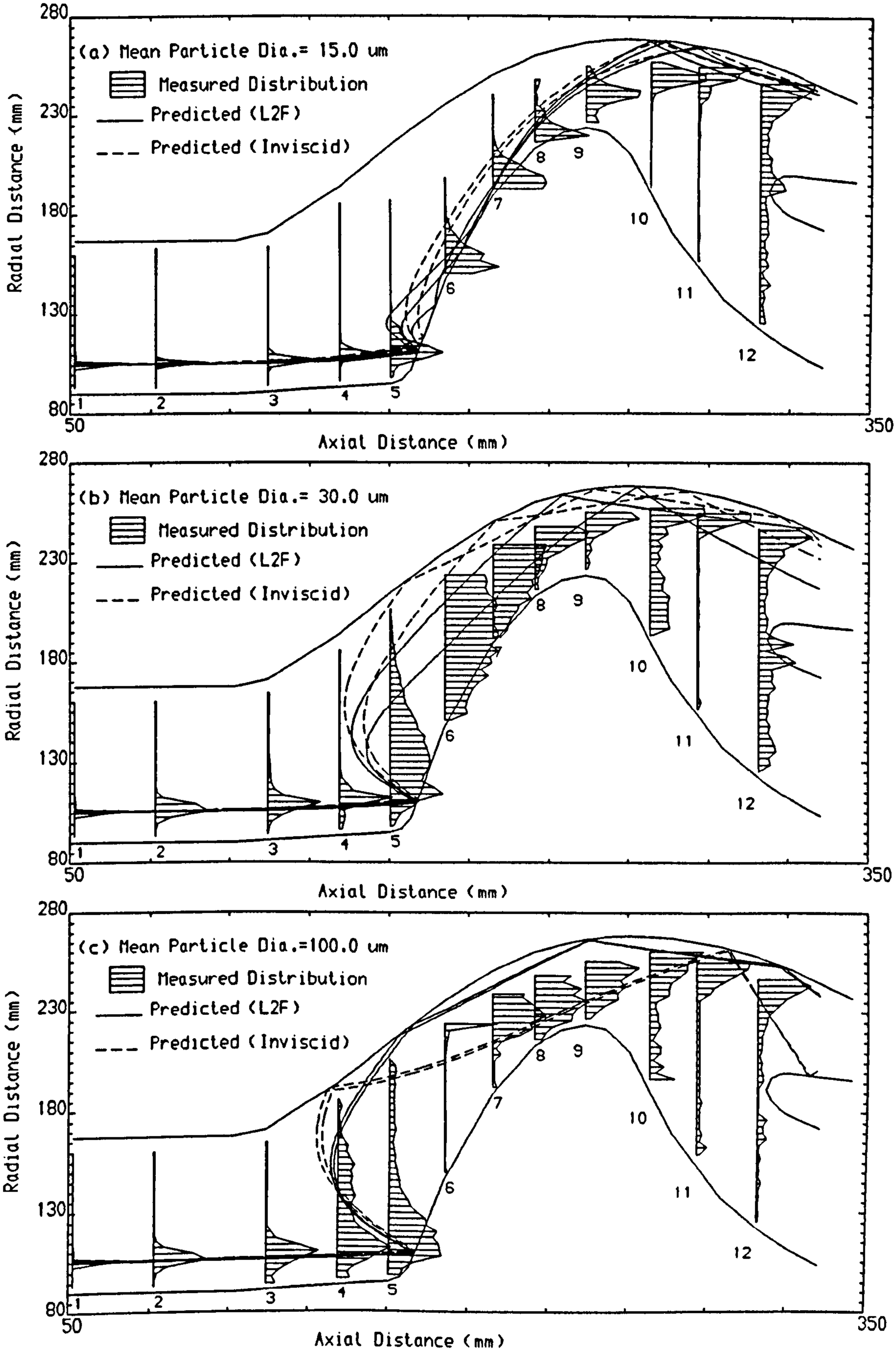

Wall matl. = AL.
Particle matl. = Ballotini
Particle initial location = 105.50 mm
Particle density = 2950.0 Kg/m3

FIG.67 MEASURED AND PREDICTED PARTICLE VELOCITIES AND ANGLES AT THE MEAN TRAJECTORY POSITIONS

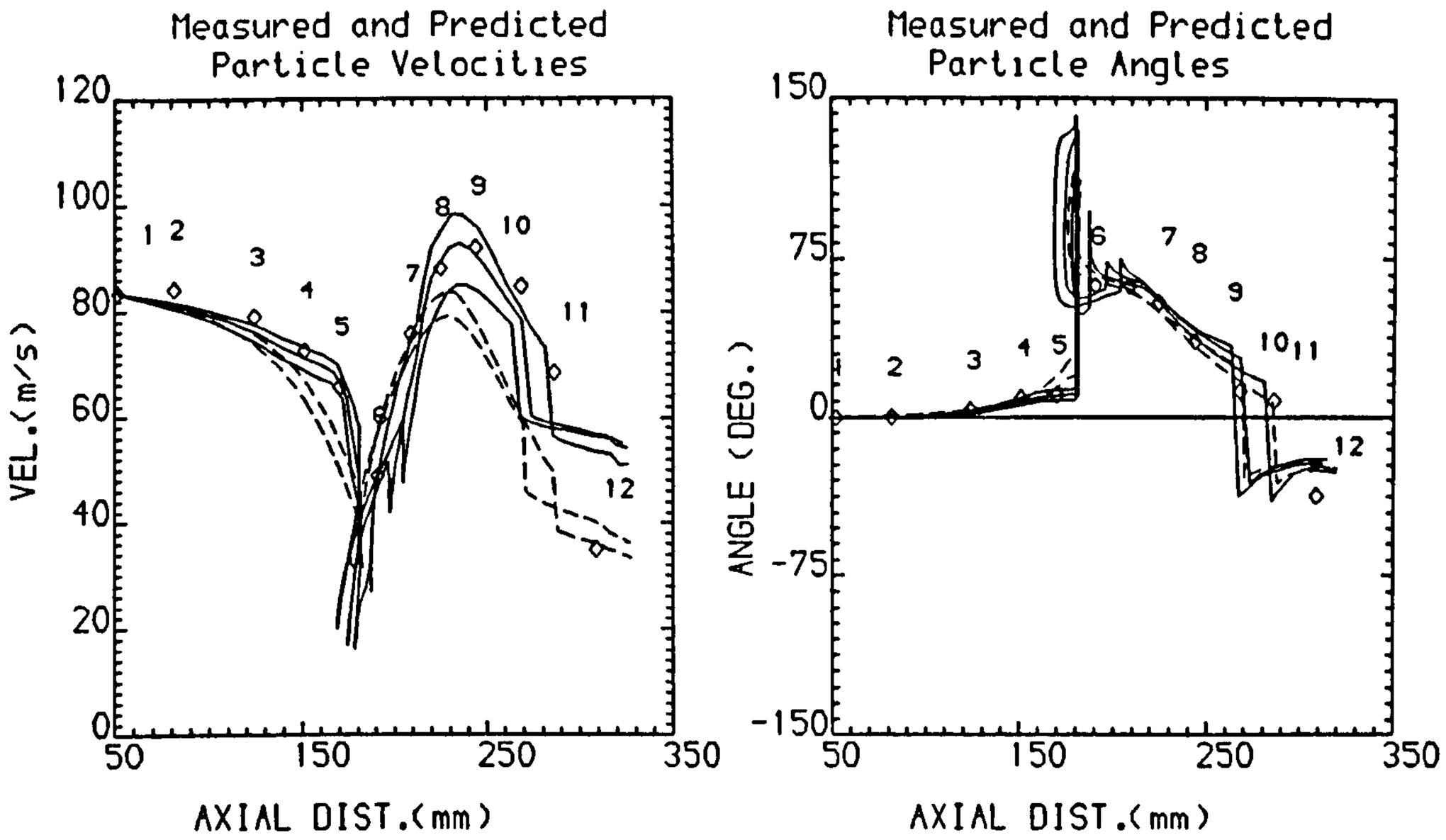

MEASURED AND PREDICTED PARTICLE TRAJECTORIES

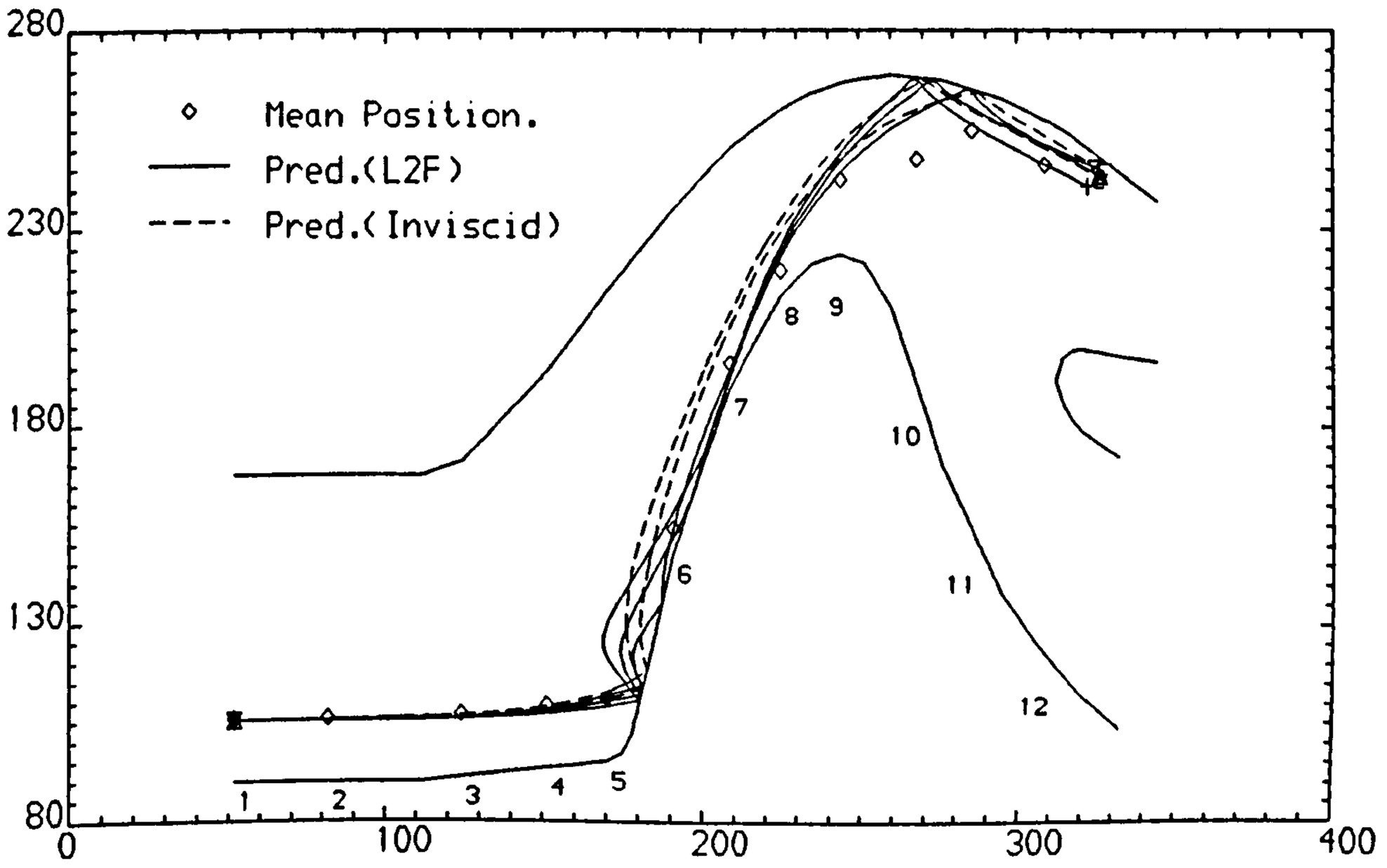

WALL MATL. = AL.
PTLE. MATL. = BALLOTINI
PTLE. DEN. = 2950.0 kg/m3
PTLE. DIAMETER = 12.0-18.0 um
PTLE. INITIAL VEL.= 83.4 m/s

FIG.68 MEASURED AND PREDICTED PARTICLE VELOCITIES AND ANGLES AT THE MEAN TRAJECTORY POSITIONS

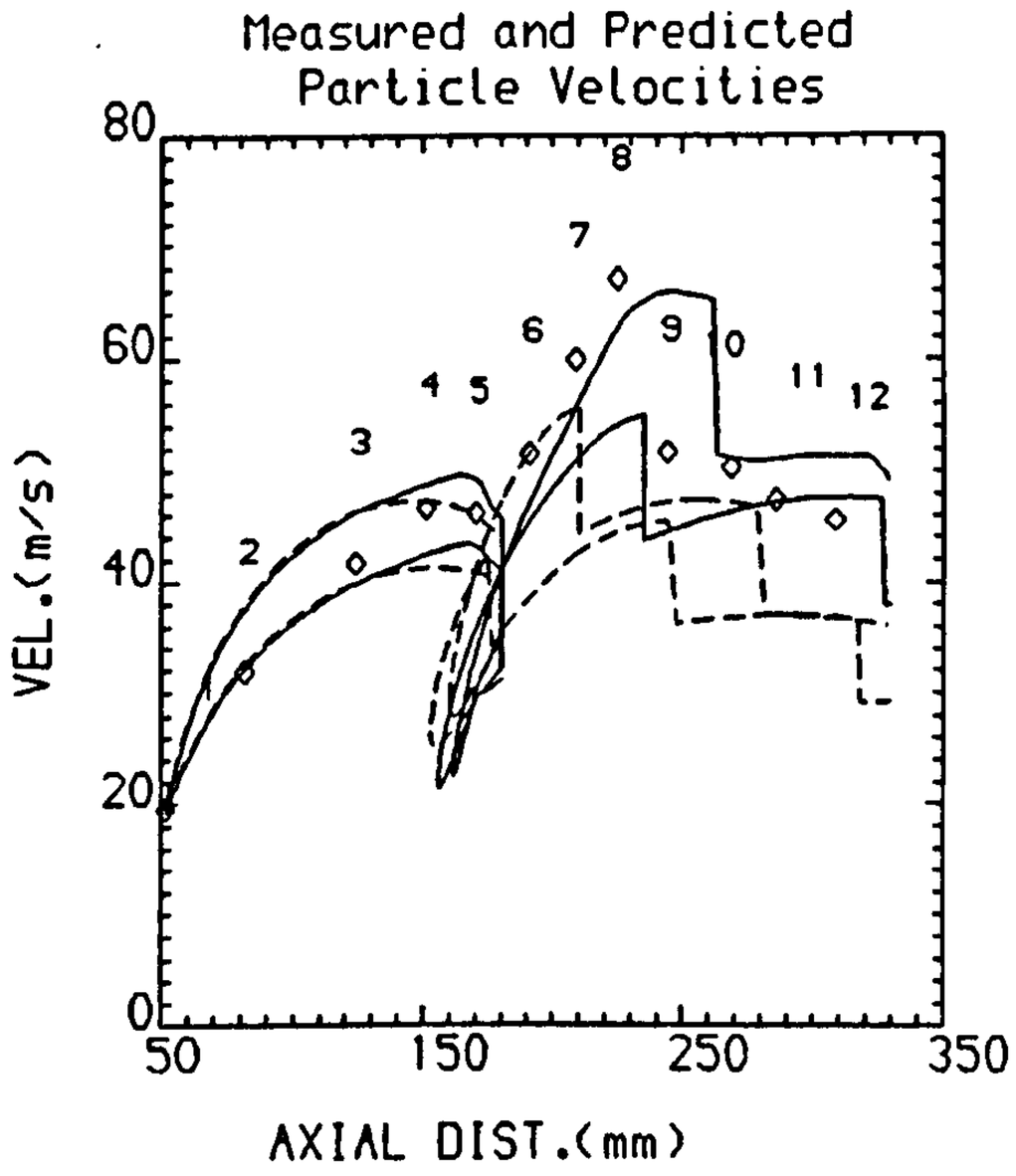

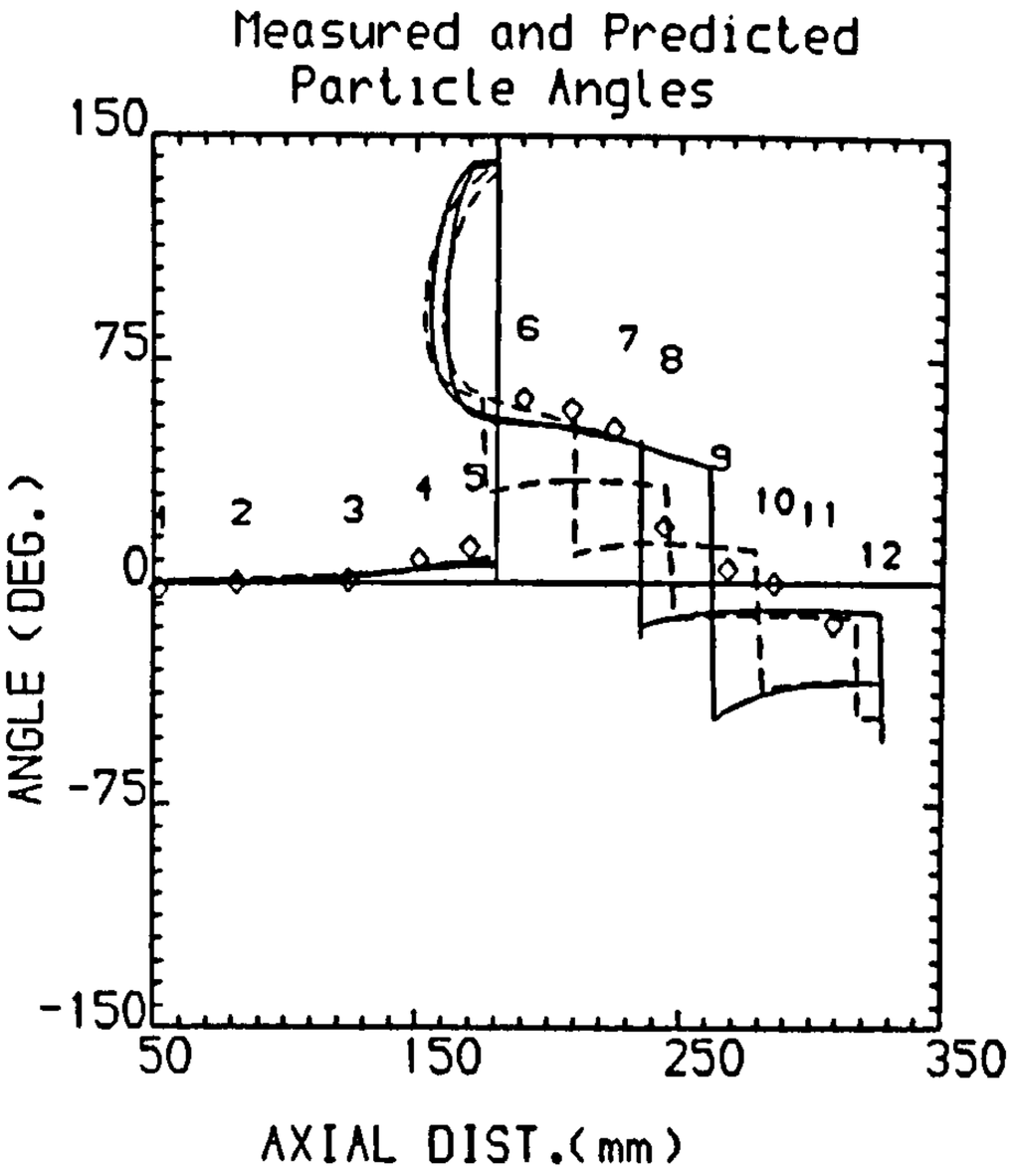

MEASURED AND PREDICTED PARTICLE TRAJECTORIES

WALL MATL. = AL.
PTLE. MATL. = BALLOTINI
PTLE. DEN. = 2950.0 kg/m3
PTLE. DIAMETER = 38.0-53.0 um
PTLE. INITIAL VEL.= 19.5 m/s

FIG.69 MEASURED AND PREDICTED PARTICLE VELOCITIES AND ANGLES AT THE MEAN TRAJECTORY POSITIONS

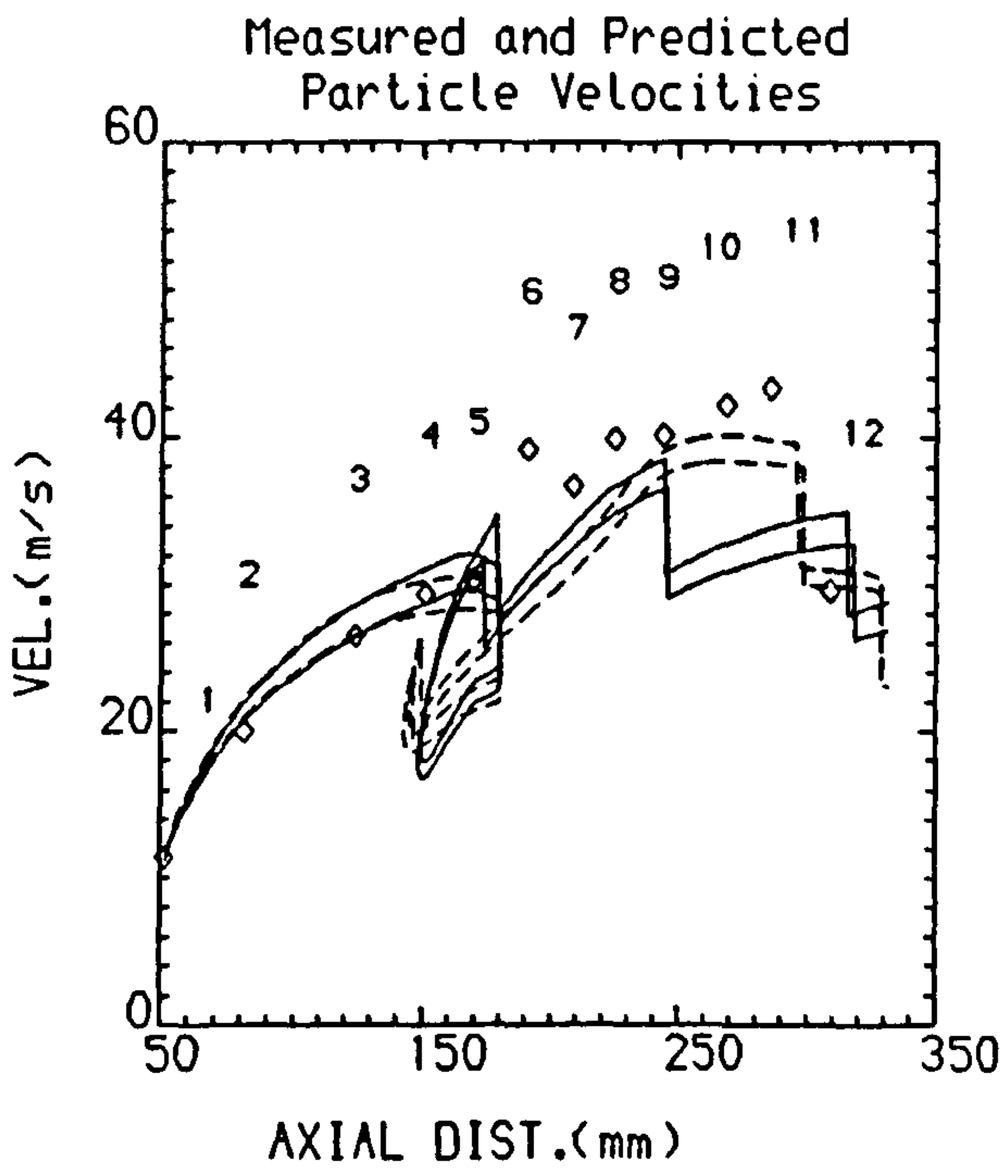

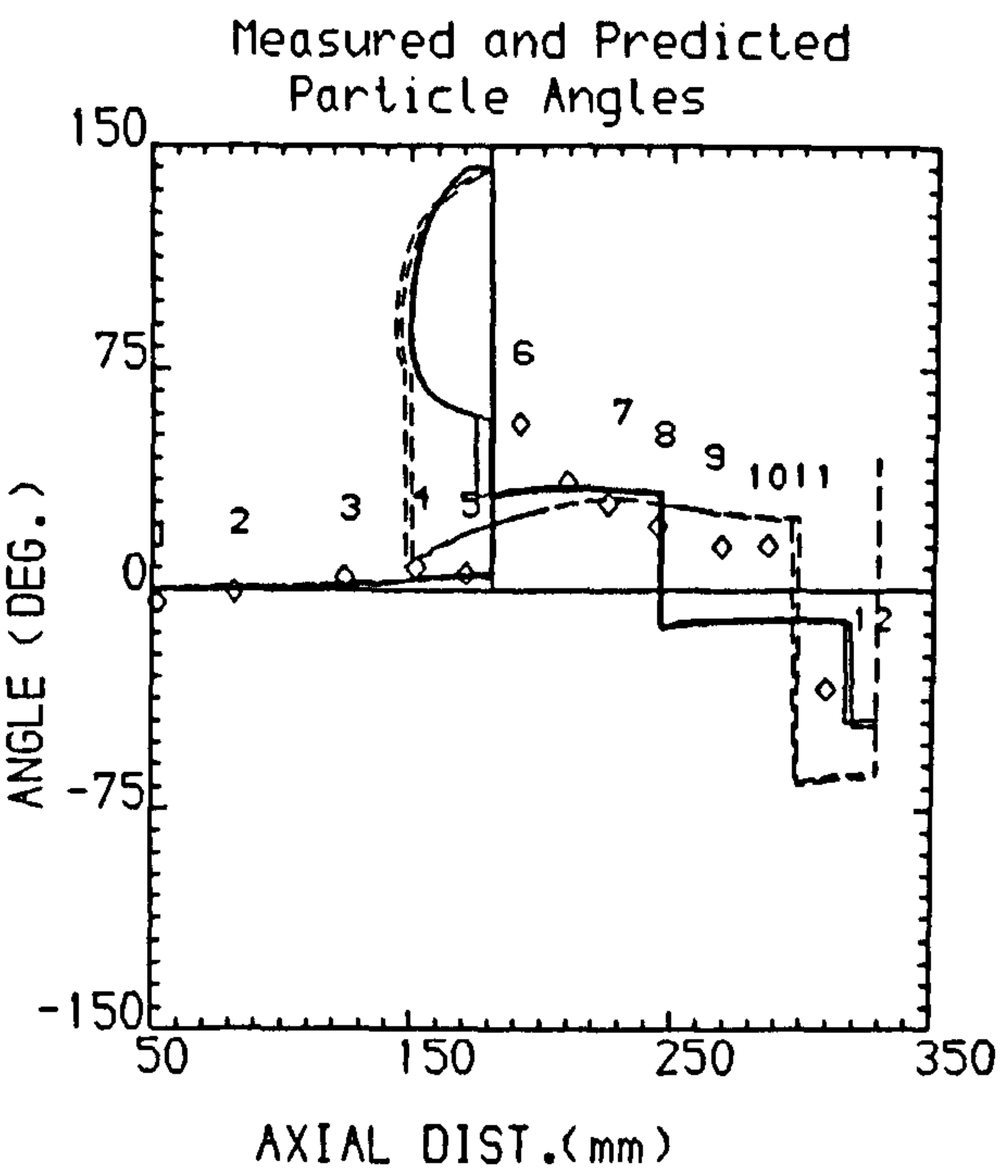

MEASURED AND PREDICTED PARTICLE TRAJECTORIES

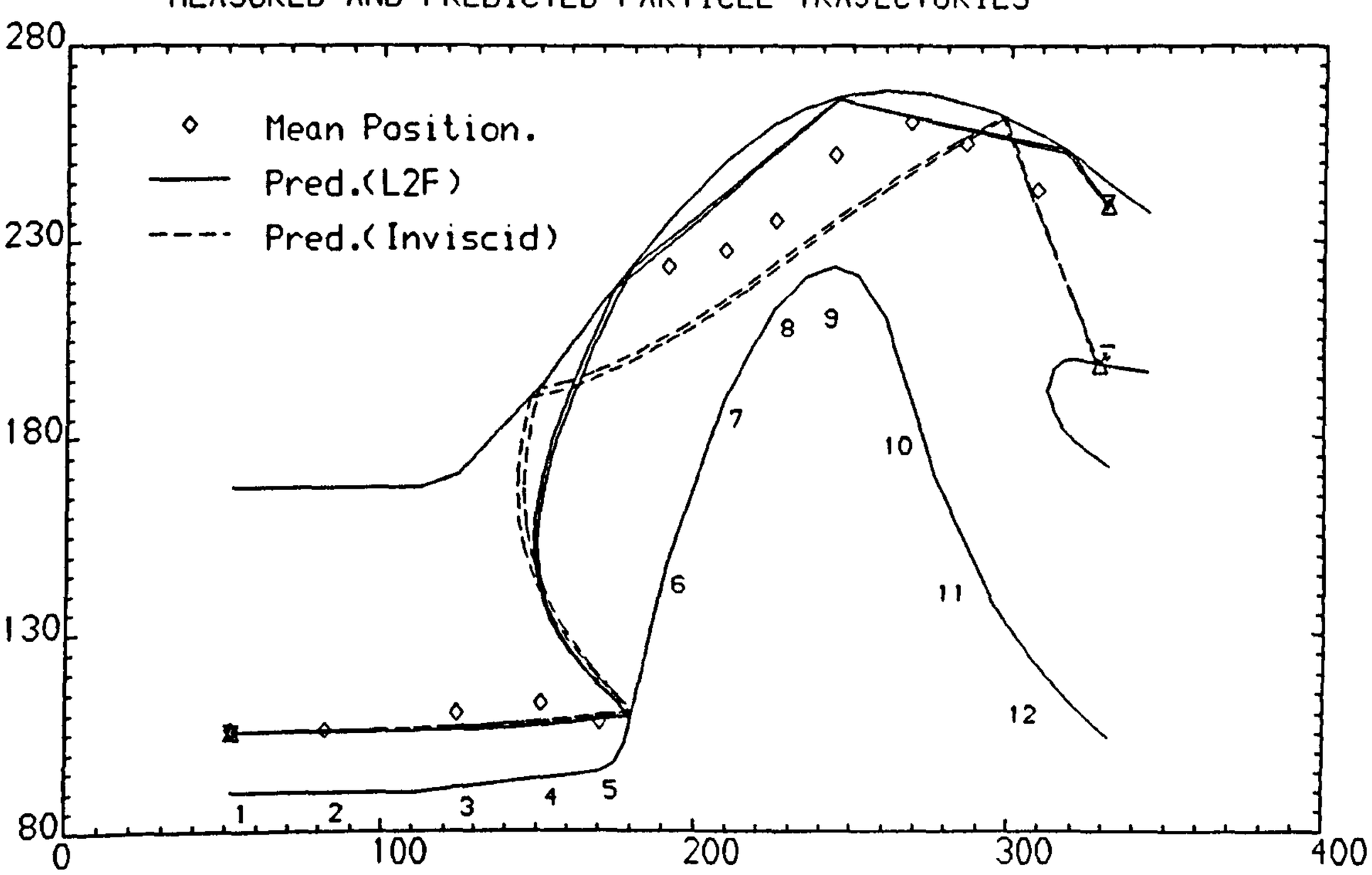

WALL MATL. = AL.

PTLE. MATL. = BALLOTINI

PTLE. DEN. = 2950.0 kg/m3

PTLE. DIAMETER = 91.0-107.0 um

PTLE. INITIAL VEL.= 11.4 m/s

FIG.70 MEASURED AND PREDICTED PARTICLE VELOCITIES AND ANGLES AT THE MEAN TRAJECTORY POSITIONS

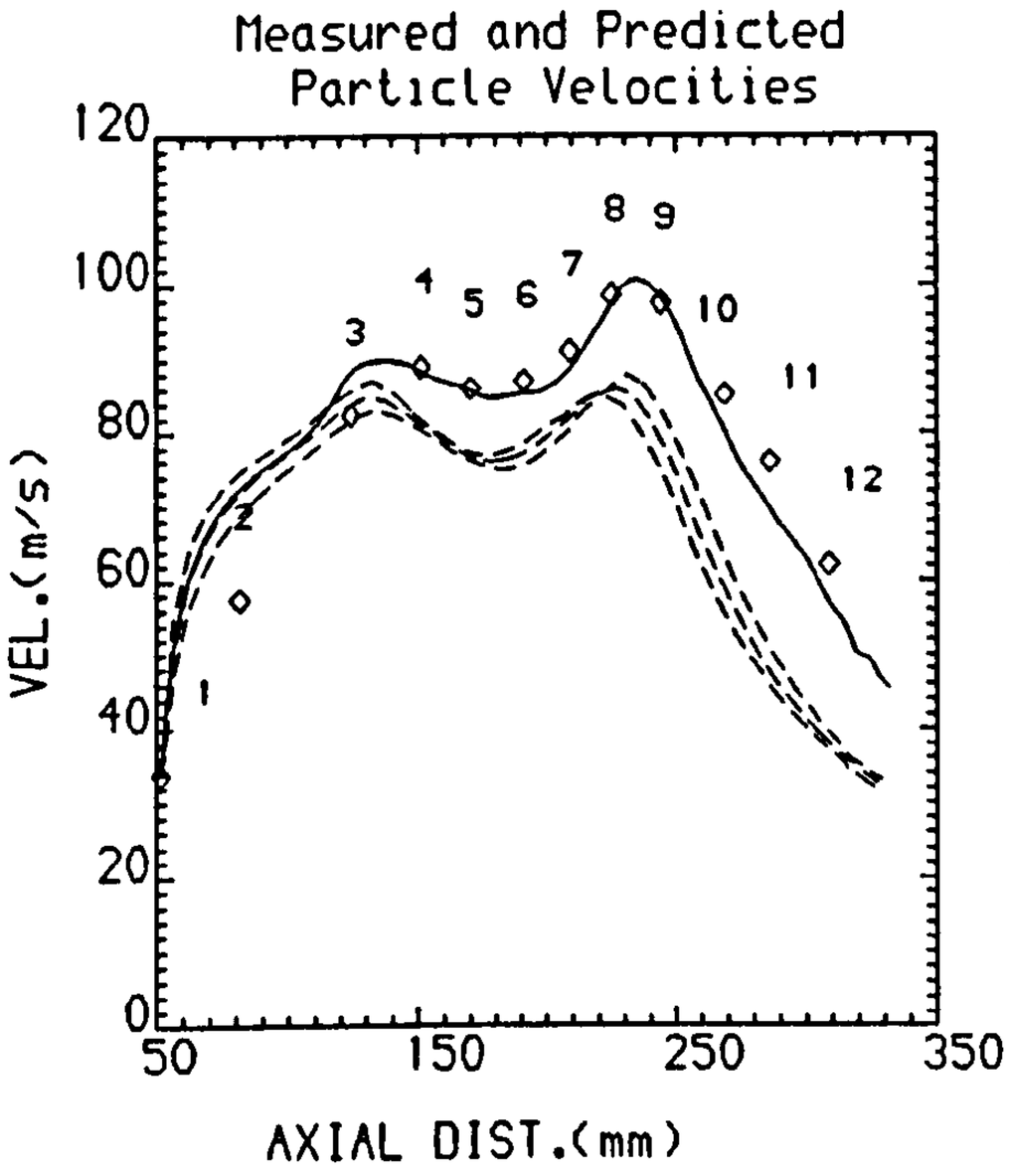

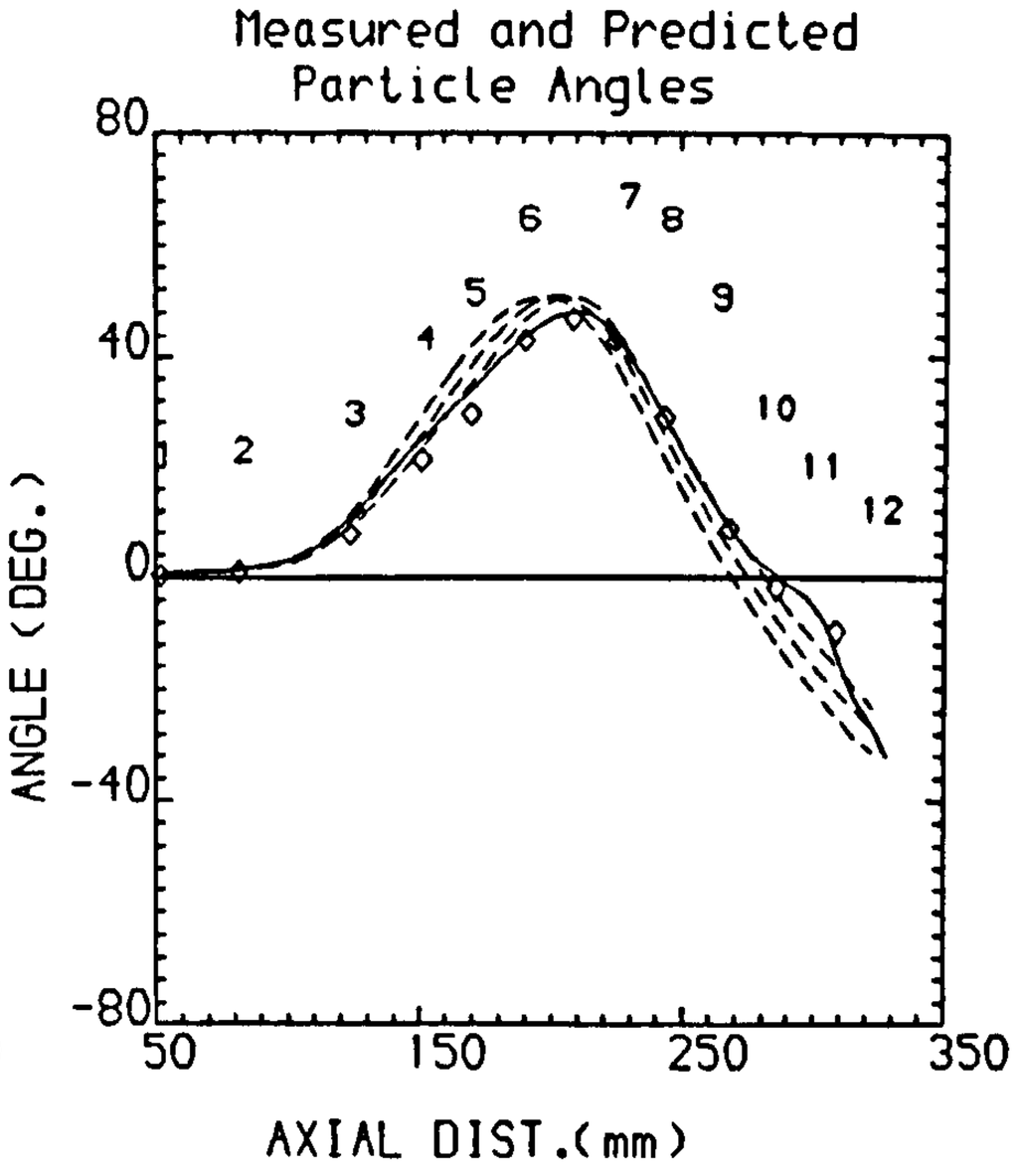

MEASURED AND PREDICTED PARTICLE TRAJECTORIES

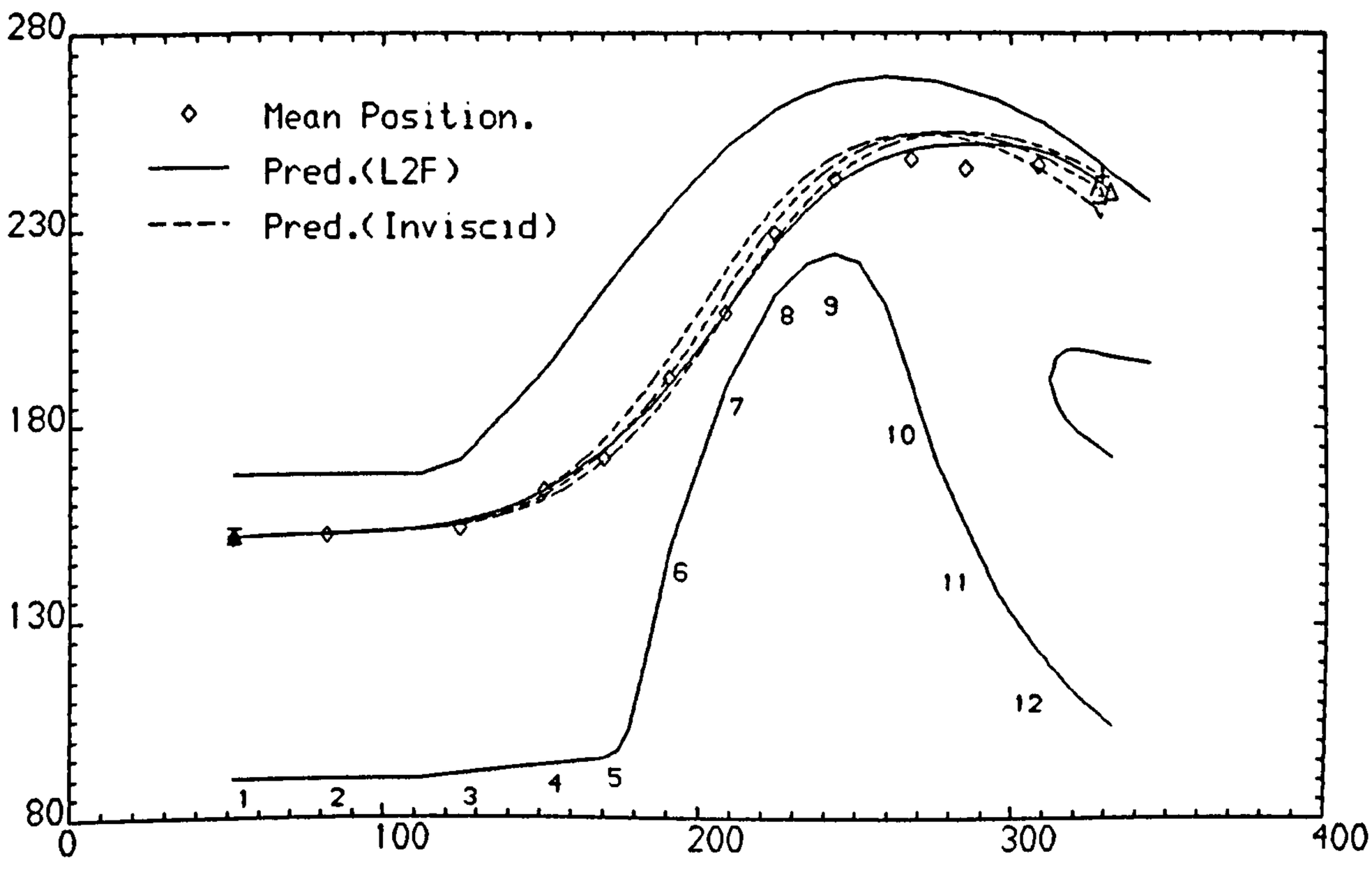

WALL MATL. = AL.	PTLE. DIAMETER = 15.0 um
PTLE. MATL. = QUARTZ	PTLE. INITIAL VEL.= 33.8 m/s
PTLE. DEN. = 2650.0 kg/m3	

FIG.71 PREDICTED AND MEASURED PARTICLE CONCENTRATION DISTRIBUTION

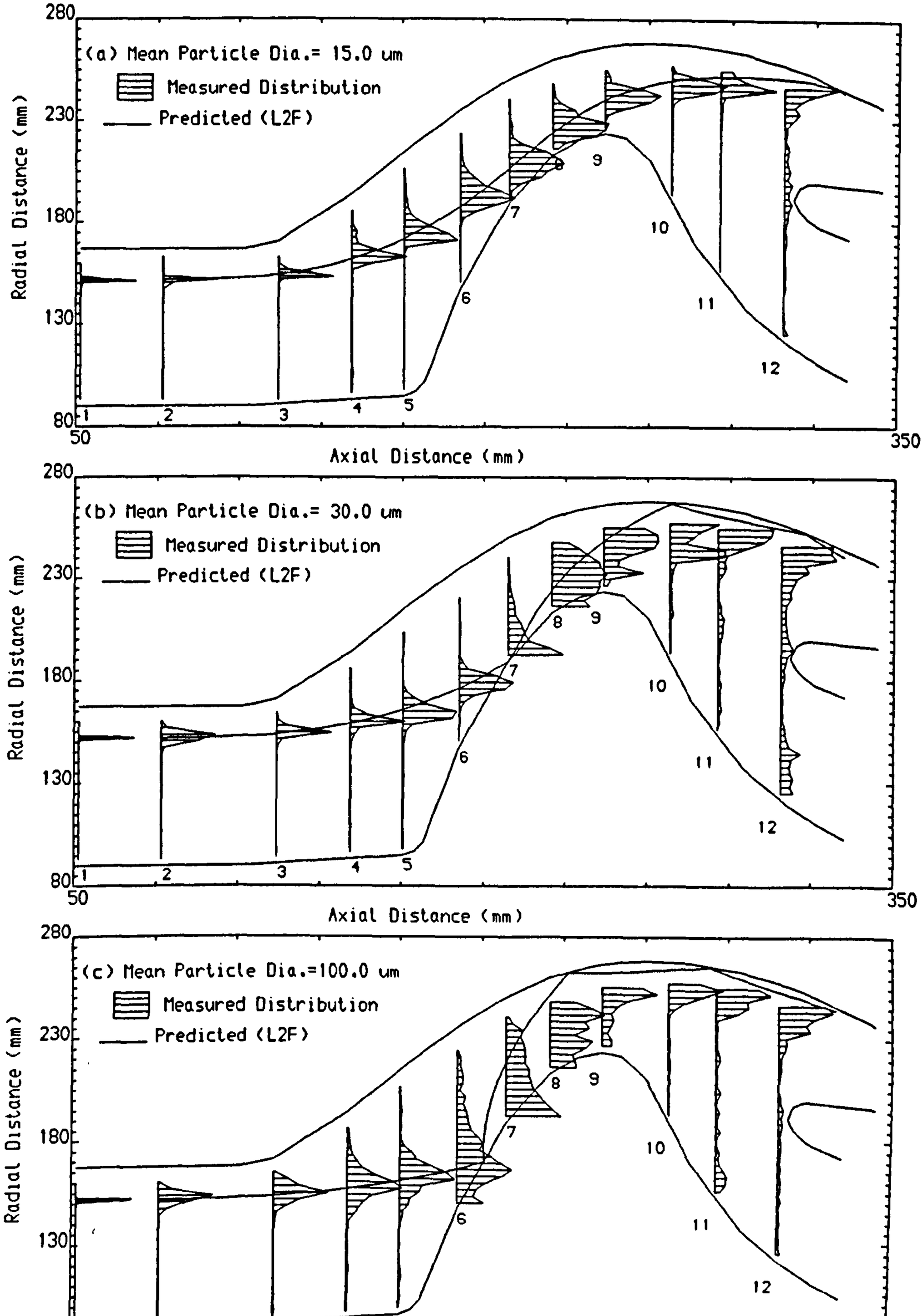

Wall matl. = AL.	Particle initial location = 151.80 mm
Particle matl. = Quartz	Particle density = 2650.0 Kg/m3

FIG.72 MEASURED AND PREDICTED PARTICLE VELOCITIES AND ANGLES AT THE MEAN TRAJECTORY POSITIONS

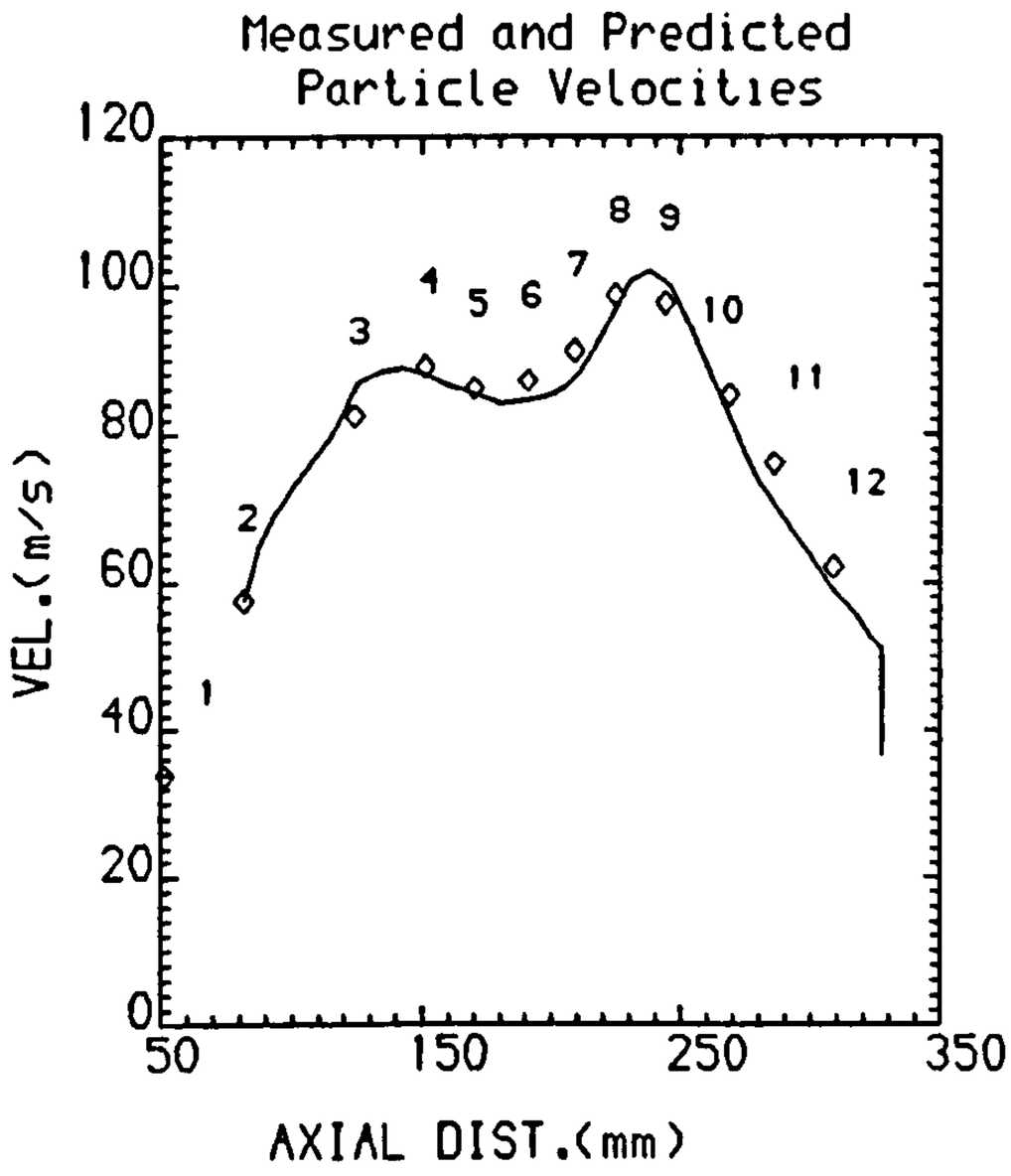

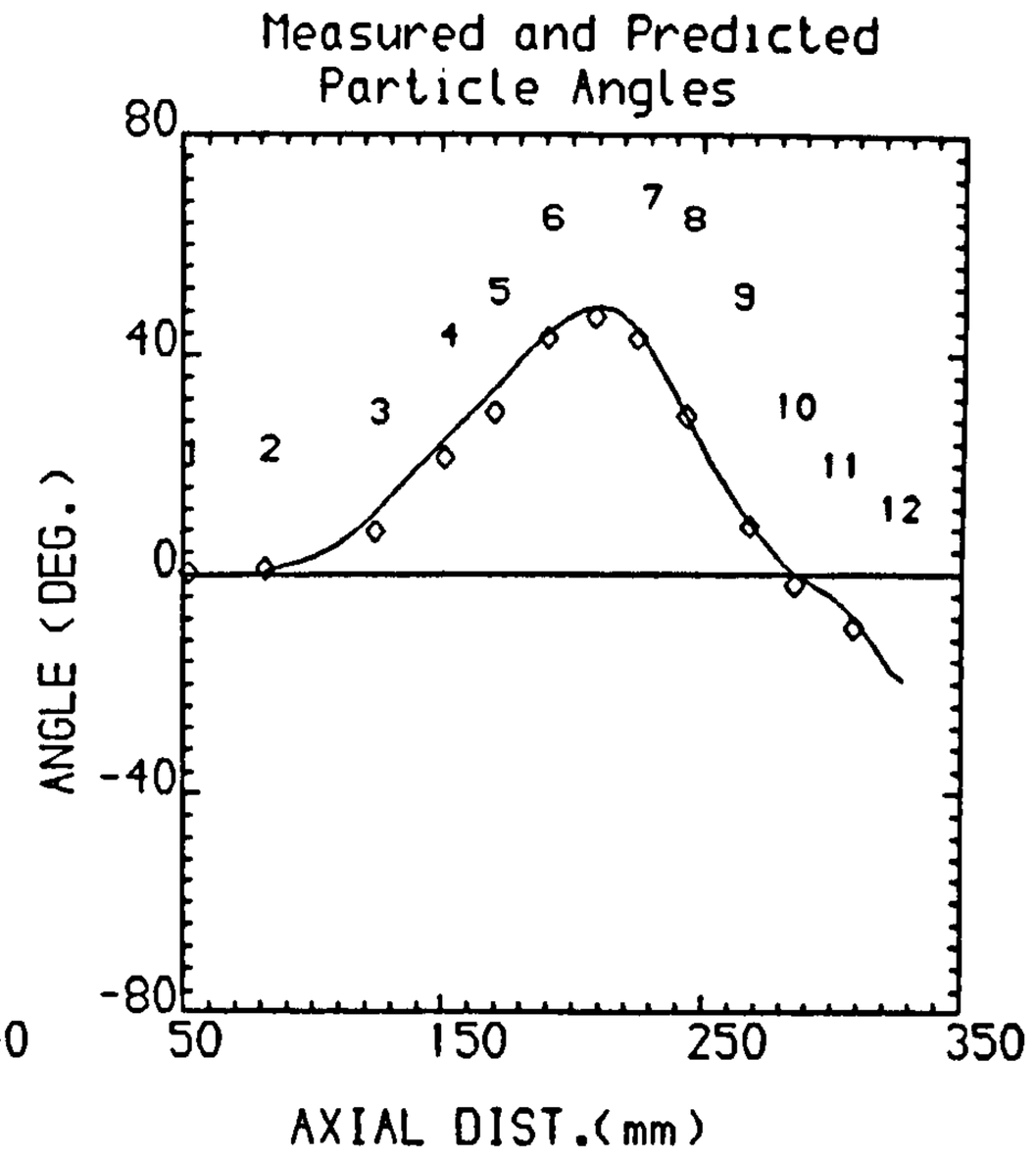

MEASURED AND PREDICTED PARTICLE TRAJECTORIES

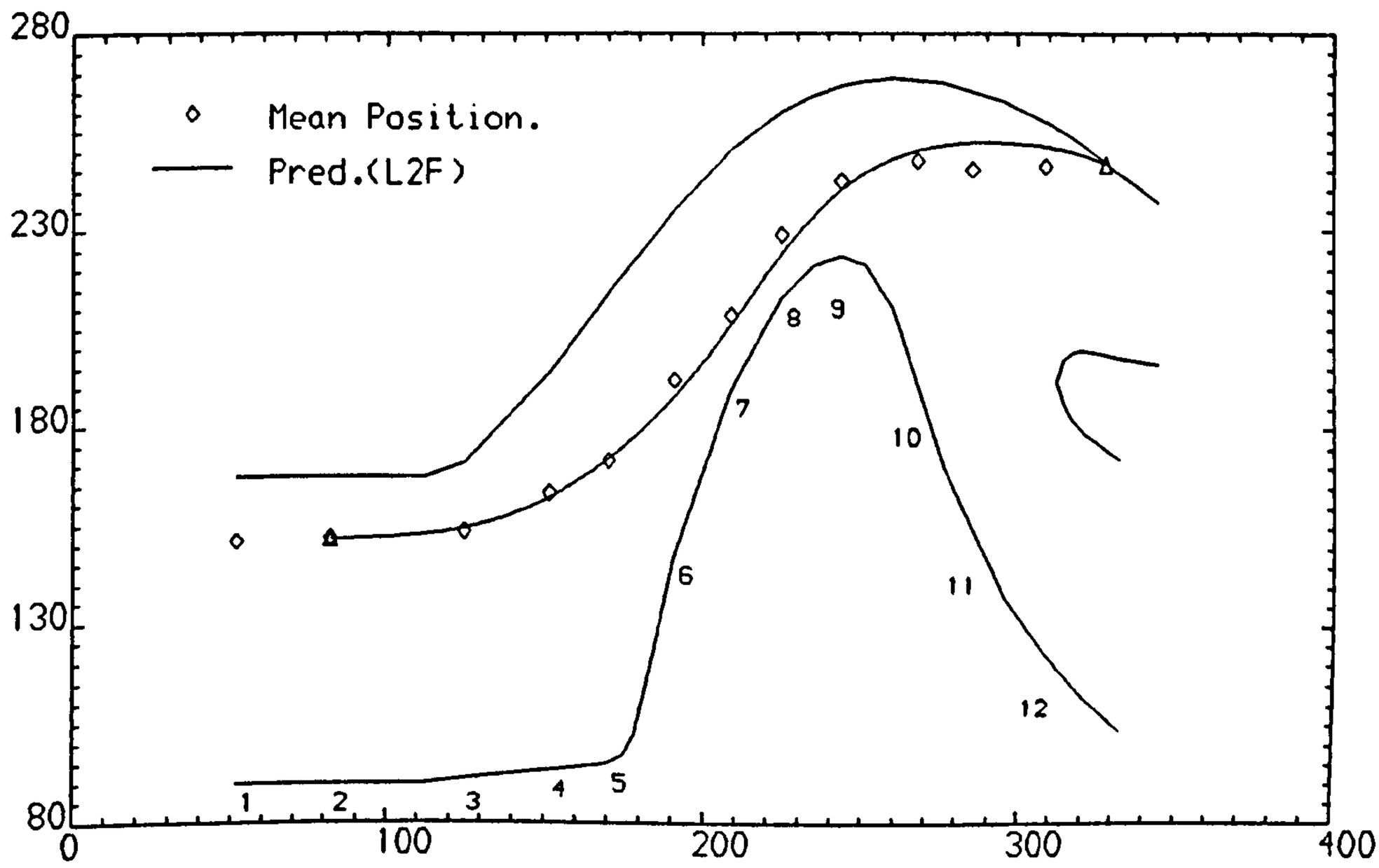

WALL MATL. = AL.	PTLE. DIAMETER = 15.0 um
PTLE. MATL. = QUARTZ	PTLE. INITIAL VEL.= 57.5 m/s
PTLE. DEN. = 2650.0 kg/m3	

FIG.73 MEASURED AND PREDICTED PARTICLE VELOCITIES AND ANGLES AT THE MEAN TRAJECTORY POSITIONS

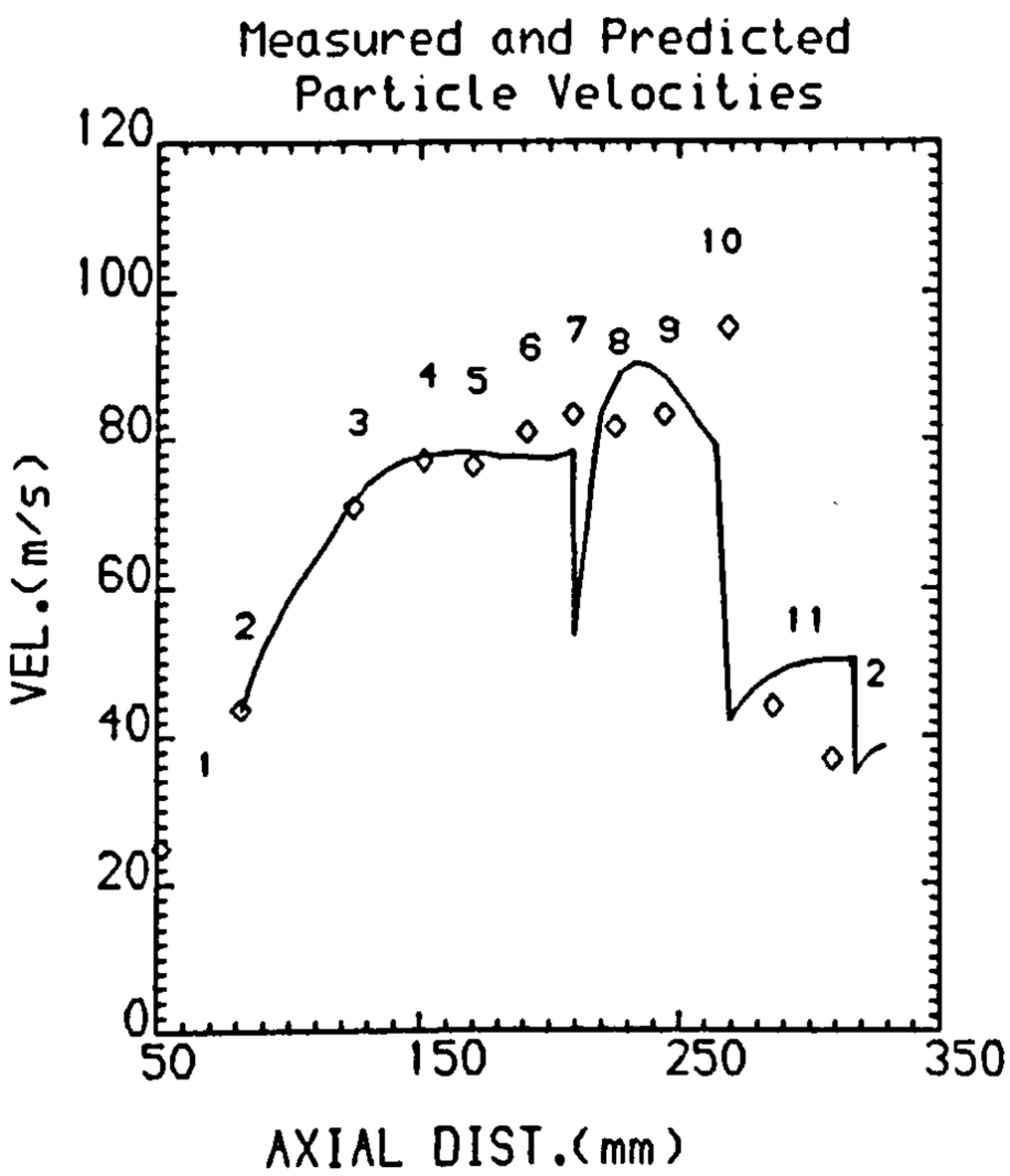

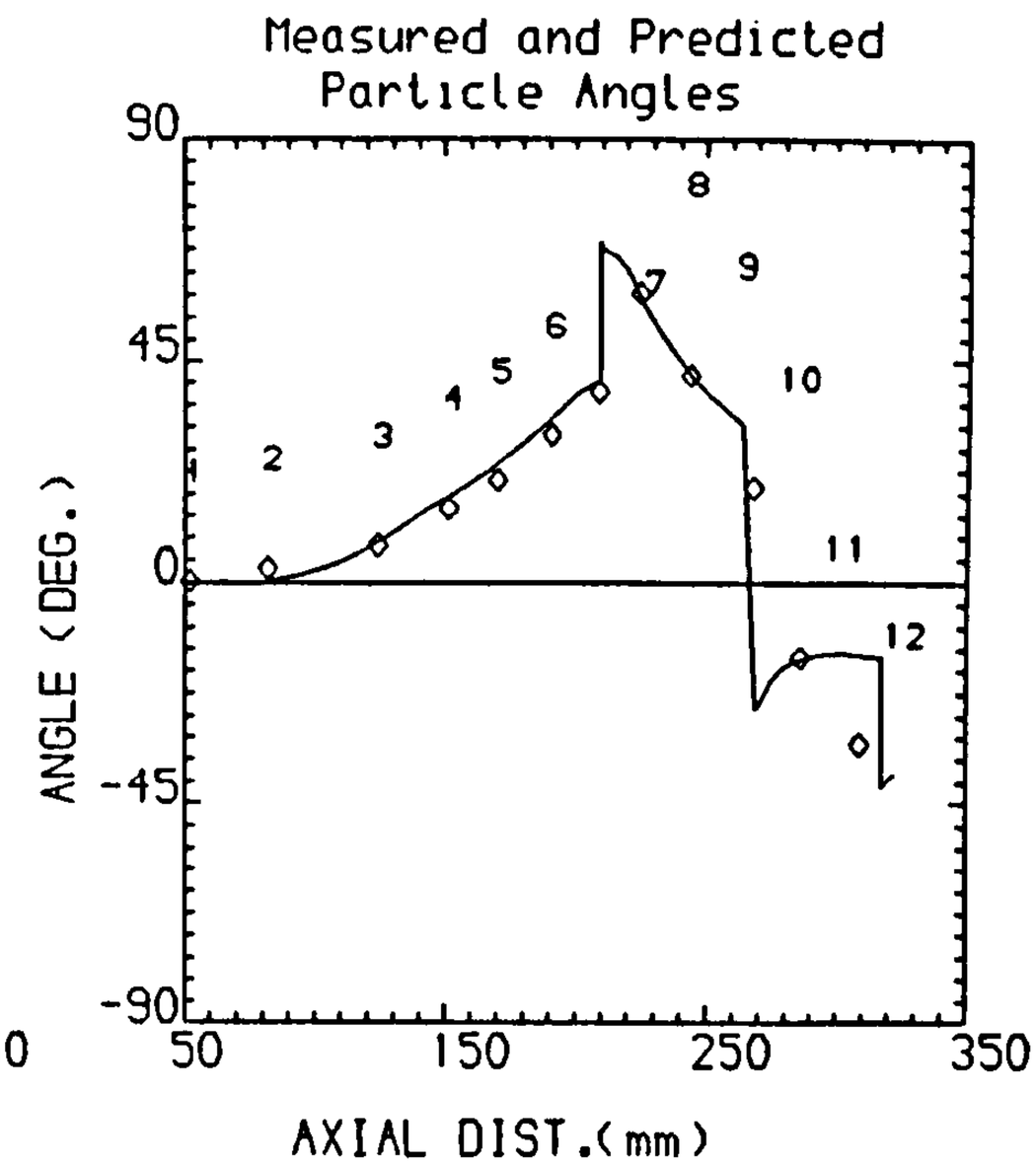

MEASURED AND PREDICTED PARTICLE TRAJECTORIES

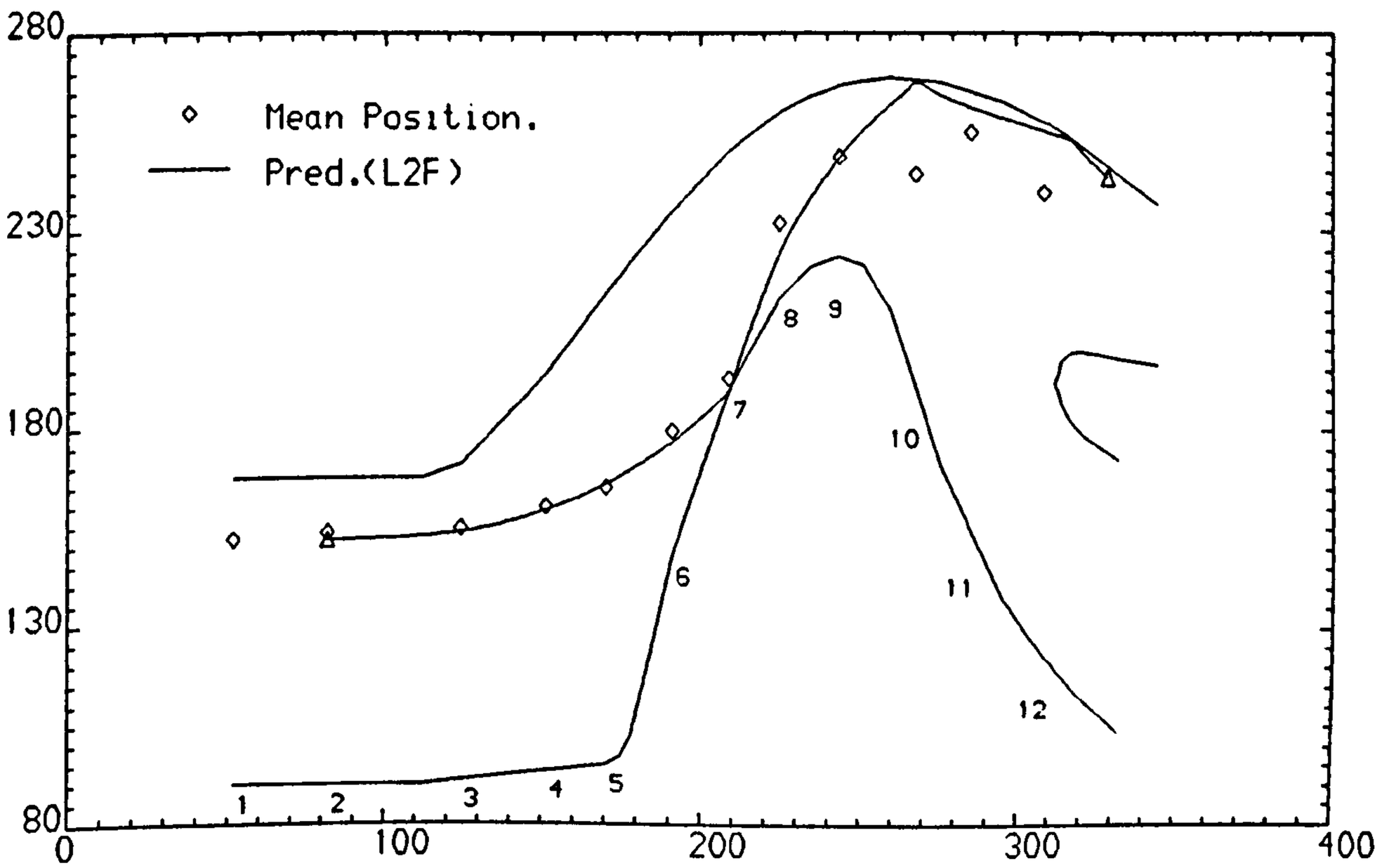

WALL MATL. = AL.
PTLE. MATL. = QUARTZ
PTLE. DEN. = 2650.0 kg/m3
PTLE. DIAMETER = 30.0 um
PTLE. INITIAL VEL.= 43.7 m/s

FIG.74 MEASURED AND PREDICTED PARTICLE VELOCITIES AND ANGLES AT THE MEAN TRAJECTORY POSITIONS

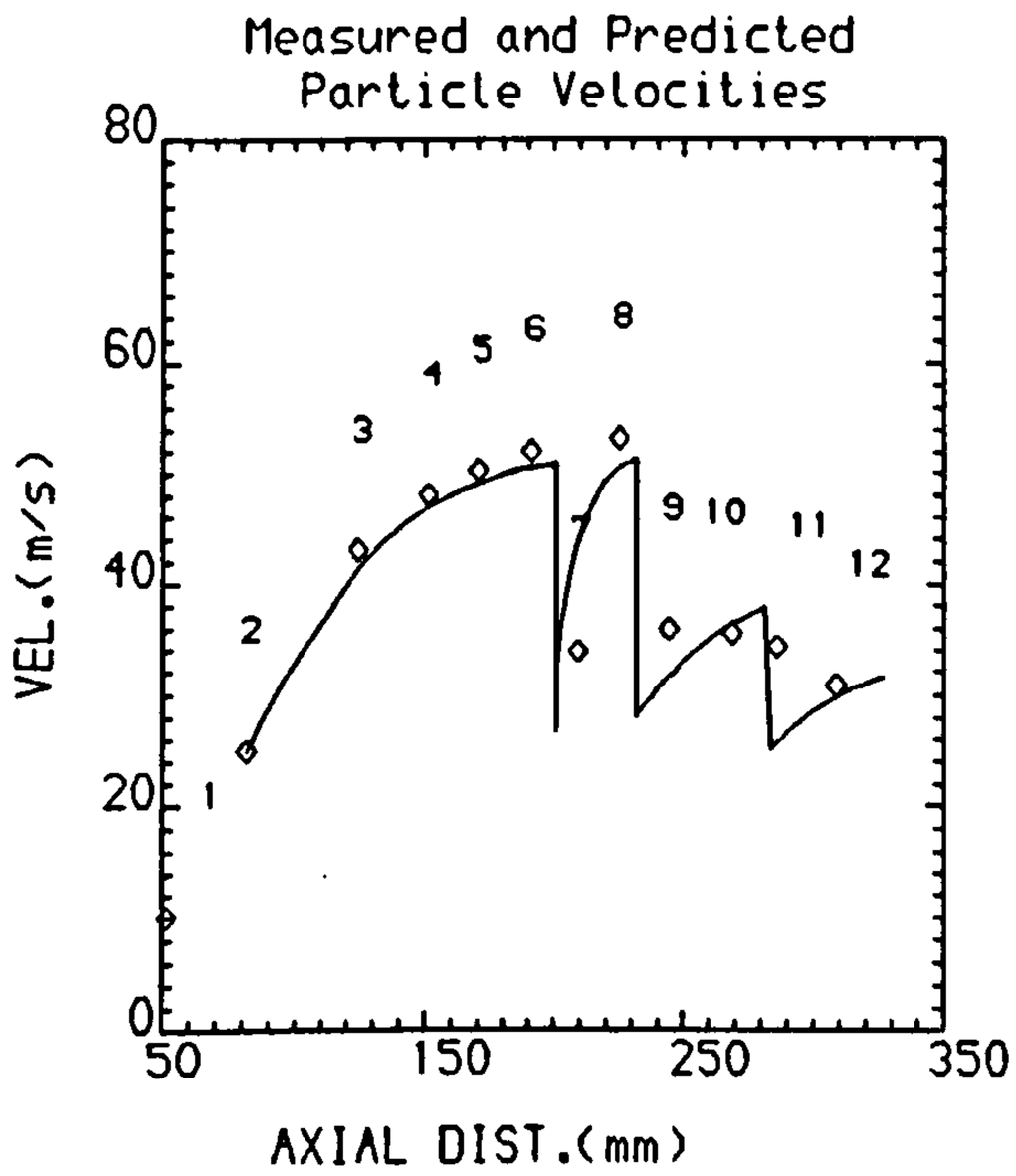

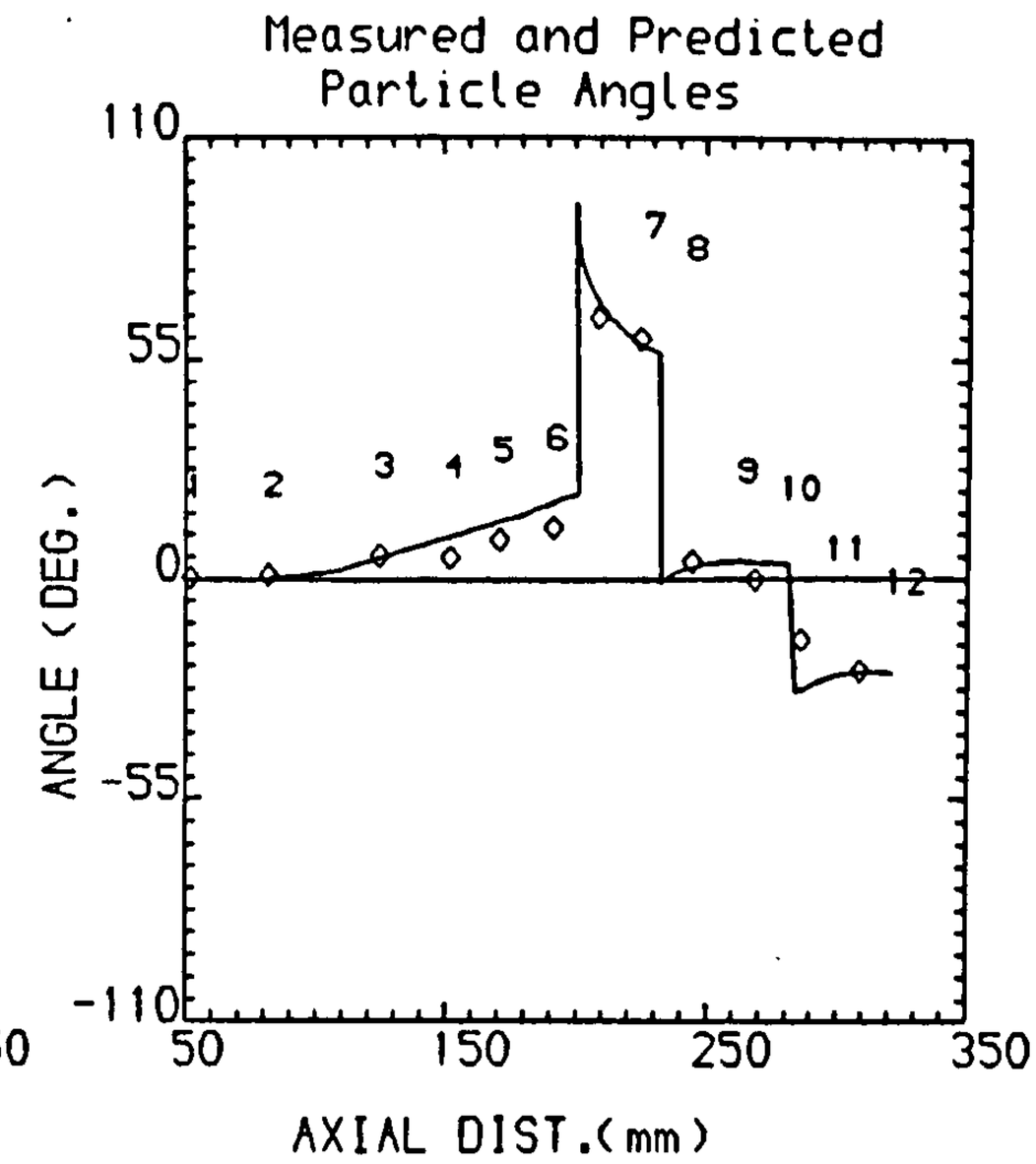

MEASURED AND PREDICTED PARTICLE TRAJECTORIES

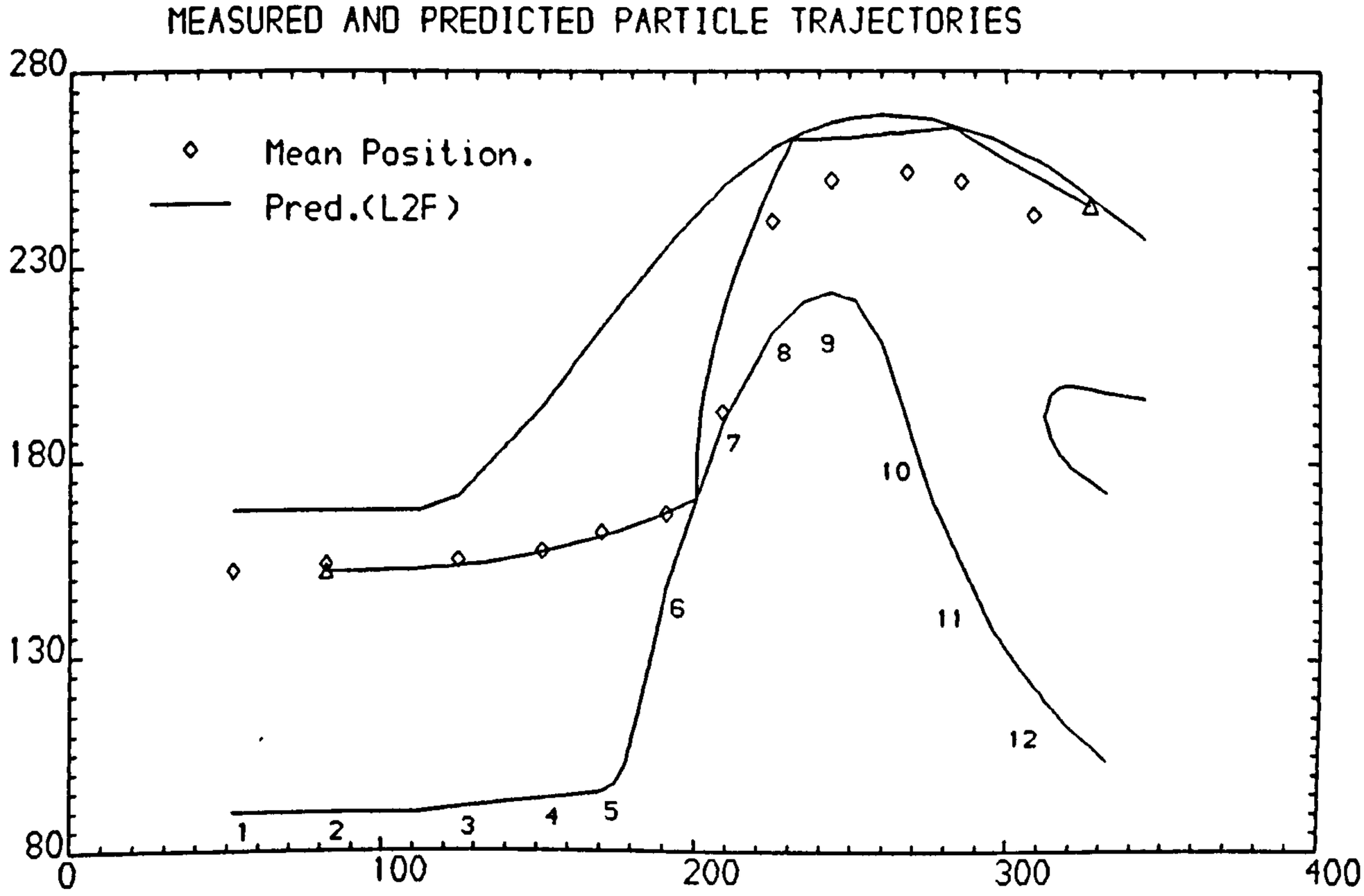

WALL MATL. = AL.
PTLE. MATL. = QUARTZ
PTLE. DEN. = 2650.0 kg/m3
PTLE. DIAMETER = 100.0 um
PTLE. INITIAL VEL.= 25.0 m/s

FIG.75 PREDICTED AND MEASURED PARTICLE CONCENTRATION DISTRIBUTION

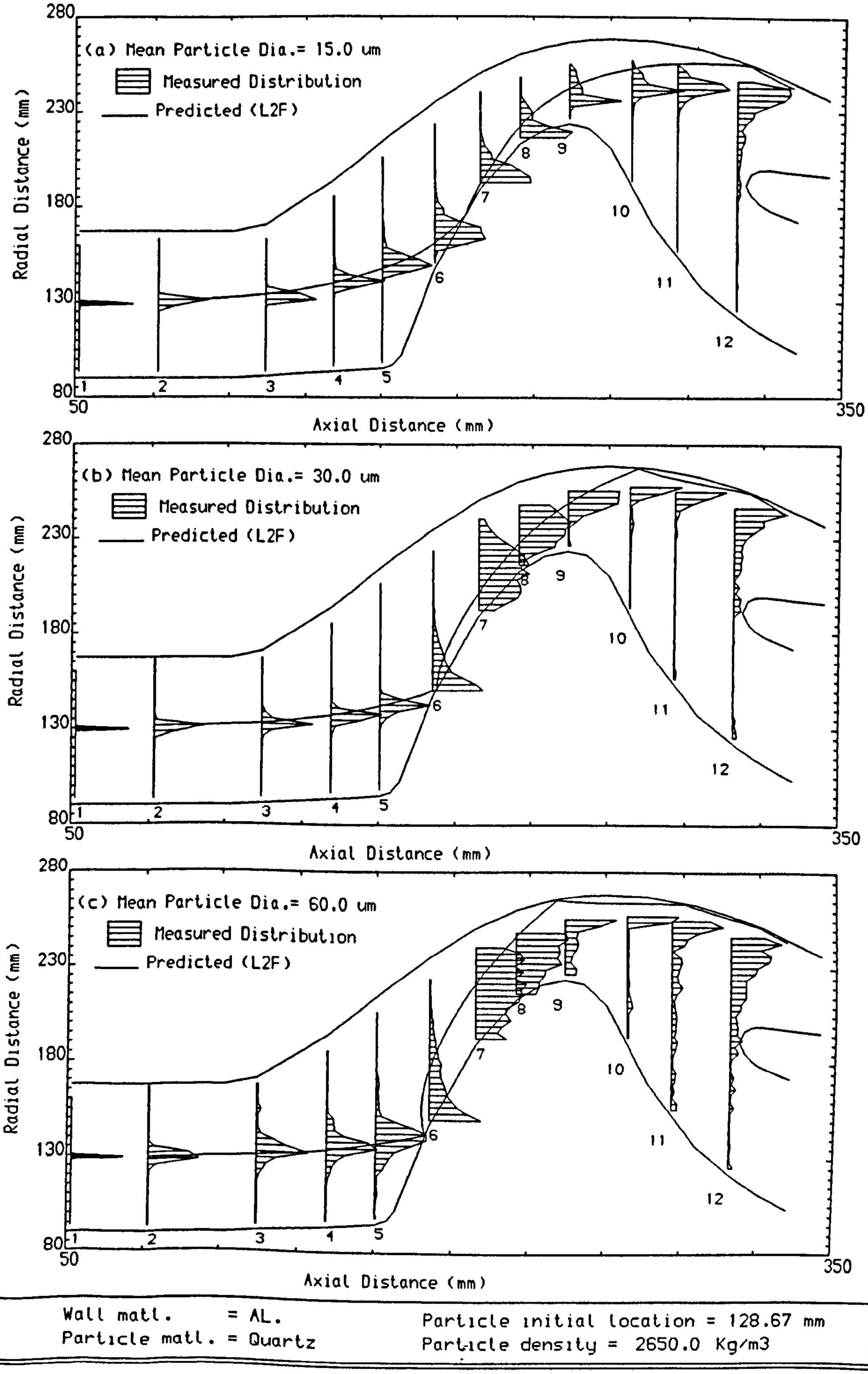

Wall matl. = AL.
Particle matl. = Quartz

Particle initial location = 128.67 mm
Particle density = 2650.0 Kg/m3

FIG.76 PREDICTED AND MEASURED PARTICLE CONCENTRATION DISTRIBUTION

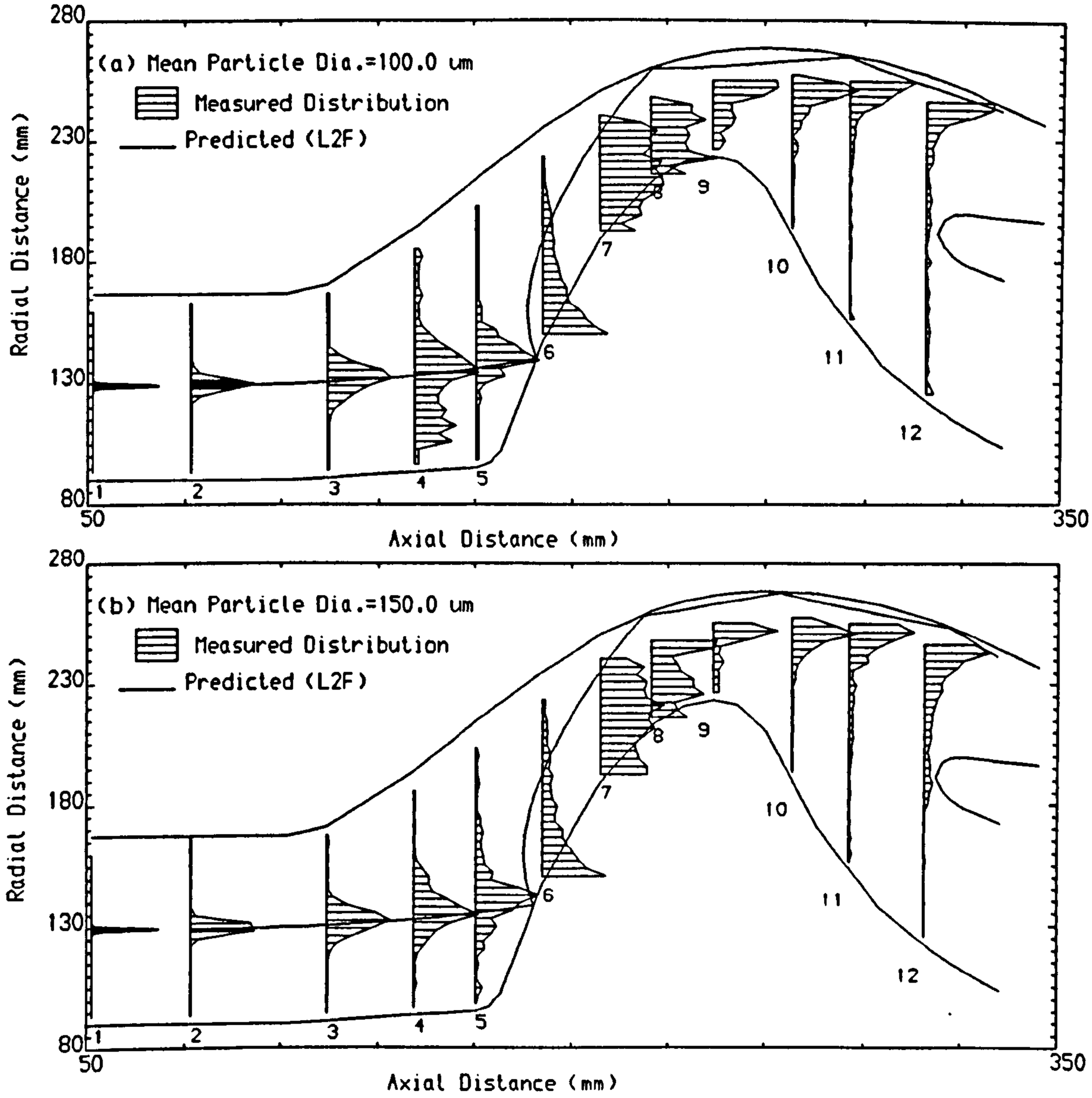

Wall matl. = AL.	Particle initial location = 128.67 mm
Particle matl. = Quartz	Particle density = 2650.0 Kg/m3

FIG.77 MEASURED AND PREDICTED PARTICLE VELOCITIES AND ANGLES AT THE MEAN TRAJECTORY POSITIONS

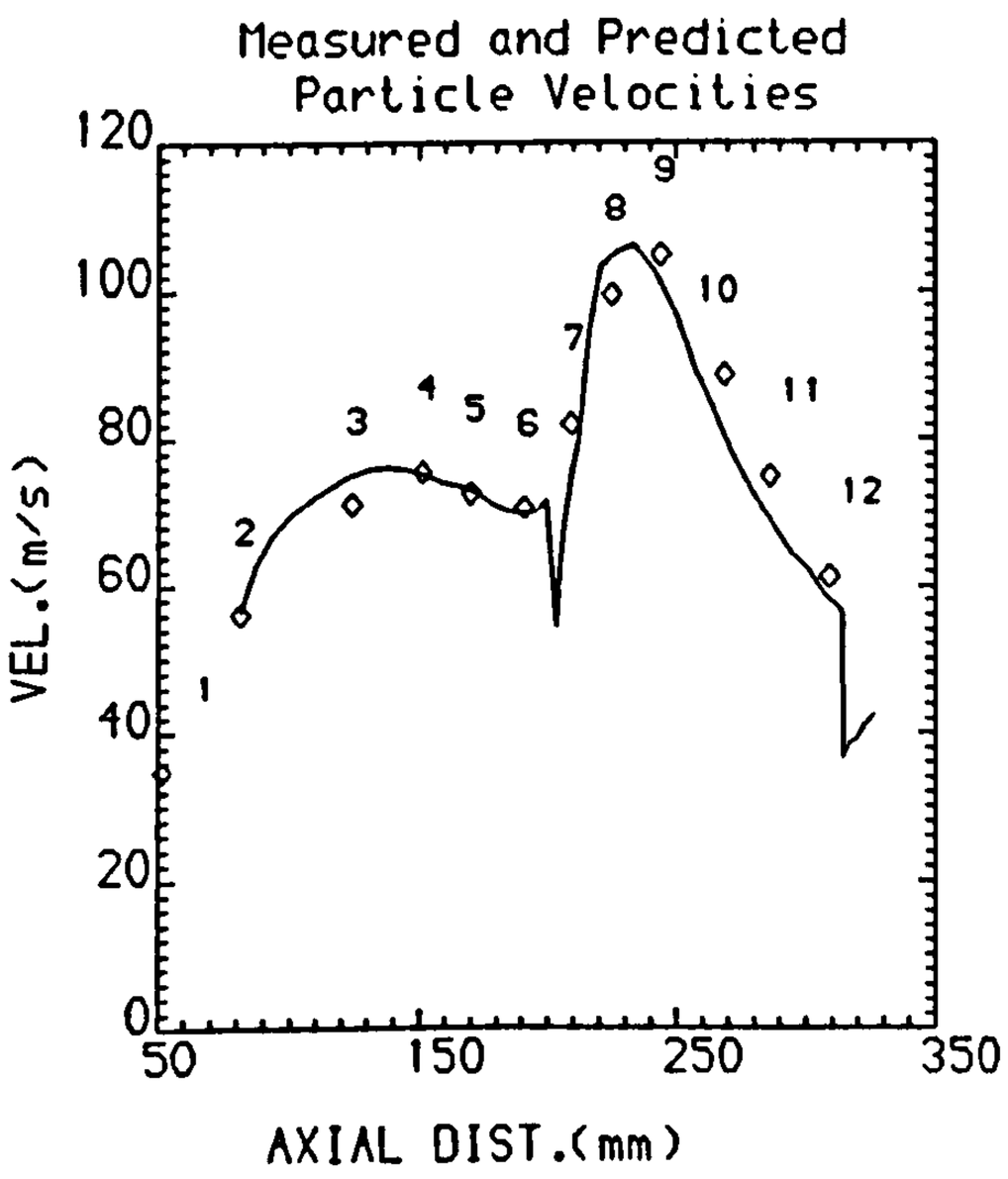

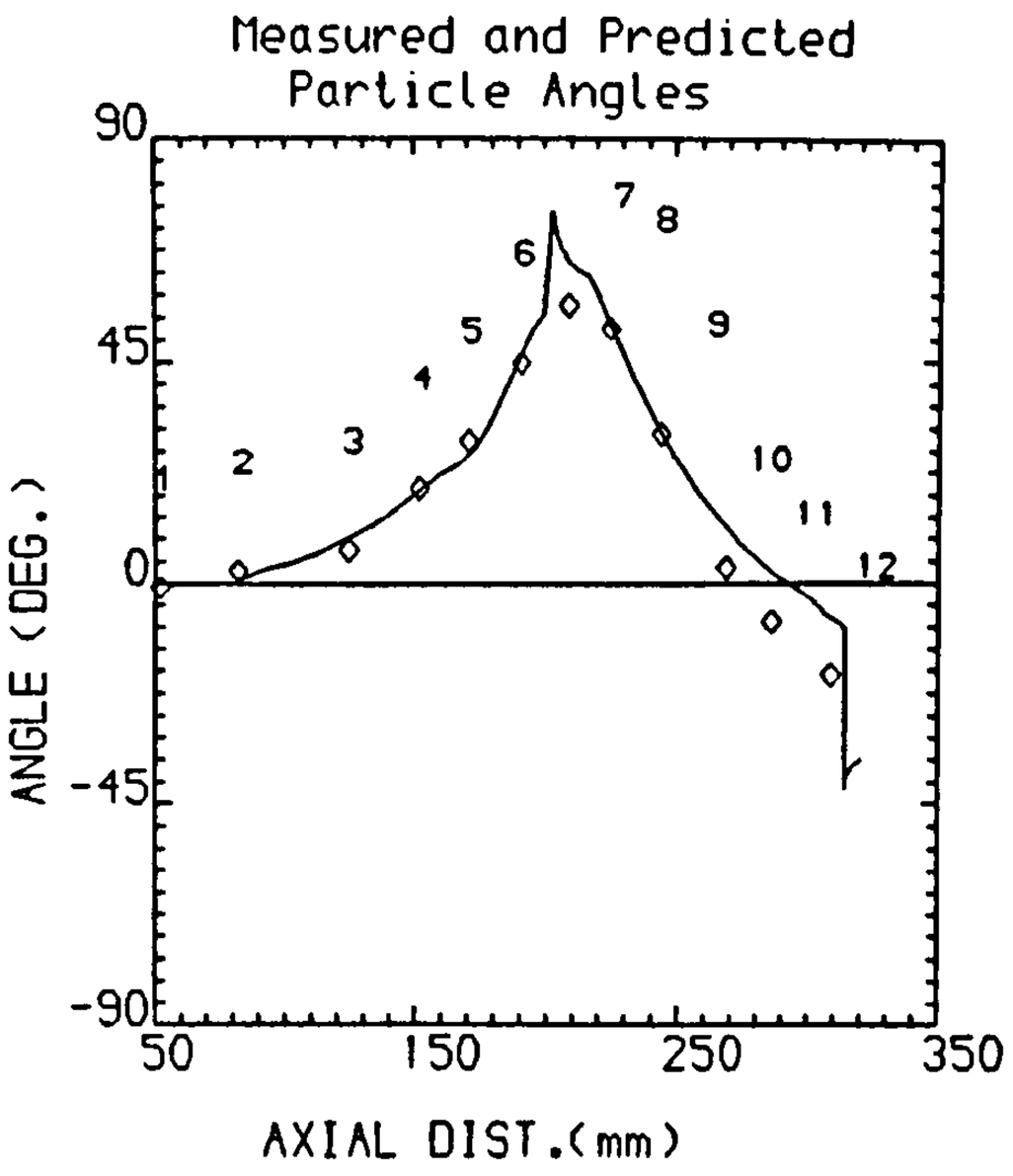

MEASURED AND PREDICTED PARTICLE TRAJECTORIES

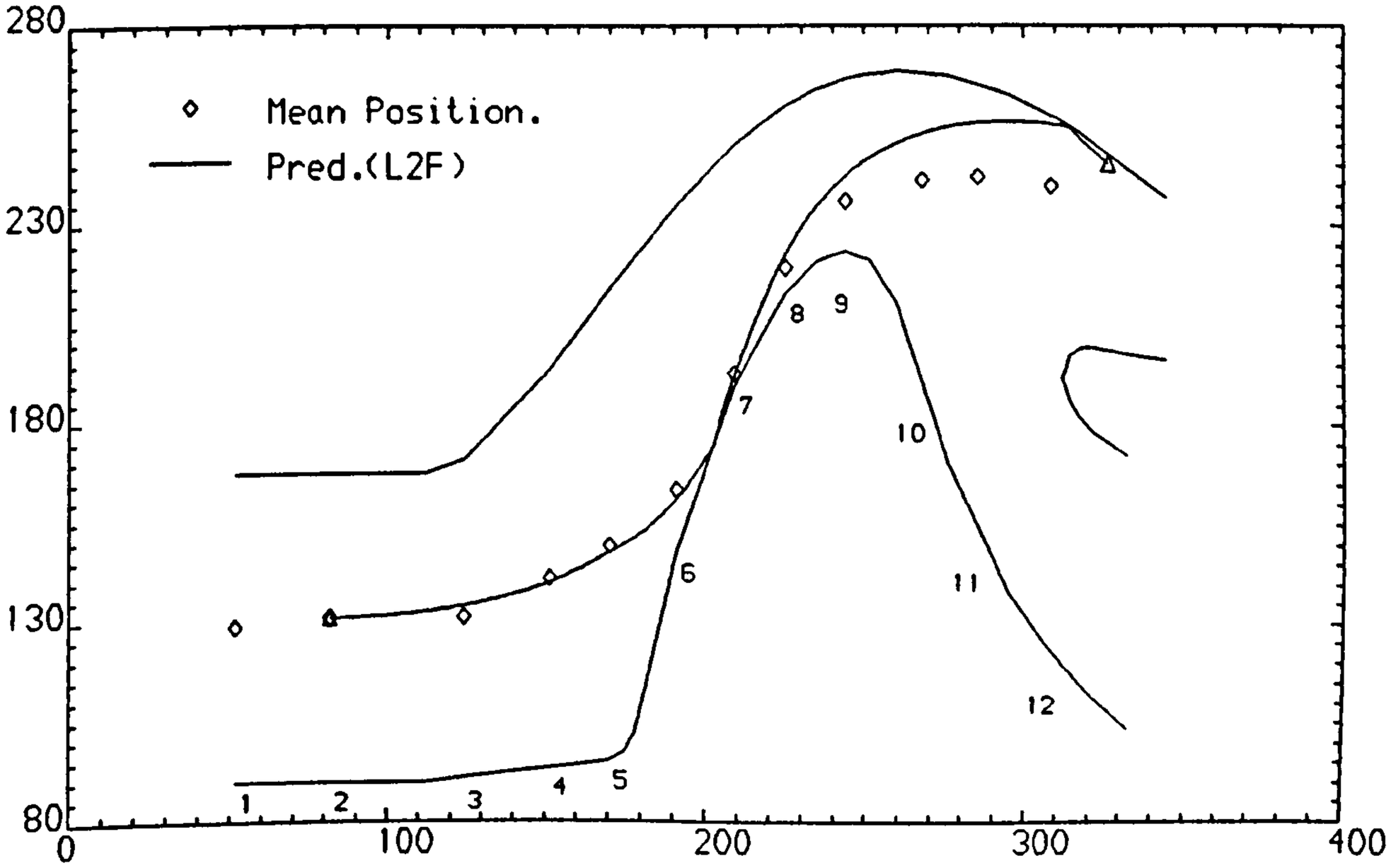

WALL MATL. = AL.
PTLE. MATL. = QUARTZ
PTLE. DEN. = 2650.0 kg/m3
PTLE. DIAMETER = 15.0 um
PTLE. INITIAL VEL.= 56.1 m/s

FIG.78 MEASURED AND PREDICTED PARTICLE VELOCITIES AND ANGLES AT THE MEAN TRAJECTORY POSITIONS

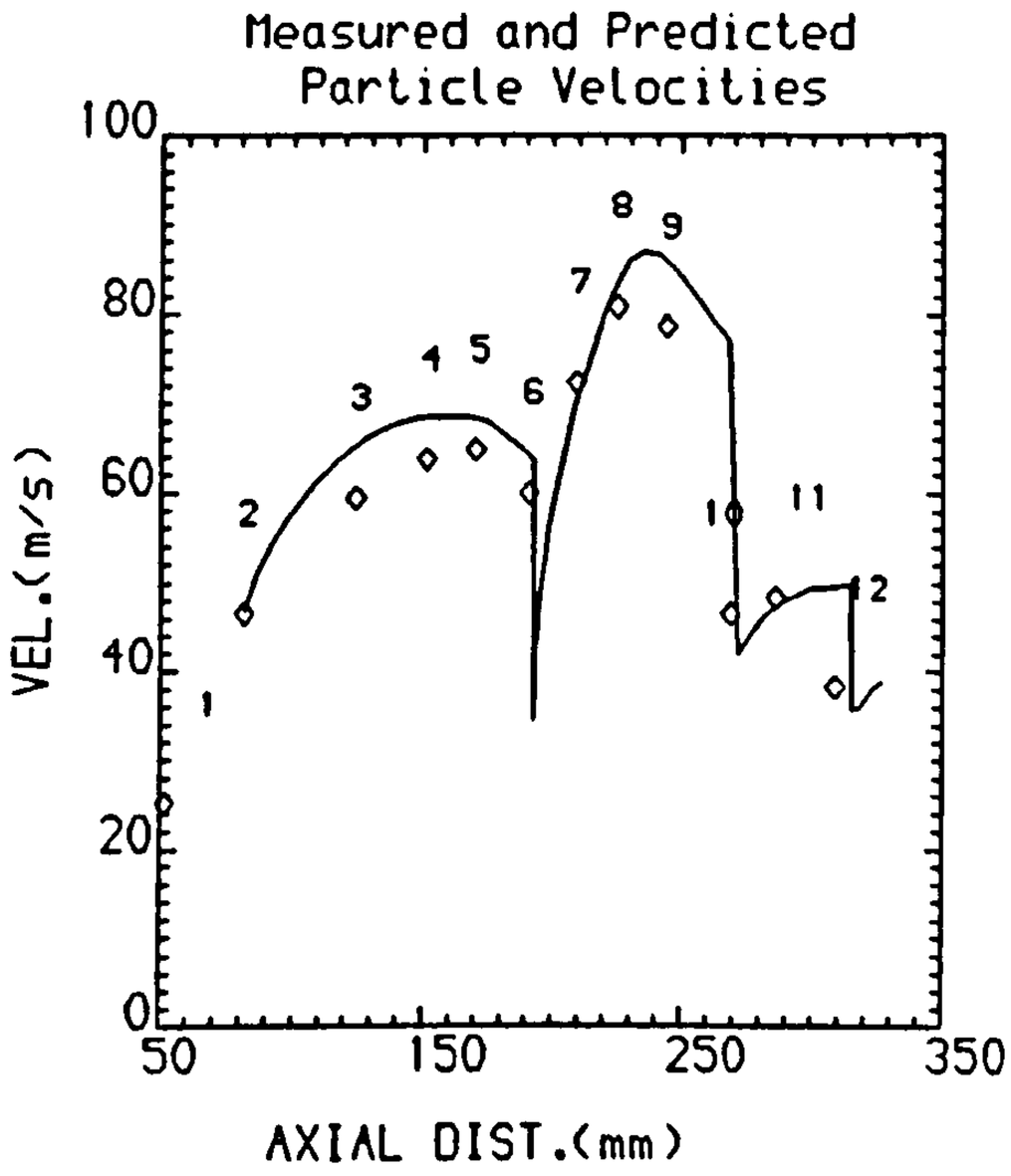

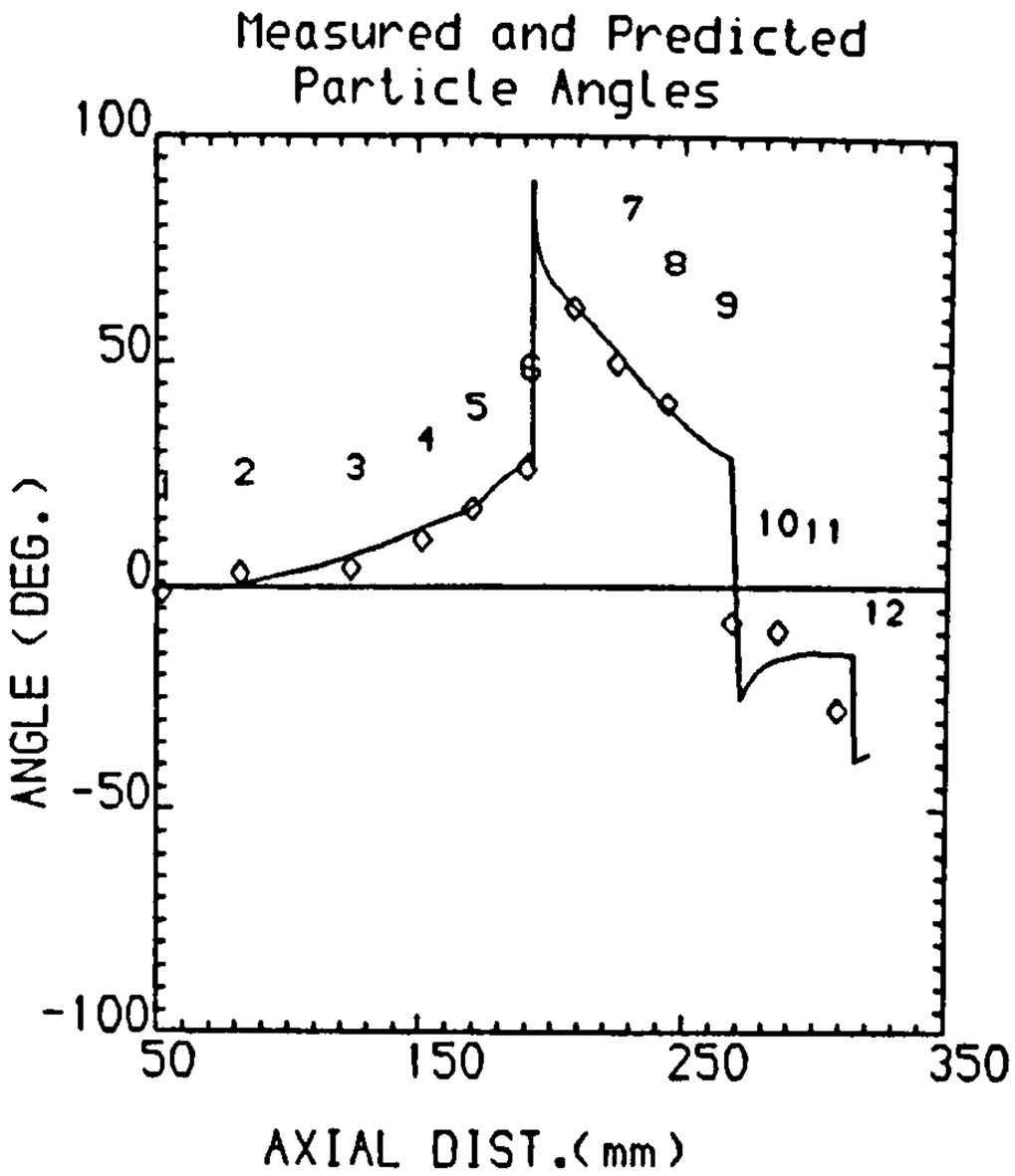

MEASURED AND PREDICTED PARTICLE TRAJECTORIES

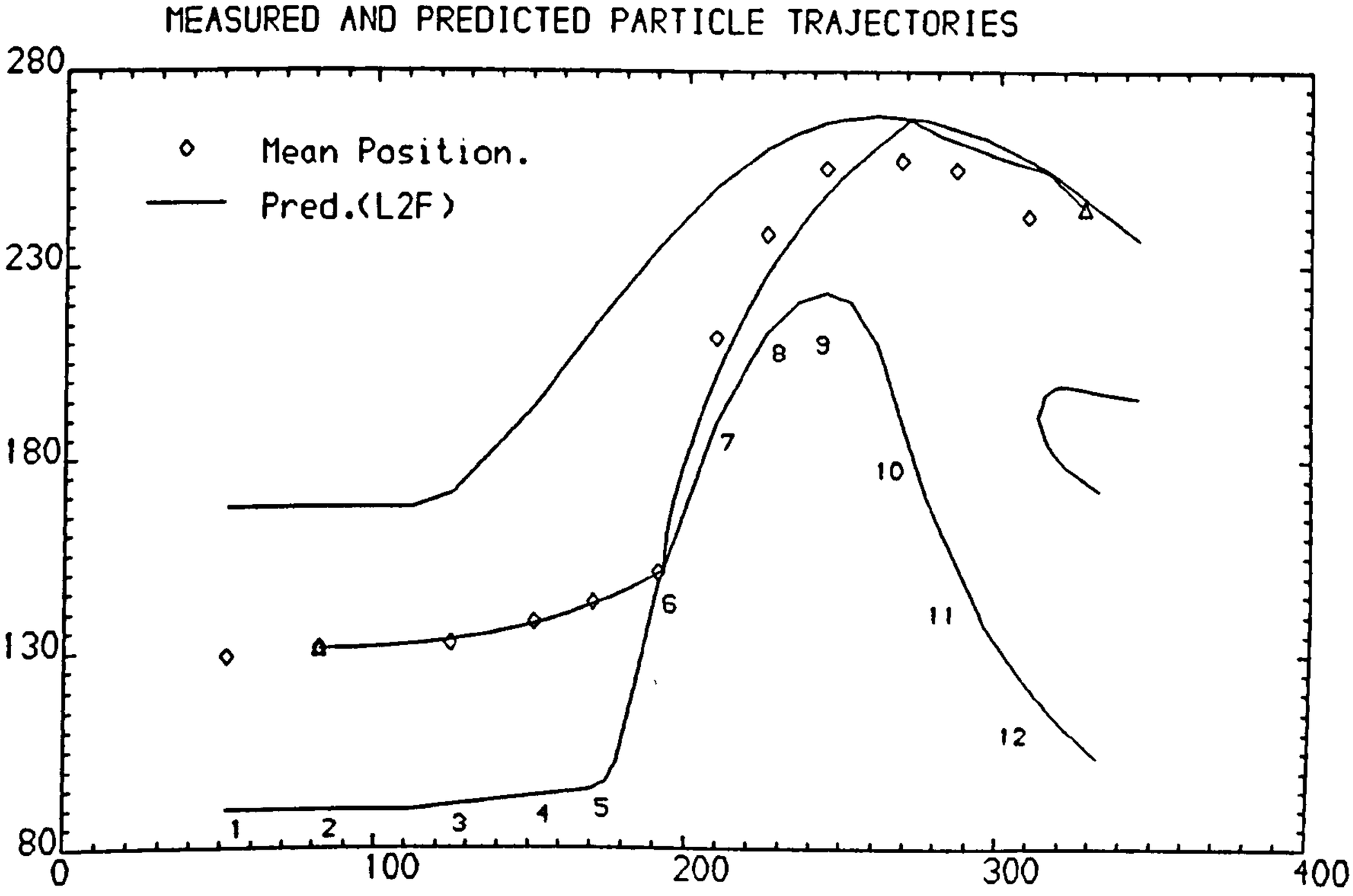

WALL MATL. = AL.
PTLE. MATL. = QUARTZ
PTLE. DEN. = 2650.0 kg/m3
PTLE. DIAMETER = 30.0 um
PTLE. INITIAL VEL.= 46.6 m/s

FIG.79 MEASURED AND PREDICTED PARTICLE VELOCITIES AND ANGLES AT THE MEAN TRAJECTORY POSITIONS

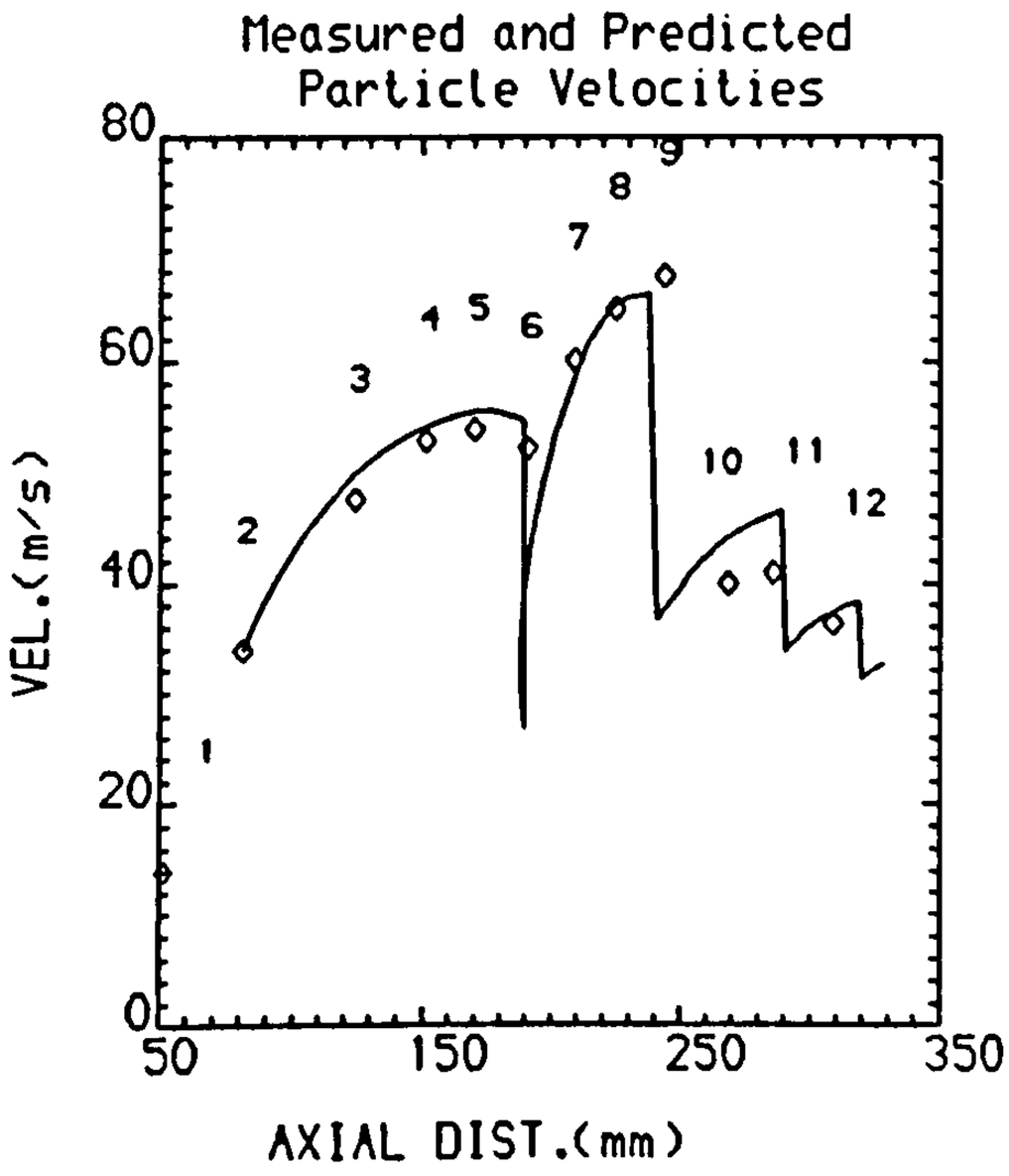

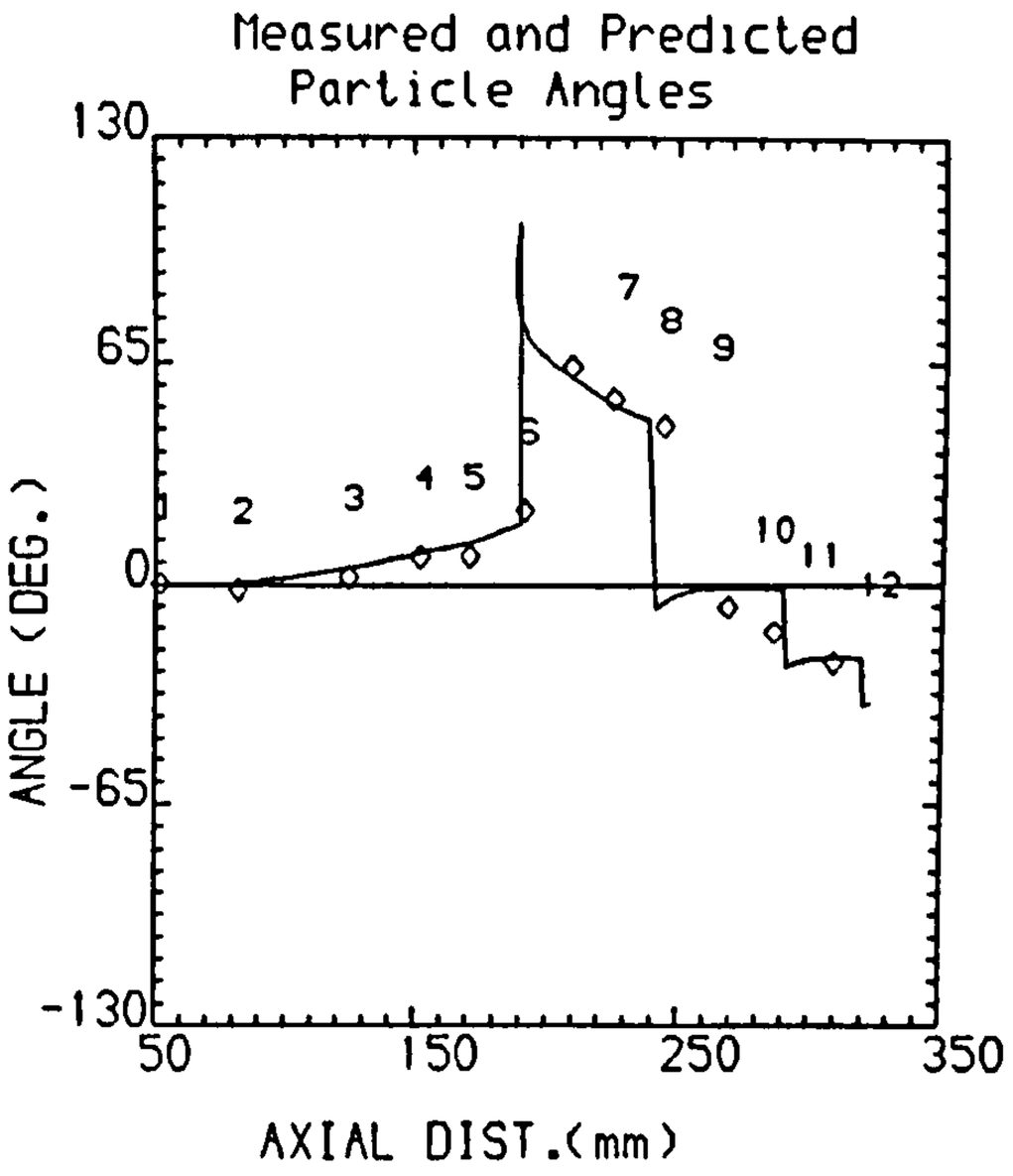

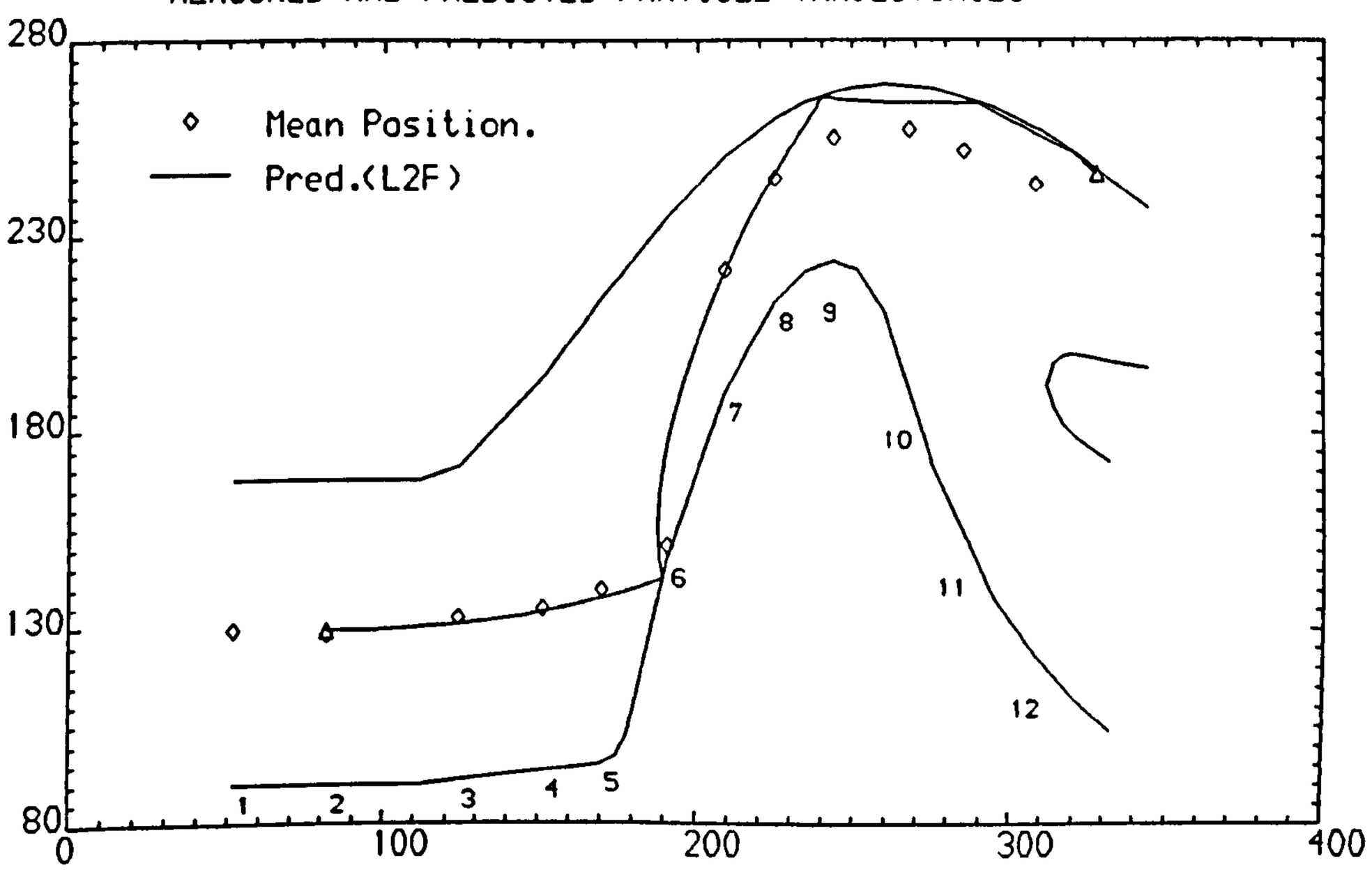

WALL MATL. = AL.	PTLE. DIAMETER = 60.0 um
PTLE. MATL. = QUARTZ	PTLE. INITIAL VEL.= 33.9 m/s
PTLE. DEN. = 2650.0 kg/m3	

FIG.80 MEASURED AND PREDICTED PARTICLE VELOCITIES AND ANGLES AT THE MEAN TRAJECTORY POSITIONS

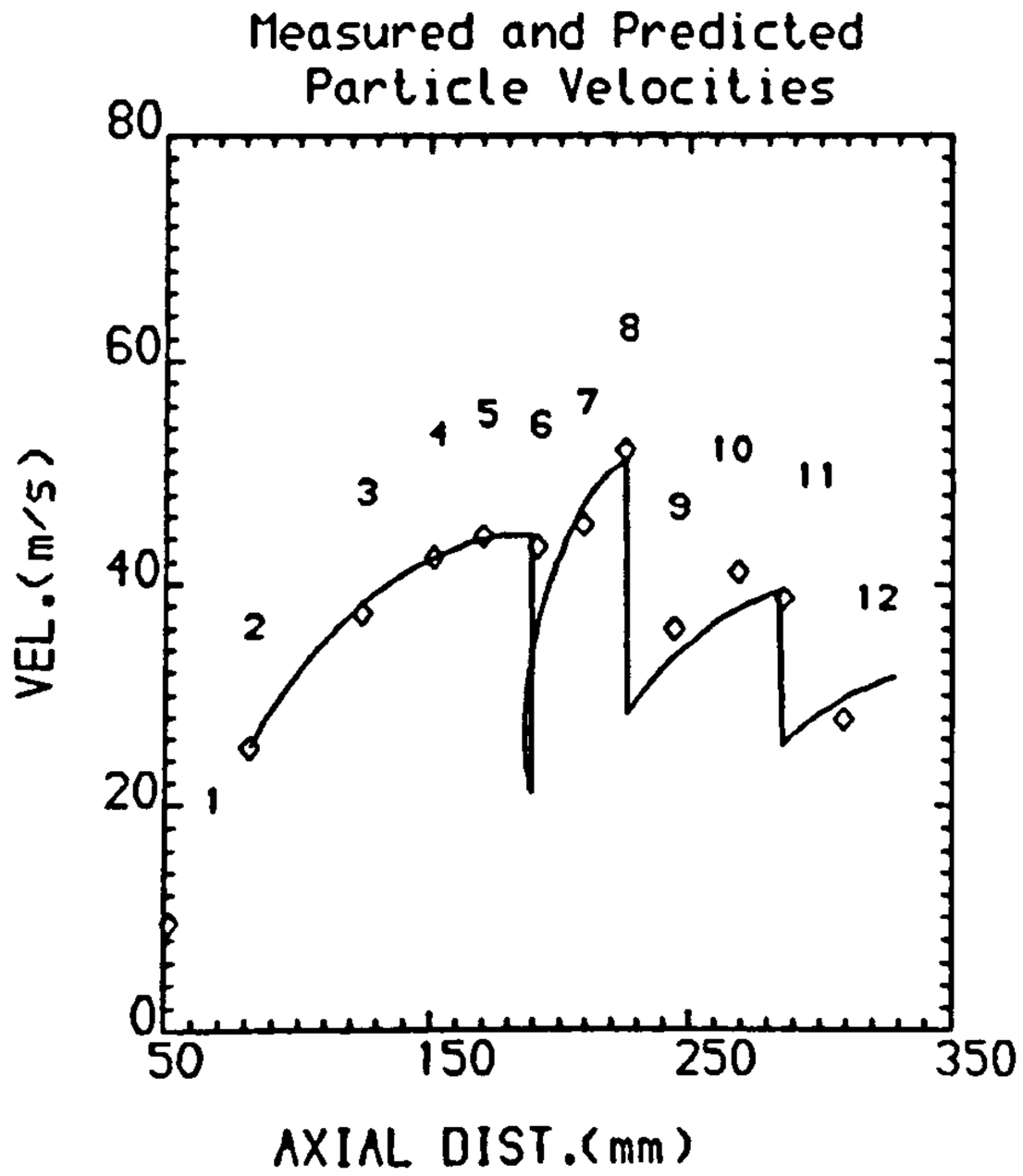

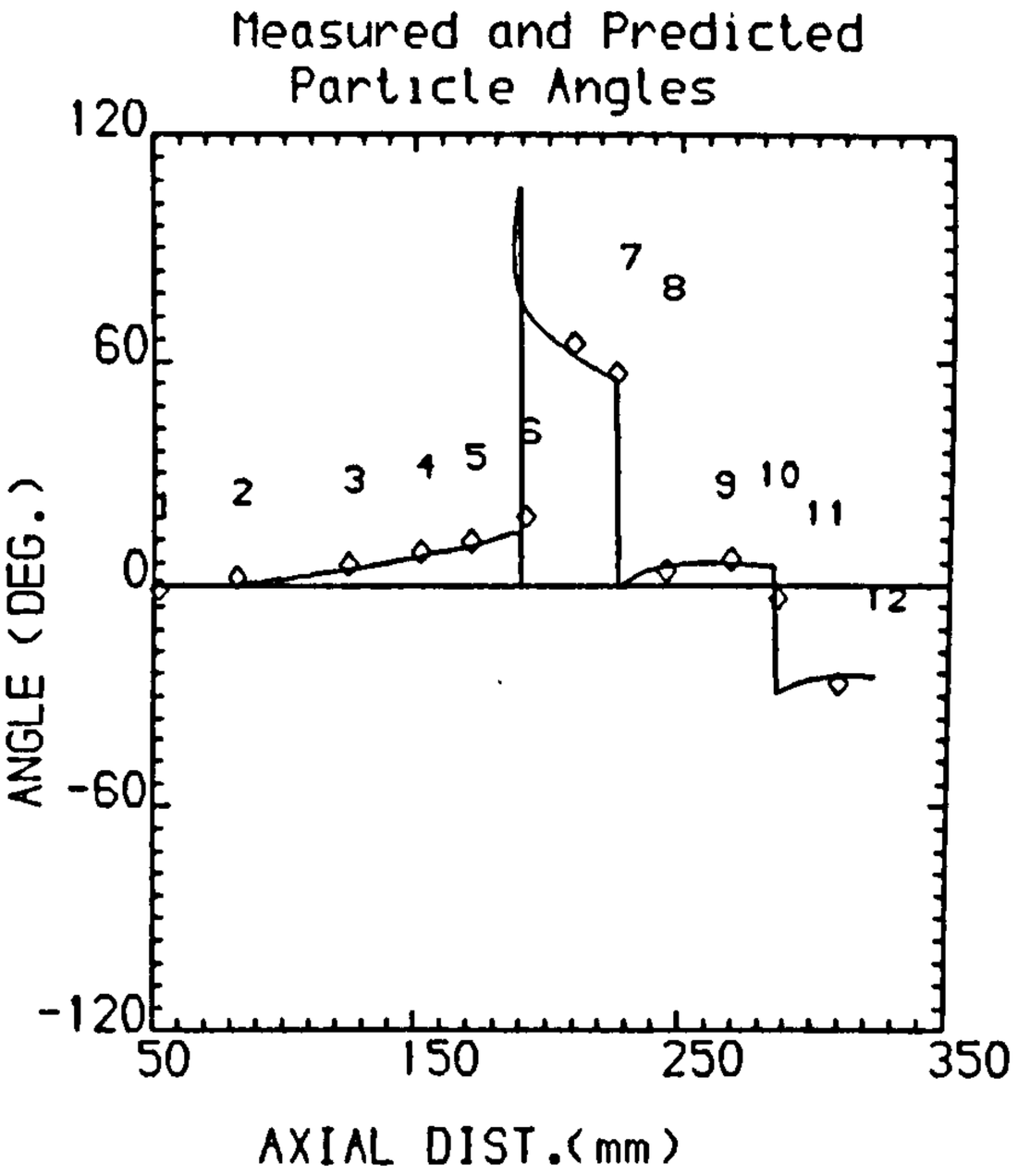

MEASURED AND PREDICTED PARTICLE TRAJECTORIES

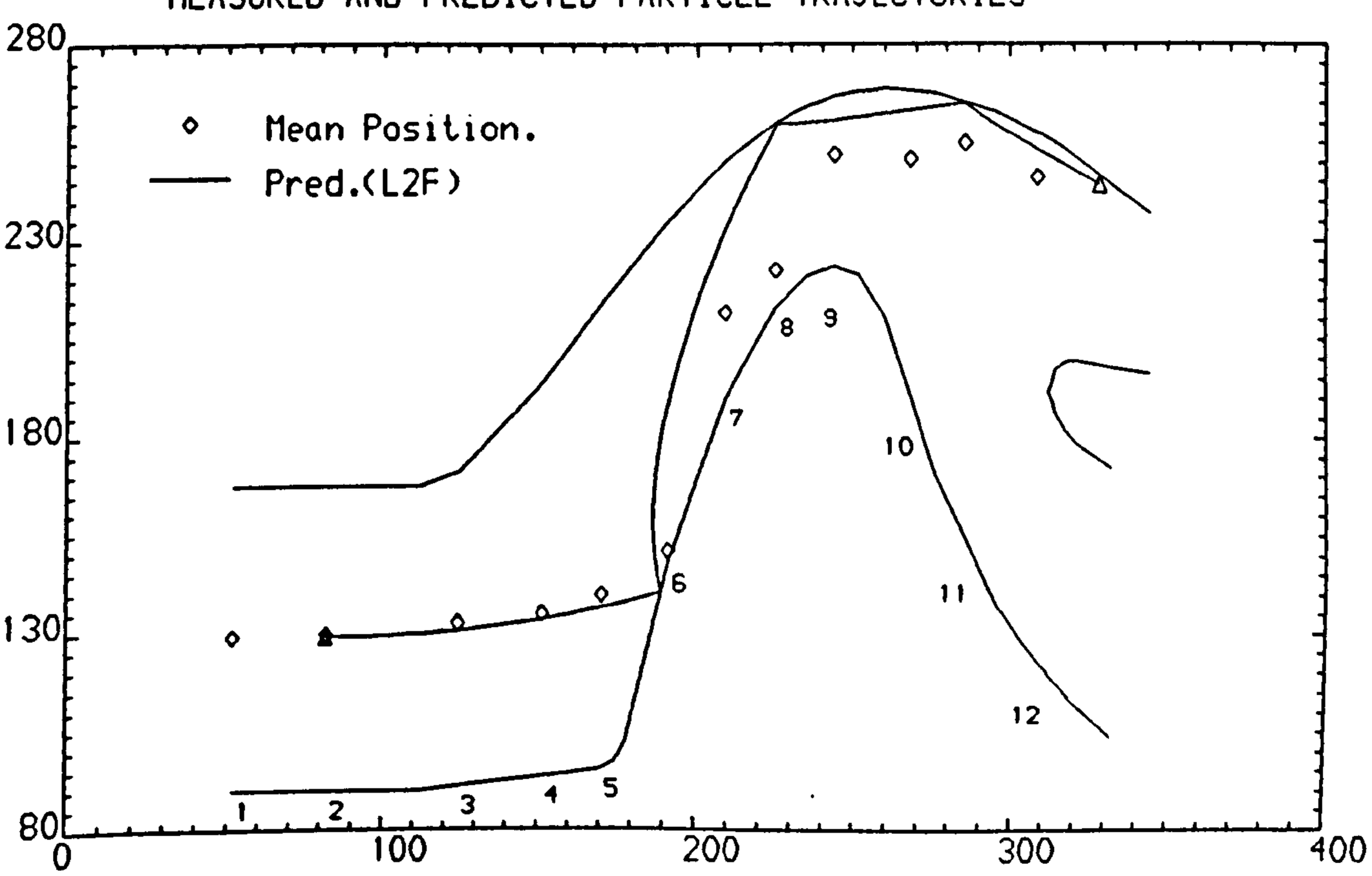

WALL MATL. = AL.
PTLE. MATL. = QUARTZ
PTLE. DEN. = 2650.0 kg/m3
PTLE. DIAMETER = 100.0 um
PTLE. INITIAL VEL.= 25.2 m/s

FIG.81 MEASURED AND PREDICTED PARTICLE VELOCITIES AND ANGLES AT THE MEAN TRAJECTORY POSITIONS

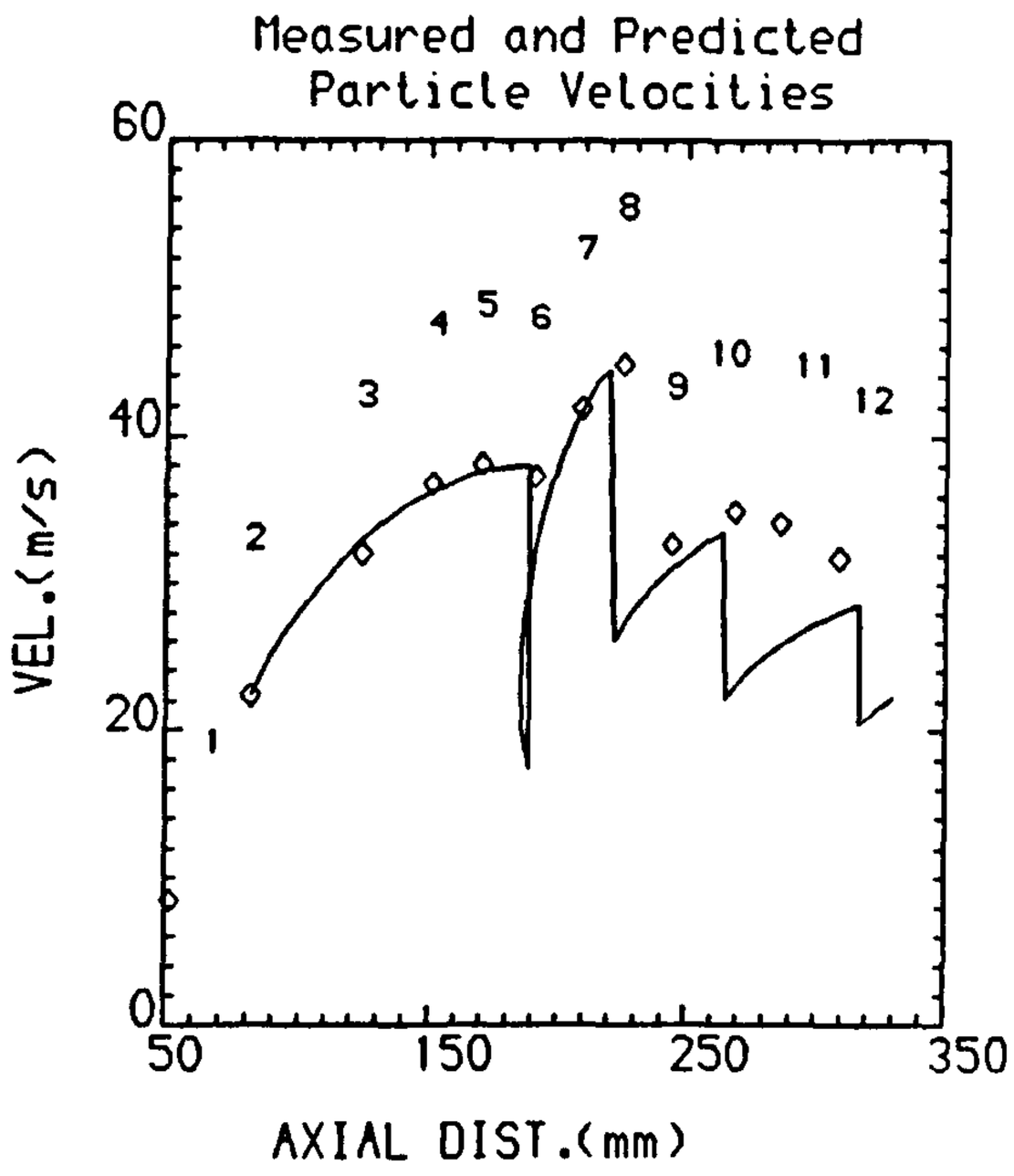

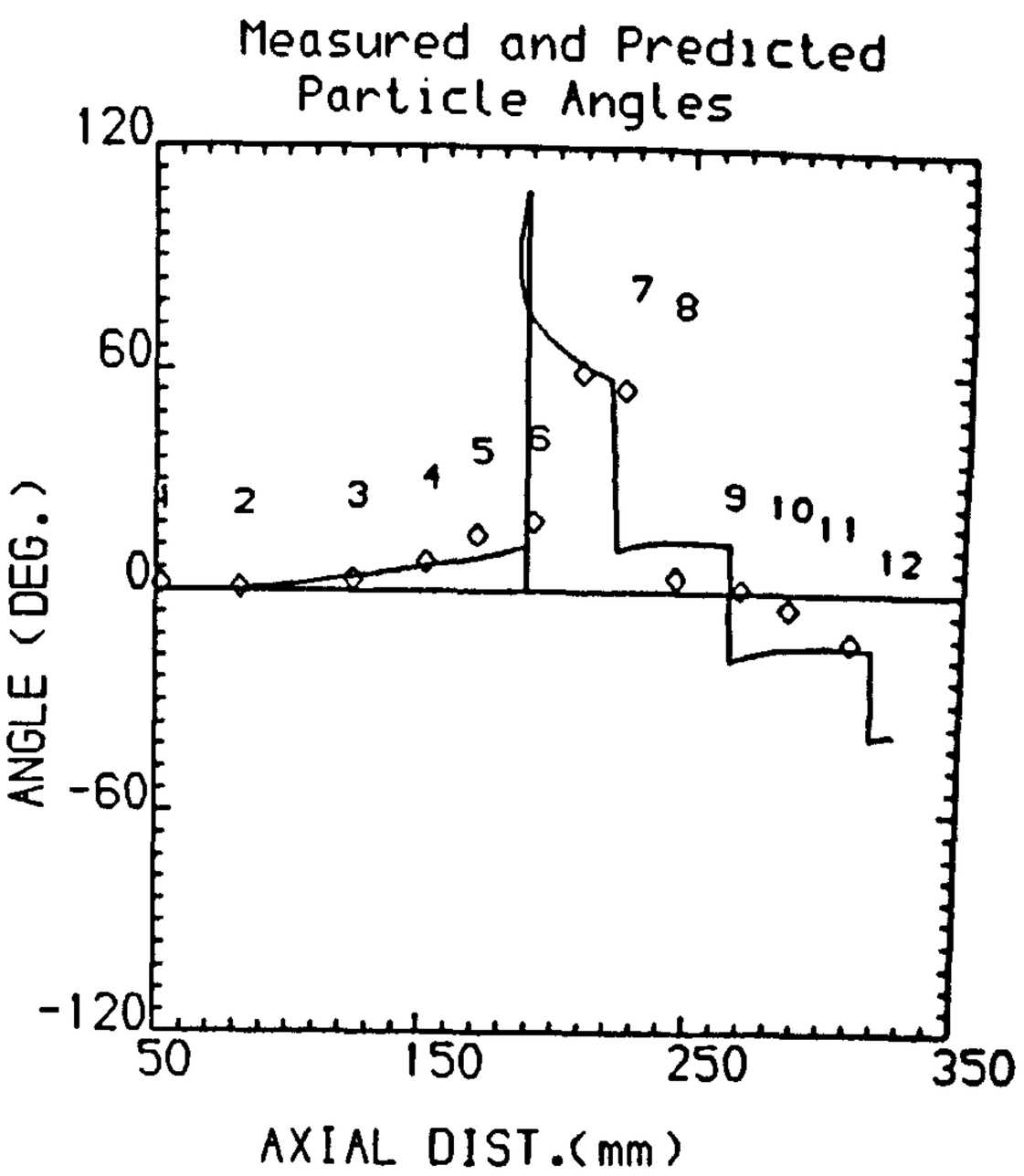

MEASURED AND PREDICTED PARTICLE TRAJECTORIES

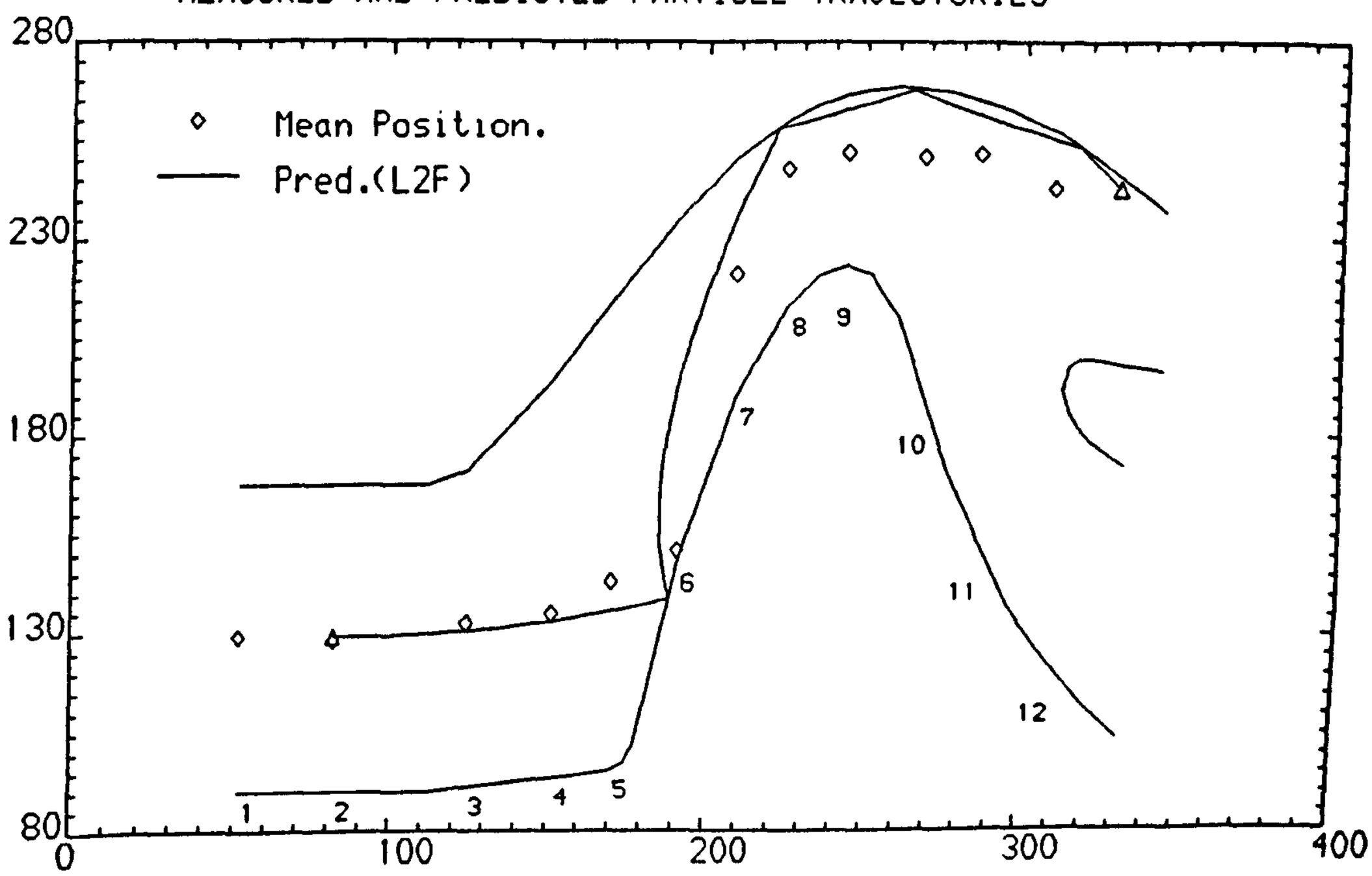

WALL MATL. = AL.	PTLE. DIAMETER = 150.0 um
PTLE. MATL. = QUARTZ	PTLE. INITIAL VEL.= 22.4 m/s
PTLE. DEN. = 2650.0 kg/m3	

FIG.82 PREDICTED AND MEASURED PARTICLE CONCENTRATION DISTRIBUTION

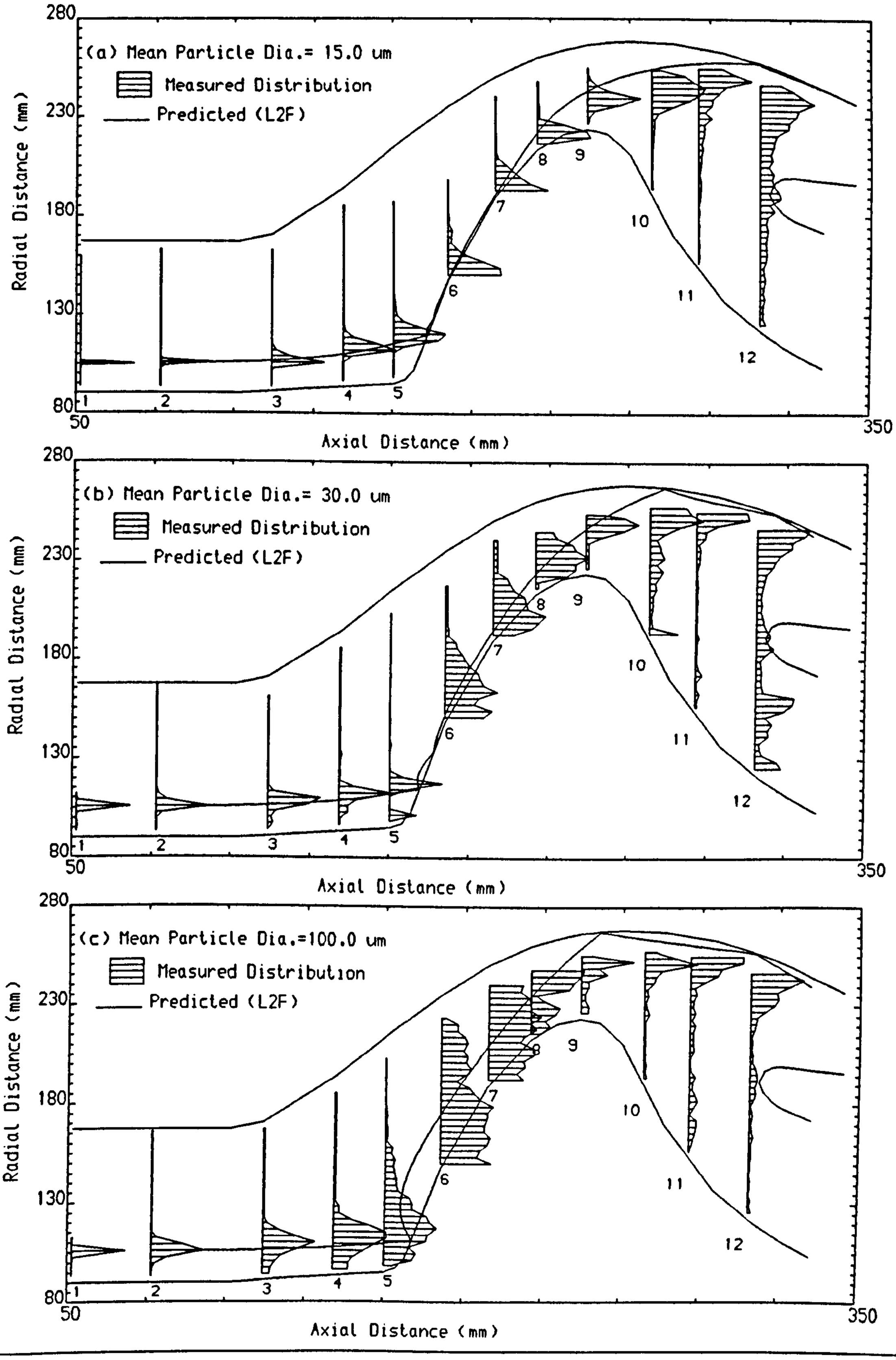

Wall matl. = AL.
Particle matl. = Quartz
Particle initial location = 105.50 mm
Particle density = 2650.0 Kg/m3

FIG.83 MEASURED AND PREDICTED PARTICLE VELOCITIES AND ANGLES AT THE MEAN TRAJECTORY POSITIONS

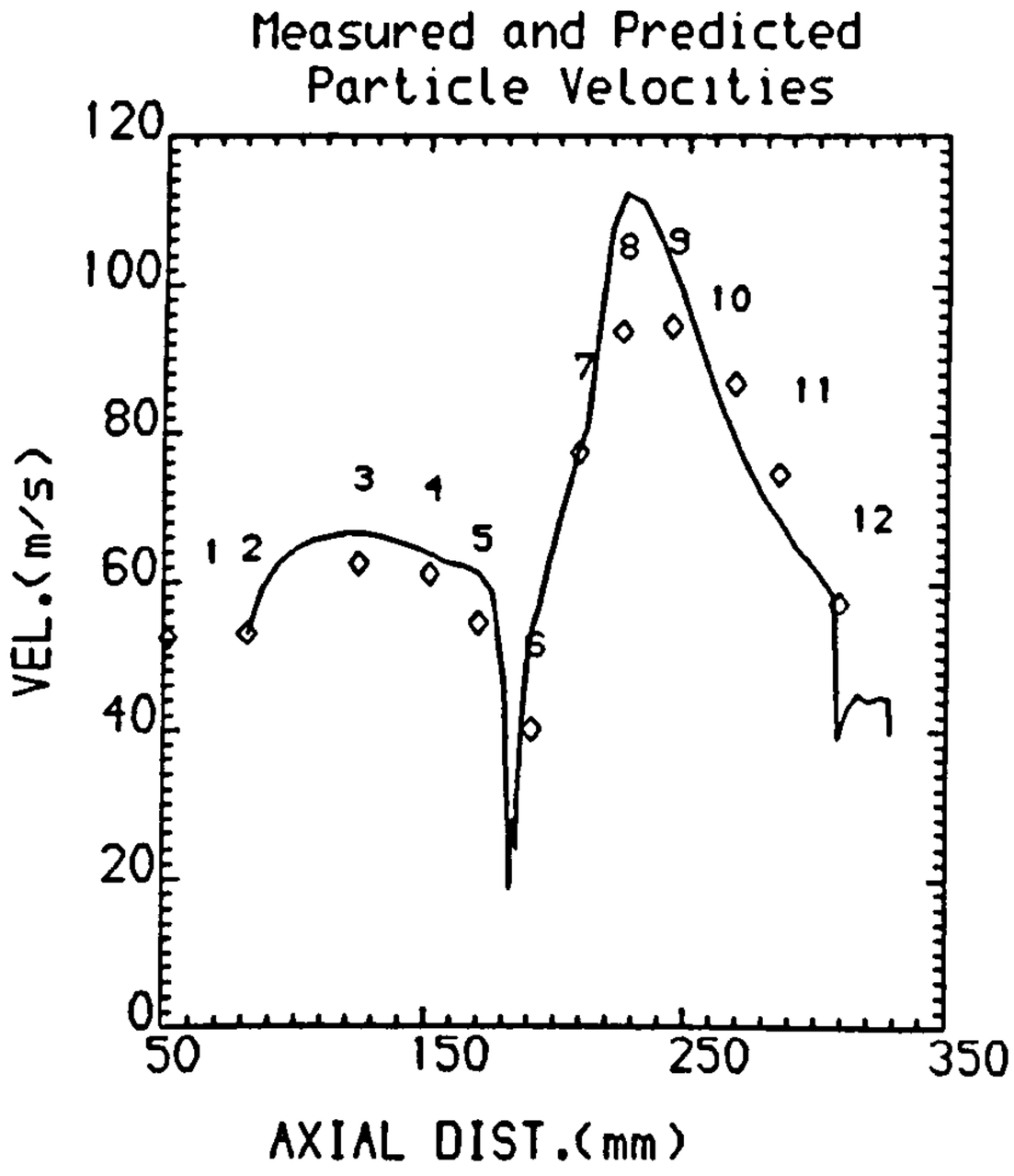

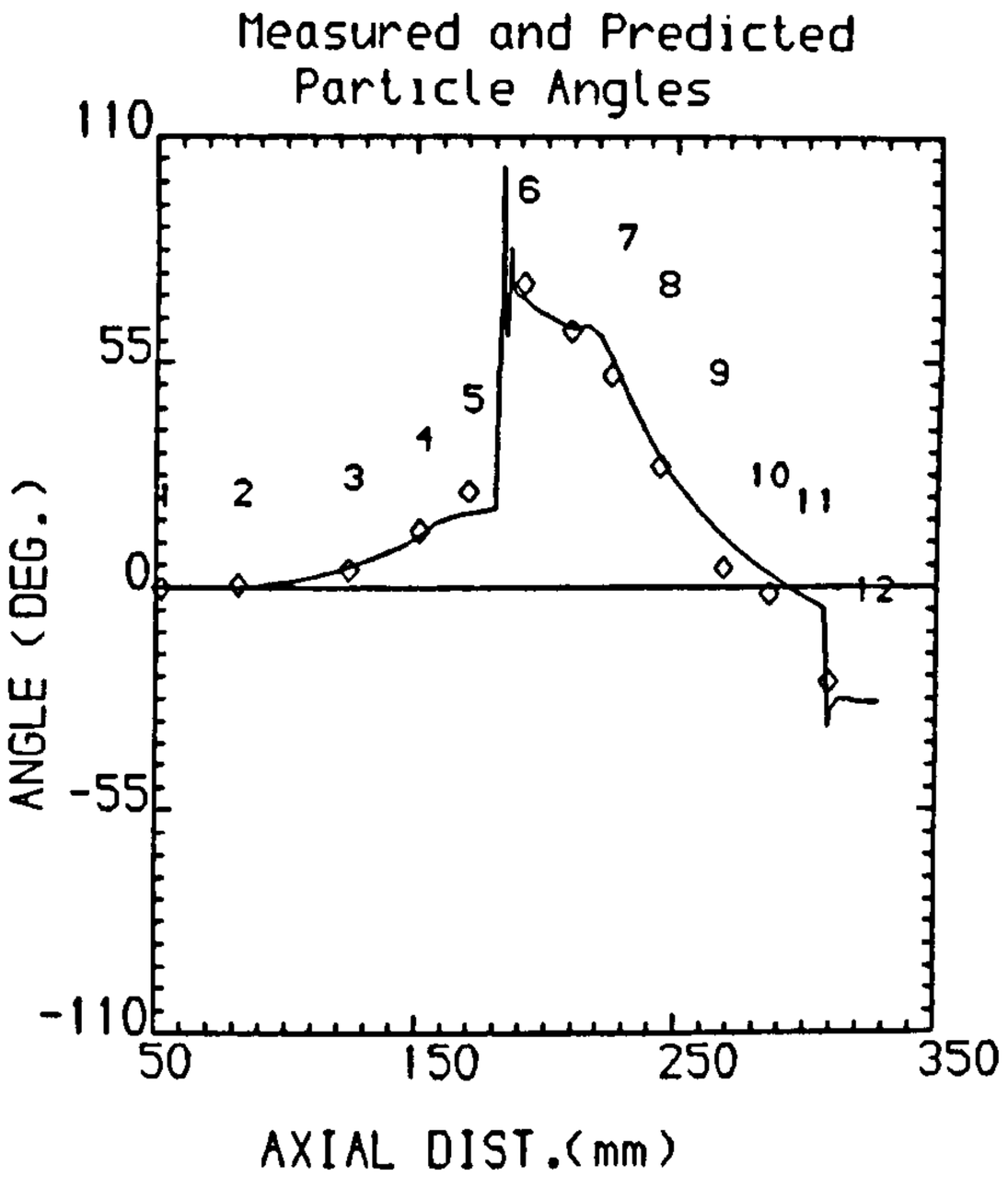

MEASURED AND PREDICTED PARTICLE TRAJECTORIES

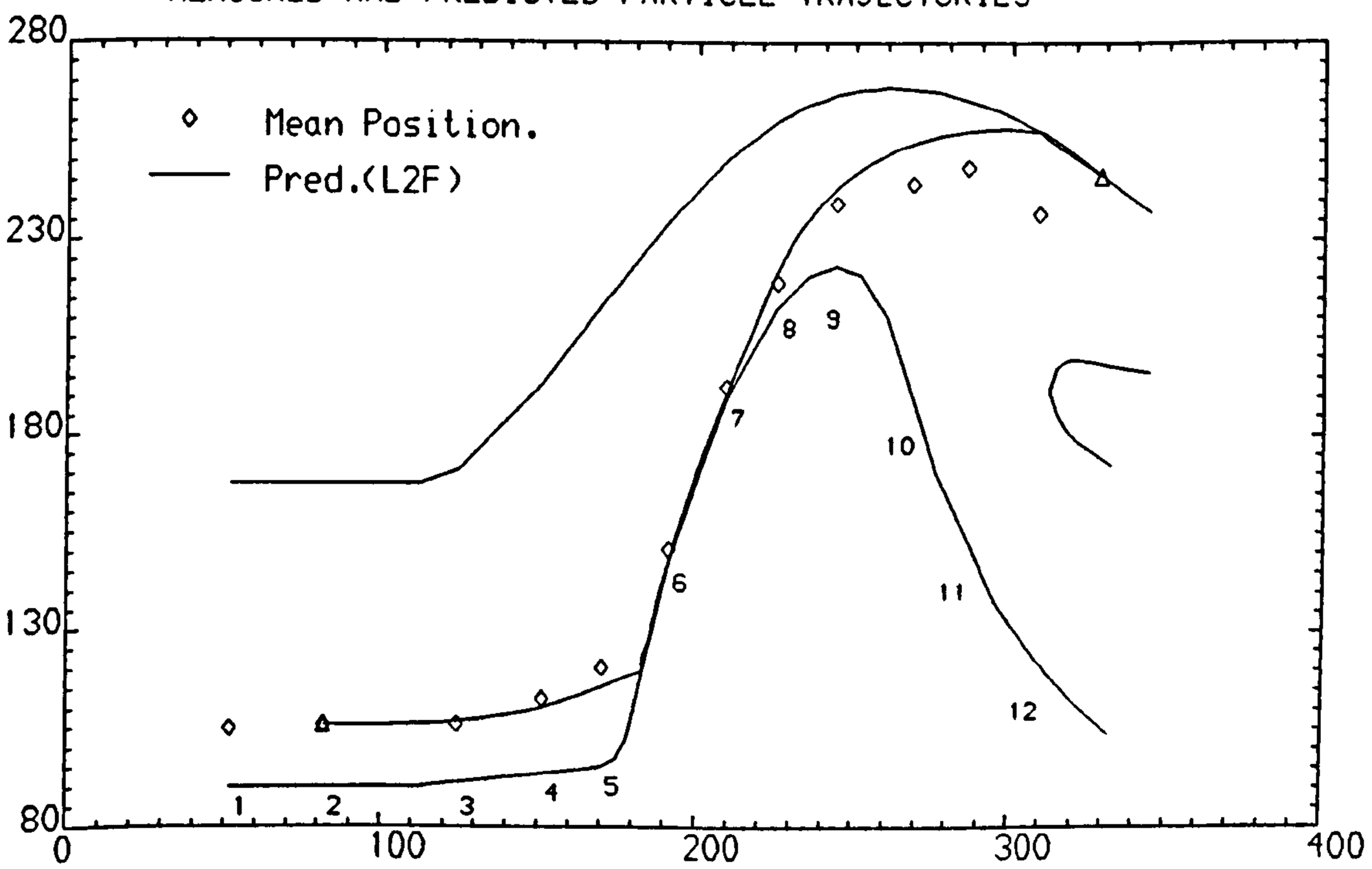

WALL MATL. = AL.
PTLE. MATL. = QUARTZ
PTLE. DEN. = 2650.0 kg/m3
PTLE. DIAMETER = 15.0 um
PTLE. INITIAL VEL.= 53.0 m/s

FIG.84 MEASURED AND PREDICTED PARTICLE VELOCITIES AND ANGLES AT THE MEAN TRAJECTORY POSITIONS

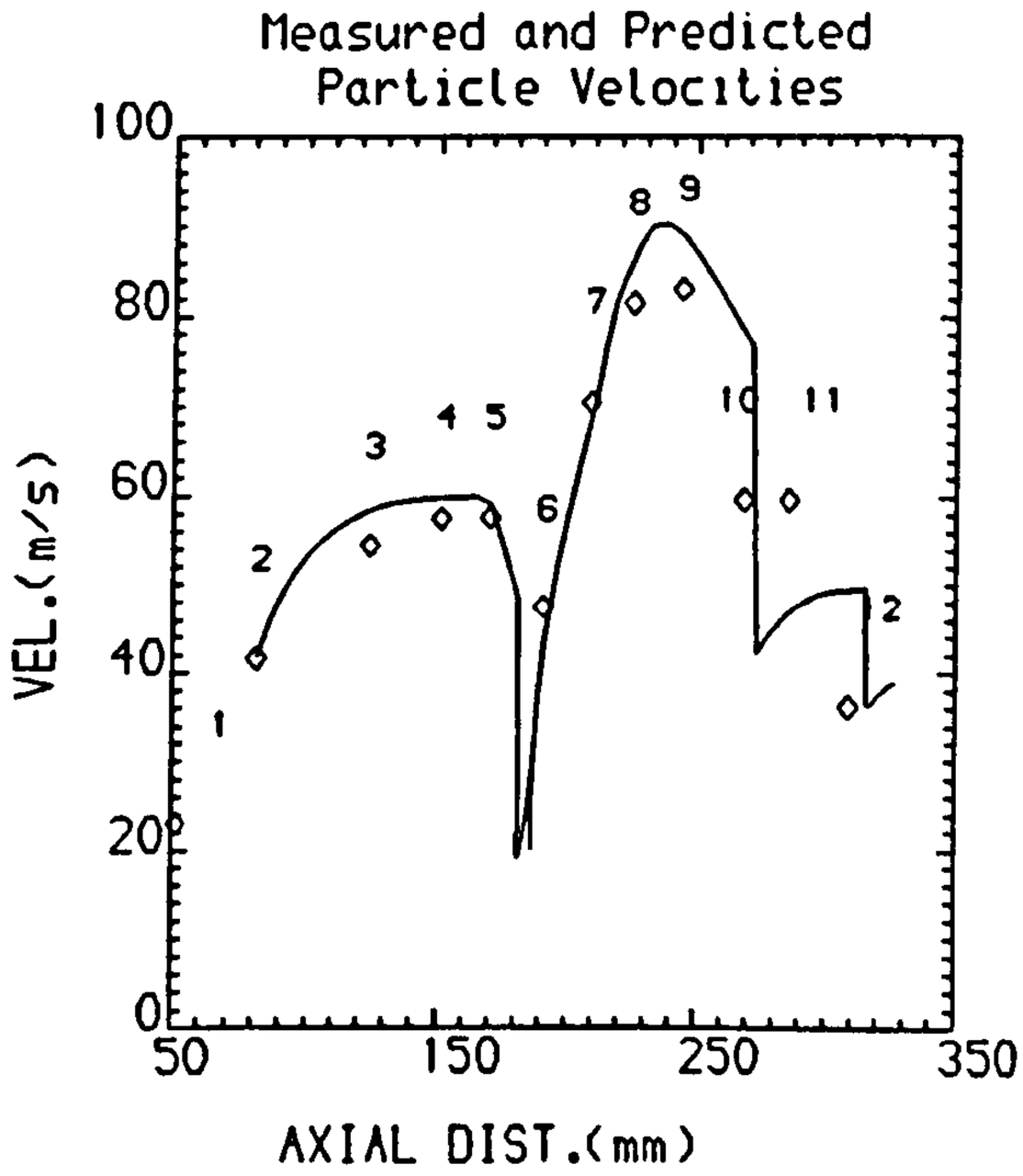

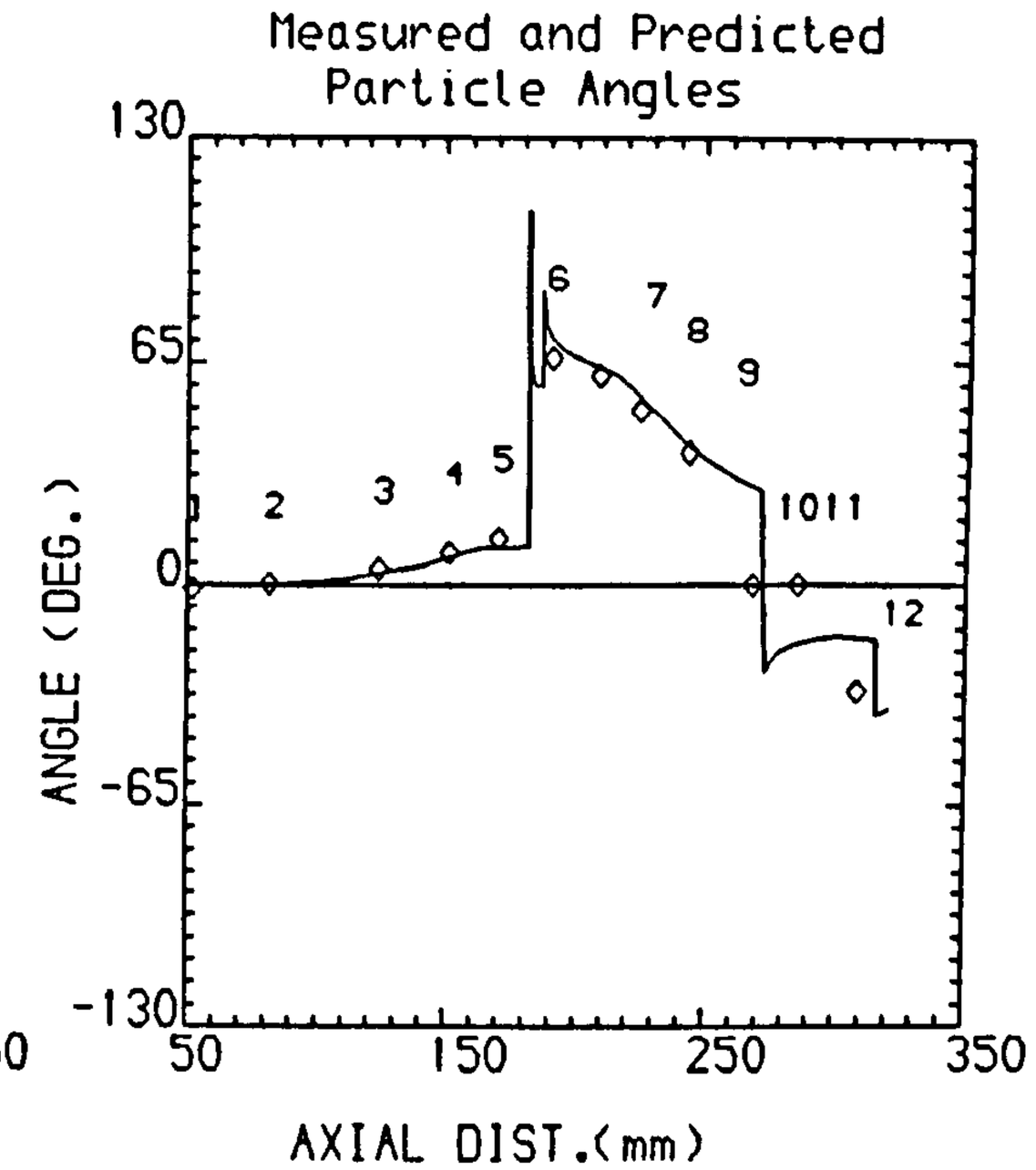

MEASURED AND PREDICTED PARTICLE TRAJECTORIES

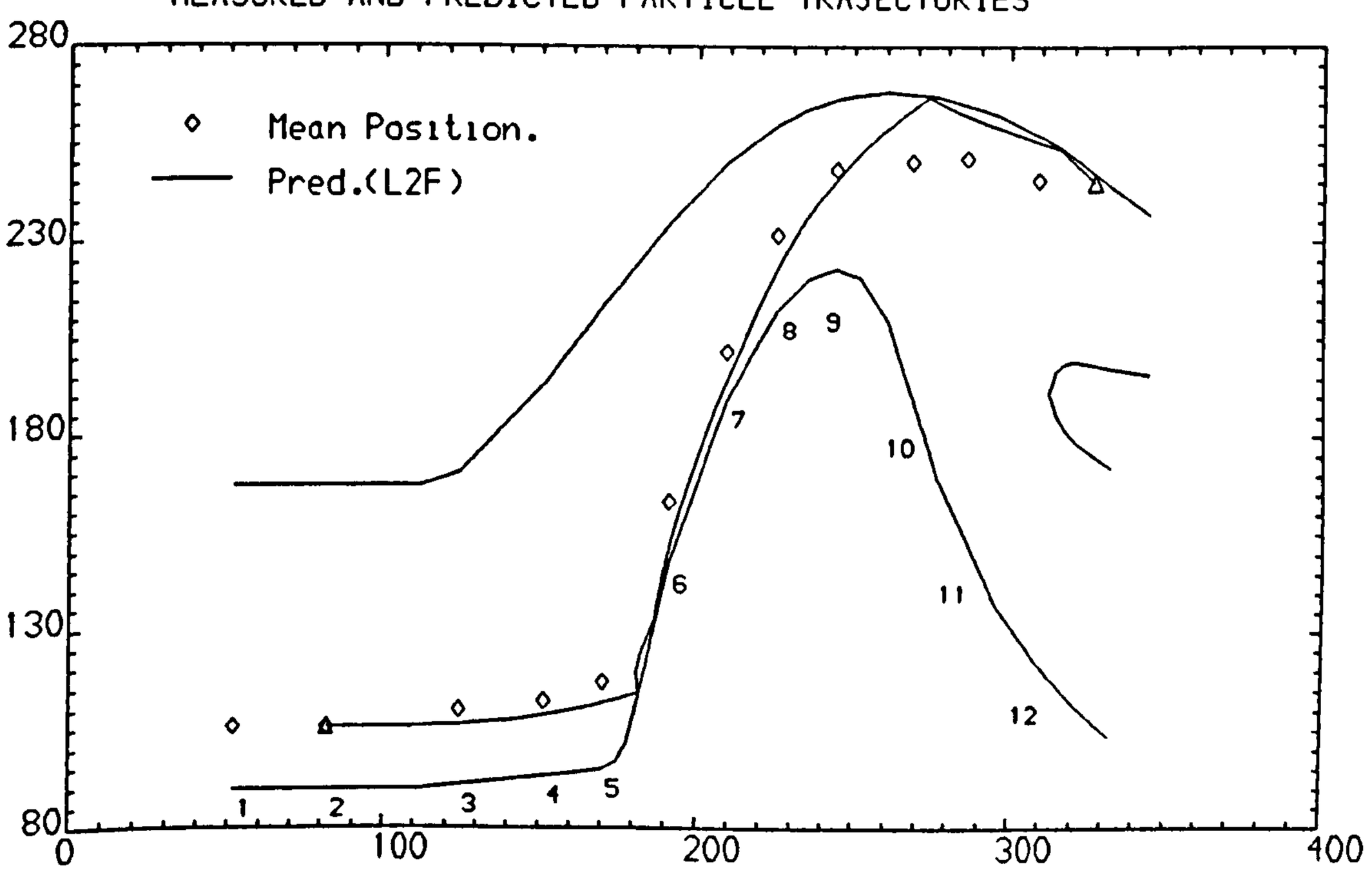

WALL MATL. = AL.
PTLE. MATL. = QUARTZ
PTLE. DEN. = 2650.0 kg/m3
PTLE. DIAMETER = 30.0 um
PTLE. INITIAL VEL.= 41.8 m/s

FIG.85 MEASURED AND PREDICTED PARTICLE VELOCITIES AND ANGLES AT THE MEAN TRAJECTORY POSITIONS

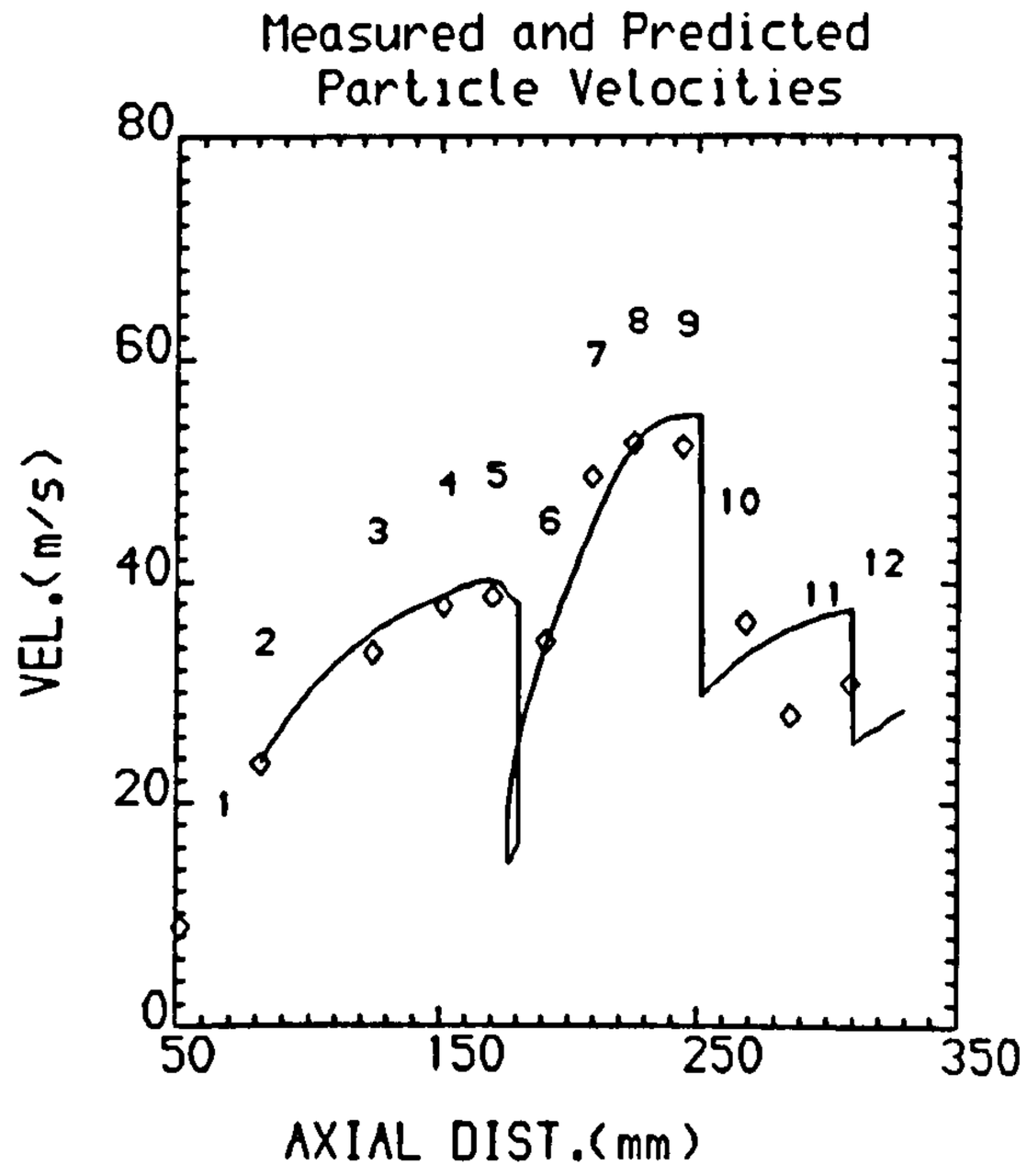

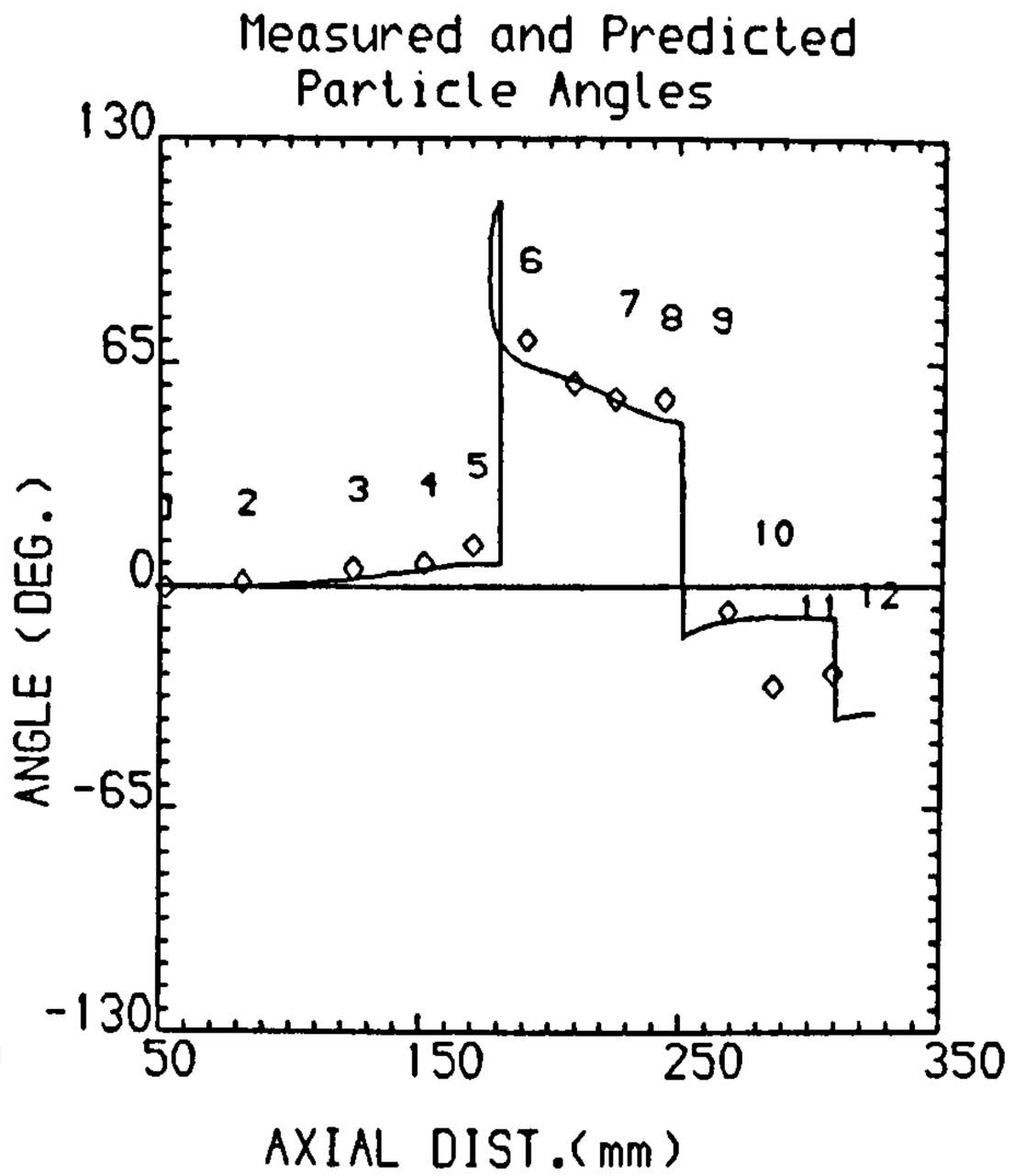

MEASURED AND PREDICTED PARTICLE TRAJECTORIES

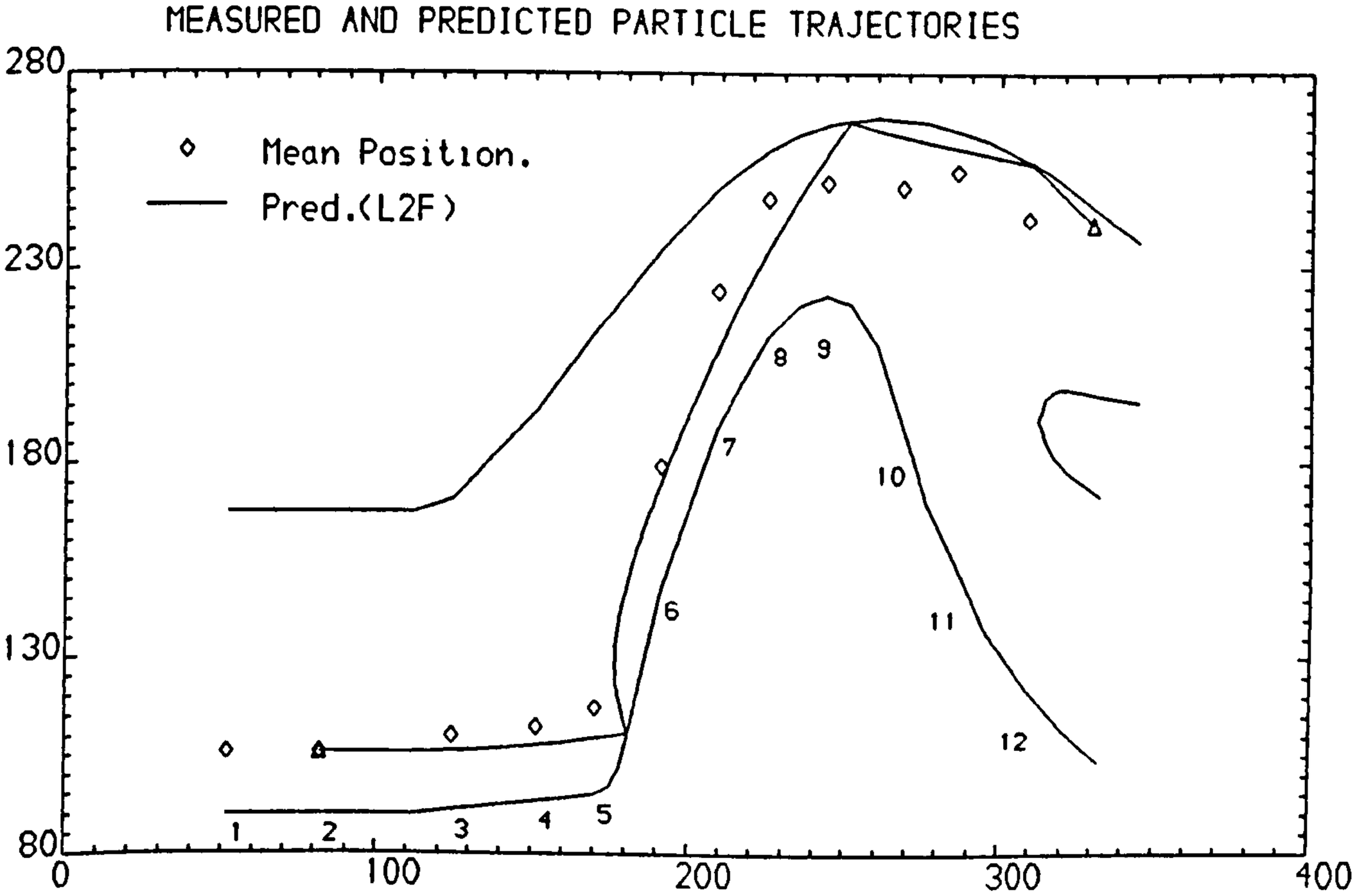

WALL MATL. = AL.

PTLE. MATL. = QUARTZ

PTLE. DEN. = 2650.0 kg/m3

PTLE. DIAMETER = 100.0 um

PTLE. INITIAL VEL.= 23.5 m/s

FIG.86 SEPARATION EFFICIENCY FOR QUARTZ AND BALLOTINI DUST

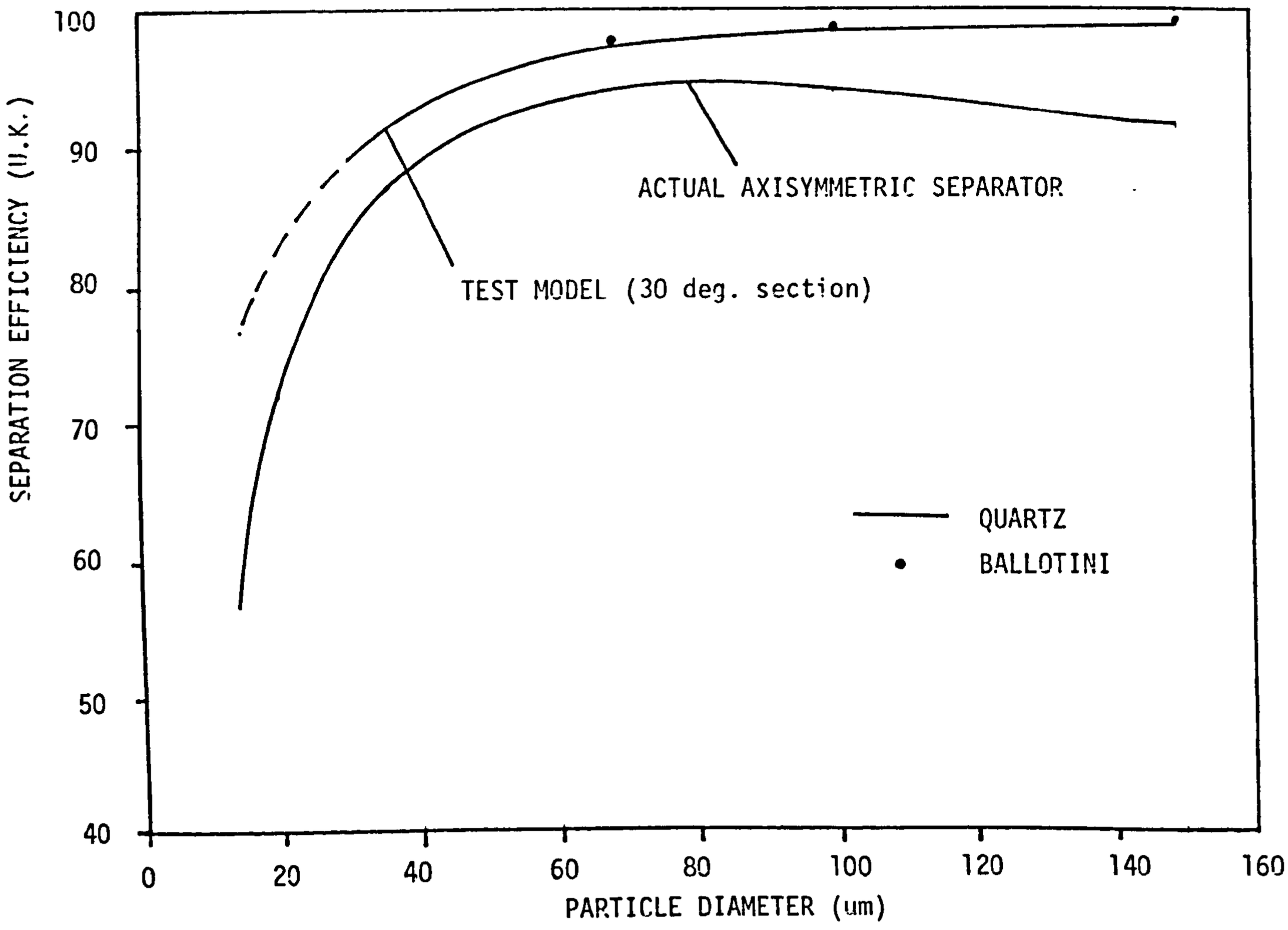

FIG.87 FLOW ABOUT A SPHERICAL PARTICLE IN A UNIFORM STREAM

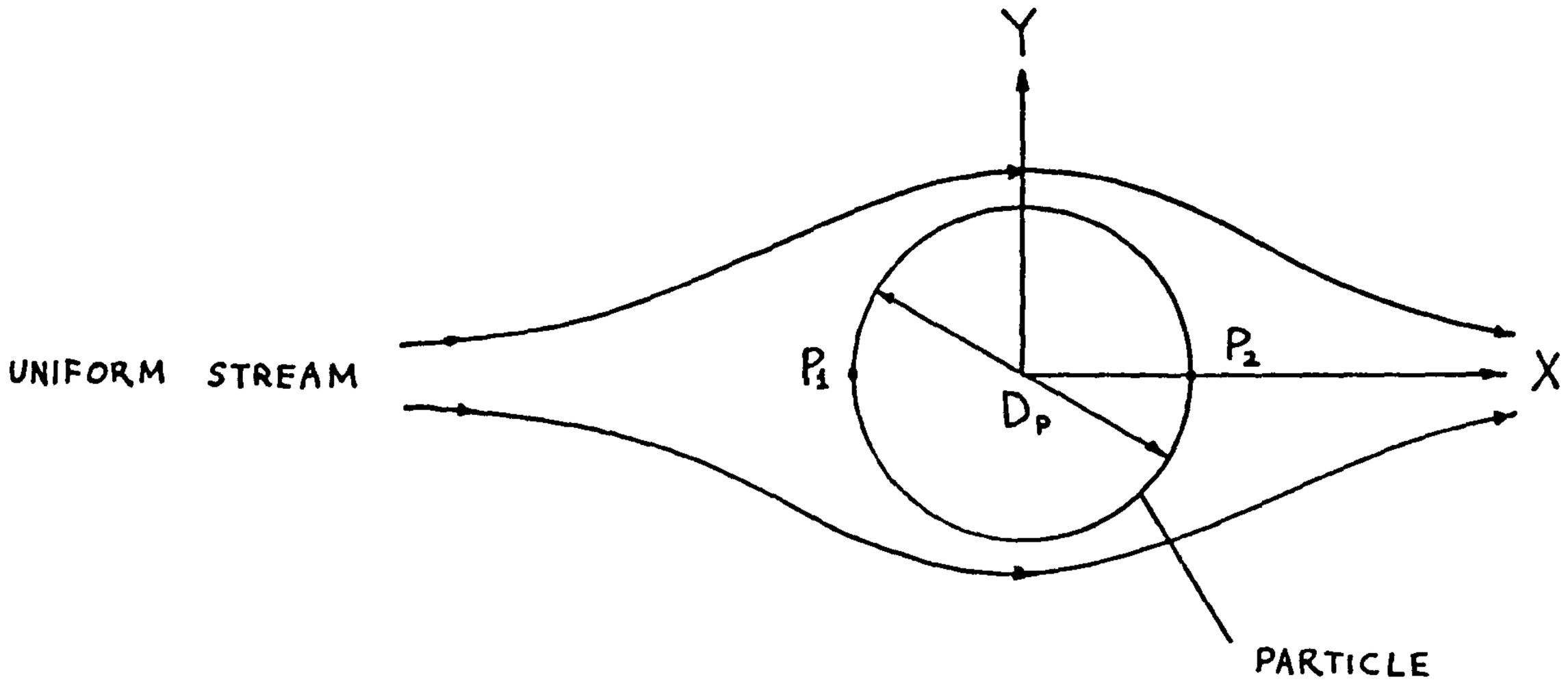

FIG 88 VECTOR NORMAL TO A SURFACE DEFINED BY Z F(X,Y)

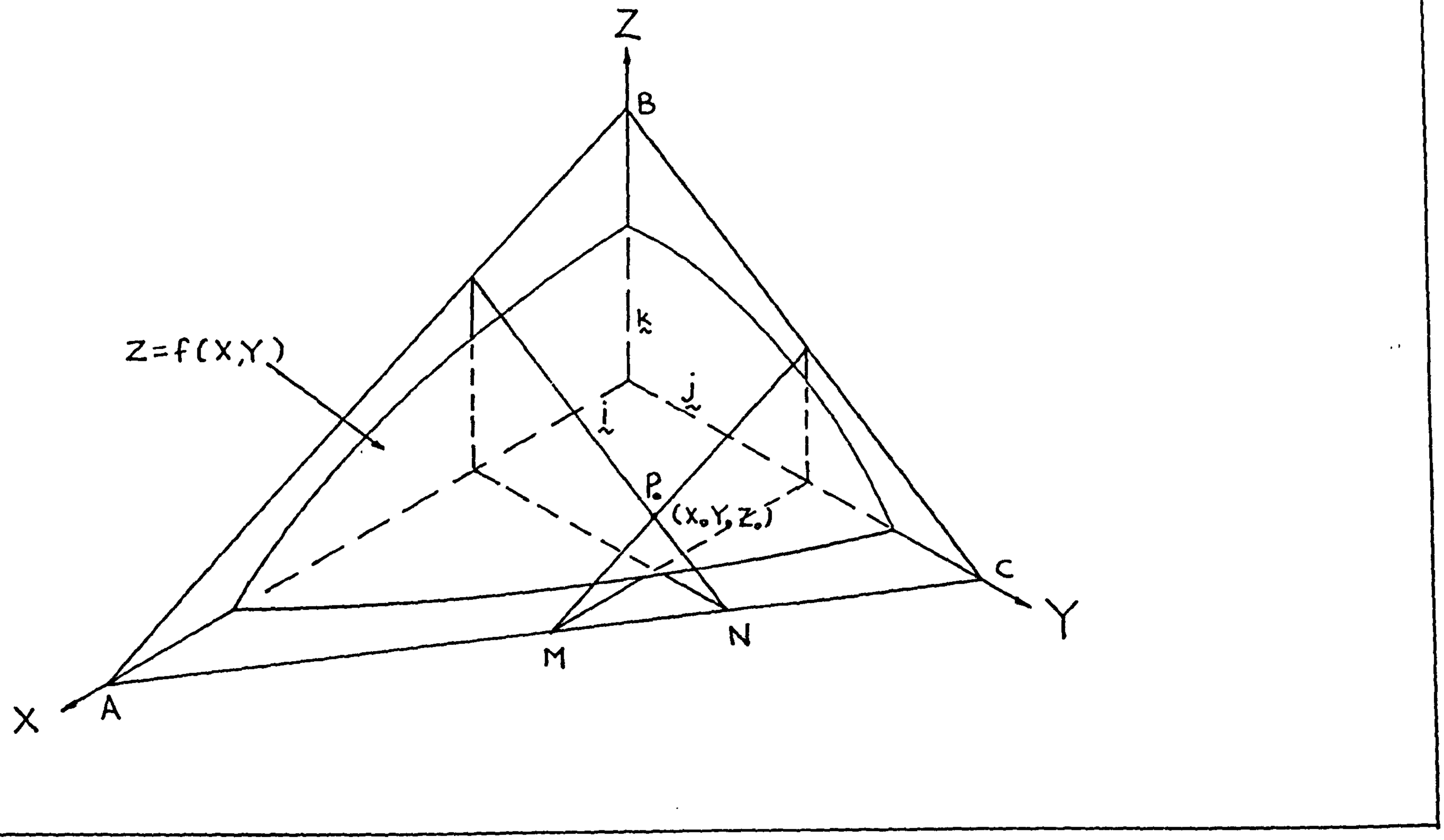

TABLE I DRAG COEFFICIENTS FOR A SPHERICAL PARTICLE

The drag coefficient equations used are

$C_d = 24{\cdot}0/R_N$ for $R_N < 0{\cdot}1$,

$C_d = 22{\cdot}73/R_N + 0{\cdot}0903/R_N^2 + 3{\cdot}69$ for $0{\cdot}1 < R_N < 1{\cdot}0$,

$C_d = 29{\cdot}1667/R_N - 3{\cdot}8889/R_N^2 + 1{\cdot}222$ for $1{\cdot}0 < R_N < 10{\cdot}0$,

$C_d = 46{\cdot}5/R_N - 116{\cdot}67/R_N^2 + 0{\cdot}6167$ for $10{\cdot}0 < R_N < 100{\cdot}0$,

$C_d = 98{\cdot}33/R_N - 2778/R_N^2 + 0{\cdot}3644$ for $100{\cdot}0 < R_N < 1000{\cdot}0$,

$C_d = 148{\cdot}62/R_N - 4{\cdot}75 \times 10^4/R_N^2 + 0{\cdot}357$ for $1000{\cdot}0 < R_N < 5000{\cdot}0$,

$C_d = -490{\cdot}546/R_N + 57{\cdot}87 \times 10^4/R_N^2 + 0{\cdot}46$ for $5000{\cdot}0 < R_N < 10000{\cdot}0$,

$C_d = -1662{\cdot}5/R_N + 5{\cdot}4167 \times 10^4/R_N^2 + 0{\cdot}5191$ for $10000{\cdot}0 < R_N < 50000{\cdot}0$.

(COURTESY OF MORSI AND ALEXANDER, REF.15)

$Re = 0 \quad C_D = 0$

$0 < Re < 1. \quad C_D = 24./Re$

$1. < Re < 400. \quad C_D = 24./Re^{0.646}$

$400 < Re < 3 \times 10^5 \quad C_D = 0.5$

$3 \times 10^5 < Re < 2 \times 10^6 \quad C_D = 3.66 \times 10^4 \times Re^{0.4275}$

$2 \times 10^6 < Re \quad C_D = 0.18$

(COURTESY OF CHUEN-YEN CHOW, REF.33)

(A) $Re < 0.01$ $\qquad C_D = 3/16 + 24/Re$

(B) $0.01 < Re \leq 20$ $\qquad \log_{10}\left[\frac{C_D Re}{24} - 1\right] = -0.881 + 0.82w - 0.05w^2$

$$\text{i.e., } C_D = \frac{24}{Re}\left[1 + 0.1315\,Re^{(0.82 - 0.05w)}\right]$$

(C) $20 \leq Re \leq 260$ $\qquad \log_{10}\left[\frac{C_D Re}{24} - 1\right] = -0.7133 + 0.6305w$

$$\text{i.e., } C_D = \frac{24}{Re}\left[1 + 0.1935\,Re^{0.6305}\right]$$

(D) $260 \leq Re \leq 1500$ $\qquad \log_{10} C_D = 1.8435 - 1.1242w + 0.1558w^2$

(E) $1.5 \times 10^3 \leq Re \leq 1.2 \times 10^4$ $\qquad \log_{10} C_D = -2.4571 + 2.5558w - 0.9295w^2 + 0.1049w^3$

(F) $1.2 \times 10^4 < Re < 4.4 \times 10^4$ $\qquad \log_{10} C_D = -1.9181 + 0.6370w - 0.0636w^2$

(G) $4.4 \times 10^4 < Re \leq 3.38 \times 10^5$ $\qquad \log_{10} C_D = -4.3390 + 1.5809w - 0.1546w^2$

(H) $3.38 \times 10^5 < Re \leq 4 \times 10^5$ $\qquad C_D = 29.78 - 5.3w$

(I) $4 \times 10^5 < Re \leq 10^6$ $\qquad C_D = 0.1w - 0.49$

(J) $10^6 < Re$ $\qquad C_D = 0.19 - 8 \times 10^4/Re$

(COURTESY OF CLIFT,R., GRACE,J.R., WEBER,M.E.)

TABLE II Coefficients of tangential and normal velocity restitution ratio

PTLE. MATL.	QUARTZ
$V_{PT2}/V_{PT1} = C_1 + C_2\beta + C_3\beta^2 + C_4\beta^3$	

TRGT. MATL.	C_1	C_2	C_3	C_4
ST. STEEL	1.0	-2.12	3.0775	-1.1
TI. ALLOY	1.0	-1.6602	2.2506	-0.76
AL. ALLOY	0.988	-1.66	2.11	-0.67

$V_{PN2}/V_{PN1} = K_1 + K_2\beta + K_3\beta^2 + K_4\beta^3$

TRGT. MATL.	K_1	K_2	K_3	K_4
ST. STEEL	1.0	-0.4159	-0.4994	0.292
TI. ALLOY	1.0	-1.1968	1.0884	-0.3995
AL. ALLOY	0.993	-1.76	1.56	-0.49

TABLE III Coefficients of Runge-Kutta-Fehlberg method of order five

	$\beta_{k\lambda}$									
k \ λ	1	2	3	4	5	6	7	α_k	c_k	$\hat{c}_k$
1	0							0	$31/384$	$7/1408$
2	$1/6$							$1/6$	0	0
3	$4/75$	$16/75$						$4/15$	$1125/2816$	$1125/2816$
4	$5/6$	$-8/3$	$5/2$					$2/3$	$9/32$	$9/32$
5	$-8/5$	$144/25$	-4	$16/25$				$4/5$	$125/768$	$125/768$
6	$361/320$	$-18/5$	$407/128$	$-11/80$	$55/128$			1	$5/66$	0
7	$-11/640$	0	$11/256$	$-11/160$	$11/256$	0		0	-	$5/66$
8	$93/640$	$-18/5$	$803/256$	$-11/160$	$99/256$	0	1	1	-	$5/66$

TABLE IV Local coordinates of a 20 - node element

NODE	ξ	η	ζ
1	1	-1	-1
2	0	-1	-1
3	-1	-1	-1
4	-1	0	-1
5	-1	1	-1
6	0	1	-1
7	1	1	-1
8	1	0	-1
9	1	-1	0
10	-1	-1	0
11	-1	1	0
12	1	1	0
13	1	-1	1
14	0	-1	1
15	-1	-1	1
16	-1	0	1
17	-1	1	1
18	0	1	1
19	1	1	1
20	1	0	1

TABLE V Dust Feedrate And Concentration for Ballotini and Quartz Particles

PARTICLE MATERIAL	BALLOTINI				QUARTZ			
PARTICLE SIZE (um)	38-53	53-65	91-107	145-162	30.0	60.0	100.0	150.0
PARTICLE FEEDRATE (g/s)	0.106	0.106	0.146	0.158	0.100	0.196	0.190	0.233
PARTICLE CONCENTRATION (g/m3)	0 228	0.228	0.314	0.340	0.216	0.421	0.409	0.480

TABLE VI Mass Flowrate And Discharge Coefficient

TRAVERSE STATIONS (D)	PIPE	ENGINE	SCAVENGE	ENGINE	SCAVENGE
	TEST NO.	A	B	C	D
-	WALL STATIC	8.4 in.Wg	4.3 in.Wg	13.5 in.Wg	12.3 in.Wg
0.026	h1 in.Wg	0.32	0.50	0.65	0.83
0.082	h2 "	0.43	0.64	0.96	1.27
0.146	h3 "	0.49	0.73	1.10	1.51
0.226	h4 "	0.54	0.78	1.20	1.68
0.342	h5 "	0.55	0.91	1.25	1.82
0.658	h6 "	0.55	0.92	1.25	1.81
0.774	h7 "	0.54	0.84	1.24	1.68
0.854	h8 "	0.49	0.74	1.15	1.51
0.918	h9 "	0.43	0.62	0.99	1.29
0.974	h10 "	0.32	0.46	0.66	0.94
-	h	4.66	7.14	10.45	14.34
-	h 6.796	6.796	8.400	10.159	11.888
-	Vmax/Vmean	1.09	1.16	1.10	1.16

TEST NO.	A	B	C	D
MASS FLOWRATE (lb/s)	0.654	0.207	0.958	0.291
DISCHARGE COEFF.	0.89	0.86	0.89	0.86

TABLE VII Separation Efficiency for Ballotini and Quartz Particles

PARTICLE MATERIAL	BALLOTINI			QUARTZ			
PARTICLE SIZE (um)	53-65	91-107	145-162	30.0	60.0	100.0	150.0
TOTAL WT. OF DUST USED (g)	751.0	842.9	1355.8	751.1	752.2	756.6	753.5
WT. OF SCAVENGE BAG BEFORE TEST (g)	215.0	219.0	220.0	218.0	215.4	215.0	214.4
WT. OF SCAVENGE BAG AFTER TEST (g)	942.3	1049.5	1565.4	874.4	930.8	957.5	959.0
WT. OF DUST IN SCAVENGE BAG (SEPARATED)	727.3	830.5	1345.4	656.4	715.4	742.5	744.6
WT. OF ENGINE BAG BEFORE TEST (g)	217.3	217.5	221.3	215.0	216.6	217.5	216.1
WT. OF ENGINE BAG AFTER TEST (g)	228.0	227.5	225.0	279.9	237.3	227.0	222.6
WT. OF DUST IN ENGINE BAG (INGESTED)	10.7	10.0	3.7	64.9	20.7	9.5	6.5
TOTAL WT. OF DUST COLLECTED (g)	738.0	840.5	1349.1	721.3	736.1	752.0	751.1
SEPARATION EFFICIENCY (BY WT.,U.S.A.)	96.8%	98.5%	99.2%	87.4%	95.1%	98.1%	98.8%
SEPARATION EFFICIENCY (U.K.)	98.3%	98.6%	99.7%	89.2%	96.6%	98.5%	98.9%

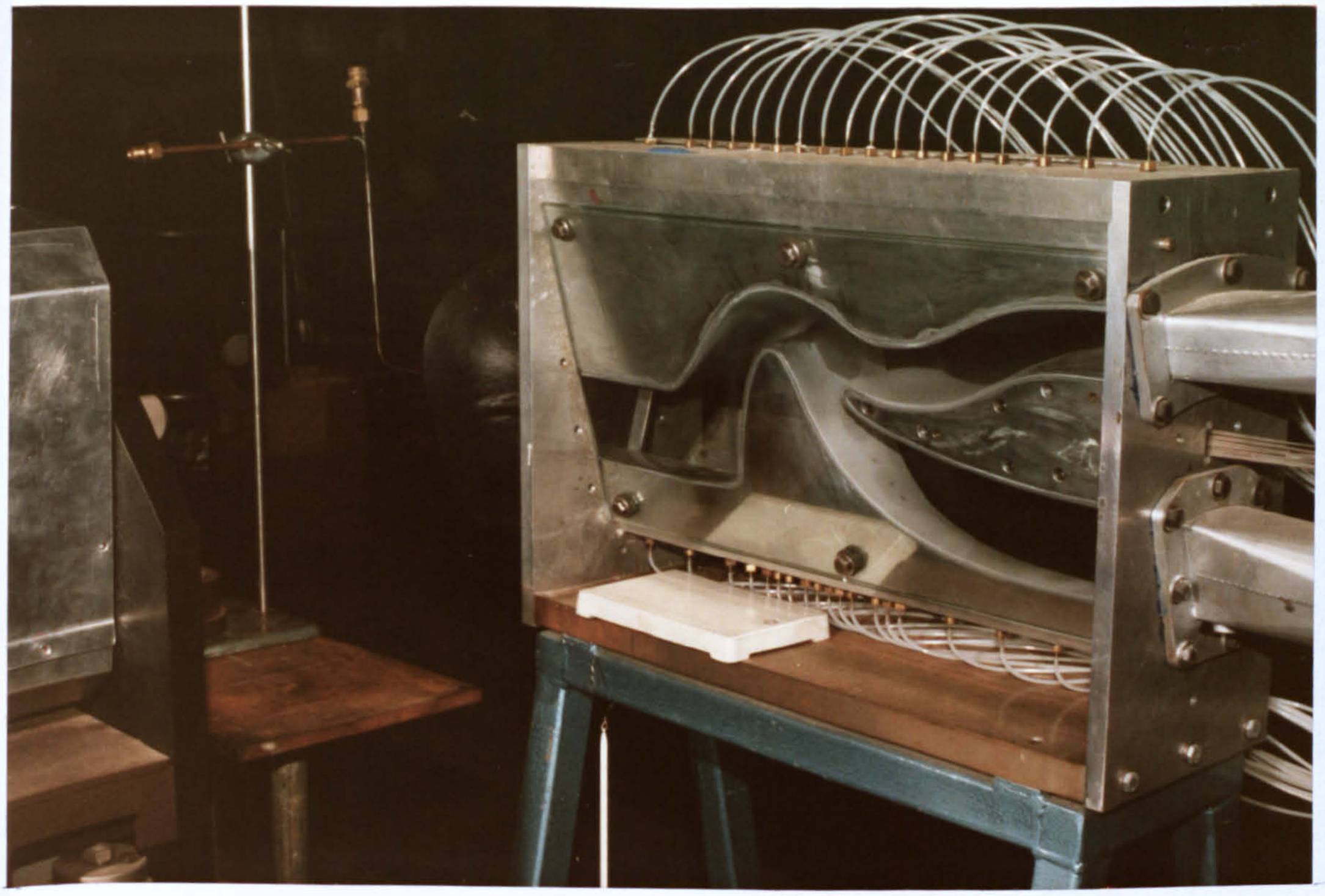

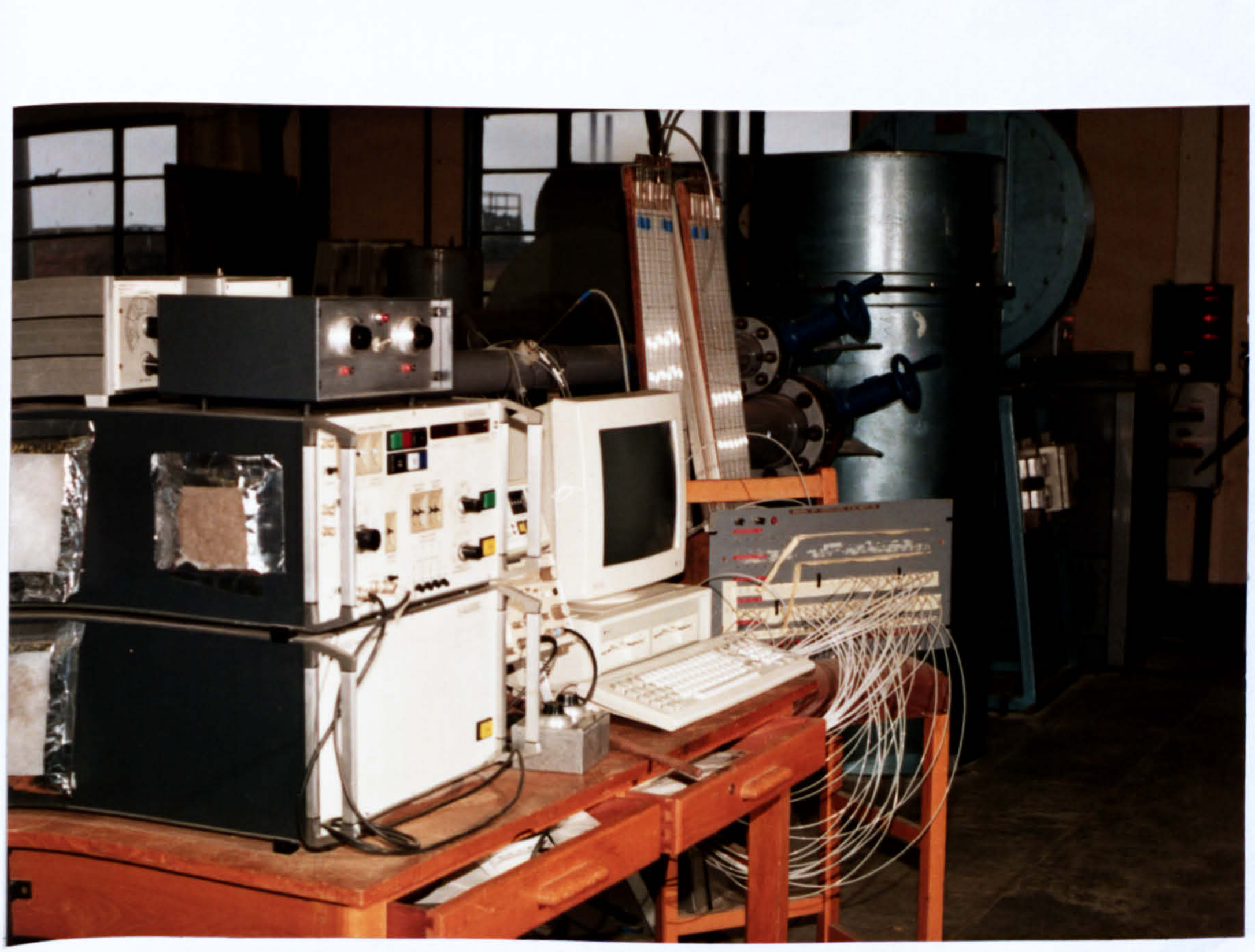

PLATE 1 EXPERIMENTAL SET-UP

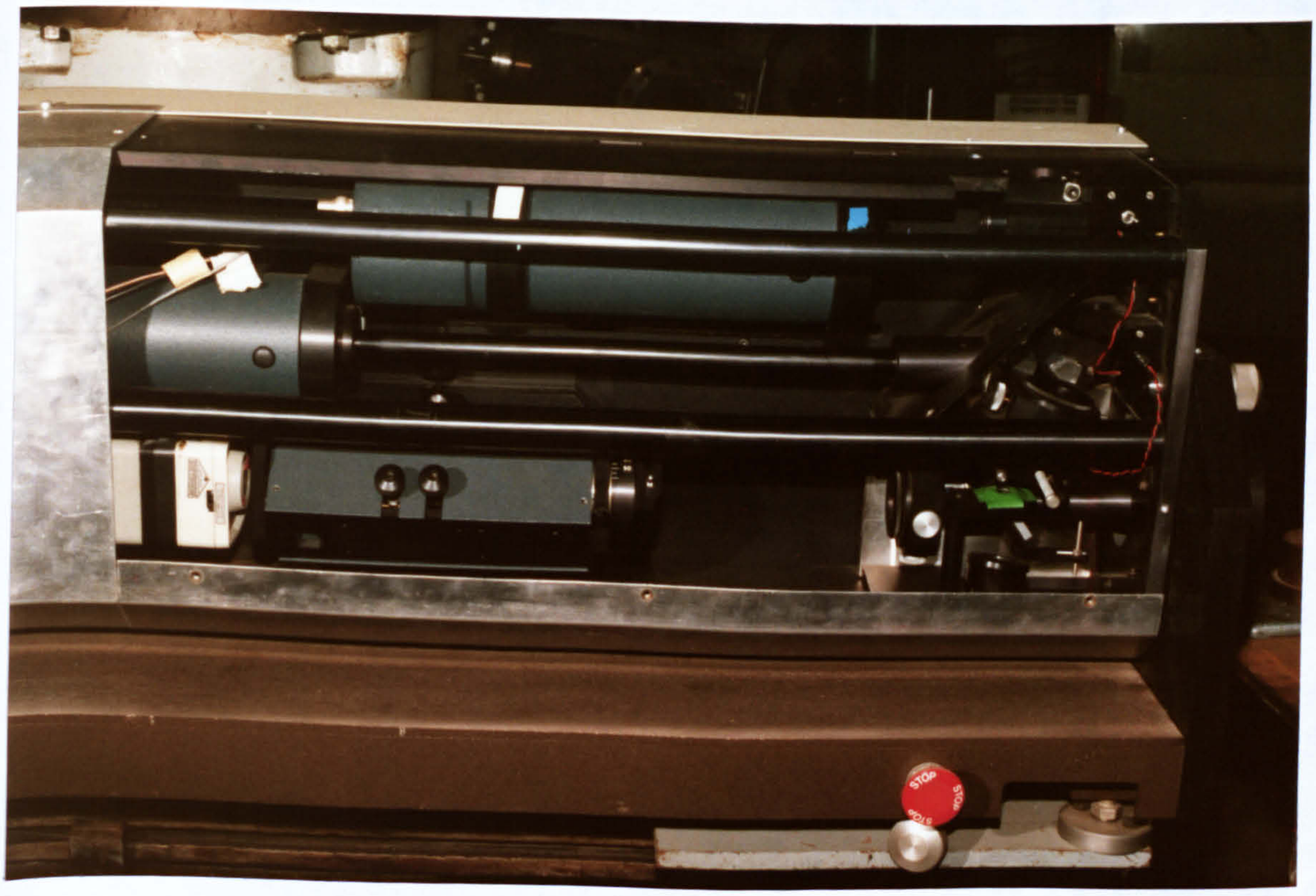

PLATE 2 LASER ANEMOMETER (L2F)

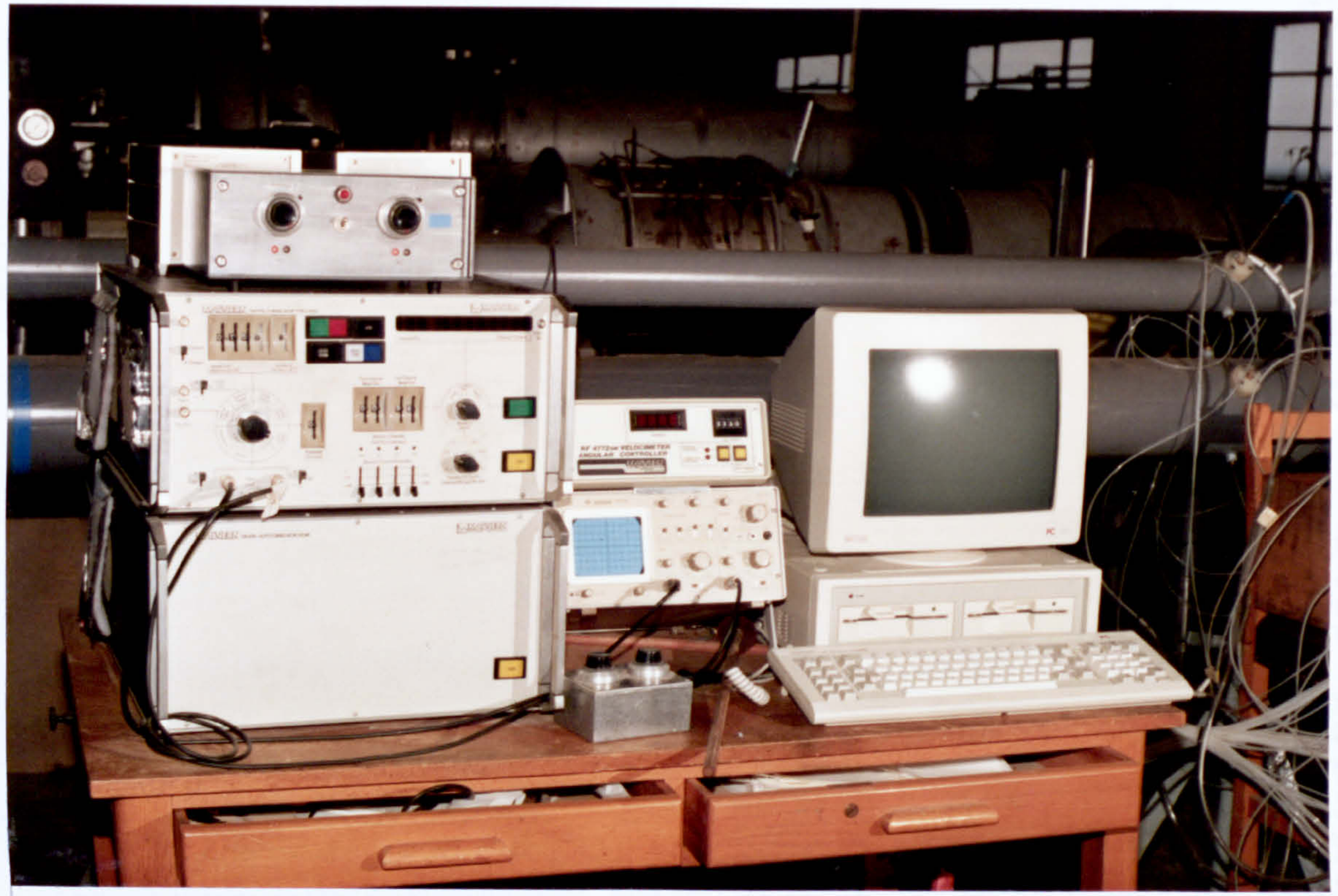

PLATE 3 DATA ACQUISITION SYSTEM

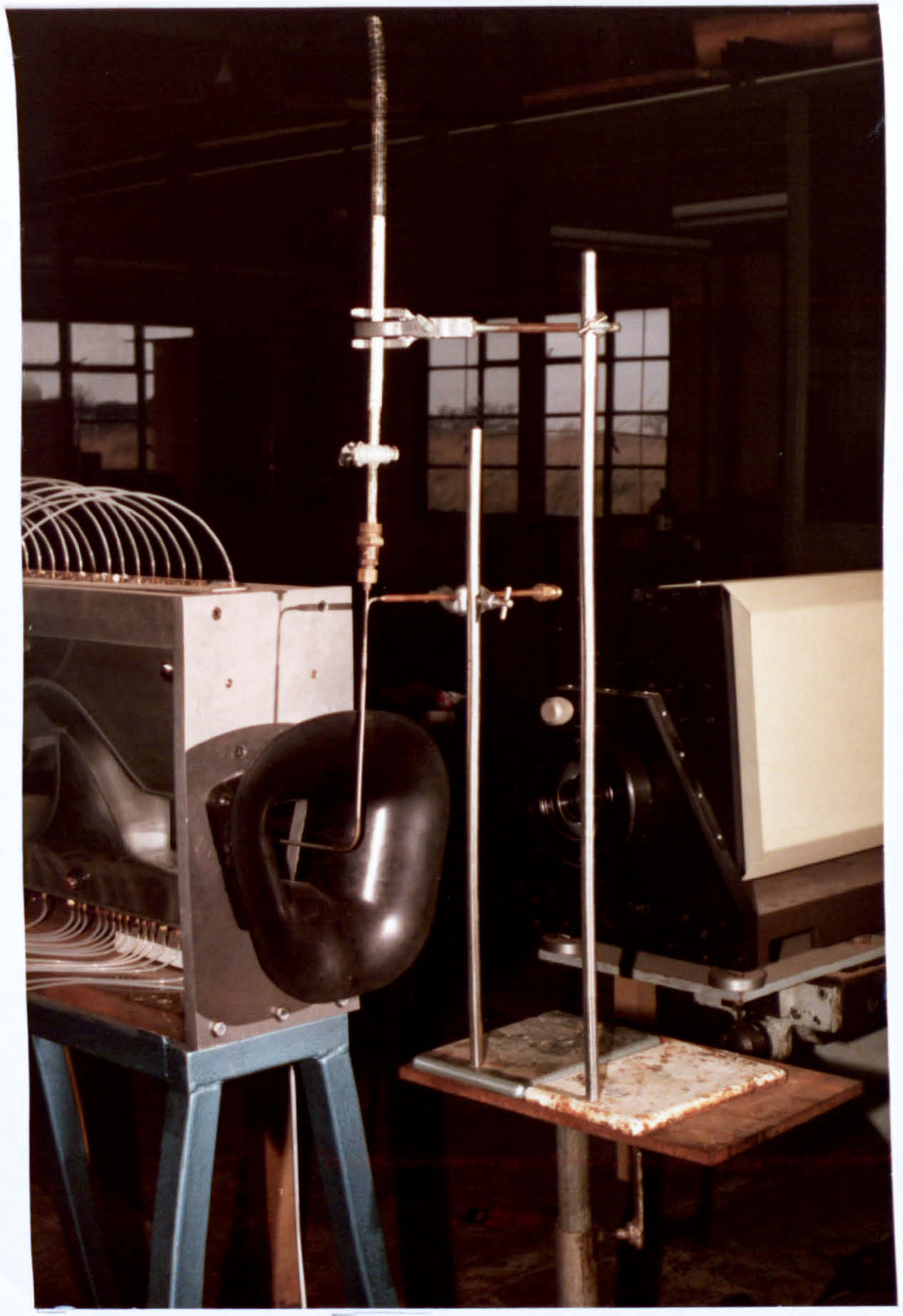

PLATE 4 DUST FEEDER NOZZLE WITH A 10 ml BURETTE

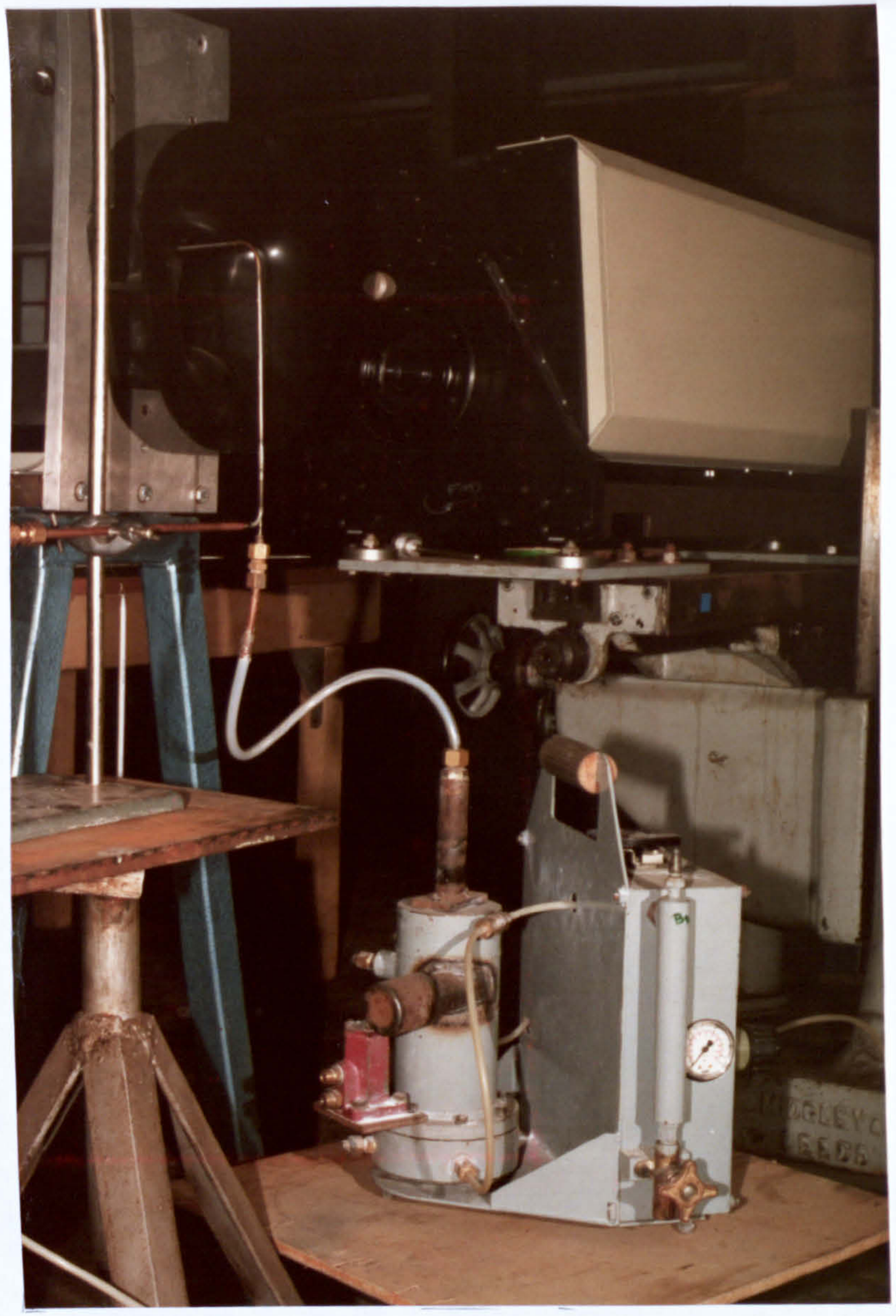

PLATE 5 DUST FEEDER NOZZLE WITH A PRESSURISED FLUIDISED BED

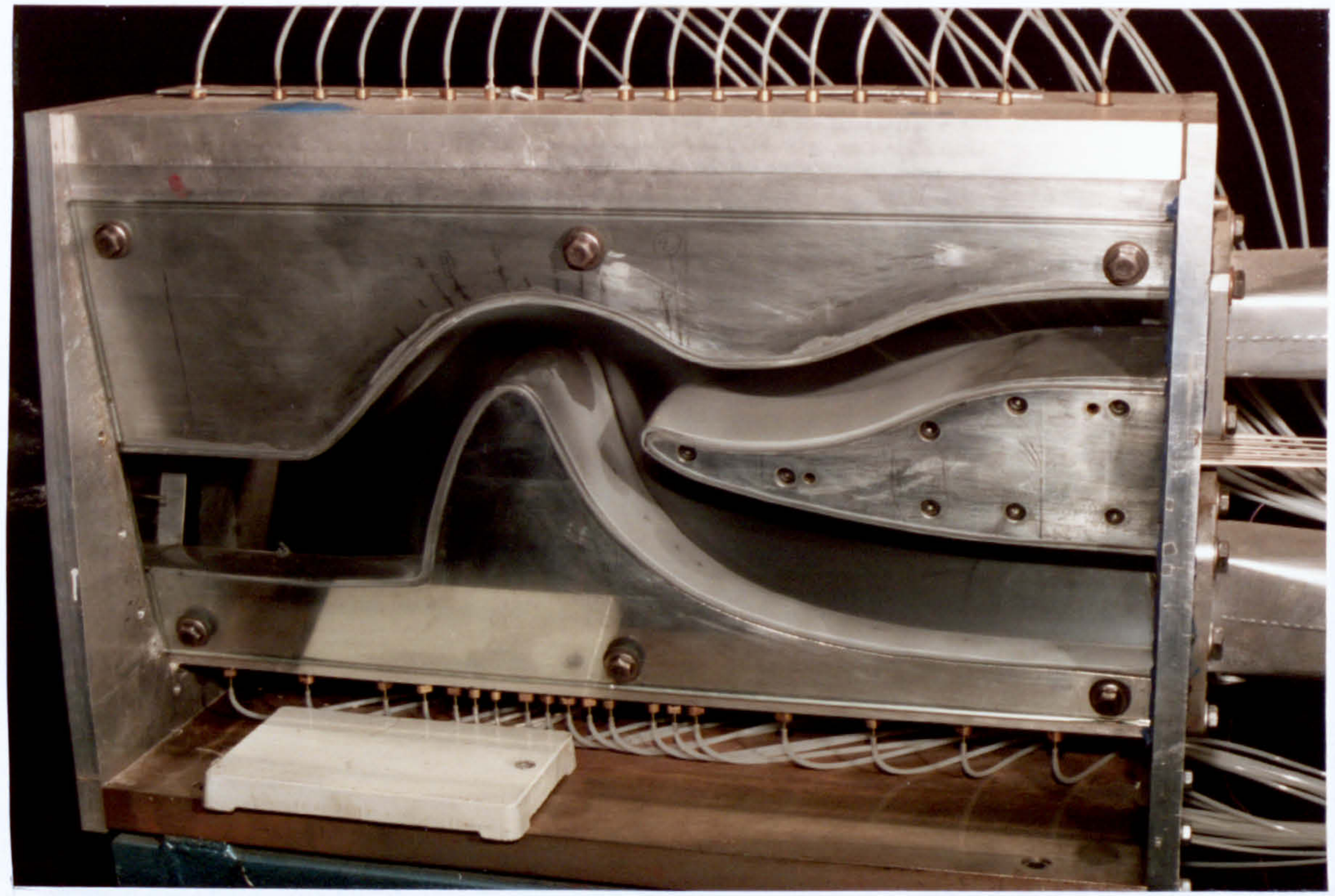

PLATE 6 TEST SECTION OF THE SEPARATOR

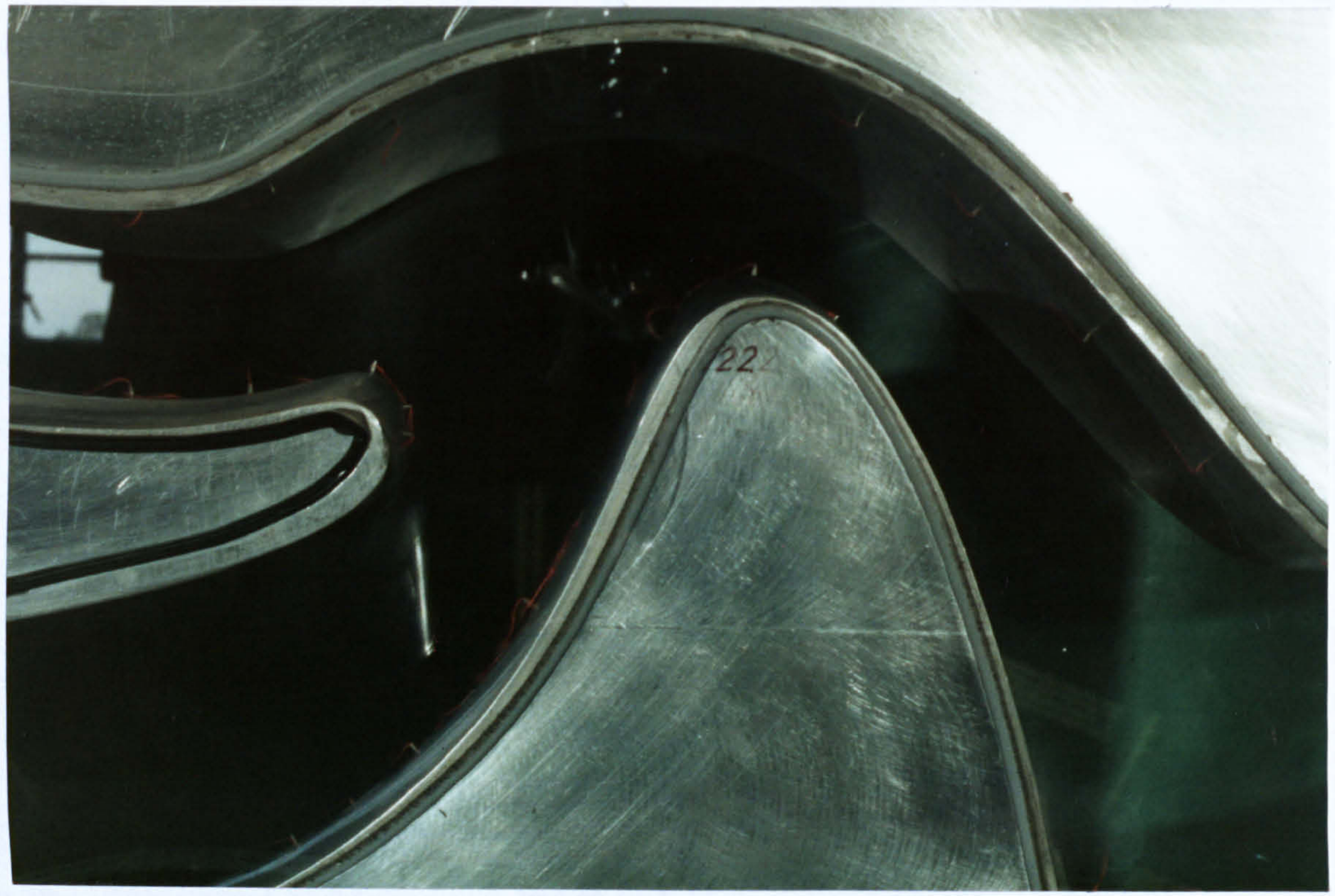

PLATE 7 OVERALL VIEW OF THE NEAR-WALL FLOW CONDITION

PLATE 8 VORTEX RE-CIRCULATION AT THE HUB SURFACE

PLATE 9 SEPARATION 'BUBBLE' AT THE HUB SURFACE

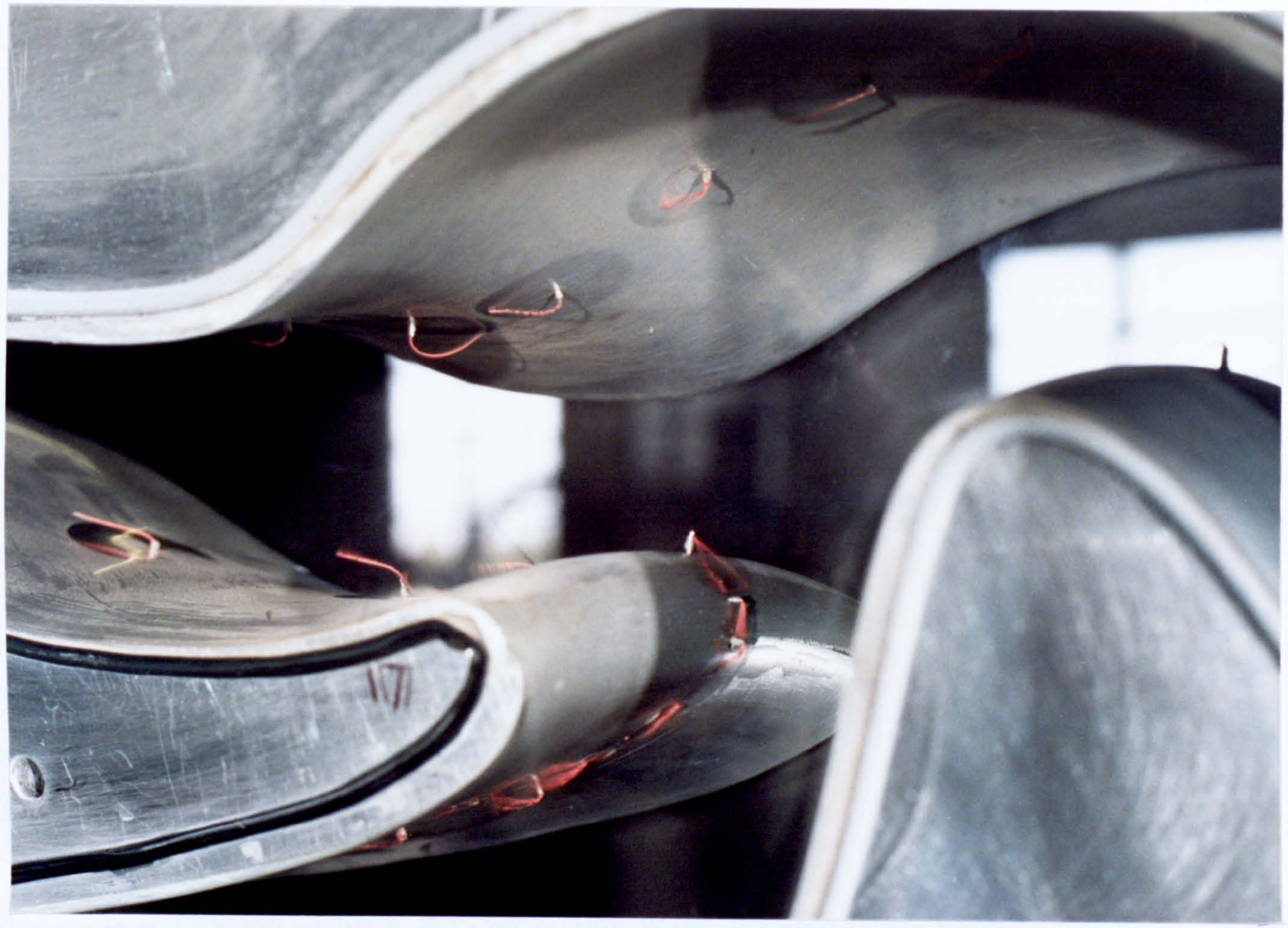

PLATE 11 FLOW ON THE UNDERSIDE OF THE SPLITTER LIP

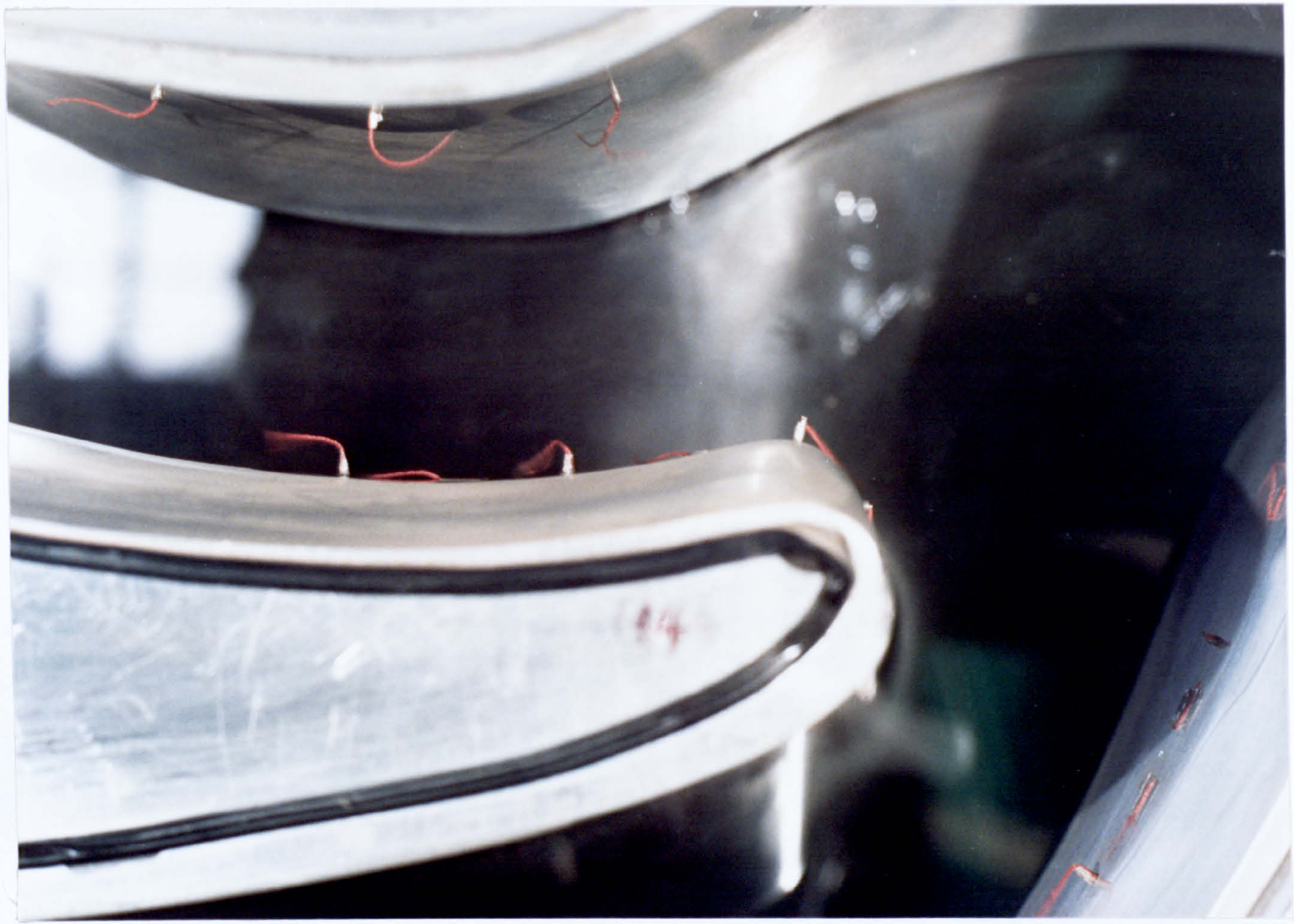

PLATE 12 STAGNATION REGION ON THE UPPERSIDE OF THE SPLITTER LIP

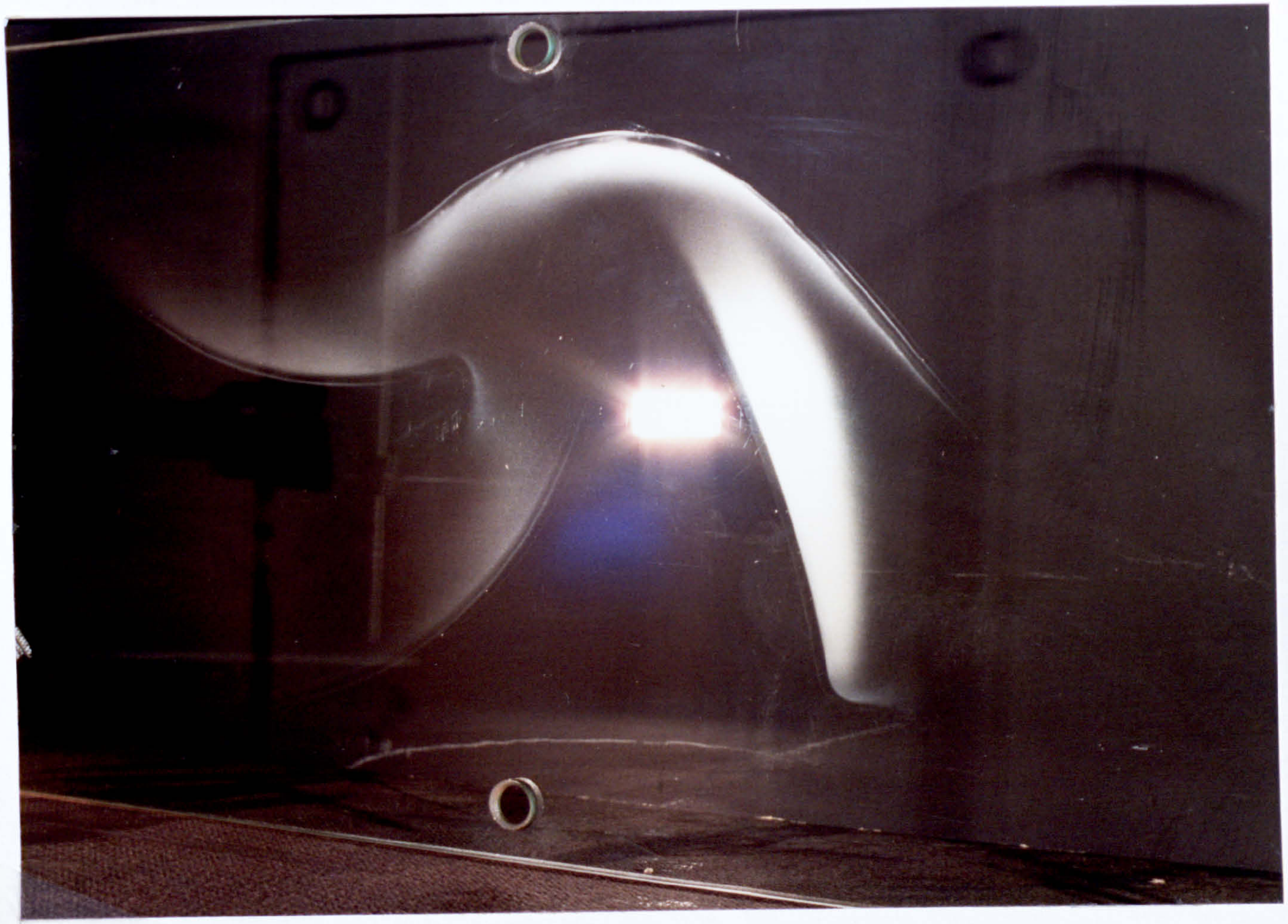

PLATE 13 EROSION PATTERN ON GLASS PLATE